Horse hunters of ancient Germany *p. 1080*

Tracing the impact that made the Moon *p. 1146*

Ruminating on the sheep genome *p. 1168*

Science

$10
6 JUNE 2014
sciencemag.org

AAAS

Rethinking the global supply chain

Smarter, cheaper, greener ways to deliver the world's goods *p. 1100*

CONTENTS

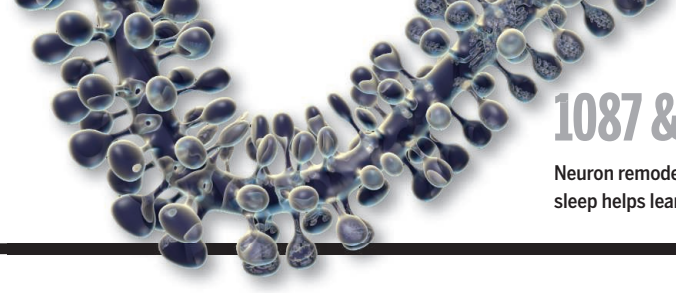

1087 & 1173
Neuron remodeling during sleep helps learning

6 JUNE 2014 • VOLUME 344 • ISSUE 6188

NEWS

IN BRIEF

IN DEPTH

FEATURES

SPECIAL SECTION

The global supply chain

Hong Kong staging dock
Photo: © Victor Fraile/Corbis

INSIGHTS

PERSPECTIVES

Published by AAAS

CONTENTS

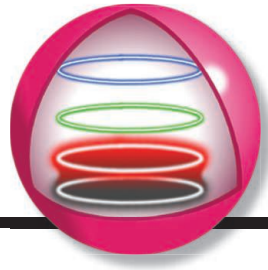

1135
An electric field manipulates terbium nuclear spin

6 JUNE 2014 • VOLUME 344 • ISSUE 6188

SCIENCE (ISSN 0036-8075) is published weekly on Friday, except the last week in December, by the American Association for the Advancement of Science, 1200 New York Avenue, NW, Washington, DC 20005. Periodicals mail postage (publication No. 484460) paid at Washington, DC, and additional mailing offices. Domestic individual membership and subscription (51 issues): $153 ($74 allocated to subscription). Domestic institutional subscription (51 issues): $1282; Foreign postage extra: Mexico, Caribbean (surface mail) $55; other countries (air assist delivery) $85. First class, airmail, student, and emeritus rates on request. Canadian rates with GST available upon request, GST #1254 88122. Publications Mail Agreement Number 1069624. **Printed in the U.S.A.**
Change of address: Allow 4 weeks, giving old and new addresses and 8-digit account number. **Postmaster:** Send change of address to AAAS, P.O. Box 96178, Washington, DC 20090–6178. **Single-copy sales:** $10.00 current issue, $15.00 back issue prepaid includes surface postage; bulk rates on request.

Published by AAAS

Science
AAAS
1200 New York Avenue, NW, Washington, DC 20005
Bateman House, 82-88 Hills Road, Cambridge, UK CB2 1LQ

INFORMATION FOR AUTHORS See pages 680 and 681 of the 7 February 2014 issue or access www.sciencemag.org/about/authors

Published by AAAS

EDITORIAL

Science diplomacy with Cuba

Over a century ago, interactions between a Cuban scientist, Carlos Finlay, and a U.S. scientist, Jesse Lazear, led to an understanding of the role of the mosquito in transmitting yellow fever and to the development of effective countermeasures. Today, new infectious diseases confront both Cuba and the United States, but a longstanding diplomatic breach between the two nations now makes such valuable joint research more complicated, if not impossible. It is time for both governments to reconsider the rules that stand in the way of scientific collaboration, before a potentially deadly outbreak spreads through both countries and beyond. In particular, the U.S. government can make a relatively straightforward change to rules that would make collaboration much easier.

The official relationship between Cuba and the United States has been frozen for over half a century, restricting scientific cooperation in many fields. However, a lack of collaboration in the public health arena poses special concerns. Cuba is only 90 miles from the United States and is the destination of over half a million U.S. citizens, many of whom are visiting relatives. Such interactions are welcome and important, but they also provide an avenue for the unintentional spread of infectious diseases. Well-known tropical diseases, such as dengue fever, and newly emerging threats, such as chikungunya, are now spreading at an alarming rate in the Caribbean and pose serious threats to both travelers and residents alike. There are already reports of these diseases in the United States. Currently, no commercial vaccines or drugs are available for treating either dread disease.

Working together more closely would allow scientists from Cuba and the United States to better share data, identify and monitor outbreaks of infectious disease, and develop more coherent responses. However, limited communication capacities, combined with regulations that make scientific meetings difficult, complicate efforts to build a more seamless discourse between U.S. and Cuban scientists. It is in both countries' national interests to change this. The general license under the U.S. Department of the Treasury's Cuban Assets Control Regulations, which presently permits nongovernmental U.S. scientists to travel to Cuba to conduct research, could be expanded to allow joint organization of scientific workshops and meetings.

Earlier this year, a group of U.S. scientists visited Havana under the auspices of the American Association for the Advancement of Science (AAAS) and the Cuban Academy of Sciences. They met with many leaders of the Cuban scientific community and visited some research facilities. The two organizations signed an agreement to cooperate that focuses on four areas: infectious disease, cancer, neurological and neurodegenerative disease, and resistance to antimicrobial drugs. But this plan of action rests in part on making it easier for U.S. scientists to get government licenses for their work in Cuba.

"...a single policy change will go a long way to ensure a more robust science relationship with great mutual benefit."

This visit was followed by a meeting last month in Washington, DC, of U.S. and Cuban marine scientists to discuss drafting an agreement to collaborate in ocean science research and conservation. A key part of that agreement is changing the U.S. general license for attending and organizing scientific conferences.

These are examples of a growing movement of "science diplomacy," a term that often seems to mean signing an agreement to cooperate. But to be effective, it must focus on deeds. Science diplomacy can facilitate addressing science-based questions whose answers are impeded because political relationships limit official interactions between the countries. There is perhaps no better modern example of this than the U.S.-Cuba relationship, where a single policy change will go a long way to ensure a more robust science relationship with great mutual benefit.

– Gerald R. Fink, Alan I. Leshner, Vaughan C. Turekian

Gerald R. Fink is president of AAAS and a professor at the Whitehead Institute of the Massachusetts Institute of Technology, Cambridge, MA. E-mail: gfink@wi.mit.edu

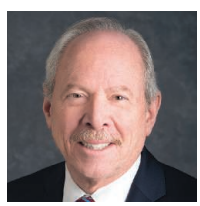

Alan I. Leshner is chief executive officer of AAAS and executive publisher of Science. *E-mail: aleshner@aaas.org*

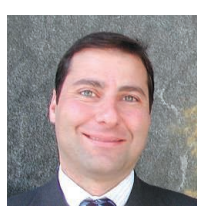

Vaughan C. Turekian is chief international officer of AAAS and director of the AAAS Center for Science Diplomacy. E-mail: vturekia@aaas.org

10.1126/science.1256312

NEWS

> "Intellectual disability is a condition, not a number."
>
> **Justice Anthony Kennedy**, writing the Supreme Court's 27 May majority decision in *Hall v. Florida*. The court ruled that states cannot decide who is mentally competent enough to qualify for the death penalty based on an IQ test score alone.

IN BRIEF

SpaceX unveils crew capsule

Enter the Dragon: On 29 May, SpaceX and its founder, billionaire Elon Musk, showed off a prototype of the company's newest Dragon capsule, which it hopes will ferry astronauts to the International Space Station in a few years. The capsule, a modified version of one that already carries cargo to the station, would hold seven astronauts. Upon reentering Earth's atmosphere, the craft would fire retrorockets and land upright, so that it might be salvaged and reused. Hawthorne, California–based SpaceX is one of three companies competing to build a crew carrier for NASA. The agency wants to have it by 2017 so that it can stop paying Roscosmos, Russia's space agency, more than $50 million apiece for rides to the space station. NASA also continues to develop its own crewed vehicle, Orion, as well as a rocket, the Space Launch System, to take astronauts beyond low-Earth orbit.

Elon Musk reveals the company's manned spacecraft.

PHOTOS: (TOP TO BOTTOM) KEVORK DJANSEZIAN/GETTY IMAGES; XINHUA/PHOTOSHOT/NEWSCOM

AROUND THE WORLD

Polio goal at risk

LONDON | The Global Polio Eradication Initiative is at "extreme risk" of, once again, missing its latest target—stopping transmission of the virus in 2014. So concludes the initiative's Independent Monitoring Board (IMB) in a just-released report. Although there were some bright spots, such as a dramatic drop in cases in Nigeria, overall global polio cases jumped from 223 in 2012 to 407 in 2013. The situation is particularly dire in Pakistan, where killings of vaccinators and political apathy have disrupted vaccination. IMB also blasts the program for not preventing new outbreaks in previously polio-free countries or stamping them out fast enough once they occur. Failure to eradicate polio is "inexcusable," IMB says. "The program is failing children and families in the poorest parts of the world."

Pakistan has little hope of stopping polio this year.

Human stem cell tests advance

MENLO PARK, CALIFORNIA | After a stalled clinical trial and a change of ownership, the first human embryonic stem cell therapy to be tested in humans appears to be back on track. Last month, Asterias Biotherapeutics announced results from an initial safety study of a potential spinal cord injury treatment; last week, it won

Published by AAAS

$14.3 million from the California Institute for Regenerative Medicine for more trials. Geron, the company that developed the cells, launched a trial in 2010, but halted it a year later to focus on anticancer therapies. Asterias took over the project in 2013, and now reports that five patients receiving the treatment saw no adverse effects. Asterias plans to test the therapy in the upper spine and to study its effect at higher dosages. http://scim.ag/Asterias

China's lunar rover languishes

BEIJING | After nearly half a year on the moon, the lunar rover Yutu, or Jade Rabbit, is alive but not kicking, according to Li Benzheng, vice commander-in-chief of China's Lunar Exploration Program. On 25 January, as Yutu was about to go dormant for the 2-week-long lunar night, it suffered a mechanical failure that prevented it from retracting its solar panels to shield its electronics from the extreme cold (*Science*, 31 January, p. 468). Engineers feared Yutu would never wake up—but it did and has survived several more lunar nights. What went wrong is a mystery, and because Yutu is still immobile, the data it still sends have little scientific value. The end is near, Li told Chinese media 28 May: "Yutu could stop working any time now."

NSF budget stays on track

WASHINGTON, D.C. | The National Science Foundation (NSF) last week withstood an assault on its 2015 budget. The Census Bureau wasn't so lucky. Despite complaints by some Republicans about NSF's support for social science research, the U.S. House of Representatives voted 321 to 87 to retain all but $10 million of a $237 million increase proposed by a House spending panel. That's more than double what the administration has asked for. At the same time, members cut $238 million from the bureau's budget request to prepare for the 2020 census, allocating the money for police protection, salmon recovery, and other purposes. The panel's chair, Representative Frank Wolf (R–VA), lamented the cuts by mockingly declaring during floor debate that "I announce that we are going to postpone the 2020 census … to 2021, or maybe to 2022." http://scim.ag/censuscuts

Researcher gives retraction OK

KOBE, JAPAN | The lead author on two controversial *Nature* papers describing a method to reprogram mature cells into stem cells has reportedly agreed to retract one of them. According to the Japanese press, stem cell researcher Haruko Obokata of the RIKEN Center for Developmental Biology indicated last week that she is willing to retract a paper detailing the capabilities of so-called stimulus-triggered acquisition of pluripotency stem cells, but not a paper explaining how to make them. The 29 January papers drew accusations of image manipulation and plagiarism. A RIKEN investigating committee ruled in April that these issues constituted research misconduct. At least two of Obokata's 10 coauthors agreed to the retraction, Japanese media reported, but the willingness to retract only one paper may indicate lingering disagreement among the researchers. http://scim.ag/_retract

Lab closings down under

SYDNEY, AUSTRALIA | Australia's cash-strapped national research body, the Commonwealth Scientific and Industrial Research Organisation (CSIRO), will shutter eight research facilities in the wake of an austerity budget announced by the federal government for 2014 to 2015. The CSIRO Directions Statement 2014, an internal planning document obtained by *Science*, identifies labs slated to close, including a horticultural facility specializing in wine, table grapes, and citrus fruit and Aspendale Laboratories, a stronghold of marine and atmospheric research. The document also details cuts to research on geothermal energy, liquid fuel, and marine biology. CSIRO has already targeted radioastronomy for heavy cuts. Even some members of Prime Minister Tony Abbott's conservative Liberal Party question the wisdom of the cuts; Dennis Jensen, an engineer and member of Parliament, told the Australian Broadcasting Corporation last week: "I'm worried about the future of science, quite frankly." http://scim.ag/Austbudcuts

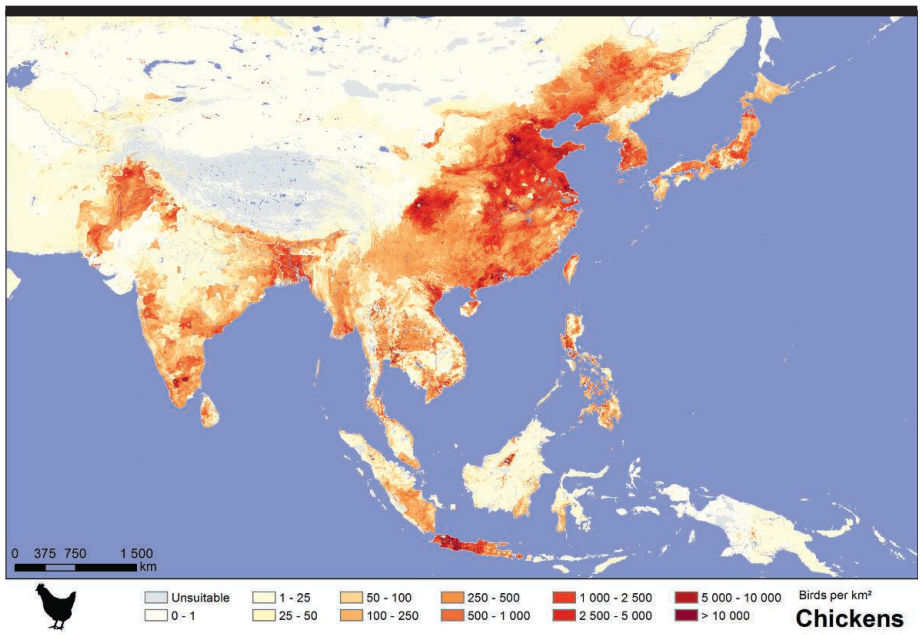

CREDIT: M. GILBERT *ET AL*., *PLOS ONE* (29 MAY), LIVESTOCK GEO-WIKI/CREATIVE COMMONS

Where are all the chickens?

There are an estimated 1 billion pigs, 1.4 billion cows, 1.9 billion sheep and goats, and 20 billion chickens in the world—but nobody knows exactly how many of the animals live where. That's a problem in addressing many scientific issues, including food security, economic development, climate change—to which livestock is a significant contributor—and zoonotic diseases such as avian influenza. Now, a team of researchers from five institutes, including the International Livestock Research Institute and the Food and Agriculture Organization of the United Nations, has assembled a new set of livestock distribution maps, using updated country estimates, advanced analytics, and new models that the scientists say provides a far better picture than the last global data set, produced in 2007. Their methods are described in a paper published in *PLOS ONE* last week. Maps and other data can be downloaded from the Livestock Geo-Wiki website, which will be updated as new census statistics become available.

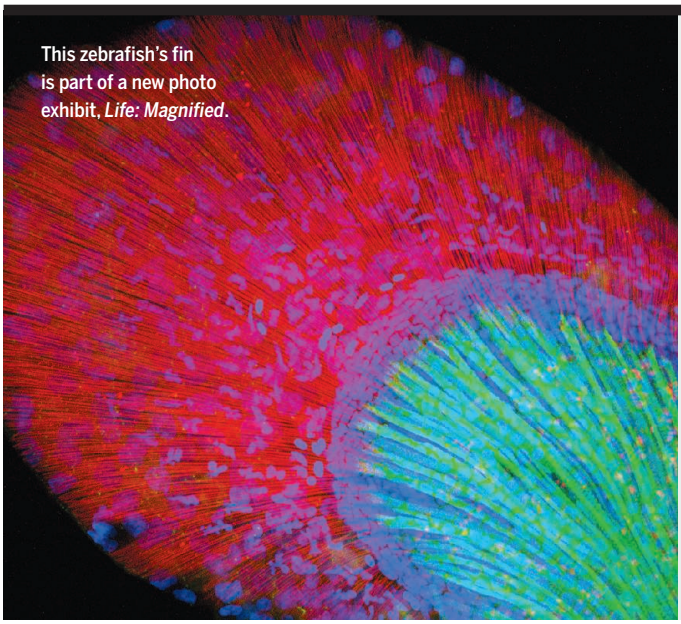

This zebrafish's fin is part of a new photo exhibit, *Life: Magnified*.

Zooming in on a fin

It's not a peacock feather, but a zebrafish's developing fin in this colorful image from the microscope of University of Wisconsin, Madison, developmental biologists. They are studying how environmental toxins can disrupt the expression of *sox9b*, which makes a protein important to skeletal development in both zebrafish and humans. (*Sox9b*'s protein is marked green, collagen is red, and DNA is blue.) The photo is among 46 stunning microscope portraits of cells and other biological structures from the plant, animal, and microbial world on display from June through November at Washington Dulles International Airport near Washington, D.C. The shots include an immune cell engulfing an anthrax bacterium, neatly patterned muscle fibers, misshapen cancer cells, spiky pollen grains, and the intricate mouthparts of a tick. The American Society for Cell Biology is sponsoring the exhibit, *Life: Magnified* (http://www.nigms.nih.gov/Life-Magnified.aspx), together with the National Institute of General Medical Sciences and the Metropolitan Washington Airports Authority.

NEWSMAKERS

Three Q's

What are your odds of becoming principal investigator (PI) of a research group? Depends on your publications, suggest computational biologist **David van Dijk** of the Weizmann Institute of Science in Rehovot, Israel, and colleagues in a 2 June paper in *Current Biology*. The team built a mathematical career model based on a scientist's publication record; *Science* talked with van Dijk in an interview edited for brevity. http://scim.ag/sciball

Q: Why study scientific careers?
A: Once in a while I like to use my skills to tackle more general questions. Every grad student dreams of a *Nature*, *Cell*, or *Science* [NCS] paper—not just for the fame, but to secure a job. We wondered whether it would be possible to quantify the effect of an NCS paper [on careers].

Q: What does your study reveal about the academic rat race?
A: The easiest, [most] sensible way to judge people you don't know is probably by past work, especially for funding agencies and hiring committees. However, this filtering method will miss some phenomenal scientists. Making the scientific community more conscious of this fact can only improve things.

Q: What effect does this paper have on your own chances of becoming a PI?
A: The model predicts that I have a 71% chance of becoming a PI. After this study is published … the model gives me a score of 81%.

Hauser report released

Four years after Harvard University completed its investigation of psychologist **Marc Hauser**, the institution's report, with redactions, is out—thanks to *The Boston Globe*, which filed a Freedom of Information Act request with the U.S. government. The pages detail an exhaustive investigation: Three committee members met 18 times and interviewed 10 people and Hauser. What they found was damning, including numerous mismatches between submitted papers and raw data. "Prof. Hauser repeatedly valued the primacy and impact of his ideas above an accurate representation of his scientific methods and the integrity of the data," the committee concluded. In 2012, the federal Office of Research Integrity found that Hauser had engaged in research misconduct. He resigned from Harvard in 2011 but continues to write about language and cognition. http://scim.ag/Hausermisc

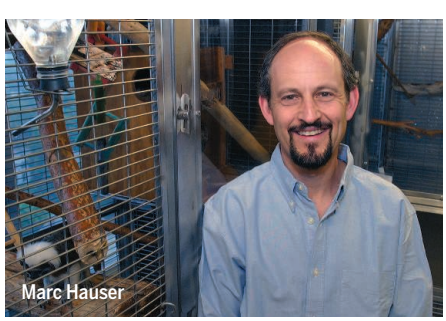

Marc Hauser

BY THE NUMBERS

55,000

"Facial recognition-quality" images intercepted by the U.S. National Security Agency each day, out of the millions of photographs published online, according to 2011 documents obtained from former agency contractor Edward Snowden.

288

Measles cases in the United States, a record since the disease was considered eliminated 15 years ago, according to the Centers for Disease Control and Prevention.

70

Percent of U.S. norovirus outbreaks from 2009 to 2012 that were linked to infected food workers; 54% of those cases involved workers touching ready-to-eat foods with bare hands, according to the Centers for Disease Control and Prevention. Only 1% of norovirus outbreaks were on cruise ships.

PHOTOS: (TOP TO BOTTOM) JESSICA PLAVICKI/UNIVERSITY OF WISCONSIN, MADISON; LISA GÖTZE; © RICK FRIEDMAN/CORBIS

IN DEPTH

Miguel Nicolelis will use EEG sensors in a high-profile demo.

PHOTO: PAULO WHITAKER/REUTERS/CORBIS

INTERVIEW

Kickoff looms for demo of brain-controlled machine

Brazilian neuroscientist Miguel Nicolelis defends his plans to show off a thought-directed exoskeleton at the World Cup

By **Kelly Servick**

During the World Cup next week, there may be 1 minute during the opening ceremony when the boisterous stadium crowd in São Paulo falls silent: when a paraplegic young person wearing a brain-controlled, robotic exoskeleton attempts to rise from a wheelchair, walk several steps, and kick a soccer ball. The neuroscientist behind the planned event, Miguel Nicolelis, is familiar with the spotlight. His lab at Duke University in Durham, North Carolina, pioneered brain-computer interfaces, using surgically implanted electrodes to read neural signals that can control robotic arms.

Symbolically, the project is a homecoming for Nicolelis. He has portrayed it as a testament to the scientific progress and potential of his native Brazil, where he founded and directs the International Institute of Neuroscience of Natal. The press has showered him with attention, and the Brazilian government chipped in nearly $15 million in support.

But scientifically, the project is a departure. Nicolelis first intended the exoskeleton to read signals from implanted electrodes, but decided instead to use a noninvasive, EEG sensor cap. That drew skepticism from Nicolelis's critics—and he has a few—that the system wouldn't really be a scientific advance. Others have developed crude EEG-based exoskeletons, they note, and it will be impossible to tell from the demo how this system compares. A bigger concern is that the event could generate false hope for paralyzed patients and give the public a skewed impression of the field's progress.

As his team prepares for the 12 June kick, Nicolelis gives *Science* a hint of the technology under the hood, and defends his decision to arrange such a conspicuous debut for a tool still in the early stages of development. This interview has been edited for brevity and clarity.

Q: Getting down to the last few weeks before the kick, how is the project progressing?

A: The scientific, the clinical, and the technological milestones have been concluded, so we're pretty happy. Our eight patients have all experienced walking in the exo[skeleton]. They all had sensations that made them report that they felt like they were walking by themselves.

Q: What's your primary goal with this demonstration?

A: My primary goal is to disseminate the passion for science around the world. I want people to know that in a country like Brazil that is well known for football, you can also do high-level science, and that high-level science can be produced by a global collaboration, in a nonprofit consortium.

Q: Are you hoping to demonstrate anything to the scientific community?

A: Not in the stadium. We are going to demonstrate a very beautiful thing, but the demonstration for the scientific community will come in the papers that will come afterward. … But we are not preparing this for peer review. This is a show for the world.

Q: How does a person move the exoskeleton, and what can they control?

A: The person has to imagine movements, and these movements are translated into commands that enact the movements in the exo. It's a concept that we published way back in 2002 called shared control. Part of the higher order decision is done by the brain, and the low-level movement is enacted by the robot. [High-order decisions include] "start walking," "stop walking," "accelerate," "slow down," "turn left," "turn right," "kick the ball."

Q: How is this system different from other exoskeletons out there?

A: There are several differences. I don't know any other exoskeleton that is taking commands from the patient's brain to be activated, move and stop, kick a ball, turn.

Number two is this thing that we call artificial skin. … When the foot touches the ground, there is a wave of signals that are generated, and they are delivered to the arms of the subject through a shirt that contains small mechanical vibration devices. The patients' brains, after a few sessions of training, associate these vibrations in the arms with either movements of the leg or touching the ground. So we documented plasticity in the brain of the patient.

That feedback creates a higher order control loop that allows them to perform much better than if they didn't have the feedback. Besides the improvements in motor performance, they have a much more vivid sensation that instead of being carried by a machine, they are literally doing it themselves.

Q: What if the brain signals the person gives on the field, under pressure, are different from the signals in previous tests?

A: We created a virtual reality room in our lab here in São Paulo where a soccer stadium is simulated while they're doing the task. So we put the noise of football fans celebrating, we put flashes of lights. … If you can do this EEG task while listening to Turkish football fans, like they did, which are the loudest fans in the world, this crowd in Brazil will look like an elementary school class in comparison. Even if they're screaming with the full strength of their Brazilian lungs, it doesn't get close to the Turkish guys, I can tell you. We measured.

Q: You originally intended to use implanted electrodes. Why the shift to EEG?

A: When I saw the results of other groups that published invasive technologies in humans, they were really mediocre and not worth the risks of implants. So I decided that it was good, in the case of locomotion, to start with the known phase of technology. We saw that we had a new algorithm for EEG that could do more than I thought we could do before.

Q: You have been critical of using EEG in neuroprosthetics.

A: Yes, I was—and I am—for upper limb control, if you want to reproduce every detail of the kinematics. That is a bogus debate, because I'm doing locomotion, which is a completely different movement.

For the upper limbs, everybody knows that if you're inside the brain, you get much better results in terms of predicting the entire trajectory. I published tons of papers on this. I pioneered the field, so I know what this is about. Unfortunately, in the U.S. there is such a belligerent, competitive environment. Some neuroscientists cannot take the fact that we are doing something different.

Q: Are you concerned that people watching won't understand how much control the person has over the movement of the exoskeleton?

A: No, because I have been very vocal and very open here in Brazil and all over, showing what is real, what is a possibility right now. This is just to raise awareness for the fact that we have 20 to 25 million people paralyzed around the world, and that science, if properly funded and supported, can do something about it. If we start now—this is just a symbolic first kick—we may be able to do something in the next few years.

The robotic exoskeleton under development at Nicolelis's lab in São Paulo.

Q: Brazil will host the Olympics in 2016. Do you have any plans for a demonstration there?

A: Oh, sure. We have plans. Our good friends would love to know them, but we'll tell them in due time. … I'll let the critics have one more month of good sleep. ■

PHOTO: MIGUEL NICOLELIS/FACEBOOK

CLIMATE CHANGE

A bold baby step on emissions

But U.S. curbs alone won't slow warming

By **Eli Kintisch**

When President Barack Obama this week announced the boldest step yet to cut U.S. emissions of greenhouse gases, he touched off both a predictable backlash and a nuanced technical debate about the long-term impacts on climate and the economy. The proposal, unveiled on 2 June by the Environmental Protection Agency (EPA), would cut carbon emissions from the U.S. power sector by up to 30% by 2030, relative to 2005 levels. It has already drawn talk of lawsuits from industry and rebuke from some powerful lawmakers in Washington, who argue that the effort will needlessly cost money and jobs. And many scientists, weighing the impact of the U.S. step in a world where other polluters are surging ahead, see the move as painfully insufficient to keep global temperature increases below dangerous levels—but still far better than nothing.

"These are a few small steps down a long, long road," says climate scientist Ken Caldeira of the Carnegie Institution for Science in Palo Alto, California. "The important thing is that these first steps do not become our last steps."

President Obama acknowledged the tightrope he's walking between critics who accuse him of being too aggressive on climate—or not strong enough. "The shift to a cleaner energy economy won't happen overnight, and it will require tough choices," he said in a video statement. But, he added, "I refuse to condemn our children to a planet that's beyond fixing."

The proposal represents an agonizing compromise between high-minded goals and brutal political reality. A high-profile effort to create a comprehensive emissions trading system died in the U.S. Senate in 2010. Since then, 10 states have taken mostly modest steps to create similar programs. EPA has also moved to limit emissions from cars and future power plants. But until this week, the federal government hadn't touched the nation's biggest

New rules could hasten the decline of coal plants, such as this one in Wyoming.

PHOTO: PHIL AUGUSTAVO/GETTY IMAGES

climate warmer, the roughly 1000 existing electricity-generating power plants responsible for spewing 40% of annual U.S. carbon emissions.

Many economists insist that charging, or taxing, industry and consumers for each ton of carbon emitted is the simplest way to create incentives for cutting emissions at the lowest cost. But a carbon tax needing congressional approval is a political nonstarter. Instead, EPA—operating under a largely untested provision of the Clean Air Act—wants to give states flexibility to reach individual reduction goals that it has set for each state.

To reach those targets, EPA has laid out four options for state regulators to impose on utilities. Plants can reduce emissions either "inside the plant fence," by increasing plant efficiency or by switching fuels from coal to natural gas, which produces less carbon dioxide. Or they can take steps "outside the fence": investing in new sources of green power, such as wind or solar, or working to reduce energy demand by their customers. States can also elect to allow trading of emissions credits.

If successful, the rules give Obama a chance to meet his 2009 promise to cut U.S. emissions from all sources by at least 17% below 2005 levels by 2020. "This plan is all about flexibility—that's what makes it ambitious, but achievable," EPA Administrator Gina McCarthy told reporters.

Opponents don't buy it. "The EPA's plan is 'all pain, no gain,' " said Representative Lamar Smith (R–TX), chair of the science committee in the U.S. House of Representatives, in a statement. "It will close power plants and drive up electricity prices. … And studies show that dramatically cutting carbon emissions in the U.S. will have little impact on global temperature in the future."

Both points—the economic and climate consequences of the rules—are likely to be the subject of technical debate in coming months. EPA estimates that the rules will prevent air pollution from coal-fired power plants—particularly mercury and soot emissions—which otherwise would cause "2,700 to 6,600 premature deaths and 140,000 to 150,000 asthma attacks in children" by 2030. The rules will modestly raise electricity costs, EPA says, but avoided impacts on health, infrastructure, and the environment could save "an estimated $55 billion to $93 billion" over the same period. But many economists are critical of the modeling underpinning such touted cost savings, because it encompasses hard-to-simulate factors like catastrophes, climate feedbacks, and political decisions. The conclusions from such models lack "theoretical or empirical" foundation, economist Robert Pindyck of the Massachusetts Institute of Technology in Cambridge recently wrote.

As for the rule's overall impact on climate, much will depend on whether the U.S. move inspires similar action by other major emitters. (China hinted at imposing a new emissions cap after the EPA announcement.) If the United States achieves its 17% emissions reduction with help from the new rules, but acts alone in sustaining the reductions over time, the global rise in emissions and temperature will barely flatten compared with business as usual, according to an analysis done for *Science* by Climate Interactive, a modeling and visualizing firm based in Washington, D.C. (see graphic). If other nations take comparable steps, however, the gains could be much greater, the modeling suggests—raising the chances of holding the future increase in average global temperature below the 2°C threshold many researchers say is advisable. Seemingly the only way to ultimately stabilize greenhouse gas concentrations and arrest the temperature rise, Caldeira says, "is for everyone to stop building things with smokestacks or tailpipes that use the sky as a waste dump."

Such debates will be largely academic if the new rules—now out for public comment but expected to be finalized next year—don't survive legal challenge. EPA's use of possible steps "outside the fence" to calculate the emissions reduction goals may be the industry's main target, says Harvard Law School professor Richard Lazarus. "The agency has never based emissions reductions on what consumers would do before," he says. But there's also nothing in the Clean Air Act, he adds, that expressly says it can't be done. ■

If U.S. goes it alone, controls will have minimal impact

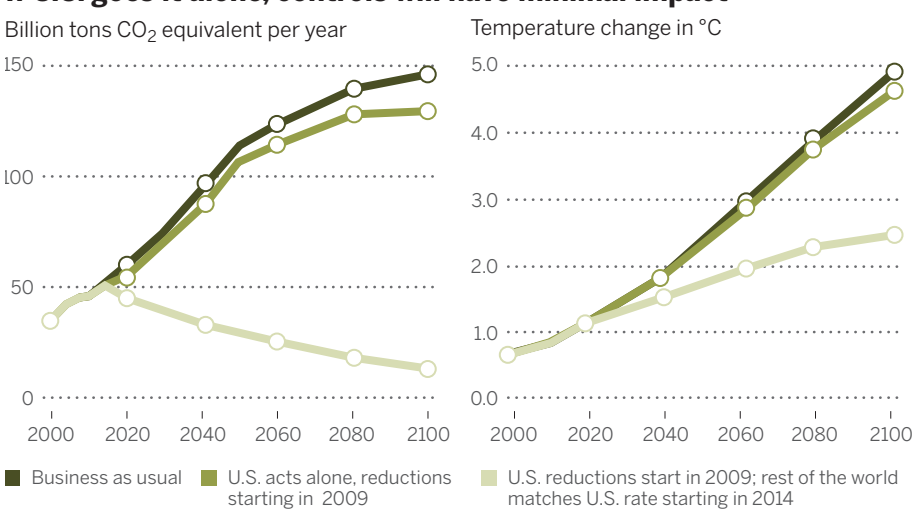

Source: C-ROADS, climateinteractive.org

ALL TOGETHER NOW? To dramatically reduce global emissions of greenhouse gases (*left*) and hold down temperature increases, other nations would have to join the United States in enacting similar controls on power plants and other sources, suggest simulations produced with C-ROADS, a climate policy modeling tool.

CELL BIOLOGY

Lengthy RNAs earn respect as cellular players

A few of these molecules are clearly important, but just how many?

By **Elizabeth Pennisi,**
Cold Spring Harbor, New York

RNA is a virtuoso molecule. What was once seen as just a cellular messenger takes multiple forms with surprising talents: It can be an enzyme, a defense against infection, a gene regulator, and much more. Now, biologists are debating whether an unusually lengthy form of RNA is a regular player in the cell or, more often, a distraction.

Surveys of cells have uncovered many thousands of RNA strands 200 bases or more long, called long non-coding RNA (lncRNA), and several groups have linked specific lncRNAs to development, cancer, pain, and inflammation. But others suggest they could be genomic trash, the spurious byproducts of gene transcription.

At the Biology of Genomes meeting held here last month, several talks offered evidence that chasing these molecules isn't a fool's errand. With the discovery that some lncRNAs are identical in many different tissues, and that a few are essential to the survival of mice, the scientific community "has gone from questions about whether they are relevant at all to how are they relevant," declared one lncRNA speaker, John Rinn, a molecular biologist at Harvard University.

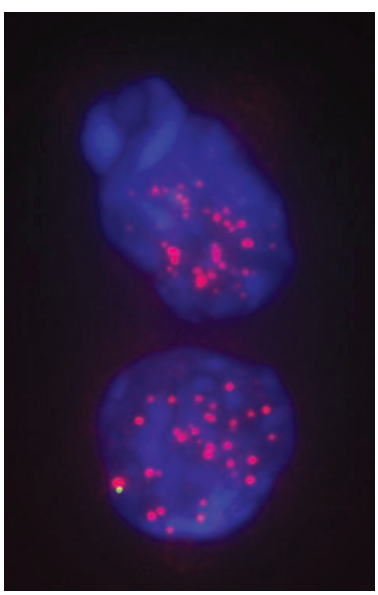

A new method for visualizing lncRNAs shows copies of one (pink) in cell nuclei (blue).

Almost 25 years ago, two lncRNAs made headlines: H19, which plays a role in cancer and in fetal growth, and Xist, which helps shut down the second X chromosome in females to ensure the proper dosage of gene activity. Those lncRNAs were considered unusual until 2005, when a large-scale project called FANTOM suggested there were 35,000 ncRNAs, exceeding the number of protein-coding genes. These findings created "a big buzz," says Adam Siepel, a computational biologist at Cornell University. "Whatever [researchers] were interested in, they wanted to see what lncRNAs had to do with it."

Researchers could envision multiple ways in which lncRNA could act, influencing gene activity by helping regulatory proteins attach to DNA or by binding to the double helix themselves, for example. But biological samples typically contained just a small number of any specific lncRNA, stoking doubts about their functionality. Chris Ponting, a genomicist at the University of Oxford in the United Kingdom, also reported that their sequences were not well conserved across species—as would be expected if most were vital to survival. For him and others, that finding cemented their doubts.

Rinn, a longtime supporter of lncRNAs, tried to settle the debate at the end of last year. In a study published on 31 December 2013 in *eLife*, he and colleagues described the effects of disabling genes for 18 lncRNAs in mice. They had carefully examined the known lncRNAs for those that did not overlap with any protein-coding genes and selected 18 to eliminate. Three of the knockout mice did not survive to adulthood; two others had growth defects. "If you take them out in mice, bad things happen," Rinn says.

Ponting, among others, was not convinced, because knocking out the lncRNA genes might also disrupt embedded regulatory DNA that might control distant protein-coding genes. "A lot of genomic real estate was taken away," he says.

The tide may now be turning in favor of lncRNAs, however. At the meeting, Philippe Batut of Cold Spring Harbor Laboratory reported comparing five fruit fly species that had diverged as much as 25 million years ago. He found that more than 1000 lncRNAs have been conserved among all the species—unlikely if the molecules have no biological role.

Ponting has also begun to come around. With Oxford's Wilfried Haerty and collaborators from the Lieber Institute for Brain Development in Baltimore, Maryland, he determined the sequences of all the RNA in preserved brain samples from 307 people. Among the thousands of lncRNAs that Ponting's team found in each person's brain tissue—many of them never identified before—about 18% show up in just one individual. Those molecules may be just randomly transcribed and of no utility, Haerty reported at the meeting. But 2728 different lncRNAs were found in more than half the samples, and 251 were expressed in every individual. Their gene sequences overlapped with chemical markers indicative of active transcription—another hint that they are functional. For Ponting, the question now is not so much whether lncRNAs matter as how many of them matter.

Rinn also offered new evidence of lncRNA functionality at the meeting. He and Harvard graduate student Moran Cabili, together with Arjun Raj from the University of Pennsylvania and Aviv Regev from the Broad Institute, have developed a way to visualize lncRNAs in single cells from different human tissues. For each lncRNA examined, they add to the cell a fluorescent-tagged probe matching the lncRNA's sequence.

The technique indicated that the distribution of many lncRNAs is not random—which Rinn argues would happen if these molecules were mere garbage. Instead, some lncRNAs are confined to the nucleus, whereas others reside only in the cytoplasm. As more lncRNAs and cells are tested, Rinn hopes to reveal whether "jackpot" cells—cells with anomalously large numbers of lncRNAs—exist. Some have suggested that jackpot cells would indicate that lncRNAs are the product of aberrant transcription in just a few cells.

Several researchers at the meeting still think lncRNAs may be minor players in biology. One who did not want to be quoted declared that no graduate student should invest time in them. "I don't like the hype," agrees Emmanouil Dermitzakis, a genomicist at the University of Geneva Medical School in Switzerland. "I don't think we should spend more money on it."

But others see progress. "We now know for sure they are not just garbage," says Mitchell Guttman, an lncRNA researcher at the California Institute of Technology in Pasadena. "But what they are doing and how they are working, we don't know." ■

PHOTO: EZGI HACISULEYMAN/ARJUN RAJ/JOHN RINN

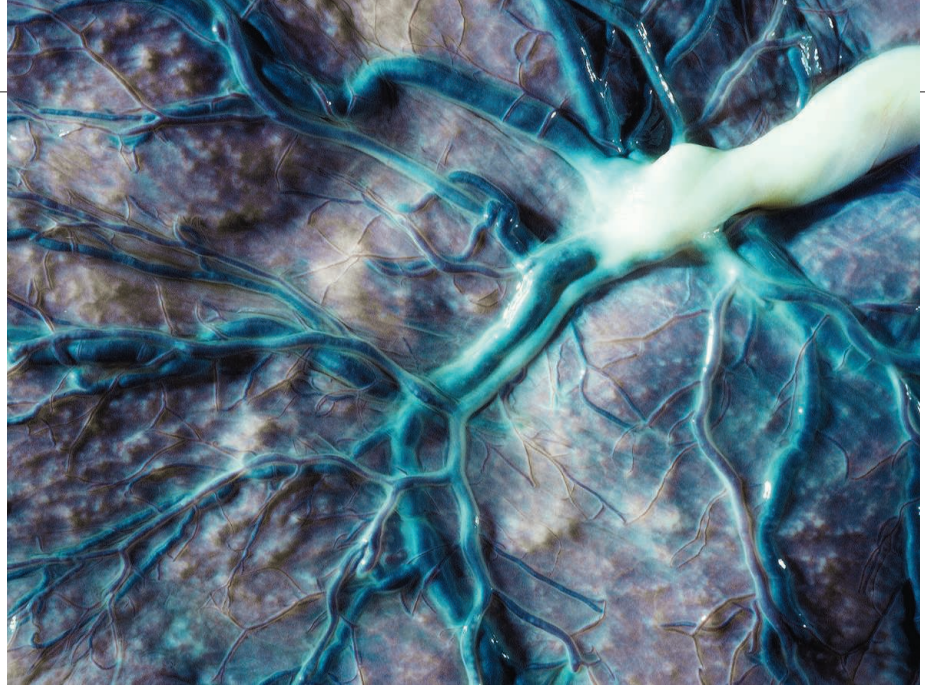

The placenta's complex vasculature (blue) sustains a fetus through its umbilical cord (white).

PHOTO: CNRI/SCIENCE PHOTO LIBRARY

REPRODUCTIVE BIOLOGY

Gearing up for a closer look at the human placenta

Workshop participants build an agenda for research on this oft-ignored bridge between mother and fetus

By **Jocelyn Kaiser,**
Potomac, Maryland

A placenta sustained you and every person ever born for 9 months, serving as your lungs and kidneys and pumping out hormones while you developed in the womb. Problems with this disk-shaped mass of tissue can contribute to everything from preterm births to diseases of middle age. Yet when a baby is born, hospitals usually throw the placenta away.

"It's the least understood human organ," says Alan Guttmacher, director of the National Institute of Child Health and Human Development (NICHD) in Bethesda, Maryland. "A large part of the scientific community never thinks about the placenta at all." He and others hope to change that, however, by rallying researchers and funders around a project to better understand the underappreciated organ. At an NICHD-sponsored workshop here last week, some 70 researchers laid out their ideas for a Human Placenta Project, including ways to better monitor the placenta during a pregnancy, and drugs to bolster it when it falters.

The human placenta forms primarily from tissue that originates in the outer layer of fetal cells that surround an early embryo. Early in pregnancy, these trophoblasts invade the uterine wall and later develop a complex network of tiny projections called villi, which contain fetal blood vessels. This treelike structure of villi absorbs oxygen and nutrients from maternal blood; fetal waste and carbon dioxide meanwhile diffuse into the maternal bloodstream. Other specialized cells link the developing placenta to the umbilical cord. To avoid rejection by the mother's immune system, the placenta employs various tricks, such as not expressing certain proteins. The placenta's role during pregnancy is "an incredibly interesting biological time" that offers lessons for everything from cancer to organ transplantation, says physician-scientist Kimberly Leslie of the University of Iowa in Iowa City.

A malfunctioning, too small, or weakly attached placenta can starve the fetus, stunting its growth. Such problems can also contribute to preeclampsia, or pregnancy-related high blood pressure, a condition that occurs in up to 6% of pregnancies and can require premature delivery of a baby. Adult diseases, too, ranging from heart disease to insulin resistance, seem to be linked to abnormal placenta morphology for poorly understood reasons (*Science*, 7 June 2013, p. 1160).

During recent strategic planning at NICHD, researchers concluded that the placenta deserved closer study. "It came up repeatedly," Guttmacher says. He expects that the Human Placenta Project will focus on understanding both the normal and abnormal placenta in real time during the course of pregnancy. It will also look for possible interventions—for example, a drug that would spur the growth of a too-small placenta.

Some at the workshop hope to adapt ultrasound and magnetic resonance imaging techniques now used to study the heart and brain to measure blood flow and oxygenation in the placenta. Injecting tracers, however, may be sensitive ethical territory. "People are very scared of doing things to pregnant women," said Nicholas Illsley, of Hackensack University Medical Center in New Jersey, at the meeting. Another idea is to probe the mother's bloodstream for cells and nucleic acids shed by the placenta as a window into the function of the organ.

Researchers also mused about creating a "placenta on a chip" that would mimic the tissue in the lab and developing molecular sensors that could monitor the placenta throughout pregnancy. "This sounds like science fiction, but if you showed me an iPhone 20 years ago, I would have said this was science fiction," said Yoel Sadovsky, of the Magee-Womens Research Institute in Pittsburgh, Pennsylvania, at the meeting.

Attendees described a few immediate goals. One is to come up with standard definitions of a normal and abnormal placenta. Placenta morphology varies widely, and those from a healthy pregnancy can still have visible abnormalities, whereas those from sick babies often look completely normal, says systems biologist Brian Cox of the University of Toronto in Canada. Even before the NICHD meeting, the international community of placenta researchers had begun to coordinate their efforts by planning a website that will list existing placenta biobanks and help match collaborators.

At a time when NICHD's budget is flat, money could be a limiting factor for the Human Placenta Project, which Guttmacher hopes will fund its first grants in 2016 and go for a decade or more. He expects that in addition to setting aside new money for the project, NICHD may give extra weight to high-quality grant applications focusing on the placenta. NICHD's own contribution may be only "in the millions" of dollars, Guttmacher says. But he says eight other NIH institutes have expressed interest in contributing, as has the March of Dimes, an organization long focused on maternal and infant health. At long last, a throwaway organ may get the attention it deserves. ■

MATERIALS SCIENCE

Solar furnace rises from the Soviet ashes in Central Asia

Clean, intense heat once exploited in military research now forges new optical materials and superconductors

By **Richard Stone,**
Parkent, Uzbekistan

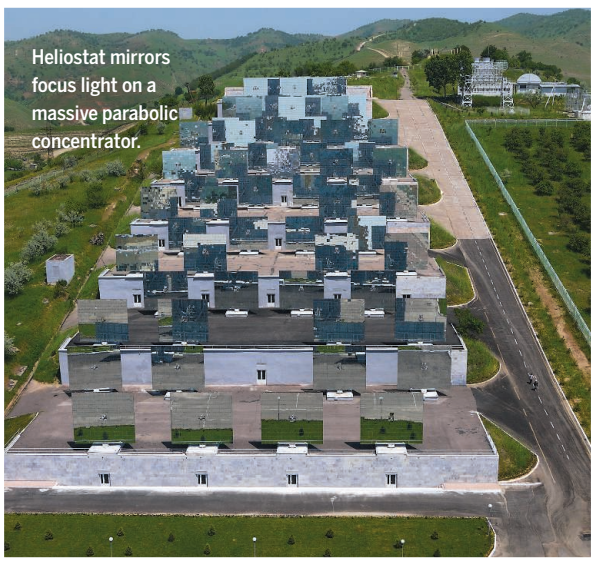
Heliostat mirrors focus light on a massive parabolic concentrator.

The sun has set on the Soviet Union, but on this hilltop about 40 kilometers east of Tashkent, the capital of Uzbekistan, it still glints off a legacy of empire: a massive solar furnace. The facility, which consists of dozens of towering mirrors that focus the sun's rays on a cauldron-sized target, was once a mecca for Soviet scientists wondering how a military bunker might hold up in a nuclear conflagration, or whether a spacecraft's heat shield could withstand reentry. Now, this aging behemoth, a near-clone of an older facility in France, is undergoing a scientific revival and creating a bright spot in the science landscape of its post-Soviet host nation.

"It's an impressive facility," says Steven Gitomer, program director for plasma physics at the U.S. National Science Foundation in Arlington, Virginia, who visited in 2009. Uzbek researchers are using its intense heat to temper high-tech materials and forge new compounds, and an international team has made a spectacular claim for one material. A cuprate compound baked in the furnace, they say, shows signs of superconductivity at a temperature far higher than any other material. If confirmed, the result "would be mind-blowing," says Wayne Reed, a polymer chemist at Tulane University in New Orleans, Louisiana, who visited last month.

The main advantages of a solar furnace over conventional ones are speed and purity: Heating is instantaneous once the solar rays are trained on the target, and the heat source produces no contaminating fumes. Only two solar furnaces in the heavyweight division—capable of focusing a full megawatt of irradiance on a square-meter target—exist in the world. In the 1960s, France built one in the sun-drenched Pyrenees, primarily to process refractory materials such as zirconia. (The French furnace, called PROMES, continues to do research in areas such as testing spacecraft heat shields and solar thermal electricity generation, says Director Gilles Flamant.) Soviet space researchers wanted a knockoff, envisioning a solar furnace smelting metals on the moon for construction of a lunar base. "That is a cool idea, even though they never pulled it off," Reed says. Construction began here in the western foothills of the Tian Shan Mountains in 1981; 6 years and $100 million later, the Institute of Materials Science's Physics-Sun facility was up and running.

An array of 62 heliostat mirrors, each 7.5 meters tall and 6.5 meters wide, tracks the sun across the sky, steadily reflecting light onto a 40-meter-tall parabolic mirror. This concentrator focuses the collected light on a tower-mounted target less than a meter wide, where temperatures can exceed 3000°C. During a brief Cold War heyday before the Soviet Union collapsed in 1991, some 1500 staff members worked at the Physics-Sun facility, says its director, materials scientist Ilkham Atabaev.


Director Ilkham Atabaev

The 160 staff members at the facility today focus on materials science work with a practical bent: making ultrahard aluminum oxide for optics, for example, and tempering ceramic spheres that are floated inside petroleum storage tanks to deter fume buildup. Industrial applications of solar furnaces are diverse enough that Uzbek researchers have built $50,000 miniature versions for metallurgical institutes in Cairo and Hyderabad, India.

Most eyebrow-raising are the experiments with novel superconductors. Physics-Sun materials scientist Dila Gulamova and colleagues at the Andronikashvili Institute of Physics in Tbilisi, Georgia, and San Jose State University in California placed a superconducting compound made from bismuth, lead, strontium, calcium, copper, and oxygen in the solar furnace. Normally, this substance becomes a superconductor at temperatures no higher than 110 kelvin. But in preliminary results, the team claims that after melting it in the furnace, islands within the material became superconducting at up to 190 K—more than 50 K above its nearest rival.

As those experiments go on in the glare of day, another group at Physics-Sun led by atmospheric physicist Mirzasulton Mamatkosimov is hatching plans for science at night. He notes that the mirrors can collect and concentrate faint flashes of Cherenkov light that flicker across the sky when cosmic rays and gamma rays from the distant universe collide with the upper atmosphere, creating a shower of particles. Analyzing Cherenkov radiation can help researchers decipher the composition and energy spectrum of the cosmic intruders. The furnace "has big potential for gamma ray astronomy," says Masahiro Teshima, director of the Max Planck Institute for Physics in Munich, Germany, and physics coordinator for the two MAGIC Cherenkov telescopes on La Palma, Canary Islands. With the right instrumentation, he says, the Uzbek facility could complement currently operating Cherenkov telescopes and the massive next-generation Cherenkov Telescope Array expected to be up and running around 2020.

Atabaev hopes to secure his furnace's future by turning it into an international facility for high-temperature testing of materials and devices. Military research at the furnace, he says, is a thing of the past: Such testing is now mostly done by computer simulation. Anyway, Atabaev says, "Russia would not do military research here now because it would be afraid that secrets would pass to America. Maybe the Americans think the same." ■

PHOTOS: (TOP TO BOTTOM) R. STONE/*SCIENCE* (2)

Drive to succeed. Richard Tapia used his Chevelle show car to lure Josef Sifuentes (*left*) into mathematics.

PHOTO: JOHN EVERETT PHOTOGRAPHY

Minority voice

Richard Tapia has prepared generations of minority students for academic jobs, but he says they still aren't welcome

By **Jeffrey Mervis**

Richard Tapia's passion for teaching and mentoring was obvious to Margaret Wright from the moment the two young applied mathematicians met at Stanford University in 1976. Wright was a newly minted Ph.D. in the operations research department, and Tapia, only 5 years older but already a tenured professor at Rice University in Houston, Texas, was teaching a course in the department.

"They gave you an 8 a.m. class?" Wright recalls asking Tapia. "That's terrible. They are the worst."

But the timing didn't seem to bother Tapia. And by the end of the semester, she says, he had transformed a group of somnolent students into excited learners. "The class received the highest ratings of any course in the history of the department," says Wright, now a professor of computer sciences at the Courant Institute of Mathematical Sciences at New York University in New York City. "It was all because of Richard."

Wright's admiration for Tapia grew over the years, fueled in part by their shared commitment to helping groups underrepresented in science—in particular, women, African-Americans, Latinos, and Native Americans. After spending a year at Stanford, Tapia returned to Rice and created what is arguably the most successful university-based program in the nation for training minorities in mathematics and computer science. The Richard Tapia Center for Excellence and Equity has helped 89 minority students earn Ph.D.s in those fields over the past dozen years, a record unmatched by any other university, much less a single professor. "Richard is amazing. He's a force of nature," Wright says.

Tapia doesn't force himself to choose between his passions: advocacy for minorities and the pursuit of a branch of mathemat-

ics called optimization algorithm research, which Tapia describes as "finding the best choices within a given class of options." "When I visit a campus," Tapia says, "I give an outreach talk on the first day, and the next day I give a math talk." That approach has lifted him to the top of his profession—election to the National Academy of Engineering in 1992, recipient of the National Medal of Science in 2011, and, just last month, winner of the highest honor bestowed by the National Science Foundation (NSF) for a lifetime of public service, the Vannevar Bush Award.

Despite these impressive accomplishments, the memory of the year Tapia spent at Stanford so long ago still rankles.

It was actually a job audition, an effort to realize a childhood dream nurtured by his parents, who came from Mexico as children with little formal education themselves but who instilled in Tapia a burning desire to succeed. "When I was growing up, anybody who wanted to be an academic, at least in California, said there are three places I want to go in my life: Stanford, [University of California,] Berkeley, or heaven," he quips.

By the end of the academic year, his chances of getting a Stanford post seemed pretty good. Along with an active research program, he says, "I had perfect teaching evaluations in three classes, and I served as faculty adviser to all Hispanic student groups."

But the department saw things differently. Although Tapia was a tenured full professor at Rice, Stanford offered him an untenured position as an associate professor. "It was a substandard offer, and I had to reject it," he says. "My extra dimensions were of negative value to them," he adds. "They made it clear that they didn't want me to be doing all these other things."

Tapia, a first-generation Mexican-American, believes that his experience at Stanford nearly 40 years ago reflected institutional racism—and that this problem, if anything, has gotten worse over the years. When he came to NSF on 6 May to accept his prize, he warned that the nation is at risk because top-tier mathematics departments don't think minority scientists have the right stuff.

Tapia's 15-minute speech to the National Science Board, NSF's presidentially appointed oversight body, was an abbreviated version of a hard-hitting and irreverent presentation he's been making at universities around the country titled "Racism in Mathematics: A Direct Factor in Underrepresentation." He chose the title in part for its shock value.

"Calling this racism is a bit hard," Tapia acknowledged in a recent e-mail to Michael Wolf, a Rice colleague who had heard the talk and objected to both its tone and its application to mathematics. "But it does get people's attention."

THE PAUCITY OF minority science faculty members at top-tier U.S. universities should be enough to get people's attention, Tapia believes. In a country whose population is 30% black and Hispanic, those two groups make up just 3.9% of the math faculty and 2.9% of the computer science faculty at the top 50 U.S. departments (see graph). Asians are the notable exception: Although making up only 5% of the U.S. population, they hold 17% of the faculty slots in mathematics and 27% in computer science at the top-tier programs.

To be sure, the pool of eligible minority candidates outside the Asian community is tiny. In 2012, some 307 mathematics departments produced 33 Latino Ph.D.s and 28 African-American Ph.D.s who were U.S. citizens. In applied mathematics, the 2012 numbers were vanishingly small—two African-Americans and seven Latinos. Those numbers represent both an injustice and a serious waste of talent, Tapia argues.

For his Vannevar Bush Award talk, Tapia bowed to his more august surroundings, changing the title to "Crisis in Higher Education: The Need for New Understanding and Leadership." But he didn't water down his message. The overt racism of the Jim Crow era may be gone, he says. But its latest incarnation—lower expectations for underrepresented minorities as both students and faculty members—is nearly as pernicious.

Those lower expectations, according to Tapia, begin when minority undergraduates planning to major in science are told that poor preparation in high school could prevent them from earning a degree from an elite school such as Rice. To make matters worse, he says, some faculty members have already discounted their students' abilities based on skin color.

To illustrate his point, Tapia tells a story from a decade ago about six talented undergraduates whom he had handpicked to take a class in functional analysis from another professor. The students were assigned no homework and made no presentations, so the professor had no work on which to grade them. Nevertheless, at the end of the term, the five white students received A's and the sole minority student—a Tapia protégé named Josef Sifuentes, a Mexican-American—got a C.

Furious, Tapia sought out the professor. "I try to discourage those who do not belong in math," his colleague told him. Tapia translated the professor's answer for the science board: "So just by looking at the student, he was saying, 'You don't belong.' "

In graduate school, Tapia says, minority students often are expected to be less productive than their majority peers. And those lower expectations can hurt them once they earn their Ph.D. and enter the academic job market. The top candidates at most top-tier math departments have published as many as eight or 10 papers, Tapia says. Such precocious productivity is often reinforced by a letter from an eminent mentor touting them as capable of winning a Fields Medal, the discipline's equivalent of a Nobel Prize.

Research prowess is certainly important, Tapia says. But he believes the current hiring standard sets the bar higher than necessary by overemphasizing a candidate's potential to be a research superstar and discounting the rest of their job description. "I couldn't get hired today" by a top-tier research university, he claims.

The first in his family to go to college, Tapia says he was an average student as a teenager. But by the time he received

Sparse representation

Low numbers of black and Hispanic faculty in math-intensive disciplines show little sign of improvement (percent, top 50 departments).

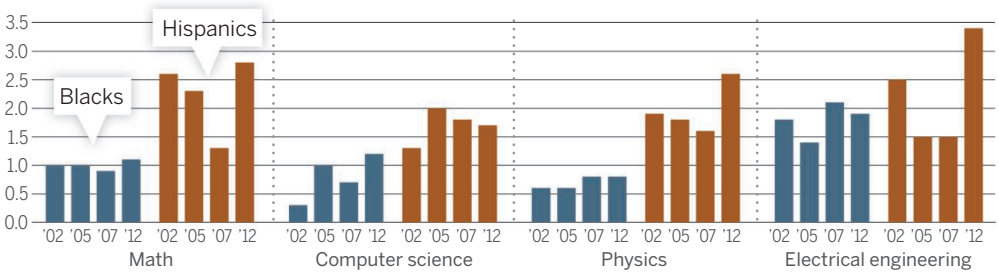

Source: Nelson Diversity Surveys; Art: K. Engman/*Science*

his mathematics Ph.D. from the University of California, Los Angeles, in 1967, he had put himself on the academic fast track. He says a postdoc at the University of Wisconsin, Madison, allowed him "to run with the big dogs" at the school's Army Mathematics Research Center. Only 2 years after arriving at Rice as an assistant professor, he was granted tenure and was on the way to becoming a big dog himself.

A founding member of the Society for Advancement of Hispanics/Chicanos and Native Americans in Science (SACNAS) in 1973, he noticed during one early gathering that only two of the 68 faculty members in the room were tenured. That statistic reinforced a pledge he had once made to himself "to start to help people after I get tenure." And once he achieved that, he began looking for ways to mentor minority students, involve them in research opportunities, and oversee their professional development.

For years it was a solo effort, something added to his other responsibilities. In 1989, the university acknowledged his mentoring work by naming him director of education and outreach programs for the NSF-funded Center for Research on Parallel Computation at Rice and giving him a $200,000 annual budget. A decade later, he snared one of the first grants in an NSF program designed to increase the number of underrepresented minorities earning STEM (science, technology, engineering, and mathematics) Ph.D.s. The program gave him contacts at other like-minded universities around the country, and in 2007 he won NSF funding to create a similar alliance to serve undergraduates.

The programs target students who are good enough academically to get into schools like Rice—a student body in which the top quarter has SAT scores of 1500 or higher (out of 1600)—but who may lack the confidence, social networks, and knowledge of higher education possessed by their wealthier peers and their college-educated parents. Sifuentes was one of those students when he arrived at Rice in 2000, and Tapia took a typically hands-on approach with him.

A high-achieving student from a Mexican-American family of modest means, Sifuentes tested into an elite high school program in Houston in which he was the only minority. At Rice, he planned to major in mechanical engineering. "Like a lot of minority students, I looked at the list of majors and said, 'Now what sounds like a good job?' " he explains.

Sifuentes was completing a summer research project that included teams from both the engineering and computational sciences when Tapia, who led the latter group, made Sifuentes an offer that changed his life.

PHOTO: JOHN EVERETT PHOTOGRAPHY

"Calling this racism is a bit hard. But it does get people's attention."

Richard Tapia, Rice University

Tapia has a passion for fast cars. As a teenager, he and his twin brother competed in drag car races in southern California and Tapia briefly held a world record. Although he abandoned the track long ago, his enthusiasm for muscle cars has never waned.

"I have a 1970 Chevelle, full custom, that I'm still working on," Tapia told Sifuentes. "I want a music video that showcases the car, which is called Heavy Metal. And I want the special effects to be based in real mathematics. You're an artist, you know how to do that, right?"

"No, I can't do that," replied Sifuentes, who was pursuing a minor in art. "I have no idea what you're talking about."

"Well, we can pay you," Tapia said.

"Sure, I can do that," Sifuentes replied.

Tapia used the video that Sifuentes created over the next 18 months to win the grand prize at the 2005 Pomona Super Chevy Show. It also made Sifuentes a minor celebrity in the applied mathematics community. Wright was so impressed by Sifuentes's talk on the video at a conference that she offered him a postdoc at Courant on the spot—only to learn that he had just begun his Ph.D. program.

TAPIA UNDERSTANDS that having a Ph.D. is no guarantee an elite department will hire you. But he says minorities face greater obstacles than simply a tight job market. One reason it's so important that Rice and other top-tier schools produce more minority graduates, he says, is that where students train is a huge factor in their careers. "Pedigree is alive and well," Tapia asserts. "So if minority students earn their degrees at minority-serving institutions, they won't get hired by Stanford."

Tapia works with graduating senior Ariel Nixon at his Rice University center.

But even a degree from a top school isn't enough to create a level playing field, Tapia adds. Minorities must also overcome an old-boy network that often excludes them from serious consideration. One science board member who heard Tapia's talk and agrees with his assessment says her institution is trying to ensure that departments cast a wider net during faculty searches.

"The idea of finding someone who is 'a good fit' is code for hiring somebody like themselves," says Deborah Ball, a mathematics educator and dean of the School of Education at the University of Michigan, Ann Arbor. "And that's no longer acceptable." Although senior university officers at Michigan don't tell departments whom to hire, she says, they have stopped searches that were insufficiently inclusive. A more diverse pool of applicants invariably leads to more minority hires, she adds.

Wolf, a former chair of the Rice mathematics department, has participated in many such searches. And although he says that Tapia has "done profound work for this country in advocating for underrepresented minorities," Wolf maintains that he exaggerates how much weight math departments place on an applicant's research history.

"If the overall record of a candidate leaves you pretty sure the person will never manage to produce research at the level of the top disciplinary journals, then the candidate does not meet your standard," Wolf says. "But my experience nationally suggests that, once a standard is met, then hiring decisions certainly take into account the other ways that a candidate would contribute, for example, in helping to mentor a diverse student population."

Wolf fears that some people will interpret his defense of high standards as prejudice. In fact, his actions demonstrate a strong commitment to diversity: Three years ago, he convinced senior university officials to fund a summer program he runs that helps a subset of the entering class—many of them minorities—acclimate to the rigors of a Rice education.

Tapia himself doesn't lay all blame for the status quo on the academic establishment. "In the 1960s you couldn't say that culture played a role because everything was about the 'system,' " he explains. "But today African-Americans and Mexican-Americans have to question certain parts of our culture. Why is the culture of Jewish-Americans or Asian-Americans so positive in terms of pursuing an academic career? And how can we enhance our culture to include some of those values?"

Sifuentes is wrestling with those issues as he hunts for a tenure-track job. Wright had stayed in touch with him after hearing his Heavy Metal talk, and in 2010 Sifuentes and his wife arrived in New York City so that he could take up a postdoctoral position at Courant.

But the high cost of living put a serious strain on their finances, he says, and the arrival of a baby meant additional responsibilities. Both he and his wife also missed their families in Texas. So in 2012 Sifuentes left Courant ahead of schedule to become a visiting assistant professor at Texas A&M University, College Station, where he was assigned undergraduate teaching duties along with his research.

In making the move to what is essentially a second postdoc, Sifuentes lost the chance to concentrate on churning out papers—in his case, on iterative methods to solve large linear systems of equations. The desire to live near their relatives led to another fateful decision, namely, to restrict his search for a faculty position to Texas. "I would like to see you rise to the top because you're so talented," Wright says she told him at one point. "And that probably means somewhere not in Texas."

In hindsight, Sifuentes admits she was right. But he doesn't think all of his wounds are self-inflicted. At one university that invited him to apply for an opening, he says, several faculty members expressed an interest in working with him and the job interview itself seemed to go well. "But then I learned they said I came across as very cocky," he says.

"Richard had told me that I'm going to hear that sort of comment a lot," Sifuentes says. " 'A white man is confident,' he would say, 'but a Mexican-American is cocky.' "

Anecdotes like that persuade Tapia that the fight against discrimination is far from over. Finding a worthy successor to a charismatic founder of an organization is never easy, however, and it may be especially hard in Tapia's case. "Richard has clout on campus. He's a fighter, and he has the respect of both the faculty and the university administration," says a former longtime colleague at the Tapia Center, Cynthia Lanius.

A Houston math teacher who left the classroom to help Tapia ramp up his center, Lanius successfully wrung money out of NSF, the Alfred P. Sloan Foundation, and other funding organizations. But last year she retired, and this year the center's current budget of $250,000—from donations and "a tiny bit from Rice," Tapia says—is half what it had been a few years ago. "We need a big hit," he admits.

It's not clear what will happen if he doesn't succeed. "Yes, I'm 75. But I don't have any plans to retire," he says. "I have tried to educate people about what I've done. And I hope that a young person will come out of the wilderness to say that they want to go forward."

Bryant York has a simple solution. Two decades ago, NSF's computer science directorate asked York, a computer scientist at Portland State University in Oregon and a national leader in efforts to broaden participation in science, what it could do to attract more minorities into the field. York worked on the project for a year. But he summed up his findings in one sentence: "If you want to solve the underrepresentation problem, clone Richard Tapia." ■

Decades-long excavations in a working coal mine have revealed evidence of startlingly early group hunting and sophisticated weapons making.

The killing ground

Clues from a German coal mine show how early hunters lived, 300,000 years ago, and how their prey died

By **Michael Balter,**
Schöningen, Germany

Just outside this sleepy town of 13,000, about 90 kilometers east of Hanover, lies a vast open coal mine, one of northern Germany's great lignite mines. The site is also rich in archaeological remains, and starting in 1983, archaeologists were let in to do "rescue excavations." They dug just ahead of the 40-meter-high mining machines that were ripping away millions of years of Earth's geological history.

One cloudy fall day in 1995, Wolfgang Mertens, a burly, bearded former forestry worker from Schöningen who had been hired by dig director Hartmut Thieme to help excavate, struck a wooden object with his trowel. "It looks like a spear," Mertens told Thieme, then with the Lower Saxony State Service for Cultural Heritage (NLD) in Hanover. But Thieme was dubious, Mertens recalls, because the object was broken in several pieces—and because they were digging in sediments dating back several hundred thousand years, before hominins were thought to have invented sophisticated hunting technologies. "Where's the spear's point?" Thieme asked.

Before long, Mertens had found it, along with two other complete spears—slender javelins about 2 meters long made from spruce trees. Closely associated with the spears were the remains of nearly 2 dozen horses, many showing signs of having been heavily butchered.

"I didn't believe it at first," says archaeologist Nicholas Conard of the University of Tübingen in Germany, whom Thieme invited to take a look. But over the next few years, excavators found several more spears, eventually identifying as many as 11. When Thieme first reported the dis-

PHOTO: JORDI SERANGELI

Published by AAAS

coveries in *Nature* in 1997, along with their initial dating—400,000 years old—they electrified the archaeological community. With one swift thrust, the paper pierced the dominant paradigm of the day, which held that hominins at that early time, well before the rise of modern humans, were scavengers rather than hunters, lacking the cognitive skills to make such sophisticated weapons or mount organized hunts for large game. To top it all, Thieme found what appeared to be four hearths, which were then considered the earliest evidence for controlled use of fire. "Schöningen was one of those sites that revolutionized our views about earlier humans," says John Shea, an archaeologist at Stony Brook University in New York. "It just goes to show that the easiest way to be wrong in paleoanthropology is to underestimate our ancestors' abilities."

But Thieme's initial report also marked the opening chapters of a detective story, as the first revelations begged further questions. How did the spearmakers actually live? What kind of environment did they inhabit? And why did they abandon so many seemingly valuable weapons in the first place? In search of answers, a multidisciplinary team led by Conard and University of Tübingen archaeologists Christopher Miller and Jordi Serangeli took over excavations in 2008 and launched intensive new investigations.

"The site still stands as critically important because of the spears," says Thomas Wynn, an archaeologist at the University of Colorado, Colorado Springs. But the new research, much of which will be reported online later this year in about 20 papers in a special issue of the *Journal of Human Evolution* (*JHE*), is changing archaeologists' views of Schöningen in important ways—and overturning some of Thieme's original interpretations. The site appears to be younger than he thought, 300,000 rather than 400,000 years old, and his claim to have found hearths has not stood up. Although the total number of horses represented at the site now stands at more than 50, researchers now doubt that they were killed in a single spectacular, coordinated orgy of mass butchery. Instead, the bones and spears are thought to represent multiple, smaller events that took place over years, decades, or even centuries, at a site that was a vibrant crossroads for wildlife and humans.

Just how those events unfolded is more mysterious than ever: The spears and horse bones were apparently deposited not on dry land but rather in a lake, under a meter or two of water. That finding has sparked hypotheses ranging from winter hunts on a frozen lake to lightning strikes. As Miller puts it, "Schöningen is so unusual, it causes archaeologists to think down crazy paths, but we have to be creative to explain it."

Schöningen has yielded as many as 11 of the oldest complete wooden spears, about 2 meters long and made of spruce and pine.

PHOTO: © E. BEHRENS AND C. S. FUCHS/NIEDERSÄCHSISCHES LANDESAMT FÜR DENKMALPFLEGE

"YOU MUST IMAGINE that there was a large lake here, and we are standing at the edge of it," says Serangeli, who supervises the excavations. Cyclical changes in water level left a layer cake of black and gray bands in the sediments, which are up to 45 meters thick and overlie the much older coal deposits. Pollen trapped in the sediments shows that the lake margin "was a very wet environment, very swampy, with a very rich plant life," says team member Brigitte Urban, a paleoecologist at Leuphana University of Lüneburg in Germany.

That's what makes the site so valuable today: Wooden objects that ended up in the muck were preserved by low oxygen levels. Defying decay, broad chunks of oak, alder, and birch trees poke through the wet sediments, the waterlogged wood still fresh after 300,000 years. For archaeology, the harvest has been extraordinary, Conard says: "Ninety percent or more of the wooden artifacts from the Middle Pleistocene"—from about 780,000 to 125,000 years ago—"are at Schöningen."

The ancient swamp was rich in wildlife and prehistoric humans, either early Neandertals or members of a species called *Homo heidelbergensis,* widely believed to be the common ancestor of Neandertals and modern humans. "It seems like a special place that attracted both horses and hominins," Miller says. Work by Urban and other team members suggests that although the lake's water level rose and fell, it persisted through 200,000 years of changing climates.

Meat was not the only attraction for the Schöningen hominins. "For daily life you need plants as food, bedding, and so on," says Gerlinde Bigga, an archaeobotanist at Tübingen. With Urban, she found that the lakeshores abounded in hazelnuts, acorns, and fruits including raspberries, as well as reeds and sedges from which bedding could have been made.

All the spears were made from spruce trees except one—which was made of pine. And yet Urban found little evidence of spruce pollen anywhere near Schöningen.

Hunting trophy. The skull of a horse on display at Schöningen's new museum is one of about 50 killed and butchered by the hunters.

That means, she says, "that people had to walk a long distance" from where the spears were made to the lake where they were used—a conclusion that Urban says conflicts with Thieme's original interpretation of Schöningen as a large "hunting camp," where hominins were resident much of the year.

Similarly, Thieme's picture of large-scale slaughter, with dozens or even hundreds of hunters attacking a large herd of horses, has not held up. Instead the hunts were small, and the kills accumulated over time, as hominins returned to the lake again and again over hundreds or even thousands of years.

The evidence comes straight from the horses' mouths. Two research subgroups, one led by archaeologist Marie-Anne Julien, now at the University of Southampton in the United Kingdom, and the other by Florent Rivals, a paleoecologist at Rovira i Virgili University, Tarragona, in Spain, analyzed the horses' teeth for strontium, oxygen, and carbon isotopes—indications of what the animals had eaten and where they had lived. They also looked at patterns of abrasion on the teeth, which hold clues about what the animals ate just before they died. The isotopes and wear pointed to considerable variation in both diet and habitat among the horses, indicating that they came from different places and were killed at different times.

Smaller scale hunting suggests less social complexity than Thieme envisioned, with groups of perhaps 20 to 30 people—much smaller than the dozens or hundreds of hunters necessary to kill 50 horses at a time, researchers say. "Thieme's interpretation is an extreme interpretation of the social complexity of early hominins," Conard says. "A lot of people would be uncomfortable attributing these kinds of behaviors to *Homo heidelbergensis*."

"A succession of single kills is a better fit with what little we know of group size from archaeological sites," Wynn adds. Shea agrees: "One, maybe two or three horses ought to be enough to leave all of a *Homo heidelbergensis* group lying on their backs, bellies distended, swearing off horse meat for the next week or two." (Thieme, who retired from the Hanover unit several years ago, could not be reached for comment despite repeated attempts to locate him.)

The spears, however, continue to astonish. They "were skillfully made, with planning and forethought," says Chris Stringer, a paleoanthropologist at the Natural History Museum in London who is not a member of the team. And they were startlingly ancient: The only other sign of weaponry this old is a 400,000-year-old fragment found in 1911 at Clacton-on-Sea in the United Kingdom. Understanding just how the Schöningen spears were made and used and the cognitive abilities they betray looms large in the team's research priorities.

PHOTO: © J. LIPTAK/NIEDERSÄCHSISCHES LANDESAMT FÜR DENKMALPFLEGE

In a 2009 paper titled "How to think a simple spear," Miriam Haidle, an archaeologist at Tübingen, detailed the elongated chain of steps required to make and use them: First, recognize that the group needed food; then procure the wood to make a wooden tool; then use the wooden tool to knap a stone tool; then carve a previously procured tree branch into a spear. Finally, the group had to wield the spears skillfully to kill an animal.

In the *JHE* special issue, the first in-depth study of the weapons and how they were manufactured adds detail to this picture. Researchers led by archaeologist Thomas Terberger of NLD found that the growth rings in the spruce shafts are narrow, indicating that the trees grew slowly in cool conditions, leading to a very hard wood. The branches used were at least 50 years old, and the hominins chose thin ones—between 2.4 and 4.7 cm in diameter—to make the slender, elegant weapons. Marks from stone tools indicate that all the bark was stripped from each branch and the wood knots were carefully trimmed off.

"The analyses demonstrate a sophisticated sequence of production steps, reflecting long experience in the manufacturing of wooden tools and weapons," the researchers conclude in their report. In experiments with replicas of the spears, the group found that they could be thrown up to 35 meters, accurately enough to hit and seriously wound large animals. Nevertheless, some experts, including Stringer and Shea, have suggested that the spears were not thrown from a distance but rather employed at close quarters as thrusting weapons. Each year, Shea says, he offers students $20 if they can hit him with a replica spear from even a fairly close distance. "Haven't had a scratch in more than 20 years," he says.

While the discovery of the Schöningen spears startled many archaeologists, who had assumed that only modern humans had the smarts to make them, researchers now say the find should not have been such a shock. The spears are "a miracle of preservation, not a cognitive threshold," says John Speth, an archaeologist at the University of Michigan, Ann Arbor. "The cognitive capacities that made this possible could easily predate Schöningen by hundreds of thousands of years." Even chimpanzees have been observed stripping leaves from slender branches, trimming them to a point, and using them to poke at prey. And Speth says researchers working at the famous Olduvai Gorge in Tanzania "have made a pretty good case that early hominins were already ambush hunting pretty large ungulates at 1.8 million years ago," although others are skeptical (*Science*, 17 September 2010, p. 1464).

The bones and spears may have been deposited in an ancient lake.

PHOTO: NICHOLAS CONARD

"The easiest way to be wrong in paleoanthropology is to underestimate our ancestors' abilities."

John Shea, Stony Brook University

FUTURE EXCAVATIONS have several mysteries to solve, starting with the possible use of fire. The ancient hunters "must have had fire, how else could they have survived?" Conard says, pointing out that the winters back then were at least as cold as today. But traces of fire use are elusive. Thieme had identified four hearths, based on a reddish color in the sediments he thought was the result of burning, along with cracks perhaps due to high heat. He preserved the hearth sediments in wooden cases for future study, and a research subgroup led by Tübingen archaeologist Mareike Stahlschmidt, and including Miller, Tübingen petrologist Bertrand Ligouis, and others, recently reopened the cases and put the sediments through a variety of tests. The results, in press in the *JHE* special issue, show no traces of burning, and the reddening that Thieme saw appears to be due to iron compounds that precipitated as the lake levels rose and fell.

Then there is the question of how the horses came to die in the middle of a lake. Both spears and horse bones appear to have been deposited in 1 to 2 meters of water, rather than on dry land. Key to this conclusion is the work of Ligouis, who found that the artifact-bearing sediments contain traces of lake algae, sponges, and small crustaceans that live only in deep water. Miller and Stahlschmidt say their own analysis of the spear-bearing sediments shows no sign that the artifacts were ever on dry land.

Team members have scrambled to come up with explanations. Miller speculates that in winter, the hominins chased horses out onto the ice and butchered them there; when the ice melted, everything sank. Serangeli proposes that some of the horses were killed by lightning while drinking from the lake and then butchered by hominins lurking nearby. That may sound far-fetched, but such strikes are fairly common; in 2012, a lightning strike killed 143 goats in Xinjiang, China. Other team members suggest that the hominins somehow killed and butchered the horses in the open water.

Conard is having none of this. He thinks that the evidence for deep water must be plain wrong. "The hunting events were probably on the margin of the lake, that's much more plausible," he says. Team member Jörg Lang, a geologist at the University of Hanover in Germany, agrees. Lang says his group has found that "the artifacts were deposited on the exposed delta plain," or perhaps in shallow pools, and quickly covered by waterlogged sediments.

Conard says the team will continue to dig at Schöningen for at least another 25 years, which may just be enough time to solve these lingering mysteries. Meanwhile, the mine will cease operating in 2017, and local authorities are discussing the idea of refilling the deeper levels with water—a process that may take decades—to reform the ancient lake. If that happens, hominins will once again roam its shores, although this time pushing strollers rather than throwing spears. ■

INSIGHTS

Biofuel models and measurements *p. 1095*

Toward better social systems through big data *p. 1097*

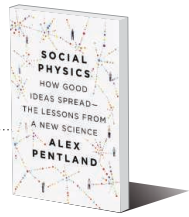

PERSPECTIVES

Cod catches at Senjahopen on the Norwegian coast.

PHOTO: GUNNAR SÆTRA/HAVFORSKNINGSINSTITUTTET/INSTITUTE OF MARINE RESEARCH

ECOLOGY

Change is coming to the northern oceans

Cod and pollock abundances and distributions shift as climate and ocean conditions change

By **Anne B. Hollowed**[1] *and* **Svein Sundby**[2]

The cold-temperate regions of the North Pacific and North Atlantic oceans, from about 40°N latitude to the Arctic fronts, support large and productive fisheries (*1*), particularly in the northernmost regions: the Bering Sea in the Pacific and the Barents Sea in the Atlantic. The two main near-bottom fish species in the Bering and Barents seas are walleye pollock (*Gadus chalcogrammus*) and Atlantic cod (*G. morhua*), respectively. In the past decade, the two species have responded differently to ocean warming. These response patterns appear to be linked to a complex suite of climatic and oceanic processes that may portend future responses to warming ocean conditions.

The largest Atlantic cod stock, Northeast Arctic (NEA, Arcto-Norwegian) cod (*2*), feeds in the Barents Sea up to the Arctic front and spawns farther south along the Norwegian coast. Year-class strength is governed by a complex suite of processes during the first year of life. Temperature serves as a proxy for several of these processes. Some studies found that strong year classes were formed at the beginning of warm phases (*3*), whereas others reported that high water temperature was a necessary but not sufficient condition for the formation of strong year classes (*4*). Interannual temperature variations influence recruitment from year to year, but longer-term variations also influence stock structure and distribution. During warming phases, the spawning stock biomass gradually builds up and the cod spawn farther north, whereas in cooling phases, spawning stock biomass decreases and spawning occurs farther south (*5*).

Since the 1980s, increasing ocean temperatures have been accompanied by a steady increase in spawning stock biomass

Published by AAAS

of NEA cod, reaching more than 2 million metric tons (see the figure, panel A) and a record-high northward distribution in 2012 (*6*). The increase in abundance and the poleward displacement of the cod stock reflects a general pattern in other components of the ecosystem, from zooplankton to plankton-eating and fish-eating fish (*6*). A similar change was observed during the mid-20th century warming from the 1920s to the 1940s (*7*).

These findings suggest that the trends in the distribution and abundance of NEA cod are related to both direct and indirect temperature influences on the cod (*5*). These effects include food web changes and changes in fishing pressure. Since 2000, reductions in NEA cod due to fishing and natural causes were below the increases due to reproduction and growth, whereas during the cool period of the 1960s and 1970s, losses due to fishing and natural causes exceeded replenishment from growth and reproduction (*6*). History has shown that it is more difficult to keep catches within the more restrictive quotas that are set during cool phases when stock size is low than in warming phases, when quotas increase due to increased productivity of the stock. This implies that historically annual fishing changes may have amplified the downward trend of the NEA cod stock abundance during cooling phases and the upward trend of the stock during warming phases.

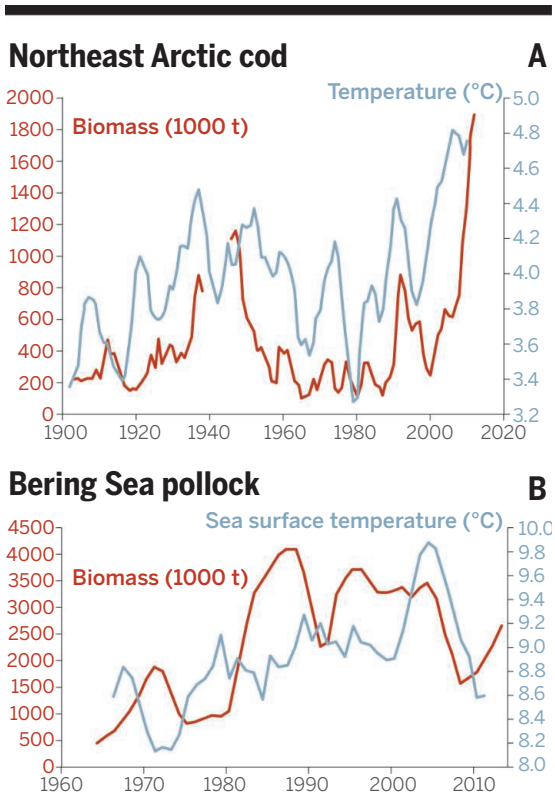

Response to seawater temperature trends. The productivity of cod in the Barents Sea and pollock in the Bering Sea varies in concert with the changing climate. (**A**) Five-year moving average of annual mean temperature, cod catches (1903 to 1938), and cod spawning stock biomass (since 1946) in the Barents Sea. (**B**) Five-year moving average SSTs over the southeast Bering Sea shelf region (July to September) and walleye pollock spawning biomass. For data sources, see (*15*).

On the opposite side of the Arctic, the Bering Sea pollock stock is the largest in the northeast Pacific Ocean. Bering Sea pollock typically spawn in the southeastern Bering Sea and feed throughout the middle and outer shelf regions. They generally avoid bottom waters below 0°C and are thus mostly found in the southern Bering Sea (*8*). In warm years, when very cold bottom waters are confined to the north, pollock tend to expand across the shelf.

The pollock spawning stock consists of several age groups, and trends in abundance therefore represent a lagged response to previous patterns in year-class strength (see the figure, panel B). Pollock year-class strength is governed by a complex suite of ecological processes, including prey quality, quantity, and availability; predation (including cannibalism); and accumulation of sufficient energy reserves to allow overwintering (*9*). Ocean temperature and timing of seasonal sea ice retreat influence these processes by affecting stratification, biogeography, and the timing and intensity of spring blooms (*10*).

Climate forcing has influenced trends in ocean temperature variation in the Bering Sea (*11*). The late 1970s marked the onset of a period of warm SSTs that persisted through the 1990s (see the figure, panel B). Since then, the region experienced an exceptional warm period from 2000 to 2005, followed by sustained cold bottom temperatures and moderate SSTs from 2006 to 2013 (*11*). Based on empirical analyses of available data, summer SSTs appear to be related to survival in the first year of life (*9*, *10*). The relation between spawning biomass and the 5-year running mean of summer SST is less clear for pollock than for cod, possibly because of nonlinear responses to environmental conditions and because the pollock stock has historically been fished at sustainable levels.

The response of seafloor fish species in the border regions between the boreal and Arctic domains to climate variability may provide clues to how future anthropogenic climate change will influence fish stocks and marine ecosystems at high latitudes. Atlantic cod has already reached the shelf break between the Barents Sea and the deep Polar Basin (*6*); no further advancement toward the North Pole is possible for this shelf species. Instead, the species may advance eastward along the Siberian Shelf as new cod habitats open due to the loss of sea ice at the Siberian shelf and the Northeast Passage. In the northern Bering Sea, sea ice is expected to continue to form in fall and winter, leaving a remnant cold pool in summer, and the northern regions of the Bering Sea are thus likely to remain generally inhospitable to pollock (*12*). Projections of annual survival of young of the year are more uncertain because of the complex suite of interacting processes that govern their survival. Interdisciplinary programs that target these processes will improve the scientific understanding of climate change impacts on these important fish stocks. ■

[1]*Alaska Fisheries Science Center, National Oceanic and Atmospheric Administration, National Marine Fisheries Service, Seattle, WA 98115, USA.* [2]*Institute of Marine Research and Hjort Centre for Marine Ecosystem Dynamics, 5005, Bergen, Norway. E-mail: anne.hollowed@noaa.gov; svein.sundby@imr.no*

REFERENCES AND NOTES

1. S. Gaichas *et al.*, *Prog. Oceanogr.* **81**, 47 (2009).
2. O. Nakken, *ICES Mar. Sci. Symp.* **198**, 212 (1994).
3. B. Sætersdal, H. Loeng, *Fish. Res.* **5**, 253 (1987).
4. B. Ellertsen, P. Fossum, P. Solemdal, S. Sundby, *Rapp. P.-V. Reun.- Cons. Int. Explor. Mer* **191**, 209 (1989).
5. S. Sundby, O. Nakken, *ICES J. Mar. Sci.* **65**, 953 (2008).
6. O. S. Kjesbu *et al.*, *Proc. Natl. Acad. Sci. U.S.A.* **111**, 3478 (2014).
7. K. F. Drinkwater, *Prog. Oceanogr.* **68**, 134 (2006).
8. S. Kotwicki, R. R. Lauth, *Deep-Sea Res. II* **94**, 231 (2013).
9. R. A. Heintz, E. C. Siddon, E. V. Farley Jr., J. M. Napp, *Deep Sea Res. II* **94**, 150 (2013).
10. F. Mueter *et al.*, *ICES J. Mar. Sci.* **68**, 1284 (2011).
11. J. E. Overland, M. Wang, K. R. Wood, D. B. Percival, N. A. Bond, *Deep-Sea Res. II* **65–70**, 6 (2012).
12. M. F. Sigler *et al.*, *Oceanography* **24**, 250 (2011).
13. International Council for the Exploration of the Sea, Report of the Arctic Fisheries Working Group, 18 to 24 April 2013 (ICES Headquarters, Copenhagen, 2013); ICES CM 2013/ACOM:05.
14. North Pacific Fishery Management Council (NPFMC), *Bering Sea Aleutian Island Groundfish Stock Assessment and Fishery Evaluation Report* (NPFMC, Anchorage, AK, 2013), chap. 1.
15. Data sources, panel A: Annual mean temperatures from Kola Section station number 4-7 at depths of 0 to 200 m, from the Polar Research Institute of Marine Fisheries and Oceanography, Murmansk (www.pinro.ru); Northeast Arctic cod catches from (*2*); Northeast Arctic spawning stock biomass from (*13*). Panel B: SSTs from (*10*); spawning stock biomass from (*14*).

ACKNOWLEDGMENTS

The authors thank R. Heintz, J. Ianelli, P. Livingston, F. Mueter, M. Sigler, and T. Van Pelt for helpful comments and suggestions. The findings and conclusions are those of the authors and do not necessarily represent the views of the National Marine Fisheries Service of the National Oceanic and Atmospheric Administration. This project was supported by NPRB and is BEST-BSIERP Bering Sea Project publication #140.

10.1126/science.1251166

PLANETARY SCIENCE

Speed metal

Meteorite dating reveals that planetary core formation is a relatively fast process

By **Tim Elliott**

As in many building booms, planets were put together pretty rapidly. Transforming nebular dust to fully formed planets took less than ~100 million years of the ~4.5 billion years of solar system history. Accurate determination of the rates of planetary growth is key for understanding these tumultuous beginnings of the solar system, but obtaining high-precision ages on short-lived events that happened so long ago is a formidable challenge. On page 1150 of this issue, Kruijer *et al.* (*1*) determine with remarkable accuracy that planetary core formation began less than 1 million years after the first solids condensed—extraordinarily fast on geological time scales.

Planets are believed to grow by progressive accretion of smaller bodies (see the figure). Planetesimals are an intermediate step. They have radii up to a few hundred kilometers, which makes them sufficiently large to retain enough heat to melt or differentiate. During differentiation, metallic melts sink to form a core and silicate melts rise to form a crust. The larger asteroids, such as 4 Vesta, represent differentiated planetesimals. Asteroids are held in orbit between Mars and Jupiter, having been thwarted from further growth by Jupiter's gravitational influence, and provide a frozen snapshot of activity that has long since run to completion elsewhere. Some meteorites—ejected fragments of asteroids that land on Earth—are derived from such differentiated bodies, and they provide samples that allow this early period of planetary growth to be studied. Kruijer *et al.* focus on the iron meteorites, which represent fragments of disrupted planetesimal cores.

The chronometer of choice is the radioactive decay of hafnium isotope ^{182}Hf to tungsten isotope ^{182}W, which has been of great value elsewhere in dating early solar system processes (*2*). The half-life of ^{182}Hf is only 9 million years, so it gives a high-resolution chronology over a period of ~50 million years at the beginning of the solar system when ^{182}Hf was extant. Although precise, such "extinct" isotope systems only provide ages relative to other dated objects (*3*). The oldest objects in the solar system, millimeter-sized calcium- and aluminum-rich inclusions (CAIs) from primitive meteorites, are often used as a reference. Over early solar system history, the decay of ^{182}Hf leads to changing ^{182}W/^{184}W. During planetary melting, W is strongly partitioned into the core-forming metal phase, while Hf is left behind in the outer silicate portion of the planet. This process effectively freezes the ^{182}W/^{184}W ratio at the time of core formation and enables the core to be dated relative to evolving planetary ^{182}W/^{184}W (expressed as ε^{182}W or the parts per 10,000 deviation of ^{182}W/^{184}W relative to a reference silicate Earth value). Thus, low (unradiogenic) ε^{182}W in iron meteorites means an early-formed core.

Kruijer *et al.* are not the first to note that extremely unradiogenic W in iron meteorites implies planetesimal core formation within the first few million years of solar system history (*4*–*6*). However, they comprehensively address what has been a major problem to the accuracy of all previous studies, namely the pernicious influence of cosmic rays in perturbing W isotope ratios at the required level of precision. The W isotope chronometer is sensitive to its past exposure to cosmic rays. Kruijer *et al.* use an elegant means to overcome this problem by making simultaneous platinum (Pt) isotope measurements to monitor the received dose of cosmic rays in each meteorite. Pt isotope ratios are more sensitive than W to the influence of cosmic rays but should be constant in all meteorites. Primary ε^{182}W can therefore be obtained by back-correcting to a common, unperturbed Pt isotope ratio. This is more easily said than done, and the coupled, high-precision Pt and W data sets presented in this study are an isotopic tour de force.

With the effects of cosmic rays removed, Kruijer *et al.* can date robustly the timing of planetesimal core formation. This endeavor is further helped by the recent reassessment of initial ε^{182}W of the CAI datum (*7*), against which ages are measured. Thus, Kruijer *et al.* demonstrate that the sinking of metal in planetesimals is indeed speedy, occurring in as little as 0.6 ± 0.3 million years after the condensation of the first dated objects (CAIs) in the solar system, presenting an appreciable constraint for numerical accretion models.

Furthermore, Kruijer *et al.* are able to discern differences in the timing of core formation between different planetesimals, represented by the different iron meteorite groups. Such differences were previously unresolvable. Kruijer *et al.* discuss an interesting model, which relates the timing of core formation to the variable amounts of sulfur (S) in the parent bodies. This approach makes good conceptual sense because the contents of volatile elements, such as S, vary widely in meteorites and planetary bodies. More S should lead to a larger amount of core formation at lower temperatures, earlier on in a planetesimal's history. In Kruijer *et al.*'s highly simplified thermal model, the time difference between initial segregation

Planetary core formation. Planets grow by accreting smaller objects. At some point, differentiation occurs where metals sink to form a core, and silicates rise to form a crust. Accurate dating of meteorites reveals that the core forms very fast, within 1 million years of the first solids condensing in the early solar system (*1*).

ILLUSTRATION: FAHAD SULEHRIA/WWW.NOVACELESTIA.COM AND SANTIAGO BILLY

School of Earth Science, University of Bristol, Queen's Road, Clifton BS8 1RJ, UK. E-mail: tim.elliott@bristol.ac.uk

of a S-rich metallic melt and final formation of S-free metallic melt is ~0.4 million years, a time scale sufficient to account for the spread in their W isotope data.

To put these ages of core formation into perspective, it is worth comparing them with ages of chondrules. These quenched melt droplets are the principal constituent of most primitive, undifferentiated meteorites, traditionally taken to be the building blocks of planets. Much recent effort has been expended in dating chondrules, and although some are as old as CAIs (*8*), most are ~1 million years younger (*9*, *10*). Thus, chondrules were being formed, before their accretion into chondrites, at the same time as fully formed planetesimals were segregating cores. Presumably the respective parent bodies of iron meteorites and chondrites formed in different parts of the nebular disk to allow these very different accretion rates. The refined, rapid time scales of core formation presented by Kruijer *et al.* underline the notion that chondritic meteorites themselves did not accrete to form planets, even if their compositions do provide a valuable guide to bulk planetary composition.

Finally, it is worth noting that the apparently youngest core formation age occurs in iron meteorites (IVB), which are also distinct in other aspects of their isotopic composition (*11*, *12*). Although Kruijer *et al.* have carefully corrected the $\varepsilon^{182}W$ for estimated effects of W isotope heterogeneity, possible differences in Pt isotopes (and thus an influence on the cosmic ray correction) and even the initial amount of ^{182}Hf remain to be assessed. This reemphasizes an age-old problem in distinguishing between time and initial isotopic composition in high-precision chronology. Nevertheless, for the majority of the samples studied here, the new data yield unprecedentedly accurate timing of the earliest stages of planetary formation. ■

REFERENCES

1. T. S. Kruijer *et al.*, *Science* **344**, 1150 (2014).
2. T. Kleine *et al.*, *Geochim. Cosmochim. Acta* **73**, 5150 (2009).
3. N. Dauphas, M. Chaussidon, *Annu. Rev. Earth Planet. Sci.* **39**, 351 (2011).
4. T. Kleine, K. Mezger, H. Palme, E. Scherer, C. Münker, *Geochim. Cosmochim. Acta* **69**, 5805 (2005).
5. A. Scherstén, T. Elliott, C. Hawkesworth, S. Russell, J. Masarik, *Earth Planet. Sci. Lett.* **241**, 530 (2006).
6. A. Markowski, G. Quitte, A. N. Halliday, T. Kleine, *Earth Planet. Sci. Lett.* **242**, 1 (2006).
7. C. Burkhardt, T. Kleine, N. Dauphas, R. Wieler, *Astrophys. J.* **753**, L6 (2012).
8. J. N. Connelly *et al.*, *Science* **338**, 651 (2012).
9. Y. Amelin, A. N. Krot, I. D. Hutcheon, A. A. Ulyanov, *Science* **297**, 1678 (2002).
10. N. T. Kita, H. Nagahara, S. Togashi, Y. Morishita, *Geochim. Cosmochim. Acta* **64**, 3913 (2000).
11. M. Regelous, T. Elliott, C. D. Coath, *Earth Planet. Sci. Lett.* **272**, 330 (2008).
12. L. P. Qin *et al.*, *Astrophys. J.* **674**, 1234 (2008).

10.1126/science.1254943

NEUROSCIENCE

Memories—getting wired during sleep

Sleep gives dendritic spines staying power

By **David R. Euston** *and* **Hendrik W. Steenland**

The idea that sleep enhances memory has a long history, but only in the last 20 years has it gained solid empirical support. Many studies have shown that sleep deprivation impairs skill learning (*1*). Moreover, learning enhances oscillations in the brain's electrical activity known as "slow waves" which occur during deeper stages of sleep. The strength of these oscillations also predicts future memory-based performance (*2*). But how exactly does sleep benefit memory? On page 1173 of this issue, Yang *et al.* (*3*) show that sleep influences changes in neuronal connectivity after learning.

Studies in invertebrates and mammals have suggested that learning increases the strength of the connections, or "synapses," between neurons (*4*). Given that skill learning is often enhanced during sleep, one would expect to see concomitant increases in synaptic strength. However, in many studies, sleep actually decreases synaptic strength. In mice, the number of dendritic spines on neurons, which correlates with the number of synapses, increased during wakefulness and decreased after a period of sleep (*5*). This led to the idea that sleep is a time for reducing the number of synaptic connections to enhance the information storage capacity of the brain (*6*). That sleep strengthens learning but weakens synapses presents a seeming paradox.

Another outstanding issue is how sleep leads to synaptic change. Theory suggests that during sleep, the brain replays or "reactivates" neural activity patterns corresponding to recently learned experiences, thus enabling the modification of synaptic connections necessary to stabilize memory (*7*). This replay of recent experiences during sleep has indeed been observed in several areas of the brain in both rodents and monkeys (*8*–*10*). What has been missing is direct evidence that this reactivation is actually tied to learning rather than being just an epiphenomenon.

To address whether synaptic strength increases or decreases during sleep, Yang *et al.* used a powerful technique to visualize dendritic spines in the motor cortex of live mice. The mice were genetically engineered to express a fluorescent protein in a subset of cortical cells. A small window was created in the skull, allowing microscopic imaging of dendritic spines repeatedly over the course of hours or even days. This technique was previously used to show that training mice to stay atop a rotating rod—an acquired skill—induced the formation of new dendritic spines in the motor cortex (*11*). Further, the rate of new spine formation was correlated with the degree of task improvement. These findings provided direct evidence that synaptic change in the mammalian cortex underlies learning. Yang *et al.* extend these findings, showing that learning-induced spine changes are segregated on specific dendritic branches. After learning, when two branches on the same dendritic arbor were examined, one typically showed many more new spines than the other. If mice were subsequently trained on a different skill (i.e., running backward on the spinning rod), the new

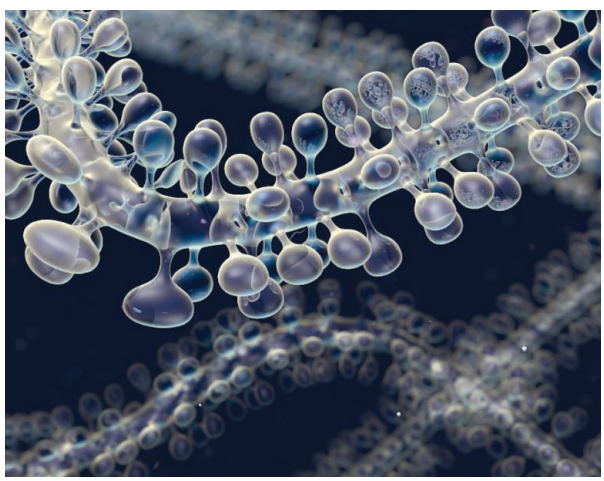

ILLUSTRATION: C. BICKEL/*SCIENCE*

Canadian Centre for Behavioral Neuroscience, University of Lethbridge, Lethbridge, Alberta T1K 3M4, Canada. E-mail: david.euston@gmail.com

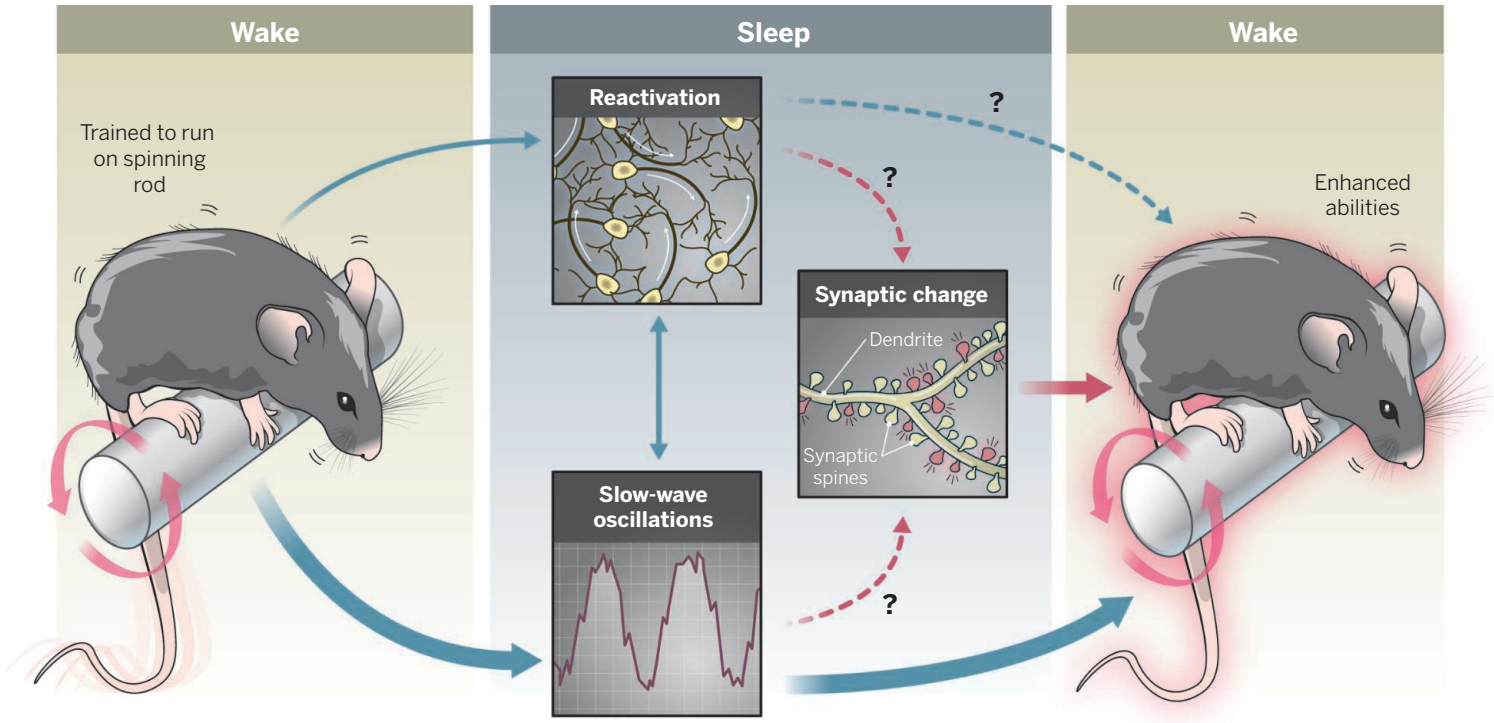

Sleep and memory. Three phenomena that occur during sleep have been linked to memory enhancement—slow-wave oscillations in brain electrical activity, reactivation of recent experiences, and changes in synaptic connectivity but the strength of the evidence (indicated by arrow thickness) varies. As shown in red, Yang *et al*. link both reactivation and slow-wave sleep to changes in synaptic connectivity that enhance learning.

spines induced by the second task grew selectively on the previously underproductive branch. Hence, different skills seem to be localized on different dendritic branches.

To test the role of sleep in spine formation, Yang *et al*. repeated their experiment with and without an 8-hour period of sleep deprivation immediately after training. Sleep deprivation markedly decreased the number of new spines. This effect also was branch-specific in that sleep deprivation reduced spine formation primarily on the dendritic branch with the higher number of new spines. Importantly, sleep had no effect on the rate of spine elimination. The authors also observed that sleep made newly formed spines much more likely to still be present 1 day later, consistent with the idea that consolidated memories are less sensitive to decay. In other words, sleep gives spines staying power.

The results of Yang *et al*. show that, at least under some circumstances, sleep can lead to the growth of new synapses (see the second figure,). What conditions promote an increase rather than downscaling? One factor may be the recency of learning. In the study of Yang *et al*., mice were trained on a motor skill just before the sleep session. In a different study, specific visual experience caused strengthening of synapses in the developing visual cortex during sleep (*12*). By contrast, studies showing reductions in connection strength typically have not involved specific training (*6*). Perhaps synapses that are forged during recent experiences undergo strengthening whereas synapses representing more distant memories undergo downscaling.

What about the relationship between reactivation of experience-dependent activity patterns and learning? Yang *et al*. used a genetically encoded calcium-sensitive indicator to visualize the firing (i.e., spiking electrical activity) of individual neurons in the motor cortex before, during, and after training on a treadmill running task. Consistent with observations in other cortical areas (*9*, *10*), motor cortex cells that fired many spikes during training tended to have elevated firing rates after training. Not only was there reactivation in the motor cortex after skill learning, reactivation was also sensitive to the same manipulations that affected dendritic spine growth. The drug MK801, which interferes with synaptic plasticity, blocked both task-induced spine growth and reactivation. Similarly, training mice on a second motor skill midway through the sleep session reduced both spine growth and reactivation. These manipulations support the supposition that reactivation is the mechanism underlying dendritic plasticity during sleep and help elucidate the mechanisms of sleep-dependent memory consolidation.

Like skill learning, the memory for places and events (i.e., "episodic memory") is also strengthened during sleep (*1*). Are episodic memories stored via synaptic changes in cortex? When do these changes occur? Using Yang *et al*.'s techniques, we may soon have the answers. Their approach brings us tantalizingly close to seeing sleep-related memory formation in action. Combining calcium-based measures of firing activity with direct imaging of dendritic spines could finally address whether, as postulated 65 years ago by neuroscientist Donald Hebb (*13*), cells that fire together, wire together and thereby form a memory. ■

REFERENCES

1. R. Stickgold, *Nature* **437**, 1272 (2005).
2. S. Diekelmann, J. Born, *Nat. Rev. Neurosci.* **11**, 114 (2010).
3. G. Yang *et al.*, *Science* **344**, 1173 (2014).
4. M. Mayford, S. A. Siegelbaum, E. R. Kandel, *Cold Spring Harb. Perspect. Biol.* **4**, a005751 (2012).
5. S. Maret *et al.*, *Nat. Neurosci.* **14**, 1418 (2011).
6. G. Tononi, C. Cirelli, *Neuron* **81**, 12 (2014).
7. J. L. McClelland *et al.*, *Psychol. Rev.* **102**, 419 (1995).
8. M. A. Wilson, B. L. McNaughton, *Science* **265**, 676 (1994).
9. K. L. Hoffman, B. L. McNaughton, *Science* **297**, 2070 (2002).
10. D. R. Euston, M. Tatsuno, B. L. McNaughton, *Science* **318**, 1147 (2007).
11. G. Yang, F. Pan, W. B. Gan, *Nature* **462**, 920 (2009).
12. S. J. Aton *et al.*, *Neuron* **61**, 454 (2009).
13. D. O. Hebb, *The Organization of Behavior; a Neuropsychological Theory* (Wiley, New York, 1949).

10.1126/science.1255649

ILLUSTRATION: C. BICKEL/*SCIENCE*

ATMOSPHERIC SCIENCE

Just add aerosols

Data from clean regions of the atmosphere show how little aerosol is needed to change clouds

By **Lorraine A. Remer**

The more carbon dioxide and other greenhouse gases in the atmosphere, the stronger the climate warming that results. Likewise, the more aerosol particles suspended in the atmosphere, the greater the ability of these particles either to scatter sunlight back to space and cool the planet or to absorb sunlight in the atmosphere, thereby warming the atmosphere while cooling Earth's surface. However, not all such climate forcing processes depend linearly on the concentrations of their forcing agent. The climatic effects of aerosols are complicated by their interactions with clouds (*1*). On page 1143 of this issue, Koren *et al.* (*2*) show that even small additions of aerosol particles to clouds in the cleanest regions of Earth's atmosphere will have a large effect on those clouds and their contribution to climate forcing.

Some aerosols act as cloud condensation nuclei, providing the seed that allows water vapor in supersaturated conditions to condense to form a cloud droplet and begin the cloud-creation process. Changing the amount of aerosol particles available to form cloud droplets directly affects the number and size of the cloud droplets in that cloud, which in turn will affect the subsequent cloud development and its climatic effect. Clouds with more or more broadly distributed cloud droplets are brighter and reflect more sunlight back to space, leading to cooling. Taller clouds have colder tops and emit less infrared radiation, leading to warming.

Observational and modeling studies have provided insights into the associations between changing aerosol concentrations and cloud properties. However, the processes are complex, spanning many orders of magnitudes from microscopic particles to large weather systems. Because of this complexity, observations tend to be uncertain and may be misinterpreted, and models can only parameterize some of the most important processes.

Part of the problem is a tendency to look for associations between clouds and aerosols in regions where aerosol concentrations are high, and especially where human activities are responsible for these high aerosol loadings. If aerosol-cloud climate forcing were monotonically and linearly linked to the concentrations of aerosol particles, then the strongest changes to clouds should occur in biomass-burning smoke plumes and downwind from highly polluted urban-industrial regions. However, this is not the case. Rather, aerosol-cloud climate forcing, through the cloud condensation nuclei process, is most pronounced at low concentrations of aerosol particles and saturates at moderate to high concentrations (*3*). Adding more particles to a location with limited water vapor availability cannot increase the number of cloud droplets indefinitely. Thus, quantifying aerosol-cloud climate forcing requires data from locations with very low aerosol concentrations, far from human activities.

Clouds in clean air. Koren *et al.* show how the addition of small amounts of aerosol changes the properties of pristine clouds, such as those shown here above the Cape Verde Islands off the western coast of Africa.

Koren *et al.* now quantify aerosol-cloud climate forcing with data from the cleanest regions of Earth's atmosphere. They find that the cloud fraction doubles under modest increase of aerosol and that this increase of bright cloud against the dark background of the ocean increases the amount of sunlight scattered back to space. This allows less solar energy to be absorbed by the Earth system, creating a negative forcing of -15 W m^{-2}. This is close to the value observed by direct satellite measurements of radiative flux changes due to enhanced aerosol over pristine ocean caused by a venting volcano (*4*). Koren *et al.* also use a numerical simulation to show that additional aerosols allow more water mass to condense in the initial stages of cloud development. The polluted cloud can then push this mass higher before the onset of mass-induced drag forces impedes cloud growth.

Without aerosol particles there would be very few clouds. A world with fewer clouds would reflect much less solar radiation back to space. Koren *et al.* suggest that the bulk of the aerosol-cloud forcing caused by human activities occurred at the beginning of the industrial era, when the world changed from pristine to slightly polluted. However, the world has always had clouds, because the atmosphere has always contained aerosols. Natural processes such as wind erosion, breaking waves, volcanoes, and biological excretions put particles into the air. In fact, the particles that Koren *et al.* analyzed in their study over the clean oceans were likely natural and not created by human activities.

Implicit in the estimates of aerosol climate forcing is the assumption that the natural processes and natural particles are constant in time and that century-long changes to the global aerosol burden are due to the overlay of human activity on the natural condition. We have no means to determine the actual preindustrial aerosol distribution to verify this assumption, though on decadal time scales we know that the background aerosol state is not constant. Volcanic eruptions are intermittent and weather patterns create droughts that change soil moisture and dust aerosol production (*5*). By focusing on pristine oceans, Koren *et al.* emphasize the necessity of characterizing background aerosol conditions and even small perturbations from those conditions, to quantify the full aerosol forcing of climate change. ■

Joint Center for Earth Systems Technology, University of Maryland Baltimore County, 5523 Research Park Drive, Baltimore, MD 21228, USA. E-mail: remer@umbc.edu

REFERENCES

1. D. Rosenfeld, S. Sherwood, R. Wood, L. Donner, *Science* **343**, 379 (2014).
2. I. Koren, G. Dagan, O. Altaratz, *Science* **344**, 1143 (2014).
3. I. Koren *et al.*, *Science* **321**, 946 (2008).
4. T. Yuan *et al.*, *Atmos. Chem. Phys.* **11**, 7119 (2011).
5. M. Chin *et al.*, *Atmos. Chem. Phys.* **14**, 3657 (2014).

10.1126/science.1255398

AGRICULTURE POLICY

EU agricultural reform fails on biodiversity

Extra steps by Member States are needed to protect farmed and grassland ecosystems

By **G. Pe'er***†, **L. V. Dicks**, **P. Visconti**, **R. Arlettaz**, **A. Báldi**, **T. G. Benton**, **S. Collins**, **M. Dieterich**, **R. D. Gregory**, **F. Hartig**, **K. Henle**, **P. R. Hobson**, **D. Kleijn**, **R. K. Neumann**, **T. Robijns**, **J. Schmidt**, **A. Shwartz**, **W. J. Sutherland**, **A. Turbé**, **F. Wulf**, **A. V. Scott**

In December 2013, the European Union (EU) enacted the reformed Common Agricultural Policy (CAP) for 2014–2020, allocating almost 40% of the EU's budget and influencing management of half of its terrestrial area. Many EU politicians are announcing the new CAP as "greener," but the new environmental prescriptions are so diluted that they are unlikely to benefit biodiversity. Individual Member States (MSs), however, can still use flexibility granted by the new CAP to design national plans to protect farmland habitats and species and to ensure long-term provision of ecosystem services.

POLICY

Agricultural expansion and intensification are important global drivers of biodiversity loss and ecosystem degradation (*1*). In Europe, habitats associated with agriculture, such as grasslands, heathlands, and peatlands, support threatened and declining species and provide important ecosystem services, yet have the worst conservation status among all ecosystems (*2*). Declines in species richness seem to have slowed for a few taxa in parts of northwestern Europe (*3*), albeit at a biodiversity-impoverished status quo.

Expansion of the EU and its common market continue driving agricultural intensification in Europe (*1*, *3*). Aided by CAP subsidies, the scale of agricultural operations is increasing throughout the EU [e.g., increasing holding size (see the chart)], with new MSs showing an increase in agrochemical inputs [e.g., fertilizers (see the chart)]. These processes, alongside peatland drainage and abandonment of seminatural grassland in less productive or accessible regions, lead to continuing decline of farmland biodiversity (*4*–*6*) (see the chart).

Certain problems relating to biodiversity decline are addressed through existing EU legislation and policies to protect the environment (e.g., directives on habitats, birds, water, nitrates, and sustainable use of pesticides), but the CAP has a much broader influence on ecosystems in the EU. With a total budget of €362.8 billion (U.S. $495.4 billion) for 2014–2020 (*7*), it provides finances, policy mechanisms, and control systems with higher environmental impact than all other policies and directives [supplementary materials (SM) part A]. Recognizing the role of the CAP for biodiversity, the EU Biodiversity Strategy for 2020 sets Target 3A to "maximise areas [...] covered by biodiversity-related measures under the CAP" (*8*). The CAP reform does not fulfill this target.

THE DILUTION OF AMBITION. When the European Commission launched the latest CAP reform in 2010, it outlined three main challenges: food security, environment and climate change, and maintaining the territorial balance and diversity of rural areas (*9*). To help address the second challenge, 30% of direct payments to farmers ("Pillar 1") were to become conditional on compliance with three "greening measures": establishing Ecological Focus Areas (EFAs) on 7% of farmed area, maintaining existing permanent grassland, and growing a minimum of three different crops on any farm with >3 ha of arable land. Yet after 3 years of negotiation (*10*), these measures now apply to roughly 50% of EU farmland, and most farmers are exempt from deploying them.

EFAs are now set at 5%, instead of 7%, and only on farms with >15 ha of arable land. Countries can reduce the requirement to 2.5% or lower in some regions (SM B). The area threshold exempts at least 88% of EU farms and over 48% of farmed area (table S1). Farms with permanent crops, grasslands, or pastures do not need EFAs. On the other hand, various land uses may qualify as EFAs, including nitrogen-fixing crops, catch crops, short-rotation coppice, and green cover. These land uses could help maintain soil and water quality

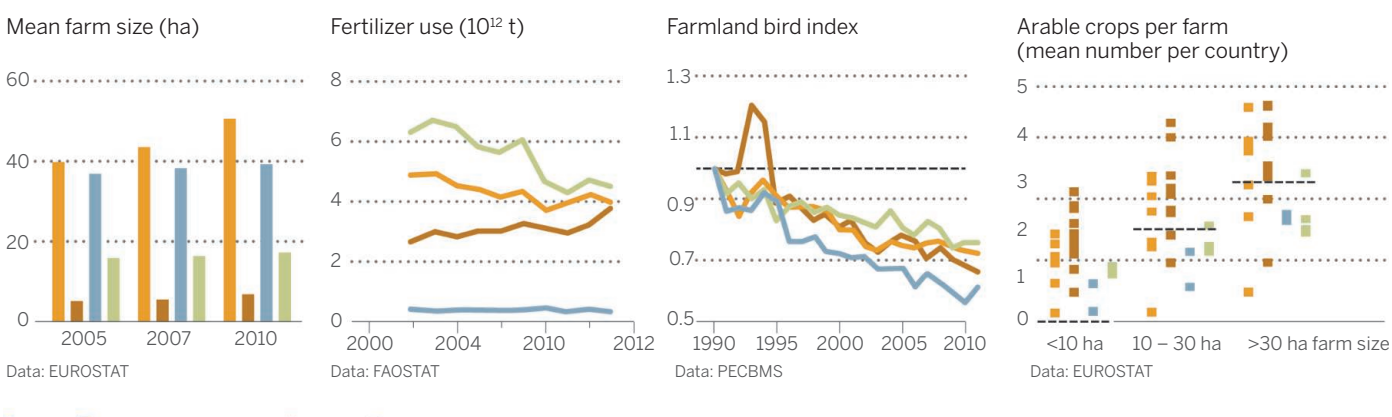

EU agriculture. (**Left**) Farm sizes are particularly large in Western and Northern Europe and have increased in Western Europe (+27%) and the new MSs (+30%) since 2005. (**Left middle**) Fertilizer use in new MSs has been increasing in the past decade (other types of agrichemical inputs show similar trends). (**Right middle**) The Farmland Bird Index (normalized to 1990 levels) declines throughout the EU. (**Right**) Average crop diversity in different MSs (symbols) compared with the minimum requirements set by the new CAP (horizontal lines). See SM for data sources and details.

but are not known to deliver benefits for biodiversity (*11*). In such a diluted form, and without specific management guidelines, EFAs will likely contribute little to biodiversity.

Permanent grasslands have decreased in cover by 6.4% between 1993 and 2011 in the EU and by 11.8% in new MSs (SM C). The new CAP aims to halt this decline, thereby reducing biodiversity loss and greenhouse gas emissions. But rather than maintaining all permanent grasslands, the reformed CAP allows a reduction of up to 5% in the net area of permanent grasslands at national or regional scales. Further degradation is permitted by the lack of habitat quality and management criteria. MSs are required to identify and protect ecologically valuable grassland within protected sites ("Natura 2000"), but outside these sites, farmers will continue receiving subsidies while converting low-input, extensively managed, species-rich grassland (*3*) to highly intensified, uniform, species-poor swards (*6*). The potential to maintain grassland biodiversity is further undermined by incomplete mapping, lack of differentiation among regions and grassland types, and a focus on net area without consideration of continuity and connectivity of existing seminatural grassland parcels.

The crop diversification measure obliges medium (10 to 30 ha) to large (>30 ha) farms to cultivate at least two or three crops, respectively (SM D). Farms with <10 ha of arable area (instead of 3 ha as originally proposed) are exempt, accounting for 92% of arable holdings in new MSs and 13% of arable area across the EU (table S4). Cultivating three crops on large, intensively managed farms is unlikely to enhance biodiversity (*11*). Moreover, in many MSs these targets are lower than current average crop diversity at the farm scale (see the chart). Combined with the absence of requirements regarding eligible crop types or rotation, this measure is unlikely to deliver benefits to biodiversity or soil quality, or to prevent further landscape homogenization.

Beyond those compulsory measures, the new CAP gives insufficient attention and financial support to sustainable farming in marginal, small-scale, and biodiversity-rich farms. Measures deployed within the framework of the Rural Development Regulation (Pillar 2), especially agri-environment-climate schemes (AESs) that farmers could take up voluntarily, can improve habitat quality and maintain biodiversity when they are well-designed, targeted, and financed (*12*). Yet funding for Pillar 2 will decrease in absolute terms by 18% from 2013 to 2020 [from €13.9 to 11.4 billion (~U.S. $19) annually, in 2011 prices] compared to a 13% reduction in Pillar 1 budget (*7*). Although the proportion of Pillar 2 funding earmarked for environmental measures has increased from 25% in the previous CAP period to 30% now, the budget needs to cover other activities, including climate change mitigation, organic farming, and so-called climate and environment investment measures—with potential for both positive and negative impacts on biodiversity (SM E).

Many EU politicians are announcing the new CAP as "greener," but the new environmental prescriptions are so diluted that they are unlikely to benefit biodiversity.

MSs have the flexibility to move some budgets from Pillar 1 to 2 ("modulation") but also vice versa ("reverse modulation"). The latter is already occurring in some MSs (SM E). Moreover, MSs still have to match Pillar 2 payments with national cofunding. Although the requirements for national cofunding were reduced in certain cases compared with the previous funding period, MSs may still lack the budgets required to unlock these resources or may prefer to allocate Pillar 2 funds to measures that are less beneficial for biodiversity. Too few developments in the new Pillar 2 regulations focus on improving cost-effectiveness in terms of uptake and biodiversity outcomes. One important advancement in some MSs, however, is encouraging farmers to act jointly toward achieving landscape-scale targets (see SM E).

Recommended immediate actions by Member States

1. Maintain or enhance the AES budget in Pillar 2 through budget modulation, prioritizing context-specific measures shown to support biodiversity and ecosystem services. Set clear and measurable targets that are coherent with the EU Biodiversity Strategy.
2. Use AESs to allow specific target groups (e.g., small holdings in marginal areas, young farmers, cooperating farmer groups) to profit from environmentally friendly practices or jointly provide landscape-scale benefits.
3. Ensure that eligible land uses for EFAs prioritize elements that benefit biodiversity and ecosystem services, including management prescriptions when necessary.
4. Complete identification and mapping of grasslands, with differentiation into types, qualities, and required management.
5. Allocate sufficient funding and effort within the Farm Advisory System to deliver ecological expertise to farmers as required.
6. Institute comprehensive provisions for monitoring biodiversity outcomes to evaluate the effectiveness of the agricultural policy against the targets set in the EU.

Agricultural intensification clearly provides some short-term economic gains for farmers and the food industry. But these have to be weighed against the loss of public goods, such as climate stability (*13*), landscape quality, and biodiversity (*13*, *14*) with associated environmental, health, and societal costs that are largely externalized from the farming economy. The EU acknowledges the importance of biodiversity through its 2020 biodiversity targets, as well as by endorsing the Aichi targets of the Convention on Biological Diversity, including strategic targets on sustainable agricultural production and consumption (goal 1, targets 4 and 7) and elimination of incentives harmful to biodiversity (target 3) (SM F). These strategic goals, developed from the evidence for the various costs of losing biodiversity and ecosystem services (*15*), would be undermined if MSs adopt the minimum requirements as set by the reformed CAP.

THE WAY FORWARD. The EU has lost an opportunity to design better guidelines to improve agricultural sustainability. Yet the increased devolution of responsibilities to individual MSs offers flexibility for promoting biodiversity and farmland ecosystems. We provide six recommendations for immediate action by MSs within the CAP implementation (see box) (SM G). In addition, we identify five actions for the EU to consider in its deliberations over the next CAP reform (details in SM H): (i) publish an evidence-based assessment of the CAP's impacts on farmland habitats, species, and ecosystem services, drawing on national-level monitoring as a base for improvements; (ii) increase the EU-wide AES budget, direct it to more effective incentives, and shift to outcome—rather than area-based targets; (iii) improve EFA effectiveness by reducing exemptions, refin-

*Author affiliations can be found in supplementary material (SM) on Science Online. †Corresponding author. guy.peer@ufz.de

ing management criteria for qualification, and expanding their total area, building on country-level evidence and experience (recommendations 3 and 6 to MSs); (iv) develop longer-term perspectives for more effective and comprehensive protection and restoration of grasslands and peatland; (v) reevaluate the usefulness of the crop diversity measure.

Our recommendations should encourage MSs and the EU to start moving toward more sustainable agriculture, securing food provision alongside biodiversity and ecosystem services for current and future generations. ■

REFERENCES AND NOTES

1. K. Henle *et al.*, *Agric. Ecosyst. Environ.* **124**, 60 (2008).
2. European Environment Agency, EU 2010 Biodiversity Baseline (Tech. Rep. No. 12/2010, EEA, Copenhagen, 2010).
3. L. G. Carvalheiro *et al.*, *Ecol. Lett.* **16**, 870 (2013).
4. T. G. Benton, J. A. Vickery, J. D. Wilson, *Trends Ecol. Evol.* **18**, 182 (2003).
5. R. D. Gregory, A. van Strien, *Ornitholog. Sci.* **9**, 3 (2010).
6. European Environment Agency, The European Grassland Butterfly Indicator: 1990–2011 (Tech. Rep. No. 11/2013, EEA, Luxembourg, 2013).
7. Directorate-General for Internal Policies, Policy Department B, Note: European Council Conclusions on the Multiannual Financial Framework 2014–2020 and the CAP (European Parliament, Brussels, 2013).
8. European Commission, Our life insurance, our natural capital: an EU biodiversity strategy to 2020 (European Commission, Brussels, 2011).
9. European Commission, The CAP towards 2020: Meeting the food, natural resources and territorial challenges of the future (European Commission, Brussels, 2010).
10. C. Rutz, J. Dwyer, J. Schramek, *Sociol. Rural.* (2013), doi: 10.1111/soru.12033.
11. L. V. Dicks *et al.*, *Conserv. Lett.* **7**, 119 (2014).
12. R. F. Pywell *et al.*, *Biol. Lett.* **8**, 772 (2012).
13. Millennium Ecosystem Assessment, *Ecosystems and Human Well-Being: Biodiversity Synthesis* (World Resources Institute, Washington, DC, 2005).
14. R. Bommarco, D. Kleijn, S. G. Potts, *Trends Ecol. Evol.* **28**, 230 (2013).
15. TEEB, *The Economics of Ecosystems and Biodiversity: Ecological and Economic Foundations* (Earthscan, London, 2010).

ACKNOWLEDGMENTS

We thank P. Ibisch, T. Vandermaesen, A. Barnett, E. Ellis, L. Podmaniczky, T. Hartel, J. Y. Humbert, M. Liebman, S. Becheva, G. Beaufoy, S. Boldogh, J. Tzanopoulos, J. Hegarty, T. Lancaster, and P. Vorisek for valuable inputs. G.P., K.H., and A.V.S. acknowledge EC FP7 projects SCALES (contract 226852), R.A. was supported by the Swiss National Science Foundation (31003A-120152) and the Swiss Government; A.A.B. and D.K. acknowledge EC FP7 project LIBERATION (311781); A.A.B. acknowledges MTA Lendület; W.J.S. acknowledges Arcadia; L.V.D. is funded by the Natural Environment Research Council (NE/K015419/1); The Pan-European Common Bird Monitoring Scheme is a joint initiative of the European Bird Census Council and the BirdLife International, funded by the EC and the Royal Society for the Protection of Birds.

SUPPLEMENTARY MATERIALS

www.sciencemag.org/content/344/6188/1090/suppl/DC1

10.1126/science.1253425

EVOLUTION

Energy at life's origin

Analysis of the bioenergetics of primitive organisms suggests that life began at hydrothermal vents

By **William F. Martin,[1] Filipa L. Sousa,[1] Nick Lane[2]**

Energy-releasing chemical reactions are at the core of the living process of all organisms. These bioenergetic reactions have myriad substrates and products, but their main by-product today is adenosine triphosphate (ATP), life's primary currency of metabolic energy. Bioenergetic reactions have been running in a sequence of uninterrupted continuity since the first prokaryotes arose on Earth more than 3.5 billion years ago, long before there was oxygen to breathe (*1*). Under what conditions did these bioenergetic processes first evolve?

Many ingenious ideas about energy at life's origins have nothing in common with modern life. It is conceivable that early life harnessed energy from volcanic pyrite synthesis (*2*), zinc sulfide–based photosynthesis (*3*), ultraviolet radiation, or lightning, yet none of these processes powers known microbial life forms. For biologists, the origin of energy-harnessing mechanisms used by real microbes is the issue. Recent studies point to parallels between the energy-harnessing systems of ancient microbes and the geochemistry of alkaline hydrothermal vents (see the figure), suggesting that natural ion gradients in such vents ignited life's ongoing chemical reaction.

How did the first cells harness energy? Because life arose in a world without molecular oxygen, some anaerobes are likely to be ancient, and anaerobic environments should harbor primitive bioenergetic reactions (*4*, *5*). Ancient anaerobic niches deep in Earth's crust often contain acetogens (bacteria) and methanogens (archaea), groups that biologists have long thought to be ancient (*4*). However, anaerobic environments harbor very little energy to harness (*6*, *7*). In the anaerobic environments of submarine hydrothermal vents, geochemically generated H_2 is the main source of chemical energy.

In addition to being strict anaerobes, acetogens and methanogens live from H_2, using the simplest and arguably most ancient forms of energy metabolism (*8*). Both synthesize ATP by reducing CO_2 with electrons from H_2 to make acetate and methane, respectively. They use a chemical mechanism called flavin-based electron bifurcation (*6*) to generate highly reactive ferredoxins—small, ancient iron-sulfur proteins (*5*) that are as central to their energy conservation as is ATP (*6*). The shared backbone of their energy metabolism is the acetyl–coenzyme A pathway, the most primitive CO_2-fixing pathway (*8*) and the one typical of subsurface microbes (*9*). Metabolism in these anaerobes is furthermore replete with reactions catalyzed by transition metals such as iron, nickel, molybdenum, or tungsten, another ancient trait (*2*, *5*–*8*).

... the primordial ATPase could have harnessed geochemically generated gradients at an alkaline hydrothermal vent.

All known life forms, including methanogens and acetogens, use two basic mechanisms to tap environmentally available energy and harness it as ATP. The first is substrate-level phosphorylation, in which highly reactive phosphate-containing compounds phosphorylate adenosine diphosphate (ADP) to make ATP (*6*, *10*). The energy conserved in ATP is released in a subsequent reaction that does chemical work for the cell or allows more sluggish reactions to go forward. The highly reactive phosphate compounds are generated during conversions of carbon compounds. Their synthesis is driven by environmental sources of chemical energy such as H_2 plus CO_2 that are harnessed during conversion to more thermodynamically stable compounds such as methane and acetate.

The second mechanism that cells use to harness energy involves ion gradients and is called chemiosmotic coupling. Here, an energy-releasing reaction is coupled to the pumping of ions across a membrane from inside the cell to the outside. The most common ions used for this purpose are protons,

[1]*Institute of Molecular Evolution, Heinrich-Heine-Universität, Universitätsstrasse 1, 40225 Düsseldorf, Germany.* [2]*Research Department of Genetics, Evolution and Environment, University College London, London WC1E 6BT, UK. E-mail: bill@hhu.de*

rendering the inside of a cell alkaline relative to the outside, but organisms in low-energy environments often use sodium (Na^+) ions (*6*, *7*). The energy stored in the ion gradient is then harnessed by an enzyme [an adenosine triphosphatase (ATPase)] to phosphorylate ADP.

Even the anaerobic energy misers, methanogens and acetogens, are chemiosmotic. They use an ATPase, but differ in the mechanism by which they generate their ion gradient (*6*–*9*, *11*). Both pump Na^+ ions, but the chemical steps that energetically support pumping differ in the two anaerobes. Acetogens pump while transferring electrons from ferredoxin to nicotinamide adenine dinucleotide (NAD^+); this energetically downhill (exergonic) reaction is catalyzed by a single protein complex (*9*). Methanogens pump while transferring a methyl group from one cofactor to another at a methyltransferase complex (*6*). These pumping reactions are far simpler and more primitive than those in oxygen-consuming respiratory chains. The anaerobic pumping systems also use chemically simple substrates (methyl groups, iron-sulfur clusters), which might be bioenergetic relics from the first free-living cells (*11*).

The chemistry that links acetogens and methanogens to each other also links them to alkaline hydrothermal vents. These vents harbor geological manifestations of both kinds of energy that are used by life: chemically reactive compounds (*12*) and natural proton gradients (*13*). And in contrast to "black smokers," which have life spans on the order of dozens of years, alkaline hydrothermal vents like Lost City (see the figure) (*14*) can remain active for up to 100,000 years (*15*), providing a constant source of gradients and chemical energy over geological time scales. This makes them unique among possible sites for life's origin. In addition, hydrothermal vents derive from reactions in Earth's crust and thus contain large amounts of catalytic transition metals (*12*, *13*). Vast networks of inorganic microcompartments in the vents provide mineral surfaces on which organic compounds can readily adsorb, providing a natural environment for concentrating these compounds on the early Earth. This process may have rendered the steep hurdles en route to chemical complexity more readily surmountable.

There are further similarities between geochemical reactions in hydrothermal vents and biological energy conversions. This is especially true for vents whose fluid contents are controlled by serpentinization, a sequence of geochemical reactions in which seawater circulating through hydrothermal systems reacts with Fe^{2+} in submarine crust, generating orders of magnitude more H_2 than acetogens or methanogens require (*6*) while also generating Fe^{3+} in the crust. At the same time, CO_2 is reduced to methane and formate, which are found at 1 and 0.1 mM concentrations, respectively, in the effluent of Lost City (*15*), one of the few alkaline vents that has been studied. Serpentinization and the accompanying CO_2 reduction are energy-releasing geochemical reactions (*14*). And chemiosmosis? The process of serpentinization not only generates a strongly reducing environment; it also makes the effluent alkaline. The Lost City effluent has a pH of about 10 (*14*, *15*), far more alkaline than ocean water, either now or 4 billion years ago, making these vents naturally chemiosmotic (*13*). The natural proton gradients at Lost City have the same magnitude and orientation as those in modern autotrophic cells.

The synthesis of high-energy bonds that underpin substrate-level phosphorylation can be catalyzed by metal ions alone (*2*); it does not require either proteins or membranes, whereas chemiosmotic synthesis of ATP requires both. This indicates that substrate-level phosphorylation came before chemiosmosis (*10*) in early bioenergetic evolution and powered the evolution of genes and proteins. The ATPase is as universal among cells as the ribosome and the genetic code and was clearly one of the earliest biological innovations. Indeed, the primordial ATPase could have harnessed geochemically generated gradients at an alkaline hydrothermal vent. This would explain why ATPase is universally conserved but ion-pumping mechanisms are not. What were the first ion-pumping mechanisms? The first step could have entailed a simple H^+/Na^+ antiporter that converted the proton gradient to a Na^+ gradient, as found in acetogens and methanogens. The invention of their simple pumping complexes, which use iron-sulfur clusters and methyl groups as substrates, would have enabled the emergence of the first free-living bacteria and archaea (*11*).

Research on the origin of life has long focused on chemical synthesis and the RNA world, neither of which pointed to specific early-Earth environments or specific groups of organisms as ancient. Hydrothermal vents like Lost City reveal exciting similarities between the energy-releasing geochemical reactions that occur there and the physiology of acetogens and methanogens. This striking convergence of geochemistry and microbiology unearths new opportunities for discovery. The chemistry of hydrothermal vents is vastly underexplored, and H_2-dependent anaerobic autotrophs are only beginning to relinquish their bioenergetic secrets. Energy-releasing processes that link the two might shed new light on biology's biggest question. ■

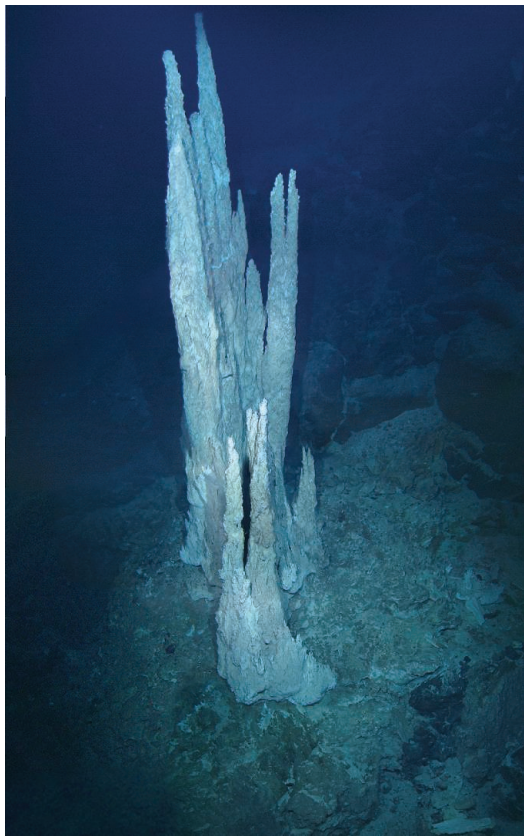

Clues to where life evolved. Similarities between bioenergetic processes and those at hydrothermal vents such as Lost City suggest that life may have evolved at such vents on the early Earth. This photo was taken at Lost City in 2005 using the remotely operated vehicle *Hercules*.

PHOTO: D. S. KELLEY AND M. ELEND/UNIVERSITY OF WASHINGTON, IFE, URI-IAO, LOST CITY SCIENCE PARTY, AND NOAA

REFERENCES AND NOTES

1. N. T. Arndt, E. G. Nisbet, *Annu. Rev. Earth Planet. Sci.* **40**, 521 (2012).
2. C. Huber, G. Wächtershäuser, *Science* **276**, 245 (1997).
3. A. Y. Mulkidjanian, A. Y. Bychkov, D. V. Dibrova, M. Y. Galperin, E. V. Koonin, *Proc. Natl. Acad. Sci. U.S.A.* **109**, E821 (2012).
4. K. Decker, K. Jungermann, R. K. Thauer, *Angew. Chem. Int. Ed. Engl.* **9**, 138 (1970).
5. R. V. Eck, M. O. Dayhoff, *Science* **152**, 363 (1966).
6. W. Buckel, R. K. Thauer, *Biochim. Biophys. Acta* **1827**, 94 (2013).
7. F. Mayer, V. Müller, *FEMS Microbiol. Rev.* **38**, 449 (2014).
8. G. Fuchs, *Annu. Rev. Microbiol.* **65**, 631 (2011).
9. D. Chivian *et al.*, *Science* **322**, 275 (2008).
10. J. G. Ferry, C. H. House, *Mol. Biol. Evol.* **23**, 1286 (2006).
11. N. Lane, W. F. Martin, *Cell* **151**, 1406 (2012).
12. J. A. Baross, S. E. Hoffman, *Orig. Life Evol. Biosph.* **15**, 327 (1985).
13. M. J. Russell, A. J. Hall, *J. Geol. Soc. London* **154**, 377 (1997).
14. T. M. McCollom, J. S. Seewald, *Elements* **9**, 129 (2013).
15. M. O. Schrenk, W. J. Brazelton, S. Q. Lang, *Rev. Mineral. Geochem.* **75**, 575 (2013).

ACKNOWLEDGMENTS

N.L. thanks the Leverhulme Trust and W.M. thanks the European Research Council for funding.

10.1126/science.1251653

INTERFACIAL CHEMISTRY

Disrupting dissolving ions at surfaces with fluid flow

Flowing solvent over a surface can dramatically change the rate of surface reactions and influence water structure

By **Glenn A. Waychunas**

Aqueous dissolution processes are not well understood on the molecular scale (*1*), and this has led to controversy, notably in geochemical systems (*2*, *3*). Charging of a solid surface, either by substitution of ions with a different valence (e.g., Ca^{2+} for Na^{+}) or by chemical binding of charged species from solution, orients the dipole moments of nearby water molecules. On the solution side of these dipoles, oppositely charged ions collect (*4*) and an electrical double layer (EDL) of different charges forms. Two prevailing assumptions about the EDL have been that water molecules and ions near the surface are not substantially perturbed by solution flow and that surfaces with low solubility have negligible effects on chemistry within the EDL. These notions are upset by the results reported on page 1138 of this issue by Lis *et al.* (*5*), who show both EDL sensitivity to flow-induced interface shear and substantial changes in surface charges as a result of dissolution processes on low-solubility surfaces.

Earth Sciences Division, Lawrence Berkeley National Laboratory, Berkeley, CA 94720, USA. E-mail: gawaychunas@lbl.gov

In the simplest case for dissolution of a surface, the coordination of a molecular species changes in a stepwise fashion, from bonding to other atoms in the solid atomic neighbors to a mixed surface-solution ligand environment and finally to a free solvated form (see the figure). These reactions are coupled to water molecules near the surface; their arrangement and reactivity depends on surface charge, interactions with local dissolved species, and hydrogen bond formation. The EDL is sensitive to this interfacial chemistry as well as the solution composition, so measurement of changes within the EDL potentially can be used to probe surface charge and obtain insight into interfacial chemistry.

Both aqueous dissolution and crystallization processes can be modeled well from several phenomenological perspectives, but the role of the solvent molecules in the various surface removal and incorporation steps is poorly known (*6*). Indeed, there is disagreement about water organization even on highly ideal surfaces (*7*). This issue, along with the technological difficulty of probing processes at a dissolving or crystallizing interface with bulk solution present, has restricted our understanding and control of aqueous interfacial processes.

Approaching these interfacial systems can be done computationally, but slow or rare process steps in systems comprising a complete EDL cannot be easily addressed [although progress is being made (*8*, *9*)]. However, experimental techniques can yield direct information on water dipole orientation, surface charge, and surface speciation at an aqueous interface. Sum-frequency generation (SFG) spectroscopy (*10*, *11*) can measure the orientation of near-surface water dipoles even under an aqueous layer thousands of times thicker. The signal obtained from the water dipoles is proportional to their net orientation in the surface field, and thus to the interfacial charge, and hence is potentially relatable to the chemical nature of the solid surface. Thus, with appropriate experimental approaches, information on the interfacial processes during a dissolution reaction might be obtained.

Lis *et al.* performed SFG experiments for calcium fluoride and fused silica surfaces using a fast-flow reactor to measure vibrational SFG spectra over the water and OH stretching regions. The spectral features in this region are highly sensitive to water dipole orientation, being minimal in amplitude if the water dipoles are random and cancel one another out, and maximal with a strong surface charge that orients the dipoles. They identified different surface processes by comparing the expected surface charges that

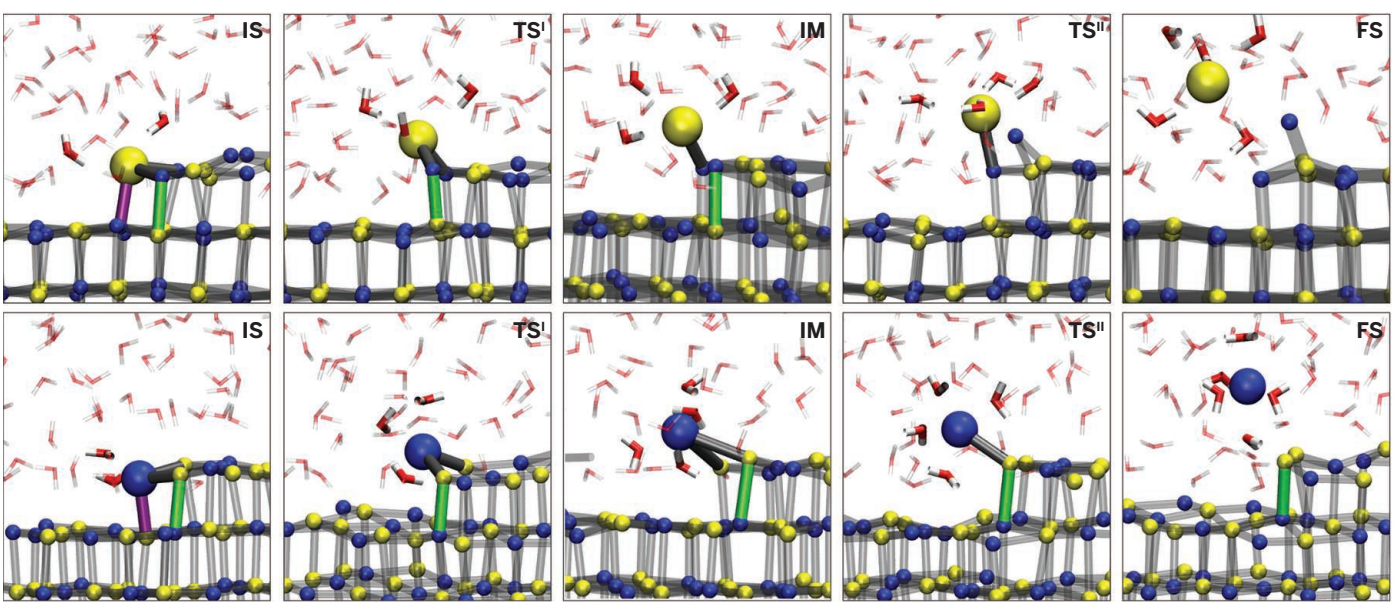

From salt to salt water. A theoretical study illustrates the steps in sodium chloride (NaCl) dissolution for (top) Cl^{-} and (bottom) Na^{+}. From left to right: initial state (IS); transition state 1 (TS^{I}); intermediate state (IM); transition state 2 (TS^{II}); and final solvated state (FS). If the solvated species are removed by flow, the back reaction (sorption or crystallization) is reduced and the forward reaction enhanced; net charge near the surface may be substantially altered [from (*9*)].

developed during hypothetical dissolution reactions and could compare interface chemistry both with and without solution flow.

In essence, Lis *et al.* show that the immediate products of dissolution are not held at the interface if there is sufficient shear induced by rapid laminar flow of fresh solution. In this case, the surface field is controlled by the immediate chemical composition of the interface and does not include contributions by the dissolution products near the interface. This result is not unforeseen, but it has not been measured directly until now. The difference between the high shear and static solution cases can change the surface charge enough to flip the average water dipole orientation 180°, which likely changes the positions and density of field-dissipating ions within the EDL. The consequences of flow effects on surface charge may be widespread.

The flow regimes used by Lis *et al.* are large compared with typical geochemical processes but could be reached near injection sites used for carbon dioxide sequestration or perhaps during fracking processes. In this case, modeling of interfacial charges and reactions may be inaccurate unless shear rate is considered. High fluid shear near pores in separation filters is another case where even small amounts of dissolution could create sensitivity to flow rates. Lis *et al.* also measured astonishingly long response times (tens to hundreds of seconds) for the interface to reestablish a steady state once the flow has been stopped. It may be possible, using pulsed flow experiments, to identify particular stages in the dissolution process. These times result from slow dissolution and finite solution diffusion rates and can be used to explore their kinetics, for example, as a function of time after the flow stops. These new observations ought to inspire others to examine molecular aqueous interfacial processes with renewed curiosity and ingenuity. ■

REFERENCES

1. C. A. Ohlin, E. M. Villa, J. R. Rustad, W. H. Casey, *Nat. Mater.* **9**, 11 (2010).
2. M. Urosevic *et al.*, *Geochim. Cosmochim. Acta* **80**, 1 (2012).
3. E. Ruiz-Agudo, C. V. Putnis, C. Rodriguez-Navarro, A. Putnis, *Geology* **40**, 947 (2012).
4. D. Henderson, D. Boda, *Phys. Chem. Chem. Phys.* **11**, 3822 (2009).
5. D. Lis, E. H. G. Backus, J. Hunger, S. H. Parekh, M. Bonn, *Science* **344**, 1138 (2014).
6. E. Vlieg, M. Deij, D. Kaminski, H. Meekes, W. van Enckevort, *Faraday Discuss.* **136**, 57, (2007).
7. J. Lützenkirchen *et al.*, *Adv. Colloid Interface Sci.* **157**, 61 (2010).
8. N. Holmberg, J.-C. Chen, A. S. Foster, K. Laasonen, *Phys. Chem. Chem. Phys.* **10**, 10.1039/c4cp00635f (2014).
9. L.-M. Liu, A. Laio, A. Michaelides, *Phys. Chem. Chem. Phys.* **13**, 13162 (2011).
10. Q. Du, E. Freysz, Y. R. Shen, *Science.* **264**, 826 (1994).
11. V. Ostroverkhov, G. A. Waychunas, Y. R. Shen, *Phys. Rev. Lett.* **94**, 046102 (2005).

10.1126/science.1254906

PHOTO: LORI ABENDROTH/IOWA STATE UNIVERSITY

PLANT SCIENCE

Best practices for biofuels

Data-based standards should guide biofuel production

By **Heather Youngs**[1] *and* **Chris Somerville**[1,2]

One reason for the use of biofuels is to reduce the greenhouse gas (GHG) emissions associated with liquid transportation fuels. However, the large amount of land needed to displace a sizable fraction of fossil fuel use has raised concerns that land will be used to produce fuels instead of animal feed and food, and that ecosystems may come under additional pressure. In considering the many different ways of producing such fuels, it is possible to envision both good and bad outcomes, depending on the approach (*1*). Thus, comments about biofuels in recent reports from Working Groups 2 and 3 (WG2 and WG3) of the Intergovernmental Panel on Climate Change (IPCC) (*2*, *3*) and a recent report by Liska *et al.* (*4*) have a special weight in the public discourse.

Since the positive treatment of biofuels in the 2007 IPCC report, a number of economic and life-cycle analysis (LCA) modeling studies have raised concerns. In particular, the use of an economic model to assess effects of indirect land-use change on GHG emissions (*5*) identified the possibility that biofuels may endanger ecosystems by stimulating expansion of agriculture but accomplish little or no reduction in GHG emissions. Subsequent studies have reduced the original estimates of such effects by an order of magnitude while accepting the basic premise (*6*). The IPCC WG3 carried out a detailed analysis of the impacts of biofuels in a special report in 2011 (*2*), which was abstracted into a series of out-of-context comments in the current IPCC WG2 report (*3*) that triggered recent criticism of biofuels. Indeed, the 2011 report emphasizes that, on the basis of LCA, biofuels can help reduce GHG emissions. However, it notes that production of biofuels must be carefully managed to prevent negative effects on food production, biodiversity, and social equity. In these and other respects, the 2011 report mirrors the academic literature, which abounds in hypothetical scenarios about possible negative effects of continued biofuel expansion. The abundance of such concerns highlights the importance of implementation, by both importing and producing nations, of standards based on verifiable sustainability criteria and good governance (*7*, *8*).

Many of the concerns about potential food-versus-fuel conflicts appear to be muted with regard to the pending development of cellulosic biofuels—liquid fuels made from the inedible body of plants. Several small commercial facilities in Europe and the United States recently began production, and several more are under construction in the United States and Brazil (see the second photo). Many of these facilities are using, or plan to use, crop residues such as wheat straw or corn stover (i.e., cobs, leaves, and stalks). Such sources seem attractive because they do not lead to land-use change or reduce the availability of grain. Thus, a recent claim by Liska *et al.*, on the basis of modeling results and a partial LCA, that the use of corn stover is unsustainable and does not result in fuels with reduced GHG emissions relative to gasoline has attracted attention.

Polyvinylchloride rings are installed to facilitate GHG measurement in a corn field site in Iowa.

Crop residues protect against erosion from wind and water, replenish mineral nutrients, and are the source of soil organic carbon (SOC) that supports soil ecosystems and contributes important physical qualities to soil. For decades, proponents of residue use (e.g., for animal feed, bedding, or biofuels) have grappled with understanding how much, if any, residue is required to provide such benefits. A recent study,

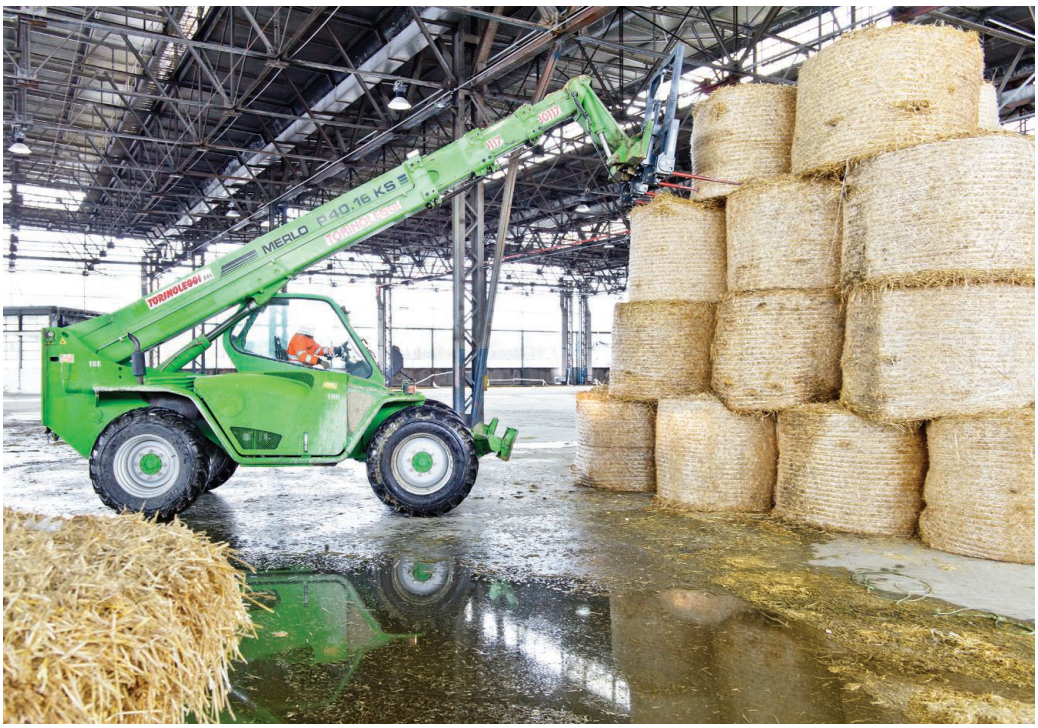

Biofuel bales. Wheat straw is readied for producing lignocellulosic ethanol at an advanced biofuels facility in Crescentino, Italy.

supported by the U.S. Department of Agriculture, reports the first 239 site-years of data collected from 36 research sites under various production systems such as no-till or conventional plowing (*9*) (see the first photo). Another study indicates that some residue can be sustainably removed from some locations, depending on factors such as biomass productivity, soil characteristics, soil management, water availability, and surface topography (*10*).

Liska *et al.* attempt to predict the SOC implications of stover removal for the entire U.S. corn crop using a model parameterized with measurements of the mineralization rate of various types of materials ranging from polysaccharides and polyphenols to microbial cells and plant residues from various locations around the world. The model correlates (within 20% error) with measurements of SOC from a single irrigated no-till continuous corn field, although the relevance of the parameters obtained in this way to corn stover at different locations around the United States is uncertain. The model output agrees with the view of soil scientists that removing all residues is detrimental; however, the story is more complicated at lower levels of removal, because of the high error ascribed to the model. One could interpret the output to indicate that 25 to 50% removal rates show no statistical difference from no removal, although a clear negative trend is evident; by contrast, the authors interpret the model to predict that removing any amount of stover tested (i.e., from 25 to 100%) will lead to soil carbon loss.

The LCA model used by Liska *et al.* does not incorporate GHG credits for using residual lignin for energy production in the bioconversion facilities, a point acknowledged by the authors, who also recognized that SOC loss might be offset by planting a fall cover crop or other management practices. Thus, ethanol from stover has not been shown to have higher GHG emissions than gasoline as reported in the general media (*11*). However, the most important unanswered question seems to be how well the model actually predicts what would happen under the diverse conditions that prevail in the corn belt soils. Soil scientists doing empirical studies emphasize that the outcome of stover removal is highly variable (*10*). It is possible that the single study site used by Liska *et al.* may not be suitable for stover removal.

Liska *et al.* also report that SOC decreased on a test site in which no stover was removed. Presumably this reflects the possibility that some corn-belt soils have not yet achieved SOC equilibrium after conversion from pre-agricultural conditions. By contrast, some high-yielding perennial grasses planted on former corn land substantially increase soil carbon, even when all aboveground biomass is removed (*12*).

The public attention associated with the report of Liska *et al.* exemplifies a disturbing trend in the treatment of model predictions as equivalent to knowledge or data based on actual measurement. Models are important tools, but they are often built on a partial state of knowledge and reflect assumptions and simplifications. Modern computing has enabled the creation of complex models with large underlying data sets, which reflect the intellectual contribution of many disparate disciplines, complicating, and possibly compromising, the peer review process of academic research. Because the model of Liska *et al.* predicts something that can be measured, the prediction will be tested by empirical studies that should ultimately settle the matter. In the interim, it is useful to bear in mind that much of the public discourse regarding biofuels is politically charged because biofuels have become a large disruptive activity that may benefit some sectors of society at the expense of others (e.g., the fossil fuels industry). It is therefore important that the scientific community remain clear about the relative power of measurements versus model predictions. ■

[1]*Energy Biosciences Institute, The University of California at Berkeley, Berkeley, CA 94720, USA.* [2]*Department of Arid Land Agriculture, Faculty of Meteorology, Environment and Arid Land Agriculture, King Abdulaziz University, Jeddah, Saudi Arabia. E-mail: crs@berkeley.edu*

REFERENCES AND NOTES

1. D. Tilman *et al.*, *Science* **325**, 270 (2009).
2. *IPCC Special Report on Renewable Energy Sources and Climate Change Mitigation*, O. Edenhofer *et al.*, Eds. (Cambridge Univ. Press, Cambridge/New York, 2011).
3. IPCC, *Climate Change 2014: Impacts, Adaptation, and Vulnerability. Contribution of Working Group II to the Fifth Assessment Report of the Intergovernmental Panel on Climate Change,* C. B. Field, V. Barros, K. Mach, M. Mastrandrea, Eds. (Cambridge Univ. Press, Cambridge/New York, 2014).
4. A. J. Liska *et al.*, *Nat. Clim. Change* **4**, 398 (2014).
5. T. Searchinger *et al.*, *Science* **319**, 1238 (2008).
6. T. W. Hertel, W. E. Tyner, *Global Food Secur.* **2**, 131 (2013).
7. G. P. Robertson *et al.*, *Science* **322**, 49 (2008).
8. N. Scarlat, J. F. Dallemand, *Energy Policy* **39**, 1630 (2011).
9. D. L. Karlen, J. M. F. Johnson, *Bioenerg. Res.* **7**, 465 (2014).
10. I. J. Bonner, D. J. Muth Jr., J. B. Koch, D. Karlen, *Bioenerg. Res.* **7**, 576 (2014).
11. D. Cappiello, Associated Press, 20 April 2014; http://bigstory.ap.org/article/study-fuels-corn-waste-not-better-gas.
12. K. J. Anderson-Teixeira *et al.*, *Ecosystems* **16**, 508 (2013).

ACKNOWLEDGMENTS

We thank S. R. Thomas and colleagues (U.S. Department of Energy, Bioenergy Technologies Office) for helpful insights and comments and L. Abendroth for the corn field site photo.

10.1126/science.1255812

PHOTO: FABRIZIO GIRALDI / WWW.FABRIZIOGIRALDI.COM AND VALENCIA RASETTO/BETA RENEWABLES

BOOKS *ET AL.*

SOCIAL NETWORKS

Stressing patterns of exchange

Social Physics
How Good Ideas Spread—The Lessons from a New Science
Alex Pentland
Penguin, 2014. 314 pp.

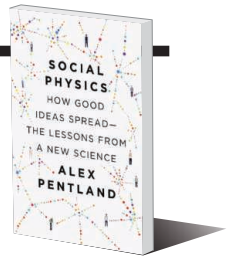

By **William P. Butz**

Who would not like to be able to predict weight gain, voting behavior, psychiatric disorders, and street crime; calculate optimum city size; encourage urban creativity; prevent waste of resources; or build a world without financial crashes or war? *Social Physics* presents an approach that aims to provide these abilities. Writing for a general readership, Alex Pentland presents a quantitative, predictive model—along with its action and policy implications—that cuts across so many phenomena and across such a wide range of scales that the total offering is "quite rare in any field of science and almost unheard of in the social sciences." Rather than focusing on markets (economics), classes (sociology), or location (geography), Pentland (MIT Media Lab) and co-investigators by the dozens hone in on the nature and number of social ties among individuals. The central hypothesis holds that with the emergence of today's hyperconnected societies, the optimal spread of new behaviors begins with an individual's broad exploration for new ideas, continues through more limited engagement to find the best ideas, and then proceeds to conversion of these to habits. The habits in the aggregate become compatible norms through social learning and social pressure. Through this process, social change occurs. Indeed, Pentland asserts that humans respond much more powerfully to social incentives than to incentives that involve only their own self-interest.

The explosion of big data documenting social interactions has made it possible to test this hypothesis and derived implications. The results might suggest how organizations and governments can employ social network incentives to alter the dynamics of the flow of ideas and thereby shape the spread of new behaviors. Pentland discusses a wide range of examples, only some of which address issues I listed above. Ultimately, the endeavor aims to engineer better social systems through a "practical science."

The study locales are as varied as the phenomena studied: from customers of a local utility, to credit card data from half the working adults in the United States, to the residents of an Italian town; from a variety of cities, to employees of large companies, to public advocacy groups around the world. Pentland refers to websites, peer-reviewed articles, and spin-off companies as well as organizations, companies, universities, and cities that have adopted policies based on the studies' findings.

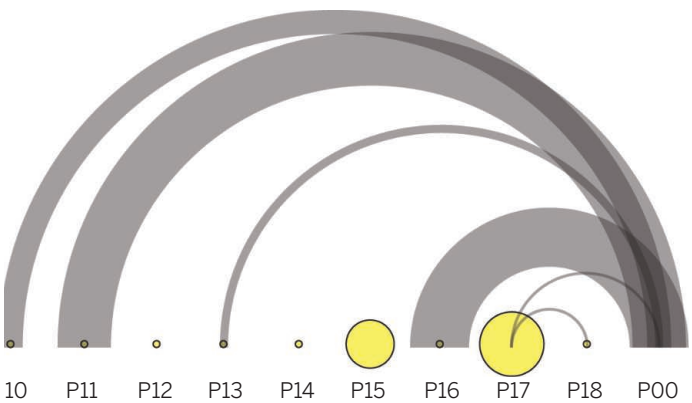

Poor exploration behavior. This "exploration dashboard" displays the pattern and amounts of interaction among (width of the arcs) and within (size of the circles) groups. Management (P00) is well engaged with only some groups, there is little other interaction between groups, and nearly all groups have almost no within-group interaction.

It is the extraordinary data that set the work Pentland discusses most apart. Gathered through a mobile sensor called a "sociometric badge" and behavior measurement software for iPhones (both developed by Pentland's team), diverse data on persons' activities and interactions are so extensive that they are measured in thousands or millions of hours. Combining these with survey data and other information on the study individuals produces scores of data sets of enormous breadth, depth, and complexity.

Regarding the research hypotheses that guide the analysis of the data, few, if any, are new, and the social sciences that have been testing them are not so hidebound as Pentland asserts. Referring to "standard" economic theory, "classic" models of class and specialization, and "historical" approaches ignores the substantial contemporary literatures on trust and social influence in economics and community effects in sociology, among other active subjects. Much imaginative and useful research refutes the blanket condemnation that "[t]he scientific method as currently practiced in the social sciences is failing us and threatens to collapse in an era of big data."

The book jacket trumpets the "stunning accuracy" of Pentland's approach, and the author assures readers that "[u]tilizing these equations, we can reliably predict what individuals will choose to do and how good their outcomes will be."

However, a thread of methodological difficulty runs through many of the reported studies. No matter the size of the sample, the fine grain of observation, or the time- and place-sequencing of hypothesized cause and effect, an investigator cannot establish the case for causality in the face of possible sample selectivity and unobserved heterogeneity. Third causes can thereby creep in, particularly where the research participants know that they are part of something special and therefore may behave differently, quite apart from any effect of the actual treatment. The resulting correlations are useful for some important purposes but not by themselves as a foundation for policy interventions. Simply recognizing the existence of these difficulties does not justify claims of causality without dealing with them directly.

Although arguably delivering neither a new science nor even a wholly new hypothesis, *Social Physics* presents considerable fresh evidence on the main hypothesis and many related questions. Pentland's informative and fascinating book may induce further use of the innovative data collection instruments that produce this evidence. It certainly advances consideration of the challenges and possibilities of using big data for organizational and social purposes. ■

10.1126/science.1254705

E-mail: william.butz@icloud.com

CREDIT: COURTESY ALEX PENTLAND/SOCIOMETRIC SOLUTIONS

LETTERS

Edited by **Jennifer Sills**

Overlooked local biodiversity loss

IN THEIR REPORT "Assemblage time series reveal biodiversity change but not systematic loss" (18 April, p. 296), M. Dornelas *et al.* summarized 100 time series of biodiversity monitoring programs and concluded that the world's biomes are "undergoing biodiversity change but not systematic biodiversity loss." This conclusion is misleading, given that Dornelas *et al.* did not account for several of the most pervasive processes known to drive biodiversity loss on the planet.

Jungle burned for agriculture in Southern Mexico.

Nowhere in their data set did Dornelas *et al.* consider the local losses of biodiversity that occurred as 13 million hectares of tropical rainforest were cleared each year from 1990 to 2010 (*1*). Nowhere in their data set did they account for local losses of biodiversity that have occurred as more than 90% of wetlands have been drained, more than 50% of grasslands destroyed, and 70% of Mediterranean and temperate woodlands cut down to make way for 4.9 billion hectares of cropland and pastures (*2*). Nowhere in their data set did the authors quantify losses of biodiversity that have occurred as 3.5 million km^2 of the world's land surface has been converted into urban environments (*3*). Their summary did not account for any direct impacts of habitat loss or land conversion, despite the fact that these are the most pervasive drivers of local diversity loss on the planet (*4*–*6*). Nor did Dornelas *et al.* account for other factors known to cause local diversity loss, such as extinctions caused by overexploitation of resources through hunting, poaching, and overfishing (*7*, *8*).

Instead, the authors focused on biodiversity trends in habitats that are mostly intact and yet to be fully exploited by humans. Because they did not make this important caveat clear, their paper could well be misinterpreted as evidence that human activities have not caused local biodiversity loss. Any accurate assessment of biodiversity change must not only include data from Earth's intact habitats; it must also account for diversity change in habitats that have already been lost, converted, and directly exploited by humanity.

Bradley Cardinale

School of Natural Resources and Environment, University of Michigan, Ann Arbor, MI 48103, USA.
E-mail: bradcard@umich.edu

REFERENCES

1. United Nations Food and Agriculture Organization (FAO), "Global Forest Resources Assessment" (FAO, Rome, 2010).
2. World Resources Institute, "Millennium ecosystem assessment, ecosystems and human well-being: Biodiversity synthesis" (Washington, DC, 2005).
3. Columbia University's Center for International Earth Science Information Network, "Global rural-urban mapping project (GRUMP)" (NASA Socioeconomic Data and Applications Center, Palisades, NY, 2011).
4. S. L. Pimm, P. Raven, *Nature* **403**, 843 (2000).
5. D. Tilman *et al.*, *Science* **292**, 281 (2001).
6. J. A. Foley *et al.*, *Science* **309**, 570 (2005).
7. J. B. C. Jackson *et al.*, *Science* **293**, 629 (2001).
8. J. Alroy, *Science* **292**, 1893 (2001).

Response

THE GOAL OF our study was to quantify biodiversity change on the planet in the recent past. Our approach was to include as many data sets as possible that met the following criteria: entire assemblages rather than just populations, standardized sampling repeated through time, and abundance of each species reported. The decision to include a data set was based exclusively on these criteria; we did not consider hypothesized drivers of change, whether habitats were pristine or modified, which taxa were sampled, or the location of samples. Strongly supporting the limited role of sampling bias in our results, another study (*1*) included mostly sites known to be heavily impacted by humans and also found, on average, little temporal change in alpha diversity of 168 terrestrial plant assemblages.

The data sets we used include both pristine and heavily exploited areas. Examples of the latter include data from a nuclear power station (*2*), an oil terminal (*3*), and fisheries data from the North East Atlantic (*4*). In our search for data, we did not find a data set that corresponded to a tropical area of active deforestation that matched our inclusion criteria. However, even a loss rate of 13 million hectares per year of tropical forest corresponds to less than 0.02% of the planet surface, making it unlikely that a before-after deforestation plot in tropical forest would be included in a random sample of the planet's surface. On the other hand, we did include a previously logged large plot of secondary tropical forest (*5*) and a 30-year data set that covers human-disturbed grassland, wetlands, and even suburban areas (*6*). Finally, as shown in Figure 2A of the original paper, our compilation included several data sets that show drastic declines in alpha diversity (the number of species at a given site), but these data sets are not the majority and are counterbalanced by other studies with increases in alpha diversity. In his Letter, Cardinale is selectively focusing on one end of the observed distribution of outcomes, and hence missing the bigger picture. Collectively, the data sets represented in our Report and in Vellend *et al.* (*1*) constitute the most rigorous bio-monitoring studies available on the planet, and their results merit careful consideration.

Cardinale implies that our paper's message is that we do not need to be concerned for the future of biodiversity. This is a misread of our results and discussion. First, we explicitly stated that our results do not contradict the fact that there is a rapid, recent decline in global biodiversity. Our analysis of alpha diversity addresses a different question at a different spatial scale. Second, our analysis of temporal beta diversity (the difference in species at one site over time) revealed that the species composition of communities is changing on average 10% each decade. Cardinale is silent about this alarming and hitherto unappreciated result, which deserves much additional attention and study. Transport of nonnative species, shifts in species geographic ranges, and the establishment of novel ecosystems are important drivers of the current biodiversity crisis, but they are acting mostly through changing which species are present, not decreasing the total number of species in any one location. This is a useful finding for conservation practice and in no way indicates that the status quo is acceptable.

The perfect data set to quantify biodiversity change would span several centuries, encompass multiple taxa, and contain a random sample of points over Earth's surface. We agree that such a data set is desirable, but it currently does not exist (*7*). These new analyses of biodiversity monitoring data [our Report and (*1*)] underline the urgent need for expanding investment and

harmonization in the collection of quality biodiversity data.

Maria Dornelas,[1]* Nicholas J. Gotelli,[2] Brian McGill,[3] Anne E. Magurran[1]

[1]Centre for Biological Diversity and Scottish Oceans Institute, School of Biology, University of St. Andrews, St. Andrews, Fife, KY16 9TH, UK. [2]Department of Biology, University of Vermont, Burlington, VT 05405, USA. [3]School of Biology and Ecology, Sustainability Solutions Initiative, University of Maine, Orono, ME 04469, USA.

*Corresponding author. E-mail: maadd@st-andrews.ac.uk

REFERENCES

1. M. Vellend *et al.*, *Proc. Natl. Acad. Sci. U.S.A.* **110**, 19456 (2013).
2. P. Henderson, R. Seaby, R. Somes, *J. Exp. Mar. Biol. Ecol.* **400**, 78 (2011).
3. J. J. Moore, C. M. Howson, "Survey of the rocky shores in the region of Sullom Voe, Shetland: A report to SOTEAG from Aquatic Survey & Monitoring Ltd." (Cosheston, Pembrokeshire, UK).
4. "Scottish West Coast Survey for Commercial Fish Species 1985–2013" (https://datras.ices.dk).
5. S. P. Hubbell, R. Condit, R. B. Foster, "Barro Colorado Forest Census Plot Data (2005)" (https://ctfs.arnarb.harvard.edu/webatlas/datasets/bci).
6. USGS Patuxent Wildlife Research Center. North American Breeding Bird Survey ftp data set, version 2014.0 (ftp://ftpext.usgs.gov/pub/er/md/laurel/BBS/DataFiles).
7. H. M. Pereira, L. M. Navarro, I. S. Martins, *Annu. Rev. Environ. Res.* **37**, 25 (2012).

Talk therapy results speak for themselves

THE NEWS FOCUS story "Talking back to madness" by M. Balter (14 March, p. 1190) highlights the importance of talk therapies as part of mainstream treatment of schizophrenia. Balter focuses largely on one form of psychotherapy, cognitive behavioral therapy (CBT), which helps positive, or psychotic, symptoms, but does not benefit other types of symptoms (*1*).

Other core features of schizophrenia, such as negative symptoms (social withdrawal, lack of motivation, and flat affect) and cognitive deficits (impairments in attention, memory, and problem-solving abilities) are more common, persist longer, and contribute more to the lifelong disability of schizophrenia. Fortunately, these symptoms also respond to psychotherapies. One meta-analysis showed that negative symptoms respond to social skills training (*1*). Another meta-analysis showed that cognitive remediation therapy improves cognitive functioning (though not other symptoms), especially when combined with psychiatric rehabilitation (*2*).

The field may have relied too much, and for too long, on antipsychotic medications as the mainstay in treating schizophrenia. Medications work, but mainly for psychosis, and are limited by side effects. It is encouraging that psychotherapies are receiving more attention. Treatment of this chronic, complex illness must involve multipronged interventions, including medications and effective talking treatments, optimally tailored to the individual patient and phase of illness.

Matcheri Keshavan

Department of Psychiatry, Harvard University, Boston, MA 02115, USA. E-mail: mkeshava@bidmc.harvard.edu

REFERENCES

1. D. T. Turner, M. van der Gaag, E. Karyotaki, P. Cuijpers, *Am. J. Psychiatr.* 10.1176/appi.ajp.2013.13081159 (2014).
2. T. Wykes, V. Huddy, C. Cellard, S. R. McGurk, P. Czobor, *Am. J. Psychiatr.* **168**, 472 (2011).

TECHNICAL COMMENT ABSTRACTS

Comment on "Engineering coherence among excited states in synthetic heterodimer systems"

Alexei Halpin, Philip J. M. Johnson, R. J. Dwayne Miller

Hayes *et al.* (Reports, 21 June 2013, p. 1431) used two-dimensional (2D) electronic spectroscopy to study molecular heterodimers and reported a general mechanism for the prolongation of electronic coherences, consistent with previous interpretations of 2D spectra for light-harvesting systems. We argue that the dynamics attributed to electronic coherences are inconclusive based on experimental inconsistencies arising from limited sample characterization and insufficient control measurements.

Full text at http://dx.doi.org/10.1126/science.1250926

Response to Comment on "Engineering coherence among excited states in synthetic heterodimer systems"

Dugan Hayes, Graham B. Griffin, Gregory S. Engel

Halpin, Johnson, and Miller contest our assignment of quantum beating signals observed in the two-dimensional electronic spectra of a series of fluorescein heterodimers to electronic coherences. Here, we present resonance Raman spectra, statistical analysis on multiple data sets, and an explanation of differences between the family of molecules described in our Report and the homodimer examined by the commenters. We contend that these results all support our assignment of the beating signals to electronic coherences.

Full text at http://dx.doi.org/10.1126/science.1251717

TECHNICAL COMMENT

CHEMISTRY

Comment on "Engineering coherence among excited states in synthetic heterodimer systems"

Alexei Halpin,[1] Philip J. M. Johnson,[1] R. J. Dwayne Miller[1,2]*

Hayes *et al*. (Reports, 21 June 2013, p. 1431) used two-dimensional (2D) electronic spectroscopy to study molecular heterodimers and reported a general mechanism for the prolongation of electronic coherences, consistent with previous interpretations of 2D spectra for light-harvesting systems. We argue that the dynamics attributed to electronic coherences are inconclusive based on experimental inconsistencies arising from limited sample characterization and insufficient control measurements.

Hayes *et al*. (*1*) report on a series of experiments on synthetic dimers to investigate the physics of electronically coupled pigments using multidimensional spectroscopy. By synthesizing rigidly linked heterodimers with tunable resonant energy gaps, they prepare systems that partially mimic the environment found in photosynthetic proteins, where long-lived coherences attributed to electronic couplings have previously been observed at ambient temperature using two-dimensional (2D) spectroscopy (*2*–*4*). The complication is that the amplitudes, frequencies, and decay rates of these coherences can also be interpreted as vibronic and not interpigment in origin. Studies of model systems, such as the halofluorescein assemblies in this work, are important tests for distinguishing these effects. The authors report "long" interpigment dephasing times for all heterodimers and infer that the rigidity of the molecules plays an essential role in suppressing dephasing, concluding that it is a general design principle employed in photosynthetic systems to preserve electronic coherence.

The approach is welcome and could address recent hypotheses regarding the interplay of vibronic coupling and electronic coherence in energy transfer between pigments (*5*, *6*). However, there are major issues with both the collection and the analysis of the four-wave mixing signals that affect the assignment and subsequent interpretation of interpigment dynamics. Despite the emphasis on the simple and tractable nature of the studied heterodimers, they are insufficiently characterized, leading to uncertainty surrounding the nature of the measured coherences.

Experimental control measurements were performed on the monomeric dyes to attempt to isolate dynamics associated with the dimeric species. This, however, does not then confirm their assignment to electronic coherences. Dimerization via covalent bonds will lead to changes in relative peak amplitudes and the appearance of new peaks in resonant Raman spectra as compared with the monomers (*7*, *8*). Without complementary infrared or Raman studies, the comparison of monomers and heterodimers using 2D spectroscopy is insufficient.

This is borne out in numerous ambiguities in the oscillatory dynamics. In figure S3 of (*1*), monomers B′ and C′ demonstrate oscillatory modes corresponding to roughly 600 cm^{-1} and 750 cm^{-1}, yet these peaks are completely absent in monomer A′. In the mixture of monomers B′ and C′ shown in figure S4 of (*1*), these peaks are still present but are now accompanied by a new intense peak in the vicinity of 700 cm^{-1}. These substantial differences in what should amount to simple control measurements cast considerable doubt on the limited interpretation of the Fourier components discussed in the text.

With these unassigned oscillatory features, and given the variability and congestion in the measured power spectra from molecule to molecule (and from monomers to dimers), the strict assignment of certain peaks to electronic coherences is unconvincing. This issue stands out dramatically for dimers AB and BC, where the "electronic" frequencies are additionally present in the mixtures of monomers in figure S4 of (*1*), further invalidating this method for reliably isolating contributions from electronic or nuclear dynamics.

Much of the above ambiguity could be resolved with a clearer understanding of the coupling induced by dimerization, which in the present work is completely absent. In the limit of very weak coupling (implied by the authors when choosing to neglect shifts in energy levels), the dimer absorption spectra should resemble those of an equimolar mixture of monomers, yet this is only the case for dimer BC [figure 2 of (*1*)], which recalls a vibronic dimer in the weak coupling regime (*9*, *10*). These absorption lineshapes raise questions about the justification for neglecting the electronic coupling entirely. Furthermore, vibronic coupling is also neglected, although it has also been shown to modify the optical response of even weakly coupled dimers (*11*).

Deeper insight into these energy levels, and the transitions that link them, is precluded by the homodyne-detected nature of the data. The main strength of 2D spectroscopy is to separate signals that are spectrally overlapped in more conventional third-order spectroscopies; however, by using homodyne detection, the authors cannot fully benefit from this decongestion to isolate spectral features which reflect interpigment coherences. Previous work has shown that the analysis of even phased absorptive 2D spectra of electronic dimers requires great care (*12*) due to strongly overlapped excited state absorption and emission peaks, acting to suppress the signatures of interpigment coherence. This suppression results in more pronounced contributions from vibrational activity to the homodyne signal. Taken together, there is no spectroscopic evidence that excludes vibrational wave-packet motion as the explanation for the observed dynamics.

Even with these open questions surrounding the oscillatory analysis, the recovered interpigment coherences are characterized as long-lived, although they persist for merely 60 fs (90 fs for dimer AB). For dimer BC, this would imply that the electronic coherence has decayed to e^{-3} of its initial amplitude upon a single period of oscillation (T ~ 165 fs). With such short dephasing times, the modes assigned to electronic coherence must have initial amplitudes much larger than the long-lived vibrational modes (we estimate by at least an order of magnitude) to result in power spectral densities of comparable magnitude after apodization. However, in the time domain data shown in figures 3 and S5 of (*1*), no signs of such large-amplitude oscillations are observed. Moreover, given the small energy gap between B′ and C′, it is surprising that the interpigment coherence in dimer BC nevertheless dephases on a time scale that is typical for optical transitions in monomeric dyes (*13*, *14*) if the combination of rigidity and exchange narrowing should indeed suffice to prolong coherences between excited states in such assemblies.

The conclusions drawn by Hayes *et al*. were cast favorably in the context of the long-lived oscillatory features observed in biological systems, but we find this comparison wanting. Instead, these results approach those observed in a rigid homodimer (*15*), where the interpigment dephasing times were found to be roughly identical to the homogeneous lifetime for the electronic transition (50 fs). Rather than shed new light on the very controversial issue of quantum coherence effects (*16*), especially in regard to light-harvesting, this work oversimplifies the relevant physics on what should be a better defined system, leading to unjustified conclusions

[1]Institute for Optical Sciences and Departments of Chemistry and Physics, University of Toronto, 80 Saint George Street, Toronto, Ontario M5S 3H6, Canada. [2]Max Planck Institute for the Structure and Dynamics of Matter, Atomically Resolved Dynamics Division, Building 99 (CFEL), Luruper Chaussee 149, 22761 Hamburg, Germany.
*Corresponding author. E-mail: dwayne.miller@mpsd.mpg.de

generalizing the role of coherence in molecular assemblies.

REFERENCES AND NOTES

1. D. Hayes, G. B. Griffin, G. S. Engel, *Science* **340**, 1431–1434 (2013).
2. E. Collini *et al*., *Nature* **463**, 644–647 (2010).
3. G. Panitchayangkoon *et al*., *Proc. Natl. Acad. Sci. U.S.A.* **107**, 12766–12770 (2010).
4. D. B. Turner *et al*., *Phys. Chem. Chem. Phys.* **14**, 4857–4874 (2012).
5. J. M. Womick, A. M. Moran, *J. Phys. Chem. B* **115**, 1347–1356 (2011).
6. V. Tiwari, W. K. Peters, D. M. Jonas, *Proc. Natl. Acad. Sci. U.S.A.* **110**, 1203–1208 (2013).
7. A. Myers Kelley, *J. Chem. Phys.* **119**, 3320 (2003).
8. W. Leng, F. Würthner, A. M. Kelley, *J. Phys. Chem. B* **108**, 10284–10294 (2004).
9. M. Kasha, *Radiat. Res.* **20**, 55–70 (1963).
10. R. L. Fulton, M. Gouterman, *J. Chem. Phys.* **41**, 2280–2286 (1964).
11. S. Polyutov, O. Kühn, T. Pullerits, *Chem. Phys.* **394**, 21–28 (2012).
12. V. Butkus, D. Zigmantas, L. Valkūnas, D. Abramavičius, *Chem. Phys. Lett.* **545**, 40–43 (2012).
13. P. C. Becker *et al*., *Phys. Rev. Lett.* **63**, 505–507 (1989).
14. J. Bigot *et al*., *Phys. Rev. Lett.* **66**, 1138–1141 (1991).
15. A. Halpin, P. J. M. Johnson, R. S. Murphy, V. I. Prokhorenko, R. J. D. Miller, *Ultrafast Phenomena XVIII, EPJ Web of Conferences* **41**, 05032 (2013).
16. S. Mukamel, *J. Phys. Chem. A* **117**, 10563–10564 (2013).

ACKNOWLEDGMENTS

R.J.D.M. acknowledges financial support by the Max Planck Society and the Natural Sciences and Engineering Research Council of Canada.

16 January 2014; accepted 30 April 2014
10.1126/science.1250926

Rethinking the global

We are all part of a global economy, capable of producing and transporting seemingly anything, from anywhere, to anyone. Its lifeblood is an interconnected network of suppliers and producers, retailers and consumers, spanning the planet. But the public typically knows far more about Apple, Nike, and other brands than the logistics empires many tiers below, where firms such as Foxconn and Pou Chen connect vast underlying commodity and labor markets that

PHOTO: © VICTOR FRAILE/CORBIS

are relatively hidden from the public eye. This sprawling web of supply chains can raise living standards, improve conditions for workers, and help alleviate poverty. But feeding its unquenchable thirst for energy, water, and other resources puts a strain on the planet. Finding ways to relieve that strain is an enormous challenge and will undoubtedly require greater traceability and transparency.

One step forward is providing better measurements and models and making efforts to standardize and coordinate

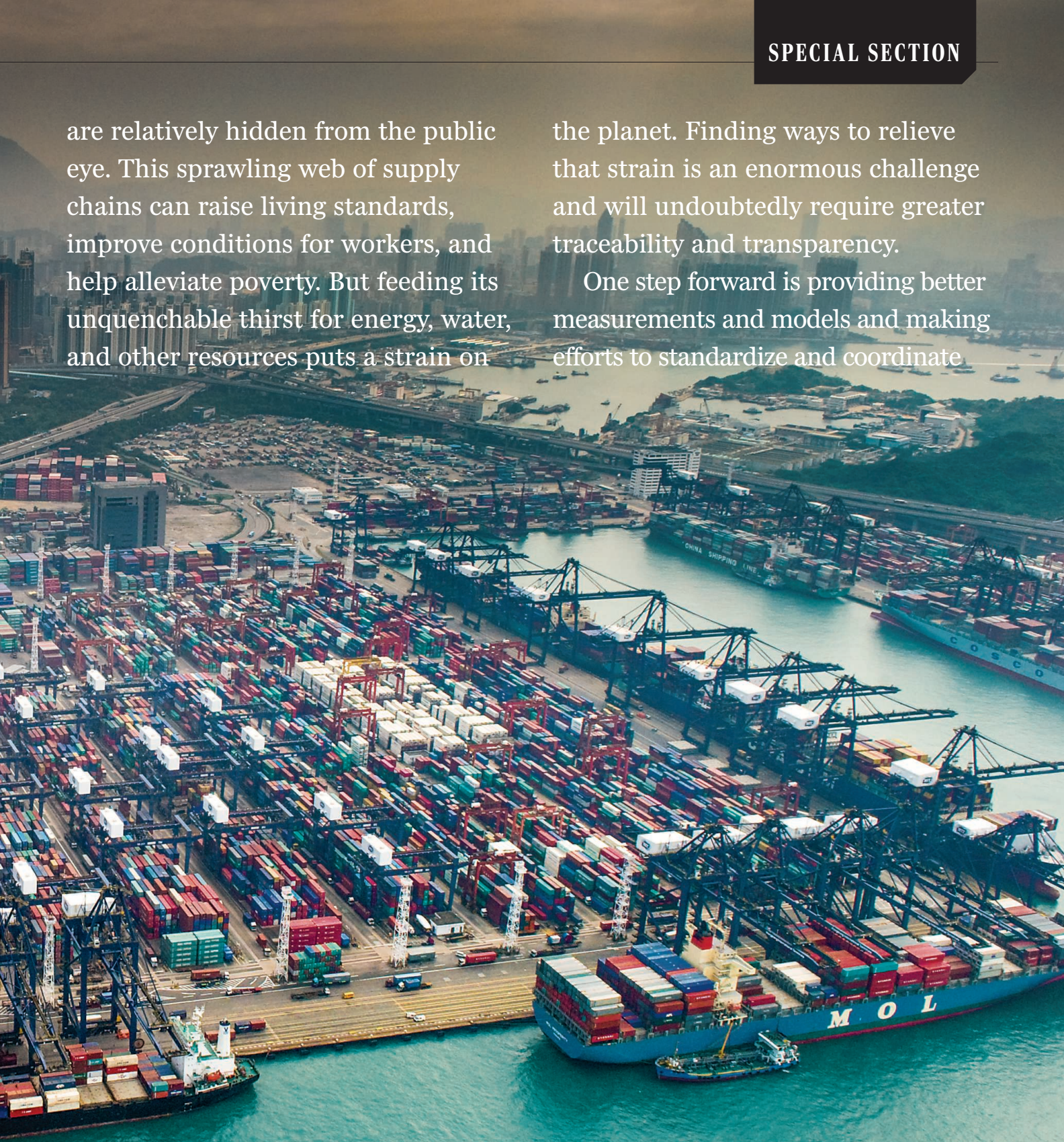

supply chain

How traceability, measurement, and standardization might tame an unwieldy web

by **Brad Wible, Jeffrey Mervis, Nicholas S. Wigginton**

Ports like Hong Kong (previous page) and warehouses like Amazon's feed global supply chains, but their social and environmental costs are largely hidden.

their use. Researchers are intensely studying how to account for supply-chain demands on ecosystems by integrating carbon, water, energy, and other "footprints" into coordinated schemes (see Hoekstra and Wiedmann, p. 1114). They are also developing better ways to inventory material and energy inputs, from the conception of a product to its grave, via life-cycle assessment tools (see Hellweg and Milà i Canals, p. 1109).

Yet academic insights alone cannot solve these problems. The large-scale cooperation of industry is essential. Many companies and industries are seeking to improve how they collect, synthesize, standardize, and communicate supply-chain data to better inform decision-making (see O'Rourke, p. 1124). A study of the Brazilian Amazon shows how supply-chain initiatives in the beef and soy industries, interacting with economic, social, and policy drivers, can slow deforestation of one of the world's major sources of biodiversity and carbon sequestration (see Nepstad *et al.*, p. 1118).

ONLINE

Podcast at www.sciencemag.org/special/supply

Logistics and transportation are also ripe for improvement. One approach is drawing inspiration from the digital Internet to create a Physical Internet. The initiative envisions using standardized "packets" and protocols for shipping, and forging the types of industry-wide partnerships that are normally anathema to a free-market system, but perhaps necessary to reduce the congestion, pollution, and inefficiency that make the current system ultimately unsustainable (see Mervis, p. 1104). Although many companies may initially be motivated by improved efficiencies and profit margins, such improvements in supply chains hold out the hope of improving conditions for humanity (see Dooley, p. 1108).

INSIDE

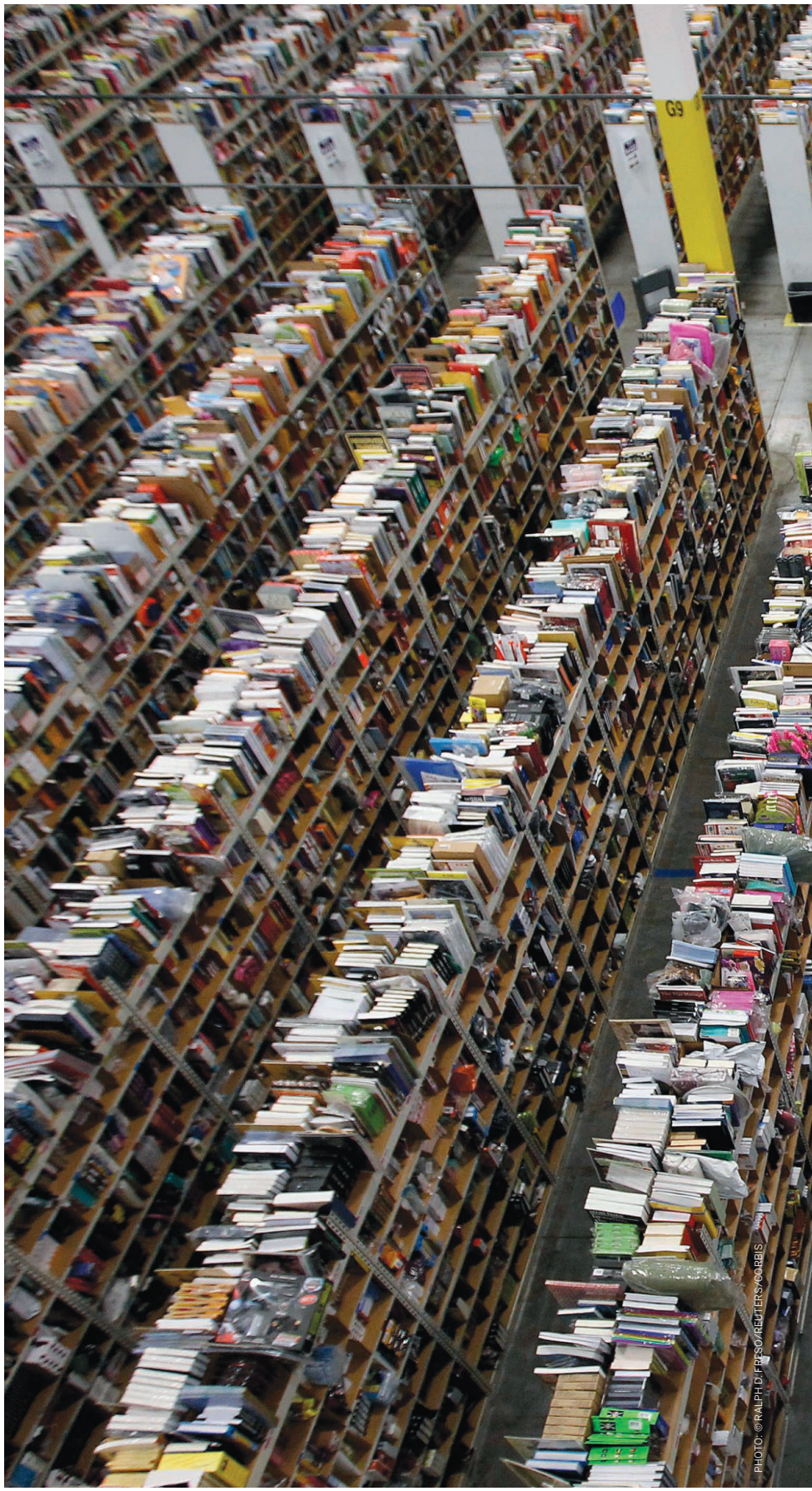

PHOTO: © RALPH D. FRESO/REUTERS/CORBIS

Published by AAAS

Shipshape. In a Physical Internet, standardized shipping containers like those crowding the deck of the *Majestic Maersk* would also take to land, simplifying the often chaotic last leg of delivery (opposite).

The information highway gets physical

The Physical Internet would move goods the way its namesake moves data

By **Jeffrey Mervis**

Sergio Barbarino is still haunted by something he once saw in a Vietnamese airport: a long line of people waiting to pick up box after box of Pampers that had just rolled out of the belly of a Lufthansa plane from Germany.

A chemical engineer who has spent his career in product development at Procter & Gamble (P&G), Barbarino was pleased that one of his company's leading brands was so popular in this growing Asian nation. But as head of P&G's global supply chain innovation center in Brussels, Barbarino was appalled that people were crowded around a baggage carousel to pluck diapers sent by relatives. Having customers who couldn't easily get a product that they wanted to buy represents a serious breakdown in logistics for one of the world's largest consumer goods companies, he realized. "My heart was bleeding, because our job is to make it easier for consumers to get their hands on our product."

Getting goods from here to there is one of humanity's oldest—and sometimes most vexing—endeavors. Today, it has spawned a complex, $60-billion-a-year logistics industry that can, in a matter of days, move a fresh flower picked in a remote South American valley to a florist in Hong Kong.

But the fundamentals of supply chain management have changed remarkably little since the first traders loaded their wares onto donkeys or carts and trundled to market. Indeed, analysts say the logistics industry is a laggard rather than a leader in adopting new technologies. That aversion to innovation has left the current global supply chain riddled with practices that waste space and energy, delay deliveries, endanger workers, increase road congestion, and pump out vast quantities of carbon dioxide. Those practices can also be bad for business, executives say—as the diaper dash in the Vietnamese airport attests.

There is a much better way, argues a small, loose-knit group of researchers that is just finding its voice. They want the world to create a "Physical Internet" that will move goods in much the same way as its digital namesake moves data. Like the cyber network, the Physical Internet would promote collaboration by developing standardized containers (think data packets), common protocols and tools (open-source software), and shared transport and technological assets (distributed computing). Manufacturers, shippers, retailers, regulators, and customers would be able to communicate seamlessly with each other and their goods. Advocates say it would also tap into underutilized capacity, improve working conditions for those in the logistics industry, relieve urban congestion, and reduce carbon emissions.

"I see what [computer scientists] did for computing as an inspiration for what we are trying to achieve in logistics," says Benoit Montreuil, an industrial engineer at Laval University in Quebec City, Canada, which last month hosted the field's first international conference. By shifting from expensive mainframe computers to

PHOTO: © NIELS QUIST PETERSEN/DEMOTIX/CORBIS

PHOTO: © XU XIAOLIN/CORBIS

personalized computing and the World Wide Web, he says, "they reinvented their field, and revolutionized society."

Montreuil concedes that there is resistance to the idea of upending a mature industry from all corners—the retailers and manufacturers, as well as those who move the goods. But he still hopes the Physical Internet can achieve a similar revolution in logistics by 2050, if not sooner.

YOU DON'T have to be FedEx, UPS, or DHL to care about what the Physical Internet could accomplish. "Everybody is affected by logistics," says J. Rod Franklin, a professor and head of executive education at Kühne Logistics University (KLU) in Hamburg, Germany. "It's the most-used industry in the world. But it's also the least visible." For most people, he adds, logistics actually has a negative connotation: "It's those guys who get in my way on the road."

One reason there are so many trucks on the road is the inefficient way in which they are deployed. One 2004 British study, for instance, studied a 24-hour cycle for 1000 food delivery trucks and found that they were actually transporting goods only 10% of the time. The rest was devoted to less productive tasks: One-quarter were offline, 16% were carrying empty loads ("shipping air" in the industry parlance), and 14% were being loaded or unloaded. Such practices help explain why logistics now accounts, on average, for more than 10% of a finished product's cost and about 15% of the world's gross domestic product.

Despite its economic importance, research on logistics has never been seen as a priority—and gets little respect within the industry. For instance, although DHL has a director of research who manages a 60-person "innovation team" outside Bonn, Germany, the company's annual report notes that DHL is "a service provider." As a result, it notes, DHL "does not engage in research and development activities … and therefore has no significant expenses to report."

That attitude may be changing, however, as governments start to pay attention. In the United States, the National Science Foundation (NSF) began funding an academia-industry consortium based at the University of Arkansas, Fayetteville, more than a decade ago. The Center for Excellence in Logistics and Distribution (CELDi) helps businesses solve logistics challenges and trains students in the field. And a few years ago, an NSF-funded study it conducted concluded that the Physical Internet initiative "represents a 'win-win-win' virtuous cycle" for raising profits and lowering pollution.

The European Union feels the same way. Its research arm is backing a €5 million project called Modulushca (Modular Logistics Units in Shared Co-modal Networks) that aims to develop a standardized, modular container for trucks and trains and the protocols needed for the container to "talk" to its handlers through radio tags and other technologies. Such a system will be essential to realizing the Physical Internet, which aims to put goods on the best possible routes from the factory to their final destination.

The Physical Internet is not just about getting packages to the right place in the most efficient manner, however. Its advocates expect it would also improve working conditions and reduce high employee turnover in the logistics industry. With pooled warehouses and transport fleets, cross-country trips by half-empty trucks would be replaced by a series of short hauls that would allow drivers to return home at night. At the same time, dank and dirty warehouses could ultimately disappear as 24-hour communications between shipments and handlers allows for just-in-time deliveries and does away with the need for intermediate storage.

The Physical Internet could also reduce urban road congestion by rationalizing and downsizing the vast fleet owned by autonomous companies that now provide last-mile delivery to homes, stores, and offices. Fewer vehicles would also mean less

air pollution and lower carbon emissions, they note.

In the last year, such potential benefits have helped the concept move out of the shadows. Last month, for example, some 200 researchers and industry officials gathered in Quebec City for the 1st International Physical Internet Conference, a 3-day opportunity to present new research, network, and spread the gospel. In the United States, White House officials have asked for a briefing on the concept from leading academics. And in April, a European working group that includes P&G and other major companies declared that "A Physical Internet Vision is possible!"

TO MAKE IT a reality, however, most companies will need to venture outside their current comfort zone. Kevin Gue, an associate professor of industrial engineering at Auburn University in Alabama and one of the keynote speakers at the Quebec City conference, tells industry executives that "it's not about a better way of doing what you now do. It's about doing things you've never thought of doing before."

One example: pooling assets, such as trucks and warehouses, that are often now locked into proprietary networks owned by individual logistics companies. Many of these players, Gue says, are reluctant to share information about customers, shipping routes, distribution networks, or markets, fearing competitors could gain an advantage. Some even consider having their own supply chain to be an integral part of their business strategy, Gue notes. "They think that, if I can lock you into my brand of material handling equipment, it'll be harder for you to switch to another company."

A few firms have formed an alliance with a competitor, says Eric Ballot, a professor of industrial management at MINES ParisTech and one of the founders of the initiative. But he reminds them that such an arrangement is not enough. "I have to say, 'Excuse me, I don't think you get it. Maybe you have a one-to-one agreement with another company. But the Physical Internet would be a network shared by many companies.' "

Achieving the Physical Internet, KLU's Franklin believes, will require companies to drop their emphasis on optimizing the use of existing assets. Instead, he says, the goal needs to be optimizing delivery of the product, using available assets regardless of who owns them. "With the Physical Internet, you wouldn't care about the route," he explains. "You care about the timeliness, the cost, and the quality of the service."

Similar challenges confront the Physical Internet's vision of developing standardized, highly modular shipping containers. In the 1950s, such containers seemed like a no-brainer to U.S. transport entrepreneur Malcom McLean, who first deployed the now ubiquitous 12-meter containers piled on ships worldwide. But it took the Vietnam War—to be precise, the U.S. military's need to transport massive amounts of material halfway around the world—to create the demand needed to realize McLean's vision. Even then, it wasn't until the 1980s that his container became the industry standard.

Unfortunately, that revolution never established a beachhead on land. It turned out that the container's dimensions are incompatible with the way trucks are loaded and how goods are stored in warehouses. "So in spite of its tremendous success on the water, transport by containers remains primarily confined to the maritime sector and in an almost forced partnership with rail," explain Ballot, Montreuil, and Russell Meller, former director of CELDi, in a new book, *The Physical Internet: The Network of Logistics Networks*.

PHOTO: © HORST OSSINGER/DPA/CORBIS
ILLUSTRATION: C. SMITH/*SCIENCE*

A better way of getting from here to there

What it would take to create the Physical Internet

The problems

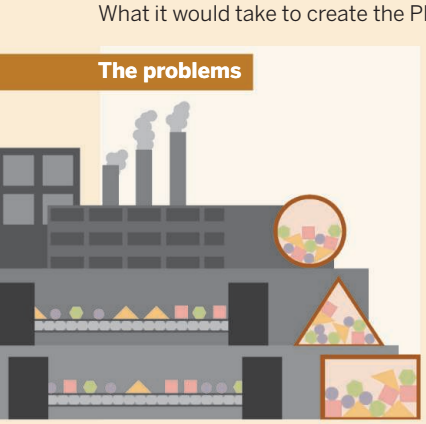

Products and shipping containers are not standard or modular.

Transportation assets are fragmented and uncoordinated.

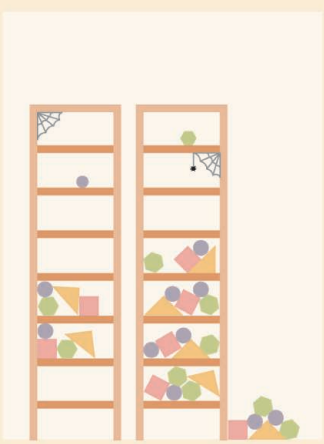

Inefficient use of storage and transfer centers.

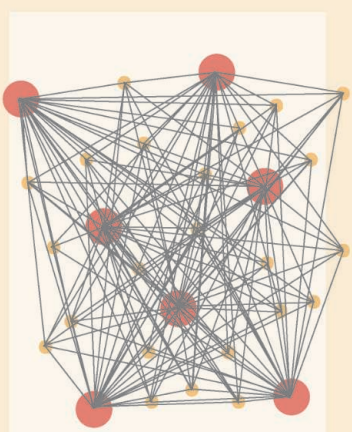

Sub-optimal delivery routes.

Packages head out to the runway at a UPS freight center in Germany.

Europe's Modulushca project hopes to change that by developing prototypes for modular, land-based containers. Having a small number of such containers would make it much easier for goods to be rolled out of factories and onto trucks and trains. Some researchers even envision containers being shuttled right to a customer's door—where they would be emptied, picked up, and reintegrated into the supply chain.

The container and pooling challenges, however, highlight one huge challenge facing proponents of the Physical Internet—remaking a mature industry—that the pioneers of the digital Internet didn't have to worry about. "Conceptually, the notion of embracing the standardization and interchangeability that's part of the Web has real appeal," says Ernest Nichols, director of the FedEx Center for Supply Chain Management at the University of Memphis in Tennessee. "But remember, you didn't have to replace your old Internet. Everybody likes the idea of standardization, as long as you agree to use my standards."

WHAT WOULD it take to move the world to adopt the needed standards? One step is to show industry that the Physical Internet is no utopian vision that is 35 years away—but something practical that could have an immediate impact. "If you talk to them about 2030 or 2050 they will stop listening," Ballot says. "So I try to be more pragmatic."

A few years ago, Ballot and Montreuil ran a Physical Internet simulation, using real logistical data provided by French retailers Carrefour and Casino. It showed that the envisioned reforms could significantly increase profits, lower prices, reduce pollution, and lead to less turnover among drivers. Now, the pair is taking the next step, conducting a pilot research project in southern France in which the two companies are using a shared distribution and scheduling system to both receive supplies and ship products.

Such proof-of-concept efforts should help persuade companies that the Physical Internet would allow them to compete on their core strengths, rather than get diverted by logistical issues. "P&G makes consumer goods, and that is what we should be concentrating on," says the company's Barbarino—not on how to get those goods to retailers and customers.

Experts expect regulators will also play a major role in developing any standards, because the logistics industry is heavily regulated. But many would prefer that governments pave the way for change by funding research and acting as a referee—enforcing rules jointly developed by private-public partnerships—rather than simply decreeing change.

Companies "are doing the best they can, considering the organization they have to work with," Ballot says. "When people start talking about shipping air and running empty trucks, the implicit message to the company is, 'You're a dummy.' Of course they would like to put more in the truck. But right now they just can't."

Auburn's Gue says he hopes to see evidence of the Physical Internet "in my lifetime—and I'm 50." He doesn't think the current logistics industry will disappear, but he does foresee major disruptions—just as the Internet is remaking the communications and publishing industries. And Montreuil says it's worth recalling the early history of the Web, which is marking just its 25th anniversary this year.

"Remember, at one time the metaphor for the digital Internet was building an information superhighway," he says. "People said, 'If we can do it for cars, why can't we do it for bits and bytes?' " He and other Physical Internet advocates are trying to reverse engineer the analogy, with the goal of making logistics as sexy as the Web. ■

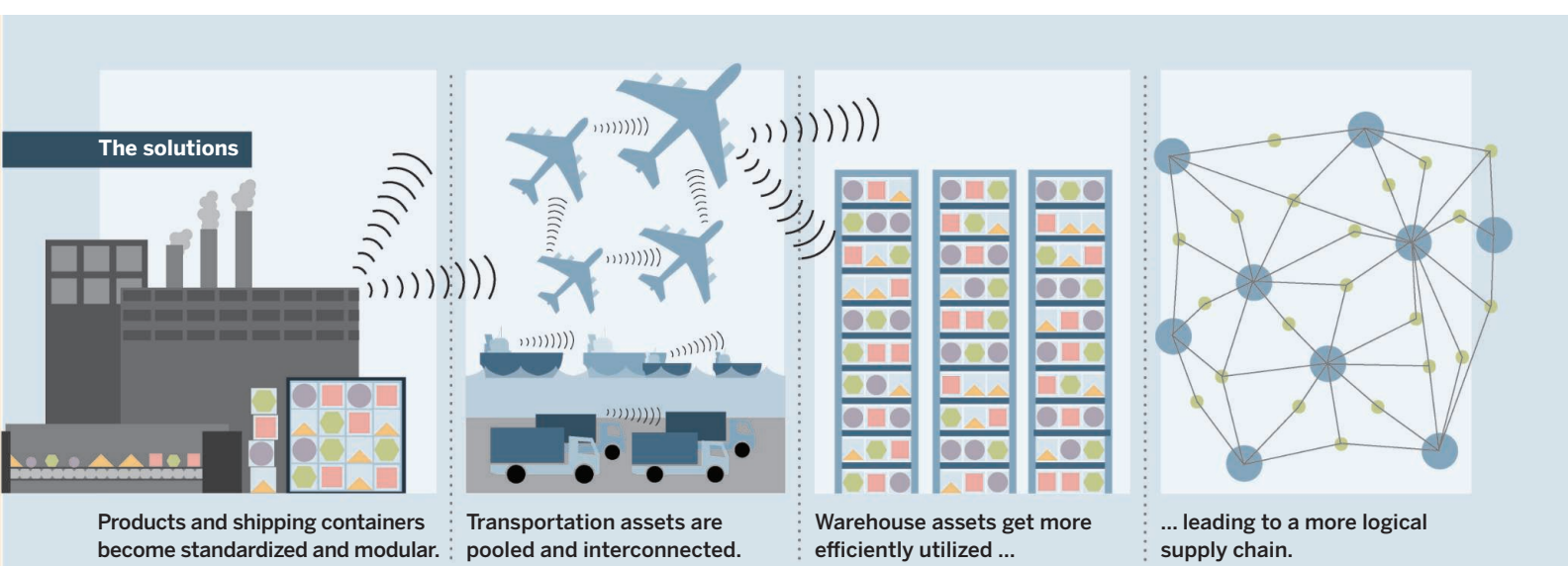

Published by AAAS

OPINION

The whole chain

A commercial port town on the East China Sea, a bustling manufacturing city in Ireland, and a scenic city on the Mediterranean coast—what ties together these regions and their people, economies, and environments? They could be part of a product's supply chain. Because the global economy rests on the maintenance of such chains, there needs to be a shift in perspective, from considering supply chains as isolated parts to optimizing them as sustainable wholes. The good news is that academia, industry, government, and civil society organizations recognize this and are seeking ways to work together to achieve sustainability across supply chains.

Decisions made by a product's designers and supply-chain managers affect the sustainability of each region that is touched by its supply chain. Consider the journey of a laptop computer, from cradle to grave. Its supply chain includes companies that mine metals and extract petroleum; manufacture the electrical and plastic components; assemble the final product; sell the computer to consumers; and, in a circular economy, recycle the device. Clearly, being part of a supply chain brings great economic opportunity to a region, but it presents challenges as well: Energy is required to run factories, water and land are demanded, and more waste must be managed. According to a 2014 report from the U.S. Environmental Protection Agency, roughly half of the greenhouse gas emissions in the United States can be linked to the supply chains of consumer products. For the laptop, factory programs could reduce the electrical demand and greenhouse gas emissions associated with producing components, and the manufacturer could design the computer to be energy-efficient. But the ultimate goal is to coordinate such efforts all along the computer's supply chain, not implement them in isolation. What is being done to achieve this?

"Science is key to holistically managing sustainable supply chains."

Science is key to holistically managing sustainable supply chains. Scientific methods such as life-cycle assessment can be used to study where improvement efforts should be concentrated. In many cases, the largest social and environmental impacts are not from the product manufacturers themselves but from their upstream suppliers or downstream consumers. For example, the manufacturers of clothing, laundry detergent, and clothes-washing machines could each work independently to reduce electricity consumption at their and their suppliers' plants. They would make far more progress in reducing global electricity consumption, however, by accommodating cold-water washing of clothes by consumers. Science also can highlight the complex tradeoffs that exist between different product solutions. Biobased materials may provide benefit through recycling or composting, but the impacts associated with growing the biomaterial have to be compared to the impacts from other materials' supply chains. And science provides an objective language for decision-makers to prioritize issues and measure and track progress. For example, because scientific studies of logistics-related transportation indicate that emissions from fuel combustion are the largest source of environmental impact, transportation carriers have worked with government, academia, and civil society to develop programs that enable public reporting of greenhouse gas emissions by carriers. This gives carriers incentives to improve and gives buyers of carrier services better information for making decisions. Because transportation logistics are a part of all product supply chains, these improvements have holistic impact.

Competing companies have similar elements in their supply chains and may compete for the same suppliers and customers. Thus, improving supply-chain sustainability eventually requires a shift to precompetitive collaboration. The Sustainability Consortium (www.sustainabilityconsortium.org), for instance, brings together stakeholders across different industry sectors and supply-chain stages to jointly prioritize product sustainability issues and create common indicators to measure and report sustainability performance. Science enables these precompetitive collaborations to be fact-based rather than opinion-based. This kind of interaction should help bring a "whole-chain" view into better focus.

– **Kevin J. Dooley**

Kevin J. Dooley is a professor in the W. P. Carey School of Business and academic director of the Sustainability Consortium at Arizona State University, Tempe, AZ. E-mail: kevin.dooley@asu.edu

10.1126/science.1256025

REVIEW

Emerging approaches, challenges and opportunities in life cycle assessment

Stefanie Hellweg[1]* and Llorenç Milà i Canals[2]

In the modern economy, international value chains—production, use, and disposal of goods—have global environmental impacts. Life Cycle Assessment (LCA) aims to track these impacts and assess them from a systems perspective, identifying strategies for improvement without burden shifting. We review recent developments in LCA, including existing and emerging applications aimed at supporting environmentally informed decisions in policy-making, product development and procurement, and consumer choices. LCA constitutes a viable screening tool that can pinpoint environmental hotspots in complex value chains, but we also caution that completeness in scope comes at the price of simplifications and uncertainties. Future advances of LCA in enhancing regional detail and accuracy as well as broadening the assessment to economic and social aspects will make it more relevant for producers and consumers alike.

The complex global supply chains, production technologies, and consumption patterns of the modern economy cause numerous environmental impacts. To identify the most effective improvement strategies and avoid burden shifting from one environmental impact to another, all impacts occurring throughout the entire value chain (supply chain plus use and disposal phases) should be accounted for. This is the goal of Life Cycle Assessment (LCA), a method to quantitatively assess the environmental impacts of goods and processes from "cradle to grave." LCA models cause-effect relationships in the environment and thus helps to understand the environmental consequences of human actions. LCA is an important decision-support tool that among other functions, allows companies to benchmark and optimize the environmental performance of products or for authorities to design policies for sustainable consumption and production.

How Does LCA work?

The currently accepted definition of LCA is the "compilation and evaluation of the inputs, outputs, and potential environmental impacts of a product system throughout its life cycle," which typically occurs in four steps (*1*). The first phase is the description of the goal and scope, which includes defining the objectives of the study and setting the system boundaries. In the LCA of freight transport, for instance, the comparison of rail and road transport to select the most sustainable option could form one objective, and the system boundaries could include the following: resource extraction and processing, the manufacture of the vehicle and infrastructure (rail tracks or roads), the operation of the vehicle, and last, disposal (Fig. 1). The second phase, inventory analysis, compiles inputs and outputs for each process in the life cycle and sums them across the whole system. Typically, several hundreds of emissions and resources are quantified.

In the third phase, life-cycle impact assessment (LCIA), emissions and resources are grouped according to their impact categories and converted to common impact units to make them comparable. For instance, CO_2 and CH_4 emissions can both be expressed as CO_2-equivalent emissions by using their Intergovernmental Panel on Climate Change (IPCC) Global Warming Potentials (this impact category, climate change, is almost identical to the so-called carbon footprint). International consensus has been reached on both the data and the modeling principles used for some impact categories, such as for the assessment of human- and eco-toxicity (*2*). For other impact categories—such as impact of land and water use, acidification, and eutrophication—diverse methods exist, and international initiatives, such as the United Nations Environment Programme (UNEP)/Society of Environmental Toxicology and Chemistry (SETAC) Life Cycle Initiative are working toward global consensus-building on impact indicators (*3*, *4*). Weighting between impact categories facilitates decision-making but, according to the International Organization for Standardization (ISO) (*1*), is not allowed for comparative assertions communicated to the public because it involves subjective judgments. The final phase is the interpretation of the inventory and impact assessment results in order to answer the objectives of the study. In the example of freight transport, outcomes obtained from an LCA include the finding that as compared with rail transport, road transport is associated with higher impacts on human health and ecosystems (Fig. 1).

How Is LCA Applied and What Are Its Potential Future Uses?

The typical use of LCA has been to assess and improve specific product systems (Fig. 2A). Many product LCAs are conducted to support corporate internal decision-making, such as for eco-design of products, process optimizations, supply-chain management, and marketing and strategic decisions. LCA has particularly high leverage at the early stage of product and process design, when there is still the freedom to make substantial changes. However, today its application is much broader. Companies are using LCA to map the key drivers of impact of their entire product portfolios (Fig. 2B) (*5*) and thus to direct their improvement strategies. Increasingly, companies are using LCA results to report on key environmental aspects on a corporate level, presenting the areas across the value chain where product portfolios generate impacts and outlining how the companies are tackling these. This can be beyond the company gates, through improvement in products and technologies, through synergies with industrial neighbors by exchanging materials and energy (*6*), and through better collaboration with other actors in the value chain. As an example, LCAs of clothes-washing have demonstrated that the largest improvement potential lies in lowering the washing temperature (*7*). Cooperation of multiple actors is needed to realize this benefit; for example, washing-powder manufacturers need to produce detergents that clean effectively at cold temperature; washing-machine producers need to manufacture machines that allow selecting cold washing temperatures; and consumers need to change their washing behavior. LCA can reveal whether collaboration between different actors would lead to a greater benefit than that of single-actor action, but making the collaboration happen also requires social and economic conditions to be fulfilled.

In the area of sustainable consumption and production, "top-down" studies of national economies help to pinpoint crucial areas of consumption and drivers of environmental impacts (Fig. 2D). For example, housing, mobility, and food (specifically, heating and cooling of buildings, car and air travel, and meat and dairy consumption) are responsible for the largest share of most environmental impacts in Europe (*8*). More detailed "bottom-up" studies of single products or product groups have also helped to determine that key drivers for impacts may not be linked to the life-cycle stages most commonly associated with high impacts, such as in the case of packaging, which was shown to be of minor importance with regard to the total greenhouse-gas emissions of food products in the UK (*9*). Such information enables the determination of the biggest impact-reduction potentials and the prioritization of political efforts. For instance, the European Commission's Energy-using Products Directive (*10*), which was built on the knowledge gathered through LCA studies, identified the use phase of

[1]Eidgenössische Technische Hochschule Zurich, Institute of Environmental Engineering, Ecological Systems Design, HPZ E 31.2, John-von-Neumann-Weg 9, 8093 Zurich, Switzerland. [2]Sustainable Consumption and Production, Division for Technology, Industry and Economics, United Nations Environment Programme (UNEP), 15 Rue de Milan, 75009 Paris, France.
*Corresponding author. E-mail: hellweg@ifu.baug.ethz.ch

household appliances as the key driver for their environmental impact and now requires electronic products to carry an energy label.

New policy initiatives go a step further by aiming to generalize the life-cycle approach in all consumption sectors, through harmonization of life-cycle–based information on a variety of impact categories to be displayed in product labeling (*11*, *12*). One challenge is how this information can be communicated to consumers in a simple and understandable manner, without hiding uncertainties. Data gaps present another challenge. Information on complete assortments of products might enable the issuing of environmental scorecards that store information on consumer-specific purchases and provide a hotspot analysis of purchases in the future (Fig. 2C). Such information would allow consumers to track the impacts of their purchases and to possibly reduce or offset them. Offsets have already been incorporated in some labels for greenhouse gas emissions but may be difficult to implement for other impacts, such as biodiversity loss (*13*). A key role is held by retailers, who are in direct contact with both consumers and producers and can serve as an information hub. In addition to product labeling (*14*), some retailers use environmental information to guide their internal decisions in supply-chain management so as to only offer products that meet minimum environmental standards (*15*).

Many LCAs have been carried out in the building sector, by urban designers, property developers, architects, engineers, and consultants. Environmental Product Declarations (*16*) have become effective mechanisms to share data about the environmental profiles of materials and semifinished products. Existing studies also assess whole building systems, considering all life-cycle stages (*17*) and even entire urban settlements (*18*, *19*). The results show that energy use within the building dominates impacts in most impact categories. Extra insulation material decreases overall life-cycle impacts in colder climates, although comparisons of low-energy to self-sufficient houses have shown that there is a tipping point at which further material use does not pay off any longer (*20*). Increasing the share of renewable energy supply systems and decreasing the per capita living space are measures with large environmental leverage (*18*). Both the impacts and the environmentally optimal design also depend on building technologies, local conditions, and the behavior of occupants (*17*, *21*).

LCA is particularly suited to support decisions in waste management. For instance, the European Waste Framework Directive (*22*) requires the use of LCA to identify cases in which it is reasonable to deviate from the classical waste hierarchy (avoid, reuse, recycle, recover, and landfill). Models and software tools for assessing the environmental impacts of recycling and disposal options are available (*23*) and have been applied in a range of cases to environmentally optimize waste management (*24*). A challenge for future research will be to widen the system boundaries beyond waste treatment and recycling to cover integrated resource management, so as not to miss improvement potentials through waste prevention and recycling-friendly product design.

LCA has been instrumental in policy-making in the energy sector. LCA can provide information on environmental benefits and costs before money is invested in new energy, grid, and storage infrastructure. For example, biofuels were once widely considered as an environmentally benign source of energy until an LCA study (*25*) showed that depending on the production conditions, biofuels from agricultural products may be responsible for larger environmental impacts than conventional fuels, mainly because of land-transformation issues. This study led the Swiss government to release a law requiring an LCA study of all nonwaste-derived biofuels, which would need to demonstrate environmental superiority over conventional fuels before any tax exemptions are granted (*26*). On a local level, mathematical optimization has been applied to propose environmentally optimal solutions for regional energy supply (*27*) and may be extended to larger regions in the future. LCA is also used to assess scenarios of energy supply mixes, to help design sustainable energy systems (*28*). A future application could be to use LCA to identify desirable scenarios and, on this basis, use backcasting to define appropriate policies.

LCAs are also applied to assess new technologies and promote proactive action, such as with nanotechnology (*29*). However, a review of LCA studies on nanostructured products (*30*) showed that almost all studies neglect nanoparticle emissions and their specific effects, thus missing a potential key concern with regard to human and ecosystem health. LCA relies on the knowledge generated in related fields (such as environmental risk assessment), and data gaps are a problem at an early stage of technology development. Another important issue is that a comparison between new and mature technologies needs to be corrected for upscaling and learning effects, which typically reduce the environmental impacts as a function of cumulated production (*31*, *32*). Last, prospective technology assessments also need models of the future industrial economy (*32*), which so far are only available for electricity generation (*28*).

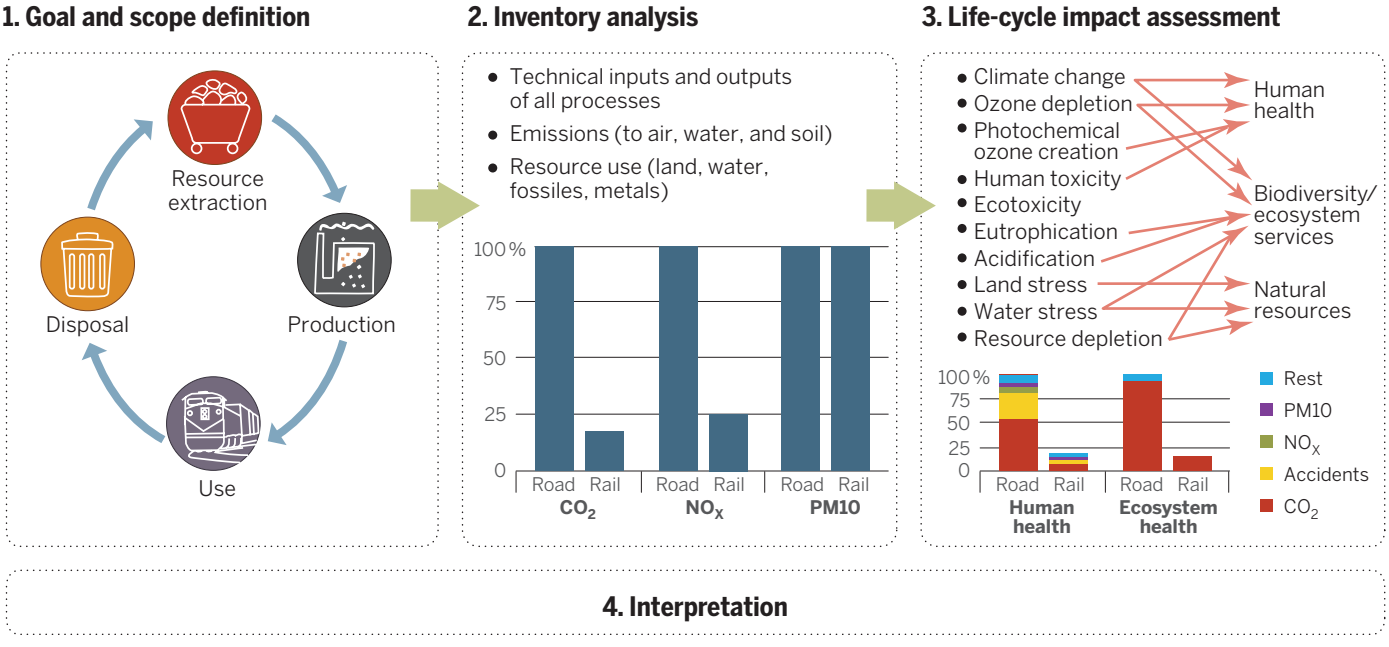

Fig. 1. The four phases of LCA for the example of freight transportation. Comparing road and rail transport for a specific freight transport chain [data are from (*68*)]. Exemplary inventory and impact assessment results (*68*) for three emissions and two damage categories, normalized to road transportation. Further details are available in the supplementary materials.

In view of the growing interest in applying LCA, enhanced coverage of inventory data and impacts is required to be able to provide answers to situations arising from increasingly complex production and consumption systems. A plethora of data must be processed on all phases of the life cycle, including consumer behavior information for the use phase. "Big Data" efforts, such as those devoted to analyzing consumer habit information, constitute a promising knowledge-generation hub (*33*). There is also a practical challenge relating to the access and interoperability of life-cycle inventory databases. Consistent data-quality guidelines are, if at all, only applied within individual databases (*34*), but not among them. Transparency and independent reviews are also crucial (*1*) to allow reproducibility and avoid hidden manipulation. Moreover, access to LCA databases should preferably be open, but this is impeded by the fact that setting up and, particularly, maintaining the quality of data are a costly task. Developments in impact assessment aiming at a better representation of cause-effect chains in the environment are also under way. At the same time, however, the mainstream application of LCA requires simplifications and standardization to enable consistent and easy use in practice (*35*). The European Commission made an attempt in this regard, defining "best practice" in impact assessment (*4*). Although on the one hand this is very helpful to harmonize LCA studies with regard to impact assessment, only LCIA methods before early 2009 were considered, and these guidelines may hamper the use of up-to-date LCIA methods. Enabling a widespread application with "stable" methods, without paralyzing the relevant methodological developments, remains a challenging task.

Emerging Approaches and Challenges in LCA

LCA results can have high uncertainties because of the large amounts of measured and simulated data and the simplified modeling of complex environmental cause-effect chains. Recent studies have highlighted the contribution that system assumptions and value choices can also make to overall uncertainty (*36*, *37*). A number of quantitative uncertainty assessments are available (*38*) but

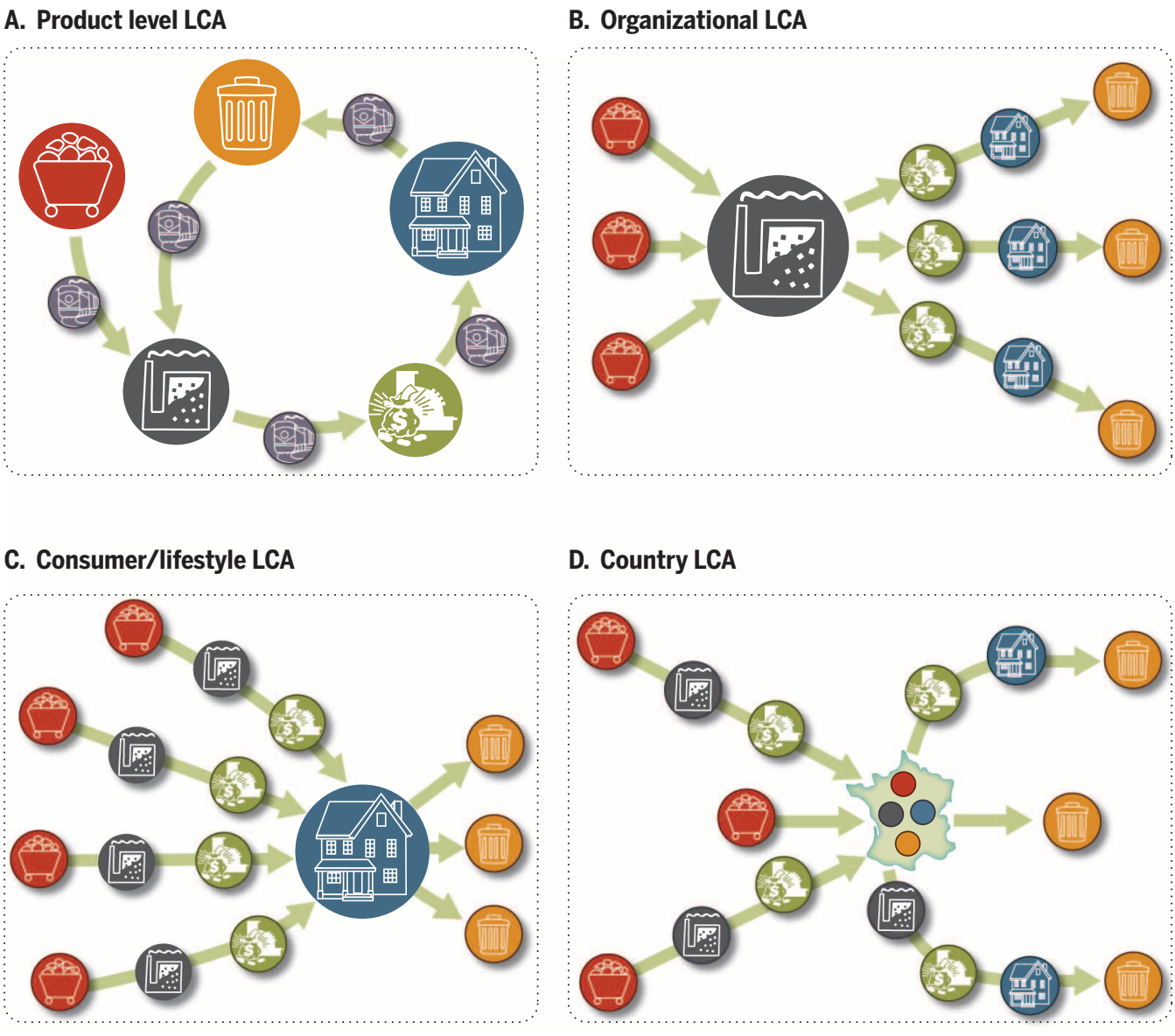

Fig. 2. The expanding nature of LCA applications. (**A**) Original product-based scope. (**B**) Organizational company LCA. (**C**) Consumer LCA (analyzing consumption patterns and lifestyles). (**D**) National-level assessments. One of the main goals in all of these application levels is the identification of environmental hotspots, which may then guide decisions on product improvement, corporate sustainability strategy (including supplier selection), consumer lifestyle and procurement options, or national sustainable consumption and production policy-setting.

are rarely used in practice. One of the key questions is, how much uncertainty is acceptable, depending on the application? In some cases, rough estimates of input values can be enough to identify supply-chain hotspots (*39*), but for other applications, such as product comparisons (*37*), the demands for more accurate values are higher. For some impact categories such as toxicity, very large differences in inventory results are needed to statistically differentiate product systems, whereas for other categories, differences of a factor of two or less may be enough (*40*). LCA practitioners should always attempt to manage the decision-maker's expectations and clarify that LCA is not always a tool to provide a single answer, but rather one that permits comprehensive understanding of a problem and its possible solutions.

Recent studies have aimed at reducing uncertainties in LCA by mapping and assessing value chains and impacts in a regionalized manner. Regionalized assessments increase the accuracy by considering site-specific production conditions as well as differences in transport and the sensitivity of ecosystems. However, acquiring spatial data constitutes a challenge. Companies may know their immediate suppliers, but only in exceptional cases do they know the whole supply chain and consumer (or post-consumer) phase. When spatial details have not been available, average market mixes have been used as an approximation. Global production mixes and trade are well known and documented for some products, such as electricity (*34*), but unfortunately, this is not the case for many other products. However, international production and trade data are becoming readily available on an industrial-sector level. Recent studies combine national production data with data on international trade flows (*41*, *42*) and are thus able to analyze the overall footprints of consuming nations, including the impacts occurring outside the national boundaries. To compare the environmental impacts between different locations of resource extraction or emission, regionalized impact-assessment methods need to be applied. Operational methods with global coverage became recently available for land-use impacts (*43*–*46*), water consumption (*47*–*50*), eutrophication (*51*, *52*), and noise (*53*). The use of Geographic Information Systems (GIS) has helped in the implementation of regionalization in LCA. An assessment of electricity generation, for example, shows that regionalization can indeed be important (Fig. 3) (*54*) and should be considered, for example, when redesigning the electricity supply mix.

Regionalization makes LCA more relevant, but matching the regionalized impact-assessment methods to regionalized emissions and resource flows is still very much a challenge. Although pilot research software systems are capable of doing this (*54*), it has yet to be implemented in commercial LCA software. An open question is, which is the most appropriate spatial (and temporal) resolution of data (*54*)? Inventory data are mostly available on the country level, with only some exceptions of finer geographical resolution [such as for agricultural processes (*55*)]. Impact-assessment methods often need a different geographical resolution, embracing the nature of the impact rather than political

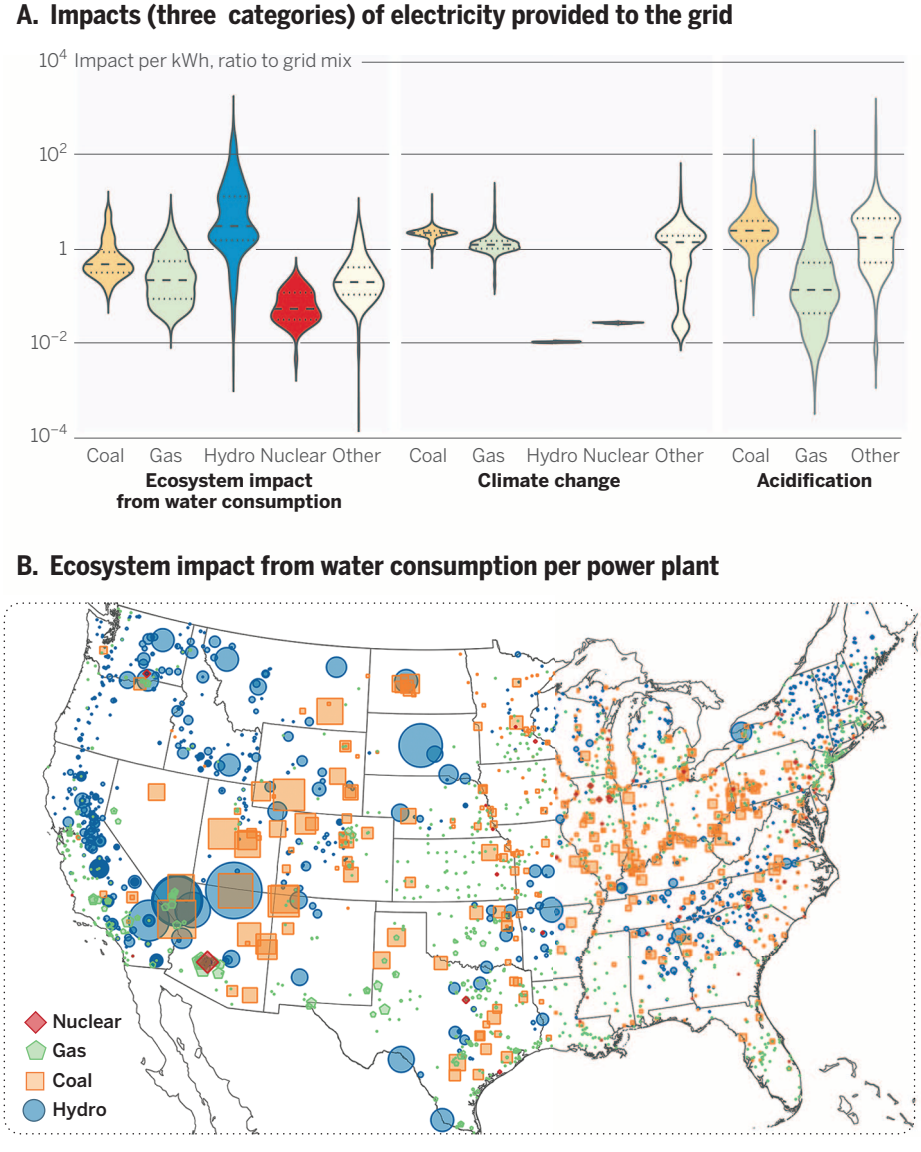

Fig. 3. Illustration of regionalized LCA of 4457 U.S. power plants. (**A**) Impact for 1 kilowatt-hour (kWh) electricity provided to the grid for three impact categories, normalized to the average impact of U.S. power production. The breadth of the "violins" reflects the frequency of data points. For impacts of climate change, differences in the technology explain the variation in impact within each power-plant type. For the other impact categories, regionalized impact assessment adds to the variability between power plants in addition to technology differences. This is illustrated by (**B**) the map, which shows total ecosystem impact from water consumption per power plant (total annual production). Impacts mainly occur in water-scarce regions with large ecosystem sensitivity. Acidification impacts of hydro and nuclear are not shown because they were negligible. Further details are available in the supplementary materials. All data are from (*54*).

boundaries. For instance, for the impacts of water consumption watersheds seem to be a logical choice. Adjusting the geographic resolution of data to a scale that warrants an appropriate assessment, without making the application too complex, is one of the challenges that remains to be confronted.

There are also new developments for global impact categories. The use of biomass for bioenergy, for example, leads to a temporary increase of carbon in the atmosphere, which acts as a greenhouse gas until it is sequestered again. Therefore, "carbon-neutral" biomass systems are not per se "climate neutral" (*56*). The importance of biogenic CO_2-emissions relative to fossil emissions depends on the rotation time as well as the temporal system boundary chosen (*56*). Discussions are also ongoing about how to model carbon storage (*57*).

One aspect that is gaining momentum in the LCA modeling community is the need to model rebound effects. Rebound effects are ones which offset the potential of a measure to reduce environmental impacts (*58*). For example, if the consumption of a good gets cheaper because of efficiency gains or if an activity becomes more time-efficient, households can use these newly available financial or temporal resources for additional consumption (*59*). Indirect effects may also occur. For example, an increased consumption of bio-based materials and energy can shift agricultural activities to rainforest areas, even if the biomass feedstock itself is not grown in rainforests. The modeling of such indirect land use requires traditional LCA modeling combined with other disciplines, such as general and partial equilibrium models from economic sciences (*60*). Although it is clear that for future-oriented decisions, it is desirable and sometimes essential to explicitly take into account the consequences of a change, including influences on the background economy and indirect effects (*61*, *62*) may compromise the transparency of the study and increase uncertainties (*32*, *63*).

Currently, LCA only addresses environmental impacts, but there is increasing demand for broader sustainability assessments covering the social and economic dimensions of sustainability (*64*). Methods for life-cycle costing exist (*65*), but methods for social assessment are still at an early development stage. A recently developed "social hotspot database" (*66*) contains country- and industrial-sector–based statistical data to screen potential hotspots at a macro level, in order to identify where more detailed social assessments about the value chain and the individual companies involved may be required. Furthermore, within the UNEP/SETAC Life Cycle Initiative, a guideline has been developed (*67*) that sets out the key elements and indicators for the assessment of the positive and negative social impacts of a product over its life cycle (for example, on human rights, working conditions, and health and safety), as well as the limitations in the approach. The point at which the environmental, economic, and social dimensions of sustainability can be assessed consistently and with sufficient detail lies at the end of a hurdled path. Such an accomplishment, however, would benefit science and society by facilitating a more thorough understanding of the impacts of human actions and identifying the proactive response required to achieve sustainability.

REFERENCES AND NOTES

1. International Organization for Standardization (ISO), *The New International Standards for Life Cycle Assessment: ISO 14040 and ISO 14044* (ISO, Geneva, Switzerland, 2006).
2. R. K. Rosenbaum *et al*., *Int. J. Life Cycle Assess.* **16**, 710–727 (2011).
3. O. Jolliet *et al*., *Int. J. Life Cycle Assess*., 10.1007/s11367 (2014).
4. M. Z. Hauschild *et al*., *Int. J. Life Cycle Assess.* **18**, 683–697 (2013).
5. L. Milà i Canals *et al*., *Int. J. Life Cycle Assess.* **16**, 50–58 (2011).
6. T. Mattila, S. Lehtoranta, L. Sokka, M. Melanen, A. Nissinen, *J. Ind. Ecol.* **16**, 51–60 (2012).
7. A. Koehler, C. Wildbolz, *Environ. Sci. Technol.* **43**, 8643–8651 (2009).
8. A. Tukker, B. Jansen, *J. Ind. Ecol.* **10**, 159–182 (2006).
9. T. Garnett, *Cooking Up a Storm. Food, Greenhouse Gas Emissions and Our Changing Climate* (Food Climate Research Network, University of Surrey, Surrey, UK, 2008).
10. European Parliament and Council, "Directive 2005/32/EC Energy-using Products" (2005).
11. C. Cros, E. Fourdrin, O. Rethore, *Int. J. Life Cycle Assess.* **15**, 537–539 (2010).
12. European Commission, *Regulation COM/2013/0196 final* (2013); available at http://eur-lex.europa.eu/legal-content/EN/ALL/?uri=CELEX:52013DC0196.
13. M. Curran, S. Hellweg, J. Beck, *Ecol. Appl.* (2013).
14. Worldwatch Institute, "Wal-Mart Scrutinizes Supply-Chain Sustainability" (2014); available at http://www.worldwatch.org/node/6200#.Uvekg3nXdAk.email.
15. F. Stoessel, R. Juraske, S. Pfister, S. Hellweg, *Environ. Sci. Technol.* **46**, 3253–3262 (2012).
16. BSI, *BS EN 15804:2012 + A1:2013 Sustainability of Construction Works* (2012); available at http://shop.bsigroup.com/ProductDetail/?pid=000000000030279721.
17. L. F. Cabeza, L. Rincón, V. Vilariño, G. Pérez, A. Castell, *Renew. Sustain. Energy Rev.* **29**, 394–416 (2014).
18. D. Saner, N. Heeren, B. Jäggi, R. A. Waraich, S. Hellweg, *Environ. Sci. Technol.* **47**, 5988–5997 (2013).
19. S. Pauliuk, K. Sjostrand, D. B. Muller, *J. Ind. Ecol.* **17**, 542–554 (2013).
20. T. Ramesh, R. Prakash, K. K. Shukla, *Energy Build.* **42**, 1592–1600 (2010).
21. K. Steemers, G. Y. Yun, *Build. Res. Inform.* **37**, 625–637 (2009).
22. European Parliament and Council, *Directive European Commission 2008/98/EC* (2008); available at http://ec.europa.eu/environment/waste/framework.
23. C. Riber, G. S. Bhander, T. H. Christensen, *Waste Manag. Res.* **26**, 96–103 (2008).
24. T. H. Christensen, F. Simion, D. Tonini, J. Møller, *Waste Manag. Res.* **27**, 871–884 (2009).
25. J. P. W. Scharlemann, W. F. Laurance, *Science* **319**, 43–44 (2008).
26. Federal Department of the Environment Transport Energy and Communications, *regulation 641.611.21* (2009) http://www.admin.ch/opc/de/classified-compilation/20080562/index.html.
27. D. Saner, thesis 20970, ETH Zurich, Switzerland (2013).
28. R. Frischknecht, in *Der Systemblick auf Innovation*, M. Decker, A. Grunwald, M. Knapp, Eds. (edition sigma, Berlin, 2012), vol. 16.
29. W. Klöpffer *et al*., *Nanotechnology and Life Cycle Assessment: A Systems Approach to Nanotechnology and the Environment* (U.S. EPA and European Commission, 2007).
30. R. Hischier, T. Walser, *Sci. Total Environ.* **425**, 271–282 (2012).
31. M. Caduff, M. A. J. Huijbregts, H.-J. Althaus, A. J. Hendriks, *Environ. Sci. Technol.* **45**, 751–754 (2011).
32. T. E. McKone *et al*., *Environ. Sci. Technol.* **45**, 1751–1756 (2011).
33. J. Cooper, M. Noon, C. Jones, E. Kahn, P. Arbuckle, *J. Ind. Ecol.* **17**, 796–799 (2013).
34. Swiss Centre for Life Cycle Inventories (Ecoinvent Centre, 2012); www.ecoinvent.ch.
35. M. Baitz *et al*., *Int. J. Life Cycle Assess.* **18**, 5–13 (2013).
36. A. M. De Schryver, S. Humbert, M. A. J. Huijbregts, *Int. J. Life Cycle Assess.* **18**, 698–706 (2013).
37. J. R. Gregory, T. M. Montalbo, R. E. Kirchain, *Int. J. Life Cycle Assess.* **18**, 1605–1617 (2013).
38. S. M. Lloyd, R. Ries, *J. Ind. Ecol.* **11**, 161–179 (2007).
39. L. Milà i Canals *et al*., *J. Ind. Ecol.* **15**, 707–725 (2011).
40. M. A. J. Huijbregts, W. Gilijamse, A. M. J. Ragas, L. Reijnders, *Environ. Sci. Technol.* **37**, 2600–2608 (2003).
41. A. Tukker *et al*., *Econ. Syst. Res.* **25**, 50–70 (2013).
42. T. O. Wiedmann *et al*., *Proc. Natl. Acad. Sci. U.S.A.* 10.1073/pnas.1220362110 (2013).
43. L. de Baan, C. L. Mutel, M. Curran, S. Hellweg, T. Koellner, *Environ. Sci. Technol.* **47**, 9281–9290 (2013).
44. R. Saad, T. Koellner, M. Margni, *Int. J. Life Cycle Assess.* **18**, 1253–1264 (2013).
45. M. Brandão, L. Mila i Canals, *Int. J. Life Cycle Assess.* **18**, 1243–1252 (2013).
46. M. Núñez, A. Anton, P. Munoz, J. Rieradevall, *Int. J. Life Cycle Assess.* **18**, 755–767 (2013).
47. M. Motoshita, N. Itsubo, A. Inaba, *Int. J. Life Cycle Assess.* **16**, 65–73 (2011).
48. S. Pfister, A. Koehler, S. Hellweg, *Environ. Sci. Technol.* **43**, 4098–4104 (2009).
49. F. Verones *et al*., *Environ. Sci. Technol.* **47**, 12248–12257 (2013).
50. A. M. Boulay, C. Bulle, J. B. Bayart, L. Deschênes, M. Margni, *Environ. Sci. Technol.* **45**, 8948–8957 (2011).
51. L. B. Azevedo, A. D. Henderson, R. van Zelm, O. Jolliet, M. A. J. Huijbregts, *Environ. Sci. Technol.* **47**, 13565–13570 (2013).
52. R. J. K. Helmes, M. A. J. Huijbregts, A. D. Henderson, O. Jolliet, *Int. J. Life Cycle Assess.* **17**, 646–654 (2012).
53. S. Cucurachi, R. Heijungs, K. Ohlau, *Int. J. Life Cycle Assess.* **17**, 471–487 (2012).
54. C. L. Mutel, S. Pfister, S. Hellweg, *Environ. Sci. Technol.* **46**, 1096–1103 (2012).
55. S. Pfister, P. Bayer, A. Koehler, S. Hellweg, *Environ. Sci. Technol.* **45**, 5761–5768 (2011).
56. F. Cherubini, G. P. Peters, T. Berntsen, A. H. Stromman, E. Hertwich, *GCB Bioenergy* **3**, 413–426 (2011).
57. A. Levasseur *et al*., *Nature Clim. Change* **2**, 6–8 (2012).
58. E. G. Hertwich, *J. Ind. Ecol.* **9**, 85–98 (2005).
59. B. Girod, P. de Haan, R. W. Scholz, *Int. J. Life Cycle Assess.* **16**, 3–11 (2011).
60. J. Hedal Kløverpris, K. Baltzer, P. H. Nielsen, *Int. J. Life Cycle Assess.* **15**, 90 (2010).
61. G. Finnveden *et al*., *J. Environ. Manage.* **91**, 1–21 (2009).
62. T. Ekvall, B. P. Weidema, *Int. J. Life Cycle Assess.* **9**, 161–171 (2004).
63. A. Zamagni, J. Guinee, R. Heijungs, P. Masoni, A. Raggi, *Int. J. Life Cycle Assess.* **17**, 904–918 (2012).
64. J. B. Guinée *et al*., *Environ. Sci. Technol.* **45**, 90–96 (2011).
65. T. E. Swarr *et al*., *Int. J. Life Cycle Assess.* **16**, 389–391 (2011).
66. C. Benoit-Norris, D. A. Cavan, G. Norris, *Sustainability-Basel* **4**, 1946–1965 (2012).
67. C. Benoit, B. Mazijn, *Guidelines for Social Life Cycle Assessment of Products* (UNEP/SETAC Life Cycle Initiative, Paris, 2009).
68. N. Fries, S. Hellweg, *Int. J. Life Cycle Assess.* **19**, 546–557 (2014).

ACKNOWLEDGMENTS

We thank C. Mutel, S. Pfister, T. Colley, and C. Raptis for their helpful assistance with figures and comments on a draft version of this paper. The views expressed in this article are those of the author and do not necessarily reflect those of UNEP.

SUPPLEMENTARY MATERIALS

www.sciencemag.org/content/344/6188/1109/suppl/DC1
Materials and Methods
References (*69*–*74*)

10.1126/science.1248361

REVIEW

Humanity's unsustainable environmental footprint

Arjen Y. Hoekstra[1*] and Thomas O. Wiedmann[2,3]

Within the context of Earth's limited natural resources and assimilation capacity, the current environmental footprint of humankind is not sustainable. Assessing land, water, energy, material, and other footprints along supply chains is paramount in understanding the sustainability, efficiency, and equity of resource use from the perspective of producers, consumers, and government. We review current footprints and relate those to maximum sustainable levels, highlighting the need for future work on combining footprints, assessing trade-offs between them, improving computational techniques, estimating maximum sustainable footprint levels, and benchmarking efficiency of resource use. Ultimately, major transformative changes in the global economy are necessary to reduce humanity's environmental footprint to sustainable levels.

Since the latter part of the 18th century, humans have been altering the Earth at an unprecedented and unsustainable rate and scale by radically transforming the landscape, increasing natural resource use, and rapidly generating waste. One way of quantifying the total human pressure on the natural environment is to calculate humanity's "environmental footprint"—an umbrella term for the different footprint concepts that have been developed during the past two decades.

Common to all environmental footprints is that they quantify the human appropriation of natural capital as a source or a sink (*1*–*4*). The basic building block of footprint accounts is the footprint of a single human activity (Fig. 1). Each specific footprint indicator focuses on one particular environmental concern (e.g., limited land, limited fresh water, and so forth) and measures either resource appropriation or waste generation, or both. The ecological footprint (EF) measures both the appropriation of land as a resource and the land needed for waste uptake (CO_2 sequestration) (*5*). The first component is separately described as the land footprint (LF) (*6*, *7*); the second component, as the energy footprint (EnF) (*8*). The water footprint (WF) measures both the consumption of fresh water as a resource and the use of fresh water to assimilate waste (*9*). The material and phosphorous footprints (MF and PF) focus on measuring resource appropriation alone (*10*, *11*). The carbon or climate footprint (CF) measures emission of greenhouse gases to the atmosphere (*12*); the nitrogen footprint (NF) measures the loss of reactive nitrogen to the environment (*13*). The biodiversity footprint (BF) measures the threat of human activity to biodiversity (*14*). Footprints are indicators of human pressure on the environment and form the basis for understanding environmental changes that result from this pressure (such as land-use changes, land degradation, reduced river flows, water pollution, climate change) and resultant impacts (such as biodiversity loss or effects on human health or economy).

Environmental Sustainability

Environmental sustainability requires that footprints remain below their maximum sustainable level, at global scale, and in some cases at smaller geographical scales as well. Sustainability depends on the size and spatiotemporal characteristics of humanity's footprint relative to Earth's carrying capacity. Environmental footprints are closely related to the concept of planetary boundaries—thresholds in Earth-system variables that, if traversed, could generate unacceptable change in the biophysical processes of the planet's natural environments (*15*). Environmental footprints measure how much of the available capacity within the planetary boundaries is already consumed.

The EF asserts that human appropriation of bioproductive area exceeds available biocapacity by 50% (*16*). The message that humanity is hence using one-and-a-half planets is one of the reasons that the EF concept has become a popular and effective tool to communicate unsustainability. It has further been estimated that humanity's blue WF, referring to consumption of surface and groundwater resources, exceeds the maximum sustainable blue WF during at least parts of the year in half of the world's river basins (*17*). Based on an analysis of nitrogen and phosphorus emissions to water, the gray WF—the WF component referring to water pollution—was found to exceed the maximum sustainable gray WF (assimilation capacity) in about two-thirds of the world's river basins (*18*). The global CF should be reduced by 60% (from 50 to 21 Gt CO_2-equiv./year) between 2010 and 2050 to achieve the climate target of a maximum 2°C of global warming (*19*).

For each type of environmental footprint there is a maximum sustainable level, but quantitatively

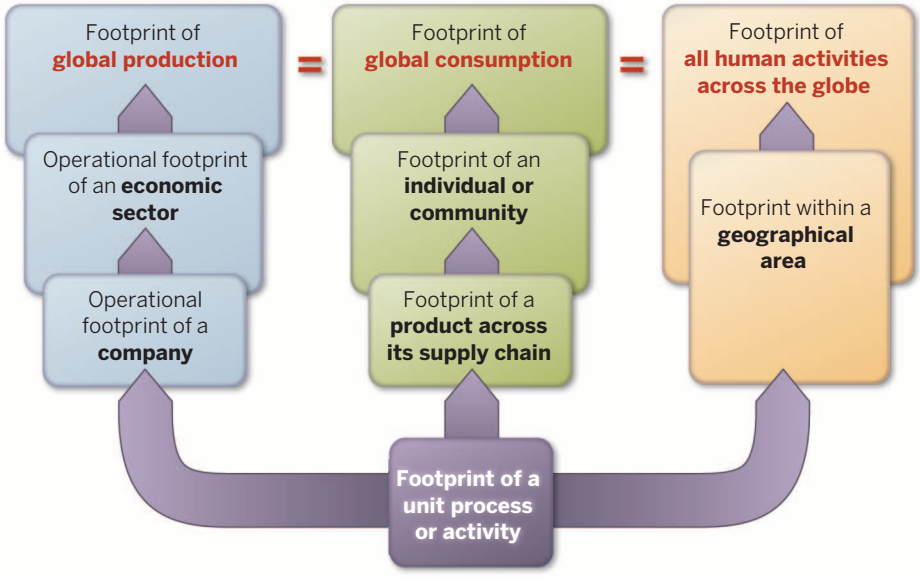

Fig. 1. The relation between footprints of different entities. At the basis of any footprint account are mutually exclusive unit footprints. A "unit footprint" is the footprint of a single process or activity and forms the basic building block for the footprint of a product, consumer, or producer or for the footprint within a certain geographical area. The footprint of global production is equal to the footprint of global consumption. Both equal the sum of the footprints of all human activities across the globe.

[1]Twente Water Centre, Institute for Innovation and Governance Studies, University of Twente, Enschede, Netherlands. [2]School of Civil and Environmental Engineering, UNSW Australia, Sydney, NSW 2052, Australia. [3]Integrated Sustainability Analysis, School of Physics A28, The University of Sydney, NSW 2006, Australia.
*Corresponding author. E-mail: a.y.hoekstra@utwente.nl

defining these levels is in its infancy (Fig. 2). Proposed maximum levels are confounded by uncertainties, ambiguity, and subjectivity. As an example of large uncertainties, the maximum sustainable level of the blue WF has been estimated to be 1100 to 4500 km^3/year at the global scale (*20*). Ambiguity exists, for example, regarding the maximum sustainable CF: Usually it is expressed as a maximum volume of Gt CO_2-equiv./year, but it has been suggested that cumulative emissions over time form a better indicator for the ultimate resultant global warming (*21*). Finally, subjectivity in setting maximum sustainable levels is an intrinsic part of the human decision-making process, exemplified by the maximum global warming threshold of 2°C, which was reached as a consensus (*22*).

At the global level, the environmental footprint of human beings shows an uninterrupted increase during the past century, owing to growing population, increasing affluence, changing consumption patterns (e.g., more meat in diets), and increasing mobility. In the period 1961 to 2008, the EF more than doubled (*16*). The blue WF grew by a factor of 5.6 in the period 1900 to 2000 (*23*), and the total amount of reactive nitrogen created by human activities (the NF) has increased ninefold during the 20th century (*24*). Global carbon emissions from fossil fuels—part of humanity's CF—increased even more: by over 16 times between 1900 and 2008 (*25*). Developing countries have now overtaken developed countries in both total territorial and total CF emissions (*26*). With business as usual, all footprints are expected to further increase during the coming few decades, rather than decrease toward sustainable levels (*19*, *27*, *28*).

Resource Efficiency and Producers

Producers compete for natural resources (e.g., land and water rights) and for their share in the limited assimilation capacity of the Earth (e.g., carbon emission and wastewater discharge permits). To get the highest benefit per unit of natural resource consumption and unit of pollution, footprints of activities and products need to be minimized. The environmental footprint has become a key performance indicator in environmental management and a way to demonstrate corporate social responsibility (*29*, *30*). Resource efficiency means a small footprint per unit of product.

The footprint of a company consists of direct (operational) and indirect (supply-chain) components. The footprint of a final product depends on the footprints of the processes in the supply chain of the product (Fig. 3). In practice, companies tend to formulate reduction targets regarding their direct footprint, thereby ignoring their indirect footprint, which is often much bigger (*31*). The indirect WF of beverage companies, for example, can constitute about 99% of their total WF (*32*). Recent developments in footprint standardization address this issue. For instance, the Corporate Value Chain (Scope 3) Accounting and Reporting Standard of the Greenhouse Gas (GHG) Protocol (*33*) provides guidance for companies and other organizations to report GHG emissions from all supply-chain, operational, and disposal activities (the "value chain") associated with their business. A major challenge remains in companies setting reduction targets for their supply-chain footprint. Current research focuses on the practicality of data compilation and reporting, the completeness of supply-chain coverage, and the accuracy and transparency of results (*29*, *34*). These issues need to be addressed to enable meaningful comparisons between companies and benchmarking based on best available technology and practice (*32*, *35*). Another challenge is to internalize the costs related to the environmental footprint of products in their price—for example, by charging carbon and water taxes along the supply chain, or a general environmental tax on final products (e.g., a tax on meat). Yet another challenge is to develop a better understanding of trade-offs between different footprints. Reducing the CF by moving toward bioenergy, for instance, will inevitably increase the LF and WF (*36*). Reducing the WF in overexploited river basins by large-scale interbasin water transfer or by increasing food imports will inevitably increase the energy footprint.

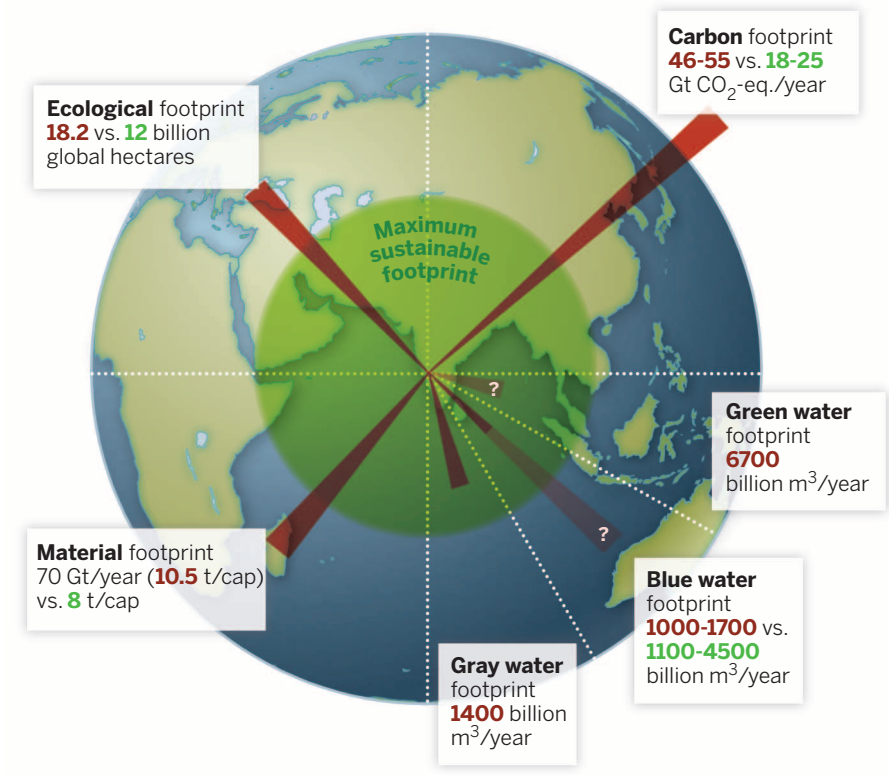

Fig. 2. Estimated global footprints versus their suggested maximum sustainable level. The inner green shaded circle represents the maximum sustainable footprint [compare (*15*)]. Red bars represent estimates of the current level of each global footprint. The EF of 18.2 billion global hectares (in 2008) exceeds the maximum sustainable EF of 12 billion global hectares by about 50% (*16*). The green WF has been estimated at 6700 billion m^3/year (average for 1996 to 2005) (*9*); a reference level is not yet available. Blue WF estimates vary from 1000 to 1700 billion m^3/year (*9*, *57*) and should be compared to the global maximum sustainable blue WF of 1100 to 4500 billion m^3/year (*20*); data on maximum blue WFs per river basin and month are provided by (*17*). The gray WF has been conservatively estimated at 1400 billion m^3/year (average for 1996 to 2005) (*9*, *57*); in two-thirds of the world's river basins, the pollution assimilation capacity for nitrogen and phosphorus has been fully consumed (*18*). The CF of 46 to 55 Gt CO_2-equiv./year (in 2010) exceeds by more than a factor of 2 the estimated maximum sustainable CF of 18 to 25 Gt CO_2-equiv./year, which must be achieved by 2050 if the maximum 2°C global warming target is to be met (*19*). The MF has been estimated at 70 Gt/year [10.5 ton/cap in 2008 (*10*)], and a reduction to 8 ton/cap has been suggested as a sustainable level (*58*).

Social Equity and Consumers

An individual's or community's consumption behavior translates into an environmental footprint. Given the huge variation in consumption patterns and related environmental burdens and the world's limited natural resources and assimilation capacity, an increasingly pressing question is who takes the biggest part of the pie, and what actually is a "fair share." Social equity implies fair sharing of limited natural resources among countries and between people within countries.

The EF of the average global citizen is 2.7 global hectares, while that of the average U.S. citizen is 7.2 (*16*). If all world citizens would have an EF

equal to the latter, the global EF would exceed Earth's biocapacity not only by the average factor of 1.5, but by a factor of 4. The current WF of the average U.S. consumer is two times the global average (*9*). To ensure that the WF of humanity as a whole will not grow under the United Nations medium population scenario, the average WF per capita will have to decrease from 1385 m^3 in 2000 to 910 m^3 in 2050 and 835 m^3 in 2100 (*32*). If we assume an equal WF share for all global citizens, the challenge is to reduce the WF over the 21st century by 22.5% for consumers in China and India and by 70% for consumers in the United States. The CF of the average U.S. consumer has been estimated to be 5.8 bigger than the global average (*37*). Footprints per capita hugely differ not only across, but also within nations (*38*). Equitable consumption in a finite world requires "contraction and convergence": The environmental footprint of humanity has to reduce toward sustainable levels, and footprints per capita have to converge to similar, more equitable shares (*32*, *39*).

Footprints per capita are determined by two factors: consumption pattern and intensity of natural resource use or waste generation per unit of product consumed (*32*). Consumers can influence the latter by buying products with high eco-efficiency (low footprint), but often this is hampered by a lack of product information. Usually, the only relevant type of information refers to the energy efficiency and sometimes the water efficiency of products. Consumers can also reduce their footprint by changing their consumption behavior. Measures that have the potential to contribute most to the reduction of the environmental footprint—at least in industrialized countries—include replacing animal with crop products (*40*, *41*), reducing food and other waste (*40*), saving energy at home and in transport (*42*), and buying second-hand, recycled products and low-footprint, dematerialized "services" rather than primary-material–based goods (*39*). However, such behavioral changes are difficult to achieve in reality because of social constraints and lock-ins (*43*). Another problem is that improvements in resource efficiency often do not result in the expected saving, since they allow overall consumption levels to increase—the so-called rebound effect (*44*). Profound, effective, socially accepted, and long-lasting changes as required for a truly sustainable transition have yet to occur.

Resource Security and the Influence of Politics

Resource security for governments means limiting national dependency on footprints that are difficult to control or influence. For companies, it means limiting corporate dependency on risk-increasing footprints in the supply chain. International trade plays an important role in this instance because it inherently shifts environmental burdens from the place of consumption in one country to the place of production elsewhere in the world. This effect of international externalization is well documented by studies of national footprints (*6*, *7*, *10*, *14*, *32*, *45*). In the United Kingdom, for example, ~40% of the CF of national consumption lies abroad (*37*) and so does 75% of the WF (*9*). Worldwide, 24% of the LF is embedded in international trade (*7*), as is 22% of the WF (*9*), 26% of the CF (*45*), and 41% of the MF (*10*). Policies aimed at increasing the sustainability of consumption therefore need to take into account and target production technologies employed abroad. Because full national self-sufficiency is generally neither possible nor desirable, international cooperation on reducing the footprint of production worldwide is the only path available to tackle unsustainability at the national scale.

This becomes evident when looking at natural resource stocks (fertile land, fossil fuels, fossil groundwater, materials) and flows (river runoff, renewable groundwater, wind and solar energy). These resources occur locally, but they have become global commodities from an economic standpoint (*46*). Comparing the environmental footprint of national consumption with its natural endowment base allows one to identify inherent and possibly critical resource dependencies (*10*, *46*). Surprisingly, countries like India and China that have EFs and WFs exceeding their sustainably available land and water resources are still net exporters of embodied land and water (*7*, *9*). Sustainable production is here at odds with the interest of export earnings.

Even though the environmental footprint of humanity is ultimately driven by consumption, governments invariably focus on "eco-efficiency" (low footprints per unit of production), leaving consumption volumes and patterns unaddressed. An example of well-intended but noneffective policy was the Kyoto Protocol that set reduction

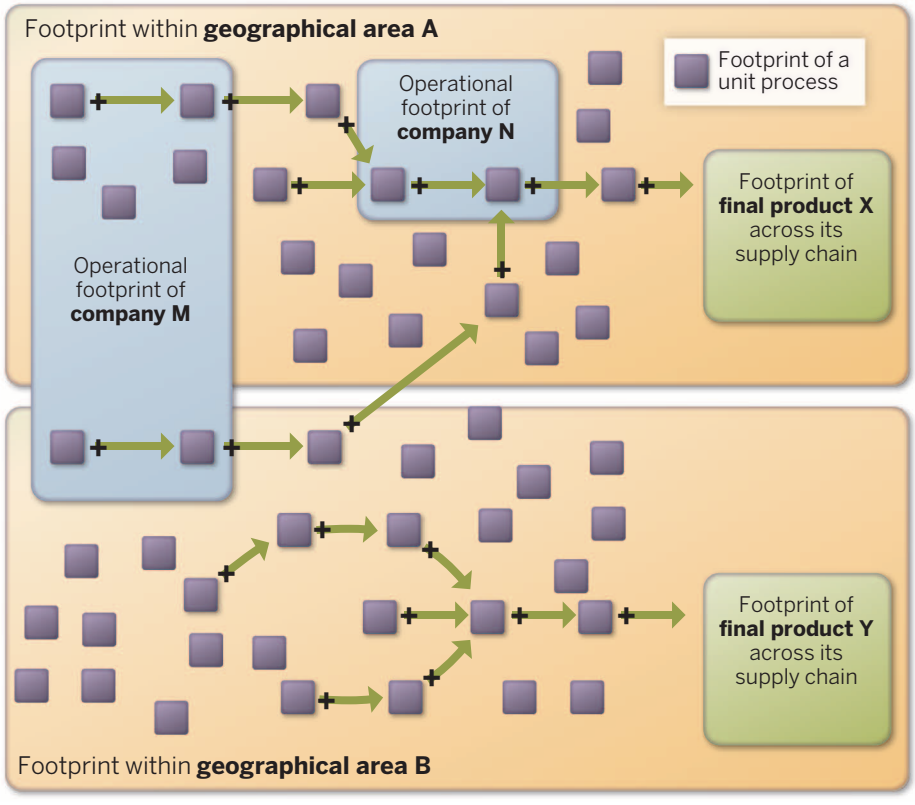

Fig. 3. Footprint accounting over supply chains. The footprint of a product is the sum of the footprints of the processes along the supply chain of the product. These processes may take place in different geographical areas. The operational footprint of a company is the sum of the footprints of its own operations. For simplicity, one-directional supply chains are drawn; in reality, supply chains of different products are interwoven and partly cyclic. Footprint-allocation procedures are applied to avoid double counting.

targets per country with respect to GHG emissions generated within the country. Relocation of production from developed to developing countries over time resulted in "carbon leakage," i.e., shifting of emissions to countries outside of the agreement's control. Even though industrialized countries could implement emission-reduction projects in other countries, this did not lead to actual reductions in national carbon footprints (*45*). In the case of setting caps on WFs by river basin, likely the same will happen: Water management is typically territorial-based and focused on increasing water-use efficiency, not related to the total volume of consumption (*32*). Efficiency may thus increase, but demand for water-intensive commodities such as meat and biofuels is rapidly rising, as well. Until this dichotomy is addressed, sustainable consumption remains a blind spot in policy-making.

Short-term resource security is still of greater interest to most governments and companies than the long-term sustainability of supplies and their consumption. This can be explained by the time frames for economic returns and political cycles. Increasingly, countries try to secure their food supply through land and water "grabbing" elsewhere (*47*). Similarly, several countries can only meet their biofuel targets through increasing imports (*48*), with associated land and water footprints elsewhere (*49*, *50*). Long-term resource security requires that imports and supply chains are truly sustainable. This is where national environmental footprint accounting can help to inform policies aimed at sustainable production worldwide.

Future Prospects

Supply-chain evaluation has only recently become an issue in corporate CF accounting, whereas it has always been a strong component of the WF. We envisage a future in which the different footprints become equally important, get elaborated to the same level of detail, and are applied by companies and governments to measure environmental performance in both operations and supply chain. We expect that footprint benchmarks will be developed for unit processes and final products as exemplified for the EnF (*51*) and the WF (*32*).

Methodologically, we expect cross-fertilization among the different footprint concepts and the gradual evolvement of a consistent analytical framework with broad but not overlapping coverage of environmental pressures (*4*). Common questions to be solved across all footprints include the difficulty of tracing along supply chains, how to avoid truncation, how to allocate to multiple products from one process, and the assessment of uncertainties. Further study is required in harmonizing footprint assessment methods, which focus on quantification of environmental pressure and assessment of sustainable, efficient, and equitable resource appropriation (*5*, *32*), and life-cycle assessment methods, which focus on quantification of environmental impacts (*52*, *53*). At a more fundamental level, a continued debate is necessary between scholars in environmental footprint assessment (EFA) and those who criticize the new field for inaccurateness and simplification (*54*). Work remains to be done also in embedding EFA in dynamic, integrated assessment models to better understand how complex processes of global change ultimately affect the natural environment and human development.

To reduce humanity's environmental footprint toward a sustainable level, it is necessary to reach consensus on footprint caps at different scales, from global to national or river-basin scale. Footprint caps need to be related to both production and consumption (*32*, *55*). The various components of the environmental footprint of humanity must be reduced to remain within planetary boundaries. Improved technologies (eco-efficiency) alone will not be sufficient to reach this goal; consumption patterns will need to alter as well (*39*). How such cultural shift and transformative change in the global economy could take place remains an open question. It is clear, however, that such change will profoundly affect all sectors of the economy. There are always several entities playing a role in causing a footprint: the investors, the suppliers, the recipients, and the regulators. Hence, the responsibility for moving toward a sustainable footprint is to be shared among them (*32*, *56*). The way societies and economies have institutionalized responsibility is clearly insufficient to warrant environmental sustainability, eco-efficiency, fair sharing, and long-term resource security. Exploring how we can better institutionalize full supply-chain responsibility is one of humanity's major research challenges toward achieving a sustainable future.

REFERENCES AND NOTES

1. A. Y. Hoekstra, *Ecol. Econ.* **68**, 1963–1974 (2009).
2. A. Galli *et al.*, *Ecol. Indic.* **16**, 100–112 (2012).
3. S. Giljum, E. Burger, F. Hinterberger, S. Lutter, M. Bruckner, *Resour. Conserv. Recycling* **55**, 300–308 (2011).
4. K. Fang, R. Heijungs, G. R. de Snoo, *Ecol. Indic.* **36**, 508–518 (2014).
5. M. Wackernagel, W. E. Rees, *Our Ecological Footprint—Reducing Human Impact on the Earth* (New Society, Gabriola Island, B.C., Canada, 1996).
6. K. Steen-Olsen, J. Weinzettel, G. Cranston, A. E. Ercin, E. G. Hertwich, *Environ. Sci. Technol.* **46**, 10883–10891 (2012).
7. J. Weinzettel, E. G. Hertwich, G. P. Peters, K. Steen-Olsen, A. Galli, *Glob. Environ. Change* **23**, 433–438 (2013).
8. T. Wiedmann, *Ecol. Econ.* **68**, 1975–1990 (2009).
9. A. Y. Hoekstra, M. M. Mekonnen, *Proc. Natl. Acad. Sci. U.S.A.* **109**, 3232–3237 (2012).
10. T. O. Wiedmann *et al.*, *Proc. Natl. Acad. Sci. U.S.A.* (2013).
11. F. Wang *et al.*, *J. Environ. Qual.* **40**, 1081–1089 (2011).
12. T. Wiedmann, J. Minx, in *Ecological Economics Research Trends*, C. C. Pertsova, Ed. (Nova Science, Hauppauge, NY, 2008), pp. 1–11.
13. A. M. Leach *et al.*, *Environ. Dev.* **1**, 40–66 (2012).
14. M. Lenzen *et al.*, *Nature* **486**, 109–112 (2012).
15. J. Rockström *et al.*, *Nature* **461**, 472–475 (2009).
16. M. Borucke *et al.*, *Ecol. Indic.* **24**, 518–533 (2013).
17. A. Y. Hoekstra, M. M. Mekonnen, A. K. Chapagain, R. E. Mathews, B. D. Richter, *PLOS ONE* **7**, e32688 (2012).
18. C. Liu, C. Kroeze, A. Y. Hoekstra, W. Gerbens-Leenes, *Ecol. Indic.* **18**, 42–49 (2012).
19. UNEP, "The emissions gap report 2012" (United Nations Environment Programme, Nairobi, Kenya, 2012).
20. D. Gerten *et al.*, *Curr. Opin. Environ. Sust.* **5**, 551–558 (2013).
21. M. R. Allen *et al.*, *Nature* **458**, 1163–1166 (2009).
22. M. Meinshausen *et al.*, *Nature* **458**, 1158–1162 (2009).
23. I. A. Shiklomanov, J. C. Rodda, *World Water Resources at the Beginning of the Twenty-First Century*. (Cambridge Univ. Press, Cambridge, UK, 2004).
24. L. Čuček, J. J. Klemeš, Z. Kravanja, *Chem. Eng. Trans.* **25**, 923–928 (2011).
25. T. A. Boden, G. Marland, R. J. Andres, "Global, Regional, and National Fossil-Fuel CO_2 Emissions" (Carbon Dioxide Information Analysis Center, Oak Ridge National Laboratory, U.S. Department of Energy, Oak Ridge, TN, 2010).
26. G. P. Peters *et al.*, *Nat. Clim. Change* **2**, 2–4 (2012).
27. D. Moore, G. Cranston, A. Reed, A. Galli, *Ecol. Indic.* **16**, 3–10 (2012).
28. A. E. Ercin, A. Y. Hoekstra, *Environ. Int.* **64**, 71–82 (2014).
29. M. Herva, A. Franco, E. F. Carrasco, E. Roca, *J. Clean. Prod.* **19**, 1687–1699 (2011).
30. L. Čuček, J. J. Klemeš, Z. Kravanja, *J. Clean. Prod.* **34**, 9–20 (2012).
31. H. S. Matthews, C. T. Hendrickson, C. L. Weber, *Environ. Sci. Technol.* **42**, 5839–5842 (2008).
32. A. Y. Hoekstra, *The Water Footprint of Modern Consumer Society* (Routledge, London, UK, 2013).
33. WRI, WBCSD, "Greenhouse Gas Protocol Corporate Value Chain (Scope 3) Accounting and Reporting Standard" (World Resources Institute and World Business Council for Sustainable Development, Geneva, Switzerland, 2011).
34. Y. A. Huang, C. L. Weber, H. S. Matthews, *Environ. Sci. Technol.* **43**, 8509–8515 (2009).
35. T. O. Wiedmann, M. Lenzen, J. R. Barrett, *J. Ind. Ecol.* **13**, 361–383 (2009).
36. W. Gerbens-Leenes, A. Y. Hoekstra, T. H. van der Meer, *Proc. Natl. Acad. Sci. U.S.A.* **106**, 10219–10223 (2009).
37. E. G. Hertwich, G. P. Peters, *Environ. Sci. Technol.* **43**, 6414–6420 (2009).
38. J. Minx *et al.*, *Environ. Res. Lett.* **8**, 035039 (2013).
39. T. Jackson, *Prosperity without Growth—Economics for a Finite Planet*. (Earthscan, London, UK, 2009).
40. J. A. Foley *et al.*, *Nature* **478**, 337–342 (2011).
41. D. Vanham, A. Y. Hoekstra, G. Bidoglio, *Environ. Int.* **61**, 45–56 (2013).
42. C. M. Jones, D. M. Kammen, *Environ. Sci. Technol.* **45**, 4088–4095 (2011).
43. T. Jackson, E. Papathanasopoulou, *Ecol. Econ.* **68**, 80–95 (2008).
44. D. Chakravarty, S. Dasgupta, J. Roy, *Curr Opin Environ Sust* **5**, 216–228 (2013).
45. G. P. Peters, J. C. Minx, C. L. Weber, O. Edenhofer, *Proc. Natl. Acad. Sci. U.S.A.* **108**, 8903–8908 (2011).
46. V. Niccolucci, E. Tiezzi, F. M. Pulselli, C. Capineri, *Ecol. Indic.* **16**, 23–30 (2012).
47. M. C. Rulli, A. Saviori, P. D'Odorico, *Proc. Natl. Acad. Sci. U.S.A.* **110**, 892–897 (2013).
48. P. Lamers, C. Hamelinck, M. Junginger, A. Faaij, *Renew. Sustain. Energy Rev.* **15**, 2655–2676 (2011).
49. M. Harvey, S. Pilgrim, *Food Policy* **36** (suppl. 1), S40–S51 (2011).
50. P. W. Gerbens-Leenes, A. R. Lienden, A. Y. Hoekstra, T. H. van der Meer, *Glob. Environ. Change* **22**, 764–775 (2012).
51. UNIDO, "Global industrial energy efficiency benchmarking: An energy policy tool" (United Nations Industrial Development Organization, Vienna, Austria, 2010).
52. J. Chenoweth, M. Hadjikakou, C. Zoumides, *Hydrol. Earth Syst. Sci. Discuss.* **10**, 9389–9433 (2013).
53. A. Kounina *et al.*, *Int J LCA* **18**, 707–721 (2013).
54. N. Fiala, *Ecol. Econ.* **67**, 519–525 (2008).
55. G. P. Peters, E. G. Hertwich, *Clim. Change* **86**, 51–66 (2008).
56. M. Lenzen, J. Murray, F. Sack, T. Wiedmann, *Ecol. Econ.* **61**, 27–42 (2007).
57. N. Hanasaki, T. Inuzuka, S. Kanae, T. Oki, *J. Hydrol.* **384**, 232–244 (2010).
58. M. Dittrich, S. Giljum, S. Lutter, C. Polzin, "Green economies around the world? Implications of resource use for development and the environment" (Sustainable Europe Research Institute, Vienna, Austria, 2012).

10.1126/science.1248365

REVIEW

Slowing Amazon deforestation through public policy and interventions in beef and soy supply chains

Daniel Nepstad,[1]* David McGrath,[1,2] Claudia Stickler,[1] Ane Alencar,[3] Andrea Azevedo,[3] Briana Swette,[1] Tathiana Bezerra,[1] Maria DiGiano,[1] João Shimada,[1] Ronaldo Seroa da Motta,[4] Eric Armijo,[1] Leandro Castello,[5] Paulo Brando,[3,6] Matt C. Hansen,[7] Max McGrath-Horn,[1] Oswaldo Carvalho,[1] Laura Hess[8]

The recent 70% decline in deforestation in the Brazilian Amazon suggests that it is possible to manage the advance of a vast agricultural frontier. Enforcement of laws, interventions in soy and beef supply chains, restrictions on access to credit, and expansion of protected areas appear to have contributed to this decline, as did a decline in the demand for new deforestation. The supply chain interventions that fed into this deceleration are precariously dependent on corporate risk management, and public policies have relied excessively on punitive measures. Systems for delivering positive incentives for farmers to forgo deforestation have been designed but not fully implemented. Territorial approaches to deforestation have been effective and could consolidate progress in slowing deforestation while providing a framework for addressing other important dimensions of sustainable development.

The prospect of ending Amazon deforestation with most of the forest still standing while agricultural production continues to grow (*1*) has improved in Brazil. Deforestation—the clear-cutting of mature forest—declined from a 10-year average of 19,500 km^2 $year^{-1}$ through 2005 to 5843 km^2 in 2013, a 70% reduction. Soy production, the most profitable Amazon land use, continued to grow (Fig. 1). The deceleration of deforestation has avoided the emissions of 3.2 Gt CO_2 to the atmosphere [see the supplementary materials (SM)] and has made Brazil the global leader in climate change mitigation. The decline in deforestation may have triggered a cascade of positive impacts, including reduced risk of regional rainfall inhibition, fewer changes in river discharge and sedimentation, and increased biodiversity conservation (*2*–*4*).

Several studies have analyzed aspects of the decline in deforestation in the Brazilian Amazon (summarized in fig. S1), but we provide a much-needed critical review of the full range of policy interventions and commodity market effects, including "supply chain" interventions involving producers, processors, and/or buyers of soy or beef, the two main historical drivers of Amazon deforestation.

Hypotheses

The deceleration of deforestation in the Brazilian Amazon is the aggregate effect of thousands of landholders and land speculators who chose to clear less forest since 2004. We examine eight hypothetical causes of this decline (table S1). Hypothesis 1 (H1): Landholders came to associate deforestation with higher risks of reduced access to markets and finance or (H2) fines, embargos on their products (SM), and even prison sentences. H3: Landholders began to realize benefits through payment for ecosystem services, price premiums from certification, and access to new credit lines by foregoing deforestation. H4: Land speculators cleared less forest because the expansion of protected areas reduced the supply of undesignated or loosely claimed forestland, and (H5) stalled highway paving projects meant that potential new supplies of such forestland were not accessible. H6: The demand for new crop- and pastureland declined when the profitability of soy production fell, (H7) when beef intensification elevated production on existing cleared lands, and (H8) when the regional cattle herd was reduced in size.

Three Phases of Deforestation

Three phases in Brazil's decline in Amazon deforestation can be distinguished as we interpret its possible causes (Fig. 2). Descriptions of the public policy and supply chain interventions and international pledges (i.e., Norway) referred to in this section are summarized in fig. S1, table S2, and accompanying supplementary text.

Phase 1: Agro-Industrial Expansion

From the late 1990s through 2004, Amazon deforestation became far more sensitive to global influences as commodity market conditions and technological advances favored the first large-scale expansion of soy and other mechanized crops into the region (*5*). During the final years of this phase, soy prices and deforestation spiked (Fig. 1A and fig. S2); more than half of this forest clearing took place in the southeastern Amazon state of Mato Grosso, Brazil's largest agricultural producer (fig. S3). Cattle production intensified, with yields increasing fivefold (Fig. 1B) (*6*–*9*).

The Brazilian Forest Code (FC) was the most important legal restriction on forest clearing on private lands. It establishes a minimum portion of each property that must be managed as a forest reserve (*reserva legal*). In the Amazon region, the *reserva legal* was increased from 50 to 80% in 1996, making compliance virtually unattainable (*10*), reducing the law's credibility (SM); enforcement was also encumbered by the lack of a rural property cadastral database. The Rural Property Environmental Licensing System (SLPR) was launched in Mato Grosso (*11*) to address this deficiency. In this phase, protected areas and indigenous reserves were established at a slow rate, far from the active agricultural frontier (*12*).

Phase 2: Frontier Governance

From 2005 through 2006, the profitability of Brazilian soy production plummeted, driving a retraction in the area of soy planted in the Brazilian Amazon (*1*, *7*) (figs. S1, S2, and S4). Law enforcement capacity increased with the launch in 2004 of the Detection of Deforestation in Real Time (DETER) system for detecting and responding to deforestation events (table S2). The "Plan for the Protection and Control of Deforestation in the Amazon" (PPCDAm) (table S2) was also created, elevating the issue of Amazon deforestation to the president's office and, facilitating coordination and collaboration across several ministries, including the federal police and the powerful public prosecutor's office (Ministério Público). In 2006, a Greenpeace-led attack on the Brazilian Amazon soy industry led to a "Soy Moratorium" that was joined by most of the buyers of Amazon soybeans (SM). Through the moratorium, farmers who grew soy on land cleared after 26 July 2006 were no longer able to sell to participating buyers (Fig. 1 and fig. S1) (*13*).

Regional planning processes organized to prepare for highway paving projects (Fig. 3A), strong political leadership, and a national commitment to expand protected areas (Amazon Region Protected Areas Program,) (table S2) resulted in rapid expansion of the protected area and indigenous territory network (*14*, *15*). From 2004 through 2012, protected areas and indigenous territories grew 68% to encompass 47% of the entire Brazilian Amazon region, with many of these areas

[1]Earth Innovation Institute, 3180 18th Street, Suite 205, San Francisco, CA 94110, USA. [2]Universidade Federal do Oeste do Pará, Bairro Fátima CEP 68040-470 Santarém, Pará, Brasil. [3]Instituto de Pesquisa Ambiental da Amazônia, SHIN CA 5, Bloco J2, Sala 309, Bairro, Lago Norte, Brasília-DF 71503-505. [4]Universidade do Estado do Rio de Janeiro, Rio de Janeiro, Brasil. [5]Virginia Polytechnic Institute and State University, Blacksburg, VA 24061, USA. [6]Carnegie Institution for Science, 260 Panama Street, Stanford, CA 94305, USA. [7]University of Maryland Department of Geographical Sciences, College Park, MD 20742, USA. [8]Earth Research Institute, University of California, Santa Barbara, CA 93106–3060, USA.
*Corresponding author. E-mail: dnepstad@earthinnovation.org

created in active agricultural frontiers (*15*) (Figs 1 and 3) (SM).

Phase 3: Territorial Performance

During this phase, the profitability of soy production began to increase, and the intensity of cattle production continued to grow (Fig. 1B and fig. S2) (*8*, *9*). A territorial performance approach to deforestation was adopted in which the geographical unit of intervention was the county (*município*) instead of the individual farm. Through a collaboration between the Central Bank and Environment Ministry, the Critical Counties program was launched, suspending access to agricultural credit for those farms and ranches located in the 36 counties with the highest deforestation rates (fig. S1 and table S2). The program stimulated collective action to reduce deforestation, mimicking some of the lessons of Brazil's successful program to eradicate foot-and-mouth disease (*5*); 11 counties succeeded in drastically reducing deforestation (*16*) (fig. S5). In response to this program, the state of Pará has launched a Green County program to help blacklisted counties reduce their deforestation rates and reestablish access to credit (table S2).

This phase also includes the first programs to create positive incentives for landholders who are making the transition to low-deforestation sustainable production systems. The National Climate Change Policy (NCCP) established the goal of an 80% reduction in Amazon deforestation by 2020 and launched a new line of farm-level low-carbon credits to help achieve this decline (SM). The Amazon Fund was created with a US$1B performance-based pledge from Norway that has been partially disbursed as deforestation has declined. Reducing Emissions from Deforestation and Forest Degradation (REDD) programs, intended to attract payments as compensation for state-wide reductions in deforestation and associated carbon emissions, were designed by the governments of most Amazon states (*1*, *17*), and some attracted investments (SM).

Property-level law enforcement capacity was also improved in 2009 through the Rural Environmental Registry [Cadastro Ambiental Rural (CAR)] in Mato Grosso and Pará. It requires landholders to submit their property boundaries to the state environmental regulatory agency (SM).

Pressured by the growing capacity of the government to enforce the FC and market demands for legal compliance (SM), a powerful faction of the agribusiness lobby sought revisions in the code. In the case of the Amazon, the 1996 increase in the *reserva legal* requirement had made compliance unattainable for most producers because it imposed more than US$2B in opportunity costs (*10*) (SM). A New Forest Code (NFC) was signed into law in 2012 (fig. S1 and table S2). Although the legal reserve requirement did not change, the NFC provided amnesty for landholders with 29 million hectares of illegal deforestation

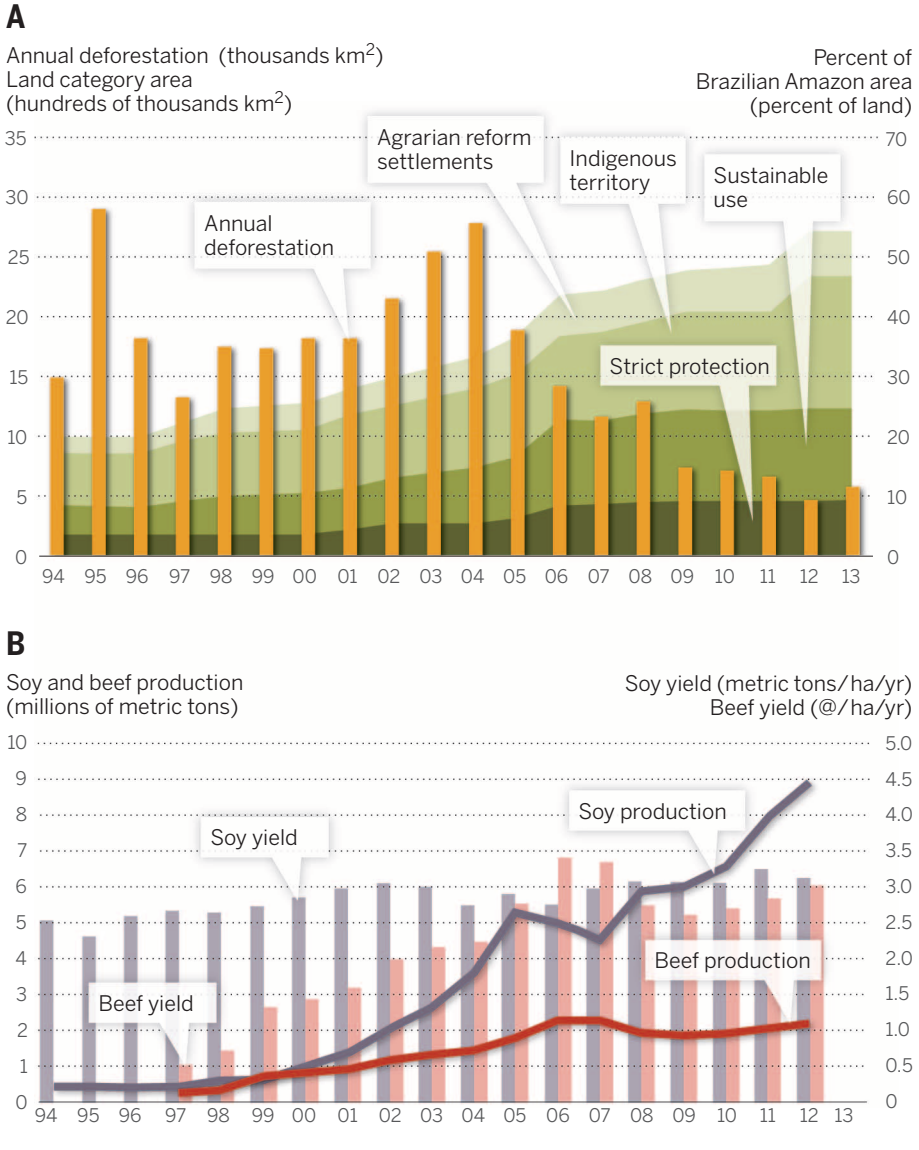

Fig. 1. Deforestation, area of land use categories, and production (beef and soy) trends in the Brazilian Amazon. (**A**) Annual deforestation and the area of indigenous territories, sustainable development reserves (e.g., extractive reserves), strict protection reserves, and agrarian reform settlements. (**B**) Soy and beef production and yields (for beef yields, @ = 15 kg of carcass weight) in the Brazilian Amazon. Annual deforestation data are from Instituto Nacional de Pesquisas Espaciais (INPE) (*26*). Indigenous territories, sustainable development reserves, and strict protection reserves are updated from Castello *et al*. (*24*), Instituto Socioambiental (ISA) (*27*), Nepstad *et al*. (*28*), and World Database on Protected Areas (WDPA) (*29*). Settlements area is from Instituto Nacional de Colonização e Reforma Agrária (INCRA) (*30*). Cattle herd and soy production data are from Instituto Brasileiro de Geografia e Estatística (IBGE) (*31*) and Nassar *et al*. (*9*).

that had taken place before July 2008 (*18*). It also introduced new measures for creating positive incentives for legal compliance (*10*). With the NFC, the farm and livestock sectors suddenly had a pathway to full legal compliance with the Amazon region's most important environmental regulation.

In 2009, a new Greenpeace campaign aimed at the Brazilian beef-processing company, Bertin—and subsequent legal proceedings against irregular slaughterhouses carried out by the Public Prosecutor's office—led to a "Cattle Agreement" in which the region's largest beef processing companies agreed to exclude from their supply chain those livestock producers who deforested after October 2009 (SM). Agricultural certification initiatives were launched during this period and are still at an early stage, as summarized in the SM (Fig. 3D).

Why Did Deforestation Decline?

The decline in deforestation during the "frontier governance" phase, from 2005 through 2007, was the result of several mutually reinforcing factors that decreased the demand for new deforestation, increased the risks to those engaged in deforestation, and reduced the supply of undesignated or loosely claimed forestland that is the target of land speculators. The demand for new deforestation declined through both a retraction in the area of soy production (supporting H6) (fig. S4), rapidly rising beef yields (H7) (Fig. 1B) and a sharp reduction in the size of the Amazon cattle herd (H8) (*9*). Deforestation became riskier through improved law enforcement, fines and embargos imposed on those associated with illegal deforestation (H2), and market rejection of deforesters through the Soy Moratorium (H3). The supply of undesignated forestland was limited through both a rapid expansion of protected areas in active agricultural frontier zones (*7*, *12*) (Fig. 1A) (H4) and delays in highway paving (H5) (SM).

The initial test of the measures implemented to slow deforestation came during the Territorial Performance phase, when soy profitability rose again and soy production increased (Fig. 1B and fig. S2). Demand for new deforestation did not come directly from the soy sector, however. The 50% expansion in soy production through 2013 took place entirely on land cleared before 2006 (fig. S6). During this period, beef production remained flat as the herd was rebuilt, gradually increasing demand for new pasture. In addition to the measures already in place, the risks associated with deforestation were further elevated through the Critical County program and the Cattle Agreement of 2009 (SM).

The contribution of each of these factors to the decline in deforestation is extremely difficult to measure because of the temporal and spatial overlap of the policy and supply chain interventions that were made. Spatial simulation modeling has found an important role of new protected areas in slowing deforestation (*12*). Econometric studies (*19*, *20*) have concluded that the rural credit restrictions implemented through the Critical Counties program contributed significantly to

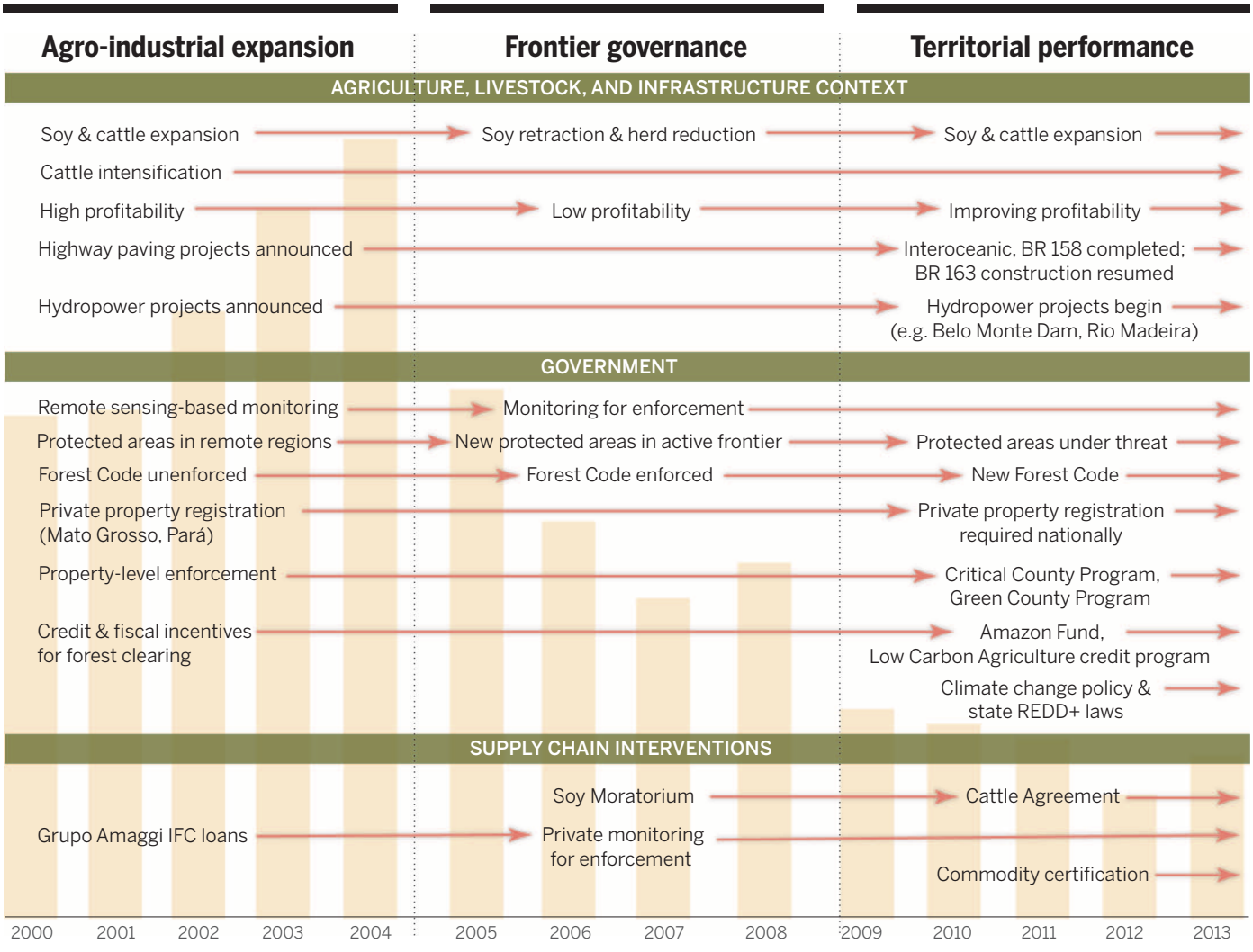

Fig. 2. Phases in the evolution of public policies and supply chain initiatives to control Amazon deforestation: 2000 to 2013. The underlying bar graph is the annual deforestation trend as shown in Fig. 1A. Sources for policy interventions are in table S2.

the decline in deforestation during this phase (table S1) (SM).

Discussion

Is the decline in deforestation sustainable, with 80% of the forest still standing? The long-term trend in deforestation will depend, in part, on continuing increases in livestock yields on existing cleared land. Cattle pasture is the main use of cleared land, and beef production has the greatest potential for yield increases compared with cropping systems (*6*). Amazon deforestation is not "decoupled" from expansion in crop and beef production, as Macedo *et al.* have concluded, unless beef yields climb fast enough to open up pastureland for soy expansion, which is a plausible scenario through 2020 (*7*, *9*). Eventually, cleared land that is suitable for soy production—the most profitable use of cleared land—will become scarce. As this scarcity sets in, the 120,000 km^2 of forests that could be profitably converted to soy in the Brazilian Amazon and that lie outside of protected areas (*4*) will become the target of deforestation pressure. Alternatively, expansion of crop and beef production could shift more heavily to the Cerrado biome to the south of the Amazon, where deforestation rates have been climbing since 2010 (*18*).

Future trends in Amazon deforestation will also depend on a continued perception of risk associated with deforestation. An important source of market access risk for soy producers is the Soy Moratorium, which is scheduled to end in 2014 because of the large number of legal soy producers who have been cut off from the market (SM). The government's command-and-control measures to fine and embargo illegal deforesters, and cut entire counties off from public agricultural credit, is precariously dependent upon the political will of government to impose these measures, which may be weakening in the face of a stagnant national economy (*21*). One early sign of a shift in political will is the reduction in size of some protected areas (*22*).

As demand for new deforestation increases, as supply chain interventions to discourage deforestation weaken, and if deforestation policies and programs lose political will, positive incentives for farmers, counties, and states that are forgoing or reducing deforestation will grow in importance. Systems for delivering these incentives are

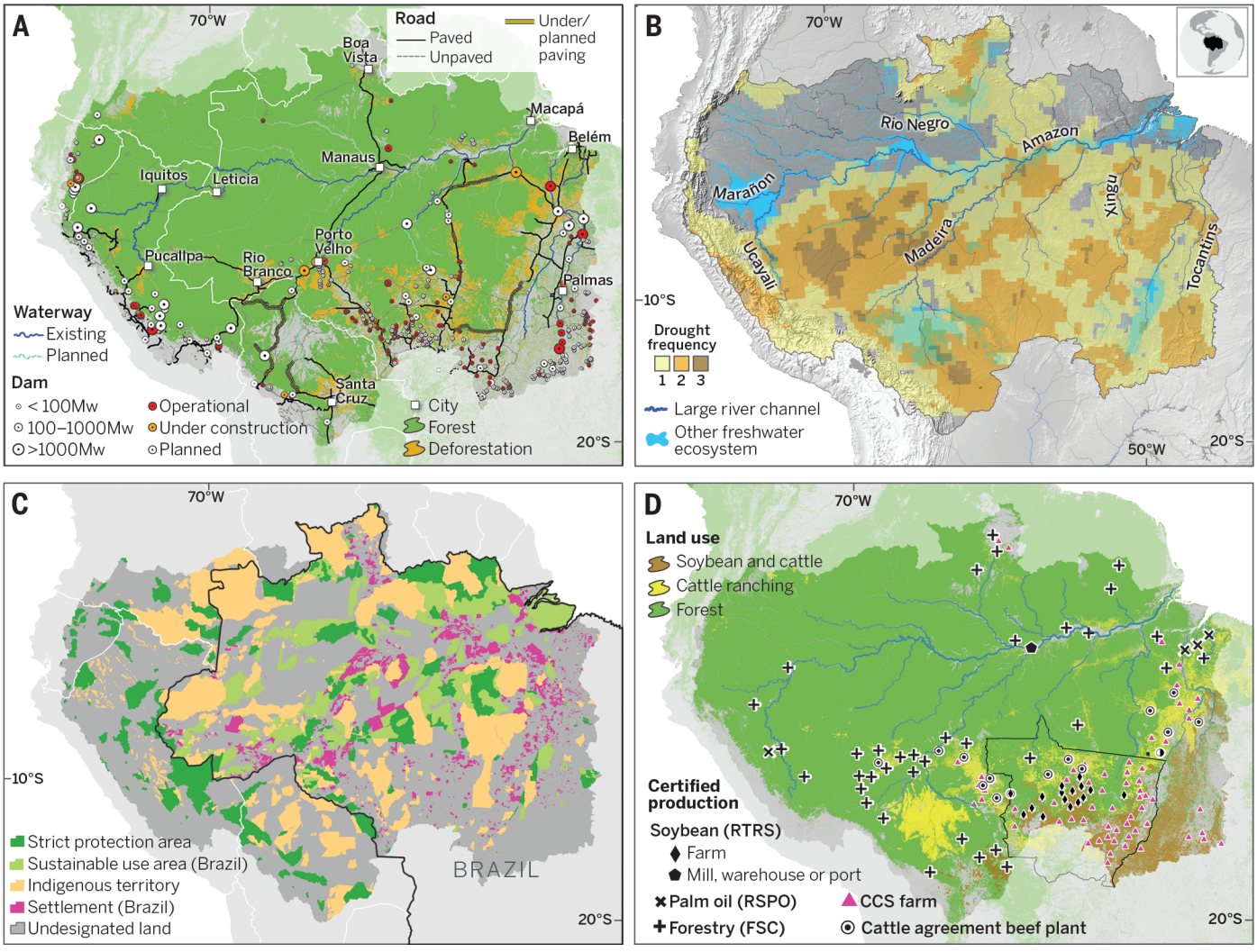

Fig. 3. The status of the Amazon region. (**A**) Infrastructure and forest loss since 2000. Highways (paved, unpaved, and planned paving), waterways (current and planned), and hydropower plants (current, under construction, and planned, with output scaled by size). Forest loss is of all forest types from 2000 through 2012 (*32*). Infrastructure updated from Soares-Filho *et al*. (*33*) and Castello *et al*. (*23*). (**B**) Rivers, other wetland ecosystems (*23*), and the number of drought episodes that exceeded the threshold of rainfall deficit [updated from Lewis *et al*. (*34*)]. (**C**) Indigenous territories, sustainable development reserves, strict protection reserves [updated from Castello *et al*. (*23*), ISA (*27*), Nepstad *et al*. (*28*), and WDPA (*29*)], agrarian reform farm settlements (Brazil only) from INCRA (*30*), and undesignated land (public and private, registered or not). (**D**) Areas of cattle and soy production (IBGE) (*31*) and locations of certified soy production and processing (Roundtable on Responsible Soy) (*35*), palm oil mills (Roundtable on Sustainable Palm Oil) (*36*), timber production (Forest Stewardship Council) (*37*, *38*), beef plants in the Cattle Agreement (*39*), and farms in the Registry of Socio-Environmental Responsibility (CCS) (*40*).

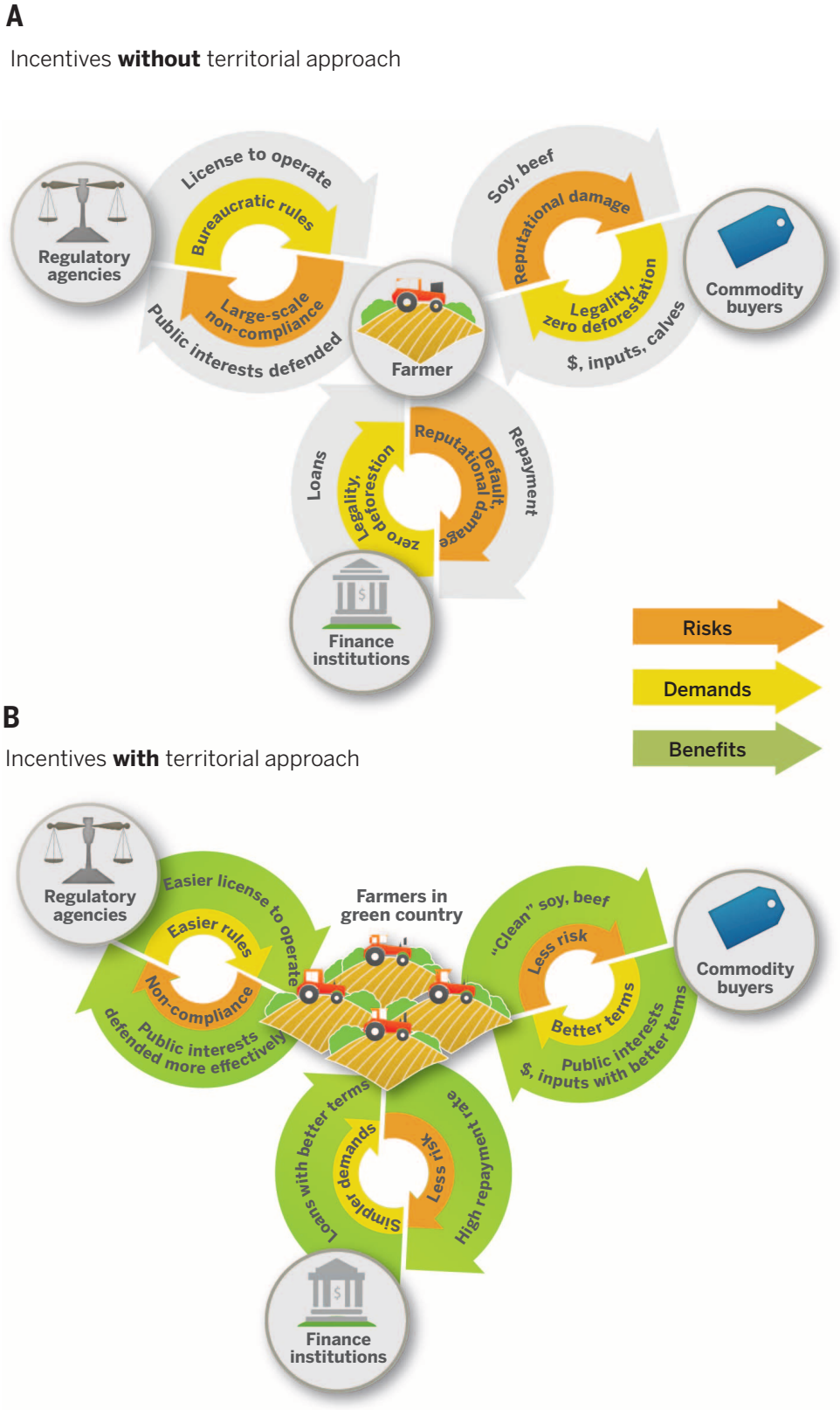

Fig. 4. Incentives for sustainable production with and without territorial performance approach. (**A**) Farmers operating in isolation are faced with many demands from regulatory agencies, commodity buyers, and financial institutions but do not receive significant positive incentives to slow deforestation. (**B**) The type of collective action to slow deforestation that is achieved in the Green County program could be reinforced through multiple incentives for territorial (county-wide) declines in deforestation. Regulatory agencies can simplify their licensing procedures, commodity suppliers can give full access to markets and better terms on preharvest loan packages, and banks can lower interest rates and improve terms (*41*).

not yet operating at scale and appear to have contributed little to the decline in deforestation (H3) even though considerable progress has been made toward establishing legal frameworks and farm-level approaches for eventually delivering these incentives (SM). Some immediate and simple positive incentives for farmers who forgo deforestation and invest in more intensive, sustainable production systems could be established without major new policies or markets for ecosystem services (Fig. 4A). Regulatory agencies could simplify their regulatory requirements or give discounts on their environmental licensing procedures, commodity suppliers could give better terms on preharvest packages, and banks could give lower interest rates or better terms on loans to legally compliant landholders. These incentives could increase for farmers in counties that have come off the Critical County black list or that are making measurable progress toward sustainable development in other ways (Fig. 4B), building on the early success of the Critical Counties program. Climate finance programs, such as the Amazon Fund, could establish innovative, competitive funding mechanisms for delivering finance to regional consortia that are ready to make the transition to low-deforestation, high-production land use systems. The new Forest Code establishes a policy framework for creating positives (*10*).

Supply chain and public policy initiatives could also become better aligned through a shared set of performance targets for further reducing deforestation that are accompanied by commitments from the relevant institutions and actors to help achieve these targets. For example, farmers; companies that produce, process, or purchase soy and beef; finance institutions; regulatory agencies; and environmental groups might agree that if counties, states, or the entire Brazilian Amazon achieve an 80% reduction in deforestation below the 10-year average, they should be considered "low deforestation" counties, conferring on the farmers in the successful territory the benefits described in Fig. 4B, including full access to markets. The target may increase to a 90% reduction in 2018. This approach could lower the costs of tracking the forest-clearing activities of millions of individual farms and ranches, which is required in the supply chain approach to deforestation. A critical issue is whether companies that have Amazon producers in their beef and soy supply chains will accept a deforestation agreement that is not absolute "zero" deforestation but that is more in line with a regional development strategy.

In the Amazon deforestation debate, little attention is paid to mechanisms for attracting investors into the Amazon region to sustainably develop its forests, fisheries, and agricultural potential. Advances in frontier governance, law enforcement, and mechanisms for punishing deforesters through restrictions on access to markets and finance succeeded in decelerating deforestation but failed to address the region's need for private investment, innovation, and enterprise. Land titling, which is fundamental to the landholder's ability to access credit, continues to progress slowly. Instead, effective campaigns by Greenpeace and others have increased the reputational risk of companies that do business in the Amazon, scaring away potential investors and market players. Consequently, the responsible agricultural and livestock companies and individuals who are needed to consolidate the progress made in reducing deforestation in the Brazilian Amazon may be driven away by the success of these campaigns.

Deforestation is only one of the threats to the Amazon region. Extensive forest fires during severe drought episodes kill mature trees, opening standing forests up to invasion by grasses and recurrent burning (Fig. 3B) (*4*, *23*). Hydropower dams, waterways (Fig. 3A), and overfishing threaten the fisheries, river ecosystems, and associated wetlands of the region, which are critical to the regional economies and to the livelihoods of indigenous and traditional communities (SM) (*24*). In addition, mining continues to degrade streams and forests through both physical disturbance and chemical pollution (*25*).

Conclusion

Brazil's remarkable decline in deforestation provides valuable lessons on the importance of public policies, monitoring systems, and supply chain interventions in slowing the advance of a vast, complex agricultural frontier. The challenge now is to build upon this progress to construct a strategy for promoting a new model of rural development in which punitive measures are complemented by positive incentives and finance at scale for landholders, indigenous communities, counties, and states to make the transition to low-deforestation, productive, sustainable rural development. Deforestation is only one dimension of the health of the Amazon Basin.

REFERENCES AND NOTES

1. D. Nepstad *et al*., *Science* **326**, 1350–1351 (2009).
2. E. A. Davidson *et al*., *Nature* **481**, 321–328 (2012).
3. P. M. Brando, M. T. Coe, R. DeFries, A. A. Azevedo, *Philos. Trans. R. Soc. Lond. B Biol. Sci.* **368**, 20120152 (2013).
4. D. C. Nepstad, C. M. Stickler, B. S. Filho, F. Merry, *Philos. Trans. R. Soc. Lond. B Biol. Sci.* **363**, 1737–1746 (2008).
5. D. C. Nepstad, C. M. Stickler, O. T. Almeida, *Conserv. Biol.* **20**, 1595–1603 (2006).
6. A. S. Cohn *et al*., *Proc. Natl. Acad. Sci. U.S.A.* (2014).
7. M. N. Macedo *et al*., *Proc. Natl. Acad. Sci. U.S.A.* **109**, 1341–1346 (2012).
8. G. L. Galford, J. Melillo, J. F. Mustard, C. E. P. Cerri, C. C. Cerri, *Earth Interact.* **14**, 1–24 (2010).
9. A. Nassar *et al*., "Brazil's pathway to low-emission rural development" (Agrolcone and Earth Innovation Institute, São Paulo, 2014); http://earthinnovation.org/wp-content/uploads/2014/05/Nassar_etal_2014.pdf.
10. C. M. Stickler, D. C. Nepstad, A. A. Azevedo, D. G. McGrath, *Philos. Trans. R. Soc. Lond. B Biol. Sci.* **368**, 20120160 (2013).
11. R. Rajão, A. Azevedo, M. C. C. Stabile, *Public Adm. Dev.* **32**, 229–244 (2012).
12. B. Soares-Filho *et al*., *Proc. Natl. Acad. Sci. U.S.A.* **107**, 10821–10826 (2010).
13. B. F. T. Rudorff *et al*., *Remote Sens.* **3**, 185–202 (2011).
14. M. T. Campos, D. C. Nepstad, *Conserv. Biol.* **20**, 1553–1556 (2006).
15. S. Schwartzman, A. Alencar, H. Zarin, A. P. Santos Souza, *J. Environ. Dev.* **19**, 274 (2010).
16. Ministerio do Meio Ambiente, Lista de Municípios Prioritários da Amazônia, (Ministerio do Meio Ambiente, Brasília, Brasil, 2014). http://www.mma.gov.br/florestas/controle-e-prevenčão-do-desmatamento/plano-de-ação-para-amazônia-ppcdam/lista-de-municípios-prioritários-da-amazônia
17. D. Nepstad, W. Boyd, C. M. Stickler, T. Bezerra, A. Azevedo, *Philos. Trans. R. Soc. B.* **368**, 20120167 (2013).
18. B. Soares-Filho *et al*., *Science* **344**, 363–364 (2014).
19. J. Assunção, C. Gandour, R. Rocha, R. Rocha, "Does Credit Affect Deforestation? Evidence from a Rural Credit Policy in the Brazilian Amazon" (Climate Policy Institute, Rio de Janeiro, 2013); www.climatepolicyinitiative.org.
20. J. Hargrave, K. Kis-Katos, *Environ. Resour. Econ.* **54**, 471–494 (2013).
21. H. Joyce, *Economist* (28 September 2013).
22. H. Martins, E. Araujo, M. Vedoveto, D. Monteiro, P. Barreto, "Desmatamento em Áreas Protegidas Reduzidas na Amazônia" (IMAZON, Belém, 2013).
23. P. M. Brando *et al*., *Proc. Natl. Acad. Sci. U.S.A.* **111**, 6347–6352 (2014).
24. L. Castello *et al*., *Conservation Letters* **6**, 217–229 (2013).
25. G. P. Asner, W. Llactayo, R. Tupayachi, E. R. Luna, *Proc. Natl. Acad. Sci. U.S.A.* **110**, 18454–18459 (2013).
26. Instituto Nacional de Pesquisas Espaciais (INPE, São Paulo, Brasil, 2013); www.obt.inpe.br/prodes/.
27. Instituto Socioambiental, Áreas Protegidas da Amazônia (São Paulo, Brasil, June 2011).
28. D. Nepstad *et al*., *Conserv. Biol.* **20**, 65–73 (2006).
29. WDPA, 2013. World Database on Protected Areas. Database accessed in February 2013 from www.protectedplanet.net/.
30. Imazon, Desmatamento nos Assentamentos de Reforma Agrária na Amazônia; available at: www.imazon.org.br/publicacoes/o-estado-da-amazonia/desmatamento-nos-assentamentos-de-reforma-agraria-na-amazonia (2011).
31. Instituto Brasileiro de Geografia e Estatística, Produção Agricola Municipal (IBGE, Rio de Janeiro, Brasil, 2013).
32. M. C. Hansen *et al*., *Science* **342**, 850–853 (2013).
33. B. S. Soares-Filho *et al*., *Nature* **440**, 520–523 (2006).
34. S. L. Lewis, P. M. Brando, O. L. Phillips, G. M. F. van der Heijden, D. Nepstad, *Science* **331**, 554 (2011).
35. Roundtable on Responsible Soy (RTRS, Buenos Aires, Argentina, 2013).
36. Roundtable on Sustainable Palm Oil (RSPO), (RSPO, Kuala Lumpur, Malaysia, 2013).
37. D. Santos, D. Pereira, A. Veríssimo, "O Estado da Amazônia: Uso da Terra" (Instituto do Homem e Meio Ambiente da Amazônia, Belém, 2013.
38. Certificación Forestal Voluntaria, Operaciones forestales certificadas. Consejo Boliviano para la Certificación Forestal Voluntaria (CFV) (2011).
39. ABIEC, Associação Brasileira das Indústrias Exportadoras de Carne, Mapa das Plantas Frigoríficas; available from www.abiec.com.br/2_mapa.asp, (2012).
40. Aliança da Terra, Mapa Geral do CCS (Aliança da Terra, Goiânia, Brasil, 2014).
41. D. C. Nepstad *et al*., *Carbon Management* **4**, 639 (2013).

ACKNOWLEDGMENTS

K. Schwalbe helped with text editing and formatting; M. Nepstad designed Fig. 4. This work was funded through grants from the Norwegian Agency for Development Cooperation (QZA-0186, QZA-13/0548), the U.S. National Science Foundation (1146206), the Gordon and Betty Moore Foundation (3980), the Linden Conservation Trust, and Roger and Vicki Sant to the Earth Innovation Institute, Instituto de Pesquisa Ambiental da Amazônia International Program, or the Woods Hole Research Center.

SUPPLEMENTARY MATERIALS

www.sciencemag.org/content/344/6188/1118/suppl/DC1
Supplementary Text
Figs. S1 to S4
Tables S1 and S2
References (*42*–*76*)

10.1126/science.1248525

REVIEW

The science of sustainable supply chains

Dara O'Rourke*

Recent advances in the science and technology of global supply chain management offer near–real-time demand-response systems for decision-makers across production networks. Technology is helping propel "fast fashion" and "lean manufacturing," so that companies are better able to deliver products consumers want most. Yet companies know much less about the environmental and social impacts of their production networks. The failure to measure and manage these impacts can be explained in part by limitations in the science of sustainability measurement, as well as by weaknesses in systems to translate data into information that can be used by decision-makers inside corporations and government agencies. There also remain continued disincentives for firms to measure and pay the full costs of their supply chain impacts. I discuss the current state of monitoring, measuring, and analyzing information related to supply chain sustainability, as well as progress that has been made in translating this information into systems to advance more sustainable practices by corporations and consumers. Better data, decision-support tools, and incentives will be needed to move from simply managing supply chains for costs, compliance, and risk reduction to predicting and preventing unsustainable practices.

A buyer for a global apparel company can see sales data in each of their retail outlets, track and communicate with consumers, monitor orders being sent to factories, and assess the location of shipments in their global distribution system (*1*). Yet it is still almost impossible to trace the cotton in a popular shirt from the store back to the farms where it was grown (although the technology for radio frequency identification tagging of cotton exists), let alone to measure the full impacts and externalized costs of the apparel supply chain.

The scale of environmental and social impacts from global production and consumption makes this lack of knowledge—and failure to manage these impacts—increasingly concerning. Analysts have estimated that there are $4.7 trillion in environmental costs externalized each year from global production systems (*2*); 6.4 billion tons of carbon dioxide emitted, more than 20% of global emissions, through production of traded goods (*3*); and 567 km^3 per year of water associated with the global food trade alone (*4*). Also, current levels of global production and consumption are using 50% more natural resources and services than ecosystems regenerate (*5*, *6*). With growth in populations and in per capita consumption levels, expanding consumer classes around the world and the production networks that support them are driving major ecological pressures.

Corporations, nongovernmental organizations (NGOs), and governments have initiated a range of programs to measure and analyze the impacts of natural resource extraction, manufacturing, transportation, retail operations, product use, and end-of-life disposal. The science of sustainability measurement has progressed alongside efforts to advance supply chain traceability and transparency, data collection, impact assessment, and aggregation of data into indicators, scorecards, and eco-certifications. Advances in life-cycle assessment (LCA) and product "footprinting" (*7*, *8*) are increasingly being deployed in efforts to turn data into decision-support tools for global brands and retailers (*6*, *9*). Some companies have begun to institute incentives for change; to ban particularly problematic practices (from child labor to hazardous chemicals); and to develop new tools to better integrate sustainability into compliance, sourcing, and design (*10*–*12*).

These actions are being motivated by four major drivers: (i) regulatory pressures (led by a mix of U.S. states and European Union legislation); (ii) competitive pressures (for both cost reductions and supply chain innovations); (iii) stakeholder pressures (particularly targeting brand reputations and demands for greater transparency); and (iv) risks from supply chain disruptions (brought about by regional resource shortages and extreme weather events) (*6*, *13*).

Firms are responding to these pressures by demanding more information than ever before from their supply chains. However, accessing data from full supply chains can be expensive, time-consuming, and, sometimes, impossible. Companies are thus joining forces to motivate suppliers to divulge information to allow them to track performance and incentivize improvements. This has motivated the creation of several new industry collaborations and software platforms to help firms track and analyze data that have been hidden in global supply chains.

However, there are continued challenges in managing these collaborations and in connecting data from global supply chains to decision-makers inside companies and government agencies (*14*). Major impact areas from production remain hidden in supply chains, with unsustainable production practices implicitly or explicitly subsidized. This creates real barriers to addressing pressing sustainability challenges (*15*, *16*). There is a critical need to improve sustainability measurement systems, data collection and sharing processes, and decision-support tools to turn data into meaningful information to help change the behavior of retailers, brands, manufacturers, and, ultimately, consumers (*17*).

Supply Chains and Sustainability

Global brands and retailers deploy complex and fluid supply-and-demand networks, connecting global systems of marketing, branding, and distribution to regional nodes supplying raw materials, components, and finished products (Fig. 1). These networks often span the globe, extend five or six tiers deep, and can reconfigure overnight in response to changes in consumer demands, commodity prices, currency fluctuations, political risks, and so on (*18*).

The public tends to know only the top brands and retailers in these systems, such as Apple, Nike, and The Gap. Only recently have tier 1 suppliers such as Foxconn (the largest electronics manufacturer in the world), Pou Chen (the largest footwear manufacturer in the world), Li & Fung (the largest apparel manufacturer in the world), and Asia Pulp and Paper (one of the largest manufacturers of paper and packaging) come to public attention. However, these manufacturers are critical nodes connecting commodity markets for fibers, chemicals, metals, ingredients, and components to fast-changing consumer markets around the world.

The speed and dynamism of modern supply chains creates challenges for incorporating sustainability into production decisions (*19*). Product cycle times have become so compressed (*20*), and sourcing from real-time commodity markets so fluid, that even knowing what to measure and manage can be challenging (*21*). In areas where it directly benefits corporations, we have seen progress in measuring and accounting for energy, water, waste, and packaging. However, sustainability initiatives without direct cost savings have not advanced as far or as fast (*13*, *22*).

Fortunately, the scope of what matters and what directly benefits corporations is expanding (*6*, *22*). Companies increasingly need to know not only cost-related matters, but also supply chain–disruption risks related to extreme weather events, resource shortages, commodity price spikes, and labor unrest (*6*, *23*). Companies also need to track impending regulatory risks and manage risks to their brand reputation from pollution incidents, labor rights controversies, and the like. Companies thus need to know more than ever before about their full

Department of Environmental Science, Policy, and Management, 130 Mulford Hall, University of California, Berkeley, Berkeley, CA 94720, USA
*Corresponding author. E-mail: orourke@berkeley.edu

supply chain impacts and risks, ideally before their stakeholders (*6*, *9*, *13*, *24*–*26*).

Mapping Supply Chain Impacts

Global production systems have global ecological impacts, both "upstream" and "downstream" of a specific manufacturer or supplier. It is thus necessary to measure factors such as energy use, carbon emissions, water use, waste emissions, and land-use conversions across the full life cycle of production (*16*, *27*, *28*). A number of industries have been working to connect environmental indicator data to their production (*29*) and, as a first step, to map their supply chains (*17*, *30*). Recent efforts by global brands and retailers to map four or five layers of suppliers, including initiatives to trace commodities such as cotton; tin, tungsten, tantalum, and gold (so-called conflict minerals); and palm oil have faced surprising challenges (*6*, *24*, *31*). As one recent survey noted, "49 percent of global manufacturing executives, and 54 percent of those in the U.S., admit that their companies do not have supply chain visibility beyond their Tier 1 suppliers" (*32*).

A growing number of firms however, are now mapping and publishing supply chain information (*6*, *13*, *33*) (Table 1). These initiatives lay the groundwork for measuring primary impacts at each stage in the life cycle of a product from raw material extraction to transport, manufacturing, retail, use, and end-of-life management.

Firms are also increasingly reporting on their global operations and impacts. The Global Reporting Initiative (GRI) has become the leading standard for supply chain–impact reporting (*15*, *34*). The GRI provides guidance for companies to produce reports covering sustainability impacts. More than 80% of the largest 250 companies in the world and almost 6000 organizations in total now publish GRI-compliant reports. It should be noted, however, that GRI does not require measurement of impacts but, instead, focuses on implementation of environmental management systems. More companies and industry associations are now emphasizing supply chain impacts in these reports, requiring reporting and disclosure of sustainability performance (*35*, *36*).

Aggregating and Analyzing Impacts

LCA has been the primary methodology for turning sustainability data into useful information for decision-makers (*7*). LCA helps companies assess the environmental impacts associated with each stage in a product's life and to identify the "hot spots," or most important environmental impacts across the supply chain (*9*, *37*). Although the International Standards Organization and the United Nations have worked to codify and standardize LCA (*9*, *37*, *38*), heated debates remain on the merits of different approaches.

LCAs require the collection of substantial amounts of data to analyze even a simple product. SAP, IBM, SAS, and other software vendors have built tools to extract energy and water data from supply-chain procurement systems. However, companies must combine this with a life-cycle

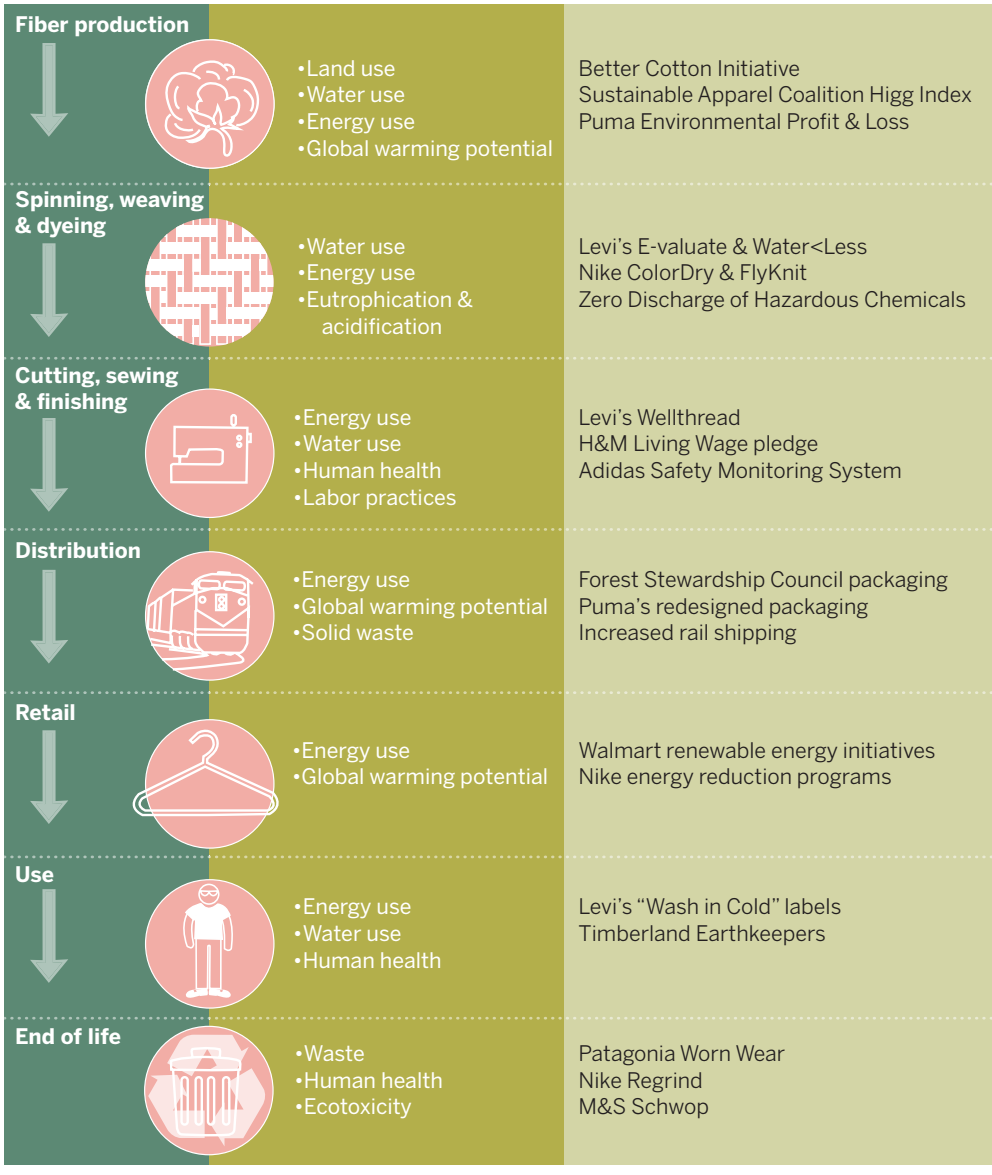

Fig. 1. Apparel supply chain initiatives. The apparel industry is an interesting sector for examining supply chain sustainability initiatives. LCA has been central to the work of the apparel industry. Leading brands and retailers have also experimented with a number of other strategies, driven by intense NGO and consumer pressures, including initiatives around traceability, impact assessment, and score-carding. Recently, a number of programs have come together within the Sustainable Apparel Coalition to develop the "Higg" sustainability index. These efforts are being translated into tools for product design, material selection, sourcing, manufacturing, use-phase interventions, and end-of-life management.

Table 1. Supply chain transparency initiatives.

Transparency type	Company initiatives
Supply chain traceability	Levi's Supplier List
	Nike Manufacturing Map
	Patagonia Footprint Chronicles
	All American Clothing
	Dole Organic banana tracker
Production processes information	ASDA—Factory web cams
	Levi's—Energy, water, chemicals commitments
	Tesco—Carbon emissions goals and performance
	Ben & Jerry's—From Cow to Cone
Production impacts	Puma's Environmental Profit and Loss Account
	Timberland—Green Index
	Nike—Our Impacts
	Apple—Environmental Footprint
	Unilever—Sustainable Living

inventory database such as the "ecoinvent" database (a collaborative effort of five Swiss research institutes) to bring together data sets covering relevant environmental flows, such as resource extractions, land use, emissions, and other material inputs (*39*).

Unfortunately, not every impact can be quantified, and some LCA data can be so variable that they lead to highly uncertain results. Data from generic upstream processes are often based on industry averages, which may not reflect a specific supply chain's impacts. Differing assumptions, system boundaries, data sets, and product uses, can influence the results of an LCA. Inconsistent rules and processes applied by LCA practitioners thus sometimes lead to contradictory conclusions (*6*, *9*, *37*).

A number of initiatives attempt to promote streamlined processes to measure product and supply chain impacts (*16*, *40*–*42*). A growing number of NGOs, academics, and government agencies are conducting "footprinting" exercises (*43*–*45*). Development of the "ecological footprint" in the early 1990s sought to create a measure of human demand on the Earth's ecosystems (*46*). The footprinting concept is now being applied to specific environmental resources, such as carbon and water (*8*). A number of analysts have built on emerging standards to develop tools for rapidly assessing thousands of products in a company's portfolio (*47*).

Use of divergent methodologies, data sets, assumptions, scopes of analysis, and system boundaries have led to confusion across footprinting initiatives (*48*). Recent efforts have thus sought to focus and constrain footprinting methods, to provide guidelines for how to conduct assessments of a specific product category (*49*), and to make the growing number of product assessments comparable (*38*).

Several large retailers are now developing their own LCA-like methods for quantifying product impacts and then turning these data into scorecards, indexes, and ratings systems (*13*, *18*, *50*, *51*). Target Corporation asked its suppliers of personal care and household chemical products to disclose product and supply chain information on ~7500 products. Target is evaluating these products and vendors for environmental and health performance, packaging, animal testing, and ingredient disclosure (via a tailored sustainability standard). Walmart has asked its suppliers to submit category-level sustainability data and is supporting the creation of a "Sustainability Index" via the Sustainability Consortium (*6*, *12*), an industry-academic collaborative working to create common sustainability measurement and reporting systems (*52*).

Decision Support

It is important to assess how these emerging footprints, indexes, and LCA results are actually used, as well as how newly gathered sustainability information is influencing decision-makers inside and outside companies (*21*). Perhaps the most ambitious strategy has been to translate environmental and social impact information into monetary terms, including, in some cases, into "profit-and-loss" statements [e.g., Puma, the footwear and apparel company (*15*, *53*)]. Companies calculate the value of the ecosystem services their supply chains draw on and estimate costs of degrading these ecosystems via their production processes (*54*). A related strategy has been to "price" resources and emissions, such as recent efforts to create internal pricing for carbon emissions at companies (such as Disney), and then to use this pricing in costing and sourcing decisions (*15*).

A related strategy has been to translate sustainability information into forms that investors can use, such as quantifying risks to a company's business (and stock value) from sustainability issues such as climate risks, stranded assets, water risks, and reputational risks. Many groups are now pressuring for companies to produce "integrated reports" in which they systematically report on financial and nonfinancial performance and risks (*36*).

A range of tools has been developed for decision-makers inside companies (*55*). These include tools for designers to incorporate sustainability concerns and trade-offs into their product decisions (*56*), for sourcing departments to incorporate analysis of resource risks into their selection of countries to source from (*17*, *18*, *56*–*58*), and for buyers inside retailers to assess the sustainability of products and brands they put on their shelves (*59*).

Finally, a number of initiatives have emerged to provide sustainability information directly to consumers. This has historically occurred through product eco-certifications (such as the Forest Stewardship Council, the Marine Stewardship Council, and Green Seal). More recently, initiatives have aggregated data from multiple public sources, including ratings and certification data, and then delivered it to consumers through Web and mobile apps at the point of purchase, such as GoodGuide.com (*12*, *15*, *17*).

Limitations of Current Science and Tools for Sustainability

There are still major debates on how best to conduct product and supply-chain sustainability assessments, as well as continued variations in methodologies, software tools, databases, and regional contexts (*6*, *22*). There are also continued limits to LCA and footprinting analyses (*9*) with researchers only recently bringing in critical issues such as biodiversity impacts (*39*) and social impacts such as working conditions and human health (*60*). Challenges also remain in connecting tier 1 data (collected by a supplier) to data for tiers two through five (which is often modeled) (*24*). Different levels of data often do not connect (*9*, *44*), and there are myriad weaknesses in publicly available data (*18*).

Tools such as LCA remain both too complicated and not specific enough (because of continued dependence on industry-average upstream data sets). Corporations complain about the cost and time required to conduct LCAs. It remains infeasible to conduct LCAs on every product in a large brand's portfolio, let alone in a major retail store. LCAs are often thus currently being used for more narrow purposes, such as identifying hot spots or supporting design improvements.

Progress in integrating sustainability analyses into core business processes and supply chain decisions (*6*, *15*) is limited. Sustainability efforts remain focused largely on finding incremental eco-efficiencies or risk reductions (*6*, *13*). A number of companies have been criticized for "greenwashing" because of poor data or of drawing system boundaries so selectively that they are representing only one node or one issue in a supply chain (*33*, *49*).

Future Prospects and Implications

Most firms still do not have good means to measure or manage upstream or downstream impacts, and very few firms are measuring their full externalities (*15*, *58*). There is thus still substantial work needed to advance the science and technology to support full supply-chain sustainability (*31*). Although some progress has been made to track conflict minerals because of recent regulation, there is a need for better tracing of supply chains, and in particular of raw materials such as cotton, minerals, and palm oil, from farms and mines all

the way through to manufacturing and retail. There is also a need for continued investment in global monitoring and assessment systems that connect upstream resource extraction to downstream consumption and disposal. The recent launch of the Global Forest Watch program hints at the potential for this kind of connected, almost–real-time monitoring and reporting.

In order for these systems to generate accurate assessments, there is a need for consistent LCA inventory data and common data sets for upstream activities (such as electricity generation, transportation, and water use) (*6*, *37*); consistent life-cycle impact factors; better uncertainty analysis; localization of LCA data sets; modeling of nonlinear responses and ecosystem dynamics; and improved systems for valuing ecosystem services (*6*, *9*, *39*).

There is also a need to bring in issues that companies do not naturally value, or do not want to pay for, such as labor and human rights, toxics, and biodiversity loss (*31*). Companies need to account for the full impacts and costs of their production chains and to integrate this information into their business models, sourcing, and innovation strategies (*31*, *56*, *61*). The market is moving toward "demand-driven supply chains," so it is critical to connect consumers not only to product design and retailing but also to the full impacts of their choices (*15*, *17*). Improved reporting systems should provide actionable information to stakeholders from CEOs to NGOs to consumers (*34*).

There is a real opportunity to connect global measurement systems, with targeted monitoring, comparative ratings, and reporting. Even as LCA scientists work through technical challenges rooted in the complex ecologies of supply chains, they must simultaneously integrate recent lessons from the behavioral sciences related to effective sustainability communication and behavior change in order to design tools that have any chance of being useful for decision-making. Better data, decision-support tools, and incentives are needed to move from policing supply chains to predicting and preventing unsustainable practices.

The future of global production and consumption can and must learn from new supply-chain management systems to improve environmental and social sustainability (*31*). Initiatives should go beyond cost-saving, compliance, and risk reduction, to literally rethinking supply chains, closing loops, moving from products to services, and changing business models (*15*, *22*, *26*, *31*, *51*). Major opportunities remain to apply innovative design, sourcing, and stakeholder engagement programs to help invent a more sustainable supply chain of the future.

REFERENCES

1. E. Chasan, "Building a speedy supply chain for fast fashion," *Wall Street Journal*, 2 August 2013; http://blogs.wsj.com/cfo/2013/08/02/building-a-speedy-supply-chain-for-fast-fashion.
2. Trucost, *Natural Capital at Risk: The Top 100 Externalities of Business* (TEEB for Business Coalition, Singapore, 2013).
3. S. J. Davis, G. P. Peters, K. Caldeira, *Proc. Natl. Acad. Sci. U.S.A.* **108**, 18554–18559 (2011).
4. C. Dalin, M. Konar, N. Hanasaki, A. Rinaldo, I. Rodriguez-Iturbe, *Proc. Natl. Acad. Sci. U.S.A.* **109**, 5989–5994 (2012).
5. S. Seuring, *Bus. Strategy Environ.* **20**, 471–484 (2011).
6. T. O'Shea, J. S. Golden, L. Olander, *Bus. Strategy Environ.* **22**, 429–441 (2013).
7. S. Hellweg, L. Milà i Canals, *Science* **344**, 1109–1113 (2014).
8. A. Y. Hoekstra, T. O. Wiedmann, *Science* **344**, 1114–1117 (2014).
9. G. Finnveden *et al.*, *J. Environ. Manage.* **91**, 1–21 (2009).
10. C. Gimenez, V. Sierra, *J. Bus. Ethics* **116**, 189–203 (2013).
11. B. Bakshi, M. J. Small, *J. Ind. Ecol.* **15**, 477–478 (2011).
12. J. S. Golden *et al.*, *Ecol. Soc.* **15**(3), no. 8 (2010); www.ecologyandsociety.org/vol15/iss3/art8.
13. P. Dauvergne, J. Lister, *Glob. Environ. Change* **22**, 36–45 (2012).
14. K. Caldeira, S. J. Davis, *Proc. Natl. Acad. Sci. U.S.A.* **108**, 8533–8534 (2011).
15. Y. Chouinard, J. Ellison, R. Ridgeway, *Harv. Bus. Rev.* **89**(10), 52–62 (2011).
16. A. Galli *et al.*, *Ecol. Indic.* **16**, 100–112 (2012).
17. L. Bonanni, M. Hockenberry, D. Zwarg, C. Csikszentmihalyi, H. Ishii, in *Proceedings of the SIGCHI Conference on Human Factors in Computing Systems*, Atlanta, GA, 10 to 15 April 2010 (Association for Computing Machinery, New York, 2010), pp. 937–946.
18. E. Hassini, C. Surti, C. Searcy, *Int. J. Prod. Econ.* **140**, 69–82 (2012).
19. A. Nagurney, M. Yu, A. H. Masoumi, L. S. Nagurney, in *Networks Against Time* (Springer, New York, 2013), pp. 117–139.
20. J. B. Schor, in *Culture of the Slow: Social Deceleration in an Accelerated World*, N. Osbaldiston, Ed. (Palgrave Macmillan, New York, 2013).
21. Z. Wu, M. Pagell, *J. Oper. Manage.* **29**, 577–590 (2011).
22. S. Freidberg, *Econ. Soc.* **42**, 571–596 (2013).
23. M. Heuer, *Bus. Strategy Environ.* **20**, 211–221 (2011).
24. J. H. Grimm, J. S. Hofstetter, J. Sarkis, "Understanding diffusion of corporate sustainability standards through sub-supplier management in the food supply chain" (Working paper 12-25, George Perkins Marsh Institute, Clark University, Worcester, MA, 2012); www.clarku.edu/departments/marsh/news/WP2012-25.pdf.
25. S. Seuring, M. Müller, *J. Clean. Prod.* **16**, 1699–1710 (2008).
26. M. E. Porter, M. R. Kramer, *Harv. Bus. Rev.* **89**(1), 62–77 (2011).
27. S. H. M. Butchart *et al.*, *Science* **328**, 1164–1168 (2010).
28. M. C. Hansen, S. V. Stehman, P. V. Potapov, *Proc. Natl. Acad. Sci. U.S.A.* **107**, 8650–8655 (2010).
29. A. Fonseca, M. L. McAllister, P. Fitzpatrick, *Miner. Eng.* **46-47**, 180–186 (2013).
30. K.-H. Lee, *J. Clean. Prod.* **19**, 1216–1223 (2011).
31. M. Pagell, A. Shevchenko, *J. Supply Chain Manage.* **50**, 44–55 (2014).
32. J. Hans, Supply chain innovations lead to 'hyper innovation' (Manufacturing.net, 2013); www.manufacturing.net/articles/2013/07/supply-chain-innovations-lead-to-'hyper-innovation'.
33. A. Prakash, M. Potoski, *J. Policy Anal. Manage.* **31**, 123–138 (2012).
34. K. Dingwerth, M. Eichinger, *Glob. Environ. Polit.* **10**, 74–96 (2010).
35. S. L. Golicic, C. D. Smith, *J. Supply Chain Manag.* **49**, 78–95 (2013).
36. R. G. Eccles, G. Serafeim, M. P. Krzus, *J. Appl. Corp. Finance* **23**, 113–127 (2011).
37. J. B. Guinée *et al.*, *Environ. Sci. Technol.* **45**, 90–96 (2011).
38. A. C. Dias, L. Arroja, *J. Clean. Prod.* **24**, 30–35 (2012).
39. R. Geyer, D. M. Stoms, J. P. Lindner, F. W. Davis, B. Wittstock, *Int. J. Life Cycle Assess.* **15**, 454–467 (2010).
40. B. R. Ewing *et al.*, *Ecol. Indic.* **23**, 1–8 (2012).
41. L. Čuček, J. J. Klemeš, Z. Kravanja, *J. Clean. Prod.* **34**, 9–20 (2012).
42. M. Herva, A. Franco, E. F. Carrasco, E. Roca, *J. Clean. Prod.* **19**, 1687–1699 (2011).
43. S. Giljum, E. Burger, F. Hinterberger, S. Lutter, M. Bruckner, *Resour. Conserv. Recycling* **55**, 300–308 (2011).
44. L. Blomqvist *et al.*, *PLOS Biol.* **11**, e1001700 (2013).
45. T. Kastner, M. Kastner, S. Nonhebel, *Ecol. Econ.* **70**, 1032–1040 (2011).
46. W. E. Rees, *Environ. Urban.* **4**, 121–130 (1992).
47. C. J. Meinrenken, S. M. Kaufman, S. Ramesh, K. S. Lackner, *J. Ind. Ecol.* **16**, 669–679 (2012).
48. V. Subramanian, W. Ingwersen, C. Hensler, H. Collie, *Int. J. Life Cycle Assess.* **17**, 892–903 (2012).
49. W. W. Ingwersen, M. J. Stevenson, *J. Clean. Prod.* **24**, 102–108 (2012).
50. R. K. Singh, H. R. Murty, S. K. Gupta, A. K. Dikshit, *Ecol. Indic.* **9**, 189–212 (2009).
51. M. Pagell, Z. Wu, *J. Supply Chain Manag.* **45**, 37–56 (2009).
52. J. S. Golden, V. Subramanian, J. B. Zimmerman, *J. Ind. Ecol.* **15**, 821–824 (2011).
53. E. J. Nelson *et al.*, *Front. Ecol. Environ.* **11**, 483–493 (2013).
54. A. P. Kinzig *et al.*, *Science* **334**, 603–604 (2011).
55. R. M. Dangelico, D. Pujari, *J. Bus. Ethics* **95**, 471–486 (2010).
56. S. I. Hallstedt, A. W. Thompson, P. Lindahl, *J. Clean. Prod.* **51**, 277–288 (2013).
57. S. U. Hoejmose, A. J. Adrien-Kirby, *J. Purchasing Supply Manage.* **18**, 232–242 (2012).
58. T. P. Gloria *et al.*, *Int. J. Life Cycle Assess.* **19**, 491–499 (2014).
59. J. Makower, "Target and GoodGuide team up to rate sustainable products" (Greenbiz.com, 2013); www.greenbiz.com/blog/2013/10/08/target-and-goodguide-team-rate-sustainable-products.
60. C. Benoît *et al.*, *Int. J. Life Cycle Assess.* **15**, 156–163 (2010).
61. H. Gmelin, S. Seuring, *J. Clean. Prod.* **69**, 1–9 (2014).

ACKNOWLEDGMENTS

The author acknowledges the research assistance of N. Lollo for this project. The author was a cofounder of GoodGuide.com, a social venture start-up that provides information to the public on the environmental, social, and health impacts of products and companies. Since 2012, GoodGuide has been owned and operated by Underwriters Laboratory. The author is now a consultant to GoodGuide and UL.

10.1126/science.1248526

RESEARCH

Neuronal surface tags are involved in sensory axonal branching
He et al. p. 1182

IN *SCIENCE* JOURNALS

Edited by **Stella Hurtley**

SHEEP GENOME

A genome for ewe and ewe

Sheep-specific genetic changes underlie differences in lipid metabolism between sheep and other mammals, and may have contributed to the production of wool. Jiang *et al*. sequenced the genome of two Texel sheep, a breed that produces high-value meat, milk, and wool. The genome information will provide an important resource for livestock production and aid in the understanding of mammalian evolution. — LMZ

Science, this issue p. 1168

SLEEP AND LEARNING

To sleep, perchance to remember

Many researchers believe sleep helps us consolidate our memories, but no one knows quite how. Yang *et al*. investigated the precise role of sleep in changing mouse brain structures (see the Perspective by Euston and Steenland). When mice learned motor tasks, small protuberances—or "spines"—formed on some of the dendritic branches of specific brain neurons. These spines represent the physical correlate of a memory. But the neurons grew and retained these spines better when the mice slept after learning the task. Neurons that fired during learning fired again during subsequent slow-wave sleep, allowing the mice to conserve the newly formed spines—and memories. — PRS

Science, this issue p. 1173; see also p. 1087

CLOUD PHYSICS

Invigorating convection in warm clouds

Atmospheric aerosols—tiny airborne particles—affect the way clouds form and how they affect climate. Koren *et al.* investigated how the formation of warm clouds, such as those that form over the oceans, depends on pollution levels (see the Perspective by Remer). Aerosols affect cloud formation in cleaner air disproportionately more than in more polluted air. Before the widespread air pollution of the industrial era, it seems, warm convective clouds may have covered much less of the oceans than they do today. — HJS

Science, this issue p. 1143; see also p. 1089

SENSORY BIOLOGY

Hold your breath or the catfish will find you

Finding prey is hard enough in the light of day, but animals that are nocturnal or live in murky conditions face even greater challenges. Caprio *et al.* describe a sense that allows a marine catfish to detect the mere "breathing" of their prey target. External sensors on the catfish's whiskers detect pH changes generated by hidden, respiring polychaete worms. — SNV

Science, this issue p. 1154

INTERFACIAL CHEMISTRY

Monitoring water interfaces in motion

Water behaves differently at interfaces—where it meets the air, or a solid surface—than it does in the middle of the liquid. Past laboratory studies of this phenomenon have mainly focused on still samples, despite the fact that in natural settings such as rivers and rain, the water moves along the surfaces.

Published by AAAS

Lis *et al.* used a microfluidics apparatus and a spectroscopy technique called sum frequency generation to study the effects of flow on aqueous chemistry at silica and fluorite surfaces (see the Perspective by Waychunas). The flow of fresh water along the surfaces disrupts the equilibrium of dissolved ions, substantially changing the surface charge and the molecular orientation of the water at the interface. — JSY

Science, this issue p. 1138; see also p. 1094

MEMBRANE BIOLOGY

How cells haul down their "eat me" flags

Dead and dying cells expose a membrane lipid called phosphatidylserine (PS) on their cell surface as a sort of "eat me" signal. Segawa *et al.* identified the membrane enzyme responsible for flipping any PS that inadvertently makes it way from the inner to the outer leaflet of the plasma membrane lipid bilayer. Without the enzyme, macrophages gobbled up healthy cells. — SMH

Science, this issue p. 1164

LUNAR FORMATION

An analysis of motes of the Moon maker

How did the Moon form? According to the prevailing hypothesis, a Mars-sized body known as Theia smashed into Earth. Herwartz *et al.* analyzed fresh basalt samples from three Apollo landing sites and compared them with several samples of Earth's mantle. The oxygen isotope values measured in these lunar rocks differ significantly from the terrestrial material, supporting the giant-impact hypothesis. — MMM

Science, this issue p. 1146

QUANTUM INFORMATION

Electrical control of nuclear spin qubits

Quantum bits of information (qubits) that are based on spins of atomic nuclei are an attractive option for quantum information processing. It can sometimes be tricky to manipulate these qubits using magnetic fields directly. Thiele *et al.* developed a technique for electrically controlling a nuclear spin qubit in the single-molecule magnet $TbPc_2$. When they hit the qubit with a microwave pulse, the microwave's electric field generated effective magnetic fields much larger than those available previously. — JS

Science, this issue p. 1135

PLANT BIOLOGY

ABA tells roots to stop and then grow

Plants initially grow a primary vertical root. The primary root then puts out horizontal lateral roots, which help to anchor the plant and take up water and nutrients from the soil. But to make the most of precious resources, plants use the hormone abscisic acid to stop lateral roots from growing in times of drought. Zhao *et al.* found that after a time, plants resume lateral root growth. This process paradoxically also uses abscisic acid, which binds to a different receptor and triggers changes in the expression of genes involved in resuming lateral root growth. — JDB

Sci. Signal. **7**, ra53 (2014).

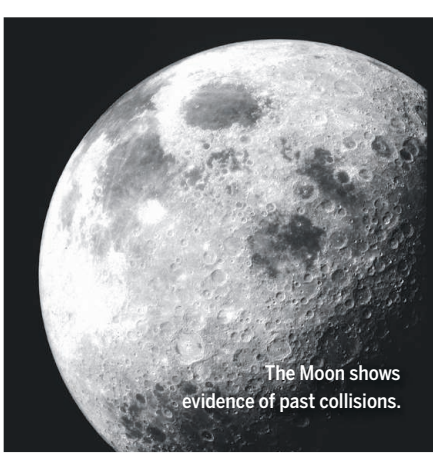

The Moon shows evidence of past collisions.

PHOTOS: (TOP TO BOTTOM) © IMAGEBROKER/ALAMY; NASA

IN OTHER JOURNALS

Edited by **Kristen Mueller** *and* **Jesse Smith**

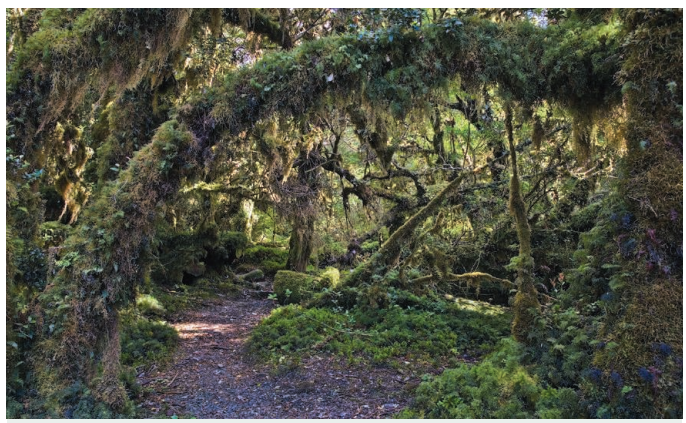

Epiphytes like mosses and lichens cover trees in a South American forest.

PLANT ECOLOGY

Lichens provide a protective coat

Lichens help even out temperatures and moisture levels in foggy deserts, according to a pioneering study of epiphytes: plants that grow on the stems and branches of larger plants. Stanton *et al*. studied the ecological role of lichens, mosses, and bromeliads inhabiting host trees in fog-fed desert ecosystems in Peru and Chile. They removed epiphytes from the columnar cacti and trees they were growing on and created artificial cacti at the field site, which they covered with collected epiphytes. Epiphytes affected the microclimatic conditions around the host plant: Their presence reduced both the amount of water that reached the ground and the amount that evaporated from the soil. They also buffered daily temperature fluctuations. Epiphytes are abundant in tropical forest ecosystems and they may play a considerable role in cycling water and nutrients. — AMS

Funct. Ecol. 10.1111/1365-2435.12249 (2014).

ENDOCYTOSIS

Galectin-3 gives cells another way to eat

Like people, cells need to eat. They use a process known as endocytosis to take up materials from their surroundings. In the best-known type of endocytosis, the cell forms a protein coat that actively pinches off small vesicles from the cell surface. However, another type of endocytosis does not use these clathrin coats—so what does it use? Lakshminarayan *et al.* found that a carbohydrate-binding protein, galectin-3, caused the cells to produce a new, morphologically distinct class of endocytic structures, termed clathrin-independent carriers (CLICs). The cell used this CLIC pathway to ingest a variety of cell-surface glycoproteins that help interacting cells to stick together and move around. — SMH

Nat. Cell Biol. 10.1038/ncb2970 (2014).

CHEMISTRY

A thinner window for shining light on shale gas

A light-powered chemical reaction ultimately could help turn shale gas into plastic. When hydrocarbons such as butane come out of the ground, the carbon atoms in each molecule are connected


Spanish flu killed many young adults.

VIRAL EVOLUTION

What made Spanish flu so deadly

The deadly pandemic Spanish flu of 1918 killed many millions, but unlike most flu strains, it targeted young adults rather than infants and the elderly. The reason remains a mystery. Worobey *et al.* used genetic and evolutionary approaches to infer that for much of the 19th century, a flu virus strain containing the same subtype of the hemagglutinin protein (H1) as the Spanish flu infected children. This gave them good immune protection from subsequent infections with H1-containing viruses. But from 1880 to 1900, the H3 subtype replaced H1 in circulating flu strains, and so people born between these times were less immune to H1. Around 1907, a novel H1-containing flu emerged, eventually becoming the deadly 1918 pandemic. With little protective immunity to H1, young adults exposed only to H3 subtypes during childhood suffered the greatest mortality. — CA

Proc. Natl. Acad. Sci. U.S.A. 10.1073/pnas.1324197111 (2014).

by single bonds. Chowdhury *et al*. show at small scale that a soluble rhodium carbonyl catalyst, activated by light, efficiently snips hydrogen atoms off the molecules to create the more reactive carbon-carbon double bonds needed to make products such as plastics. Past efforts to remove hydrogen photochemically without creating by-products tended to be inefficient, but the authors suspected that flask walls might have been partly responsible by blocking some of the light. Using thin-walled glass flasks and an additive that activated the catalyst, the authors achieved on the order of 100 turnover cycles per hour for a range of different hydrocarbons. — JSY

Angew. Chem. Int. Ed. **53**, 10.1002/anie.201402287 (2014).

MATERIALS SCIENCE

Rupturing cells gently with a spiky membrane

Researchers need to rupture cells before they can analyze the proteins and nucleic acids inside, but they should do it as gently as possible. So *et al*. decorated silicon membranes with hierarchical layers of pointy spikes, using a single-step etching process. When they attached the membrane to the end of a syringe as part of a filter holder, the cells ruptured as the syringe pushed them past the membrane.

Compared to other techniques for breaking cells open, such as those based on chemical or acoustic methods, the spiky-membrane method provides higher concentrations of proteins and nucleic acids in a shorter time. Another plus: The membrane collects the debris from the cell, giving a cleaner solution. — MSL

ACS Appl. Mater. Interfaces 10.1021/am501221b (2014).

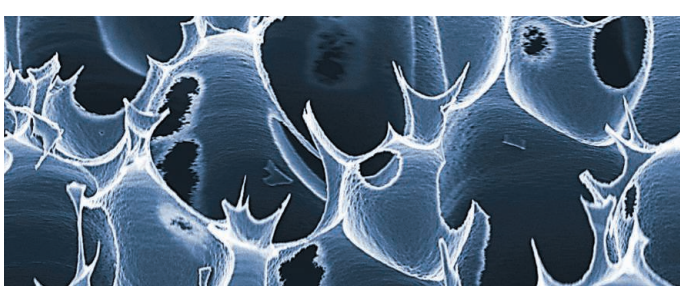
Ultrasharp silicon nanospikes for efficiently shredding cells.

ECONOMICS

Public health insurance costs jobs?

What is the relationship between employment rates and access to public health insurance? Garthwaite *et al*. analyzed what happened in 2005, when the state of Tennessee discontinued Medicare health insurance coverage for about 4% of its non-elderly adult population, many of them nondisabled low-income adults without children at home. With a new need for private health insurance, which is often provided by employers, many of these people found new jobs. State employment rose by 6 percentage points from 2004 to 2006. This change mirrors the Congressional Budget Office projections of the decline in employment due to the expansion of public health insurance mandated in the U.S. Affordable Care Act. — GJC

Q. J. Econ. **129**, 653 (2014).

GEOPHYSICS

An anti-earthquake cloak for buildings?

Scientists studying how to shield vulnerable buildings from destructive seismic waves are getting ideas from optics. Drawing on techniques for controlling the flow of light and electromagnetic radiation, Finnochio *et al*. show how to arrange resonators into mechanical metamaterials that could deflect seismic waves. In a large-scale field experiment, Brule *et al*. used a similar approach and placed engineered resonators in the ground. Their arrangement worked: When they generated seismic activity nearby, the resonators modified the energy's distribution, making it less destructive. — ISO

Appl. Phys. Lett. **104**, 191903 (2014).
Phys. Rev. Lett. **112**, 174302 (2014).

NEUROLOGY

Parenting Rewires the Male Brain

Women aren't the only gender hardwired for parenthood: Caring for children awakens similar brain circuits in men. Abraham *et al*. investigated two family types: mother-father couples with the mother as primary caregiver, and homosexual male couples sharing caregiving. The team videotaped parents and children together, then the parents underwent functional magnetic resonance imaging brain scanning. All showed activation of a "parenting network," including an amygdala-centered network that handles strong emotions and reward, and regions handling learning and experience. In the traditional couples, mothers showed stronger activation in the amygdala network and fathers in experience-dependent regions (amygdala activation was proportional to time spent with the baby). But activity in the homosexual fathers' brains mirrored the mothers' brain activity. — EN

Proc. Natl. Acad. Sci. U.S.A. 10.1073/pnas.1402569111 (2014).

ONLINE IN *SCIENCE*

Edited by **Stella Hurtley**

CALCIUM CHANNELS

Allowing calcium to leak across a membrane

Cells maintain a balance between calcium in the cytosol and calcium stored in organelles—too much stored calcium kills cells. Transmembrane Bax inhibitor motif (TMBIM) proteins form channels in organelle membranes that allow calcium to leak out. Chang *et al*. show that this calcium leak is pH-dependent. A bacterial homolog of TMBIM proteins converts between an open channel at low pH and a closed channel at high pH. Although the channel is open at low pH, calcium leakage is low because the inside of the channel remains at a neutral pH. Thus, at physiological pH, these channels will be in equilibrium between the open and closed states, so that excess calcium can leak through. — VV

Science, this issue p. 1131

PLANETARY FORMATION

The chronology of planetary embryos

Protoplanets, or early planetary embryos such as iron meteorite parent bodies, formed in the early protoplanetary disk from dust, debris, and planetesimals. Defining the precise chronology of accretion and differentiation—including core formation—of these planetary embryos will aid in a richer understanding of the chemical evolution of the solar system. Through high-precision tungsten isotope measurements, Kruijer *et al*. show that the timing of accretion and core formation for iron meteorite groups falls within 0.6 to 2 million years of the age of the solar system (see the Perspective by Elliott). Differences of timing within this group are probably a function of volatile contents of the parent bodies or spatial and chemical heterogeneity within the protoplanetary disk. — NW

Science, this issue p. 1150; see also p. 1086

PLURIPOTENCY PROGRAM

Predicting stem cell renewal or differentiation

Predicting complex mammalian cell behavior is extremely challenging. Dunn *et al.* developed a computational model that predicts when embryonic stem cells will self-renew or differentiate. The model revealed an essential program governing pluripotency and identifies a minimal set of components and interactions that accurately predict responses to genetic perturbation. — BAP

Science, this issue p. 1156

SCHIZOPHRENIA

Genes, synapses, and hallucinations

In a schizophrenia mouse model, Chun *et al.* found that an abnormal increase of dopamine D2 receptors in the brain's thalamic nuclei caused thalamocortical synapse deficits owing to reduced glutamate release. Antipsychotic agents or a dopamine receptor antagonist reversed this down-regulation. The defect was associated with the loss of a component of the microRNA processing machinery encoded by the *dgcr8* gene. — PRS

Science, this issue p. 1178

PLANT GROWTH

Emerging from the shade into the light

As a growing seedling emerges into the light, it needs to shift its developmental program to grow toward the light. Signaling components that flip the switch from growth in the shade to growth in the light include phytochromes, which are sensitive to red light, and transcription factors that drive the shade-adapted pattern of development. Ni *et al*. now show how phosphorylation sets these signaling partners up for destruction. The signaling established by red light invokes photomorphogenesis by promoting the destruction of the photoreceptor and its signaling partner. — PJH

Science, this issue p. 1160

NEURODEVELOPMENT

Wiring the developing insect brain

Developmental brain wiring requires a complex set of cellular interactions often orchestrated by a large number of surface receptors. Thousands of Dscam1 receptor isoforms function as "surface tags" endowing neurons with unique molecular identities. These isoforms are important for neuronal self-recognition and dendrite self-avoidance. He *et al*. report that the diversity of Dscam1 isoforms is also essential for complex axonal branching of sensory neurons in developing fruit flies. — BAP

Science, this issue p. 1182

RESEARCH ARTICLE

CALCIUM CHANNEL STRUCTURE

Structural basis for a pH-sensitive calcium leak across membranes

Yanqi Chang,[1] Renato Bruni,[1] Brian Kloss,[1] Zahra Assur,[2] Edda Kloppmann,[1,3] Burkhard Rost,[1,3] Wayne A. Hendrickson,[1,2,4,5] Qun Liu[1,4]*

Calcium homeostasis balances passive calcium leak and active calcium uptake. Human Bax inhibitor–1 (hBI-1) is an antiapoptotic protein that mediates a calcium leak and is representative of a highly conserved and widely distributed family, the transmembrane Bax inhibitor motif (TMBIM) proteins. Here, we present crystal structures of a bacterial homolog and characterize its calcium leak activity. The structure has a seven-transmembrane-helix fold that features two triple-helix sandwiches wrapped around a central C-terminal helix. Structures obtained in closed and open conformations are reversibly interconvertible by change of pH. A hydrogen-bonded, pK_a (where K_a is the acid dissociation constant)–perturbed pair of conserved aspartate residues explains the pH dependence of this transition, and biochemical studies show that pH regulates calcium influx in proteoliposomes. Homology models for hBI-1 provide insights into TMBIM-mediated calcium leak and cytoprotective activity.

Calcium (Ca^{2+}) is a ubiquitous intracellular messenger that regulates cellular and physiological activities. Cytosolic Ca^{2+} is kept at a low level to assure responsiveness to Ca^{2+} signals, but subcellular organelles such as the endoplasmic reticulum (ER) and Golgi apparatus maintain calcium stores. Upon activation, Ca^{2+} is mobilized to cross membrane barriers through calcium-release channels and calcium-uptake pumps (*1*). Under resting conditions, intracellular and subcellular calcium homeostasis is dynamically regulated to equilibrate between active calcium uptake and passive calcium leak. Calcium homeostasis is cytoprotective (*2*, *3*). An overloaded ER calcium content promotes cell death (*4*); inversely, lowering of ER calcium content by antiapoptotic proteins Bcl-2, Bcl-xL, or Bax inhibitor-1 (BI-1) elicits a survival signal (*5*–*7*). Bcl-2, Bcl-xL, and BI-1 have been suggested to regulate ER calcium leak, either directly by forming a leaky pore or by modulating calcium-release channels such as inositol 1,4,5-trisphosphate (IP_3) receptors (IP3Rs) (*8*–*10*).

Human BI-1 (hBI-1) was discovered as a human gene product that can block lethality of the pro-apoptotic Bax protein in yeast (*8*). hBI-1 is localized to the ER membrane, where, among other functions, it mediates a calcium leak downstream of Bcl-2 and Bcl-xL (*8*, *11*). By sequence similarity to hBI-1, a highly conserved TMBIM (transmembrane Bax inhibitor motif) family was identified (*12*) and assigned the Pfam (*13*) name of Bax1-I (identification code PF01027). TMBIM proteins are present in prokaryotes, fungi, plants, and metazoans, including invertebrates and mammals (*12*) (fig. S1). Humans have six identified TMBIM proteins (TMBIM1 to 6), each containing seven presumed transmembrane helices (*14*) and with variations mainly in their N-terminal extensions (fig. S2). Besides hBI-1 (TMBIM6) in the ER membrane, human Golgi antiapoptotic protein (hGAAP/TMBIM4) is in the Golgi membrane, where it mediates Golgi calcium leak, providing another identified connection to calcium and apoptosis (*15*). Other human TMBIM proteins are diversely localized and less well characterized (*12*).

Accumulating evidence has demonstrated the calcium-leak activity of the TMBIM proteins and their regulatory roles in apoptosis (*11*, *15*); however, little is known about the structure or mechanism of action for these proteins beyond recent topological studies on hBI-1 and hGAAP (*16*, *17*). Seeking structural clues into the mechanism of calcium flux activity, we undertook structural studies of TMBIM proteins. Here, we present crystal structures of a bacterial homolog in interconvertible conformational states dependent on pH, we demonstrate pH-sensitive calcium permeation by this protein consistent with the calcium-leak activity of hBI-1 and hGAAP, and we build homology models of hBI-1 to provide structural insights into the calcium leak and antiapoptotic functions of the TMBIM family.

Structural Analyses

To address the structural challenge of the TMBIM family, we identified prokaryotic homologs of hBI-1 that might provide structural insights into function. After screening 51 bacterial relatives for expression in *Escherichia coli*, we identified YetJ from *Bacillus subtilis* (BsYetJ), a previously uncharacterized protein, as a family member with satisfactory biochemical properties. The detergent-extracted protein was purified and crystallized in two crystal forms.

Form-1 crystals grew at pH 8 in space group $P6_522$ with one protein molecule per asymmetric unit. We solved this structure by native single-wavelength anomalous diffraction (SAD) (*18*) using relatively low energy x-rays (~6 keV) to enhance anomalous signal-to-noise ratios. The eight ordered sulfur atoms contributed a Bijvoet-diffraction ratio of ~1.4%. Diffraction data up to 2.8 Å spacings were measured from 12 crystals, and 10 of these met criteria for statistical equivalence (fig. S3A). Previously established analytical procedures (*18*) allowed both substructure determination and native-SAD phasing. The resulting electron-density map (fig. S3B) permitted automatic tracing of a nearly complete model, which was further refined at 1.95 Å resolution against a separate high-energy data set (table S1 and fig. S3C).

Form-2 crystals grew at pH 6 in space group $C222_1$ and have one molecule per asymmetric unit. Native crystals diffracted x-rays only to ~4.5 Å with severe anisotropy. Attempts at structure solution by molecular replacement from the form-1 structure did not succeed, suggesting a different conformation. Fortunately, a platinum derivative diffracted better; the structure was determined by Pt-SAD phasing at 3.6 Å resolution (fig. S3D), and a

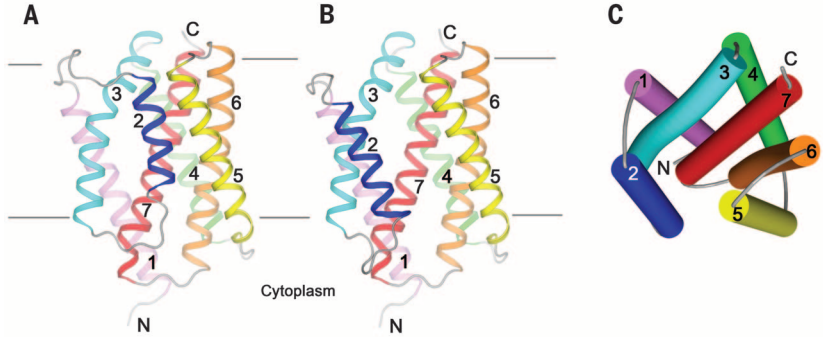

Fig. 1. Structures of BsYetJ. (**A**) Ribbon drawing of form-1 structure determined at pH 8. (**B**) Ribbon drawing of form-2 structure determined at pH 6. The views of (A) and (B) are from the membrane, and each structure has its seven TMs color-coded. All connecting loops are colored in gray. (**C**) A cylinder diagram of the form-2 structure to show the structural features from a periplasmic view. The coloring is as for (B).

[1]New York Consortium on Membrane Protein Structure, New York Structural Biology Center, New York, NY 10027, USA. [2]Department of Physiology and Cellular Biophysics, Columbia University, New York, NY 10032, USA. [3]Department of Bioinformatics and Computational Biology, Fakultät für Informatik, Technische Universität München, Garching, Germany. [4]New York Structural Biology Center, National Synchrotron Light Source (NSLS) X4, Brookhaven National Laboratory, Upton, NY 11973, USA. [5]Department of Biochemistry and Molecular Biophysics, Columbia University, New York, NY 10032, USA.
*Corresponding author. E-mail: qunliu@bnl.gov

conformationally distinct model was built with reference to the form-1 structure, mainly by displacing one helix. We also found that BsYetJ can undergo an intracrystalline transition when form-1 crystals, as grown, are soaked in medium at pH 6. The resulting low pH conformation is almost identical to that in the orthorhombic form-2 crystals (fig. S3E). The converted structure in the hexagonal form-1 lattice diffracted better and could be refined to 2.5 Å resolution (table S1), and this structure was used for further structural characterization.

Structural Features

The structure of BsYetJ in each of its conformations comprises seven transmembrane helices (7 TMs), which by structure-based alignment compares with anticipated helix boundaries for the entire family of TMBIM proteins (fig. S2). The higher-pH form has a compact, closed conformation (Fig. 1A and fig. S4), whereas the lower-pH form has an opened conformation with helix TM2 displaced (Fig. 1B). On the basis of topology assays of the human homologs (*16*, *17*), TMBIM proteins have their N-termini in the cytoplasm, which is consistent with the positive-inside rule (*19*) as applied to the electrostatic potential surfaces of the BsYetJ structures (fig. S5). The tightly packed helices of the closed form give this structure a barrel-like shape. The barrel is about 56 Å long by 34 Å in diameter and, judged by electrostatics, its axis is tilted in the lipid bilayer by 9° so that 31 Å is embedded in lipid bilayer. The open conformation produces a pore through the lipid bilayer (fig. S5, E to H) that is wide open (11 Å) at the periplasmic side and narrows to a 5 Å–wide bottleneck near the cytoplasmic side.

The polypeptide folding in BsYetJ is topologically different from that of any known structures, as revealed by a DALI search (*20*). As best seen in the open conformation, conceptually the overall structure has three components: TM1 to 3, TM4 to 6, and TM7 (Fig. 1C). TM1 to 3 and TM4 to 6 are similar, each forming a triple-helix sandwich substructure: TM3 is clamped by helix-loop-helix TM1 and 2; TM6 is clamped by helix-loop-helix TM4 and 5 (Figs. 1C and 2, A and B). In forming the triple-helix sandwich, short side-chain hydrophobic residues on the TMs are crucial (*21*) because they provide sticky patches to allow close TM1-TM3 and TM4-TM6 contacts for clamping (Fig. 2, A and B, insets). TM3 and TM6 are each bent at the sticky patch. Although there is no obvious sequence similarity between TM1 to 3 and TM4 to 6, the two components are superimposable when inverted by a pseudo-twofold symmetry viewed from within the membrane (Fig. 2, C and D). C-terminal helix TM7 is in the center of the structure, parallel to TM3 and antiparallel to TM6; these three helices together form a central layer that is sandwiched by the four peripheral helices TM1, 2, 4, and 5 (Fig. 1C).

As a 7-TM protein, BsYetJ compares with heterotrimeric guanine nucleotide–binding protein–coupled receptors (GPCRs) (*22*) and recent CAAX metalloprotease structures (*23*, *24*). The fold of BsYetJ is distinct from these (fig. S6). The CAAX protease helices encompass an intramembrane chamber, and cross-sectional registrations of these helices are unrelated. The GPCR fold has TM3 somewhat central, which has been proposed to have functional importance in ligand binding and signal transduction (*25*). For BsYetJ, TM7 has the central position, and it too has functional importance, as suggested by sequence conservation and biochemical analyses on its human relative, hBI-1 (*17*). By topology, BsYetJ somewhat resembles insect olfactory receptors, a special family of 7-TM proteins that also have their N-termini

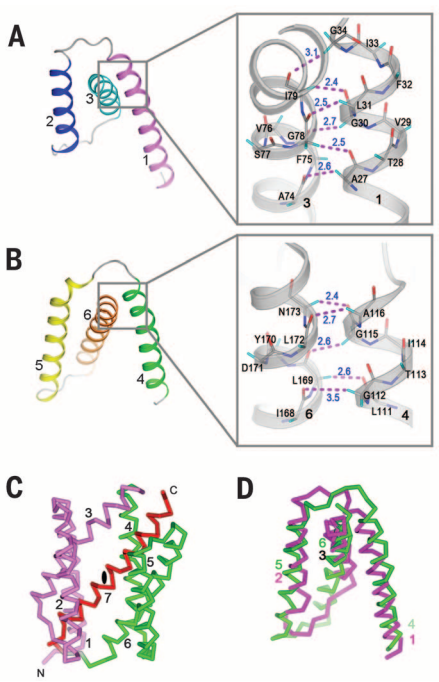

Fig. 2. Structural features. (**A** and **B**) Two triple-helix sandwich substructures consist of TM1 to 3 (A) and TM4 to 6 (B). The color scheme is as Fig. 1B. Insets in (A) and (B) are, respectively, the close α-helical contacts between TM1 and TM3 and between TM4 and TM6. Cα-H·····O contacts between 2.3 and 3.5 Å were drawn as magenta dashes. A, Ala; D, Asp; F, Phe; G, Gly; H, His; I, Ile; L, Leu; N, Asn; S, Ser; T, Thr; V, Val; and Y, Tyr. (**C**) Overall pseudo-inverse symmetry with the triple-helix sandwiches in magenta for TM1 to 3 and green for TM4 to 6. The pseudo-twofold axis is on the middle of the red TM7. (**D**) Superposition of the two symmetric components.

Fig. 3. Pore opening and closing regulated by pH. (**A** and **B**) Superposition of the two conformationally different structures at pH 8 (cyan and blue) and at pH 6 (gray and magenta). (A) is cytoplasmic view, and (B) is membrane view. (**C**) Electron density of the pH-7 structure showing alternative conformations of TM2. The $2F_o–F_c$ electron densities were drawn as gray isomeshes at 0.8σ. The side chains of TM2 in closed and open conformations were drawn respectively as blue and magenta sticks. (**D**) Overall pH-7 structure with two alternative conformations. Deviated side chains are shown as sticks: cyan for closed conformation and gray for open conformation.

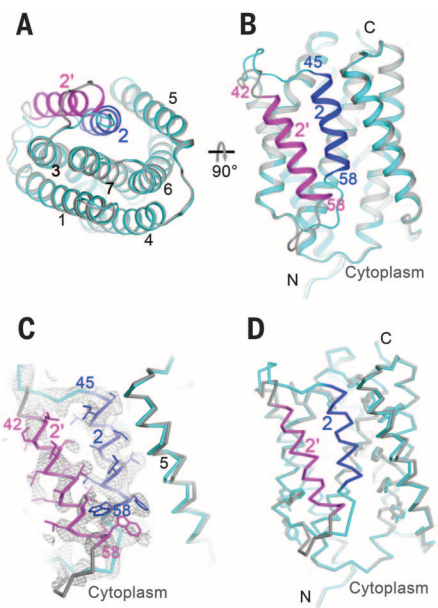

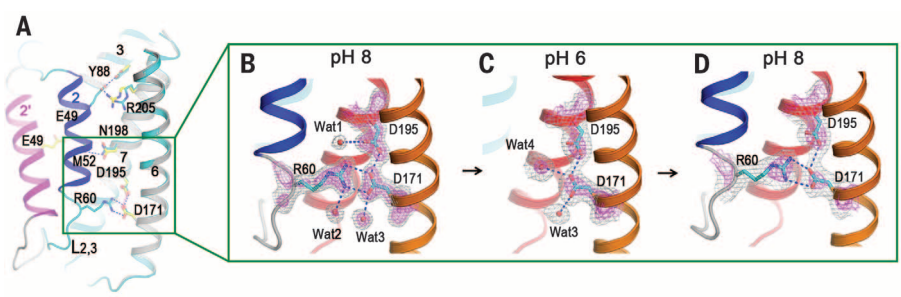

Fig. 4. Di-aspartyl pH sensor. (**A**) H-bond interactions within the pore of the closed-conformation structure. E, Glu; M, Met; and R, Arg. (**B** to **D**) Successive structures from intracrystalline transitions with superposed $2F_o–F_c$ electron densities contoured at two levels, 1.2σ (gray) and 3.0σ (magenta). (B) Starting form-1 structure at pH 8. (C) Structure after soaking a form-1 crystal into a medium at pH 6, disrupting the interactions between Arg^{60} and Asp^{171}. (D) Structure after reversal, from first soaking at pH 6 and then back-soaking to pH 8, thereby reclosing the pore and restoring the interactions between Arg^{60} and Asp^{171}.

MS no:	Emp no:	Date / Time:	PE's:	AA's:	Comments:	Art no:
RA1252043/TW/BIOCHEM	cw32	6-2-2014/11:38			1132	Figs. 2–4 - 4/C

inside (*26*); however, sequence alignments did not reveal any homology between the two families.

Regulation of Pore Opening and Closing by pH

The facts that the pore-closed and pore-open conformations were obtained at pH 8 and pH 6 and that the pore can be opened by intracrystalline transition (Fig. 3, A and B) suggest a role for pH in regulation of conformational transition. Superposition of the pore-open and pore-closed structures indicates substantial structural changes for TM2 and the two loops connecting it to TM1 and TM3 (Fig. 3, A and B). Relative to the closed conformation, TM2 in the open conformation swings away by as far as 13.5 Å to form a transmembrane pore bordered by it, TM5 to 7, and the presumed lipid bilayer (Fig. 3A and fig. S5F). In the closed conformation, TM2 is rather short (14 residues); whereas in the open conformation TM2 is extended by roughly one helical turn at its N terminus. The transformation from the closed to open conformation (rotation χ = 38.6°; translation t_χ = 3.4 Å) displaces TM2 away from contact with TM6 and also moves it along its axis toward the cytoplasm (Fig. 3B).

During the pH 6 to pH 8 transition, the *c* axis of the $P6_522$ lattice shrinks from 289 to 276 Å, but the resulting open-conformation structure is essentially the same as that obtained in the $C222_1$ lattice as grown at pH 6 (fig. S3E). To test for reversibility of this pH-driven conformational transition, we soaked the closed-form crystals at pH 6; took diffraction images to confirm unit-cell shrinkage, the hallmark of pore-opening upon soaking; and then back-soaked the exact crystals to pH 8. This reestablished pH-8 structure, which has a diagnostic *c* axis of 293 Å, is reclosed to be almost identical to the initial pore-closed conformation. Thus, pH can regulate the opening and closing of the pore.

To further test the pH-driven conformational changes, we moved the opened crystals from pH 6 to pH 7 and determined this pH-7 structure by molecular replacement, using the back-soaked pH-8 structure because their lattice parameters were nearly identical (table S1). Electron density was seen for TM2 in both closed and open conformations, consistent with alternate states in equilibrium (Fig. 3C). The ratio of closed:open component was determined as 60:40 by occupancy refinement with the program PHENIX (*27*). The pH-7 structure as refined with two alternative conformations shows differences propagated into neighboring helices with associated main-chain and side-chain shifts (Fig. 3D). Thus, the conformation of BsYetJ is pH sensitive, and we presume that the ratio of TM2 occupancies reflects the conformational equilibrium. On the basis of the 60:40 closed:open ratio at pH 7, the apparent pK_a (where K_a is the acid dissociation constant) of the protein in the crystal may be estimated to be slightly below pH 7.

Di-Aspartyl pH Sensor

When closed at pH 8, TM2 and cytoplasmic loop $L_{2,3}$ (TM2-TM3 connection) engage in several hydrogen bonds with residues from TM3, 6, and 7; and all of these are disrupted in the open conformation at pH 6 (Fig. 4A). A key interaction at the closed-conformation interface appears to be a latch of Arg^{60} with the TMBIM-conserved di-aspartyl unit Asp^{171}-Asp^{195} (Fig. 4B). The guanidinium moiety from Arg^{60} forms a doubly hydrogen-bonded salt bridge with Asp^{171} when the protein is at pH 8 (Fig. 4B), but this is broken at pH 6 (Fig. 4C) and reestablished upon back-soaking to pH 8 (Fig. 4D). In all cases, the carboxylate groups of the two aspartates are hydrogen-bonded to one another. Electron density that is continuous through the di-aspartate unit, even for the 1.95 Å–resolution structure, and refined O-O distances of 2.55 Å at pH 8 and 2.71 Å at pH 6 demonstrate the hydrogen bonding and anomalous aspartate protonation.

The structural presumption based on the pH-8 structure would have Asp^{195} as the protonated group, leaving Asp^{171} free to form its salt bridge with Arg^{60}. This presumption is validated by pK_a calculations from the program PROPKA (*28*). For the closed conformation, the pK_a values of Asp^{171} and Asp^{195} are 3.1 and 11.2, respectively, one depressed and the other elevated resulting from a presumed coupling effect (*28*). For the open conformation, the respective

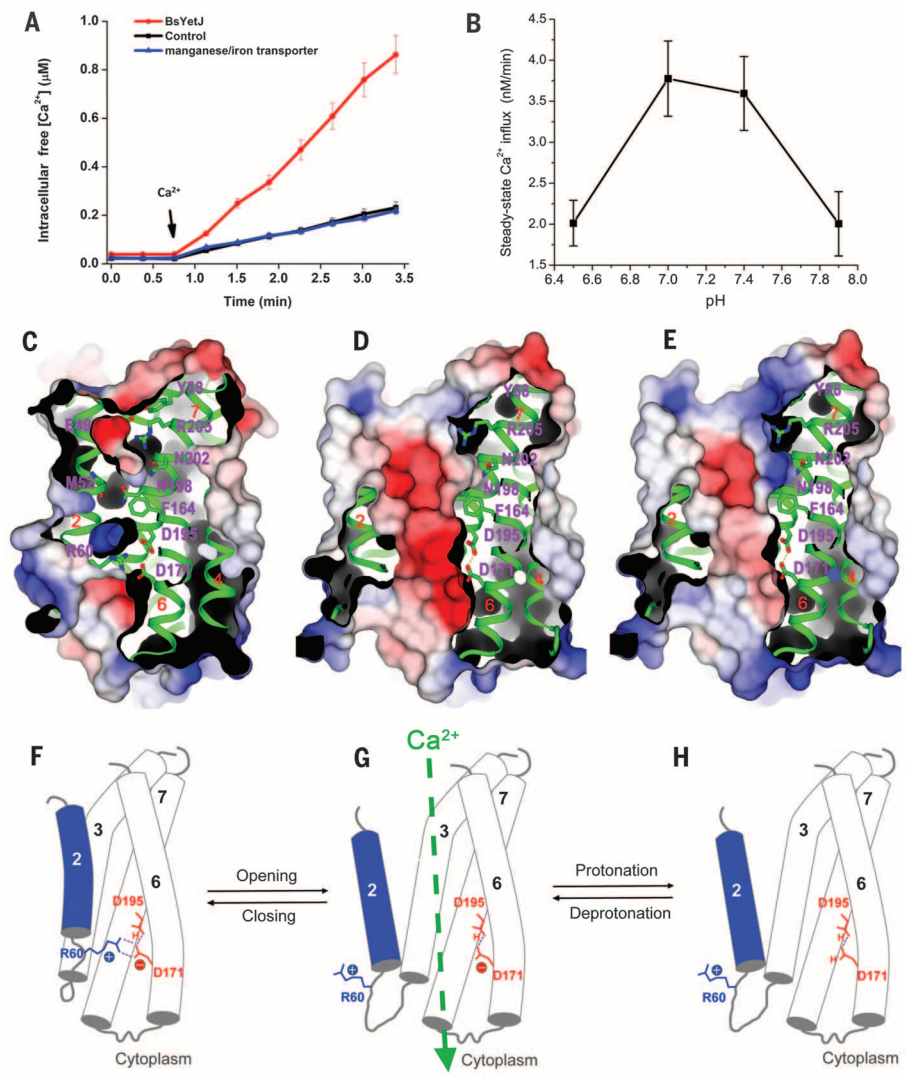

Fig. 5. Structural and functional characterization of calcium leak. (**A**) Calcium influx into bacteria overexpressing BsYetJ. An empty plasmid and a manganese transporter were used as negative controls. Error bars indicate ±SEM (*n* = 9 experiments). (**B**) Calcium influx into proteoliposomes. Error bars, ±SEM (*n* = 3). (**C**) Electrostatic surface of the closed-conformation structure showing charged surface concavities and internal cavities but a blocked pore. (**D**) Electrostatic surface of the open-conformation structure at pH 7.4, where the cleft is electronegative. (**E**) Electrostatic surface for the open-conformation structure at pH 6, where the cleft is more neutral. The contour level of the electrostatic surface is at ±5 kT/e. Red, negative potential; blue, positive potential. (**F** to **H**) A proposed model for pH-sensitive calcium leak. (F) At higher pH (e.g., 8), Asp^{195} is protonated and Asp^{171} is deprotonated. Asp^{171} forms two H bonds with positively charged Arg^{60}, and the Arg^{60}-Asp^{171} latch closes the pore. (G) When in the open conformation at a more neutral pH (e.g., 7.4), Asp^{171} may equilibrate between protonated and deprotonated states. Calcium passage occurs only when Asp^{171} is transiently deprotonated. (H) At lower pH (e.g., 6), the equilibration will favor more complete protonation of Asp^{171}, disfavoring calcium passage due to pore neutralization. Cartoons (F) to (H) correspond to structures (C) to (E) directly above.

MS no:	Emp no:	Date / Time:	PE's:	AA's:	Comments:	Art no:
RA1252043/TW/BIOCHEM	cw32	6-2-2014/11:38			1133	Fig. 5 - 4/C

values are 6.2 and 12.0. The increased pK_a of Asp^{171} in the open conformation may account for the equilibrated conformational states seen in our pH 7 structure. Thus, in absence of the guanidinium interaction, Asp^{171} is more readily protonated; alternatively, Asp^{171} when protonated is incompatible with Arg^{60} engagement. We suggest that the pH control of Asp^{171} thereby regulates the conformational transition and pore opening or closing. Asp^{195} is protonated throughout pH 6 to 8. Aspartate residues at positions 171 and 195 are strictly conserved in the TMBIM family (fig. S2), suggesting that a di-aspartyl pH sensor may be a family trait. The latch partner Arg^{60} is also conserved in TMBIM1 to 4 but not in TMBIM5 and 6, opening a question of alternative latch partners.

Both Arg^{60}-bearing loop $L_{2,3}$ and loop $L_{1,2}$, which connects TM2 to TM1, are quite flexible, as seen in B-factor plots (fig. S7). This mobility is consistent with ready displacement of TM2 when the latch to Asp^{171} is broken at lower pH. When TM2 is displaced from its van der Waals contacts with TM5, both it and TM5 have increased flexibility. Thus, we picture a pH-sensitive conformational equilibrium between a rather flexible pore-open state seen at lower pH and a pore-closed state seen at higher pH.

Calcium Leak

Both hBI-1 and hGAAP are able to mobilize calcium leak into the cytoplasm from stores in ER and Golgi compartments, respectively (*7*, *11*, *15*). To test whether our bacterial homolog has calcium-leak activity, we overexpressed BsYetJ in *E. coli*, added calcium extracellularly, and measured the intracellular calcium concentration with the fluorescent calcium dye Fura-2/AM. Upon addition of external calcium, intracellular calcium concentration increased steadily in cells overexpressing BsYetJ but not for controls of an empty plasmid or an unrelated membrane protein transporter (Fig. 5A). Thus, BsYetJ is a bona fide functional bacterial TMBIM homolog with calcium-leak activity.

Having shown that BsYetJ can produce a calcium leak in bacteria and that pH can control pore opening in BsYetJ, we explored the effect of pH on calcium influx. We constructed BsYetJ proteoliposomes at various pHs, preloaded them with the Fura-2 dye, and measured calcium influx when exposed to externally added calcium. We observed pH-dependent influxes of calcium, typically accumulating more rapidly at the outset of calcium application and then slowing somewhat to steady-state levels after ~10 min (fig. S8). The steady-state calcium influx was substantially lower when the pH was lower (pH 6.5) or higher (pH 7.9) than when under near-neutral conditions (pH 7.0 or 7.4) (Fig. 5B). We conclude that pH-sensitive calcium-leak activity is intrinsic to BsYetJ because we prepared the proteoliposomes from pure components.

Multiple hydrophilic residues lie within the core of closed-conformation BsYetJ (Glu^{49}, Arg^{205}, Asp^{202}, Asn^{198}, Asp^{195}, Asp^{171}, and Arg^{60}), lining up from the periplasmic side to the cytoplasmic side (Fig. 5C). These residues border concave surfaces that invaginate from either side and form two charged internal cavities along with these residues. This incipient passageway for calcium ions is structurally blocked in the closed conformation by hydrophobic residue Phe^{164} (Fig. 5C). When TM2 is moved away from the closed conformation, the separated concave surfaces and internal cavities unify to form a transmembrane pore, largely electronegative at a physiological pH (7.4; Fig. 5D) and less electronegative at a lower pH (6.0; Fig. 5E).

The pore at a more neutral pH appears conducive to calcium passage; however, we did not detect calcium ions in the pore of any BsYetJ crystal structure even though calcium was included in all crystallization and soaking experiments. Evidently, the structure does not feature discrete calcium binding sites in the pore but does allow calcium passage with only transient interactions within the pore. On the basis of the alternative conformations in our pH-7 structure, we imagine BsYetJ in the lipid bilayer to be in a facile equilibrium between open and closed conformations.

Why is the flux rate higher at pH 7, where the pore is in equilibrium, than at pH 6, where it is open? Fluctuations in the open/closed equilibrium may permit a calcium leak by opening a pore that is electronegative when at physiologically neutral pHs (Fig. 5D), as in our assays for uptake of calcium into bacteria and proteoliposomes (Fig. 5, A and B), whereas either closure at higher pH or reduced electronegativity at lower pH will counteract calcium passage. A working model for this pH-sensitive calcium-leak activity is given in Fig. 5, F to H. We propose that BsYetJ exists equilibrated among three states: closed, open deprotonated, and open protonated. At higher pH, Asp^{171} is predominantly deprotonated and forms a doubly hydrogen-bonded salt bridge with Arg^{60} (Fig. 5F); with this Arg^{60}-Asp^{171} latch in place, the structure is closed and the pore is sealed (Fig. 5, C and F). At a more neutral pH, the open conformation becomes accessible, even if transiently (Fig. 5G); the opened pore is electronegative with Asp^{171} remaining deprotonated, and a calcium leak is then facilitated along the calcium gradient into the cytosol (Fig. 5, D and G). At lower pH, the protonated state of Asp^{171} is favored because its pK_a is raised in the open conformation, which precludes formation of the Arg^{60}-Asp^{171} latch (Fig. 5H). In this state, electronegativity of the pore is reduced and calcium influx is impeded (Fig. 5E).

We conclude that BsYetJ is a pH-sensitive calcium-leak channel. Its molecular architecture is distinct from that known for other calcium channels and exchangers (*29*–*33*), and its pH-dependent changes in conformation and electrostatics are compatible with observed calcium-flux activities. hBI-1 also exhibits pH-sensitive calcium-leak activities, proposed to be mediated by aspartic acid residues on TM7 (*34*) or by the C-terminal lysine-rich motif (*35*). Our results are consistent with the TMBIM-conserved di-aspartyl pH sensor, but not the C-terminal lysine-rich motif, as a shared mechanism for the pH-sensitive calcium leak.

Insights into the BI-1–Mediated Calcium Leak and Antiapoptosis

To explore the structural linkage of BsYetJ to human homologs, we constructed homology models of hBI-1, the most studied of TMBIM proteins, by using structure-based sequence alignment (fig. S2) and the program MODELLER (*36*).

Because BsYetJ is homologous with its human TMBIM relatives (21% for TMBIM4 and 18% for TMBIM6), the hBI-1 models are highly similar to their BsYetJ templates but with instructive differences. The di-aspartyl pH sensor Asp^{188}-Asp^{213} (Asp^{171}-Asp^{195} in BsYetJ) is intact in both states; however, the Arg^{60} latch of BsYetJ (and TMBIM1 to 4) is replaced by His^{78} in hBI-1. In the closed conformation of hBI-1, His^{78} forms an alternative latch by hydrogen-bonding to Asp^{209} (Ser^{191} in BsYetJ) (Fig. 6A). In the open conformation, Asp^{209} is freed from its interaction with His^{78}, and it will likely exacerbate the pK_a elevations of Asp^{188}-Asp^{213} expected by analogy with BsYetJ. At a suitably low pH, we expect that Asp^{209} will adopt an alternative conformation and form a hydrogen bond with protonated Asp^{188} (Fig. 6B). Analogous to residues in BsYetJ, side chains of Leu^{71}, Thr^{74}, and Met^{181} (Phe^{164} in BsYetJ) are expected to provide pore-sealing functions in the closed state, separating concave indentations from the opposing membrane surfaces. Although many residues that line the open-state pore differ in hBI-1 as compared with BsYetJ, the shape and electrostatic features of the two pores remain very similar; particularly, the narrow opening on the cytoplasmic side of the hBI-1 pore is like that of BsYetJ.

On the basis of topology studies, hBI-1 was proposed to have a 6-TM topology with both N- and C-termini in the cytoplasm, where the predicted TM7 segment is either disordered or hemi-penetrant

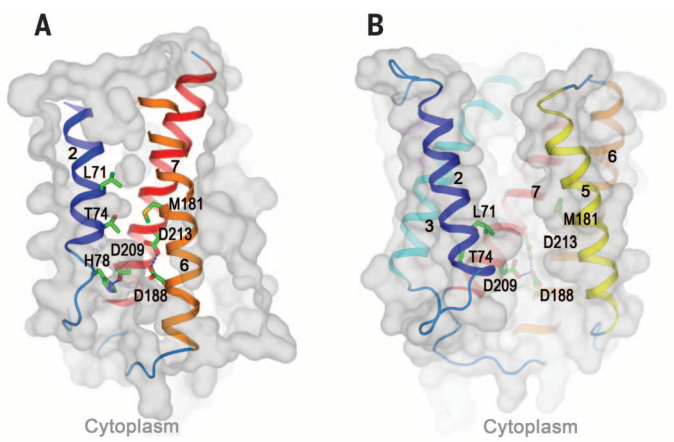

Fig. 6. Homology models of hBI-1. (**A** and **B**) Homology models of hBI-1 in its closed (A) and open (B) conformations. The conserved di-aspartyl Asp^{188}-Asp^{213} unit is shown within the membrane in each case, and a third aspartate, Asp^{209}, is shown interacting with His^{78} in (A) and with Asp^{188} in (B). In (A), the indicated pore-sealing residues, Leu^{71}, Thr^{74}, and Met^{181}, separate concave surfaces invaginating from opposite membrane face.

MS no:	Emp no:	Date / Time:	PE's:	AA's:	Comments:	Art no:
RA1252043/TW/BIOCHEM	cw32	6-2-2014/11:38			1134	Fig. 6 - 4/C

back into the membrane (*16*, *17*). On the other hand, TM7 is in the middle of the 7-TM structure of BsYetJ, where it forms extensive interactions with other TM helices. These include the conserved diaspartyl pH sensor between TM6 and TM7 and a contact between TM4 and TM7 ($Thr^{104/121}$ and $Phe^{200/218}$ in BsYetJ and hBI-1, respectively). The hydrophobicity analysis, secondary structure predictions, and conservation also suggest that hBI-1 has a 7-TM topology like that in BsYetJ (fig. S9).

Besides calcium-leak activity, which has been observed for TMBIM proteins wherever tested, TMBIM interactions with other proteins have also been identified. For example, hBI-1 and hGAAP coimmunoprecipitate with IP3R and modulate IP_3-induced Ca^{2+} release (*9*, *15*), and hBI-1 interacts with Bcl-2 as shown by in vivo cross-linking and coimmunoprecipitation (*8*, *11*). On the basis of the BsYetJ structures and the homology models for hBI-1, a plausible mode of TMBIM-mediated protein-protein interactions would have a TM from the partner protein taking the place of TM2 after its displacement in the open conformation of the TMBIM protein (fig. S10, A and B).

It has been reported that Bax and Bak activation and mitochondria outer membrane permeabilization (MOMP) are enhanced by overloaded calcium stores (*2*). The protective role of hBI-1 in decreasing ER Ca^{2+} concentration is expected to reduce MOMP and thus suppress the activation of Bax and Bak toward the initiation of apoptosis. We propose that human TMBIM proteins function in maintaining a dynamic homeostasis of stored Ca^{2+} concentration and cytosolic Ca^{2+} concentration through the pH-sensitive calcium-leak mechanism. The overexpression of hBI-1 in various cancers, including prostate, breast, glioma, uterine, ovarian, and lung, presumably reflects recruitment of its antiapoptotic activity (*37*–*40*). Knockdown of hBI-1 expression by RNA interference has shown effectiveness in inducing spontaneous apoptosis of cancer cells in prostate and breast (*37*, *38*). The structures of BsYetJ and its derivative hBI-1 models provide substantial insights into the functioning of TMBIM proteins and offer therapeutic prospects for intervention of anti-apoptotic functions in treatment of cancers.

REFERENCES AND NOTES

1. M. J. Berridge, M. D. Bootman, H. L. Roderick, *Nat. Rev. Mol. Cell Biol.* **4**, 517–529 (2003).
2. S. S. Smaili *et al.*, *Curr. Mol. Med.* **13**, 252–265 (2013).
3. S. Orrenius, B. Zhivotovsky, P. Nicotera, *Nat. Rev. Mol. Cell Biol.* **4**, 552–565 (2003).
4. L. Scorrano *et al.*, *Science* **300**, 135–139 (2003).
5. A. E. Palmer, C. Jin, J. C. Reed, R. Y. Tsien, *Proc. Natl. Acad. Sci. U.S.A.* **101**, 17404–17409 (2004).
6. Y. Ihara-Ohori, M. Nagano, S. Muto, H. Uchimiya, M. Kawai-Yamada, *Plant Physiol.* **143**, 650–660 (2007).
7. B. C. Westphalen, J. Wessig, F. Leypoldt, S. Arnold, A. Methner, *Cell Death Differ.* **12**, 304–306 (2005).
8. Q. Xu, J. C. Reed, *Mol. Cell* **1**, 337–346 (1998).
9. S. Kiviluoto *et al.*, *Cell Death Dis.* **3**, e367 (2012).
10. C. W. Distelhorst, M. D. Bootman, *Cell Calcium* **50**, 234–241 (2011).
11. C. Xu, W. Xu, A. E. Palmer, J. C. Reed, *J. Biol. Chem.* **283**, 11477–11484 (2008).
12. N. Henke *et al.*, *Cell Calcium* **50**, 251–260 (2011).
13. M. Punta *et al.*, *Nucleic Acids Res.* **40**, D290–D301 (2012).
14. L. Käll, A. Krogh, E. L. Sonnhammer, *Nucleic Acids Res.* **35** , W429–W432 (2007).
15. F. de Mattia *et al.*, *Mol. Biol. Cell* **20**, 3638–3645 (2009).
16. G. Carrara, N. Saraiva, C. Gubser, B. F. Johnson, G. L. Smith, *J. Biol. Chem.* **287**, 15896–15905 (2012).
17. G. Bultynck *et al.*, *J. Biol. Chem.* **287**, 2544–2557 (2012).
18. Q. Liu *et al.*, *Science* **336**, 1033–1037 (2012).
19. G. von Heijne, *J. Mol. Biol.* **225**, 487–494 (1992).
20. L. Holm, S. Kääriäinen, P. Rosenström, A. Schenkel, *Bioinformatics* **24**, 2780–2781 (2008).
21. A. Senes, I. Ubarretxena-Belandia, D. M. Engelman, *Proc. Natl. Acad. Sci. U.S.A.* **98**, 9056–9061 (2001).
22. S. G. Rasmussen *et al.*, *Nature* **450**, 383–387 (2007).
23. A. Quigley *et al.*, *Science* **339**, 1604–1607 (2013).
24. E. E. Pryor Jr. *et al.*, *Science* **339**, 1600–1604 (2013).
25. A. J. Venkatakrishnan *et al.*, *Nature* **494**, 185–194 (2013).
26. R. Benton, S. Sachse, S. W. Michnick, L. B. Vosshall, *PLOS Biol.* **4**, e20 (2006).
27. P. D. Adams *et al.*, *Acta Crystallogr. D* **66**, 213–221 (2010).
28. C. R. Søndergaard, M. H. M. Olsson, M. Rostkowski, J. H. Jensen, *J. Chem. Theory Comput.* **7**, 2284–2295 (2011).
29. J. Liao *et al.*, *Science* **335**, 686–690 (2012).
30. X. Hou, L. Pedi, M. M. Diver, S. B. Long, *Science* **338**, 1308–1313 (2012).
31. A. B. Waight *et al.*, *Nature* **499**, 107–110 (2013).
32. M. Wu *et al.*, *Proc. Natl. Acad. Sci. U.S.A.* **110**, 11367–11372 (2013).
33. T. Nishizawa *et al.*, *Science* **341**, 168–172 (2013).
34. S. Kiviluoto *et al.*, *Cell Calcium* **54**, 186–192 (2013).
35. H. R. Kim *et al.*, *J. Biol. Chem.* **283**, 15946–15955 (2008).
36. A. Fiser, A. Sali, *Methods Enzymol.* **374**, 461–491 (2003).
37. M. Grzmil *et al.*, *J. Pathol.* **208**, 340–349 (2006).
38. M. Grzmil *et al.*, *Am. J. Pathol.* **163**, 543–552 (2003).
39. R. Tanaka *et al.*, *Cancer* **106**, 648–653 (2006).
40. R. Sano *et al.*, *Genes Dev.* **26**, 1041–1054 (2012).

ACKNOWLEDGMENTS

We thank J. Schwanof and R. Abramowitz at NSLS beamlines X4A and X4C for their assistance in data collection, J. Love for help in initial high-throughput screening, M. Punta for help in initial target selection, M. Su for help with the phylogenetic presentation, and F. Mancia and L. Shapiro for discussions. This work was supported in part by NIH grants GM095315 and GM107462. Beamlines X4A and X4C of the NSLS at Brookhaven National Laboratory, a U.S. Department of Energy facility, is supported by the New York Structural Biology Center. Atomic coordinates and structure factor files have been deposited in the Protein Data Bank (PDB) under the accession codes 4PGR for closed-form at pH 8, 4PGS for open-form at pH 6 by soaking, 4PGU for closed/open-form at pH 7 by back-soaking, 4PGV for closed-form at pH 8 by back-soaking, and 4PGW for open-form in $C222_1$ lattice. Q.L., Y.C., and W.A.H. are inventors on a patent application filed by the New York Structural Biology Center on uses of the three-dimensional structures of BsYetJ and homology models of hBI-1.

SUPPLEMENTARY MATERIALS

www.sciencemag.org/content/344/6188/1131/suppl/DC1
Materials and Methods
Figs. S1 to S10
Table S1
References (*41*–*63*)

10 February 2014; accepted 14 May 2014
10.1126/science.1252043

REPORTS

QUANTUM INFORMATION

Electrically driven nuclear spin resonance in single-molecule magnets

Stefan Thiele,[1,2] Franck Balestro,[1,2,3] Rafik Ballou,[1,2] Svetlana Klyatskaya,[4] Mario Ruben,[4,5] Wolfgang Wernsdorfer[1,2]*

Recent advances in addressing isolated nuclear spins have opened up a path toward using nuclear-spin–based quantum bits. Local magnetic fields are normally used to coherently manipulate the state of the nuclear spin; however, electrical manipulation would allow for fast switching and spatially confined spin control. Here, we propose and demonstrate coherent single nuclear spin manipulation using electric fields only. Because there is no direct coupling between the spin and the electric field, we make use of the hyperfine Stark effect as a magnetic field transducer at the atomic level. This quantum-mechanical process is present in all nuclear spin systems, such as phosphorus or bismuth atoms in silicon, and offers a general route toward the electrical control of nuclear-spin–based devices.

The realization of a functional quantum computer is currently one of the most ambitious technological goals. Among existing concepts (*1*–*3*), devices in which the quantum bits (qubits) are encoded by spins are very attractive, as they benefit from the steady progress in nanofabrication and allow for electrical readout of the qubit states (*4*–*6*). Nuclear-spin–based devices are better isolated from the environment than their electron spin counterparts (*7*), but their detection and manipulation remain challenging.

Operating nuclear spin qubits have been demonstrated with devices based on nitrogen vacancy centers (*8*), single-molecule magnets (*9*–*11*), and silicon (*12*). Yet, their integration remains limited by the on-chip microcoils (*13*) used to manipulate the spin. The parasitic crosstalk to neighboring spin qubits and the large currents necessary to perform quantum operations are serious limiting factors. Using electric fields instead of magnetic fields to manipulate the spin would alleviate this problem, as only small displacement currents are required; in addition, electric fields can be easily focused and shielded within a small volume. The coupling of the spin to the electric field is established by the hyperfine Stark effect, which transforms the electric field into a local magnetic field. Moreover, the static hyperfine Stark effect can be used

[1]CNRS, Inst NEEL, F-38042 Grenoble, France. [2]Université Grenoble Alpes, Inst NEEL, F-38042 Grenoble, France. [3]Institut Universitaire de France, 103 boulevard Saint-Michel, 75005 Paris, France. [4]Institute of Nanotechnology, Karlsruhe Institute of Technology, 76344 Eggenstein-Leopoldshafen, Germany. [5]Institut de Physique et de Chimie des Materiaux de Strasbourg, CNRS, 67034 Strasbourg, France.
***Corresponding author. E-mail: wolfgang.wernsdorfer@neel.cnrs.fr**

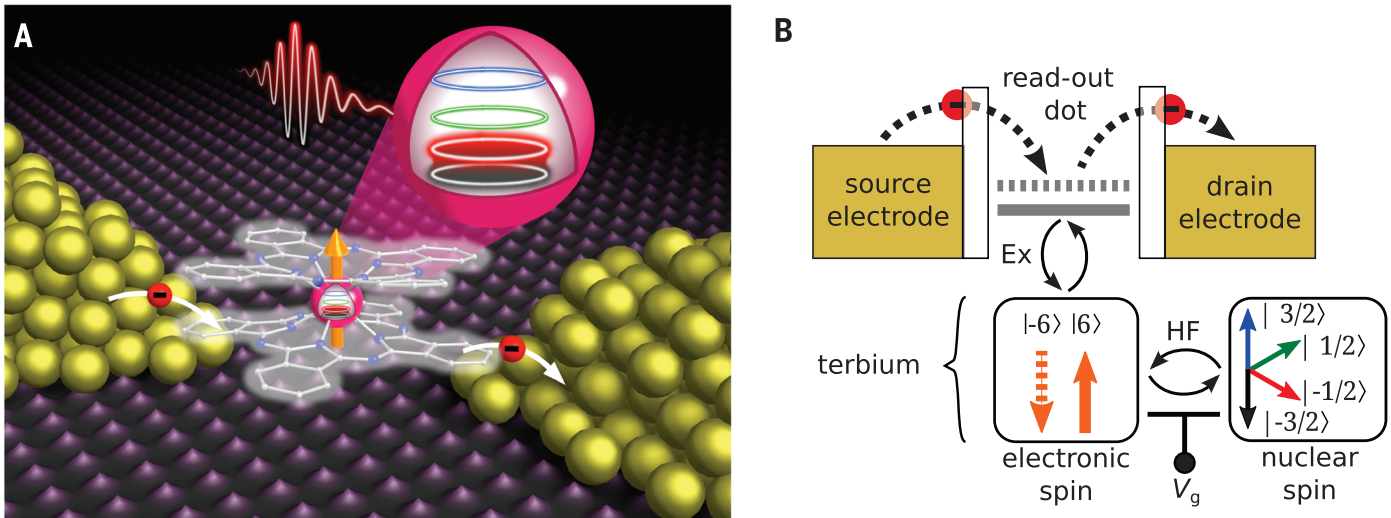

Fig. 1. Nuclear spin qubit transistor and its detection scheme. (**A**) Artist's view of a nuclear spin qubit transistor based on a single $TbPc_2$ molecular magnet. The molecule, consisting of a Tb^{3+} ion (pink) sandwiched between two Pc-ligands (white), is coupled to source, drain, and gate (not shown) electrodes. The four anisotropic nuclear spin states of the Tb^{3+} (colored circles) can be manipulated with an electric field pulse. (**B**) Three coupled subsystems of the transistor: (i) The four-level nuclear spin qubit is hyperfine (HF) coupled to (ii) an Ising-like electronic spin, which in turn is antiferromagnetically exchange (Ex) coupled to (iii) a readout quantum dot.

to tune individual nuclear qubits in and out of resonance (*14*) and thus allows for the individual addressability of different nuclear spin qubits.

To perform our experiments, we used a three-terminal nuclear spin qubit transistor (*9*) (Fig. 1A). We studied the transistor, consisting of a $TbPc_2$ single-molecule magnet coupled to source, drain, and gate electrodes, by performing electrical transport measurements inside a dilution refrigerator at 40 mK. We can associate the device with three coupled quantum systems (Fig. 1B):

(i) A nuclear spin qubit emerging from the atomic core of the Tb^{3+} ion. It possesses a nuclear spin $I = 3/2$ leading to four different qubit states: $|-3/2\rangle$, $|-1/2\rangle$, $|+1/2\rangle$, and $|+3/2\rangle$.

(ii) An electronic spin arising from the 4f electrons of the terbium. Its electronic configuration is $[Xe]4f^8$ resulting in a total spin of $S = 3$ and a total orbital momentum of $L = 3$. A strong spin-orbit coupling yields an electronic spin with a total angular magnetic moment of $J = 6$. In addition, the ligand field, generated by the two Pc's, leads to a well-isolated electron spin ground state doublet of $|\uparrow\rangle$ and $|\downarrow\rangle$ with a uniaxial anisotropy axis perpendicular to the Pc plane. The degeneracy of the doublet is lifted by the hyperfine coupling to the nuclear spin qubit and splits each electronic spin ground state into four different quantum states. At zero external field, the energy levels are intrinsically separated by $\nu_{01} \approx 2.(5)$ GHz, $\nu_{12} \approx 3.(1)$ GHz, and $\nu_{23} \approx 3.(7)$ GHz, where the index 0 corresponds to the ground state, and indices 1, 2, and 3 to the first, second, and third excited states, respectively (Fig. 2A).

(iii) A readout quantum dot created by the Pc ligands. Their delocalized π-electron system is tunnel-coupled to the source and drain terminals, creating a quantum dot in the vicinity of the electronic spin carried by the Tb^{3+} ion. Furthermore, an overlap of the delocalized π-electron system with the terbium's 4f wave functions gives rise to an exchange coupling of $E_{ex} \approx 1.66$ T between the readout quantum dot and the electronic spin (*15*).

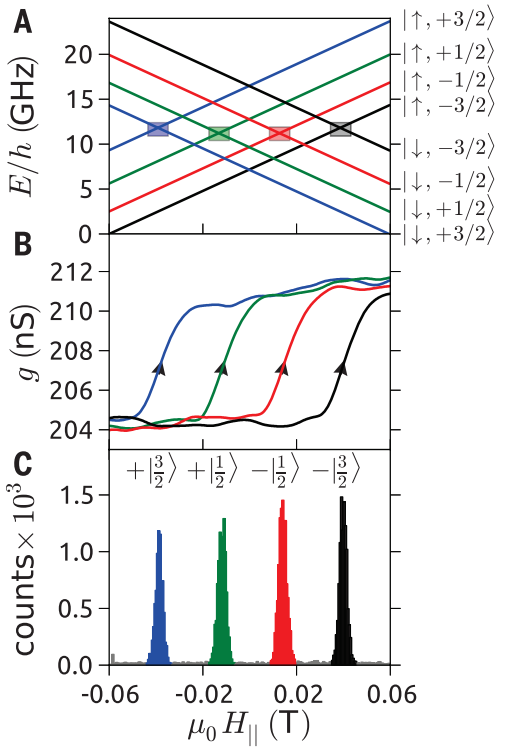

Fig. 2. Zeeman diagram and nuclear spin detection procedure. (**A**) Zeeman diagram of the $TbPc_2$ molecular magnet, showing the hyperfine split electronic spin ground state doublet $|\uparrow\rangle$ and $|\downarrow\rangle$ as a function of the external magnetic field $H_{||}$ parallel to the easy-axis of magnetization. The ligand-field–induced avoided level crossings (colored rectangles) allow for tunneling of the electron spin. (**B**) The jumps of the conductance g of the readout quantum dot during magnetic-field sweeps are nuclear-spin dependent. (**C**) Histograms of the positions of about 75,000 conductance jumps, showing four nonoverlapping Gaussian-like distributions; each conductance jump can be assigned to a nuclear spin state.

To perform the readout of the single-nuclear spin state, we exploit the different interactions between the three quantum systems.

First, the hyperfine interaction splits each electronic ground state doublet into four nuclear-spin–dependent levels (Fig. 2A). Electronic levels corresponding to the same nuclear spin state are mixed owing to the off-diagonal terms in the ligand-field Hamiltonian; in an external magnetic field, this results in avoided level crossings of $\Delta E \approx 1\ \mu K$ (rectangles in Fig. 2A). Sweeping the magnetic field slowly enough over such an anti-crossing gives rise to the quantum tunneling of magnetization (QTM) (*16*, *17*), which reverses the electronic spin according to the Landau-Zener probability (*18*, *19*). Because the magnetic field position of the QTM is nuclear spin dependent, we can use this process to measure the state of the nuclear spin qubit (*9*–*11*).

In the second stage, the electronic spin is mapped onto the readout dot's conductance through use of the exchange interaction (*15*). It

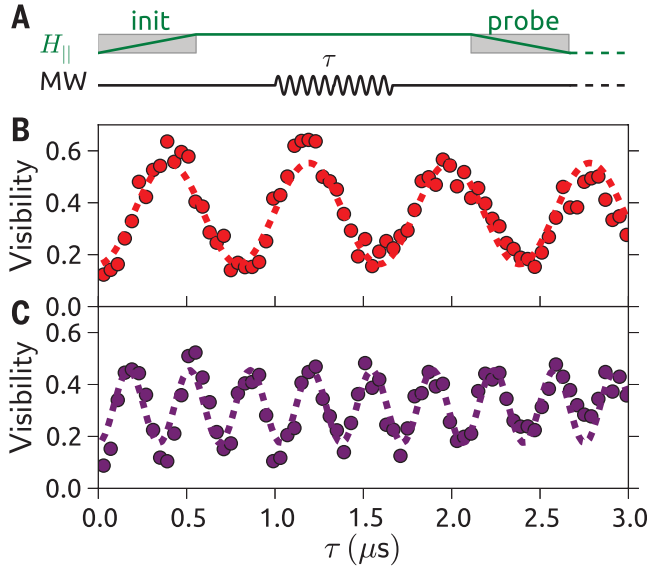

Fig. 3. Rabi oscillations of a single nuclear spin qubit. (**A**) Time-dependent external magnetic field $H_{||}$ and pulse sequence. The nuclear spin is first initialized in the lower $|3/2\rangle$ state (init sequence). A subsequent MW pulse of frequency ν_0 and duration τ induces an effective oscillating magnetic field resulting in coherent manipulation of the two lower states of the nuclear spin qubit. Finally, $H_{||}$ is swept back to probe the final state of the nuclear spin qubit. (**B** and **C**) Rabi oscillations between $|3/2\rangle$ and $|1/2\rangle$ states obtained by repeating the above sequence 100 times at each τ, for two different MW powers, (**B**) P_{MW} = 1 mW and (**C**) P_{MW} = 1.58 mW.

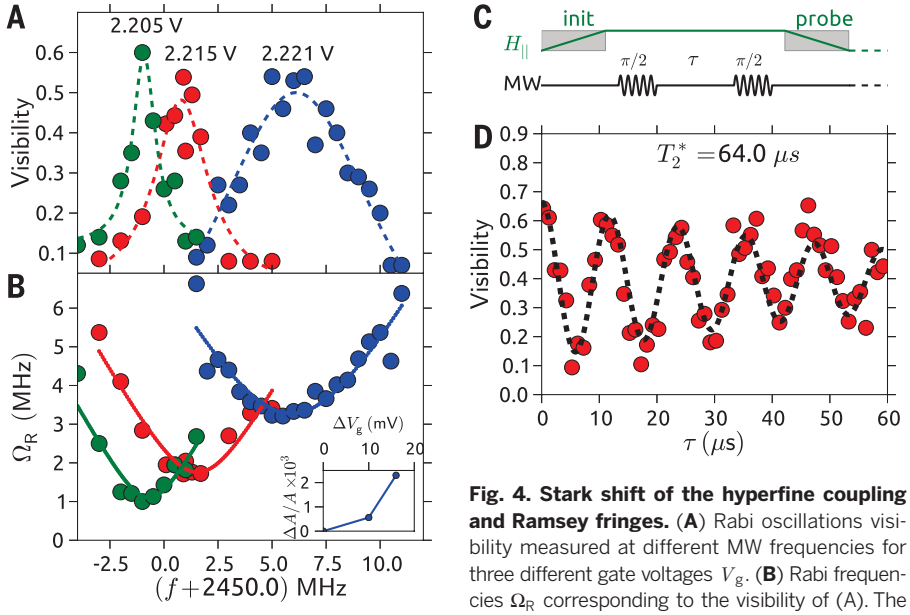

Fig. 4. Stark shift of the hyperfine coupling and Ramsey fringes. (**A**) Rabi oscillations visibility measured at different MW frequencies for three different gate voltages V_g. (**B**) Rabi frequencies Ω_R corresponding to the visibility of (A). The continuous lines are fit to the experimental points following the theoretical expression of the Rabi frequency dependence (see text). (Inset) The relative change $\Delta A/A$ with respect to the applied V_g. (**C**) Time-dependent external magnetic field $H_{||}$ and pulse sequence. Initialization and probe of the nuclear spin qubit are performed by using the identical protocol as in Fig. 3A. The MW sequence consists of two $\pi/2$ pulses, with an increasing interpulse delay τ. (**D**) Ramsey interference fringes obtained by repeating the procedure of (C) 100 times. V_g = 2.205 V, corresponding to a Rabi frequency Ω_R = 1.136 MHz and a resonant frequency ν_0 = 2.449 MHz of the nuclear spin qubit. The measured coherence time $T_2^* \approx 64$ μs.

induces a slight modification of the readout quantum dot's chemical potential depending on whether the electronic spin is $|\uparrow\rangle$ or $|\downarrow\rangle$. Therefore, when sweeping the magnetic field at constant bias and gate voltages, the reversal of the electronic spin results in a conductance jump (Fig. 2B). The amplitude of the jump is typically about 3% and its position in the magnetic field is nuclear spin state dependent.

For statistical analysis, we swept the magnetic field back and forth 75,000 times while monitoring the conductance of the readout quantum dot. By plotting the magnetic field position of all the detected conductance jumps into a histogram, we obtained four nonoverlapping peaks (Fig. 2C), which enabled us to unambiguously assign a nuclear qubit state to each detected jump. The error induced by our nuclear spin readout procedure is mainly due to inelastic electronic spin reversals, which were misinterpreted as a QTM event, and is estimated to be less than 4% (*20*). For the device presented here, we found relaxation times T_1 of ≈34 s for $m_I = \pm 3/2$ and T_1's of ≈17 s for $m_I = \pm 1/2$ (*15*).

We turn now to the electrical manipulation of a single nuclear spin. The hyperfine Stark effect describes the change of the hyperfine constant A in the Hamiltonian $H_{HF} = A\mathbf{I}\cdot\mathbf{J}$ as a function of an external electric field (*21*, *22*). Writing the Hamiltonian as $H_{HF} = g_N \mu_N \mathbf{I} \cdot \mathbf{B}_{eff}(A, J)$ demonstrates how the modification of A is converted into a change of the effective magnetic field $\mathbf{B}_{eff}(A, J)$ at the center of the nucleus. Given a HF constant of A = 24.9 mK (*23*) and $J = 6$, we obtain an effective static field of 329 T. Thus, a periodic modulation of A by 1/1000 of its value is sufficient to generate local magnetic field oscillations of ±329 mT. Because the orientation of the quantization axis of the molecule with respect to the electric field is not well determined, the effective magnetic field will have components in the x and z direction. However, in terms of oscillating fields, only the component in the x direction can rotate the nuclear spin, whereas the z component induces additional decoherence. Moreover, even moderate electric field amplitudes of 1 mV/nm are sufficient to induce a controlled fine tuning of the HF constant, which is on the order of 1% (*15*).

For the experimental demonstration of the single–nuclear-spin manipulation, we focused on the nuclear qubit subspace of $|+3/2\rangle$ and $|+1/2\rangle$, whose eigenstates are separated by $\nu_{01} \approx 2.45$ GHz [the exact value is device dependent (*23*, *24*)]. We initialize the nuclear spin qubit by sweeping the external magnetic field back and forth between ±60 mT at 80 mT/s (Fig. 3A) until a QTM transition is measured at –38 mT, which is the signature of the $|+3/2\rangle$ qubit state (Fig. 2C). We then apply a microwave (MW) pulse of duration τ and a local field amplitude on the order of ≈1 mV/nm while keeping the external magnetic field constant (Fig. 3A); the pulse modulates the hyperfine constant A at the MW frequency. Finally, we detect the resulting state by sweeping back the external magnetic field on a time scale faster than the measured relaxation times of both nuclear spin states. The entire sequence is rejected when the final state is not detected because of a missing QTM transition. Repeating this procedure resulted in coherent Rabi oscillations (Fig. 3, B and C). The visibility of the Rabi oscillations as a function of the applied MW frequency (Fig. 4A) has a maximum at the resonant frequency ν_0 and decreases for increasing detuning $\Delta = |\nu - \nu_0|$. In addition, a clear dependence of the nuclear qubit resonance frequency on the gate voltage is observed in Fig. 4A. This effect can be attributed to the static HF Stark shift, owing to the additional electric field induced by the gate voltage, which shows our ability to tune the HF constant A between the electronic spin and the nuclear spin qubit. Only the z component of the effective magnetic field will modify the level splitting. Applying a static gate voltage offset of 16 mV shifts the resonant frequency of the nuclear spin qubit by $\Delta\nu_0 \approx 7$ MHz, corresponding to $\Delta A/A \approx 0.23\%$ (Fig. 4B, inset).

To extract the Stark shift–induced effective ac magnetic driving field at the nuclei, used to

coherently manipulate the nuclear spin qubit, we measured the Rabi frequency Ω_R evolution as a function of the applied MW frequency for the three different gate voltages (Fig. 4B). The horizontal shift of the minimum is again induced by the static gate voltage, whereas the vertical evolution indicates an increasing effective ac field in the x direction, which is probably caused by the nonlinearity of the HF Stark effect. The solid lines are fits to $\Omega_R = \sqrt{\Delta^2 + (\sqrt{3} g_N \mu_N B_x / h)^2}$, with g_N being the nuclear g-factor [≈1.354 for Tb (*25*)], μ_N the nuclear magneton, and B_x the effective magnetic field in the x direction. The equation gives B_x = 62, 98, and 183 mT for V_g = 2.205, 2.215, and 2.221 V, respectively, up to two orders of magnitude higher than magnetic fields created by on-chip microcoils. The electric driving field is induced along the source-drain direction, and only the x component of the corresponding effective magnetic field is responsible for the nuclear spin rotation.

We turn now to the measurements of the Ramsey fringes to assess the dephasing time T_2^* of the nuclear spin qubit, which is tantamount to the average duration over which the coherence of the quantum superposition is preserved. As shown by the pulse sequence presented in Fig. 4C, the nuclear spin qubit is first initialized in the $|3/2\rangle$ state. Subsequently, two $\pi/2$ MW pulses are generated with an interpulse delay τ. Finally, the readout of the final state is probed with the same procedure as explained previously. Repeating this procedure results in the Ramsey fringes shown in Fig. 4D. The data follow an exponentially decaying cosine function revealing a coherence time $T_2^* \approx 64\ \mu s$. Detailed studies suggest that the major contribution to the decoherence was caused by charge noise, which induced magnetic field fluctuations of about 10 mT via the HF Stark effect. Therefore, we expect that more stable gate oxides would increase T_2^* by one or two orders of magnitude.

Our results show the general feasibility of establishing an all-electrical control of a single nuclear spin through use of the hyperfine Stark effect and should be transferable to other spin qubit devices with a large hyperfine interaction.

REFERENCES AND NOTES

1. C. Monroe, D. M. Meekhof, B. E. King, W. M. Itano, D. J. Wineland, *Phys. Rev. Lett.* **75**, 4714–4717 (1995).
2. A. Wallraff *et al.*, *Nature* **431**, 162–167 (2004).
3. L. DiCarlo *et al.*, *Nature* **467**, 574–578 (2010).
4. D. Loss, D. P. DiVincenzo, *Phys. Rev. A* **57**, 120–126 (1998).
5. J. M. Elzerman *et al.*, *Nature* **430**, 431–435 (2004).
6. F. H. L. Koppens *et al.*, *Nature* **442**, 766–771 (2006).
7. P. C. Maurer *et al.*, *Science* **336**, 1283–1286 (2012).
8. P. Neumann *et al.*, *Science* **329**, 542–544 (2010).
9. R. Vincent, S. Klyatskaya, M. Ruben, W. Wernsdorfer, F. Balestro, *Nature* **488**, 357–360 (2012).
10. M. Urdampilleta, S. Klyatskaya, M. Ruben, W. Wernsdorfer, *Phys. Rev. B* **87**, 195412 (2013).
11. M. Ganzhorn, S. Klyatskaya, M. Ruben, W. Wernsdorfer, *Nat. Nanotechnol.* **8**, 165–169 (2013).
12. J. J. Pla *et al.*, *Nature* **496**, 334–338 (2013).
13. T. Obata *et al.*, *Rev. Sci. Instrum.* **78**, 104704 (2007).
14. B. E. Kane, *Nature* **393**, 133–137 (1998).
15. Materials and methods are available as supplementary materials on *Science* Online.
16. J. R. Friedman, M. P. Sarachik, J. Tejada, R. Ziolo, *Phys. Rev. Lett.* **76**, 3830–3833 (1996).
17. L. Thomas *et al.*, *Nature* **383**, 145–147 (1996).
18. L. Landau, *Physics of the Soviet Union* **2**, 46 (1932).
19. C. Zener, *Proc. R Soc. Math. Phys. Eng. Sci.* **137**, 696–702 (1932).
20. S. Thiele *et al.*, *Phys. Rev. Lett.* **111**, 037203 (2013).
21. R. Haun, J. Zacharias, *Phys. Rev.* **107**, 107–109 (1957).
22. R. Rahman *et al.*, *Phys. Rev. Lett.* **99**, 036403 (2007).
23. N. Ishikawa, M. Sugita, W. Wernsdorfer, *Angew. Chem. Int. Ed.* **44**, 2931–2935 (2005).
24. C. Hutchison, E. Wong, *J. Chem. Phys.* **29**, 754 (1958).
25. J. M. Baker, J. R. Chadwick, G. Garton, J. P. Hurrell, *Proc.R. Soc. Math. Phys. Eng. Sci.* **286**, 352–365 (1965).

ACKNOWLEDGMENTS

This work was partially supported by MoQuaS FP7-ICT-2013-10, the Deutsche Forschungsgemeinschaft Programs no. SPP 1459 and TRR 88 3Met, ANR-12-JS10-007, ANR-13-BS10-0001 MolQuSpin, and European Research Council Advanced Grant MolNanoSpin no. 226558. The samples were manufactured at the NANOFAB facilities of the Neel Institute. We acknowledge E. Bonet, O. Buisson, Y. Deschanels, F. Evers, E. Eyraud, O. Gaier, M. Ganzhorn, C. Godfrin, C. Grupe, C. Hoarau, D. Lepoittevin, T. Meunier, N. Roch, C. Thirion, M. Urdampiletta, and R. Vincent.

SUPPLEMENTARY MATERIALS

www.sciencemag.org/content/344/6188/1135/suppl/DC1
Materials and Methods
Supplementary Text
Figs. S1 to S10
References (*26*–*35*)

16 December 2013; accepted 7 May 2014
10.1126/science.1249802

INTERFACIAL CHEMISTRY

Liquid flow along a solid surface reversibly alters interfacial chemistry

Dan Lis,[1]* Ellen H. G. Backus,[2] Johannes Hunger,[2] Sapun H. Parekh,[2] Mischa Bonn[2]*

In nature, aqueous solutions often move collectively along solid surfaces (for example, raindrops falling on the ground and rivers flowing through riverbeds). However, the influence of such motion on water-surface interfacial chemistry is unclear. In this work, we combine surface-specific sum frequency generation spectroscopy and microfluidics to show that at immersed calcium fluoride and fused silica surfaces, flow leads to a reversible modification of the surface charge and subsequent realignment of the interfacial water molecules. Obtaining equivalent effects under static conditions requires a substantial change in bulk solution pH (up to 2 pH units), demonstrating the coupling between flow and chemistry. These marked flow-induced variations in interfacial chemistry should substantially affect our understanding and modeling of chemical processes at immersed surfaces.

The chemistry taking place at the interface between a solid material and an aqueous solution is relevant for a variety of disciplines, including geology, environmental sciences, and catalysis (*1*–*3*). The local chemical composition at the interface strongly influences the reactivity of the system, as has been demonstrated, for example, in geological studies of weathering (*4*). Similarly, the abrasion and dissolution of materials immersed in aqueous solutions is at the heart of environmental concerns. Dissolution of ocean organisms' shells and skeletons stemming from increasing acidification of water could lead to potentially devastating consequences for marine life (*5*). Accurate knowledge of the composition of both the solid material and the aqueous solution locally at the surface is essential to understand, model, and predict these interfacial chemical processes.

Previous studies have shown that the structure of liquid water at a solid interface is different from that of the bulk phase (*6*–*8*) and can resemble the ice structure (*9*) because of the specific physico-chemical properties of the surface (e.g., charge, morphology, wetting properties). Generally speaking, interfacial water possesses a more structured hydrogen bonding network than bulk water. Among various factors, the solid surface holding a net electric charge acts to align the static dipole of water molecules at the surface (Fig. 1A, top). The length over which the electric field extends into the solution from the surface is referred to as the Debye length (*10*) and correlates with the distance from the surface that water retains its preferential alignment (~ 1 to 10 nm).

In addition to causing water alignment at the surface, the charge present at the interface also attracts ions from the solution to the interface, causing surface-charge screening and leading to the formation of the so-called electrical double layer (*10*). Accordingly, the composition, as well as the structure, of the fluid adjacent to the surface can vary substantially compared with the bulk (*11*–*14*). Molecular dynamics simulations have shown, for instance, that the interfacial pH can be quite different from the bulk (*11*). Although substantial progress regarding interfacial composition and molecular organization has been achieved, in nearly all of these studies on solid-liquid

[1]Department of Physics, University of Namur, Rue de Bruxelles 61, 5000 Namur, Belgium. [2]Department of Molecular Spectroscopy, Max Planck Institute for Polymer Research, Ackermannweg 10, 55128 Mainz, Germany.
*Corresponding author. E-mail: dan.lis@unamur.be (D.L.); bonn@mpip-mainz.mpg.de (M.B.)

interfacial chemistry, the liquid is not collectively in motion (that is, at rest) (*6*, *9*, *12*, *14*–*22*). This is despite the fact that macroscopic fluid flow is ubiquitous in nature (e.g., oceans, rivers, and rainfall).

In this work, we used vibrational sum frequency generation (SFG) spectroscopy (*9*, *13*, *16*, *23*) to demonstrate that liquid flow along an interface substantially, yet reversibly, perturbs the interfacial chemistry and water arrangement at the nanoscale. The observation of this effect on two different types of solid interfaces suggests that this is a generic phenomenon. SFG is a class of second-order nonlinear optical spectroscopy that provides surface-specific vibrational spectra and has been successfully applied to elucidate interfacial water organization at solid interfaces (*6*, *9*, *12*, *14*, *15*, *19*–*22*, *24*, *25*). In an SFG experiment, an infrared (IR) laser pulse is overlapped at the surface in both time and space with a visible (VIS) pulse, leading to the generation of new photons at the sum-frequency of the IR and VIS frequencies (Fig. 1A, bottom). Vibrational information is obtained when the IR frequency is tuned into resonance with a vibrational mode; for example, the OH stretch vibration of water molecules. SFG owes its surface specificity to the selection rule that requires the inversion symmetry (present in isotropic liquids such as water) to be broken to generate a signal, which precisely occurs at an interface. The SFG signal for water is then generated only by those molecules that are preferentially aligned; for example, by the electrostatic field at the solid-water interface (*6*, *21*).

The magnitude of the SFG signal scales with the degree of alignment of those water molecules and is thus tightly related to the surface charge (*26*, *27*). From the SFG vibrational spectrum of interfacial water (plotted as SFG intensity versus IR frequency), it is thus possible to glean information on the orientation of the water molecules and water structure in the interfacial region. We employ SFG to study the interface between a solid and various aqueous solutions within a microfluidic flow cell (Fig. 1A, bottom, and fig. S1). The shear rate in the flow cell is ~10^4 s^{-1} (typical Reynolds number of 1000), ensuring a fully developed laminar flow at the center of the cell (fig. S1). All SFG experiments reported here were performed under standard atmospheric conditions (e.g., room temperature and air environment), using *s*, *s*, *p* polarizations for SFG, VIS, and IR fields, respectively. Further details about the experimental setup can be found in the supplementary materials.

The first solid surface that we studied was polycrystalline calcium fluoride (CaF_2, Crystran), with a surface RMS roughness of ~1.5 nm over a 10 μm by 10 μm area. Under ambient conditions the CaF_2 surface assumes positive, neutral, or negative charge, depending on the pH of the contacting solution (*28*, *29*). The point of zero charge (pzc) of CaF_2—that is, the pH at which the surface is charge-neutral—has been shown to vary from pH 6 to 10, depending on the sample preparation and measurement conditions (*15*, *28*, *30*). For a neutral CaF_2 surface, no electrostatic interaction exists to preferentially align water molecules at the liquid-solid interface. Under this condition, a near-zero SFG intensity has been observed (*14*, *15*, *31*). Black traces in Fig. 1, B and C, show the SFG response of water at the positively [~+60 mV surface potential at pH 3 (*28*)] and negatively [~–30 mV surface potential at pH 12 (*28*, *30*)] charged CaF_2

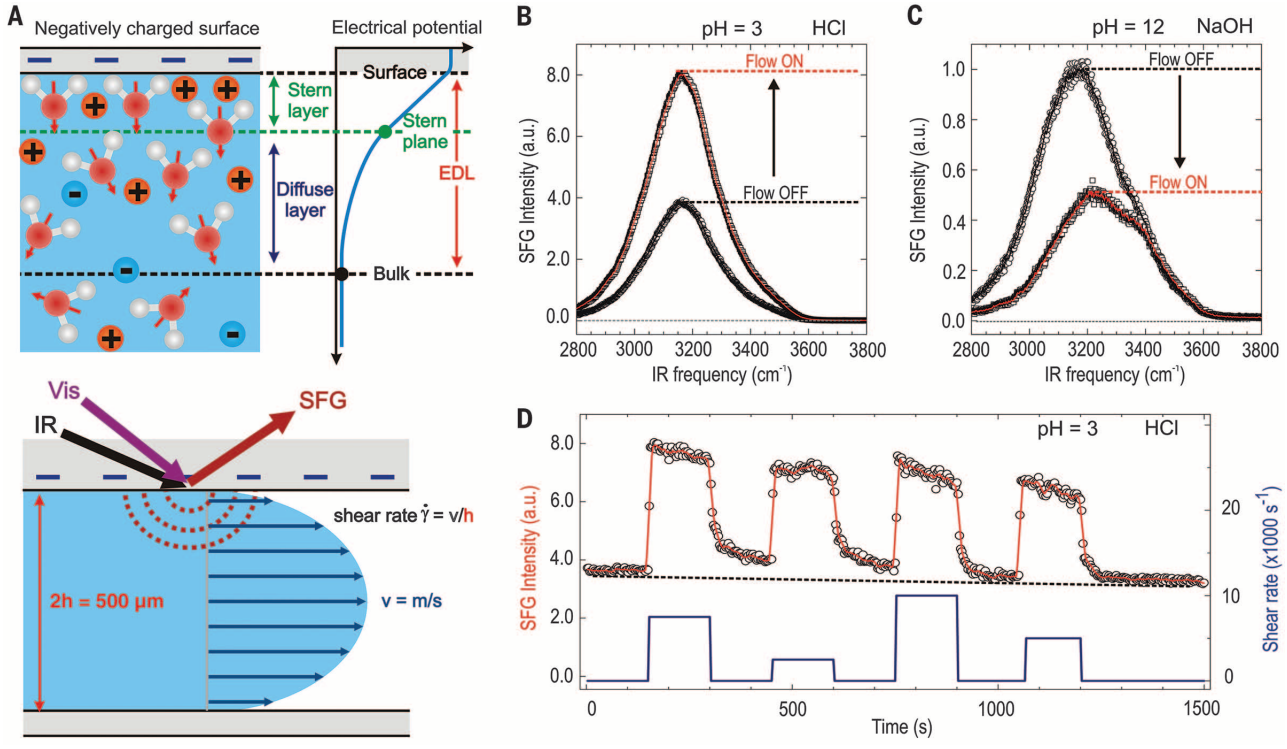

Fig. 1. Experimental scheme and the effect of flow on the SFG signal at the CaF_2-water interface. (**A**) (Top) Schematic representation of the molecular arrangement at the charged solid-water interface in presence of electrolytes. For a negatively charged surface, the water dipole moments are aligned away from the interface. Cations (red spheres) form a compact layer adjacent to the surface (Stern layer) with water and partially screen the negative surface charge. Anions (blue spheres) are mostly repelled from the surface. EDL, electrical double layer. (Bottom) Schematic representation of the SFG experimental geometry with respect to the flow cell. Incident VIS and IR beams generate sum frequency light at the solid-liquid interface. v, flow velocity at the center of the channel; h, distance from center of the channel to the surface. (**B**) SFG spectrum in the OH stretch region of the CaF_2-water interface at pH 3 (1 mM HCl) under static (black) and flow (red) conditions. a.u., arbitrary units. (**C**) SFG spectrum of the CaF_2-water interface at pH 12 (10 mM NaOH). (**D**) Plot of the time dependence of the integrated SFG intensity (black circles) for the water-CaF_2 interface at pH 3 under multiple flow on-off cycles (blue curve). The red solid line on the SFG data is a five-point average to guide the eye. In all panels, the SFG intensity is normalized by the maximal intensity of the flow-off SFG curve at pH 12 shown in Fig. 1C. Further information on the OH peak center positions can be found in the supplementary materials (*33*).

surface, with water molecules preferentially aligned with their dipoles toward and away from the surface, respectively. Figure S2 shows that between these two pH values, an inversion of the molecular alignment occurs when crossing the pzc (*32*).

At both pH 3 and 12, the SFG vibrational signature of the water at rest displays a broad resonance centered at 3160 cm^{-1} and attributed to the OH stretching mode (*14*, *15*, *23*, *33*) (fig. S2). For the low-pH solution, we observe a ~100% increase in the SFG intensity (Fig. 1B, red curve) when flowing water along the surface under laminar conditions at a modest shear rate (10^4 s^{-1}). Conversely, for a basic solution, we observe the opposite behavior—a 50% decrease in the SFG signal—in addition to a shift of the primary SFG spectral peak to 3200 cm^{-1} (Fig. 1C, red curve). For comparison, to achieve such a drop in the SFG intensity for a static system, a pH 10 liquid is required (fig. S3A); that is, the effect of the flow is equivalent to a 100-fold decrease of the bulk OH^- concentration. From Fig. 1, B and C, it is clear that flowing the solution along a charged solid surface modifies the vibrational response in opposite ways depending on surface charge. As shown in Fig. 1D, the changes recorded in the integrated SFG intensity are only very weakly dependent on the flow speed within the range of shear rates accessible with our experimental setup (5×10^2 to 10^4 s^{-1}). The changes in SFG intensity are also independent of the flow direction (fig. S3B). Moreover, the flow-induced changes occur on the ~10-s time scale of the experiment and are reversible when flow is turned off (Fig. 1D). Clearly, a major rearrangement of the interfacial water ensues as a result of the flow.

The observed flow-induced changes in the interfacial water response are not specific to CaF_2. Figure 2 shows SFG spectra of a fused silica interface in contact with a 10 mM NaCl solution under flow and at rest for various pH values. Fused silica is glass consisting of silicon dioxide (SiO_2), which represents 28% of Earth's crust and has its pzc at pH ~2 (*18*). Therefore, a SiO_2 surface will be increasingly negatively charged as pH rises above 2. The SFG spectrum of the (negatively charged) fused silica-water interface at pH 6.5 is shown in black in Fig. 2A and displays a maximum intensity at 3200 cm^{-1} with a shoulder at ~3460 cm^{-1} (see fig. S4 for peak details) (*18*, *21*). Similar to observations for the negatively charged CaF_2, the presence of flow (shear rate = 6×10^3 s^{-1}) causes a very large (50%) decrease in SFG intensity (Fig. 2A, red curve). However, at both low and high pH, the reduction in SFG intensity upon flow is very small (Fig. 2, B and C), in contrast to what is observed for CaF_2. It takes tens of minutes for the SFG intensity to reach the static value after stopping the flow (Fig. 2D).

Under specific solution conditions, turning on flow dramatically changes the SFG intensity for both CaF_2 and SiO_2, albeit at different solution conditions for each surface. As mentioned earlier, the magnitude of the SFG signal reflects the degree of alignment of water molecules due to the electrostatic field at the surface. The large changes in the SFG intensity triggered by the flowing liquid therefore reflect a considerable change in the interfacial water alignment. The water arrangement at the surface is influenced by three primary factors: (i) the magnitude of the surface charge (potential), (ii) the penetration depth of the resulting electric field into the liquid, and (iii) the ability of the surface field to maintain alignment of water dipoles. One could imagine that the flow displaces ions from the surface, thus decreasing the screening of the interfacial charge and increasing the penetration depth of the electric field; that is, increasing the Debye length. However, such a mechanism would always result in an increased water dipole alignment and corresponding increase in SFG intensity upon flow, regardless of the sign of the surface charge, which is clearly not borne out by the data (Figs. 1, B and C, and 2A). It is also plausible that the flow perturbs the field-induced preferential alignment of water at the surface, which would lead to a decrease in the SFG signal but again would not result in different behavior based on surface charge. Furthermore, the reorientational motion of water and the re-equilibration of displaced ions due to diffusion in the near-surface region are both too fast to be consistent with the slow recovery times observed after stopping the flow (Figs. 1D and 2D). These arguments make both hypotheses (ii) and (iii) incompatible with our results and indicate that changes in the surface charge are responsible for the altered water arrangement at the interface when the flow is turned on.

The slow recovery after stopping the flow suggests the onset of a new chemical equilibrium: Chemical reactions occurring at the interface appear to underlie the change in surface charge and, therefore, water alignment. Although the solubility of CaF_2 and SiO_2 in water is extremely low, it is not negligible (supplementary materials section 7). For SiO_2, the dissolution reaction is dominated by the hydrolysis of the Si-O-Si bond (*34*)

$$\equiv Si{-}O{-}Si(OH)_2O^- + H_2O \rightleftharpoons \equiv Si{-}OH + Si(OH)_3O^-(aq)(pH > pzc) \quad (1)$$

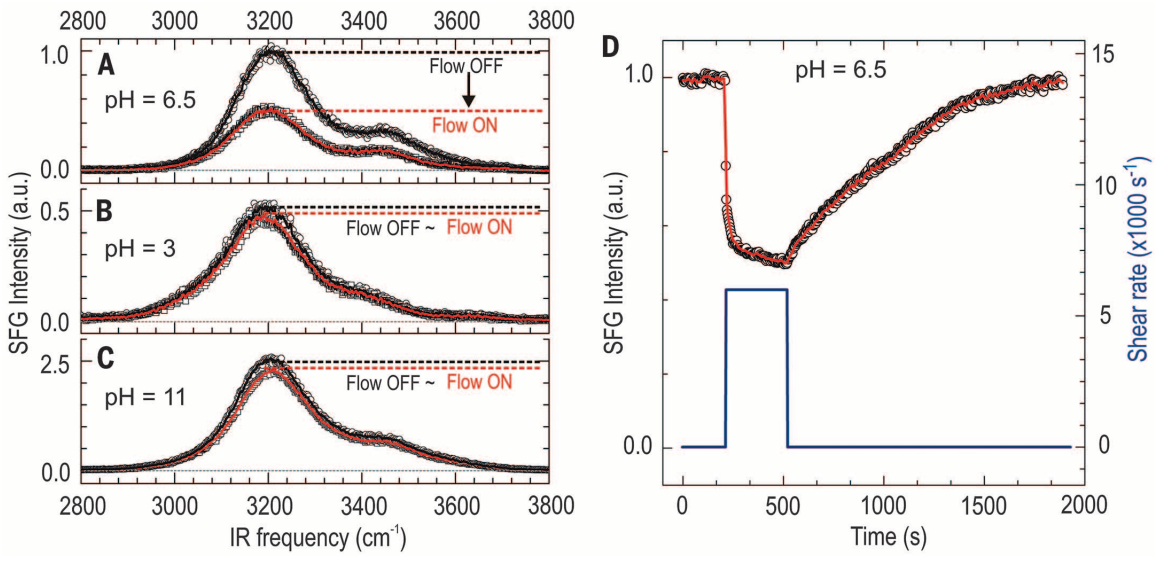

Fig. 2. The effect of flow on the interfacial vibrational spectra of water at the SiO_2-water interface. (**A**) pH 6.5 (10 mM NaCl), (**B**) pH 3 (1 mM HCl, 10 mM NaCl), and (**C**) pH 11 (1 mM NaOH, 10 mM NaCl) at rest (black) and under flow (red). (**D**) Plot of the time-dependence of the integrated SFG spectrum (black circles) at pH 6.5 as a function of time for a liquid flow cycle (blue curve). The solid red line over the SFG data is a five-point average to guide the eye. All intensity curves are normalized to the flow-off intensity at pH 6.5.

Equation 1 shows that for pH values above the pzc, where the SiO_2 surface is (on average) negatively charged, hydrolysis entails a loss of the negative surface charge. For water at rest, the effective forward and backward reaction rates balance each other when the solution near the surface is nearly saturated with silicic acid. The onset of the flow lowers the silicic acid concentration near the surface by introducing fresh water, not yet saturated with the solute. This provides a driving force for surface hydrolysis that sharply biases the equilibrium in Eq. 1 toward the right-hand side, effectively removing negative charges from the surface and thereby lowering the SFG intensity. However, subsequent deprotonation of the newly formed neutral Si-OH surface state (Si-OH → $Si\text{-}O^- + H^+$) will partially restore the negative surface charge. These two competing reactions create a new steady state with a possibly changed surface charge. As shown in Fig. 2A by the large drop in SFG intensity at pH 6.5 after turning on flow, the interfacial water is not as strongly aligned, indicating that the SiO_2 surface has become less negatively charged. The substantial change in the SFG signal upon flow directly implies that deprotonation of the surface Si-OH is slower than silica hydrolysis by water at pH 6.5 (Eq. 1).

After stopping the flow, dissolution of the silica surface results in slow accumulation of silicic acid that gradually tapers off as the near-surface region becomes saturated. This slow saturation, along with the deprotonation of Si-OH surface groups, results in the delayed recovery to the at-rest (more negative) surface charge and thus provides a rationale for the observed slow recovery (Fig. 2D). Equation 1 represents only one elementary step in the dissolution reaction. The $Si(OH)_3O^-$ can be further protonated in solution (depending on the solution pH); however, its global concentration remains too low (compared with the 10 mM NaCl) to substantially change the ionic strength or pH of the solution.

The situation is different at low pH, where at equilibrium, the surface is less negative (more Si-OH rather than $Si\text{-}O^-$), on average. Equation 2 shows that for this case, silica hydrolysis at the surface is essentially neutral in terms of surface charge

$$\equiv Si{-}O{-}Si(OH)_2OH + H_2O \rightleftharpoons \equiv Si{-}OH + Si(OH)_3OH(aq)\,(pH < pzc) \quad (2)$$

Thus, at low pH, the liquid flow, although still driving away silicic acid, is expected to have minimal effect on the surface charge (and equivalently the SFG signal), consistent with our experimental observation (Fig. 2B).

At high pH, we also observe that flow minimally affects the SFG signal (Fig. 2C). Although the dissolution of silicic acid due to hydrolysis certainly alters the charge (Eq. 1), the subsequent deprotonation of Si-OH following silica hydrolysis is expected to be much faster than at pH 6.5. The combination of hydrolysis and fast subsequent deprotonation does not lead to a substantial shift of the surface charge. Alkaline cleavage of the Si-O-Si bond is also possible at high pH and is consistent with the data we see here (see supplementary materials section 8). Taken together with Fig. 2, this demonstrates that flow-induced changes in chemical dissolution equilibria can modulate the SiO_2 surface charge, which is ultimately reflected by changes in the interfacial water alignment, as detected by the SFG measurements.

Coming back to the CaF_2 surface, we now similarly relate a change in surface charge triggered by flow with dissolution of CaF_2, which was verified by inductively coupled plasma optical emission spectrometry (see supplementary materials section 7). The main equations that govern the ion dissolution from the surface are

$$\equiv(CaF_2)_X \rightleftharpoons \equiv(CaF_2)_{X-1} + \equiv(CaF)^+ + F^-(aq) \quad (3)$$

$$\equiv(CaF_2)_X \rightleftharpoons \equiv(CaF_2)_{X-1} + \equiv(F)_2^{2-} + Ca^{2+}(aq) \quad (4)$$

From these reactions, we see that the surface charge does not originate from protonation or deprotonation of surface sites, but rather from dissolution of F^- or Ca^{2+} ions from the surface. For CaF_2 it has been shown that dissolution of F^- (Eq. 3) is favored over Ca^{2+} dissolution (Eq. 4), due to the strong, energetically favored hydration of F^- (*29*, *35*). Therefore, when the fluid is at rest, a slight stoichiometric excess of F^- will be present in the near-surface region, which makes the CaF_2 surface positively charged (at low pH), according to Eq. 3.

As in the silica case, turning on the flow introduces fresh water near the surface, dispersing near-surface dissolved Ca^{2+} and F^- ions into the bulk fluid and biasing the dissolution equilibria toward the release of ions. Our measurements in Fig. 1B show that the SFG signal increases by nearly 100% when pH 3 water is flowed over CaF_2, reflecting a more positively charged surface. This observation directly shows that dissolution of F^- is faster than Ca^{2+}. This explanation implicitly assumes that the change of the fluoride concentration upon flow dominates the magnitude of the change of the surface charge, whereas the change in near-surface Ca^{2+} concentration has little effect. This is confirmed by control experiments. Figure S5 shows that the flow effect is seen for a solution with a 10-fold higher Ca^{2+} concentration than is theoretically available from CaF_2 dissolution. In contrast, figs. S6 and S7 show that the flow effect is completely suppressed in the presence of excess F^-. Because the free concentration of F^- ions in a saturated solution is nearly constant from pH

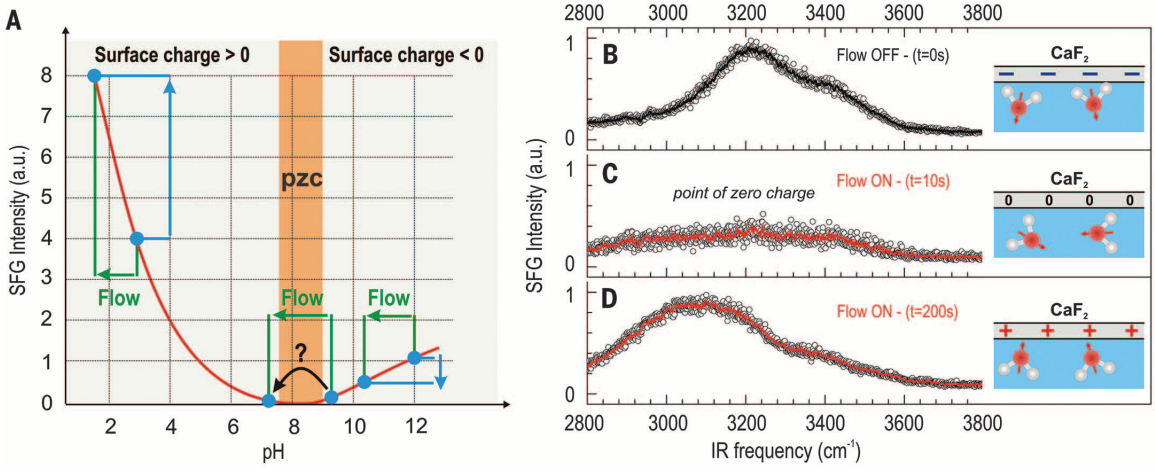

Fig. 3. Flow induces charge inversion at the CaF_2 interface. (**A**) Trend of the SFG signal intensity as a function of aqueous solution pH for the CaF_2 interface. (**B**) SFG spectra of the CaF_2-water interface at pH 9.5, where the surface is weakly negatively charged, with flow off (time t = 0 s). (**C**) The water flow is turned on, and the SFG signal decreases to essentially zero at t = 10 s. (**D**) At t = 200 s after turning flow on, the SFG intensity increases in a red-shifted band. The solid lines over the SFG data are five-point averages to guide the eyes. All curves have been normalized by the flow-off maximal intensity.

from 3 to 12 (*28*), the dissolution equilibria are not expected to depend strongly on pH, and the surface should always become more positively charged in the presence of flow, regardless of pH in our experiments.

Although Eqs. 3 and 4 predict the CaF_2 surface to be positive regardless of pH (*28*–*30*), it has been shown that at typical ambient conditions, dissolution of atmospheric CO_2 and subsequent formation of CO_3^{2-} lead to surface carbonation with increasing pH (that is, surface F^- is replaced by CO_3^{2-}), eventually making the surface negatively charged above pH 10 (*28*). Thus, at high pH the contribution of carbonate must also be considered, making the surface reactions more complicated. Despite these complications, we again find that the F^- concentration mediates the decreased SFG intensity upon flow at high pH, and that carbonate contributions can be excluded as being responsible for the flow-induced changes (for details, see figs. S8 and S9). Our results show that dissolution of F^- plays the key role for changing the surface charge (Eq. 3) up to at least pH 12. Therefore, upon flow at acidic pH, the surface charge becomes more positive, causing the SFG intensity to increase (Fig. 1B), whereas upon flow at basic pH (above the pzc), the surface becomes less negative, thereby decreasing the SFG signal (Fig. 1C).

The notion that flow modifies the surface charge by altering the near-surface ionic distribution, thereby shifting the chemical equilibrium, has interesting and important consequences near the pzc for CaF_2. Because the surface is always predicted to become more positive (or less negative) upon flow, regardless of the pH of the solution, and the effect of flow is similar to reducing the pH by ~2 units (fig. S3), a surface-polarity reversal should be observable near the pzc (Fig. 3A). The polarity of the CaF_2 surface charge is expected to flip from negative to positive upon turning on flow if the solution pH is slightly above the pzc. Accordingly, this charge inversion should lead to a corresponding flow-induced flip-flop or orientation reversal of water molecules at the interface (*32*).

Indeed, this is borne out experimentally. Starting with water at pH 9.5, the CaF_2 surface charge is slightly negative under our experimental conditions (due to the presence of carbonate). The water molecules are expected to be weakly aligned because of the small surface charge, with their dipoles directed away from the substrate, on average. The SFG spectrum shown in Fig. 3B displays a broad resonance with a peak intensity at 3220 cm^{-1} that is 10-fold weaker than at pH 12 (Fig. 1C) because of the proximity to the pzc. Furthermore, observing the primary peak blue-shifted (with respect to its location for pH 12) to 3220 cm^{-1} in the SFG spectrum is only possible for CaF_2 when approaching the pzc from a highly alkaline solution (fig. S10A).

Upon starting the flow, the SFG intensity drops in a matter of seconds in response to generation of a less negative surface, according to Eq. 3. This results in the total surface charge approaching zero, at which point the SFG signal has essentially vanished (Fig. 3C). At this moment, the surface reaches the pzc and is electrically neutral, so it does not induce any preferential water alignment (*15*, *32*). As the flow continues, the SFG signal evolves and increases to give a very different SFG spectrum with a peak intensity shifted to 3080 cm^{-1} (Fig. 3D). This peak location in the SFG spectrum, combined with the more than 100-fold weaker SFG intensity than at pH 3 (Fig. 1B), is only observable when approaching the pzc from acidic pH (fig. S10B). Figure 3D is thus the SFG spectrum from a CaF_2-water interface that is now slightly positively charged. This spectrum therefore reflects water dipoles pointing, on average, slightly toward the surface. Figure 3, B to D, directly demonstrates that flow along the CaF_2-water interface generates sufficient positive charge as a result of fluoride dissolution to invert the polarity of the surface and the average direction of water dipoles. The flip-flop behavior predicted based on flow-induced inversion of the surface charge via the dissolution reaction in Eq. 3 is clearly observed in our experiments. Upon switching off the flow, the surface again changes polarity back to negative, and the reversibility can be seen in fig. S11.

The coupling of liquid flow with interfacial chemistry has clear implications for interpretation of flow-based electrokinetic measurements. Streaming potential experiments (*36*) will likely present a surface charge influenced by the flow conditions, if surface reactions are not suppressed. Besides flow modulating the electrostatics at the interface, our results additionally imply that (electro-) chemical reactions are inevitably affected as a result of the modified surface potential. Therefore, this work is expected to have a substantial impact on the understanding, modeling (*37*), and sensing (*38*, *39*) of (geo-) chemistry and physics at immersed interfaces.

REFERENCES AND NOTES

1. G. E. Brown Jr. *et al.*, *Chem. Rev.* **99**, 77–174 (1999).
2. R. T. Wilkin, D. C. Digiulio, *Environ. Sci. Technol.* **44**, 4821–4827 (2010).
3. A. Putnis, *Science* **343**, 1441–1442 (2014).
4. J. P. Icenhower, P. M. Dove, *Geochim. Cosmochim. Acta* **64**, 4193–4203 (2000).
5. R. F. Service, *Science* **337**, 146–148 (2012).
6. K. C. Jena, D. K. Hore, *Phys. Chem. Chem. Phys.* **12**, 14383–14404 (2010).
7. A. Nilsson, L. G. M. Pettersson, *Chem. Phys.* **389**, 1–34 (2011).
8. P. Wernet *et al.*, *Science* **304**, 995–999 (2004).
9. Q. Du, E. Freysz, Y. R. Shen, *Phys. Rev. Lett.* **72**, 238–241 (1994).
10. R. B. Schoch, J. Han, P. Renaud, *Rev. Mod. Phys.* **80**, 839–883 (2008).
11. R. Vácha, D. Horinek, M. L. Berkowitz, P. Jungwirth, *Phys. Chem. Chem. Phys.* **10**, 4975–4980 (2008).
12. S. C. Flores, J. Kherb, N. Konelick, X. Chen, P. S. Cremer, *J. Phys. Chem. C* **116**, 5730–5734 (2012).
13. H. C. Allen, N. N. Casillas-Ituarte, M. R. Sierra-Hernández, X. Chen, C. Y. Tang, *Phys. Chem. Chem. Phys.* **11**, 5538–5549 (2009).
14. P. A. Covert, K. C. Jena, D. K. Hore, *J. Phys. Chem. Lett.* **5**, 143–148 (2014).
15. K. A. Becraft, G. L. Richmond, *Langmuir* **17**, 7721–7724 (2001).
16. K. B. Eisenthal, *Chem. Rev.* **96**, 1343–1360 (1996).
17. P. A. Fenter, N. C. Sturchio, *Prog. Surf. Sci.* **77**, 171–258 (2004).
18. K. C. Jena, D. K. Hore, *J. Phys. Chem. C* **113**, 15364–15372 (2009).
19. I. Li, J. Bandara, M. J. Shultz, *Langmuir* **20**, 10474–10480 (2004).
20. H. Noguchi *et al.*, *Phys. Chem. Chem. Phys.* **10**, 4987–4993 (2008).
21. Z. Yang, Q. Li, K. C. Chou, *J. Phys. Chem. C* **113**, 8201–8205 (2009).
22. S. Ye, G. Liu, H. Li, F. Chen, X. Wang, *Langmuir* **28**, 1374–1380 (2012).
23. M. Sovago *et al.*, *Phys. Rev. Lett.* **100**, 173901 (2008).
24. M. Maccarini, *Biointerphases* **2**, MR1–MR15 (2007).
25. G. J. Holinga *et al.*, *J. Am. Chem. Soc.* **133**, 6243–6253 (2011).
26. Note that due to the presence of the surface field, the SFG signal does not originate solely from a second-order nonlinear process, but also from a third-order process (*27*). However, both the second- and third-order contributions reflect the surface potential, which is relevant to the discussion of the present results.
27. K. C. Jena, P. A. Covert, D. K. Hore, *J. Phys. Chem. Lett.* **2**, 1056–1061 (2011).
28. J. D. Miller, J. B. Hiskey, *J. Colloid Interface Sci.* **41**, 567–573 (1972).
29. J. D. Miller, K. Fa, J. V. Calara, V. K. Paruchuri, *Colloids Surf. A Physicochem. Eng. Asp.* **238**, 91–97 (2004).
30. S. Assemi, J. Nalaskowski, J. D. Miller, W. P. Johnson, *Langmuir* **22**, 1403–1405 (2006).
31. K. A. Becraft, F. G. Moore, G. L. Richmond, *Phys. Chem. Chem. Phys.* **6**, 1880–1889 (2004).
32. M. S. Yeganeh, S. M. Dougal, H. S. Pink, *Phys. Rev. Lett.* **83**, 1179–1182 (1999).
33. Because the experiments were performed in total internal reflection geometry, it is challenging to record a reliable reference of the IR spectral profile transmitted through the prism. Therefore, the spectra shown here have not been normalized by the IR spectral profile. However, because only relative comparison between vibrational bands is made, the lack of normalization does not affect the conclusions. Details are provided in the supplementary materials.
34. A. Seidel, M. Löbbus, W. Vogelsberger, J. Sonnefeld, *Solid State Ion.* **101–103**, 713–719 (1997).
35. Y. Hu, Y. Lu, S. Veeramasuneni, J. D. Miller, *J. Colloid Interface Sci.* **190**, 224–231 (1997).
36. A. V. Delgado, F. González-Caballero, R. J. Hunter, L. K. Koopal, J. Lyklema, *Pure Appl. Chem.* **77**, 1753–1805 (2005).
37. D. L. Suarez, S. Goldberg, *Modeling Soil Solution, Mineral Formation and Weathering*, R. B. Bryant, R. Arnold, Eds. (U.S. Department of Agriculture–Agricultural Research Service, Riverside, CA, 1994)
38. M. R. Sheffer, D. W. Oldenburg, *Geophys. J. Int.* **169**, 839–848 (2007).
39. P. W. J. Glover, E. Walker, M. D. Jackson, *Geophysics* **77**, D17–D43 (2012).

ACKNOWLEDGMENTS

We gratefully acknowledge D. Bonn, H.-J. Butt, and G. Auernhammer for fruitful discussions, as well as the anonymous referees for their insightful comments that resulted in a more accurate interpretation of our results. We thank P. Lambin and F. Cecchet for reading the manuscript, H. Burg for measuring the surface roughness of the CaF_2 prism, and M. Steiert for the inductively coupled plasma optical emission spectrometry measurements. D.L. is supported by the Belgian Fund for Scientific Research—Fonds de la Recherche Scientifique (F.R.S.-FNRS). S.H.P. and E.H.G.B. are supported by the Marie Curie Foundation, with grants CIG322284 and CIG334368, respectively.

SUPPLEMENTARY MATERIALS

www.sciencemag.org/content/344/6188/1138/suppl/DC1
Materials and Methods
Supplementary Text
Figs. S1 to S11
Reference (*40*)

24 March 2014; accepted 2 May 2014
10.1126/science.1253793

CLOUD PHYSICS

From aerosol-limited to invigoration of warm convective clouds

Ilan Koren,[1]* Guy Dagan,[1] Orit Altaratz[1]

Among all cloud-aerosol interactions, the invigoration effect is the most elusive. Most of the studies that do suggest this effect link it to deep convective clouds with a warm base and cold top. Here, we provide evidence from observations and numerical modeling of a dramatic aerosol effect on warm clouds. We propose that convective-cloud invigoration by aerosols can be viewed as an extension of the concept of aerosol-limited clouds, where cloud development is limited by the availability of cloud-condensation nuclei. A transition from pristine to slightly polluted atmosphere yields estimated negative forcing of ~15 watts per square meter (cooling), suggesting that a substantial part of this anthropogenic forcing over the oceans occurred at the beginning of the industrial era, when the marine atmosphere experienced such transformation.

How changes in aerosol concentrations (and properties) affect clouds and what are the derived cloud feedbacks are challenging questions that carry with them a substantial part of the uncertainty in our understanding of anthropogenic effects on climate (*1*, *2*). The hypothesis of cloud invigoration by aerosols links the cloud's vertical development to aerosol loading. A chain of processes and feedbacks ties the aerosol effect on the droplet-size distribution to dynamic effects, resulting in deeper and bigger clouds (*3*–*6*). Because the natural variation in convective systems is large and sensitive to environmental conditions, compelling evidence for the invigoration effect is difficult to obtain. Most studies that do suggest invigoration link the effect to deep convective clouds with a warm base and mixed-phase or cold top (*4*, *7*). A few observational studies have suggested warm clouds' invigoration by aerosols (*8*, *9*), but most of the modeling studies suggest smaller warm clouds in a higher aerosol-loading environment resulting from enhanced evaporation (*10*, *11*).

Cloud-drop formation requires aerosols that serve as cloud-condensation nuclei (CCN) to lower the energy barrier for activation. A hypothetical aerosol-free atmosphere would probably be mostly cloud-free. Therefore, theoretically, in such a clean environment, a small increase in aerosol loading could produce a very dramatic change from a cloud-free to partly cloudy atmosphere. When do clouds stop being aerosol-limited? Here, we argue that the aerosol-invigoration effect can be viewed as an extension of the concept of aerosol-limited clouds, where cloud development (by measures of liquid water mass, for example) is limited by the availability of CCN (*12*–*14*). We propose that the two regimes can be combined and that the cloud-invigoration concept simply suggests that, in many cases, clouds are aerosol-limited up to much higher aerosol concentrations, well within the anthropogenic aerosol levels.

To reduce the inherent complexity and to focus on the transition from aerosol-limited to cloud invigoration, we looked for pristine areas with low variability of meteorological conditions that support the formation of warm-but-developed convective clouds. Our working hypothesis was that, despite the fact that we are focusing on areas with environmental conditions that favor deeper clouds, the forming clouds would often be less developed because of the clean conditions. Figure 1 shows that clean areas are more prevalent over the Southern Hemisphere. In particular, there is an atmospheric clean belt that marks the subtropical high in the vicinity of the so-called Horse Latitudes. The black contour marks clean areas that are characterized mainly by warm convective clouds. During June to August 2007, the area that showed the optimal conditions was over the southern Pacific (13°S to 22°S, 121°W to 130°W; Fig. 1, green box). The analysis was also performed over the southern Atlantic and Indian oceans (Fig. 1, yellow boxes, and fig. S4) (*15*).

Understanding the aerosol effect on developed warm convective clouds forming in a pristine region with relatively low cloud coverage and relatively steady meteorological conditions has several critically important qualities: (i) it provides a hint as to the relevant transition from preindustrial to industrial atmosphere; (ii) some of the key microphysical processes are nonlinear with respect to aerosol concentration, showing the highest sensitivity in the transition from clean to slightly polluted conditions; (iii) focusing on regions with relatively steady meteorology (fig. S1) can reduce the likelihood of changes in meteorological conditions explaining changes in both cloud and aerosol properties; (iv) measuring aerosol near clouds poses many challenges (*16*), such as cloud contamination (*17*), aerosol humidification (*18*), and cloud secondary illumination [three-dimensional (3D)] effects (*19*). Therefore, studying the aerosol effect on clouds in regimes that exhibit a small cloud fraction dramatically reduces the likelihood of encountering such challenges; (v) moreover, the dynamic interactions between clouds within a given cloud field are smaller in regimes with a small cloud fraction, further reducing complexity; (vi) last, one cannot understand aerosol effects

[1]Department of Earth and Planetary Sciences, Weizmann Institute, Rehovot 76100, Israel.
*Corresponding author. E-mail: ilan.koren@weizmann.ac.il

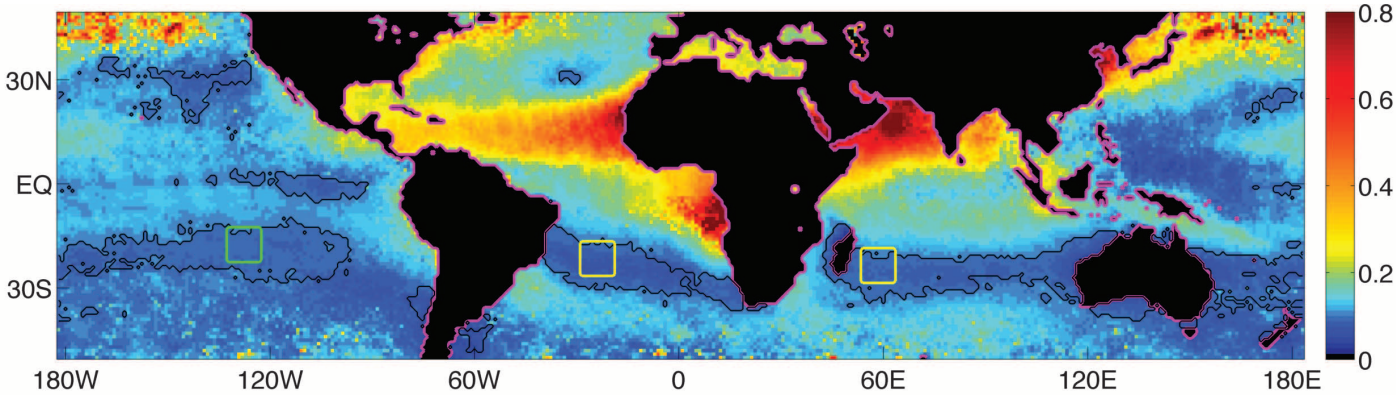

Fig. 1. Averaged AOD over the oceans for June, July, and August 2007. Areas marked by a black contour represent pristine oceanic regions with AOD < 0.1 and warm convective clouds. The green box marks the main study area over the Pacific, and the yellow boxes mark the study areas over the Atlantic and Indian oceans (all boxes are 9° by 9°). EQ, Equator.

on deep convective clouds with mixed and cold parts without fully understanding how aerosols change the warm processes that serve as the initial and boundary conditions for the upper parts.

Three types of global daily databases for 92 days between June and August 2007 were used. Moderate Resoluation Imaging Spectroradiometer (MODIS) Aqua data were used for cloud properties and aerosol optical depth (AOD) (*20*, *21*), serving as a proxy for CCN concentration (*22*). Rain rates were obtained from the Tropical Rainfall Measuring Mission (TRMM) satellite measurements (*23*) and meteorological data from the Global Data Assimilation System (GDAS) (*24*). All data sets were projected to the Aqua passage time [1:30 pm local time (*25*)]. Cloud fraction, cloud top pressure, cloud top temperature (both are measures of vertical cloud development), and rain rate were sorted as a function of AOD and averaged, creating 100 scatter points (Fig. 2, top row).

Positive trends between aerosol loading and cloud properties are not always an indication of causality. Before declaring an aerosol effect on clouds, one should check that changes in the environmental conditions (meteorology) cannot explain the observed correlations. Which atmospheric variables can approximate well the dependency of clouds on the environmental conditions over the study areas? To answer this question, we analyzed 286 GDAS meteorological variables against the measured aerosol, cloud, and rain properties (fig. S2) (*16*). We found a range of geopotential heights (Z_g, between 300 and 700 hPa) that correlated relatively well with cloud properties but not with aerosols (*15*). Restricting Z_g to a narrow range can limit the variation in the meteorological conditions that control warm convective cloud formation in our study areas while applying no (or very small) restriction on AOD levels. The data set was divided into three equal-sized subsets of high, medium, and low Z_g ranges at the 400 hPa level (Z_{400}) (fig. S4). The analysis of AOD versus cloud and rain properties was performed for each subset separately. The middle and bottom rows in Fig. 2 show the trends for the subsets with mean Z_{400} of ~7530 m and ~7590 m, respectively. The former represents conditions that promote deeper clouds and consequently higher rain rates. An orthogonal microphysical effect is observed in all subsets.

By focusing on the transition from clean background aerosol conditions of AOD = 0.06 (*26*, *27*) [equivalent to ~100 CCN/cm^3 (*22*)] to slightly polluted conditions of AOD = 0.1 (~300 CCN/cm^3; in many urban areas AOD = 0.1 is as clean as it gets), Fig. 2 reveals important changes in all cloud properties. For the convection-promoting subset (middle row), a significant decrease in the cloud top pressure is shown, suggesting an over-1-km increase in the cloud's vertical extent with the increase in AOD. In addition, we see an increase in the cloud fraction from 0.3 to 0.6 and a significant increase in rain rate from almost no rain to ~2 mm/hour. For the subset characterized by a larger geopotential height that dictates shallower clouds (bottom row in Fig. 2), we see an increase of a few hundreds of meters in the cloud top, an increase in the cloud fraction from ~0.2 to ~0.4, and no significant change in the low rain rates. Identical trends were observed over the Atlantic and Indian oceans (fig. S4). Cloud fraction, cloud top height, and rain rates all showed an increase with the increase in AOD.

To further explore the transition from aerosol-limited to cloud invigoration, we ran a detailed numerical experiment using a bin-microphysical model. The Tel Aviv University bin-microphysics axisymmetric model (TAU-CM) was used with detailed treatment of warm microphysical processes (*15*, *28*, *29*). We define here the effective terminal velocity (V_e) as the average, mass-weighted, terminal velocity of the water droplets within a given volume element. Similar measure was used before in the context of rain (*30*). An analysis of V_e for cloud droplets revealed how aerosol effects on the redistribution of droplet sizes on a microscale propagate to affect the vertical water distribution on the macroscale of the entire cloud. It can be shown that V_e measures the vertical displacement in time of the center of gravity (*31*) of the liquid water within the volume element for a zero updraft reference. Therefore, the superposition of V_e and the air vertical velocity estimates the center of gravity displacement taking into account all processes (*15*).

Conceptually, the aerosol's microphysical effects can be divided into a bulk effect on vapor-consumption efficiency and a series of delays in the onset of collection-related processes. Clouds that form in a very clean environment exhibit limitations on the droplet surface area available for condensational growth, and therefore the ambient supersaturation is weakly (slowly) consumed, allowing the sparse droplets to grow relatively fast. The condensed mass is small,

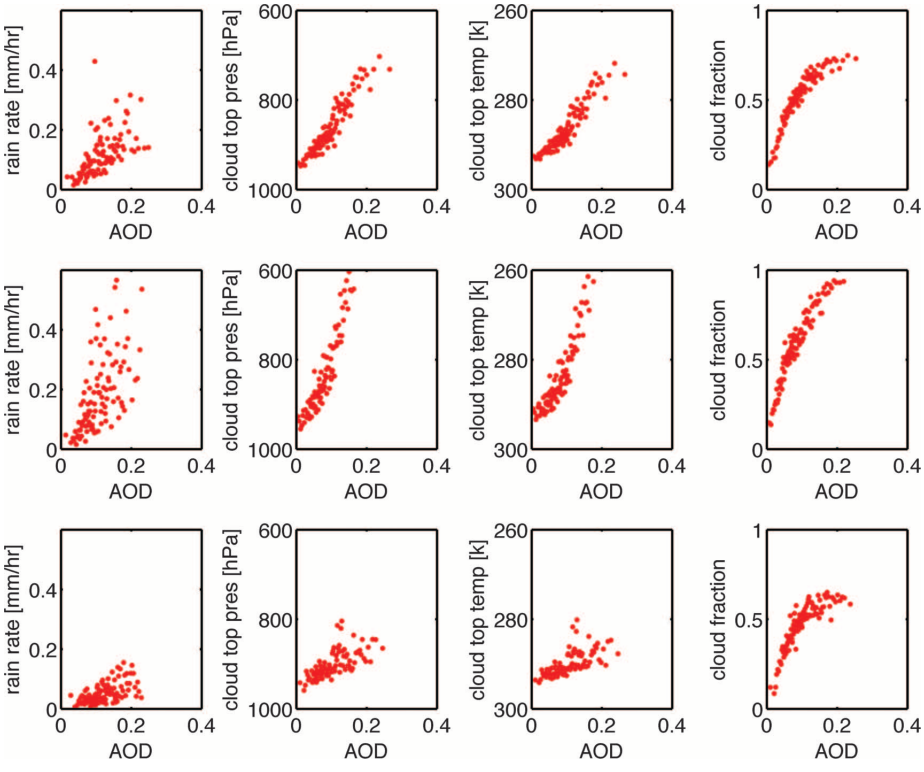

Fig. 2. Associations between cloud properties and aerosol loading (estimated by AOD). (**Top**) All data. (**Middle**) Data filtering by the 400-hPa geopotential height using only the lower one-third subset. (**Bottom**) Data filtering by using the upper one-third of the 400-hPa geopotential height subset. First (left) column shows rain rates versus AOD. Second column, cloud top pressure (P) versus AOD. Lower P values (or colder cloud top temperature, third column) indicate deeper clouds. Fourth (right) column, cloud fraction versus AOD.

and there is early initiation of the collection process. The collecting drops quickly fall as a weak rain. An increase in the CCN concentration leads to a larger condensed mass (Fig. 3, A and B). The effect of aerosols on the droplet-size distribution drives the above-mentioned delays. The initial one is the delay in the onset of the collision-coalescence process that transforms the mass from smaller to larger droplet bins (Fig. 3C). This delay initiates an additional delay in the onset of significant V_e (Fig. 3, E and F), and both imply a delay in the onset of precipitation (Fig. 3D).

Driven by these delays, the invigoration of warm clouds occurs in the first stage of the cloud's evolution, when polluted clouds condense more water mass, release more latent heat, and push this mass higher in the atmosphere before the onset of significant V_e and the development of significant (mass-driven) drag forces. Such delays provide the time for the extra cloud development. Later, once the collection process starts in the polluted cloud, more mass is transferred to the larger size bins, and V_e increases to larger falling velocities, leading to a stronger depletion of the cloud's water as reflected by stronger rain rates (Fig. 3D). In addition, an increase in the entrainment process is expected in polluted clouds, driven by more efficient evaporation of the smaller droplets and stronger velocities [for further discussion on the modeling results, see (*15*)].

Starting our analysis from the extreme clean cases [concentrations below ~25 CCN/cm^3 (*32*–*34*)] makes it easier to argue that such clouds cannot condense or hold significant amounts of water. Indeed, the sharper changes in cloud properties, shown from both observational and numerical results (Figs. 2 and 3 and fig. S4) (*6*), occur when the aerosol loading shifts from extremely pristine to slightly polluted. Nevertheless, clouds do not stop being aerosol-limited in this range. The invigoration effect tends to saturate at much higher aerosol loading. Both the observational and modeling analyses suggest that the cloud's liquid water mass, horizontal and vertical extent, and rain rates will continue to increase up to polluted conditions of a few hundred CCN/cm^3 (AOD ~0.3). The model results demonstrate that polluted clouds exhibit a series of delays in the onset of collection processes, significant V_e and rain. All act to enhance the vertical and horizontal dimensions of the polluted cloud.

Clouds can be viewed as a complex system with many coupled processes acting together and orchestrated along a delicate timeline. The exact timing of each process's initiation and its magnitude control the overall properties of the cloud. The use of a single-cloud model allowed us to separate key processes and to follow their magnitude and timing. However, such a model has some limitations, because it does not account for interactions between clouds or for the impact of clouds on their environment. Our satellite data analysis is also not completely free of residual cloud contamination on the aerosol retrieval and of some environmental effects that are not captured by the meteorological slicing. Nevertheless, we show a trend that survives restrictions on the meteorological variance in three different places over the pristine oceans. The effect is shown in the transition from extremely clean to slightly polluted conditions for low cloud fractions where cloud contamination and interactions between clouds are minor.

To understand the anthropogenic aerosol effect on the climate system, we have to know what the aerosol conditions were in the preindustrial era (*35*–*38*). It has been recently argued that this is one of the toughest challenges we face (*39*). The average AOD of the pristine oceanic atmosphere today is estimated to be ~0.06 (*26*, *27*). This by itself suggests that, over large marine areas, clouds are aerosol-limited. In fact, our results suggest that clouds forming in a pristine atmosphere may be the most sensitive to changes in aerosol loading (*40*). We hypothesize that, over the pristine oceans, higher pollution levels could push more clouds to cross the freezing level and to undergo ice processes.

Cloud invigoration produces two opposing radiative effects. On one hand, larger and thicker clouds increase the reflected shortwave (SW) radiation back to space and cool the atmosphere. On the other hand, deeper clouds have colder tops and therefore emit less longwave (LW) radiation to space, hence warming the atmosphere (*41*). By using the Clouds and the Earth's Radiant Energy System (CERES) data (*42*), we analyzed trends in top-of-atmosphere SW and LW fluxes as a function of AOD. Indeed they show (fig. S7) a strong increase in the SW flux (cooling), partly compensated by a decrease in the LW flux. Specifically, in the all-data case the AOD transition from 0.05 to 0.15 produces a cooling effect of 27 W/m^2 in the SW, whereas half of the forcing is counteracted by warming in the LW, yielding a net cooling effect of ~14 W/m^2. These results obtained over pristine aerosol regimes suggest that a great portion of the anthropogenic forcing over the oceans occurred in the early stages of the industrial era, when the average marine atmosphere changed

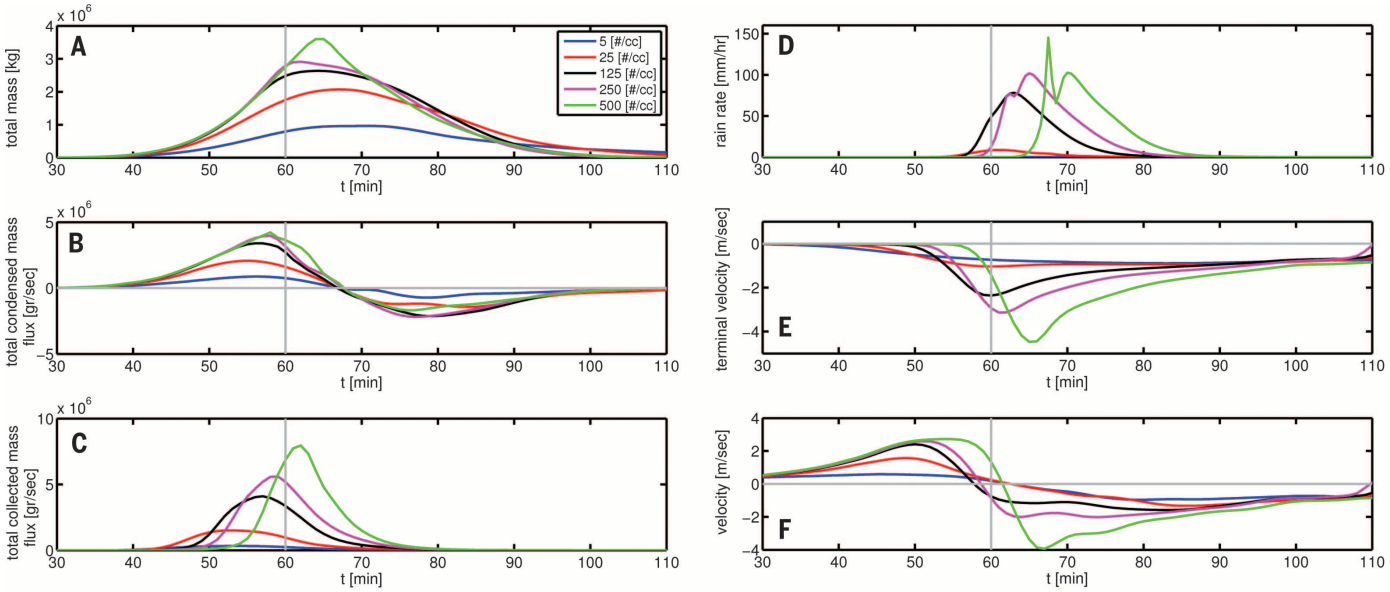

Fig. 3. Total cloud view of key processes as a function of time (*t*) for five aerosol levels. (**A**) Total mass of the cloud, (**B**) total condensed mass per unit time (mass transferred from water vapor to liquid), (**C**) total collected mass per unit time (mass transferred from the smaller bins to the bigger ones), (**D**) rain rate, (**E**) effective terminal velocity, and (**F**) integrated view of the velocities as the sum of the air vertical velocity and the effective terminal velocity. Blue curves show results for 5 aerosols per cm^3 (#/cc); red, 25; black, 125; magenta, 250; green, 500.

from pristine to slightly polluted (*35*). If this is true, it means that the preindustrial globe should be considered differently from today's globe. At least over the oceans, the coverage of warm clouds should be regarded as having been much smaller than it is today.

REFERENCES AND NOTES

1. P. Forster *et al.*, in *Climate Change 2007: The Physical Science Basis. Contribution of Working Group I to the Fourth Assessment Report of the Intergovernmental Panel on Climate Change* (Cambridge Univ. Press, Cambridge, 2007), pp. 129–234.
2. U. Lohmann, J. Feichter, *Atmos. Chem. Phys.* **5**, 715–737 (2005).
3. M. O. Andreae *et al.*, *Science* **303**, 1337–1342 (2004).
4. W.-K. Tao, J.-P. Chen, Z. Li, C. Wang, C. Zhang, *Rev. Geophys.* **50**, RG2001 (2012).
5. I. Koren, Y. J. Kaufman, D. Rosenfeld, L. A. Remer, Y. Rudich, *Geophys. Res. Lett.* **32**, L14828 (2005).
6. D. Rosenfeld *et al.*, *Science* **321**, 1309–1313 (2008).
7. D. Rosenfeld, S. Sherwood, R. Wood, L. Donner, *Science* **343**, 379–380 (2014).
8. Y. J. Kaufman, I. Koren, L. A. Remer, D. Rosenfeld, Y. Rudich, *Proc. Natl. Acad. Sci. U.S.A.* **102**, 11207–11212 (2005).
9. T. Yuan, L. A. Remer, H. Yu, *Atmos. Chem. Phys.* **11**, 7119–7132 (2011).
10. H. L. Jiang, G. Feingold, *J. Geophys. Res. Atmos.* **111**, D01202 (2006).
11. H. W. Xue, G. Feingold, B. Stevens, *J. Atmos. Sci.* **65**, 392–406 (2008).
12. P. Reutter *et al.*, *Atmos. Chem. Phys.* **9**, 7067–7080 (2009).
13. D. Rosenfeld, R. Wood, L. J. Donner, S. C. Sherwood, in *Climate Science for Serving Society*, G. R. Asrar, J. W. Hurrell, Eds. (Springer, Dordrecht, Netherlands, 2013), pp. 105–149.
14. M. B. Baker, R. J. Charlson, *Nature* **345**, 142–145 (1990).
15. See supporting data on *Science* Online.
16. I. Koren, G. Feingold, L. A. Remer, *Atmos. Chem. Phys.* **10**, 8855–8872 (2010).
17. I. Koren, L. A. Remer, Y. J. Kaufman, Y. Rudich, J. V. Martins, *Geophys. Res. Lett.* **34**, L08805 (2007).
18. O. Altaratz, R. Bar-Or, U. Wollner, I. Koren, *Environ. Res. Lett.* **8**, 034025 (2013).
19. G. Wen, A. Marshak, R. F. Cahalan, L. A. Remer, R. G. Kleidman, *J. Geophys. Res.* **112**, D13204 (2007).
20. S. Platnick *et al.*, *IEEE Trans. Geosci. Rem. Sens.* **41**, 459–473 (2003).
21. L. A. Remer *et al.*, *J. Atmos. Sci.* **62**, 947–973 (2005).
22. M. O. Andreae, *Atmos. Chem. Phys.* **9**, 543–556 (2009).
23. G. J. Huffman *et al.*, *J. Hydrometeorol.* **8**, 38–55 (2007).
24. D. F. Parrish, J. C. Derber, *Mon. Weather Rev.* **120**, 1747–1763 (1992).
25. I. Koren *et al.*, *Nat. Geosci.* **5**, 118–122 (2012).
26. Y. J. Kaufman *et al.*, *Geophys. Res. Lett.* **32**, L17804 (2005).
27. H. Yu *et al.*, *J. Geophys. Res. Atmos.* **114**, D10206 (2009).
28. S. Tzivion, T. Reisin, Z. Levin, *J. Appl. Meteorol.* **33**, 252–267 (1994).
29. T. Reisin, S. Tzivion, Z. Levin, *J. Appl. Meteorol.* **35**, 1416–1434 (1996).
30. G. J. Tripoli, W. R. Cotton, *J. Appl. Meteorol.* **19**, 1037–1063 (1980).
31. I. Koren, O. Altaratz, G. Feingold, Z. Levin, T. Reisin, *Atmos. Chem. Phys.* **9**, 155–161 (2009).
32. S. S. Yum, J. G. Hudson, *J. Geophys. Res.* **109**, D06204 (2004).
33. E. E. Hindman, W. M. Porch, J. G. Hudson, P. A. Durkee, *Atmos. Environ.* **28**, 3393–3403 (1994).
34. D. A. Hegg, L. F. Radke, P. V. Hobbs, *J. Geophys. Res.* **96**, 18727–18733 (1991).
35. M. O. Andreae, *Science* **315**, 50–51 (2007).
36. M. O. Andreae, D. Rosenfeld, *Earth Sci. Rev.* **89**, 13–41 (2008).
37. M. Wang, J. E. Penner, *Atmos. Chem. Phys.* **9**, 239–260 (2009).
38. J. R. Pierce, P. J. Adams, *Atmos. Chem. Phys.* **9**, 1339–1356 (2009).
39. K. S. Carslaw *et al.*, *Nature* **503**, 67–71 (2013).
40. S. Twomey, P. Squires, *Tellus* **11**, 408–411 (1959).
41. I. Koren, L. A. Remer, O. Altaratz, J. V. Martins, A. Davidi, *Atmos. Chem. Phys.* **10**, 5001–5010 (2010).
42. B. A. Wielicki *et al.*, *IEEE Trans. Geosci. Rem. Sens.* **36**, 1127–1141 (1998).

ACKNOWLEDGMENTS

The research leading to these results received funding from the European Research Council (ERC) under the European Union's Seventh Framework Programme (FP7/2007-2013)/ERC Grant agreement no. 306965 (CAPRI).

SUPPLEMENTARY MATERIALS

www.sciencemag.org/content/344/6188/1143/suppl/DC1
Materials and Methods
Supplementary Text
Figs. S1 to S7
References (*43*–*47*)

24 February 2014; accepted 5 May 2014
10.1126/science.1252595

LUNAR FORMATION

Identification of the giant impactor Theia in lunar rocks

Daniel Herwartz,[1,2]* Andreas Pack,[1] Bjarne Friedrichs,[1] Addi Bischoff[3]

The Moon was probably formed by a catastrophic collision of the proto-Earth with a planetesimal named Theia. Most numerical models of this collision imply a higher portion of Theia in the Moon than in Earth. Because of the isotope heterogeneity among solar system bodies, the isotopic composition of Earth and the Moon should thus be distinct. So far, however, all attempts to identify the isotopic component of Theia in lunar rocks have failed. Our triple oxygen isotope data reveal a 12 ± 3 parts per million difference in $\Delta^{17}O$ between Earth and the Moon, which supports the giant impact hypothesis of Moon formation. We also show that enstatite chondrites and Earth have different $\Delta^{17}O$ values, and we speculate on an enstatite chondrite–like composition of Theia. The observed small compositional difference could alternatively be explained by a carbonaceous chondrite–dominated late veneer.

Earth's Moon is distinct among the >150 moons of our solar system (*1*). Most other moons are either captured planetesimals, or they formed along with the planet in a common accretion disc. In contrast, it is hypothesized that our satellite formed ~4.5 billion years ago from the debris of a giant collision between the proto-Earth and another smaller proto-planet [giant impact hypothesis (*2*, *3*)]. Some of the distinct features of the Moon—such as the depletion in moderately volatile elements and water, the small lunar core, and the angular momentum of the Earth-Moon system—are interpreted as products of the energetic collision with Theia (*1*).

Most numerical models of the collision assume that Theia was about the size of Mars and collided with the proto-Earth at an oblique angle. These classic collision models predicted that the Moon is made of 70 to 90% Theia [mass fraction of impactor (M_i)] and only 10 to 30% proto-Earth [mass fraction of proto-Earth ($M_\oplus$)] material (*2*, *3*). Such a large fraction of Theia in the Moon, however, is difficult to reconcile with the observed isotopic similarity between the Moon and Earth (*4*). Recent simulations take this into account and aim to decrease the compositional difference between Earth and the Moon (see below).

Measurements of isotope ratios of terrestrial, martian, and asteroidal samples show that the bodies in the early solar system were isotopically heterogeneous (*5*). It is therefore expected that Theia and proto-Earth were isotopically distinct. If the Moon formed predominantly from fragments of Theia, as predicted by most numerical models, the Moon and Earth should differ in their isotopic composition. However, no isotopic differences between Earth and the Moon have yet been recognized; for instance, for O (*6*–*10*), Ti (*11*), Ca (*12*), Si (*13*), or W (*14*). We argue herein that careful reinvestigation of the published data sets for O and Ti hint at small variations between Earth and the Moon.

Three explanations exist for the paradox of identical isotopic compositions of Earth and the Moon: (i) formation of proto-Earth and Theia at similar heliocentric distances from the same isotopic reservoir, resulting in identical compositions of proto-Earth and Theia (*8*); (ii) isotopic reequilibration in the aftermath of the giant impact that has obliterated the initial heterogeneity (*4*); or (iii) less compositional difference between Earth and the Moon than predicted by classic numerical simulations (*15*–*17*).

Recent collision models that aim to be consistent with isotope measurements proposed a larger (*15*), smaller (*16*), or faster impactor (*16*, *17*). In models with small impactors that assume a fast-spinning proto-Earth (*16*), the Theia component in

[1]Georg-August-Universität Göttingen, Geowissenschaftliches Zentrum, Abteilung Isotopengeologie, Goldschmidtstraße 1, 37073 Göttingen, Germany. [2]Universität zu Köln, Institut für Geologie und Mineralogie, Zülpicher Straße 49a, 50674 Köln, Germany. [3]Westfälische Wilhelms-Universität Münster, Institut für Planetologie, Wilhelm-Klemm-Straße 10, 48149 Münster, Germany.
*Corresponding author. E-mail: d.herwartz@uni-koeln.de

Table 1. Triple oxygen isotope analysis of terrestrial, lunar, and enstatite chondrite samples. Delta prime notations (δ′) are calculated according to (*19*), and $\Delta^{17}O$ is equal to $\delta'^{17}O - 0.5305 * \delta'^{18}O$. The enstatite chondrite samples identified by "MS" (from Sudan) represent individual meteorite fragments of high- and low-iron enstatite chondrites of various petrological types from the Almahata Sitta polymict breccia (*31*). *n* indicates the number of single analysis.

Sample	Type	Locality (mission)	$\delta^{18}O$	$\delta^{17}O$	$\delta'^{18}O$	SD	SEM	$\delta'^{17}O$	SD	SEM	$\Delta^{17}O$	SD	SEM	*n*
						*Earth mantle**								
Ava opx*	Opx	Avachinsky, Kamchatka	5.86	3.01	5.84	0.2	–	3.00	0.1	–	−0.098	0.010	–	1
WR21*	Ol	Antarctica	5.49	2.81	5.47	0.11	0.05	2.81	0.06	0.03	−0.098	0.006	0.003	4
M. Maar*	Ol	Eifel, Germany	5.16	2.63	5.15	0.09	0.05	2.63	0.05	0.02	−0.101	0.014	0.007	4
Ah ol*	Ol	Aheim, Norway	5.61	2.88	5.60	0.2	–	2.87	0.1	–	−0.098	0.024	–	1
SC ol*	Ol	San Carlos, USA	5.25	2.68	5.23	0.19	0.03	2.67	0.10	0.02	−0.102	0.009	0.001	39
SC cpx*	Cpx	San Carlos, USA	5.72	2.94	5.70	0.13	0.10	2.93	0.07	0.05	−0.095	0.007	0.005	2
SC opx*	Opx	San Carlos, USA	6.03	3.09	6.01	0.22	0.12	3.08	0.11	0.06	−0.106	0.021	0.012	3
SC spl*	Spl	San Carlos, USA	4.39	2.23	4.38	0.22	0.11	2.23	0.11	0.06	−0.096	0.012	0.006	4
MORB*	Glass	Unknown	5.60	2.86	5.58	0.18	0.07	2.86	0.10	0.04	−0.101	0.014	0.006	6
Aple Arami*	Grt	Central Alps, Switzerland	5.59	2.86	5.57	0.2	–	2.86	0.1	–	−0.097	0.014	–	1
Weighted average*											**−0.101**	**0.003**	**0.002**	**65**
UWG-2*	Grt	Gore Mountain, USA	5.98	3.06	5.96	0.14	0.06	3.06	0.07	0.03	−0.102	0.006	0.003	5
						APOLLO samples								
10071.122	High Ti basalt	Apollo 11	5.42	2.78	5.40	0.18	0.07	2.78	0.07	0.04	−0.087	0.007	0.003	7
61224,52	Low Ti gabbro	Apollo 16	5.99	3.08	5.97	0.07	0.03	3.08	0.03	0.02	−0.088	0.007	0.003	5
12018, 267	Low Ti basalt	Apollo 12	5.68	2.92	5.67	0.17	0.06	2.92	0.06	0.03	−0.091	0.009	0.004	8
Weighted average											**−0.089**	**0.008**	**0.002**	**20**
						Enstatite chondrites								
Pillistfer	EL6	Pillisfer, Estonia	6.21	3.25	6.19	0.25	0.11	3.24	0.12	0.05	−0.045	0.021	0.009	5
MS-D	EL6	Sudan	6.42	3.36	6.40	0.20	0.14	3.36	0.12	0.08	−0.038	0.008	0.006	2
MS-52	EL6	Sudan	6.22	3.23	6.20	0.26	0.19	3.22	0.13	0.09	−0.063	0.008	0.005	2
MS-MU-007	EL6	Sudan	6.17	3.24	6.15	0.2	–	3.23	0.1	–	−0.028	0.052	–	1
MS-201	EL5	Sudan	6.05	3.21	6.03	0.18	0.13	3.20	0.11	0.08	0.002	0.017	0.012	2
MS-MU-002	EL3	Sudan	6.26	3.25	6.24	0.2	0.1	3.25	0.1	0.03	−0.062	0.032	0.023	2
Weighted average											**−0.041**	**0.026**	**0.007**	**14**
Qingzhen	EH3	Qingzhen, China	6.08	3.16	6.07	0.17	0.07	3.16	0.11	0.04	−0.059	0.030	0.012	6
MS-MU-009	EH4/5	Sudan	6.61	3.41	6.59	0.21	0.12	3.41	0.10	0.06	−0.086	0.013	0.007	3
MS-192	EH4/5	Sudan	5.82	3.03	5.80	0.2	–	3.03	0.1	–	−0.050	0.068	–	1
Weighted average											**−0.066**	**0.027**	**0.009**	**10**
Weighted average											**−0.051**	**0.029**	**0.006**	**24**

*Terrestrial samples from Pack and Herwartz (*19*).

the Moon can be reduced down to ~8 weight percent (wt %), whereas Earth receives ~2 wt % (*16*); the Moon and the postimpact mantle then differ by only a few weight percent. Simulations with very large impactors can produce a Moon and Earth that are each composed of ~50% Theia material, and in such cases, the Moon and the postimpact Earth are compositionally identical down to the 0.1–wt % level (*15*).

The size of Theia is unknown, so to report compositional variation between Earth and the Moon independent of that size, we introduce the value δf_T

$$\delta f_T = \left(\frac{F_{M,tar}}{F_{P,tar}} - 1\right) * 100$$

where F is the mass fraction of proto-Earth material (target) in the Moon ($F_{M,tar}$) and in the final planet ($F_{P,tar}$), respectively. The δf_T quantifies the percent compositional deviation of the Moon (or disk) from Earth (*15*, *17*). Most models predict fractionally more impactor material in the Moon than in Earth; thus, δf_T is usually negative. However, some simulations with large impactors also predict positive δf_T and, thus, larger fractions of Theia in Earth than in the Moon (*15*).

The predicted range of δf_T is large, and from the numerical models alone it is impossible to decide which one is the most likely. Independent estimates of δf_T or M_i can thus help to constrain the kinematics of the collision. To our knowledge, only one independent estimate exists, which is based on the variable Nb/Ta ratio in Earth's mantle (14.0 ± 0.3), the Moon (17.0 ± 0.8), and chondrites (19.9 ± 0.6) (*18*). The depletion in Nb relative to Ta in the bulk silicate Earth probably results from the more siderophilic nature of Nb over Ta at high pressures and sequestration of some Nb in Earth's core. Assuming that Theia was Mars-sized and had a chondritic Nb/Ta ratio, the most likely mass fraction of Theia in the Moon was estimated to M_i ~ 30 to 50 wt % (*18*). This translates to δf_T ~ −21 to −44 for the assumed Mars-sized impactor.

If the giant impact hypothesis holds, the isotopic composition of lunar rocks is a function of impactor composition and impactor mass fraction. Large isotopic variations among solar system bodies are observed for O (*5*, *7*). Oxygen has three stable isotopes (^{16}O, ^{17}O, and ^{18}O) and displays large mass-independent variations among solar system bodies that are expressed in the form of the $\Delta^{17}O$ value (*5*). Oxygen isotopes are therefore ideal for tracing the isotope composition of Theia in lunar rocks. Previous oxygen isotope studies did not find any difference between Earth and the Moon (*6*–*10*), and Wiechert *et al.* (*8*) concluded from their high-precision data that Earth and the Moon are identical within 5 parts per million (ppm) [0.005 per mil (‰)] in $\Delta^{17}O$. However, careful reinvestigation of the three

high-precision data sets (*8*–*10*) reveals that lunar samples are elevated, on average, by 9 ppm compared with the terrestrial UWG-2 standard used in all three studies (fig. S1). With an improved analytical technique (*19*), we are able to measure variations in parts per million (0.00*x*‰) in $\Delta^{17}O$ (see supplementary materials and methods), allowing us to detect the isotopic differences between Earth and the Moon.

We first attempted to use lunar meteorites to determine the isotope composition of the Moon. Our data show that terrestrial weathering modified the $\Delta^{17}O$ of the studied lunar meteorites, making identification of small variations impossible (fig. S2). Therefore, we have analyzed fresh basalt samples from three Apollo landing sites that were provided by NASA. We compared the composition of the lunar basalts with the composition of Earth mantle xenoliths and mantle-derived melts [mid-ocean ridge basalt (MORB)] (Table 1 and Fig. 1).

The bulk silicate Earth (BSE) is constrained to a $\Delta^{17}O$ value of −0.101 ± 0.002‰ [1σ SEM, n = 65 measurements (*19*)] from mantle xenoliths and MORB from seven localities around the world [for definitions and analytical details, see (*19*, *20*)]. Earth mantle minerals and MORB fall on a common mass-fractionation line, with a slope of θ = 0.532 ± 0.006, in the $\delta'^{17}O$ versus $\delta'^{18}O$ space. This slope is, within uncertainty, identical to the high-temperature approximation for equilibrium oxygen isotope fractionation of 0.5305 (*21*). The $\Delta^{17}O$ values of Earth mantle minerals and MORB are identical within the uncertainty. This is in agreement with mass fractionation upon melt extraction along a slope of ~0.53 for high-temperature processes (*19*, *21*). Because the same slope must apply to melt extraction from the lunar mantle, we can safely use the lunar basalts as analogs for the bulk silicate Moon (BSM) with respect to $\Delta^{17}O$.

The three lunar basalts span a small range in $\delta^{18}O$ and have an average $\Delta^{17}O$ = −0.089 ± 0.002‰ (1σ SEM, n = 20). We suggest that this value is representative of the BSM. Thus, the $\Delta^{17}O$ of the Moon is 12 ± 3 ppm (0.012 ± 0.003‰) higher than that of Earth (Fig. 2). This unequivocally identifies an isotopic difference between Earth and the Moon and supports the view that the Moon formed by a giant collision of the proto-Earth with Theia.

The reevaluation of lunar O isotope data from three previous studies (*8*–*10*) is consistent with our finding within the respective uncertainties (fig. S1) (*20*). Thus, our new data are not in conflict with previous studies, and the slightly elevated $\Delta^{17}O$ composition of the Moon was already present in these data sets (*8*–*10*).

Carbonaceous chondrites and BSE differ considerably, not only in $\Delta^{17}O$, but also in their Ti, Cr, and Ni isotope composition (*22*), making a carbonaceous chondrite composition of Theia unfeasible. Rather, Theia formed from the same large noncarbonaceous chondrite (*22*) reservoir as Earth, Mars, ordinary chondrites (OCs), enstatite chondrites (ECs), and other noncarbonaceous chondrites and achondrites (*22*). All numerical simulations, except some with very large impactors, predict that the Moon received fractionally more impactor material than Earth (negative δf_T). Hence, the $\Delta^{17}O$ of Theia was most likely higher than that of Earth and the Moon. The solar system bodies from the noncarbonaceous chondrite (*22*) reservoir with a higher $\Delta^{17}O$ than that of Earth are Mars and the parent asteroids of OC and R-chondrites (*7*). Admixing only 4% of material isotopically resembling Mars would be sufficient to explain the observed 12 ppm difference between Earth and the Moon. For an OC or R-chondrite composition, less than 2% would be required in the Moon. Such small proportions are inconsistent with most numerical models (*2*, *3*, *15*–*17*) that generally suggest larger fractions of Theia in the Moon (Fig. 3A). This implies that the composition of Theia was only slightly higher in $\Delta^{17}O$ than that of Earth.

We have obtained new data on ECs that were previously assumed to be identical to Earth in $\Delta^{17}O$ (*23*, *24*). Our data show a difference of 59 ± 8 ppm (1σ SEM, n = 14) between Earth and EL (low iron) enstatite chondrites and 35 ± 10 ppm (1σ SEM, n = 10) between Earth and more metal-rich EH (high iron) enstatite chondrites.

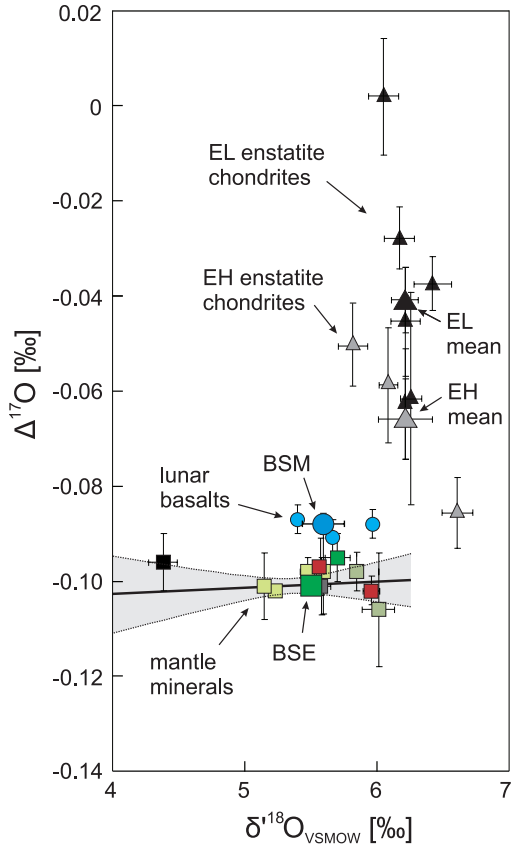

Fig. 1. Terrestrial (squares) and lunar (circles) samples and ECs (triangles) in $\delta'^{18}O$ versus $\Delta^{17}O$ space. VSMOW, Vienna standard mean ocean water. Error bars denote 1σ SEM.

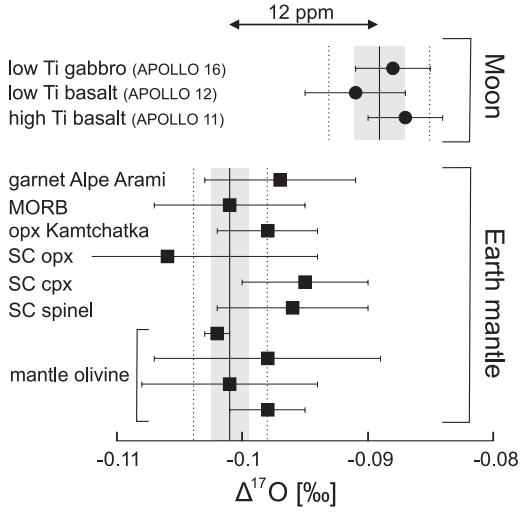

Fig. 2. $\Delta^{17}O$ composition for terrestrial and lunar samples. A slope of 0.5305 and zero intercept (VSMOW) is used to calculate $\Delta^{17}O$ (*19*, *20*). Error bars are 1σ SEM. Solid vertical lines denote mean values for the BSE and the Moon. Gray shaded areas represent 1σ SEM, and dotted lines represent 2σ SEM.

If the oxygen isotopic composition of Theia resembled that of EL or EH chondrites, δf_T is –21 ± 9% for EL and –36 ± 15% for EH, respectively (Fig. 3B). Assuming a Mars-sized impactor ($m_{Theia}/m_{\oplus}$ = 0.12), this translates to M_i = 30 ± 8% (EL) or 43 ± 13% (EH), respectively (Fig. 3B). These estimates are in good agreement with the more recent numerical models (*15*–*17*) and estimates from Nb/Ta mass balance considerations (Fig. 3A) (*15*–*18*).

If Theia compositionally resembled EC, one would expect the Moon to fall on a mixing trend for isotope systems that show differences between ECs and Earth. High-precision Ti isotope measurements suggest that Earth and ECs are different (*11*). The datum for the Moon indeed falls between Earth and ECs (fig. S3) (*20*). [Note that Zhang *et al.* (*11*) argued for an identical ^{50}Ti composition of Earth and the Moon.] Earth and ECs also differ slightly in Ca (*12*) and Si isotopes (*13*), but variations between Earth and the Moon were not detected. Thus, only the O and possibly the Ti isotopes indicate that Theia may have resembled ECs. The Moon is a mixture between Theia and proto-Earth, not only isotopically, but also chemically. For refractory lithophile elements, mass balance modeling shows that an EC composition of Theia is feasible (fig. S4). The elevated FeO content in the lunar mantle, however, is not consistent with the reduced state and, thus, low FeO content of ECs, although their bulk Fe content is high (EH = 33 wt % and EL = 24 wt %) (*25*).

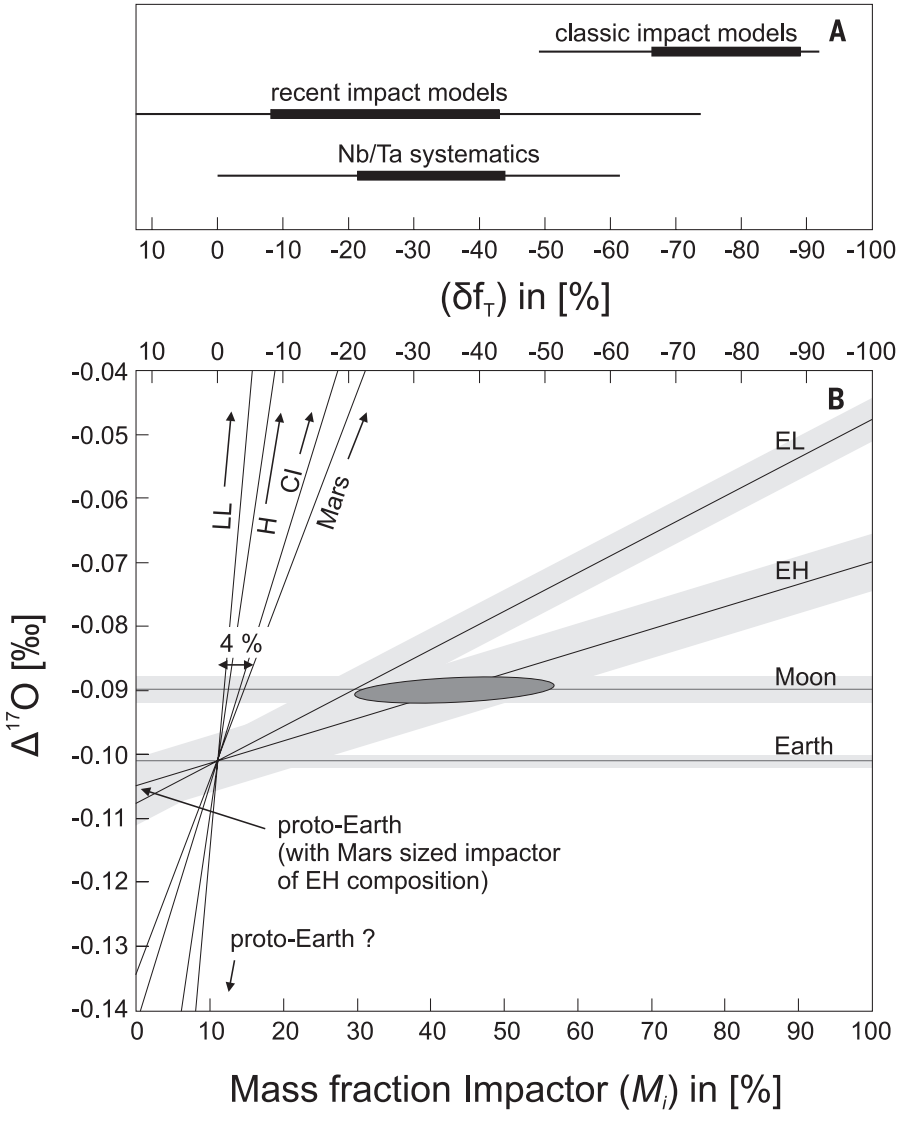

Fig. 3. Mass balance between possible impactors and proto-Earth. (**A**) The percent compositional difference (δf_T) between the Moon and Earth, as predicted by classical (*2*, *3*) and more recent (*15*–*17*) numerical simulations. Estimates derived from Nb/Ta systematics (*18*) are displayed for comparison (assuming a Mars-sized impactor). Black lines represent the range of most simulations; black bars represent typical values for seemingly realistic model runs. (**B**) Mass balance estimates for oxygen isotopes between Earth and several possible impactors (LL and H ordinary chondrites, CI, Mars, EL, and EH). Because δf_T and M_i are related for a given impactor size, both quantities can be displayed on the same figure. A Mars-sized impactor with $m_{Theia}/m_{\oplus}$ = 0.12 is used to estimate M_i; thus, Earth contains ~11% of Theia component. Mixing lines (black lines) between the possible impactors and proto-Earth are defined by their Δ^{17}O isotopic composition (i.e., Δ^{17}O at 100% M_i) and the fraction of Theia material in Earth (i.e., Δ^{17}O = 0.101‰ at 11% M_i). Extrapolation of the mixing lines to 0% M_i indicates potential Δ^{17}O proto-Earth compositions for the given Mars-sized impactor. Shaded areas represent 1σ SEM. A Mars-sized impactor with EH composition would result in a moon within the dark grey ellipse with M_i ~ 43%.

Enstatite chondrites are sometimes regarded as the sole building blocks of Earth (*25*). This highly debated theory was supported by the isotopic similarity of EC and Earth in O (*23*, *24*), Cr (*26*), or Ni (*27*), but it has been disputed, for instance, on the basis of Si isotopes (*13*). The differences between ECs and Earth found for Δ^{17}O (this study), Ti (*11*), and Ca isotopes (*12*) are also inconsistent with ECs as the sole building blocks of Earth (*25*).

Hence, there is no chondrite group that can be regarded as the sole building blocks of Earth. Likewise there is probably no meteorite group that is identical in composition to Theia. Although Theia may have been compositionally similar to ECs, its composition was probably distinct and is not represented by any known meteorite group.

Pahlevan and Stevenson (*4*) have modeled likely compositions of potential impactors in terms of oxygen isotopic composition. In this model, >10% of all impactors would have a Δ^{17}O value that is more similar to proto-Earth than to EH chondrites (fig. S5). This would allow more than 43 wt % Theia in the Moon and would give numerical models more elements of freedom (*15*–*17*). If impact models that predict >70% impactor component in the Moon are correct, the Δ^{17}O of Theia must have been <18 ppm higher in Δ^{17}O than the proto-Earth. This conforms to ~6% of all modeled impactors (*4*). Thus, a small chance remains that numerical models predicting a large fraction of Theia in the Moon hold (*2*, *3*).

The size of Theia is not known, and current assumptions for the impactor–to–proto-Earth mass ratio ($m_{Theia}/m_{\oplus}$) range over one order of magnitude ($m_{Theia}/m_{\oplus}$ = 0.025 to 0.45) (*15*, *16*). If a reservoir on Earth exists that has escaped equilibration with the Theia component in Earth, Theia's size could be constrained. Theia has changed the composition of the proto-Earth as a function of $m_{Theia}/m_{\oplus}$ and impactor composition. If Theia was Mars-sized ($m_{Theia}/m_{\oplus}$ ~ 0.12) with an EC-like composition, proto-Earth was 4 ppm lower in Δ^{17}O before mixing with Theia. For smaller impactors ($m_{Theia}/m_{\oplus}$ = 0.025 to 0.048) (*16*), this effect shrinks to 1 to 2 ppm, as less material is added to the proto-Earth. In contrast, a large impactor with $m_{Theia}/m_{\oplus}$ = 0.4 to 0.45 (*15*) would suggest a value of Δ^{17}O that is 14 to 27 ppm lower for the proto-Earth than for BSE today (Fig. 3 and fig. S6). Currently, no reservoir on Earth is known to have escaped equilibration

with Earth's Theia component; thus, it is presently not possible to obtain information on $\Delta^{17}O$ of the proto-Earth.

An alternative explanation for the isotope difference between Earth and the Moon is that the $\Delta^{17}O$ value of Earth was modified by late-accreting material (late veneer) after the formation of the Moon. Such material may have had a $\Delta^{17}O$ value lower than that of Earth. In the following scenario, Earth and the Moon had identical $\Delta^{17}O$ compositions after the giant impact (*4*, *8*, *15*–*17*), with the Moon now representing the composition of Earth before the late veneer.

From the overabundance of siderophile elements in Earth's mantle, late veneer masses between 0.1 and 0.5% of BSE have been suggested (*28*). Higher estimates between 0.3 to 0.8% of BSE are derived from ^{182}W isotope systematics (*29*). Here, we use 0.5% for mass balance considerations. The only groups of undifferentiated meteorites that have $\Delta^{17}O$ much lower than that of Earth are carbonaceous chondrites (*30*). Assuming that the late veneer component had an oxygen isotope composition of CV carbonaceous chondrites ($\Delta^{17}O$ = –4‰) (*30*), incorporation of 0.5% late veneer component would decrease the $\Delta^{17}O$ of Earth by as much as ~20 ppm. Similar proportions of material resembling CO, CR, or CH carbonaceous chondrites would also be sufficient to explain the observed difference of 12 ppm between Earth and the Moon.

If this scenario is correct, the observed difference in $\Delta^{17}O$ between Earth and the Moon points toward a late veneer that is dominated by carbonaceous chondrites. Among the carbonaceous chondrites, the most water-rich meteorites are found. It would thus be feasible that part of the ocean water was delivered by the late veneer impactors. Evidence for this scenario may be found in old crust that has escaped mixing with the late veneer component (*29*).

REFERENCES AND NOTES

1. S. R. Taylor, in *Encyclopedia of the Solar System*, L.-A. McFadden, P. R. Weissman, T. V Johnson, Eds. (Academic Press, San Diego, ed. 2, 2007), pp. 227–250.
2. A. G. W. Cameron, W. Benz, *Icarus* **92**, 204–216 (1991).
3. R. M. Canup, E. Asphaug, *Nature* **412**, 708–712 (2001).
4. K. Pahlevan, D. J. Stevenson, *Earth Planet. Sci. Lett.* **262**, 438–449 (2007).
5. R. N. Clayton, L. Grossman, T. K. Mayeda, *Science* **182**, 485–488 (1973).
6. R. N. Clayton, T. K. Mayeda, *Proc. Lunar Sci. Conf.* **6**, 1761–1769 (1975).
7. R. N. Clayton, T. K. Mayeda, *Geochim. Cosmochim. Acta* **60**, 1999–2017 (1996).
8. U. Wiechert *et al.*, *Science* **294**, 345–348 (2001).
9. M. Spicuzza, J. Day, L. Taylor, J. Valley, *Earth Planet. Sci. Lett.* **253**, 254–265 (2007).
10. L. J. Hallis *et al.*, *Geochim. Cosmochim. Acta* **74**, 6885–6899 (2010).
11. J. Zhang, N. Dauphas, A. Davis, I. Leya, A. Fedkin, *Nat. Geosci.* **5**, 251–255 (2012).
12. J. I. Simon, D. J. De Paolo, *Earth Planet. Sci. Lett.* **289**, 457–466 (2010).
13. C. Fitoussi, B. Bourdon, *Science* **335**, 1477–1480 (2012).
14. M. Touboul, T. Kleine, B. Bourdon, H. Palme, R. Wieler, *Nature* **450**, 1206–1209 (2007).
15. R. M. Canup, *Science* **338**, 1052–1055 (2012).
16. M. Ćuk, S. T. Stewart, *Science* **338**, 1047–1052 (2012).
17. A. Reufer, M. M. M. Meier, W. Benz, R. Wieler, *Icarus* **221**, 296–299 (2012).
18. C. Münker *et al.*, *Science* **301**, 84–87 (2003).
19. A. Pack, D. Herwartz, *Earth Planet. Sci. Lett.* **390**, 138–145 (2014).
20. See supplementary materials on *Science* Online.
21. E. Young, A. Galy, H. Nagahara, *Geochim. Cosmochim. Acta* **66**, 1095–1104 (2002).
22. P. H. Warren, *Earth Planet. Sci. Lett.* **311**, 93–100 (2011).
23. R. N. Clayton, T. K. Mayeda, A. E. Rubin, *J. Geophys. Res.* **89**, C245–C249 (1984).
24. J. Newton, I. A. Franchi, C. T. Pillinger, *Meteorit. Planet. Sci.* **35**, 689–698 (2000).
25. M. Javoy *et al.*, *Earth Planet. Sci. Lett.* **293**, 259–268 (2010).
26. A. Trinquier, J. Birck, C. Allègre, *Astrophys. J.* **655**, 1179–1185 (2007).
27. M. Regelous, T. Elliott, C. D. Coath, *Earth Planet. Sci. Lett.* **272**, 330–338 (2008).
28. R. J. Walker, *Chem. Erde* **69**, 101–125 (2009).
29. M. Willbold, T. Elliott, S. Moorbath, *Nature* **477**, 195–198 (2011).
30. R. N. Clayton, T. K. Mayeda, *Geochim. Cosmochim. Acta* **63**, 2089–2104 (1999).
31. A. Bischoff, M. Horstmann, A. Pack, M. Laubenstein, S. Haberer, *Meteorit. Planet. Sci.* **45**, 1638–1656 (2010).

ACKNOWLEDGMENTS

We thank NASA for providing samples; Z. Sharp, F. Wombacher, C. Münker, and H. Palme for discussions; three anonymous reviewers for constructive comments; and E. Barkan and B. Luz for analyzing our reference O_2 relative to SMOW. All data are provided within the manuscript or the supplementary materials.

SUPPLEMENTARY MATERIALS

www.sciencemag.org/content/344/6188/1146/suppl/DC1
Materials and Methods
Supplementary Text
Figs. S1 to S6
Table S1
References (*32*–*41*)

21 January 2014; accepted 8 May 2014
10.1126/science.1251117

PLANETARY FORMATION

Protracted core formation and rapid accretion of protoplanets

T. S. Kruijer,[1,2] M. Touboul,[3] M. Fischer-Gödde,[1] K. R. Bermingham,[3] R. J. Walker,[3] T. Kleine[1]

Understanding core formation in meteorite parent bodies is critical for constraining the fundamental processes of protoplanet accretion and differentiation within the solar protoplanetary disk. We report variations of 5 to 20 parts per million in ^{182}W, resulting from the decay of now-extinct ^{182}Hf, among five magmatic iron meteorite groups. These ^{182}W variations indicate that core formation occurred over an interval of ~1 million years and may have involved an early segregation of Fe-FeS and a later segregation of Fe melts. Despite this protracted interval of core formation, the iron meteorite parent bodies probably accreted concurrently ~0.1 to 0.3 million years after the formation of Ca-Al–rich inclusions. Variations in volatile contents among these bodies, therefore, did not result from accretion at different times from an incompletely condensed solar nebula but must reflect local processes within the nebula.

Magmatic iron meteorites are generally considered to sample the metal cores of differentiated protoplanetary bodies that formed after the segregation and subsequent crystallization of metallic melts (*1*). Each of the magmatic iron meteorite groups represents metal from a distinct parent body. The groups are primarily distinguished by different contents of moderately volatile elements such as Ga and Ge, relative to Ni. The order-of-magnitude variations in volatile depletion probably arise from chemical fractionations induced by processes within the solar nebula, suggesting that the conditions of parent body accretion varied in time and/or space.

Precise determination of the timing of core formation for each magmatic iron meteorite group is critical for determining the accretion rate for each parent body, for identifying the heat sources responsible for melting and differentiation, and for assessing whether the timing of accretion played a role in establishing the different degrees of volatile depletion observed in the magmatic iron meteorite groups. The extinct ^{182}Hf-^{182}W chronometer [half-life ($t_{1/2}$) = 8.9 million years (My)] is ideally suited to precisely constrain the time of core formation, but its application to iron meteorites has been hampered by cosmic ray–induced neutron capture effects on W isotope compositions (*2*–*5*). Thus, although previous studies have shown that core formation in most iron meteorite parent bodies probably occurred within ~2 My after the formation of Ca-Al–rich inclusions (CAIs), it has not yet been possible to resolve differences in the timing of accretion and core formation (*6*).

We used Pt isotope compositions to quantify and correct measured W isotope compositions of iron meteorites for the effects of neutron capture (*7*, *8*) and obtained combined high-precision Pt

[1]Institut für Planetologie, Westfälische Wilhelms-Universität Münster, Wilhelm-Klemm-Strasse 10, DE-48149 Münster, Germany. [2]ETH Zürich, Inst. of Geochemistry and Petrology, Clausiusstrasse 25, CH-8092 Zürich, Switzerland. [3]Department of Geology, University of Maryland, College Park, MD 20742, USA.

and W isotope data for metal samples from the major iron meteorite groups (IIAB, IID, IIIAB, IVA, and IVB) (*9*). All iron meteorite groups exhibit well-defined empirical ε^{182}W-ε^{196}Pt correlations, whose intercepts provide pre-exposure ε^{182}W (the ^{182}W/^{184}W unbiased by galactic cosmic rays) for each group (Fig. 1 and table S1). Our results reveal small but resolvable differences in pre-exposure ε^{182}W among magmatic iron meteorite groups, with the IID iron meteorites having the highest pre-exposure ε^{182}W of −3.15 ± 0.07 (±95% confidence) and the IIAB iron meteorites having the lowest value of −3.40 ± 0.03. Model ages of metal segregation in the iron meteorite parent bodies, relative to the formation of CAIs, can be calculated as the time of Hf/W fractionation from an unfractionated reservoir with chondritic ^{180}Hf/^{184}W of 1.28 ± 0.03 (*10*, *11*). At face value, the distinct pre-exposure ε^{182}W values yield resolved and very precise Hf-W ages spanning a total range of ~0.7 to ~2.9 My after CAI formation (table S6).

With the exception of the IID iron meteorites, the pre-exposure ε^{182}W values exhibit inverse correlations with Ga/Ni and S contents, estimated for the bulk compositions of each core (Fig. 2). This suggests that the degree of volatile element depletion exerted some control on the timing of core formation. The inverse correlation of core formation model age with the degree of volatile depletion is remarkable because it is opposite to what might be expected for the accretion time of iron meteorite parent bodies. Volatile-poor bodies (such as IVA and IVB) would be expected to have accreted earlier, at a time when the solar nebula was yet not fully condensed, in comparison to more volatile-rich bodies (such as IIAB) (*12*, *13*). Our data, however, suggest that core formation in the IVA and IVB iron meteorite parent bodies occurred later than in the IIAB parent body (Fig. 2 and table S1). This may indicate that the IVA and IVB, as well as the IID, parent bodies accreted later than or over a longer period of time than the IIAB parent body. However, linking the time of core formation to an age of accretion requires knowledge of the temperature at which melting and metal segregation occurred. This temperature is largely controlled by the S content of the iron meteorite parent bodies (*14*, *15*), and thus was different for each body. The IIAB iron meteorites have the highest S content and hence the lowest liquidus temperature of ~1330°C, whereas the IVB iron meteorites exhibit the lowest S content and highest liquidus temperature of ~1600°C. The inverse ε^{182}W-versus-S correlation observed among the magmatic iron meteorites therefore may primarily reflect different melting temperatures of the metal within their parent bodies.

To quantify the relation between accretion age and time of melting and metal segregation, we consider two end-member models for core formation (*9*). After the initial accretion, the still undifferentiated iron meteorite parent bodies probably consisted of an unequilibrated mix of different components, including metallic Fe, FeS, and silicates. Upon heating, due primarily to the presence of ^{26}Al, melting probably began at the Fe-FeS eutectic temperature (~1000°C at 1 atm) (*14*) (Fig. 3). The first model assumes that this Fe-FeS melt did not segregate, but that heating continued to the liquidus temperature of the core, and only then did the metal melt segregate to form the core. In this model, the observed ~1-My time difference in core formation model ages between the IIAB and IVA parent bodies is consistent with the time required to raise the temperature inside the parent body from the liquidus temperature of the IIAB to that inferred for the IVA iron meteorites (Fig. 3). Despite their different core formation ages, the IIAB, IIIAB, and IVA iron meteorite parent bodies, therefore, could have accreted within a narrow time

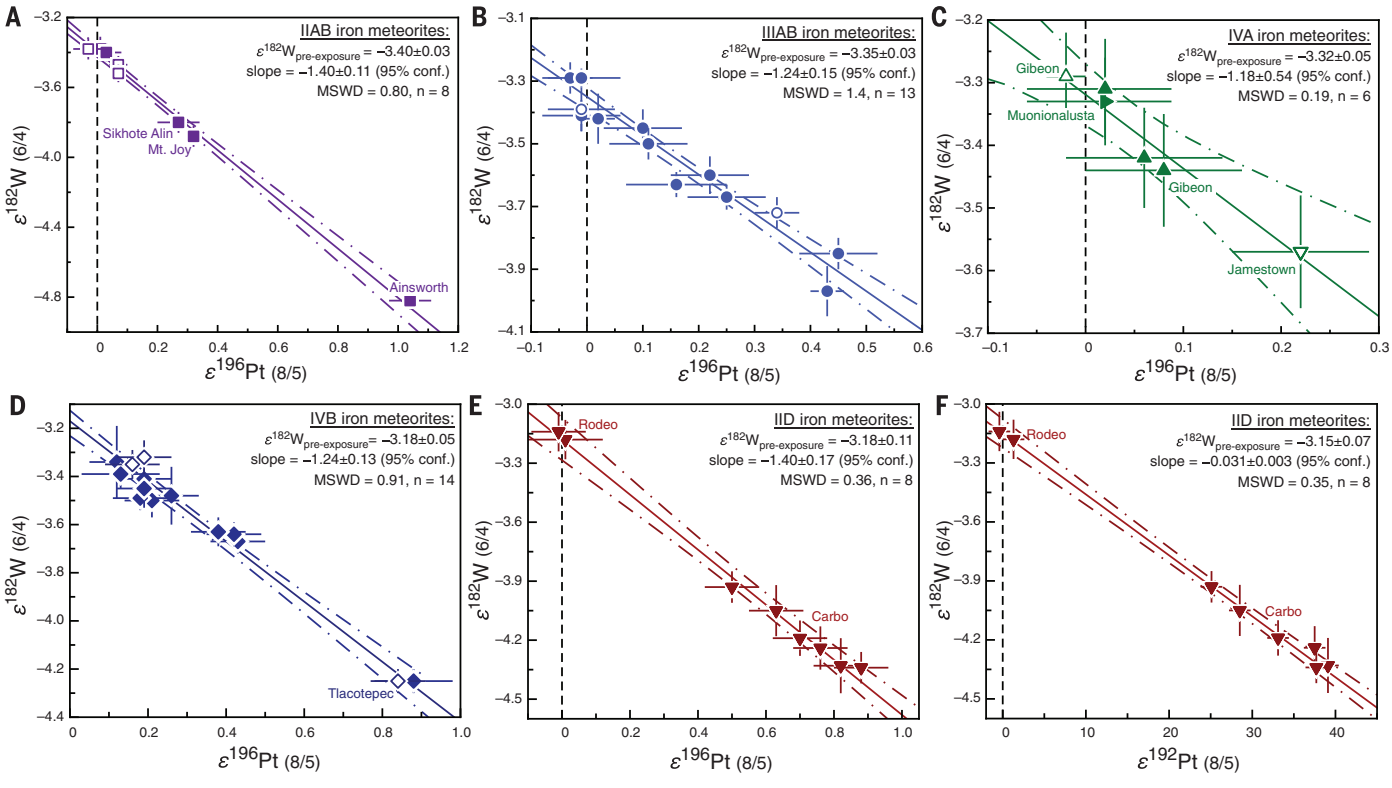

Fig. 1. ε^{182}W versus ε^{i}Pt for the major magmatic iron meteorite groups. (**A** to **F**) IIAB, IIIAB, IVA, IVB, and IID iron meteorites, respectively. ε^{182}W (6/4) and ε^{19i}Pt (8/5) are 0.01% deviations from the terrestrial ^{182}W/^{184}W ratios (normalized to ^{186}W/^{184}W, denoted 6/4) and ^{i}Pt/^{195}Pt ratios (normalized to ^{198}Pt/^{195}Pt, denoted 8/5). Solid lines are best-fit regressions through the data with their 95% confidence envelopes (dashed lines) and pre-exposure ε^{182}W intersecting the ordinate at ε^{i}Pt = 0. W isotope analyses were performed using multicollector inductively coupled plasma mass spectrometry (solid symbols) or thermal ionization mass spectrometry (open symbols). Error bars represent external uncertainties (2 SD for Pt and 95% confidence for W). The investigated IID iron meteorites Carbo and Rodeo have nearly identical Ir/Pt, so in this specific case, ε^{182}W (6/4) versus ε^{192}Pt (8/5) also show a well-defined correlation (Fig. 1F), providing an additional precise estimate of the pre-exposure ε^{182}W (*7*). Small downward corrections for nucleosynthetic heterogeneity have been made to the IID and IVB data points (*7*, *9*).

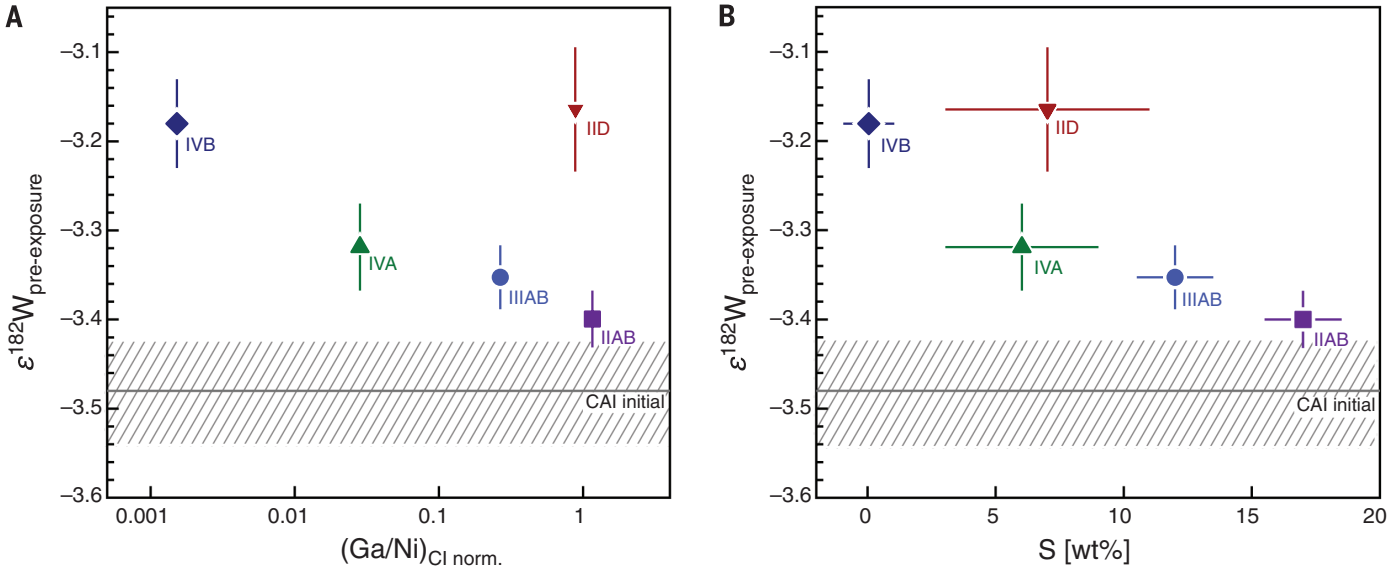

Fig. 2. ε^{182}W versus volatile element ratios and bulk S contents. (**A**) Pre-exposure ε^{182}W versus CI chondrite–normalized Ga/Ni. (**B**) Pre-exposure ε^{182}W versus inferred S concentration (weight %) in the core (*9*). Error bars on ε^{182}W represent 95% confidence limits of the mean. The Ge, Ga, and Ni concentrations are from (*19*) and references therein.

interval, between ~0.1 and ~0.3 My after the formation of CAIs. However, for a given accretion time, this model cannot explain the higher ε^{182}W of the IID and IVB iron meteorites, which plot to the right of the heating curves of the IIAB, IIIAB, and IVA groups (Fig. 3).

The second model assumes that, as a consequence of their high densities, the Fe-FeS eutectic melts rapidly segregated by permeable flow to form cores (*16*). The parent bodies subsequently continued to heat, eventually leading to the melting of silicates and finally of pure Fe metal at ~1600°C (*14*). Therefore, in this model, core formation and metal-silicate separation began with eutectic melting of Fe-FeS but probably did not resume until pure Fe metal melted at higher temperatures (Fig. 3). Because melting was a multistage process occurring over a period of time, the early-segregated Fe-FeS melts would have had less radiogenic ε^{182}W than the later-segregated pure Fe metal melts. In addition, as the early-segregated Fe-FeS melts removed some W to the initial cores, the residual mantles would have developed suprachrondritic $^{180}Hf/^{184}W$, potentially leading to considerably higher ε^{182}W in the mantles over a short period of time. The final W isotope compositions of the metal cores therefore would reflect particular mixes of early- (having lower ε^{182}W) and late- (having higher ε^{182}W) segregated metal fractions. Consequently, for different bodies with uniform formation ages, the metal cores of S-rich bodies would be characterized by lower ε^{182}W as compared to S-poor bodies, because they would contain a larger fraction of the early-segregated Fe-FeS melt.

We modeled the ^{182}W evolution in the iron meteorite parent bodies, accounting for the $^{180}Hf/^{184}W$ in the mantles after a first melt extraction (Fig. 4A). For an accretion time of 0.25 My, our thermal model predicts that the first Fe-FeS melts formed at ~0.7 My (t_1 in Fig. 4) and that the melting temperature of pure Fe metal was reached ~0.6 My later, at ~1.3 My (t_2 in Fig. 4). For an earlier accretion time, at ~0.1 My, the difference between t_1 and t_2 becomes much smaller, leaving too little time for the generation of a significant ^{182}W difference between early- and late-segregated metal. For accretion times later than ~0.3 My, the onset of melting is too late to explain the low ε^{182}W of –3.40 ± 0.03 of the IIAB iron meteorites. The $^{180}Hf/^{184}W$ of the mantle after extraction of an Fe-FeS melt at t_1 is obtained by estimating the fraction of Fe metal melted at the eutectic, using the S content of each iron meteorite group (*9*). The $^{180}Hf/^{184}W$ values of the mantles reached after a first melt extraction are different for each parent body, because the amount of early-segregated Fe-FeS melt decreases with decreasing S content of the bulk core. Thus, the mantles of S-rich bodies (such as IIAB and IID) initially have higher $^{180}Hf/^{184}W$ than those of S-poor bodies (such as IVA) (Fig. 4A). After extraction of a Fe-FeS melt, the mantles of the iron meteorite parent bodies evolved to ε^{182}W values between ~ –3.3 and –3.1 until the melting temperature of pure Fe metal was reached (Fig. 4A). At that point, all Fe metal segregated to the core and was mixed with the earlier-segregated Fe-FeS melts. The IIAB iron meteorites have a very low ε^{182}W of –3.40 ± 0.03 that is only slightly elevated as compared to the

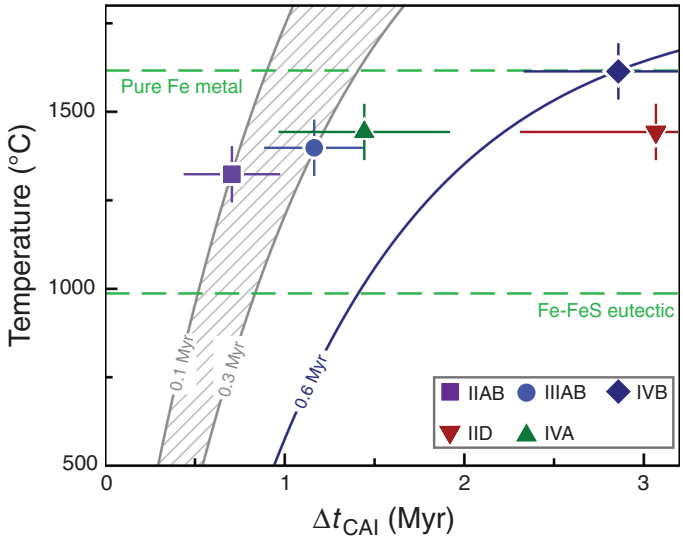

Fig. 3. Internal temperature versus time after CAI formation for iron meteorite parent bodies assuming a single event of metal segregation. Solid symbols show the model ages of metal segregation inferred for the iron meteorite parent bodies. Also shown are model results for postaccretional internal heating by ^{26}Al decay of a spherical protoplanet with a radius of 40 km (*9*). Solid curves show the temperature evolution at half the radius (i.e., at 20 km depth) in planetesimals accreted at 0.1 to 0.3 My (hashed area) after CAI formation, and for 0.6 My in the case of the IVB iron meteorites (dark blue curve). Horizontal dashed lines show the eutectic melting temperature in the Fe-FeS system and that of pure Fe at atmospheric pressure.

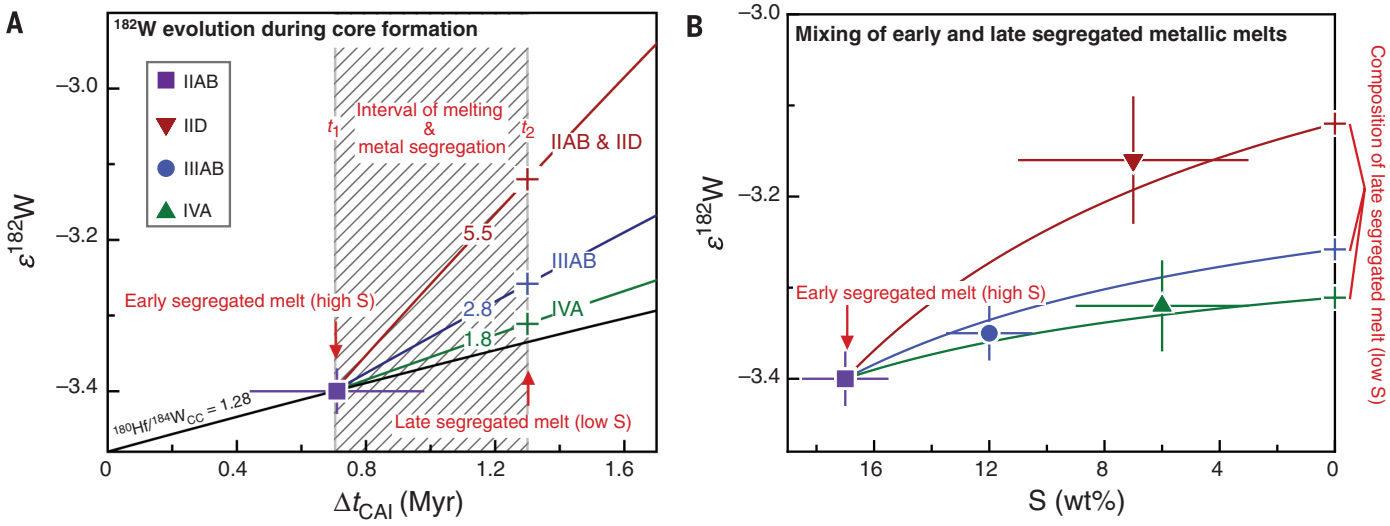

Fig. 4. History of core formation for a two-stage metal segregation process. (**A**) ε^{182}W evolution diagram illustrating the effect of a two-step metal segregation history of the IIAB, IIIAB, IVA, and IID parent bodies, shown for an accretion time of 0.25 My after CAI formation. For a given accretion time, the thermal model constrains the time interval (hashed area) of melting and core formation between the early (t_1) and late (t_2) metal segregation step. Dashed lines show modeled ε^{182}W curves for different ^{180}Hf/^{184}W ratios of the IID, IIIAB, and IVA residual mantles after early core segregation at t_1, represented by the IIAB iron meteorites. The modeled ε^{182}W compositions of the late-segregated (low-S) core fractions at t_2 are also plotted. (**B**) Diagram of ε^{182}W versus S for the IIAB, IID, IIIAB, and IVA iron meteorite groups with mixing curves demonstrating that the pre-exposure ε^{182}W of the IID, IIIAB, and IVA iron meteorites can be explained by mixing of (i) an early- (high-S) segregated melt, represented by the IIAB iron meteorites, and (ii) the modeled ε^{182}W compositions of the residual mantles, which supplied a late- (low-S) segregated melt.

solar system initial value of −3.48 ± 0.06, indicating that melting and metal segregation in the IIAB iron meteorite parent body must have started very early. The IIAB composition, therefore, is dominated by the early-segregated Fe-FeS melt and as such represents one end member in the mixing model. The mixing of early- and late-segregated metal to form bulk iron cores illustrates that the variable ε^{182}W, as well as the inverse ε^{182}W–versus-S correlation of the magmatic iron meteorites, can be reproduced (Fig. 4B). The mixing model also reproduces the offset of the IID iron meteorites from the ε^{182}W–versus-S correlation, which reflects the high ^{180}Hf/^{184}W of the IID mantle after extraction of an early Fe-FeS melt.

Only the IVB iron meteorites appear inconsistent with the models presented above. They are strongly depleted in volatile elements, including S (*17*, *18*). Therefore, only a very minor early-segregated Fe-FeS metal fraction could form, and so this body evolved with chondritic ^{180}Hf/^{184}W until pure Fe melted at high temperature and subsequently segregated to form the core. However, for accretion times of ~0.1 to 0.3 My, our model predicts that the melting temperature of pure Fe is reached between ~0.7 and 1.3 My after CAI formation (Fig. 3); that is, earlier than suggested by the Hf-W model age of 2.9 ± 0.5 My for the IVB iron meteorites. Thus, either the IVB parent body accreted later than the other iron meteorite parent bodies (at ~0.6 My after CAI formation; Fig. 3), or the precursor material of the IVB parent body had higher-than-chondritic Hf/W. The inferred bulk composition of the IVB parental melt is strongly fractionated relative to chondrites, indicating substantial high-temperature processing of the precursor materials in the solar nebula before parent body accretion (*17*, *18*). Relative to other refractory siderophile elements, W is depleted, reflecting either core formation under relatively oxidized conditions—where W becomes less siderophile—or subchondritic W abundances of the bulk IVB parent body with a bulk ^{180}Hf/^{184}W as high as ~2 (*9*). Using a ^{180}Hf/^{184}W of 2 results in a Hf-W model age of metal segregation of 1.8 ± 0.3 My after CAI formation, which is in good agreement with the timing of pure Fe metal melting inferred for the IIAB, IID, IIIAB, and IVA parent bodies (Fig. 4). The IVB parent body, therefore, may have accreted at about the same time as the other bodies.

The Hf-W results indicate that core formation in iron meteorite parent bodies occurred over at least ~1 My. Differences in the time of metal segregation reflect either distinct melting temperatures of the metal or variations in the proportions of early- and late-segregated metal fractions, which in turn are controlled by the bulk S concentrations of the parent bodies. Regardless of differences in the time of core formation, the parent bodies of the IIAB, IID, IIIAB, IVA, and IVB iron meteorites probably accreted at about the same time, between ~0.1 and ~0.3 My after CAI formation. Our data, therefore, rule out the possibility that strongly volatile-depleted parent bodies (IVA and IVB) accreted much earlier than less depleted bodies (IIAB), indicating that the variable depletions of moderately volatile elements in the iron meteorite parent bodies do not mirror the increasing condensation of the moderately volatile elements in the solar nebula over time. Rather, they seem to reflect more local processes within the nebula, resulting in spatially distinct chemical heterogeneities and thus variable volatile depletions of the dust accreting to planetesimals. This is consistent with the observation that the IVB iron meteorites, which are among the most strongly volatile-depleted meteorites, formed from material that underwent substantial high-temperature processing before parent body accretion.

REFERENCES AND NOTES

1. E. R. D. Scott, J. T. Wasson, *Rev. Geophys.* **13**, 527 (1975).
2. T. Kleine, K. Mezger, H. Palme, E. Scherer, C. Münker, *Geochim. Cosmochim. Acta* **69**, 5805–5818 (2005).
3. A. Scherstén, T. Elliott, C. Hawkesworth, S. Russell, J. Masarik, *Earth Planet. Sci. Lett.* **241**, 530–542 (2006).
4. A. Markowski, G. Quitte, A. Halliday, T. Kleine, *Earth Planet. Sci. Lett.* **242**, 1–15 (2006).
5. L. Qin, N. Dauphas, M. Wadhwa, J. Masarik, P. E. Janney, *Earth Planet. Sci. Lett.* **273**, 94–104 (2008).
6. T. Kleine *et al.*, *Geochim. Cosmochim. Acta* **73**, 5150–5188 (2009).
7. T. S. Kruijer *et al.*, *Earth Planet. Sci. Lett.* **361**, 162–172 (2013).
8. N. Wittig, M. Humayun, D. Brandon, S. Huang, I. Leya, *Earth Planet. Sci. Lett.* **361**, 152–161 (2013).
9. Materials and methods and supplementary text are available on *Science* Online.
10. T. S. Kruijer, T. Kleine, M. Fischer-Gödde, C. Burkhardt, R. Wieler, Hf-W isochron for bulk CAI: Evidence for homogeneity of ^{26}Al and ^{182}Hf. Paper presented at the 45th Lunar and Planetary Science Conference, Houston, TX, 17 to 21 March 2014, no. 1786.
11. T. Kleine, K. Mezger, C. Münker, H. Palme, A. Bischoff, *Geochim. Cosmochim. Acta* **68**, 2935–2946 (2004).
12. A. P. Boss, in *Origin of the Earth*, H. E. Newsom, J. Jones, Eds. (Oxford Univ. Press, Oxford, 1990), pp. 3–15.
13. M. Humayun, P. Cassen, in *Origin of the Earth and Moon*, R. Canup, K. Righter, Eds. (Univ. of Arizona Press, Tucson, AZ, 2000), pp. 3–23.
14. R. Brett, P. M. Bell, *Earth Planet. Sci. Lett.* **6**, 479–482 (1969).
15. Y. Fei, C. M. Bertka, L. W. Finger, *Science* **275**, 1621–1623 (1997).
16. T. Yoshino, M. J. Walter, T. Katsura, *Nature* **422**, 154–157 (2003).

17. A. J. Campbell, M. Humayun, *Geochim. Cosmochim. Acta* **69**, 4733–4744 (2005).
18. R. J. Walker *et al.*, *Geochim. Cosmochim. Acta* **72**, 2198–2216 (2008).
19. G. K. Benedix, H. Haack, T. J. McCoy, in *Treatise on Geochemistry* (Elsevier, Amsterdam, ed. 2, 2014), pp. 267–285.

ACKNOWLEDGMENTS

We thank T. Elliott, A. Halliday, and an anonymous reviewer for their comprehensive and constructive reviews. We gratefully acknowledge the Field Museum of Natural History (Chicago), the Smithsonian Institution (Washington, DC), and the American Museum of Natural History (New York City) for providing the samples for this study. We also thank R. Wieler, J. Wasson, R. Hin, F. Nimmo, and W. van Westrenen for discussions and U. Heitmann for technical support during sample preparation. This study was supported by a Förderungsprofessur to T.K. of the Swiss National Science Foundation (grant no. PP00P2_123470) and NASA Cosmochemistry grant NNX13AF83G to R.J.W.. The data reported in this paper are tabulated in the supplementary materials (tables S1 to S6).

SUPPLEMENTARY MATERIALS

www.sciencemag.org/content/344/6188/1150/suppl/DC1
Materials and Methods
Supplementary Text
Figs. S1 to S5
Tables S1 to S6
References (*20*–*39*)

4 February 2014; accepted 28 April 2014
10.1126/science.1251766

SENSORY BIOLOGY

Marine teleost locates live prey through pH sensing

John Caprio,[1]* Mami Shimohara,[2] Takayuki Marui,[3] Shuitsu Harada,[4] Sadao Kiyohara[2]

We report that the Japanese sea catfish *Plotosus japonicus* senses local pH-associated increases in H^+/CO_2 equating to a decrease of ≤0.1 pH unit in ambient seawater. We demonstrated that these sensors, located on the external body of the fish, detect undamaged cryptic respiring prey, such as polychaete worms. Sensitivity is maximal at the natural pH of seawater (pH 8.1 to 8.2) and decreases dramatically in seawater with a pH <8.0.

Locating food is essential for the survival of any heterotrophic organism. Sensory systems such as vision, hearing, and chemoreception aid in this critical endeavor, because each can provide key information for identifying and locating prey at a distance. Vision is of limited use for species that are nocturnal and/or live in murky environments (such as fish). Chemoreception, however, is especially important for many aquatic organisms in acquiring food (*1*).

While investigating how chemical stimulus information is encoded by the taste system in fish, we discovered a remarkable sensitivity of the Japanese sea catfish (*Plotosus japonicus*) to small transient increases in ambient H^+/CO_2. Extracellular electrophysiological recordings from specific fibers of the facial [cranial nerve VII)/cranial nerve V (trigeminal)] nerve complex that innervates the maxillary barbel (the "whisker") of the catfish (*2*) (Fig. 1A) were excited by slight transient declines in the pH of the ambient seawater (SW) that contacted its barbel (Fig. 1B). These fibers characteristically elicited large-amplitude (hundreds of microvolts to 1 mV) action potentials that were often about double the amplitude of those evoked by other fibers of the nerve complex recorded extracellularly. The recordings revealed that the fibers responded to a decline of ≤0.1 pH unit in SW that washed over the maxillary barbel (Fig. 1B and table S1) (*3*), a similar sensitivity to pH as that observed for respiratory chemosensitive neurons (*4*) and associated astrocytes (*5*) in the mammalian medulla. Not only did small-volume transients (fig. S1) (*3*) and repetitive (fig. S2) (*3*) declines in pH in the SW bathing the barbel receptive field (RF) activate the "pH fibers," the fibers also responded to larger transient drops, even those into the slightly acidic range (Fig. 1C). If the pH of the SW bathing the RF was lowered to <pH 8.0 and maintained for several minutes, either a greater drop in pH was required to activate the same fibers or the fibers became inactivated (table S1 and Figs. 1D, 2, and 3) (*3*). When the flow of control SW (pH ~8.2) over the RF was resumed, however, sensitivity to falling pH was restored (Figs. 1D and 4).

Because sea catfish are benthic nocturnal feeders (*6*) whose stomach contents contain polychaete worms (*7*), we hypothesized that a function of the highly sensitive H^+/CO_2 system of the catfish is to detect polychaete worms, which live in semipermanent U- or Y-shaped burrows in coastal marine sediments (*8*) and release punctate

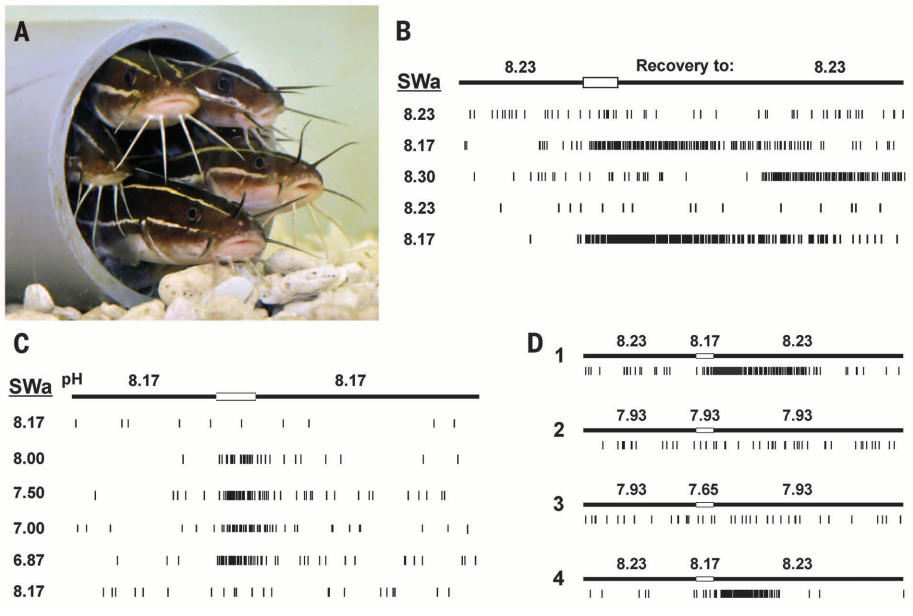

Fig. 1. Representative single nerve fibers that innervate the maxillary barbel respond to the falling pH of ambient SW. (**A**) Sea catfish, *Plotosus japonicus*. (**B**) Only falling pH activates the fiber. Artificial SW (SWa) of pH 8.23 flows over the barbel into which SW of either pH 8.23 (control), 8.17, or 8.3 is added (marked by the clear portion of the stimulus bar). Only falling pH activates the pH fiber (at stimulus onset for SW of pH 8.17 or with a delay after the onset of pH 8.30 SW) as the pH 8.23 SW background replaces the brief application of pH 8.30 SW. (**C**) A typical pH fiber is excited by brief applications of SW of pH < ambient, even to pH values into the acidic range. (**D**) SW of pH <8.0 that continuously bathes the barbel reduces the sensitivity of the sensor and sometimes inactivates the sensor (traces 2 and 3); however, sensitivity recovers to approximately control level (trace 4) after the barbel is bathed in pH 8.23 SW. The clear portion of the stimulus bar represents a 0.5-s stimulus presentation. Fibers shown in (B) to (D) are from different preparations.

[1]Department of Biological Sciences, Louisiana State University, Baton Rouge, LA 70803, USA. [2]Graduate School of Science and Engineering, Department of Chemistry and BioScience, Kagoshima University, Kagoshima 890-0065, Japan. [3]409 Koyocho, Sukagawa, Fukushima, 962-0401, Japan. [4]Department of Oral Physiology, Graduate School of Medical and Dental Sciences, Kagoshima University, Kagoshima 890-8544, Japan.
*Corresponding author. E-mail: jcap@lsu.edu

amounts of H^+/CO_2 into the surrounding water during respiration. To test this hypothesis, we first examined whether the respiratory transients of H^+/ CO_2 of the worm would be of sufficient magnitude to be detectable by sea catfish. Therefore, we recorded the pH of the SW within a 1-liter glass beaker every 5 s over 45 min at distances of 5 and 15 mm from the outflow end of a glass U tube used as an artificial burrow containing a single worm. With an electrode distance of 5 mm from the U-tube, the pH was transiently lowered by 0.15 to 0.25 pH units (Fig. 2A), a change in pH that was sufficiently within the range of sensitivity of the pH sensors of the sea catfish (table S1 and Fig. 1B) (*3*); at 15 mm from the U tube containing the worm, pH fluctuations were absent because of the buffering ability of the SW.

We next tested the hypothesis that sea catfish would be attracted to the region of the aquarium that contained a worm in its burrow. All behavioral experiments occurred in the dark (Fig. 2B) and were monitored with an infrared camera. Initial observations showed that sea catfish would approach a U tube containing a worm and suck it out of the tube (Fig. 2C and movie S1) (*3*). For the experimental tests, each of four catfish was placed in a separate aquarium filled with pH 8.0 to 8.1 SW and allowed to acclimate for 1 month. One hour before testing, a glass U tube, covered with netting, either empty or containing a live worm, was placed within the coral substrate of each aquarium at a location distant from the fish's nest; the netting was to prevent ingestion of the worm by the fish during the tests (Fig. 2D). Each 15-min test was conducted over 8 consecutive days. The results indicated that the catfish spent significantly more time within the designated partition of the tank containing the U tube with the worm than in the part of the tank with the U tube that lacked the worm (Fig. 2F).

Although the sensory systems used by the sea catfish to locate the worm in the preceding tests could have been mechanoreception, electroreception, and/or chemoreception, we hypothesized that the respiratory transients of increased H^+/ CO_2 from the worm were a sufficient stimulus to attract the catfish. We therefore tested whether a release from the U tube of SW of pH slightly less than that of the SW within the aquarium (pH 8.0 to 8.1) would result in the catfish spending more time in that region of the aquarium than when only control SW (pH 8.1 to 8.3) flowed from the U tube. A small length of polyethylene tubing was placed in one end of the U tube, and the other end was connected to a peristaltic pump located outside the aquarium that delivered SW at either pH 8.0 to 8.1 (control) or pH 7.8 to 7.9 (test) into the U tube (Fig. 2, B, E, and G). Four fish different than those tested previously were each placed in separate aquaria for at least 1 month before experimentation and were then tested over 8 consecutive days. For each test, 20 ml of pH-adjusted SW was pumped into the aquarium at a rate of 4 ml/min. The results indicated that the catfish spent significantly more time in the partition of the aquarium containing the U tube that emanated the lower-pH SW than when control SW was released (Fig. 2G). Further, the catfish were highly active and in an appetitive search mode when swimming in the vicinity of the U tube emitting the lower-pH SW. The catfish also frequently bit at the end of the U tube, a behavior never observed when control SW at the pH of the aquarium water was released (movie S2)

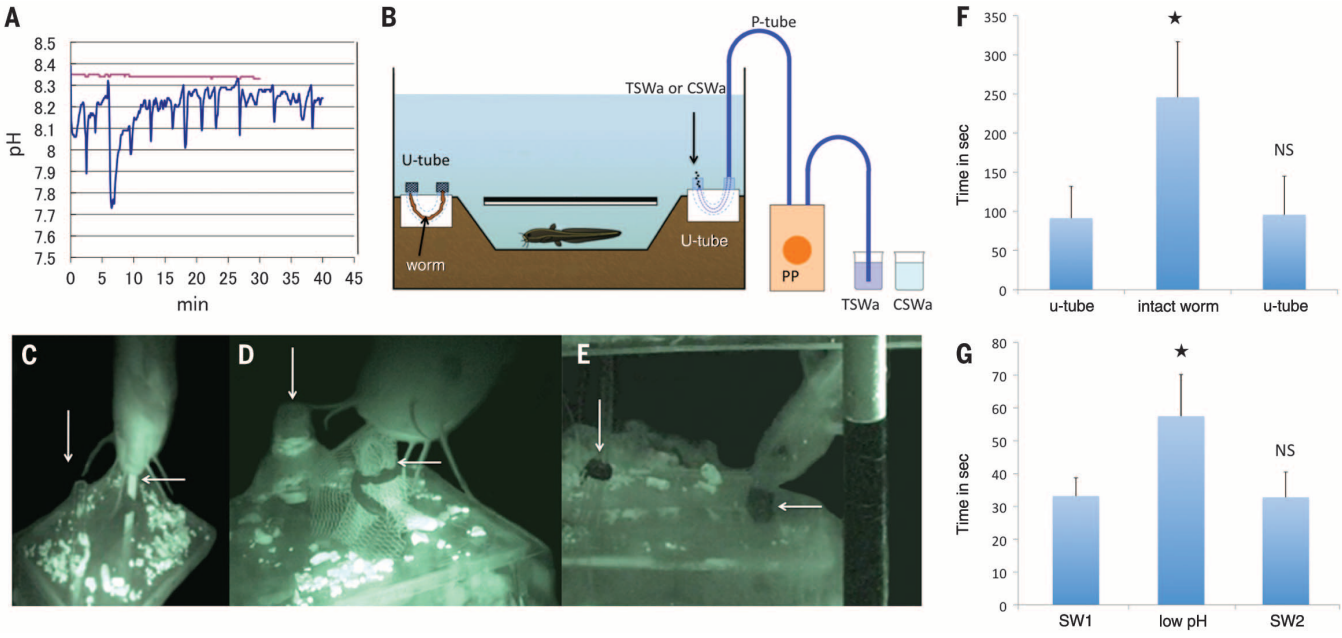

Fig. 2. Chemosensory response of the Japanese sea catfish to polychaetes and falling pH. (**A**) Recorded fluctuations in pH (by 0.15 to 0.25 pH unit) due to polychaete respiration recorded at 5 mm from the outflow end of a U tube containing the worm (blue) immersed in a 1-liter glass beaker containing pH ~ 8.35 SW; no change in pH was detected at 15 mm from the U tube (red). (**B**) Experimental setup: A single catfish constructed a nest within the coral substrate. A glass U tube was inserted into the substrate, containing either a live worm (left) or an empty U tube (right) emitting SW of slightly lower pH than that of the aquarium water. PP, peristaltic pump; TSWa, test SW; CSWa, control SW. (**C**) A catfish biting one end of the U tube and beginning to suck out the worm (movie S1). (**D**) A catfish biting the netting covering one end of the U tube that housed a worm. (**E**) A catfish attracted to and biting at the outflow end of a U tube lacking a worm, but emitting SW of lower pH (7.9) than ambient (pH 8.3) (movie S2). Arrows in (C) to (E) indicate the positions of the two openings of the U tube. (**F**) Catfish spent significantly more time in the quadrant of the aquarium containing a U tube with a worm (asterisk) than in the portion without a worm. Each of four catfish received three treatments (control-test-control) and eight replicates of each treatment; the mean of the eight replicates for each of the four animals was used in the statistical analyses to avoid pseudoreplication. The data were analyzed with a one-factor block design analysis of variance (ANOVA) ($F[2,6] = 27.51$, $P = 0.00095$), followed by a priori one-tailed t tests, $P < 0.05$; NS, not significantly different from the first bar. (**G**) Catfish spent significantly more time in the quadrant of the aquarium containing a U tube that emitted pH 7.9 SW (asterisk) than that emitting pH 8.3 SW, the same pH as the aquarium SW. Each of four catfish different from those tested in (F) received three treatments (control-test-control) with 8 to 10 replicates of each treatment, and the mean of the 8 to 10 replicates for each of the four animals was used in the statistical analyses to avoid pseudoreplication. These data were analyzed with a one-factor block design ANOVA ($F[2,6] = 8.21$, $P = 0.019$), followed by a priori one-tailed t tests, $P < 0.05$; NS, not significantly different from the first bar. Error bars in (F) and (G) are SEM.

(*3*). These results clearly showed that an elevation in ambient H^+/CO_2 alone was sufficient to attract the catfish to the worm prey.

The sensory origin of this extraordinary sensitivity to H^+/CO_2 is currently unidentified, because recordings were obtained from fibers within the facial/trigeminal complex that innervate the head, including the barbels (*9*, *10*). The sensors could be located in cells within taste buds innervated by VII fibers (*10*) and/or within solitary chemosensory cells (SCCs) that are scattered across the surface epithelium innervated by either V or VII fibers (*11*–*13*). Because both tastebuds (*10*, *14*, *15*) and SCCs (*16*) also occur along the flank of catfishes, the sensors might also be located within flank tastebuds innervated by VII nerves or on SCCs innervated by either VII and/or spinal sensory nerves (*17*, *18*). It is possible that the entire surface epithelium is H^+/CO_2-sensitive, as it is to amino acid stimuli (*19*). The molecular sensors of the sea catfish to H^+/CO_2 are unknown; however, if the sea catfish sensors are activated by H^+, they could possibly be related to acid-sensing (ASIC) (*20*, *21*) or TASK-2 (*22*) channels. If, however, the sensors detect CO_2, they might be related to connexin 26 hemichannels found in medullary respiratory neurons (*23*) or to currently unknown sensors located on neuroepithelial cells in fish gills (*24*). Whether the olfactory system of the sea catfish is also sensitive to H^+/CO_2 is unknown.

The decline in sensitivity of the H^+/CO_2–detecting system in SW <pH 8.0 suggests the possibility of compromised feeding behavior of these fish in their estuarine habitat due to transient drops in ambient pH commonly occurring in that environment (*25*). It is possible, however, that other sensory systems of the sea catfish not so affected during times of pH transients could compensate for locating prey. In addition to transitory alterations in the pH of the marine environment, anthropogenic activities are causing ocean acidification that can adversely affect marine organisms over the long term. The pH of ocean waters has been reduced from 8.2 to 8.1, a 30% rise in acidity since preindustrial times, and is predicted to decline to ~7.8, a 150% rise in acidity, by the end of the 21st century (*26*, *27*). Declining oceanic pH is shown to be detrimental to numerous aquatic species, including fish populations, because it alters various neurosensory systems and natural behaviors that affect species survival (*28*–*32*). If the rapidity of ocean acidification exceeds the plasticity (*24*) of the H^+/CO_2-sensing system of the Japanese sea catfish to adapt and reset its sensitivity to a lower-pH environment, then this detection system along with possibly other sensory systems will be compromised. Whether such a highly sensitive prey-detecting system is common among other benthic teleosts and how ocean acidification might impinge on the sensory capabilities of those organisms remain unknown.

REFERENCES AND NOTES

1. P. W. Sorensen, J. Caprio, in *The Physiology of Fishes*, D. H. Evans, Ed. (CRC Press, Boca Raton, FL, ed. 2, 1997), pp. 375–405.
2. T. Yoshino, H. Kishimoto, *Bull. Natl. Mus.Nat. Sci. Ser. A* **2** (suppl.), 1 (2008).
3. Supplementary information is available on *Science* Online.
4. P. G. Guyenet, R. L. Stornetta, D. A. Bayliss, *J. Comp. Neurol.* **518**, 3883–3906 (2010).
5. A. V. Gourine *et al.*, *Science* **329**, 571–575 (2010).
6. M. Kasai, S. Kiyohara, *J. Comp. Physiol. A Neuroethol. Sens. Neural Behav. Physiol.* **196**, 901–912 (2010).
7. E. Clark, D.R. Nelson, M.J. Stoll, Y. Kobayashi, *Aqua* **17**, 211 (2011).
8. E. Kristensen, *Geochem. Trans.* **2**, 92 (2001).
9. S. Kiyohara, H. Houman, S. Yamashita, J. Caprio, T. Marui, *Brain Res.* **379**, 353–357 (1986).
10. T. E. Finger, *J. Comp. Neurol.* **165**, 513–526 (1976).
11. K. Reutter, *Cell Tissue Res.* **149**, 143–146 (1974).
12. T. E. Finger *et al.*, *J. Comp. Neurol.* **373**, 129–138 (1996).
13. T. E. Finger, *Brain Behav. Evol.* **50**, 234–243 (1997).
14. J. Atema, *Brain Behav. Evol.* **4**, 273–294 (1971).
15. T. E. Finger, S. K. Drake, K. Kotrschal, M. Womble, K. C. Dockstader, *J. Comp. Neurol.* **314**, 55–66 (1991).
16. K. Kotrschal, *Environ. Biol. Fishes* **35**, 273–282 (1992).
17. E. Scharrer, S. W. Smith, S. L. Palay, *J. Comp. Neurol.* **86**, 183–198 (1947).
18. W. L. Silver, T. E. Finger, *J. Comp. Physiol. A Neuroethol. Sens. Neural Behav. Physiol.* **154**, 167–174 (1984).
19. C. J. Davenport, J. Caprio, *J. Comp. Physiol. A Neuroethol. Sens. Neural Behav. Physiol.* **147**, 217–229 (1982).
20. A. Springauf, S. Gründer, *J. Physiol.* **588**, 809–820 (2010).
21. X. Chen, G. Polleichtner, I. Kadurin, S. Gründer, *J. Biol. Chem.* **282**, 30406–30413 (2007).
22. S. Wang *et al.*, *J. Neurosci.* **33**, 16033–16044 (2013).
23. L. Meigh *et al.*, *eLife* **2**, e01213 (2013).
24. S. F. Perry, S. Abdallah, *Respir. Physiol. Neurobiol.* **184**, 309–315 (2012).
25. G. E. Hofmann *et al.*, *PLOS ONE* **6**, e28983 (2011).
26. K. Caldeira, M. E. Wickett, *Nature* **425**, 365 (2003).
27. R. F. Service, *Science* **337**, 146–148 (2012).
28. D. L. Dixson, P. L. Munday, G. P. Jones, *Ecol. Lett.* **13**, 68–75 (2010).
29. P. L. Munday *et al.*, *Proc. Natl. Acad. Sci. U.S.A.* **106**, 1848–1852 (2009).
30. S. D. Simpson *et al.*, *Biol. Lett.* **7**, 917–920 (2011).
31. M. C. O. Ferrari *et al.*, *PLOS ONE* **7**, e31478 (2012).
32. G. E. Nilsson *et al.*, *Nat. Clim. Change* **2**, 201–204 (2012).

ACKNOWLEDGMENTS

We thank A. Nikonov, M. Brown, and J. Belanger for aid in preparation of Fig. 1; A. Kiyohara for Fig. 1A; C. Derby, A. Hansen, W. C. Michel, W. Silver, D. Mulkey, and T. Dietz for their constructive comments on the manuscript; and C. Derby for statistical aid. We also thank M. Kirino, T. Ikenaga, R.Kawabata and K. Kawano for assitance in the laboratory. Supported in part by the NIH U.S.-Japan Brain Research Cooperative Program (grant NS-04-014) and the George C. Kent Professorship (Louisiana State University College of Science) to J.C. and a grant (22580205) to S.K. from the Ministry of Education, Science, Sports, and Culture of Japan. All primary electrophysiological data (VCR tapes) are archived in the Department of Biological Sciences, Louisiana State University. The authors declare no competing financial interests. Readers are welcome to comment on the online version of the paper. Correspondence and requests for materials should be addressed to J.C. (jcap@lsu.edu).

SUPPLEMENTARY MATERIALS

www.sciencemag.org/content/344/6188/1154/suppl/DC1
Materials and Methods
Figs. S1 and S2
Reference (*33*)
Movies S1 and S2
Databases S1 and S2 (Excel spreadsheets)

27 February 2014; accepted 8 May 2014
10.1126/science.1252697

PLURIPOTENCY PROGRAM

Defining an essential transcription factor program for naïve pluripotency

S.-J. Dunn,[1]* G. Martello,[2]*†‡ B. Yordanov,[1]* S. Emmott,[1] A. G. Smith[2,3]†

The gene regulatory circuitry through which pluripotent embryonic stem (ES) cells choose between self-renewal and differentiation appears vast and has yet to be distilled into an executive molecular program. We developed a data-constrained, computational approach to reduce complexity and to derive a set of functionally validated components and interaction combinations sufficient to explain observed ES cell behavior. This minimal set, the simplest version of which comprises only 16 interactions, 12 components, and three inputs, satisfies all prior specifications for self-renewal and furthermore predicts unknown and nonintuitive responses to compound genetic perturbations with an overall accuracy of 70%. We propose that propagation of ES cell identity is not determined by a vast interactome but rather can be explained by a relatively simple process of molecular computation.

Mouse embryonic stem (ES) cells exhibit the capacity to self-renew indefinitely, the plasticity to generate all somatic lineages and germ cells, and the ability to reenter embryogenesis after blastocyst injection. Collectively these properties are described as ground-state pluripotency (*1*). The pluripotent state of mouse ES cells has been considered as controlled by a vast network of genetic interactions (*2*–*6*). However, only a limited number of transcription factors (TFs) have been validated rigorously. Two have been found to be indispensable: Oct4 and Sox2. In contrast, factors such as Nanog, Klf4, and Esrrb are individually dispensable, yet their overexpression can support self-renewal (*7*–*9*).

[1]Computational Science Laboratory, Microsoft Research, Cambridge CB1 2FB, UK. [2]Wellcome Trust–Medical Research Council Cambridge Stem Cell Institute, University of Cambridge, Cambridge CB2 1QR, UK. [3]Department of Biochemistry, University of Cambridge, Cambridge, UK.
*These authors contributed equally to this work. **†Corresponding author. E-mail: graziano.martello@unipd.it (G.M.); austin.smith@cscr.cam.ac.uk (A.G.S.)** ‡Present address: Department of Molecular Medicine, University of Padua, 35131 Padua, Italy.

Culture environments for efficiently sustaining mouse ES cells have been progressively refined. Currently optimized conditions comprise the cytokine leukemia inhibitory factor (LIF), together with two selective inhibitors (2i) of glycogen synthase kinase 3 (Chiron99021, CH) and mitogen-activated protein kinase kinase (Mek) (PD0325901, PD) (*10*). A number of direct transcriptional targets downstream of LIF, CH, and PD have been identified (fig. S1A) (*8*, *9*, *11*–*14*). Although there is evidence of extensive cross-regulation between the TFs, it is not understood how the environmental signals are processed to stabilize the network and to ensure self-renewal. Characterizing this circuitry should allow us to explain and predict the self-renewal behavior of ES cells.

ES cells can be stably cultured as a substantially homogeneous population in four different environments: 2i+LIF, 2i, LIF+CH, and LIF+PD (Fig. 1A and fig. S2, A to C). Under these conditions, cells show no signs of differentiation, self-renew at clonal density, homogeneously express pluripotency markers, and form germline-competent chimeras after blastocyst injection (fig. S2E). This system permits us to study gene expression of pluripotency factors at steady state in different culture conditions with similar abilities to maintain ES cells. Furthermore, cells can be efficiently transitioned from one culture condition to another without affecting pluripotency or cell survival (fig. S2D), allowing adjustments in gene expression circuitry to be measured over time.

We analyzed gene expression for 17 factors implicated in ES cell maintenance and inferred to be cross-regulatory (Fig. 1B) (*1*). To identify plausible TF interactions, we examined expression correlation between all possible TF pairs across the different culture conditions. Steady-state data were obtained from ES cells grown in each condition for 10 days, and time-course data were obtained from cells cultured for 10 days in each of 2i, LIF+CH, and LIF+PD before adding the third component to reconstitute 2i+LIF (Fig. 1B). By way of example, the strong negative correlation observed between estrogen-related receptor β (Esrrb) and transcription factor 7–like 1 (Tcf7l1, also known as Tcf3) (Fig. 1C) suggests a repressive interaction.

We used the Pearson coefficient as a metric to quantify the correlation between any two TFs (fig. S3A). Accordingly, we constructed a "meta-model" of the pluripotency network (Fig. 1D), defined as a set of possible undirected interactions, each suggested by the Pearson correlation data (supplementary materials section S1J). The meta-model therefore consists of a set of models, each a unique instantiation of possible interactions that might explain ES cell behavior. Inferred interactions are assumed to be functional but not necessarily direct.

The possible combinations of interactions between the TFs exceed the billions of billions. Distillation to only those models that capture observed behavior, and can explain ES cell information processing and decision-making, necessitated development of a new computational approach.

We adopted Boolean network formalism to abstract gene expression levels as low or high within the endogenous expression range. Computational analyses were performed by using a bespoke software tool designed to encode possible genetic interactions and behavioral constraints (supplementary materials section S1I). The tool implements formal verification procedures (*15*) to synthesize those interaction combinations and gene-regulation functions that provably satisfy experimental data, thereby constraining the set of possible models. Moreover, the tool enables interrogation of the entire constrained meta-model to generate predictions of behavior under genetic and environmental perturbations.

We defined a set of 23 experimental constraints, comprising conversion between culture conditions, loss of signals, and gain- or loss-of-gene-function experiments (Fig. 2A and supplementary materials section S1K). Each constraint consists of an initial and final gene expression pattern that must be reached in a finite number of steps. Starting from the meta-model, we

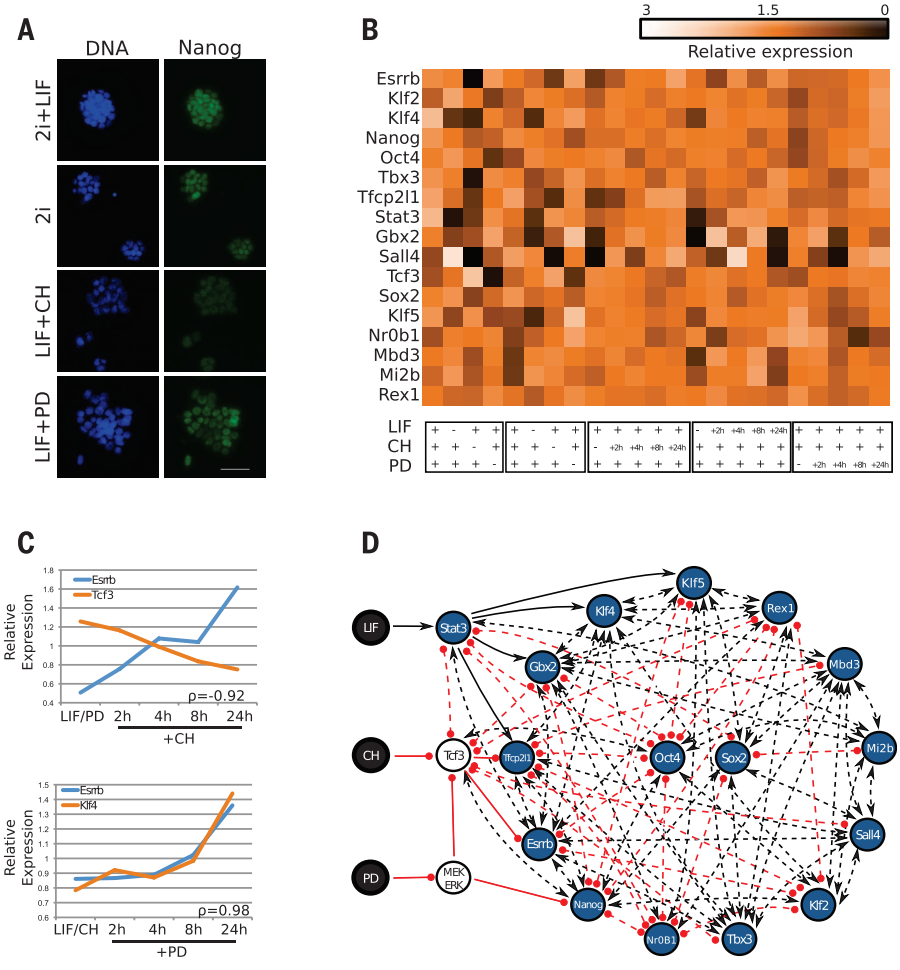

Fig. 1. Flexible culture conditions for mouse ES cells allow deduction of possible interactions between pluripotency factors. (**A**) Under different combinations of LIF, CH, and PD, ES cells show homogeneous expression of Rex1, Oct4, Esrrb, and Nanog. See also fig. S2, A to C. Scale bar indicates 50 μm. (**B**) Gene expression for the set of 17 pluripotency-associated TFs (gastrulation brain homeobox 2, GBX2; transcription factor CP2–like 1, Tfcp2l1; sal-like 4, Sall4) from five experiments under different culture conditions. Columns 1 to 4 and 5 to 8 are biological replicates in the indicated steady-state conditions, whereas columns 9 to 23 illustrate the change in gene expression over time from cells in LIF+PD, 2i, or LIF+CH switched to 2i+LIF. Gene expression was measured by quantitative reverse transcription polymerase chain reaction and normalized to mean expression level. β-actin was used as an internal control. (**C**) Examples showing negative correlation between Esrrb and Tcf3 and positive correlation between Esrrb and Klf4 under time-series experiments. The Pearson correlation coefficient is indicated on each plot. (**D**) The meta-model derived from a Pearson coefficient threshold of 0.7, with the expected gene expression under 2i+LIF conditions. Gene expression is discretized to high (blue) or low (white). Positive regulation indicated by a black arrow; negative regulation indicated by a red circle-headed line. Dashed lines indicate optional interactions; solid lines indicate definite interactions. ERK, extracellular signal–regulated kinase.

identified a subset of models that can reproduce all 23 constraints simultaneously.

To reduce model complexity and to maximize the predictive capability of the meta-model (supplementary materials section S1M), we sought only those components and interactions that are essential. A high Pearson correlation threshold is desirable to select only possible interactions between genes that show strong correlations in expression. The maximum Pearson correlation threshold that identified the smallest set of interactions needed to satisfy all experimental constraints simultaneously is 0.792. This gave a set of 70 possible interactions. We found that, in addition to known signal targets, 11 of the possible interactions were present in all of these models. We conclude that these are essential interactions for the pluripotency network (Fig. 2B). We further found that five components are not required and can be eliminated: zinc finger protein 42 (Zfp42, also known as Rex1); nuclear receptor subfamily 0, group B, member 1 (Nr0b1); methyl-CpG binding domain protein 3 (Mbd3); chromodomain helicase DNA binding protein 4 (Chd4, also known as Mi-2β; and Kruppel-like factor 5 (Klf5) (Fig. 2B, in gray). We thus derived a first set of minimal models to explain the 23 known behaviors of ES cells.

The set of possible interactions were compared with those inferred from open-source microarray data after genetic perturbations and also with chromatin immunoprecipitation sequencing data. We found that our set of possible interactions are supported by these independent data but that a set of interactions derived only from perturbation data was insufficient to satisfy experimental observations (supplementary materials section S2A and figs. S4 and S5). Second, we compared our computational approach with Bayesian network inference (*16*). The latter yielded fewer interactions and only one model that was inconsistent with experimental observations (fig. S5B).

ES cells cultured in 2i+LIF show a remarkable degree of robustness because they can tolerate the singular loss of key TFs such as Nanog homeobox (Nanog) or Esrrb (*8*, *9*). However, the response of ES cells to compound perturbations is unknown, difficult to predict, and time-consuming to investigate by unsupervised experimental tests. We used the complete set of data-constrained models to predict the response of ES cells to single and double knockdowns in 2i+LIF.

We determined whether a given knockdown was predicted to result in maintenance or collapse of self-renewal (supplementary materials section S1L) (*17*–*19*). We accepted predictions only when all of the candidate models were in agreement. This led to 11 predictions from the 24 possible double knockdowns and one single knockdown prediction (Fig. 3A, left prediction column).

To test the predictions, we used small interfering RNA (siRNA) transfection followed by clonal assay, which provides a quantitative measure of self-renewal capacity (Fig. 3A, left exp. validation column). A subset of predictions was also tested by using knockout ES cells (fig. S6, B and C). The experimental results confirmed all predictions with the sole exception of the *Tbx3*/*Klf2* double knockdown. Several predictions were non-intuitive: for example, the effect of *Klf2*/*Sall4*

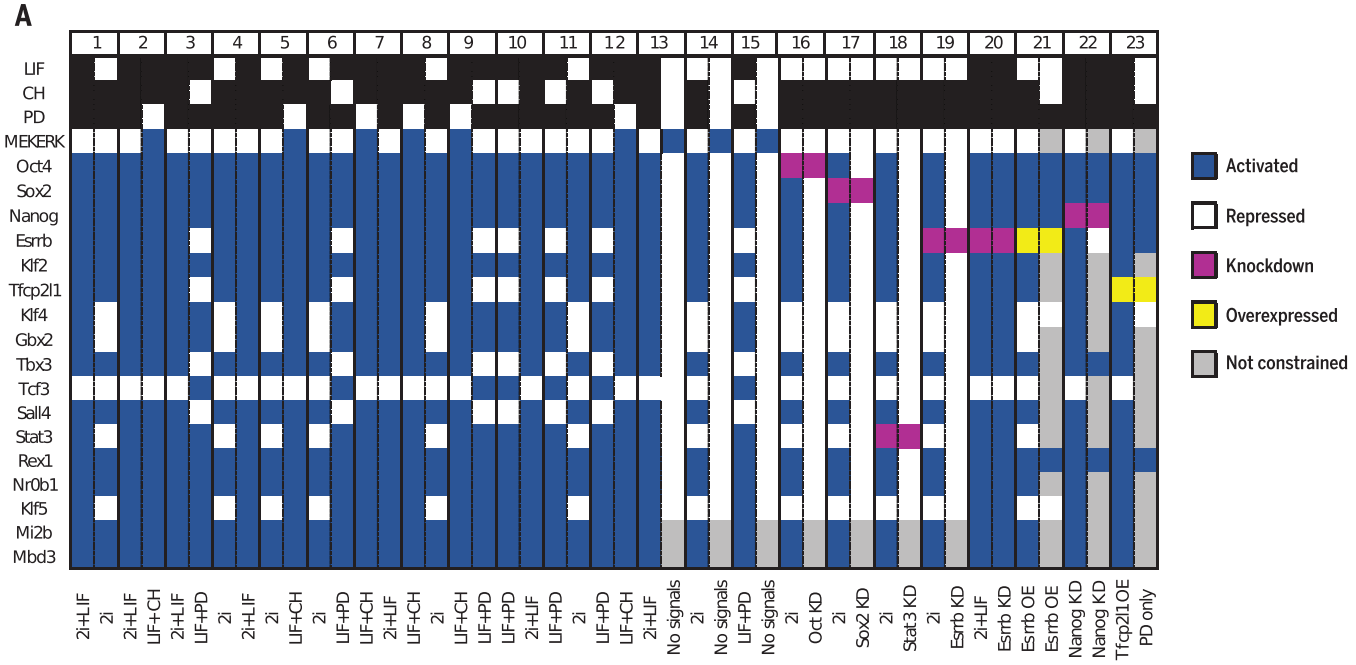

Fig. 2. Iteration with experimental observations reduces model complexity. (**A**) Twenty-three experimental constraints are defined, each with initial (left column) and final (right column) conditions (supplementary materials section 1K). (**B**) The meta-model derived from a Pearson correlation threshold of 0.792, constrained to satisfy the expected experimental behavior (A). Eleven of the possible interactions are present in all possible models, and the remaining possible interactions are shown by dashed gray lines. All of the constraints can be satisfied without including five components of the network (gray).

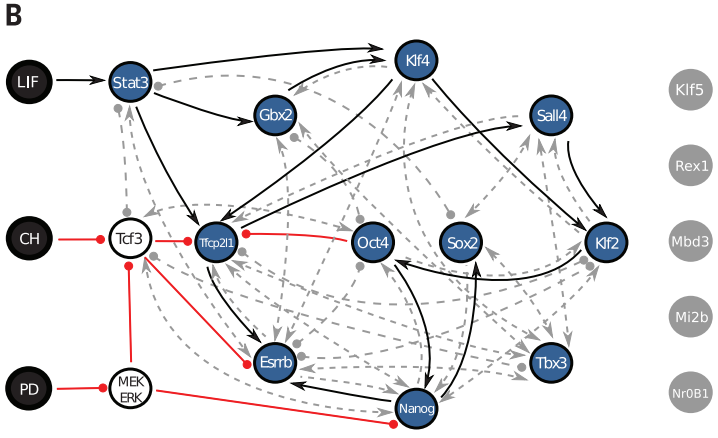

double knockdown could not be inferred from single knockdown results (Fig. 3B).

No single model within the meta-model is capable of producing the observed behavior after *Tbx3*/*Klf2* double knockdown. We therefore used this incorrect prediction as a new experimental constraint to derive a more accurate set of models by incrementally lowering the Pearson coefficient threshold to identify the most-supported subset of interactions (supplementary materials section S1M). We found that including an optional positive interaction between octamer-binding transcription factor 4 (Oct4) and sex-determining region Y–box 2 (Sox2) was sufficient to introduce the necessary flexibility to the network.

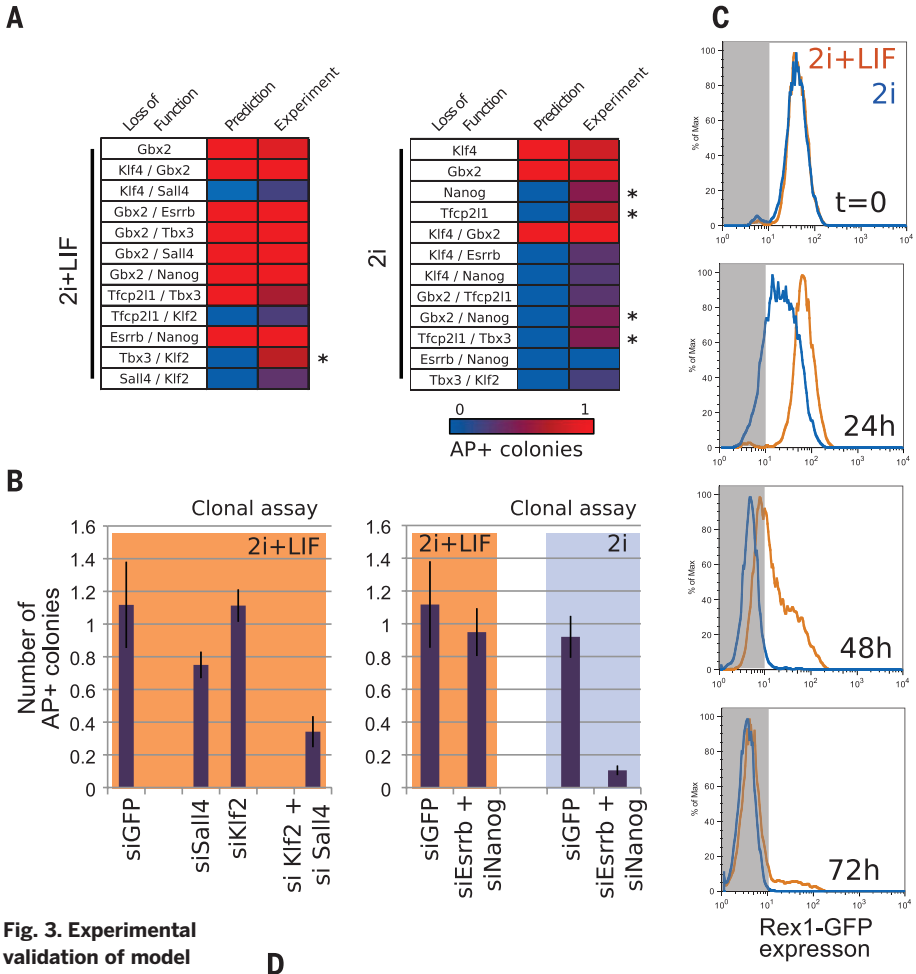

Fig. 3. Experimental validation of model predictions. (**A**) Summary of model predictions and experimental validation. Incorrect predictions are highlighted with an asterisk. Each box in the Exp. Validation column indicates the number of alkaline phosphate–positive (AP+) colonies obtained in a clonal assay. See also fig. S6. (**B**) Clonal assay of ES cells in the indicated culture conditions. For each sample, the number of AP+ colonies, relative to nontargeting siRNA-transfected cells, is indicated. Each bar represents the mean and SEM of at least four independent experiments. (**C**) Rex1GFPd2 flow profile of cells withdrawn from either 2i+LIF or 2i conditions for the indicated time. Cells taken from 2i down-regulate the reporter more rapidly. (**D**) The simplest model of 16 interactions and 12 components required to satisfy all experimental constraints. The complete set of constrained models is shown in fig. S7.

With the refined meta-model, we sought predictions of the response to genetic perturbations in different conditions (Fig. 3A, right, and fig. S6, F and G). In 2i, LIF+CH, and LIF+PD conditions, we found that 17 of 28 tested predictions were correct (Fig. 3A and fig. S6D).

The outcomes of some double knockdowns, including *Esrrb*/*Nanog*, were predicted to be strictly dependent on the culture environment: impeding self-renewal in 2i but not in 2i+LIF (Fig. 3B). Thus, our modeling approach can accurately recapitulate the behavior of the network in response to input signals.

The meta-model predictions suggest that the pluripotency network is less resistant to genetic perturbation in 2i than in 2i+LIF (compare charts in Fig. 3A). We tested whether a similar difference in robustness could be observed upon environmental perturbation. We transferred ES cells from either 2i+LIF or 2i only into unsupplemented medium then, after different periods, performed a clonogenicity assay by replating in 2i+LIF. The number of self-renewing cells declined more rapidly for 2i than 2i+LIF cultures (fig. S6, H and I). Rex1GFP (GFP, green fluorescent protein) was also down-regulated faster from 2i (Fig. 3C). These results suggest that the pluripotent state collapses more readily in 2i ES cells, consistent with the network being less stable than in 2i+LIF.

To identify the simplest among the set of equally valid candidate models constrained using the additional experimental data from knockdowns in 2i+LIF, we explicitly sought those with the fewest interactions. Only 16 interactions between 12 components may be required, because T-box 3 (Tbx3) is dispensable as a regulator of any other component (supplementary materials section S1N). There is only one valid model of this size, representing the minimal possible transcriptional program governing ES cell self-renewal (Fig. 3D). Of note, a repressive effect of Esrrb on Oct4 is required in all of the constrained models.

Our results reveal that ES cell decision-making is not necessarily dependent on a vast gene network, as widely considered, but instead can be explained by a program that, in its simplest version, consists of just 16 interactions, 12 components, and three inputs. This example model from the meta-model identifies the most parsimonious network that could maintain naïve pluripotency under four different culture conditions. Environmental signals are processed via interactions between pluripotency factors to stabilize the gene expression pattern that defines a self-renewing, pluripotent cell. The program itself is unchanging under the action of different inputs but computes the appropriate stable state as a consequence of these inputs. This conclusion is consistent with the proposition that individual cell states are attractors (*20*).

It will be instructive to learn how the current meta-model can be refined further to explain how cells exit from the pluripotent state for differentiation and how this state is generated in the developing embryo or by reprogramming. Furthermore, the general design of our computational approach means that it can be applied to understand biological computation in other cell systems.

REFERENCES AND NOTES

1. J. Nichols, A. Smith, *Cold Spring Harb. Perspect. Biol.* **4**, a008128 (2012).
2. X. Chen *et al.*, *Cell* **133**, 1106–1117 (2008).
3. R. Lu *et al.*, *Nature* **462**, 358–362 (2009).
4. D. L. C. van den Berg *et al.*, *Cell Stem Cell* **6**, 369–381 (2010).
5. A. Som *et al.*, *PLOS ONE* **5**, e15165 (2010).
6. J.-C. Yeo, H.-H. Ng, *Cell Res.* **23**, 20–32 (2013).
7. I. Chambers *et al.*, *Nature* **450**, 1230–1234 (2007).
8. G. Martello *et al.*, *Cell Stem Cell* **11**, 491–504 (2012).
9. G. Martello, P. Bertone, A. Smith, *EMBO J.* **32**, 2561–2574 (2013).
10. Q.-L. Ying *et al.*, *Nature* **453**, 519–523 (2008).
11. J. Silva *et al.*, *Cell* **138**, 722–737 (2009).
12. J. Hall *et al.*, *Cell Stem Cell* **5**, 597–609 (2009).
13. C.-I. Tai, Q.-L. Ying, *J. Cell Sci.* **126**, 1093–1098 (2013).
14. F. Lanner *et al.*, *Stem Cells* **28**, 191–200 (2010).
15. B. Yordanov, C. M. Wintersteiger, Y. Hamadi, H. Kugler, in *NASA Formal Methods: 5th International Symposium, NFM 2013, Moffett Field, CA, USA. May 14–16 2013*, G. Brat, N. Rungta, A. Venet, Eds. (vol. 7871 of Lecture Notes in Computer Science, Springer, New York, 2013), pp. 78–92.
16. B. Wilczyński, N. Dojer, *Bioinformatics* **25**, 286–287 (2009).
17. S. Masui *et al.*, *Nat. Cell Biol.* **9**, 625–635 (2007).
18. N. Ivanova *et al.*, *Nature* **442**, 533–538 (2006).
19. H. Niwa, J. Miyazaki, A. G. Smith, *Nat. Genet.* **24**, 372–376 (2000).
20. T. Enver, M. Pera, C. Peterson, P. W. Andrews, *Cell Stem Cell* **4**, 387–397 (2009).

ACKNOWLEDGMENTS

We thank T. Kalkan, H. Kugler, and S. Dupont for stimulating discussions and comments on this manuscript and B. Simons for reading the manuscript. G.M. was a recipient of a Human Frontier Science Program fellowship. A.G.S. is a Medical Research Council Professor and is also funded by the Wellcome Trust.

SUPPLEMENTARY MATERIALS

www.sciencemag.org/content/344/6188/1156/suppl/DC1
Materials and Methods
Supplementary Text
Figs. S1 to S6
Tables S1 to S3
References (*21*–*32*)

25 November 2013; accepted 7 May 2014
10.1126/science.1248882

PLANT GROWTH

A mutually assured destruction mechanism attenuates light signaling in *Arabidopsis*

Weimin Ni,[1,2]* Shou-Ling Xu,[3,4]* James M. Tepperman,[1,2] David J. Stanley,[3] Dave A. Maltby,[3] John D. Gross,[3] Alma L. Burlingame,[3] Zhi-Yong Wang,[4] Peter H. Quail[1,2]†

After light-induced nuclear translocation, phytochrome photoreceptors interact with and induce rapid phosphorylation and degradation of basic helix-loop-helix transcription factors, such as PHYTOCHROME-INTERACTING FACTOR 3 (PIF3), to regulate gene expression. Concomitantly, this interaction triggers feedback reduction of phytochrome B (phyB) levels. Light-induced phosphorylation of PIF3 is necessary for the degradation of both proteins. We report that this PIF3 phosphorylation induces, and is necessary for, recruitment of LRB [Light-Response Bric-a-Brack/Tramtrack/Broad (BTB)] E3 ubiquitin ligases to the PIF3-phyB complex. The recruited LRBs promote concurrent polyubiquitination and degradation of both PIF3 and phyB in vivo. These data reveal a linked signal-transmission and attenuation mechanism involving mutually assured destruction of the receptor and its immediate signaling partner.

The mechanisms by which cells perceive and adapt to external signals remains an area of central interest in the biosciences. The capacity to respond rapidly and robustly to such signals is frequently coupled to a capacity to subsequently modulate the intensity of that response through feedback attenuation of the signaling process (*1*). Whereas the initial robust burst of signaling activity is presumably necessary for the induction of the consequent adaptational or developmental switch, unfettered prolongation of the elevated activity can be harmful to the organism. A plethora of attenuation mechanisms have been identified (*1*, *2*). Defects in these mechanisms are under increasing scrutiny as evidence increases that they are major causes of human malignancies (*3*).

The initial emergence of seedlings from subterranean darkness into sunlight triggers a rapid and extensive redirection of gene expression that drives a developmental switch from skotomorphogenic to photomorphogenic development, which is observed as the production of normal green seedlings (*4*, *5*). The red and far-red wavelengths inducing this switch are perceived by the phytochrome family of sensory photoreceptors (phyA to phyE) by virtue of a capacity to convert reversibly between biologically inactive Pr (red-absorbing) and biologically active Pfr (far-red-absorbing) conformers (*6*). Photoactivation of the cytoplasmically localized photoreceptors triggers their rapid translocation into the nucleus, where they interact directly with a subfamily of basic helix-loop-helix (bHLH) transcription factors, termed PIFs [Phytochrome-Interacting Factors; PIF1 to PIF8 (*4*, *7*)]. This interaction induces multisite phosphorylation, ubiquitination, and degradation of the PIFs via the 26*S* proteasome system (*4*, *8*–*14*), altering the transcription of target genes within minutes (*4*, *5*, *15*). The PIFs promote skotomorphogenic development in the dark (*16*), but their red-light–induced degradation represses this activity, inducing the switch to the photomorphogenic pathway (*4*).

In addition to their direct function in phytochrome signal transduction, the PIFs also desensitize cells to red light through negative feedback regulation of phyB levels (*17*–*19*). We showed recently that Pfr-induced multisite phosphorylation of PIF3 is not only necessary for the degradation of PIF3, but also for concomitant PIF-interaction–induced degradation of phyB (*8*). Although there is evidence that E3 ligases assembled with COP1 are involved in ubiquitylation and degradation of phyB in a PIF-promoted manner (*20*), the signaling mechanism has remained unclear.

To address this question, we performed mass-spectrometric analysis of affinity-purified PIF3 to identify components associated with PIF3 in a light-dependent manner. Dark-grown seedlings transgenically expressing yellow fluorescent protein (YFP)–PIF3 were either kept in the dark or irradiated with 10 min of red light before protein extraction and affinity purification by using an antibody to green fluorescent protein (GFP). Quantitative spectral count analysis, not unexpectedly, identified all five phytochromes (phyA to phyE) specifically in the red light–treated samples (table S1). In addition, components of a Bric-a-Brack/Tramtrack/Broad (BTB)–Cullin3-type E3 ubiquitin ligase were also identified as red-light–specific, PIF3-interacting proteins in three biological replicates (table S1 and fig. S1). BTB proteins are substrate-specific proteins that bridge target proteins to Cullin3 for ubiquitin ligation (*21*, *22*). The two highly conserved BTB proteins [Light-Response-BTB1 (LRB1) and LRB2] identified here were shown previously to be nuclear-localized and required genetically for proteasome-mediated phyB protein degradation in the light, but whether the involvement is direct or indirect was not determined (*23*). A third LRB homolog (LRB3) was not detected in our mass spectrometric analysis, possibly because of the lower expression level than those of the other two (*23*).

To further investigate the light-dependent interaction of PIF3 with the LRBs in vivo, we generated transgenic lines expressing both PIF3:MYC and YFP:LRB2. Immunoprecipitation using YFP:LRB2 as bait showed considerably higher levels of PIF3:MYC

[1]Department of Plant and Microbial Biology, University of California, Berkeley, Berkeley, CA 94720, USA. [2]Plant Gene Expression Center, Agriculture Research Service (ARS), U.S. Department of Agriculture (USDA), Albany, CA 94710, USA. [3]Department of Pharmaceutical Chemistry, University of California, San Francisco, San Francisco, CA 94143, USA. [4]Department of Plant Biology, Carnegie Institution for Science, Stanford, CA 94305, USA.
*These authors contributed equally to this work. †Corresponding author. E-mail: quail@berkeley.edu

coprecipitation from red-treated than dark-control seedlings (Fig. 1A). The red-treated samples also displayed enrichment of the mobility-shifted forms of PIF3:MYC in the immunoprecipitates compared with the input (Fig. 1A), suggesting preferential binding of in vivo–phosphorylated PIF3 to the LRB protein. Together with previous evidence that red light induces LRB-Cullin3 interaction in vivo (*23*), our present findings indicate that this interaction is promoted by light-induced binding of phospho-PIF3 to the LRBs.

In vitro pulldown assays with recombinant LRB2:MYC as bait were also performed to further probe the molecular mechanism of the interaction with PIF3. Because phyB does not display autonomous light-activated protein kinase activity toward PIF3 in our hands, and no other kinase has been identified, we examined the LRB-binding behavior of a set of mutant PIF3 variants. Previously, using mass spectrometric analysis and transgenic expression of targeted missense mutants of PIF3, we identified 20 light-induced phosphorylated residues in the protein that are functionally necessary for its rapid degradation in vivo (*8*). When expressed in a Hela cell lysate, the phospho-dead PIF3 mutant protein (A20) showed no apparent binding to LRB2, whereas PIF3 with phospho-mimic mutations in the majority of the light-induced residues (D19), or simply the six most strongly light-induced residues (D6), exhibited high binding affinity toward LRB2 (Fig. 1B). The absence of binding to PIF3-A6 and YFP-MYC further supports the specificity of phosphorylation-dependent binding of LRB2 to PIF3 (Fig. 1C). The in vitro–expressed wild-type PIF3 intrinsically displayed multiple bands, which is reminiscent of the pattern from light-treated seedlings, and only the slower migrating form showed high affinity for LRB2 through coimmunoprecipitation (Fig. 1, B and C). Moreover, the slower migrating band of wild-type PIF3 was sensitive to alkaline phosphatase treatment (Fig. 1, B and D). These results suggest that recombinant wild-type PIF3 expressed in Hela cell lysates is phosphorylated by an unknown kinase in the lysate. Moreover, it appears that one or more of the strongly light-induced sites (*8*) in PIF3 is phosphorylated by this kinase because the PIF3-A6 variant, mutated at six of

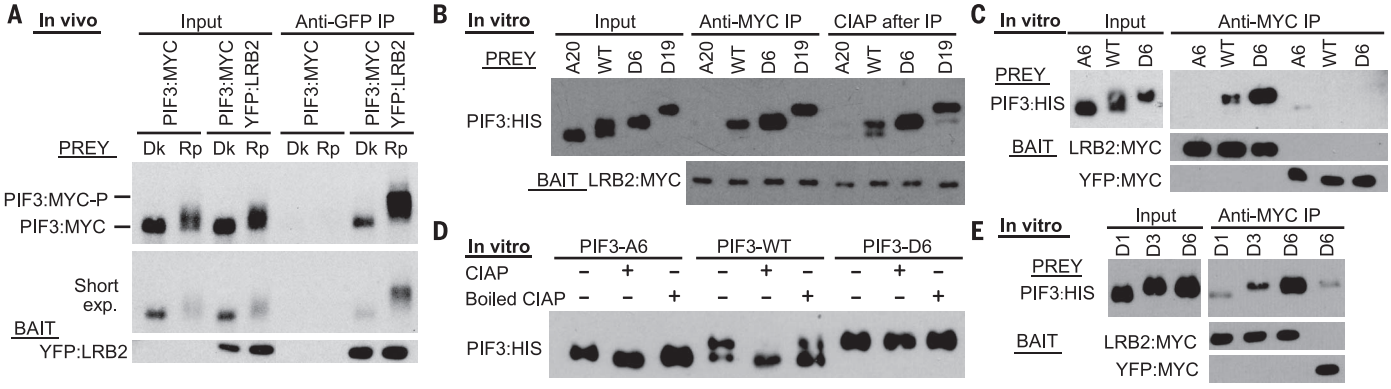

Fig. 1. Light-induced phosphorylation of PIF3 promotes interaction with Cullin E3-ligase substrate-recognition subunit LRB2. (**A**) Light induces LRB2 and PIF3 interaction in vivo. Dark-grown seedlings from either PIF3:MYC or PIF3:MYC/YFP:LRB2 double-transgenic lines were pretreated with MG132 then either kept in the dark (Dk) or irradiated with a pulse of red light (Rp) before protein extraction and coimmunoprecipitation (Co-IP) with an antibody to GFP. The proteins were analyzed by means of Western blot with antibody either to MYC (Prey, top and middle) or to GFP (Bait, bottom). (**B** to **D**) Phosphorylation or phosphomimic mutations of the light-induced phosphosite residues in PIF3 promote its association with LRB2 in vitro. In (B) and (C), in vitro–expressed recombinant LRB2 or YFP-control (Bait) proteins were precipitated with a MYC antibody then incubated with normal [wild-type (WT)] PIF3 or the indicated light-induced–phosphosite mutant variants (A6, A20, D6, and D19) of PIF3 (Prey). Bait and prey proteins were detected by means of Western blot with antibody to MYC and to His, respectively. All proteins were expressed in Hela cell lysate. A, Ser/Thr to Ala substitutions; D, Ser/Thr to Asp substitutions; A6/D6, PIF3 with substitutions in the six strongly light-induced phosphosite residues (fig. S4A) (*8*); A20/D19, PIF3 with substitutions in the majority of the light-induced phosphosite residues. Co-IP products were treated with alkaline phosphatase (CIAP) in (B). (D) PIF3-A6, PIF3-WT, or PIF3-D6 expressed in Hela cell lysates were either treated (+) or not (–) with CIAP or with heat-inactivated CIAP before Western blot analysis with antibody to His. (**E**) High-affinity interaction of LRB2 and PIF3 in vitro requires multisite phosphorylation of PIF3. Immunoprecipitations and Western blots are as in (C). PIF3 mutant-variant substitutions are D1, S88D; D3, S58/S88/S102D. All S to A or D substitutions are provided in fig. S4A.

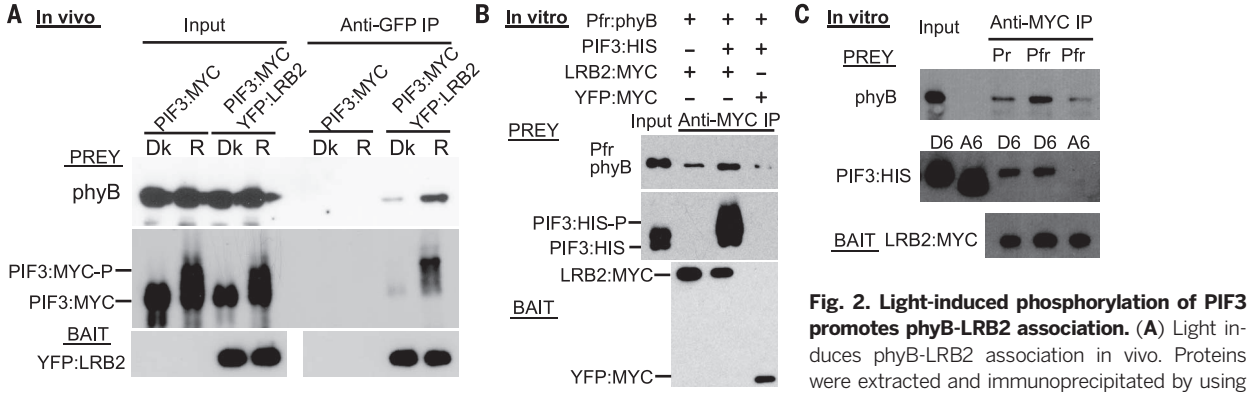

Fig. 2. Light-induced phosphorylation of PIF3 promotes phyB-LRB2 association. (**A**) Light induces phyB-LRB2 association in vivo. Proteins were extracted and immunoprecipitated by using the same lines and procedure as in Fig. 1A and then subjected to Western blot analysis by using antibody to phyB (Prey, top), to MYC (Prey, middle), or to GFP (Bait, bottom). (**B**) Phosphorylated PIF3 promotes phyB-LRB2 association in vitro. In vitro–expressed recombinant LRB2:MYC or YFP:MYC-control bait proteins were incubated with phyB-Pfr in the presense (+) or absence (–) of PIF3:His prey proteins and immunoprecipitated with antibody to MYC. Western blots were probed with antibody to phyB (top), to His-epitope (middle) or to MYC (bottom). (**C**) PIF3-D6 phosphomimic (fig. S4A) (*8*) promotes Pfr-dependent phyB-LRB2 association in vitro. In vitro–expressed recombinant LRB2:MYC bait protein was incubated with phyB (as Pr or Pfr) and PIF3:His [D6- or A6-mutant (fig. S4A) (*8*)] prey proteins and immunoprecipitated with antibody to MYC. Western blots are as in (B).

these sites, did not have a similarly slower migrating form (Fig. 1, C and D). In addition, in vitro pulldown assays with LRB2 as prey also indicated that PIF3-WT, D6, and D19, but not A20, bind LRB2 with high affinity (fig. S2) and that both LRB1 and LRB3 are able to bind PIF3-D6 with high affinity in vitro, similarly to LRB2 (fig. S3).

Because the six most strongly light-induced phosphosites in PIF3 are predominantly responsible for rapid degradation in vivo (*8*), we tested here whether binding to LRB2 in vitro also requires these multiple phospho-sites. Phosphomimic substitutions in individual (variants 1, D1, or 3) or three (variants 4 or D3) of these sites were introduced into the PIF3-A6 sequence (fig. S4A). In vitro pulldown assays showed that none of these mutant variants has LRB2 binding affinity comparable with that of PIF3-D6 (Fig. 1E and fig. S4B), suggesting that high-affinity binding to LRB2 requires between three and six light-induced phosphosites in PIF3. In addition, PIF3-D6 showed relatively low binding to either the N- or C- terminal domain of LRB2 (fig. S5B), suggesting that determinants in both domains are required for its strong binding to PIF3. These data favor the model that the cooperative action of multiple low-affinity sites between PIF3 and LRBs enable light-induced degradation of PIF3, similar to that proposed for yeast Sic1 degradation (*24*).

Because light-induced phosphorylation of PIF3 is also required for its negative feedback-regulation of phyB levels, despite not being required for phyB-PIF3 binding per se (*8*), we examined the possibility that phosphorylated PIF3 bridges the interaction of LRBs and phyB-Pfr in vivo. Pull-down

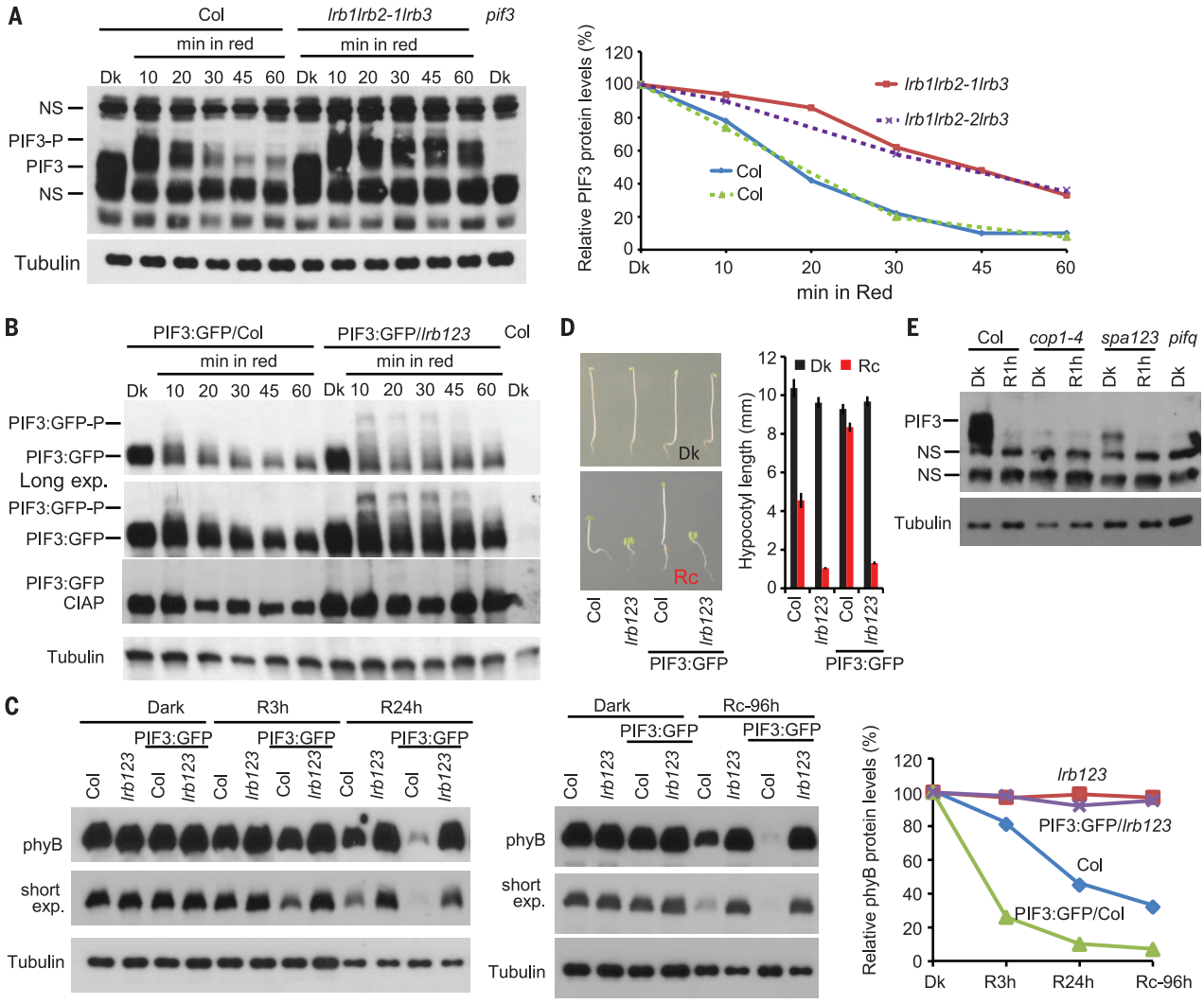

Fig. 3. LRBs function in both PIF3 and PIF3-mediated–phyB degradation in the light. (**A**) Endogenous PIF3 degradation is reduced in the *lrb1lrb2lrb3* triple-mutant (*lrb123*) compared with Col WT seedlings in the light. Dark-grown seedlings of Col and *lrb123* were irradiated with red light (R) for the period indicated before protein extraction and Western blot analysis with antibody to PIF3 (left). PIF3, unphosphorylated PIF3; PIF3-P, phosphorylated PIF3; NS, nonspecific bands. Right shows the quantification of the Western blot results from both left (blue and red curves) and fig. S6B (green and purple curves) after normalization to the Tubulin loading control. The dark PIF3 level was set as 100%. (**B**) PIF3:GFP accumulates in the phosphorylated form in the *lrb123* triple mutant in the light. Seedling growth was as in (A). Extracted proteins were either analyzed directly (top and top middle) or after phosphatase (CIAP) treatment (bottom middle) by means of Western blot with antibody to GFP. (**C**) LRBs are essential for light-induced, PIF3-promoted feedback degradation of phyB. Light-induced degradation of phyB (accelerated by PIF3:GFP overexpression) is absent in the *lrb123* mutant background. Dark-grown seedlings of the indicated genotypes were irradiated with 3 (R3h), 24 (R24h), or 96 (Rc96h) hours of continuous red light before protein extraction and Western blot analysis with an antibody to phyB (left and middle). Tubulin was used as a loading control. Right shows the quantification of the relative phyB/Tubulin protein levels shown to left and middle. Dark levels were set as 100%. (**D**) PIF3:GFP overexpression does not complement the short-hypocotyl phenotype of the *lrb123* mutant in the light. Seedlings of the indicated genotypes were grown for 4 days in the dark (Dk) or continuous red light (Rc). Visible phenotypes are shown at left; hypocotyl lengths are shown at right. Error bars represent SE. (**E**) Endogenous PIF3 levels are strongly reduced in dark-grown seedlings of the *cop1* and *spa123* mutants.

assays from seedling extracts with YFP:LRB2 as bait showed light-dependent coimmunoprecipitation of phyB and PIF3 with LRB2 (Fig. 2A). In vitro binding assays indicated that LRB2 itself has some apparent affinity for phyB-Pfr alone, but that PIF3 binding enhances LRB2-phyB-Pfr association (Fig. 2, B and C).

To examine the functional role of the LRBs in PIF3 and PIF3-mediated–phyB degradation, we used a set of single, double, and triple *lrb* mutants (*23*). Dark-grown seedlings of both the *lrb3* single and *lrb1lrb2* double mutants have normal PIF3 protein levels and normal light-induced PIF3 degradation (fig. S6A). In contrast, the *lrb1lrb2lrb3* (*lrb123*) triple mutant exhibits a reduced rate of light-induced endogenous PIF3 degradation (Fig. 3A and fig. S6, B and C). In addition, the light-induced, slower-migrating forms of PIF3 display accumulation in the *lrb123* triple mutant, compared with rapid degradation in the wild type (Fig. 3A and fig. S6B). A similar pattern was observed for a PIF3:GFP fusion protein transgenically expressed under control of the constitutive CaMV *35S* promoter in the *lrb123* mutant background (Fig. 3B, top and top middle, and fig. S6C), indicating that LRB regulation is exerted at the posttranslational level. Phosphatase treatment reversed the mobility shift of the accumulated slower migrating PIF3:GFP bands (Fig. 3B, bottom middle). These data indicate that PIF3 accumulates in the phosphorylated form in the light when the LRBs are mutated. The reason for the retention of higher relative levels of PIF3:GFP than endogenous PIF3 in prolonged red light (fig. S6C) is undetermined but could reflect the higher absolute levels of PIF3:GFP than endogenous PIF3.

We showed previously that overexpression of PIF3 markedly accelerates the rate of phyB degradation in response to light (*8*). This finding indicates that the absolute rate of PIF3 degradation is rate-limiting to the concurrent degradation of phyB. Because the relative rate of phyB degradation is only ~2% that of PIF3 in the wild-type seedling (*8*, *18*, *19*, *25*), this observation suggests in turn that phyB is substantially more abundant than PIF3. The data for phyB in the Col wild type and the Col transgenic line overexpressing PIF3:GFP in Fig. 3C support this notion, showing the accelerated degradation of phyB in the overexpressor line. However, the light-induced degradation of phyB is absent in both the *lrb12* double (fig. S6D) and *lrb123* triple (Fig. 3C) mutants, with or without overexpression of PIF3:GFP, in the latter case. These data are consistent with previous evidence for the *lrb* mutants (*23*) and establish that LRB1 and LRB2 are essential for the PIF3-mediated, light-induced degradation of phyB. The absence of accelerated phyB degradation by overexpression of the PIF3-A20 variant (*8*) that cannot bind LRB2 (Fig. 1B) is similarly in agreement with this conclusion.

The morphogenic phenotypes of these lines are consistent with these findings. Whereas seedlings overexpressing PIF3 in wild-type Col show an etiolated-like phenotype in the light, seedlings overexpressing a similarly high or higher level of PIF3:GFP or endogenous PIF3 in the *lrb123* mutant (Fig. 3, A and B, and fig. S6C) remain hypersensitive to red light, like the *lrb123* mutant itself (Fig. 3D) (*23*). These data are in accord with the levels of phyB in these lines under prolonged red light (Fig. 3C), in which the depletion of phyB in the wild-type Col PIF3-overexpressor results in hyposensitivity to the light signal, and the stability of phyB in the *lrb123* background (*23*) results in hypersensitivity, despite high levels of PIF3 (Fig. 3, A and B, and fig. S6C). These results indicate that the suppressive activity of high phyB levels overrides the antagonistic promotive activity of PIF3 on hypocotyl growth (*17*). This effect could result from phyB activity independent of PIF3, reduced intrinsic activity of PIF3, or phyB-induced dissociation of PIF3 from its DNA binding sites.

COP1-assembled E3 ligases were reported to be an important negative regulator of phyB levels (*20*). However, in agreement with other data (*14*, *16*) we observed that PIF3 levels are reduced in dark-grown seedlings of both the *cop1* and *spa123* mutants, and no accumulation is observed in the light (Fig. 3E). These data suggest that the reduction in light-induced phyB degradation in the *cop1* mutant partially is due to an indirect effect of the reduced levels of PIF3 (and possibly other PIFs) initially present in the dark. Regardless, the absence of detectable light-induced phyB degradation in the *lrb123* mutant (Fig. 3C) indicates that COP1 is not sufficient for phyB degradation in the absence of the LRBs. Consistent with previous data that LRB1 and LRB2 are not directly involved in phyA degradation (*23*), we found that LRB3 also has no detectable role (fig. S7).

Regulated protein degradation through the 26*S* proteasome requires E3 ligase-mediated polyubiquitination of target proteins (*21*, *22*). In support of the LRBs being components of an E3 ligase responsible for PIF3 polyubiqutination, light-induced ubiquitination of PIF3:GFP (fig. S8) is reduced in the *lrb123* mutant (Fig. 4A). Moreover, photoactivated phyB, which coimmunoprecipitates with PIF3:GFP from extracts of light-treated seedlings, also displays high–molecular weight–shifted bands in wild-type but not in *lrb123* mutant seedlings (Fig. 4B), which is suggestive of a subfraction of light-dependent, LRB-generated polyubiquitinated phyB molecules. More definitively, precipitation of total ubiquitinated proteins from the seedling extracts—followed by immunoblot detection of either phyB, PIF3:GFP, or endogenous PIF3—

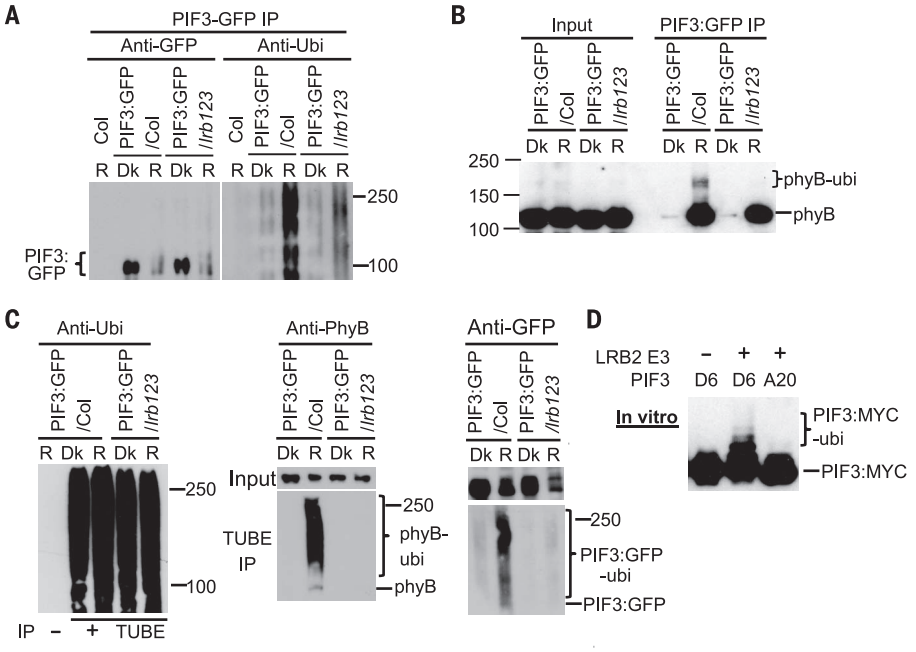

Fig. 4. LRB E3 ligases function in polyubiquitination of both PIF3 and phyB. (**A**) Light-induced polyubiquitination of PIF3 is reduced in the *lrb123* mutant. Dark-grown wild-type (col) or *lrb123*-mutant seedlings, transgenically, or not, expressing PIF3:GFP (PIF3:GFP/col and PIF3:GFP/*lrb123*, respectively) were irradiated with 10 min of red light (R), or not (Dk), before protein extraction and immunoprecipitation (IP) with antibody to GFP. The IP products were then analyzed by means of Western blot with antibody to GFP (left) or to ubiquitin (right). (**B**) Light-induced mobility shift of PIF3-bound phyB (phyB-ubi) is absent in the *lrb123* mutant. Co-IP products prepared as in (A) were analyzed with antibody to phyB. (**C**) Light-induced polyubiquitination of both phyB and PIF3 is strongly reduced in the *lrb123* mutant. Seedling growth and extraction was as in (A). Total ubiquitinated proteins were immunoprecipitated with TUBEs (tandem ubiquitin binding entities), then analyzed by means of Western blot with antibody to ubiquitin (left), to phyB (middle), or to GFP (right). (**D**) A Cullin3-LRB2 E3 ubiquitin-ligase complex ubiquitinates phosphomimic PIF3 (D6) in vitro. A Cullin3 E3 ubiquitin ligase complex was assembled with recombinant LRB2 protein and incubated with D6 or A20 PIF3:MYC (D6 is provided in fig. S4A) (*8*) variants in vitro (supplementary materials, materials and methods) before Western blot analysis with antibody to MYC.

indicates that both phyB and PIF3 are polyubiquitinated in the wild-type in the light and that this concomitantly induced, bimolecular ubiquitination is undetectable (Fig. 4C) or markedly reduced (fig. S9) in the *lrb123* mutant.

Last, to examine whether LRB2 has the capacity to directly catalyze ubiquitination of PIF3, we assembled a Cullin3-based E3 ligase complex in vitro using recombinant LRB2 and human Cullin3/RBX1 and performed an in vitro ubiquitination assay. The data show that this complex can indeed ubiquitinate PIF3 in a phosphomimic-dependent manner, which is consistent with its PIF3 recognition mechanism and confirms its biochemical function (Fig. 4D and fig. S10). Although the evidence for LRB-dependent, light-induced ubiquitination of phyB in vivo is compelling (Fig. 4C), for undetermined reasons we were unable to detect such activity using the above in vitro assay.

We propose a mechanistic model (fig. S11), in which light-activated phyB induces multisite phosphorylation of PIF3 upon direct binding, enhancing the affinity of PIF3 for the LRBs, which then bind to Cul3, forming an active E3 ligase complex, which ubiquitinates both PIF3 and phyB, targeting them for degradation by the 26*S* proteasome. This mechanism of attenuation thus embodies a mutually assured destruction configuration of bidirectional signaling, directly at the receptor–primary-signaling-partner interface, that is unusual among reported mechanisms (*1*–*3*). Indicative of additional complexity, however, whereas light-induced phyB ubiquitination and degradation is essentially eliminated in the *lrb123* mutant, light-induced PIF3 ubiquitination and degradation is slowed but not eliminated (Figs. 3 and 4 and fig. S6, C and D). This observation suggests the existence of partial functional redundancy between the LRBs and yet another unknown E3 ligase (or ligases) for PIF3 degradation and uncovers a dichotomy between PIF3 and phyB regulation.

REFERENCES AND NOTES

1. R. Avraham, Y. Yarden, *Nat. Rev. Mol. Cell Biol.* **12**, 104–117 (2011).
2. Y. Yarden, *Oncologist* **15**, (Suppl 5), 1–7 (2010).
3. I. Amit *et al.*, *Nat. Genet.* **39**, 503–512 (2007).
4. P. Leivar, P. H. Quail, *Trends Plant Sci.* **16**, 19–28 (2011).
5. Y. Jiao, O. S. Lau, X. W. Deng, *Nat. Rev. Genet.* **8**, 217–230 (2007).
6. N. C. Rockwell, Y. S. Su, J. C. Lagarias, *Annu. Rev. Plant Biol.* **57**, 837–858 (2006).
7. M. Ni, J. M. Tepperman, P. H. Quail, *Nature* **400**, 781–784 (1999).
8. W. Ni *et al.*, *Plant Cell* **25**, 2679–2698 (2013).
9. H. Shen *et al.*, *Plant Cell* **20**, 1586–1602 (2008).
10. S. Lorrain, T. Allen, P. D. Duek, G. C. Whitelam, C. Fankhauser, *Plant J.* **53**, 312–323 (2008).
11. G. Bae, G. Choi, *Annu. Rev. Plant Biol.* **59**, 281–311 (2008).
12. Y. Shen, R. Khanna, C. M. Carle, P. H. Quail, *Plant Physiol.* **145**, 1043–1051 (2007).
13. B. Al-Sady, W. Ni, S. Kircher, E. Schäfer, P. H. Quail, *Mol. Cell* **23**, 439–446 (2006).
14. D. Bauer *et al.*, *Plant Cell* **16**, 1433–1445 (2004).
15. Y. Zhang *et al.*, *PLOS Genet.* **9**, e1003244 (2013).
16. P. Leivar *et al.*, *Curr. Biol.* **18**, 1815–1823 (2008).
17. P. Leivar, E. Monte, M. M. Cohn, P. H. Quail, *Mol. Plant* **5**, 734–749 (2012).
18. B. Al-Sady, E. A. Kikis, E. Monte, P. H. Quail, *Proc. Natl. Acad. Sci. U.S.A.* **105**, 2232–2237 (2008).
19. R. Khanna *et al.*, *Plant Cell* **19**, 3915–3929 (2007).
20. I. C. Jang, R. Henriques, H. S. Seo, A. Nagatani, N. H. Chua, *Plant Cell* **22**, 2370–2383 (2010).
21. Z. Hua, R. D. Vierstra, *Annu. Rev. Plant Biol.* **62**, 299–334 (2011).
22. R. J. Deshaies, C. A. Joazeiro, *Annu. Rev. Biochem.* **78**, 399–434 (2009).
23. M. J. Christians, D. J. Gingerich, Z. Hua, T. D. Lauer, R. D. Vierstra, *Plant Physiol.* **160**, 118–134 (2012).
24. X. Tang *et al.*, *Proc. Natl. Acad. Sci. U.S.A.* **109**, 3287–3292 (2012).
25. E. Monte *et al.*, *Proc. Natl. Acad. Sci. U.S.A.* **101**, 16091–16098 (2004).

ACKNOWLEDGMENTS

We thank R. J. Chalkley, A. Pfeiffer, M. Zhuang, and B. A. Schulman for materials and technical assistance and S. McCormick for comments on the manuscript. We also thank the Salk Institute and Arabidopsis Biological Resource Center for the *Arabidopsis* T-DNA insertion lines. The plasmid pGEX-CUL3 (split 'n' coexpress)–Rbx1 used in the in vitro ubiquitination assays was provided by B. A. Schulman under a materials transfer agreement with St. Jude Children's Research Hospital. For access to this reagent, contact B. A. Schulman. The supplementary materials contain additional data. This work was supported by the National Institutes of Health (NIH) (2R01 GM-047475), the U.S. Department of Energy (DOE) (DEFG03-87ER13742), and USDA ARS Current Research Information System (5335-21000-032-00D) to P.H.Q; by NIH (5R01GM066258) and DOE (DEFG02-08ER15973) to Z.Y.W.; by NIH (8P41GM103481) to A.L.B; and by NIH (P50 GM082250) to J.D.G.

SUPPLEMENTARY MATERIALS

www.sciencemag.org/content/344/6188/1160/suppl/DC1
Materials and Methods
Figs. S1 to S11
Tables S1 and S2
References (*26*, *27*)

13 January 2014; accepted 13 May 2014
10.1126/science.1250778

MEMBRANE BIOLOGY

Caspase-mediated cleavage of phospholipid flippase for apoptotic phosphatidylserine exposure

Katsumori Segawa,[1] Sachiko Kurata,[1] Yuichi Yanagihashi,[1] Thijn R. Brummelkamp,[2] Fumihiko Matsuda,[3] Shigekazu Nagata[1,4]*

Phospholipids are asymmetrically distributed in the plasma membrane. This asymmetrical distribution is disrupted during apoptosis, exposing phosphatidylserine (PtdSer) on the cell surface. Using a haploid genetic screen in human cells, we found that ATP11C (adenosine triphosphatase type 11C) and CDC50A (cell division cycle protein 50A) are required for aminophospholipid translocation from the outer to the inner plasma membrane leaflet; that is, they display flippase activity. ATP11C contained caspase recognition sites, and mutations at these sites generated caspase-resistant ATP11C without affecting its flippase activity. Cells expressing caspase-resistant ATP11C did not expose PtdSer during apoptosis and were not engulfed by macrophages, which suggests that inactivation of the flippase activity is required for apoptotic PtdSer exposure. CDC50A-deficient cells displayed PtdSer on their surface and were engulfed by macrophages, indicating that PtdSer is sufficient as an "eat me" signal.

In eukaryotic cells, phospholipids are asymmetrically distributed between the outer and inner leaflets of the plasma membrane (*1*). Phosphatidylcholine (PtdCho) and sphingomyelin are located primarily in the outer leaflet, whereas phosphatidylserine (PtdSer) and phosphatidylethanolamine (PtdEtn) are restricted to the cytoplasmic leaflet. Disruption of asymmetrical phospholipid distribution—in particular, PtdSer exposure on the cell surface—is important in various biological processes. For example, platelet activation leads to PtdSer exposure, which in turn activates clotting factors (*1*), and apoptotic cells expose PtdSer as a signal to be engulfed by phagocytes (*2*). Scramblases nonspecifically transport phospholipids bidirectionally (*1*). TMEM16F is essential for PtdSer exposure in activated platelets (*3*), whereas Xkr8 (XK-related protein 8) supports phospholipid scrambling after being cleaved by caspase during apoptosis (*4*). Flippases transport aminophospholipids from the extracellular to the cytoplasmic side (*1*). Some members (mammalian ATP8A1 and its orthologs in yeast and *Caenorhabditis elegans*, and ATP11C) of the type 4 subfamily of P-type adenosine triphosphatases (P4-ATPases) have been proposed to act as flippases (*5*–*8*). Earlier studies reported that the flippase is inactivated during apoptosis (*9*, *10*), but its identity is unclear, as is the mechanism of its inactivation.

[1]Department of Medical Chemistry, Graduate School of Medicine, Kyoto University, Yoshida-Konoe, Kyoto 606-8501, Japan. [2]Netherlands Cancer Institute, Plesmanlaan 121, 1066 CX Amsterdam, Netherlands. [3]Center for Genomic Medicine, Graduate School of Medicine, Kyoto University, Yoshida-Konoe, Kyoto 606-8501, Japan. [4]Core Research for Evolutional Science and Technology, Japan Science and Technology Corporation, Kyoto 606-8501, Japan.
***Corresponding author. E-mail: snagata@mfour.med.kyoto-u.ac.jp**

We used a haploid genetic screen in human KBM7 cells (*11*) to identify the plasma membrane PtdSer flippase. KBM7 cells incorporated 1-oleoyl-2-{6-[(7-nitro-2-1,3-benzoxadiazol-4-yl)amino]hexanoyl}-*sn*-glycero-3-PtdSer (NBD-PS), NBD-PtdEtn (NBD-PE), and NBD-PtdCho (NBD-PC) with different efficiencies (Fig. 1A). KBM7 cells were mutagenized with a gene trap vector. About 1.0% of the cells defective in NBD-PS internalization were expanded and subjected to a second sorting step to obtain "low flipping" (LF) cells (Fig. 1B). Gene trap insertion sites were recovered by polymerase chain reaction from LF cells and identified by deep sequencing (*12*). A proximity index (*12*) for genomic regions containing multiple insertions in close proximity identified two genes: *CDC50A* (cell division cycle protein 50A) and *ATP11C* (ATPase type 11C) (Fig. 1B). Information from a genome database (http://genome.ucsc.edu/cgi-bin/hgTracks?org=human) and 5′-RACE (rapid amplification of cDNA end) analysis (fig. S1) indicated that most of the insertions were assigned to intron 1 in the transcriptional direction (Fig. 1C).

ATP11C is a member of the P4-ATPase family, and CDC50A is its β subunit (fig. S2A) (*13*, *14*). They were expressed in various tissues (fig. S2B). Cloned cell lines (ATP11C^{GT} and CDC50A^{GT}) that lost the expression of *ATP11C* or *CDC50A* (fig. S2C) were isolated. The ability to incorporate NBD-PS and NBD-PE, but not NBD-PC, was reduced in ATP11C^{GT} cells; transformation with human (h)*ATP11C* rescued this ability (Fig. 1D). The incorporation of phospholipids in ATP11C^{GT} was inhibited by orthovanadate (Fig. 1E), which suggests that the remaining flippase activity was due to other P4-ATPases in KBM7 cells (fig. S2D). Among three members, only *CDC50A* was expressed in KBM7 cells (fig. S2D), and the internalization of NBD-PS was completely defective in CDC50A^{GT} cells but could be rescued with h*CDC50A* (Fig. 1D). CDC50A^{GT} cells, but not ATP11C^{GT} cells, exposed PtdSer on the cell surface (Fig. 1F); this result suggests that the residual PtdSer flippase in ATP11C^{GT} cells was sufficient to maintain asymmetrical PtdSer distribution. The ability to internalize NBD-PC was also reduced in CDC50A^{GT} cells (Fig. 1D), indicating that some P4-ATPases in KBM7 cells may promote PtdCho flipping.

To study the effect of the PtdSer flippase on apoptotic PtdSer, we chose mouse W3 cells that undergo apoptosis upon treatment with Fas ligand (FasL) (*15*). W3 cells expressed several P4-ATPases (fig. S3A) and incorporated NBD-PS, NBD-PE, and NBD-PC with different efficiencies (fig. S3B). *ATP11C* in W3 cells was mutated using the CRISPR/Cas (clustered regulatory interspaced short palindromic repeats/CRISPR-associated) system (*16*) (fig. S3C). Two cloned cell lines (ATP11C^{ED22} and ATP11C^{ED23}) carrying biallelic ATP11C truncations lost the ability to internalize NBD-PS and NBD-PE (Fig. 2A and fig. S3D). Apoptotic PtdSer exposure is accompanied by the loss of PtdSer flippase activity (*9*, *10*). Treating W3 cells with FasL reduced ATP11C from 120 to 50 kD (Fig. 2B); this reduction was prevented by a caspase inhibitor, QVD-OPh [quinolyl-valyl-*O*-methylaspartyl-(2,6-difluorophenoxy)-methyl ketone]. A search using Cascleave (http://sunflower.kuicr.kyoto-u.ac.jp/~sjn/Cascleave) revealed three caspase recognition sequences (sites 1 to 3) in the nucleotide-binding (N) domain of hATP11C (fig. S4A). Mutants in sites 1 to 3 were generated (fig. S4B), tagged by green fluorescent protein (GFP) at the C terminus, and expressed in *ATP11C*^{ED22} cells. The transformants were treated with FasL and analyzed by immunoblotting with antibodies to GFP (Fig. 2C). The FasL treatment caused a shift of the wild-type and doubly mutated hATP11C-GFP from 140 to 80 kD. But little cleavage was observed with the triply mutated hATP11C-GFP (*CasR*). Incubation of the membrane fraction carrying hATP11C-GFP with caspases revealed that hATP11C was cleaved by caspases 3, 6, and 7 (fig. S5). ATP11C^{ED22} cells expressing *CasR* (ATP11C^{ED22}-*CasR*) incorporated NBD-PS as efficiently as those expressing wild-type *ATP11C* (ATP11C^{ED22}-*hATP11C*) (Fig. 2D) and could not expose PtdSer upon FasL treatment (Fig. 2E), although caspase-3 was activated (Fig. 2E). Transformation of W3-Ildm cells [a derivative of W3 cells (*17*)] and human Jurkat cells with *CasR*, but not with wild-type h*ATP11C*, blocked the FasL-induced PtdSer exposure (fig. S6). CasR had no effect on the FasL-induced scramblase, as measured by NBD-PC incorporation (Fig. 2F). FasL-induced cell death, cell shrinkage, and DNA fragmentation were also normal in *CasR*-expressing cells (fig. S7). The FasL-treated W3-Ildm cells and the h*ATP11C* transformants were efficiently engulfed by thioglycollate-elicited peritoneal macrophages (thio-pMacs), whereas the *CasR* transformants were not (Fig. 2G); this suggests that the flippase must be inactivated by caspase for engulfment of apoptotic cells.

CDC50A was then mutated using the CRISPR/Cas system in W3-Ildm cells that expressed only CDC50A in the CDC50 family (fig. S8A). Cloned cell lines (CDC50A^{ED29} and CDC50A^{ED62}) carrying a biallelic truncation (fig. S8B) could not support the localization of hATP11C-GFP at the plasma membrane (Fig. 3A), could not internalize NBD-PS (Fig. 3B), and exposed PtdSer (Fig. 3C and fig. S9A). Transformation of CDC50A^{ED} cells with h*CDC50A* supported the localization of ATP11C at the plasma membrane, rescued the flippase activity, and blocked PtdSer exposure, confirming the chaperone-like function of CDC50 for P4-ATPase (*5*, *13*, *14*). W3 cells expressing a constitutively active form of TMEM16F (D430G-L) (*3*, *18*) internalized NBD-PS (Fig. 3B) and bound MFG-E8, a PtdSer-binding protein (*19*), in HEPES-buffered saline containing 2.5 mM $CaCl_2$ but not in Iscove's modified Dulbecco's medium with 10% fetal calf serum (IMDM–10% FCS) (Fig. 3D). In contrast, CDC50A^{ED} cells bound MFG-E8 in IMDM–10% FCS. Observation by microscope confirmed the binding of MFG-E8 to CDC50A^{ED} cells. The doubling time of CDC50A^{ED29} cells (13.7 ± 0.14 hours) was slightly longer than that of W3-Ildm cells (12.2 ± 0.39 hours) (fig. S9B), but CDC50A^{ED29} cells responded normally to FasL for apoptosis (fig. S9C).

When living CDC50A^{ED} cells were cultured with thio-pMacs in medium containing 1.0% methylcellulose, more than 20% of the macrophages engulfed CDC50A^{ED} cells (Fig. 4A). The thio-pMacs did not engulf W3-Ildm cells, W3-D430G-L cells, or CDC50A^{ED}-h*CDC50A* cells. The engulfment of CDC50A^{ED} cells was inhibited by D89E [a mouse MFG-E8 (milk fat globule EGF factor 8) mutant carrying a point mutation in the RGD domain], which masks PtdSer (*19*). Similar to the engulfment of apoptotic cells (*20*), living CDC50A^{ED} cells were not engulfed by *MerTK*$^{-/-}$ thio-pMacs (Fig. 4B). Among 132 engulfment events observed (Fig. 4C and movies S1 and S2), about 80% were with living cells, while 20% involved apoptotic cells. As reported for the entosis of epithelial cells (*21*), the engulfment of living CDC50A^{ED} cells was reversible until a certain point. About 3% of the engulfed cells were released from the macrophages before they were transferred into lysosomes (Fig. 4D and movie S3). The release of engulfed cells was not observed with caspase-positive cells. Examination with electron microscopy showed that the engulfed living cells had a swollen morphology (Fig. 4E) different from the apoptotic cells with a condensed morphology. Engulfment of living PtdSer-exposing cells by thio-pMacs was also observed with *CDC50A*-null KBM7 cells (fig. S10). Subcutaneous transplantation of W3-Ildm cells into nude mice induced tumors in 8 of 11 recipients, and the tumor size was approximately 4.3 g after 4 weeks (Fig. 4F). CDC50A^{ED} cells, but not their h*CDC50A* transformants, lost the ability to induce tumors, which suggests that CDC50A^{ED} cells were cleared in vivo.

Our results show that ATP11C can function as a PtdSer flippase at the plasma membrane. *ATP11C*-deficient KBM7 cells and W3 cells exhibited reduced PtdSer flippase activity, whereas *CDC50A*-null cells almost completely lost the activity. Most, if not all, P4-ATPases require CDC50 family proteins as a functional subunit or chaperone (*5*, *22*, *23*). KBM7 cells and W3 cells expressed only CDC50A among CDC50 proteins, but also expressed ATP11C and other P4-ATPases, some of which may also function as a PtdSer flippase. PtdSer flippase has been considered to be specific for aminophospholipids (*14*). But, as reported previously with Jurkat cells (*24*), *CDC50A*-null KBM7 cells lost the ability to transport PtdCho, which suggests that some P4-ATPases may flip PtdCho. In apoptosis, Xkr8's scramblase is activated (*4*) and ATP11C's flippase is inactivated to expose PtdSer. The PtdSer exposure in activated platelets and lymphocytes is Ca^{2+}-dependent (*3*, *25*). Because a high Ca^{2+} concentration inhibits P4-ATPases (*26*), PtdSer exposure in these processes may be mediated by the Ca^{2+}-dependent activation of scramblases coupled to the Ca^{2+}-mediated down-regulation of flippase activity. Once cellular Ca^{2+} levels are reduced, ATP11C and/or other P4-ATPases would reestablish the asymmetric phospholipid distribution in the plasma membrane. On the other hand, caspase-mediated apoptotic PtdSer exposure is irreversible, leading to engulfment by macrophages.

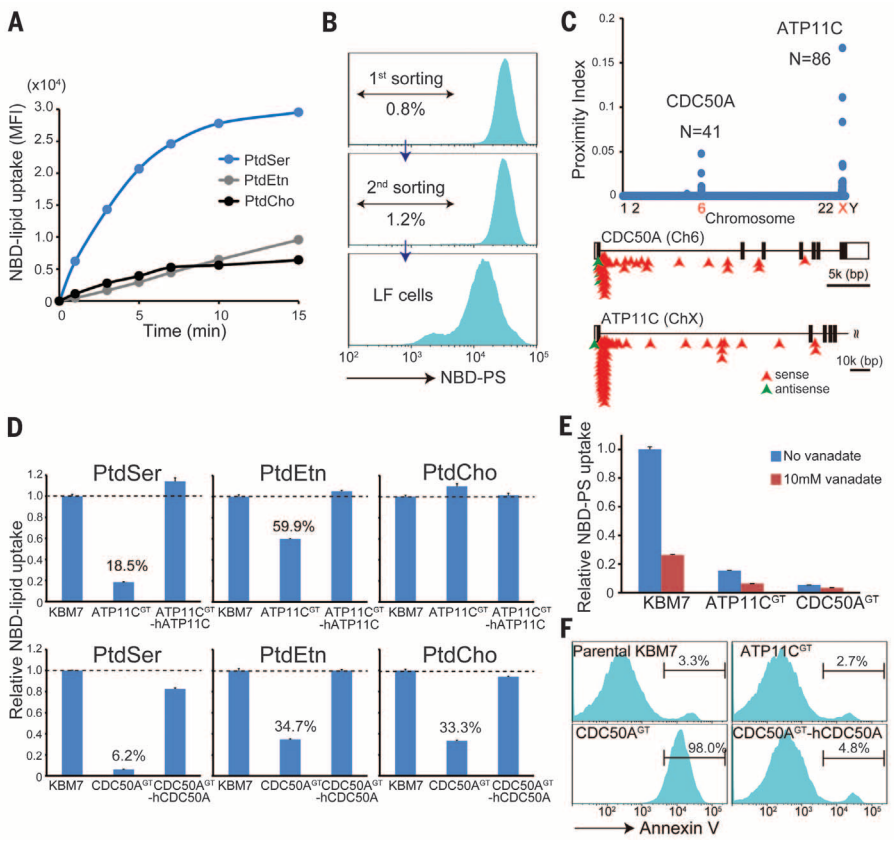

Fig. 1. Screening for phospholipid flippase. (**A**) KBM7 cells were incubated with 1.5 μM NBD-phospholipids, treated with bovine serum albumin (BSA), and analyzed by fluorescence-activated cell sorting (FACS). Mean fluorescence intensity (MFI) is plotted. (**B**) Mutagenized KBM7 cells that incorporated low levels (~1%) of NBD-PS were collected and sorted to generate LF (low flipping) cells. (**C**) Identification of gene trap insertions. Proximity index is plotted for human chromosome with number (N) of insertions. Arrowheads denote insertion positions for sense (red) and antisense orientation (green). (**D**) Incorporation of NBD-phospholipids into ATP11C^{GT}, ATP11C^{GT}-h*ATP11C*, CDC50A^{GT}, or CDC50A^{GT}-h*CDC50A* cells, relative to incorporation into KBM7 cells (n = 3). Error bars denote SD. (**E**) Effect of vanadate on NBD-PS incorporation into KBM7, ATP11C^{GT}, and CDC50A^{GT} cells, relative to incorporation into KBM7 cells in the absence of vanadate (n = 3). Error bars denote SD. (**F**) Annexin V staining profile of KBM7, ATP11C^{GT}, CDC50A^{GT}, and CDC50A^{GT}-h*CDC50A* cells; percentages of Annexin V–positive cells are shown.

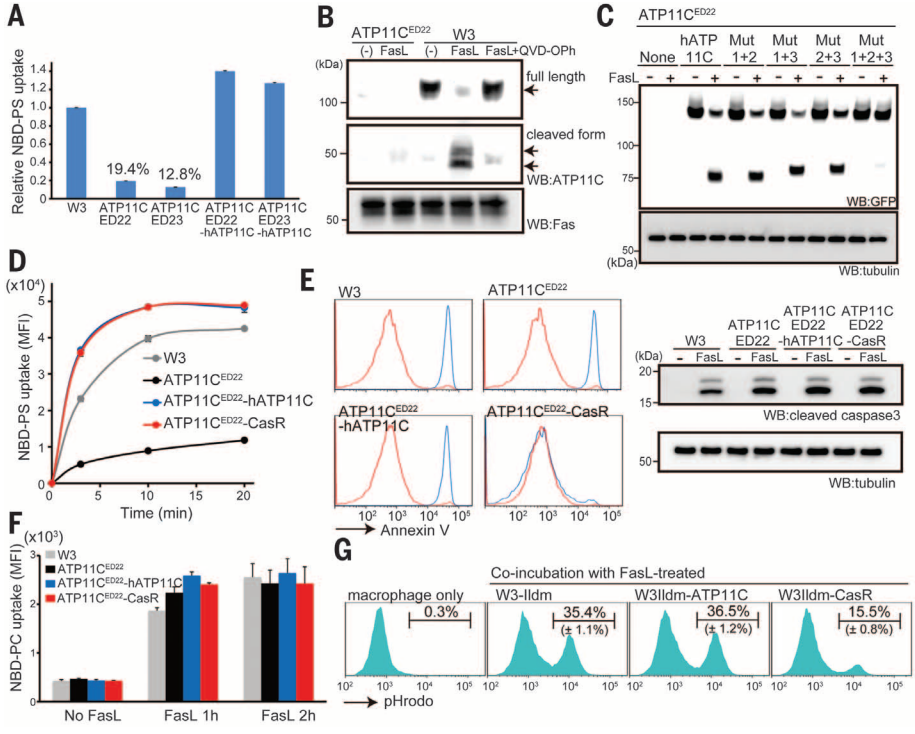

Fig. 2. Cleavage of ATP11C during apoptosis. (**A**) Incorporation of NBD-PS into ATP11C^{ED22}, ATP11C^{ED23}, ATP11C^{ED22}-h*ATP11C*, and ATP11C^{ED23}-h*ATP11C* cells, relative to incorporation into W3 cells (n = 3). Error bars denote SD. (**B**) W3 and ATP11C^{ED22} cells were incubated for 1 hour with FasL in the presence or absence of 20 μM QVD-OPh. Membrane fractions were analyzed by immunoblotting with antibodies to mATP11C or Fas. Middle panel, longer exposure. (**C**) ATP11C^{ED22}, ATP11C^{ED22}-h*ATP11C*-GFP, or ATP11C^{ED22}-mutant h*ATP11C*-GFP cells were incubated for 45 min with FasL, and analyzed by immunoblotting with antibody to GFP or tubulin. (**D**) W3, ATP11C^{ED22}, ATP11C^{ED22}-h*ATP11C*, and ATP11C^{ED22}-*CasR* cells were incubated with NBD-PS, treated with BSA, and analyzed by FACS. MFI is plotted (n = 3). Error bars denote SD. (**E**) Annexin V staining profile of W3, ATP11C^{ED22}, ATP11C^{ED22}-h*ATP11C*, and ATP11C^{ED22}-*CasR* cells that were untreated (red) or FasL-treated for 2 hours (blue). Right panel: Immunoblotting of the cell lysates with antibody to cleaved caspase 3 or tubulin. (**F**) W3, ATP11C^{ED22}, ATP11C^{ED22}-h*ATP11C*, and ATP11C^{ED22}-*CasR* cells were treated for 1 or 2 hours with FasL, incubated with 0.5 μM NBD-PC for 4 min, and analyzed by FACS. MFI is plotted (n = 3). Error bars denote SD. (**G**) W3-lldm, W3lldm-h*ATP11C*, and W3lldm-*CasR* cells were treated with FasL, labeled with pHrodo (a pH indicator), incubated for 1 hour with thio-pMacs, and analyzed by FACS.

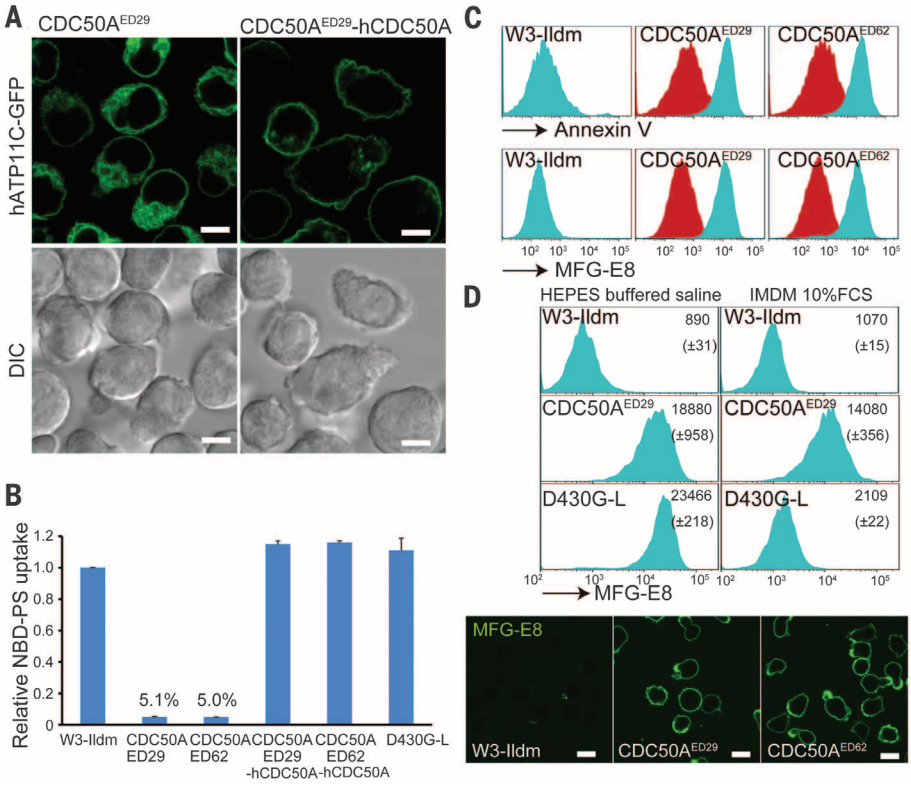

Fig. 3. PtdSer exposure in *CDC50A*$^{-/-}$ cells. (**A**) Observation of hATP11C-GFP expressed in CDC50A^{ED29} or CDC50A^{ED29}-h*CDC50A* cells by confocal fluorescence microscopy. DIC, differential interference contrast. Scale bar, 5 μm. (**B**) Incorporation of NBD-PS into CDC50A^{ED29}, CDC50A^{ED62}, CDC50A^{ED29}-h*CDC50A*, CDC50A^{ED62}-h*CDC50A*, and W3-D430G-L cells, relative to incorporation into W3-lldm cells (n = 3). Error bars denote SD. (**C**) W3-lldm, CDC50A^{ED29}, and CDC50A^{ED62} cells and their h*CDC50A* transformants (red) were stained with Cy5–Annexin V or fluorescein isothiocyanate (FITC)–MFG-E8 in Annexin V buffer. (**D**) W3-lldm, CDC50A^{ED29}, and W3-D430G-L cells were incubated at room temperature for 5 min with FITC-MFG-E8 in HEPES-buffered saline or in IMDM–10% FCS. MFI is indicated (n = 3). Lower panels: W3-lldm, CDC50A^{ED29}, and CDC50A^{ED62} cells were stained with FITC-MFG-E8 in IMDM–10% FCS and observed by confocal fluorescence microscopy. Scale bar, 10 μm.

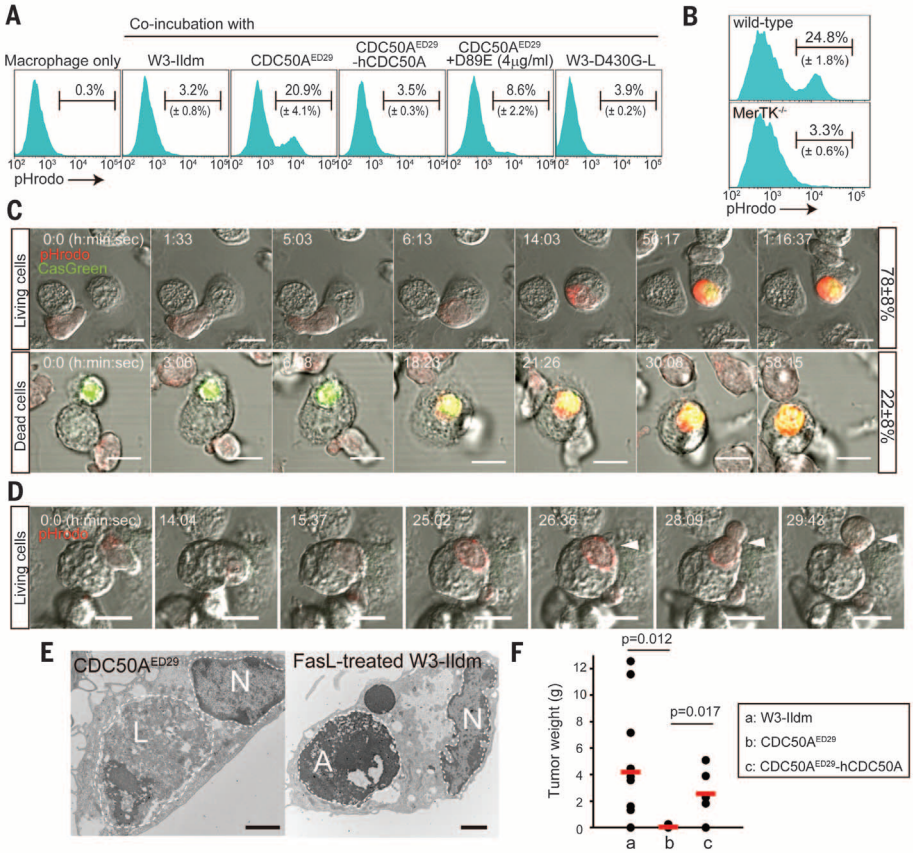

Fig. 4. Engulfment of viable cells. (**A**) Thio-pMacs were incubated for 2 hours with pHrodo-labeled W3-lldm, CDC50A^{ED29}, CDC50A^{ED29}-h*CDC50A*, or W3-D430G-L cells in the presence or absence of D89E (4 μg/ml) and analyzed by FACS. (**B**) Wild-type or *MerTK*$^{-/-}$ thio-pMacs were incubated for 2 hours with pHrodo-CDC50A^{ED29} and analyzed by FACS. (**C**) pHrodo-CDC50A^{ED29} was incubated with thio-pMacs in the presence of CellEvent Caspase-3/7 Green Detection Reagent (Life Technology). Images for pHrodo (red), CellEvent (green), and DIC were captured every 1.5 min. Scale bars, 10 μm. Engulfment of CellEvent-negative (living) and -positive (dead) cells was followed for at least 130 events in 30 fields of three independent experiments. Percentages of dead or living cell engulfment are at right. (**D**) Release of engulfed CDC50A^{ED29} (arrowhead) from thio-pMacs. Scale bars, 10 μm. (**E**) Transmission electron micrograph of thio-pMacs engulfing CDC50A^{ED29} or FasL-treated W3-lldm cells. Scale bars, 2 μm. N, macrophage nucleus; L, engulfed living cells; A, engulfed apoptotic cells. (**F**) W3-lldm, CDC50A^{ED29}, and CDC50A^{ED29}-h*CDC50A* (10^6 cells) were transplanted subcutaneously into nude mice (N = 6 to 11) and tumors were weighed 4 weeks later.

The engulfment of living cells by neighboring cells or macrophages has been reported in various systems (*21*, *27*, *28*). Our finding that macrophages engulf PtdSer-exposing *CDC50A*-null cells supports the idea (*28*) that when PtdSer is exposed, even viable cells can be engulfed. The engulfment of living cells may be involved in diseases such as hemophagocytosis, neurodegeneration, and cancer (*29*). *ATP11C*-defective mice lose a large number of B cells during differentiation from progenitor B cells to precursor B cells in bone marrow (*7*, *30*), and a weak defect in the PtdSer internalization has been detected in progenitor B cells (*7*). One possible explanation is that among the P4-ATPases promoting flippase activity, only ATP11C is expressed in the early stage of B cell development. Thus, *ATP11C*-defective cells expose PtdSer and are engulfed by macrophages.

REFERENCES AND NOTES

1. P. A Leventis, S. Grinstein, *Annu. Rev. Biophys.* **39**, 407–427 (2010).
2. S. Nagata, R. Hanayama, K. Kawane, *Cell* **140**, 619–630 (2010).
3. J. Suzuki, M. Umeda, P. J. Sims, S. Nagata, *Nature* **468**, 834–838 (2010).
4. J. Suzuki, D. P. Denning, E. Imanishi, H. R. Horvitz, S. Nagata, *Science* **341**, 403–406 (2013).
5. K. Tanaka, K. Fujimura-Kamada, T. Yamamoto, *J. Biochem.* **149**, 131–143 (2011).
6. X. Tang, M. S. Halleck, R. A. Schlegel, P. Williamson, *Science* **272**, 1495–1497 (1996).
7. M. Yabas *et al.*, *Nat. Immunol.* **12**, 441–449 (2011).
8. T. T. Sebastian, R. D. Baldridge, P. Xu, T. R. Graham, *Biochim. Biophys. Acta* **1821**, 1068–1077 (2012).
9. B. Verhoven, R. A. Schlegel, P. Williamson, *J. Exp. Med.* **182**, 1597–1601 (1995).
10. D. L. Bratton *et al.*, *J. Biol. Chem.* **272**, 26159–26165 (1997).
11. M. Kotecki, P. S. Reddy, B. H. Cochran, *Exp. Cell Res.* **252**, 273–280 (1999).
12. J. E. Carette *et al.*, *Nat. Biotechnol.* **29**, 542–546 (2011).
13. H. Takatsu *et al.*, *J. Biol. Chem.* **286**, 38159–38167 (2011).
14. J. A. Coleman, F. Quazi, R. S. Molday, *Biochim. Biophys. Acta* **1831**, 555–574 (2013).
15. M. Tanaka, T. Suda, T. Yatomi, N. Nakamura, S. Nagata, *J. Immunol.* **158**, 2303–2309 (1997).
16. L. Cong *et al.*, *Science* **339**, 819–823 (2013).
17. H. Sakahira, M. Enari, S. Nagata, *Nature* **391**, 96–99 (1998).
18. K. Segawa, J. Suzuki, S. Nagata, *Proc. Natl. Acad. Sci. U.S.A.* **108**, 19246–19251 (2011).
19. R. Hanayama *et al.*, *Nature* **417**, 182–187 (2002).
20. H. M. Seitz, T. D. Camenisch, G. Lemke, H. S. Earp, G. K. Matsushima, *J. Immunol.* **178**, 5635–5642 (2007).
21. M. Overholtzer *et al.*, *Cell* **131**, 966–979 (2007).
22. B. Chen *et al.*, *PLOS Genet.* **6**, e1001235 (2010).
23. L. M. van der Velden *et al.*, *J. Biol. Chem.* **285**, 40088–40096 (2010).
24. R. Chen, E. Brady, T. M. McIntyre, *J. Immunol.* **186**, 3215–3225 (2011).
25. J. I. Elliott *et al.*, *Nat. Cell Biol.* **7**, 808–816 (2005).
26. D. L. Daleke, J. V. Lyles, *Biochim. Biophys. Acta* **1486**, 108–127 (2000).
27. P. A. Oldenborg *et al.*, *Science* **288**, 2051–2054 (2000).
28. M. Darland-Ransom *et al.*, *Science* **320**, 528–531 (2008).
29. G. C. Brown, J. J. Neher, *Trends Biochem. Sci.* **37**, 325–332 (2012).
30. O. M. Siggs, B. Schnabl, B. Webb, B. Beutler, *Proc. Natl. Acad. Sci. U.S.A.* **108**, 7890–7895 (2011).

ACKNOWLEDGMENTS

We thank B. H. Cochran for KBM7 cells, K. Higasa and M. Shimizu for help in next-generation sequencing, K. Okamoto-Furuta and H. Kohda for support in electron microscope analysis, and M. Fujii for secretarial assistance. This work was supported in part by grants-in-aid from the Ministry of Education, Science, Sports, and Culture, Japan. Kyoto University has filed a patent entitled "Method of screening agents for the treatment or prevention of cancer or apoptosis-related diseases" (inventors, Shigekazu Nagata, Katsumori Segawa; reference number: 61/978415). Plasmids encoding human ATP11C or CDC50A, human KBM7 cells lacking ATP11C or CDC50A, and mouse W3 cell lines lacking ATP11C or CDC50A are all available under material transfer agreements. T.R.B. is a co-founder, shareholder, and member of the scientific advisory board of Haplogen, an early-phase biotech company based on haploid genetics.

SUPPLEMENTARY MATERIALS

www.sciencemag.org/content/344/6188/1164/suppl/DC1
Materials and Methods
Figs. S1 to S10
References (*31*–*41*)

3 March 2014; accepted 13 May 2014
10.1126/science.1252809

SHEEP GENOME

The sheep genome illuminates biology of the rumen and lipid metabolism

Yu Jiang,[1,2,3*] Min Xie,[4*] Wenbin Chen,[4*] Richard Talbot,[5] Jillian F. Maddox,[6†] Thomas Faraut,[7] Chunhua Wu,[8‡] Donna M. Muzny,[9] Yuxiang Li,[4] Wenguang Zhang,[1,10,11] Jo-Ann Stanton,[12] Rudiger Brauning,[13] Wesley C. Barris,[2§] Thibaut Hourlier,[14,21] Bronwen L. Aken,[14,21] Stephen M. J. Searle,[14] David L. Adelson,[2||] Chao Bian,[4] Graham R. Cam,[2¶] Yulin Chen,[3] Shifeng Cheng,[4] Udaya DeSilva,[2#] Karen Dixen,[15] Yang Dong,[1] Guangyi Fan,[4] Ian R. Franklin,[2] Shaoyin Fu,[10] Pablo Fuentes-Utrilla,[5] Rui Guan,[4] Margaret A. Highland,[16,17] Michael E. Holder,[9] Guodong Huang,[4] Aaron B. Ingham,[2] Shalini N. Jhangiani,[9] Divya Kalra,[9] Christie L. Kovar,[9] Sandra L. Lee,[9] Weiqing Liu,[4] Xin Liu,[4] Changxin Lu,[4] Tian Lv,[4] Tittu Mathew,[9] Sean McWilliam,[2] Moira Menzies,[2] Shengkai Pan,[4] David Robelin,[7] Bertrand Servin,[7] David Townley,[2††] Wenliang Wang,[4] Bin Wei,[4,18] Stephen N. White,[16,17] Xinhua Yang,[4] Chen Ye,[4] Yaojing Yue,[19] Peng Zeng,[4] Qing Zhou,[4] Jacob B. Hansen,[15] Karsten Kristiansen,[20] Richard A. Gibbs,[9] Paul Flicek,[21] Christopher C. Warkup,[22] Huw E. Jones,[22] V. Hutton Oddy,[23] Frank W. Nicholas,[24] John C. McEwan,[13] James W. Kijas,[2] Jun Wang,[4,20,25,26] Kim C. Worley,[9‡‡] Alan L. Archibald,[27‡‡] Noelle Cockett,[8‡‡] Xun Xu,[4‡‡] Wen Wang,[1‡‡] Brian P. Dalrymple[2‡‡]**

Sheep (*Ovis aries*) are a major source of meat, milk, and fiber in the form of wool and represent a distinct class of animals that have a specialized digestive organ, the rumen, that carries out the initial digestion of plant material. We have developed and analyzed a high-quality reference sheep genome and transcriptomes from 40 different tissues. We identified highly expressed genes encoding keratin cross-linking proteins associated with rumen evolution. We also identified genes involved in lipid metabolism that had been amplified and/or had altered tissue expression patterns. This may be in response to changes in the barrier lipids of the skin, an interaction between lipid metabolism and wool synthesis, and an increased role of volatile fatty acids in ruminants compared with nonruminant animals.

Sheep and goats are thought to be the first domesticated livestock species and thus integral to animal husbandry. Sheep are ruminants, digesting plant material in a four-chambered stomach (*1*). The largest compartment is the rumen, which uses microbial flora to ferment the feed, facilitating the conversion of lignocellulose-rich plant materials, of low value in the human diet, to animal protein (*2*). The rumen is thought to have evolved about 35 to 40 million years ago (*3*), coinciding with the emergence of grasslands, in a cooler climate and atmosphere containing lower CO_2 than today (*4*, *5*). Ruminants are now the dominant terrestrial herbivores. The rumen microbial flora also generate volatile fatty acids (VFAs) (*6*), requiring specialized energy and lipid metabolism in ruminants, and produce the greenhouse gas methane, which may be relevant to climate change (*7*). Another feature of sheep is wool, which has a substantial proportion of its weight made up of lanolin, formed primarily from wax esters (*8*, *9*). Thus, synthesis of wool may be linked to fatty acid metabolism. Given these unusual evolutionary traits, sheep provide an area for exploration of the genetic underpinnings of digestion and fatty acid metabolism.

We assembled the reference genome sequence of the sheep (Fig. 1) from two individuals of the Texel breed totaling ~150-fold sequence coverage (table S1) using linkage and radiation hybrid maps (tables S2 and S3) to order and orient the super-scaffolds (*10*). The final sheep genome assembly, Oar v3.1, has a contig N50 length of ~40 kb and a total assembled length of 2.61 Gb, with ~99% anchored onto the 26

autosomes and the X chromosome (table S4) (*10*). About 0.2% of each Texel's genome are heterozygous loci—i.e., SNPs (single-nucleotide polymorphisms) (Fig. 1, C and D)—a quarter of which are heterozygous in both animals. Due to selection for a beneficial muscle hypertrophy phenotype in the Texel breed (*11*) (Online Mendelian Inheritance in Animals 001426-9940), both sheep share a long run of homozygosity spanning the *MSTN* gene (Fig. 1, C and D). The SNPs also enabled us to identify allele-specific gene expression (Fig. 1E) (see the supplementary text) (*10*).

We identified segmental duplications in sheep (Fig. 1A and table S5) (*10*) and compared the genome assemblies of sheep, goat, and cattle (fig. S1), identifying 141 breakpoints between sheep and cattle (Fig. 1B and table S6) (see the supplementary text). We compared the sequences of sheep, goat, cattle, yak, pig, camel, horse, dog, mouse, opossum, and human proteins and identified 4850 single-copy orthologous genes from which we constructed a phylogenetic tree (Fig. 2 and fig. S2) (*10*). The separation of sheep from goats and the diversification of the bovids occurred contemporaneously with the expansion of the C4 grasses (which first fix CO_2 into a four-carbon rather than a three-carbon compound) in the late Neogene (*4*). RNA-Seq transcriptome data were generated from 94 tissue samples (from 40 tissues), including 83 from four additional Texel individuals (table S7) (*10*). A protein clustering analysis among the 11 mammalian species identified 321 expanded subfamilies in the ruminant branch, of which 73 were ruminant specific (tables S8 and S9) (*10*). We identified sheep genes exhibiting changes in copy number (e.g., lysozyme C–related proteins, prolactin-related proteins, pregnancy-associated glycoproteins, *RNASE1*, *ASIP*, *MOGAT2*, and *MOGAT3*) and changes in tissue specificity of gene expression (e.g., *MOGAT2*, *MOGAT3*, and *FABP9*) (Figs. 1 and 2) (*10*).

The mammalian epidermal development complex (EDC) region contains up to 70 genes encoding proteins involved in keratinized epidermal structure development, including the rumen, skin, and wool (*12*). The sheep EDC region (Figs. 1, 3) included several previously unidentified, or poorly annotated, genes in any mammalian genome (table S10). One such gene in the top 0.1% of all genes expressed in the rumen, but not expressed in the skin (Fig. 3A), is predicted to encode a large S100 fused-type protein (*12*). This protein has homology to trichohyalin (TCHH) (*12*), which is highly expressed in the skin, and we designated it Trichohyalin-like 2 (TCHHL2) (figs. S3 and S4). Expressed sequence tag (EST) data indicate that *TCHHL2* is also expressed in the rumen of cattle (see the supplementary text). Although not previously annotated, syntenically conserved orthologous genes to *TCHHL2* were detected in many mammalian genomes—including a marsupial, the Tasmanian devil, and a monotreme, the platypus (fig. S3)—

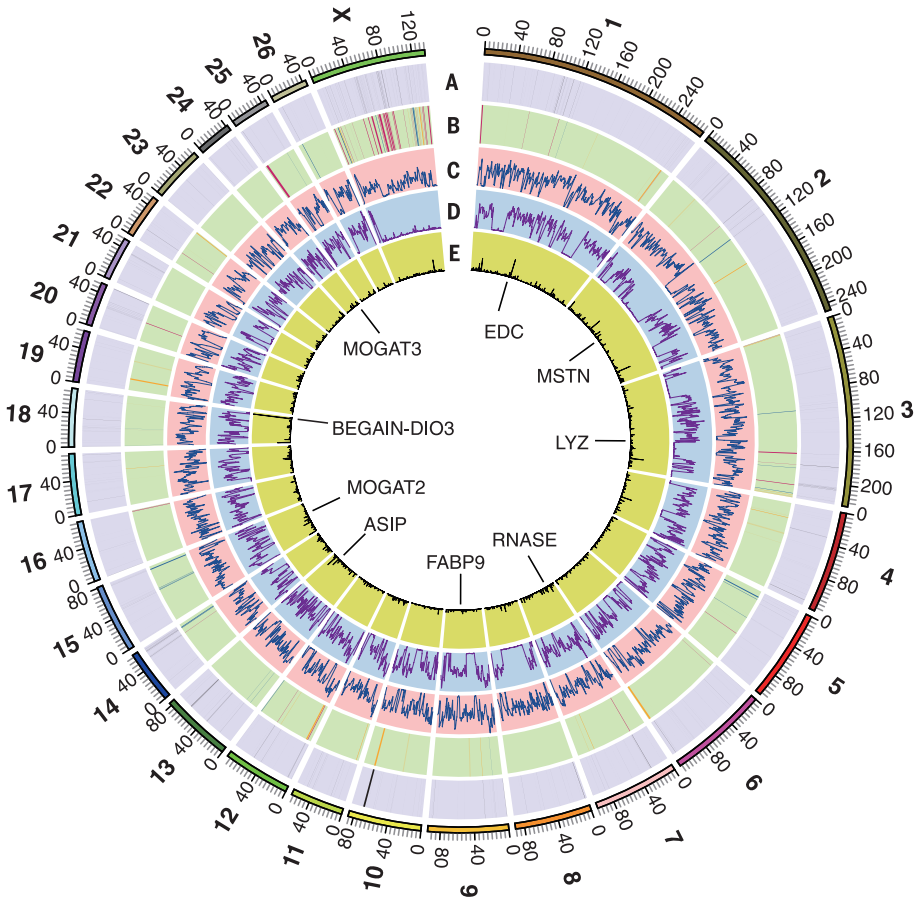

Fig. 1. The genome of sheep. (**A**) A total of 1097 segmental duplications (length >5 kb) in the two Texel sheep (*10*). (**B**) Sheep versus cattle chromosome break points (*10*); gaps in Oar v3.1 are red; probable misassemblies in UMD 3.1 are yellow; and probable true structural differences are blue. (**C**) Distribution of SNPs in the Texel ewe in 1-Mb nonoverlapping windows; range of values 1 to 4954. (**D**) Distribution of SNPs in the Texel ram in 1-Mb nonoverlapping windows; range of values 3 to 5676. (**E**) Distribution of mono-allelically expressed SNPs in 500-kb sliding windows, range of values 0 to 42 (*10*). The scale is in Mb. Positions of loci discussed in the text are indicated.

[1]State Key Laboratory of Genetic Resources and Evolution, Kunming Institute of Zoology, Chinese Academy of Sciences, Kunming 650223, China. [2]Commonwealth Scientific and Industrial Research Organisation Animal Food and Health Sciences, St Lucia, QLD 4067, Australia. [3]College of Animal Science and Technology, Northwest A&F University, Yangling 712100, China. [4]BGI-Shenzhen, Shenzhen 518083, China. [5]Ediburgh Genomics, University of Edinburgh, Easter Bush, Midlothian EH25 9RG, UK. [6]Utah State University, Logan, UT 84322-4815, USA. [7]Institut National de la Recherche Agronomique, Laboratoire de Génétique Cellulaire, UMR 444, Castanet-Tolosan F-31326, France. [8]Utah State University, Logan, UT 84322–1435, USA. [9]Human Genome Sequencing Center, Baylor College of Medicine, Houston, TX 77030, USA. [10]Inner Mongolia Agricultural University, Hohhot 010018, China. [11]Institute of ATCG, Nei Mongol Bio-Information, Hohhot, China. [12]Department of Anatomy, University of Otago, Dunedin 9054, New Zealand. [13]AgResearch, Invermay Agricultural Centre, Mosgiel 9053, New Zealand. [14]Wellcome Trust Sanger Institute, Wellcome Trust Genome Campus, Hinxton, Cambridge, CB10 1SA, UK. [15]Department of Biology, University of Copenhagen, DK-2100 Copenhagen Ø, Denmark. [16]U.S. Department of Agriculture Agricultural Research Service Animal Disease Research Unit, Pullman, WA 99164, USA. [17]Department of Veterinary Microbiology and Pathology, Washington State University, Pullman, WA 99164, USA. [18]Maize Research Institute, Sichuan Agricultural University, Chengdu 611130, China. [19]Lanzhou Institute of Husbandry and Pharmaceutical Science, Lanzhou, 730050, China. [20]Department of Biology, University of Copenhagen, DK-2200 Copenhagen N, Denmark. [21]European Molecular Biology Laboratory, European Bioinformatics Institute, Wellcome Trust Genome Campus, Hinxton, Cambridge, CB10 1SA, UK. [22]Biosciences Knowledge Transfer Network, The Roslin Institute, Easter Bush, Midlothian, EH25 9RG, UK. [23]School of Environmental and Rural Science, University of New England, Armidale, NSW 2351, Australia. [24]Faculty of Veterinary Science, University of Sydney, NSW 2006, Australia. [25]Princess Al Jawhara Center of Excellence in the Research of Hereditary Disorders, King Abdulaziz University, Jeddah 21589, Saudi Arabia. [26]Macau University of Science and Technology, Macau 999078, China. [27]The Roslin Institute and Royal (Dick) School of Veterinary Studies, University of Edinburgh, Easter Bush, Midlothian EH25 9RG, UK.

*These authors contributed equally to this work. †Present address: 16 Park Square, Port Melbourne, VIC 3207, Australia. ‡Present address: Huntsman Cancer Institute, Salt Lake City, UT 84112, USA. §Present address: Cobb-Vantress, Siloam Springs, AR 72761, USA. ||Present address: School of Molecular and Biomedical Science, University of Adelaide, Adelaide, SA 5005, Australia. ¶Present address: Genomic Strategies, Post Office Box 123, Lawson, NSW 2783, Australia. #Present address: Department of Animal Science, Oklahoma State University, Stillwater, OK 74078, USA. **Present address: 11 Fourth Road, Belair, SA 5052, Australia. ††Present address: Illumina Cambridge Ltd, Chesterford Research Park, Saffron Walden CB10 1XL, UK. **‡‡Corresponding author. E-mail: brian.dalrymple@csiro.au (B.P.D.); wwang@mail.kiz.ac.cn (W.W); xuxun@genomics.cn (X.X.); alan.archibald@roslin.ed.ac.uk (A.L.A.); kworley@bcm.edu (K.C.W.); noelle.cockett@usu.edu (N.C.)**

but not in the chicken, suggesting that *TCHHL2* may be specific to mammals. All *TCHHL2* orthologs encode a protein containing up to 70 tandem copies of a highly variable 15 amino acid repeat, rich in arginine, glutamic acid, aspartic acid, and proline, which does not appear to be rumen specific (fig. S3). A short array of seven copies of the 15 amino acid repeat unit has been duplicated in the common ancestor of ruminants (Fig. 3B and fig. S4). S100 fused-type proteins are substrates for transglutaminase-mediated cross-linking to themselves and to other proteins, including keratins, during epidermal cornification and hair/wool development (*12*), suggesting that TCHHL2 may play a role in cross-linking the keratins at the rumen surface. *TCHHL2* was expressed in other sheep epidermal tissues, but >1000-fold lower than in rumen; thus, it may have a similar, but less extensive, role in these tissues.

PRD-SPRRII (*13*) is also in the EDC region and the top 0.1% of genes expressed in the rumen, but not in any other tissue sampled, including skin (Fig. 3A). *PRD-SPRRII* is homologous to the *SPRR2* gene family (*12*, *14*) but encodes a protein with a distinctive proline- and histidine-rich sequence that disrupts the glutamine-rich amino-terminus present in SPRR2 proteins, potentially affecting its transglutamination sites (Fig. 3C) (*15*). We identified four additional genes related to *PRD-SPRRII* in the sheep EDC region, two of which were also highly expressed in the rumen but not in any other tissue sampled, including the skin (Fig. 3A), and eight related genes in the cattle EDC region also expressed in the rumen but none in nonruminants (Fig. 3C) (see the supplementary text). Thus, it appears that the ruminant-specific *PRD-SPRRII* family genes, resulting from the amplification and sequence divergence of an SPRR2 gene, have gained a new expression pattern, altered amino-terminal sequence, and modified function during rumen evolution. By analogy with SPRR2 (*12*, *16*), the PRD-SPRRII family proteins are predicted to be major structural proteins and may function in the cornification of the keratin-rich surface of the rumen.

The primary role of the skin and wool, an important economic product of sheep, is to form a barrier between the organism and the external environment, reducing water and heat loss and pathogen entry (*17*). The sheep EDC gene, LOC101122906, which we designated *LCE7A*, represents a previously unrecognized subfamily of the late cornified envelope (LCE) genes (*12*, *18*) (fig. S5). We identified *LCE7A* coding sequence in the genomes of most mammals, although it has not been previously annotated (fig. S5). *LCE7A* is expressed in sheep (Fig. 3A and table S10), cattle, and goat skin (see the supplementary text), but not in the rumen or any other tissue examined (Fig. 3A). In situ hybridization showed *LCE7A* expression in Merino wool follicles, including the inner root sheath (fig. S6). LCE7A contains the transglutaminase target site present in most LCE proteins (fig. S5) and is likely to be a substrate for transglutaminase-mediated cross-linking of proteins in the epidermis, inner root sheath, or wool (*18*). *LCE7A* also appears to be under positive selection in the sheep lineage, with a sheep versus cattle ratio of the number of nonsynonymous substitutions per nonsynonymous site to the number of synonymous substitutions per synonymous site of 2.5 ($P < 0.005$), possibly reflecting an association of LCE7A with wool development.

Wool grease (lanolin), secreted from the sebaceous glands attached to the wool follicles, constitutes 10 to 25% of the wool weight (*9*). The wool follicles are located in the dermal layer between the surface keratinocytes, which synthesize surface lipids (*19*), and the subcutaneous adipose tissue. We identified the genes encoding lipid metabolic enzymes expressed in the skin (table S11) and positioned them on known and putative lipid metabolic pathways likely to be involved in the storage and mobilization of long-chain fatty acid components of the sebum and epidermal lipids (Fig. 4A). Unexpectedly, the skin transcriptome revealed high expression of *MOGAT2* and *MOGAT3*, members of the acylglycerol O-acyltransferase (*DGAT2/MOGAT*) gene family that are involved in the synthesis of diacylglyceride (DAG) and triacylglyceride (TAG) from monoacylglyceride (MAG) (Fig. 4A). In humans, MOGAT3 is an essential and rate-limiting

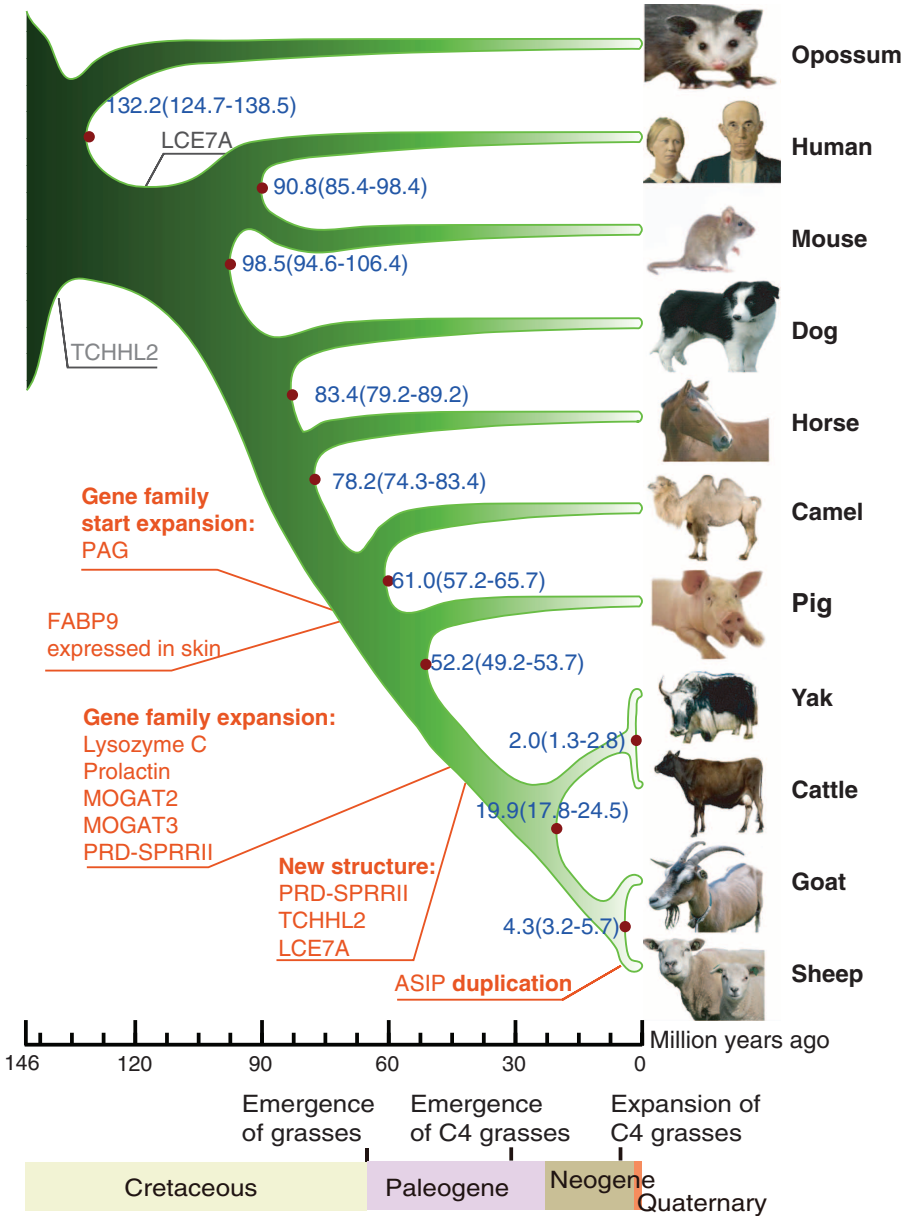

Fig. 2. Sheep relative to human and livestock evolution. A phylogenetic tree generated using single-copy orthologous genes (*10*). The origins (black) and amplifications (red) of genes discussed in the text are marked. The scale is in millions of years ago (Ma). Blue numbers on the nodes are the divergence time from present (Ma) and its confidence interval. Dates for major events in the evolution of grasses are from (*4*) and (*5*).

step for the absorption of dietary fat in the small intestine (*20*) and is an important liver enzyme (*21*). *MOGAT2* and *MOGAT3* are single-copy genes in almost all mammals with available data. However, in ruminants, both genes have undergone tandem gene expansions, indicative of evolving functionality. (Fig. 4B and figs. S7 and S8). *MOGAT2* has more than five tandemly duplicated copies in sheep, with the first copy expressed in the duodenum and the last copy expressed in the skin and with no expression of any copy detected in the liver (fig. S7). Three nearly identical *MOGAT3* copies were highly expressed in sheep skin and at a much lower level in white adipose and omentum (Fig. 4B). In contrast to humans, we detected no expression of functional *MOGAT3* in sheep duodenum or liver. The skin had two *MOGAT3* splice

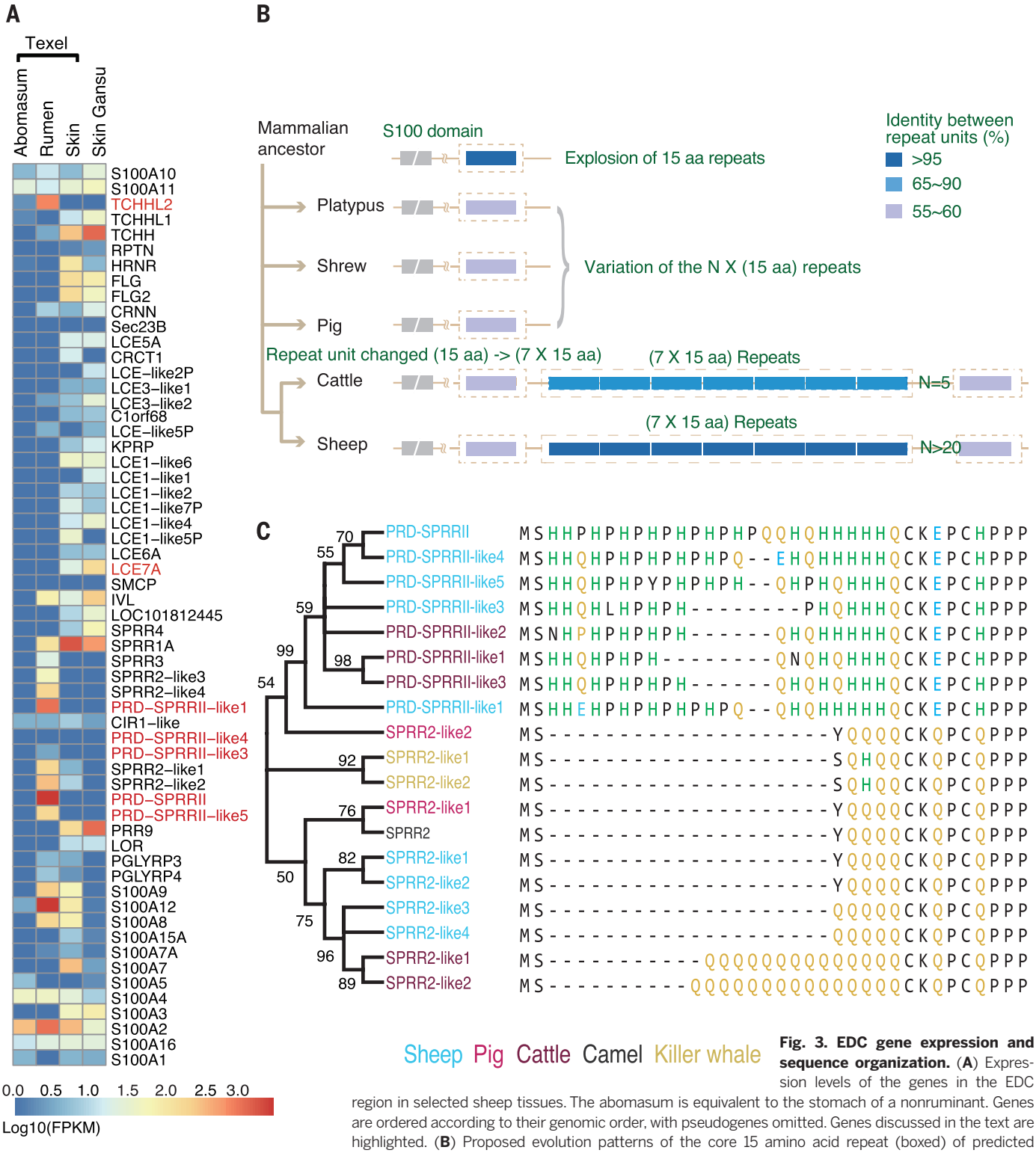

Fig. 3. EDC gene expression and sequence organization. (**A**) Expression levels of the genes in the EDC region in selected sheep tissues. The abomasum is equivalent to the stomach of a nonruminant. Genes are ordered according to their genomic order, with pseudogenes omitted. Genes discussed in the text are highlighted. (**B**) Proposed evolution patterns of the core 15 amino acid repeat (boxed) of predicted TCHHL2 proteins. Percent identity between repeat units is within each species. (**C**) Maximum likelihood phylogenetic tree of PRD-SPRRII and SPRR2 proteins. For clarity, three representative PRD-SPRRII-like cattle sequences are shown. Bootstrap values ≥50% (500 replicates) are shown.

variants (fig. S9): The most common transcript encodes a predicted protein orthologous to the typical mammalian MOGAT3; the second contains a predicted alternate start codon and amino-terminal sequence that is missing the probable membrane anchor (fig. S10), predicted to be uncoupled from the endoplasmic reticulum membrane-bound TAG synthesis pathway (Fig. 4A).

The presence of MOGAT2 and MOGAT3 in sheep skin indicates that there may be an alternative pathway for DAG synthesis, either from recycling MAG generated from the mobilization of TAG stored within a cell to generate fatty acids for incorporation into other products, or from external sources of MAG (Fig. 4A). The MOGAT pathway does not generate glycerol, which requires phosphorylation in the liver before reuse for TAG synthesis in the skin via the glycerol-3-phosphate (G3P) pathway (Fig. 4A), potentially increasing the efficiency of recycling of the glycerol backbone in sheep skin. The MOGAT pathway also bypasses 1-acyl-lysophosphatidic acid (LPA) and phosphatidic acid (PA) synthesis (Fig. 4A). Skin produces a lipase (LIPH) to cleave PA into 2-acyl LPA, which has a role in controlling hair-follicle development (*22*). *LIPH* mutations in several mammalian species result in wool-like hair due to changes in follicle shape (*23*). Thus, the MOGAT pathway in sheep skin may also reduce the coupling between TAG and PA synthesis, skin barrier lipid synthesis, and follicle development signaling, facilitating wool production.

In ruminants, the liver is primarily a gluconeogenic organ using propionate (a VFA) as the source of carbon. It contributes little to the synthesis of lipids, or to the uptake of lipids from circulation, and is inefficient at exporting TAG (*24*, *25*). The apparent loss of *MOGAT3* expression in the intestines and both *MOGAT2* and *MOGAT3* in the liver may reflect the greater importance of VFAs and the reduced importance of the liver in long-chain fatty acid metabolism in ruminants compared with nonruminants.

We identified major genomic signatures associated with interactions between diet, the digestive system, and metabolism in ruminants. These include two extensions of their biochemical capabilities that have been extensively exploited by humans: the production of wool by sheep and the evolution of an organ that houses a diverse community of microorganisms that enable efficient digestion of plants.

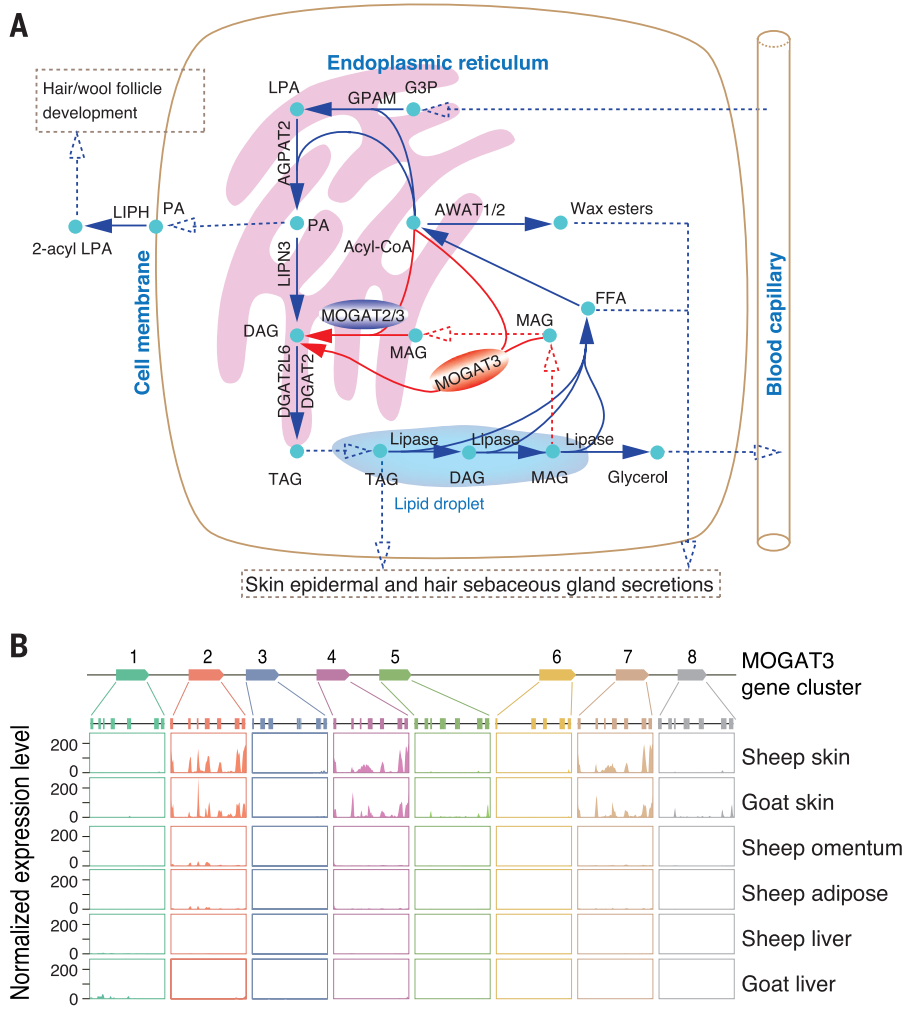

Fig. 4. Proposed sheep-skin lipid metabolic pathways and the expression of the *MOGAT3* region. (**A**) Proposed sheep-skin lipid metabolic pathways. The proposed nonmembrane form of MOGAT3 is red; the membrane form of MOGAT2/3 is blue. The glycerol-3-phosphate and MOGAT pathways to DAG are in blue and red arrows, respectively. Dashed lines represent transport or diffusion of products. (**B**) Expression of eight *MOGAT3* genes in sheep skin (Gansu fine wool); sheep omentum, white adipose, and liver (Texel); goat skin (Shanbei Cashmere); and goat liver (Yunling Black).

REFERENCES AND NOTES

1. R. R. Hofmann, *Oecologia* **78**, 443–457 (1989).
2. M. J. Wolin, *Science* **213**, 1463–1468 (1981).
3. T. J. Hackmann, J. N. Spain, *J. Dairy Sci.* **93**, 1320–1334 (2010).
4. C. A. E. Strömberg, *Annu. Rev. Earth Planet. Sci.* **39**, 517–544 (2011).
5. E. J. Edwards *et al.*, *Science* **328**, 587–591 (2010).
6. E. N. Bergman, *Physiol. Rev.* **70**, 567–590 (1990).
7. K. A. Johnson, D. E. Johnson, *J. Anim. Sci.* **73**, 2483–2492 (1995).
8. M. E. Stewart, in *Biology of the Integument*, J. Bereiter-Hahn, A. G. Matoltsy, K. S. Richards, Eds. (Springer, Berlin Heidelberg, 1986), vol. 2, pp. 824–832.
9. M. L. Schlossman, J. P. McCarthy, *J. Am. Oil Chem. Soc.* **55**, 447–450 (1978).
10. Material and methods are available as supplementary material on *Science* Online
11. A. Clop *et al.*, *Nat. Genet.* **38**, 813–818 (2006).
12. M. Kypriotou, M. Huber, D. Hohl, *Exp. Dermatol.* **21**, 643–649 (2012).
13. L. Wang, R. L. Baldwin 6th, B. W. Jesse, *Biochem. J.* **317**, 225–233 (1996).
14. H. J. Song *et al.*, *Genomics* **55**, 28–42 (1999).
15. J. Deng, R. Pan, R. Wu, *J. Biol. Chem.* **275**, 5739–5747 (2000).
16. P. M. Steinert, E. Candi, T. Kartasova, L. Marekov, *J. Struct. Biol.* **122**, 76–85 (1998).
17. K. R. Feingold, *J. Lipid Res.* **48**, 2531–2546 (2007).
18. D. Marshall, M. J. Hardman, K. M. Nield, C. Byrne, *Proc. Natl. Acad. Sci. U.S.A.* **98**, 13031–13036 (2001).
19. F. P. W. Radner, S. Grond, G. Haemmerle, A. Lass, R. Zechner, *Dermatoendocrinology* **3**, 77–83 (2011).
20. D. Cheng *et al.*, *J. Biol. Chem.* **278**, 13611–13614 (2003).
21. A. M. Hall *et al.*, *J. Lipid Res.* **53**, 990–999 (2012).
22. A. Kazantseva *et al.*, *Science* **314**, 982–985 (2006).
23. A. Inoue *et al.*, *EMBO J.* **30**, 4248–4260 (2011).
24. G. Bobe, J. W. Young, D. C. Beitz, *J. Dairy Sci.* **87**, 3105–3124 (2004).
25. D. L. Ingle, D. E. Bauman, U. S. Garrigus, *J. Nutr.* **102**, 617–623 (1972).

ACKNOWLEDGMENTS

The International Sheep Genomics Sequencing Consortium is grateful to the following for funding support for the sheep genome sequencing project: one 973 Program (no. 2013CB835200) and one CAS Program (XDB13000000) to Kunming Institute of Zoology, China; BGI-Shenzhen (ZYC200903240077A and ZYC200903240078A); China National GeneBank-Shenzhen for support for the storage of samples and data; Inner Mongolia Agricultural University (30960246 and 31260538); The Roslin Institute, University of Edinburgh and Biotechnology and Biological Sciences Research Council, UK (BBSRC): BB/1025360/1, BB/I025328/1, Institute Strategic Programme, and National Capability Grants; The Roslin Foundation; The Scottish Government, UK; Department for Environment, Food and Rural Affairs/Higher Education Funding Council/Scottish Higher Education Funding Council Veterinary Training and Research Initiative, UK; USDA-ARS, USA, USDA-National Research Initiative Competitive Grants Program, USA (grant nos. 2008-03923 and 2009-03305); Wellcome Trust (grant nos. WT095908 and WT098051), BBSRC (grant nos. BB/I025506/1 and BB/I025360/1) and European Molecular Biology Laboratory; USDA-NRSP-8, USA; USDA-ARS grant 5348-32000-031-00D; Meat and Livestock Australia and Australian Wool Innovation Limited through SheepGENOMICS, Australia; Australian Government International Science Linkages Grant (CG090143), Australia; University of Sydney, Australia; CSIRO, Australia; AgResearch, NZ, Beef + Lamb NZ through Ovita,

New Zealand; INRA and Agence Nationale de la Recherche project SheepSNPQTL, France; European Union through the Seventh Framework Programme Quantomics (KBBE222664) and 3SR (KBBE245140) projects; the Ole Rømer grant from Danish Natural Science Research Council, BGI-Shenzhen, China; the Earmarked Fund for Modern China Wool & Cashmere Technology Research System (no.nycytx-40-3); and the Australian Department of Agriculture Food and Fisheries, Filling the Research Gap project, "Host control of methane emissions." We thank B. Freking (USDA-ARS-U.S. Meat Animal Research Center) for provision of Texel ram tissue samples for DNA extraction and sequencing. We thank the sequencing teams and other contributors; full details are in the acknowledgements section of the supplementary materials. We thank SheepGENOMICS and Utah State University for access to the genotyping data for the SheepGENOMICS and Louisiana State University flocks, respectively. We thank L. Goodman for help with condensing the text. The genome assemblies have been deposited in GenBank, Oar v1.0 (GCA_000005525.1), and Oar v3.1 (GCA_000298735.1) and in GigaDB, Oar v2.0 (http://dx.doi.org/10.5524/100023). The Ensembl annotation of the Oar v3.1 assembly is available at http://e74.ensembl.org, and the gene builds are available from ftp://ftp.ensembl.org/pub/release-74/bam/ovis_aries/genebuild/. The RNA-Seq data sets have been deposited in public databases: 83 samples from The Roslin Institute (European Nucleotide Archive (ENA) study accession PRJEB6169), seven tissues from the genome-sequenced Texel ewe and Gansu alpine fine wool sheep skin (GenBank accession GSE56643), and three blood samples (GenBank BioProject accession PRJNA245615). The methylated DNA immunoprecipitation sequencing (MeDIP-seq) raw reads from the Texel ewe liver have been deposited in GenBank (GSE56644). The bacterial artificial chromosome sequence assembly has been deposited in GenBank (KJ735098). The raw reads of the genome sequencing projects have been deposited in public nucleotide databases: Texel ewe (GenBank accession SRA059406), Texel ram (ENA study accession PRJEB6251, GenBank accession SRP015759), and 0.5-fold coverage 454 sequencing of six animals (GenBank accessions SRP000982, SRP003883, and SRP006794). The authors declare no competing financial interests.

SUPPLEMENTARY MATERIALS

www.sciencemag.org/content/344/6188/1168/suppl/DC1
Materials and Methods
Supplementary Text
Figs. S1 to S33
Tables S1 to S27
References (*26*–*112*)

3 March 2014; accepted 7 May 2014
10.1126/science.1252806

SLEEP AND LEARNING

Sleep promotes branch-specific formation of dendritic spines after learning

Guang Yang,[1,2] Cora Sau Wan Lai,[1] Joseph Cichon,[1] Lei Ma,[1,3] Wei Li,[3] Wen-Biao Gan[1]*

How sleep helps learning and memory remains unknown. We report in mouse motor cortex that sleep after motor learning promotes the formation of postsynaptic dendritic spines on a subset of branches of individual layer V pyramidal neurons. New spines are formed on different sets of dendritic branches in response to different learning tasks and are protected from being eliminated when multiple tasks are learned. Neurons activated during learning of a motor task are reactivated during subsequent non–rapid eye movement sleep, and disrupting this neuronal reactivation prevents branch-specific spine formation. These findings indicate that sleep has a key role in promoting learning-dependent synapse formation and maintenance on selected dendritic branches, which contribute to memory storage.

Sleep has an important role in learning and memory consolidation (*1*–*5*). During sleep, neurons involved in wakeful experiences are reactivated in multiple brain regions (*6*–*12*), and neuronal networks exhibit various patterns of rhythmic activity (*13*, *14*). Given the crucial function of neuronal activity in synaptic plasticity, sleep likely modulates synaptic connections that are important for long-term memory formation (*15*–*18*). Nevertheless, the role of sleep in experience-dependent changes of synaptic connections remains controversial (*19*–*22*). Overall synaptic strength and numerous synaptic proteins are up-regulated during wakefulness and down-regulated during slow-wave sleep (*23*, *24*). A net loss of synapses is found during sleep in the developing mouse cortex (*25*, *26*) and in the invertebrate nervous system (*27*, *28*). These observations support the hypothesis that sleep is important for the downscaling of synaptic connectivity that has been potentiated during wakefulness (*29*). However, ocular dominance plasticity and cortical-evoked local field potential increase rather than decrease after a slow-wave sleep episode (*30*, *31*). The expression of several proteins required for synaptic plasticity increases during the early hours of sleep (*32*, *33*). Furthermore, the number of synapses increases during early development when animals sleep the most (*34*, *35*). Together, these studies support the opposing view that sleep promotes, rather than down-regulates, synaptic plasticity related to learning and memory.

We examined how sleep affects the remodeling of postsynaptic dendritic spines induced by motor learning in the mouse primary motor cortex. Rotarod motor learning increases dendritic spine formation on apical tuft dendrites of layer V pyramidal neurons in the motor cortex within 2 days (*18*, *36*). To investigate whether sleep is involved in this process, we first determined the time course of spine remodeling in mice that were trained to run forward on an accelerated rotating rod. Yellow fluorescent protein (YFP)–labeled dendrites in the hind limb region of the motor cortex were imaged in awake head-restrained mice before and in the hours after training with transcranial two-photon microscopy (*18*, *37*). The formation rate of new spines in trained mice was significantly higher within 6 hours after training and continued to increase within the first day when compared to that in untrained controls ($P < 0.05$) (Fig. 1, A and B). In contrast, rotarod training had no significant effect on the elimination rate of existing spines within 6 to 48 hours (Fig. 1C).

We observed that, 24 hours after motor training, only a fraction (~30%) of apical tuft branches (average branch length: 62.7 ± 1.3 μm) in trained mice showed a higher rate of spine formation than the branches in untrained mice (Fig. 1D and fig. S1). When spine formation on two sibling branches sharing the same parent branch was compared, the difference in spine formation, but not spine elimination, between sibling branches was also significantly larger in trained mice than in untrained controls (Fig. 1, D to F) ($P < 0.0001$ for spine formation; $P = 0.52$ for spine elimination) (fig. S2). To investigate this branch-specific spine formation further, we classified the sibling branch with higher spine formation as a "high-formation branch" (HFB) and the other as a "low-formation branch" (LFB) (Fig. 1G). Twenty-four hours after training, the average rate of spine formation on HFBs in trained mice (15.3 ± 1.3%) was 2.4 to 3.5 times that of HFBs (6.4 ± 0.8%) or LFBs (4.4 ± 0.9%) in untrained control mice ($P < 0.0001$) (Fig. 1H). The difference in spine formation between HFBs and LFBs was statistically larger for sibling branches than for randomly paired branches ($P < 0.0001$) (Fig. 1I). However, spine formation on LFBs in trained mice (5.2 ± 0.5%) was not significantly different from that on either HFBs ($P = 0.19$) or LFBs ($P = 0.49$) in untrained controls. There was also no significant difference in spine elimination between HFBs and LFBs in both trained ($P = 0.15$) and untrained animals ($P > 0.9$) (Fig. 1J).

[1]Skirball Institute, Department of Neuroscience and Physiology, New York University School of Medicine, New York, NY 10016, USA. [2]Department of Anesthesiology, New York University School of Medicine, New York, NY 10016, USA. [3]Drug Discovery Center, Key Laboratory of Chemical Genomics, Peking University Shenzhen Graduate School, Shenzhen, 518055, China.
*Corresponding author. E-mail: gan@saturn.med.nyu.edu

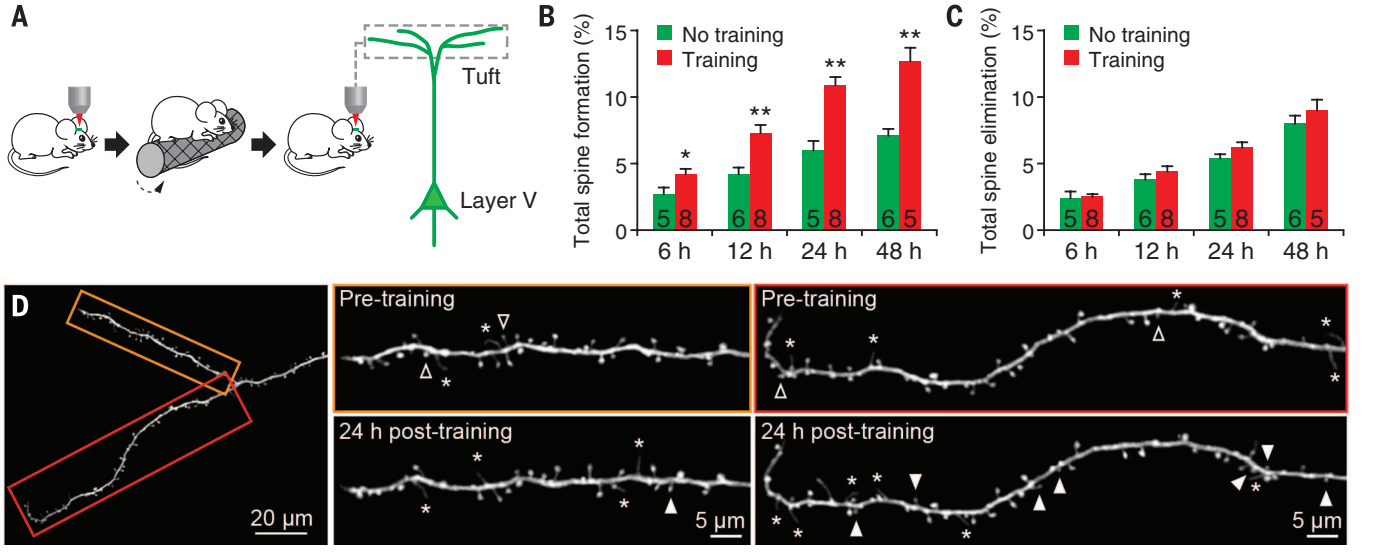

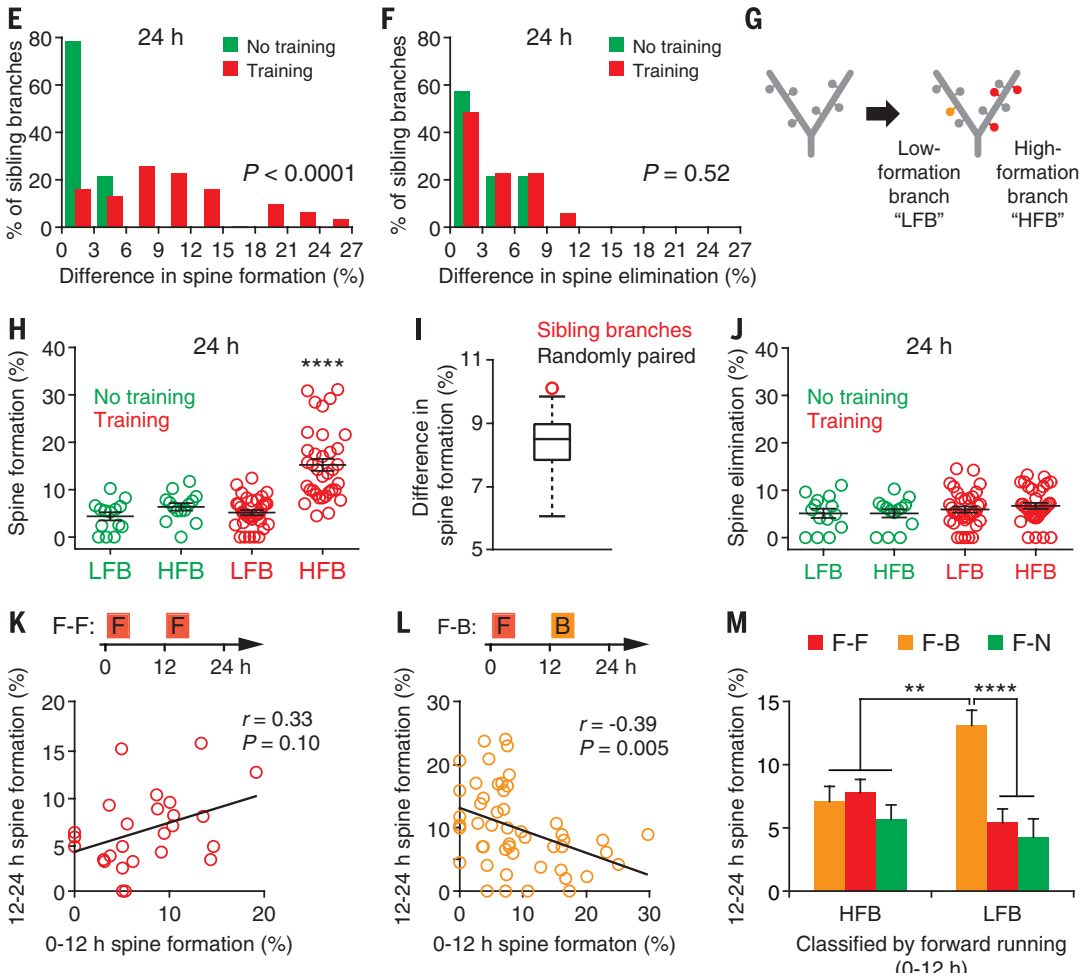

Fig. 1. Motor learning induces branch-specific spine formation. (**A**) Transcranial two-photon imaging in the primary motor cortex of awake, head-restrained mice before and after rotarod motor training. (**B** and **C**) The percentage of dendritic spines formed (B) and eliminated (C) over time after one session of rotarod training (20 trials). Motor training progressively increased new spine formation over the course of 6 to 48 hours. No significant difference in the rate of spine elimination was observed within 48 hours after training. The number of animals is indicated on each column. (**D**) An example of two sibling apical tuft branches with different degrees of spine formation 24 hours after training. Filled arrowheads indicate newly formed dendritic spines and open ones indicate eliminated spines over a 24-hour interval. Asterisks indicate dendritic filopodia. (**E**) Motor training–induced spine formation was significantly different between sibling branches (15 trained mice and 8 control mice). (**F**) No significant difference in spine elimination between sibling branches. (**G**) Classification of sibling dendritic branches to HFBs and LFBs on the basis of the spine formation rate relative to each other. (**H**) Motor training significantly increased the rate of spine formation on HFBs 24 hours after training. (**I**) The average of measured difference in spine formation between HFBs and LFBs was statistically larger ($P < 0.0001$) for sibling branches (red circle) than for randomly paired branches (box plot of results from 100 simulations of random pairing). The simulation was performed to test the null hypothesis that learning-induced spine changes are distributed randomly across all branches. (**J**) There was no significant difference in spine elimination between HFBs and LFBs 24 hours after training. (**K** and **L**) Mice were first trained to run forward on an accelerating rotarod and, 12 hours later, to run either forward (F-F) or backward (F-B). Correlation of spine formation rate on individual branches between 0–12 hours and 12–24 hours. The correlation was positive when animals were subjected to the same forward training [(K) n = 6 mice] and negative when the animals were trained with a backward running task [(L) n = 8 mice]. (**M**) Experimental designs are shown in (K) and (L). Sibling branches were classified as HFBs and LFBs on the basis of the degree of spine formation induced by the initial forward training from 0 to 12 hours. There is a significant increase in spine formation on LFBs than on HFBs after backward training, not after forward running or no training, from 12 to 24 hours. Data are presented as means ± SEM. *$P < 0.05$. **$P < 0.01$. ****$P < 0.0001$, nonparametric test.

Different motor learning tasks often activate the same neurons in the motor cortex (*38*). We wondered whether different learning tasks lead to spine formation on the same or different dendritic branches. To address this question, we trained mice to run forward and, 12 hours later, to run either forward or backward (Fig. 1, K and L). When mice were subjected to the second session of forward running 12 hours after the initial forward-running session, new spines formed during 0 to 12 hours and 12 to 24 hours tended to occur on the same set of branches, although the effect was not statistically significant (Fig. 1K). In contrast, running backwards induced spine formation on a set of branches that showed little formation of new spines in response to the previous forward running (Fig. 1L). Furthermore, when sibling branches were classified as HFBs and LFBs based on the degree of spine formation induced by the initial forward training, we found that backward running, not forward running or no training, induced spine formation mainly on the LFBs but not on the HFBs during the second 12 hours (Fig. 1M).

Our results thus far have revealed task- and branch-specific spine formation over the course of 24 hours after motor skill learning. To test a potential role of sleep in this process, we examined spine formation in mice that were subjected to rotarod training (one 40-trial session of forward running, ~1 hour) and then sleep deprived (SD) for 7 hours by gentle handling (Fig. 2A). Electroencephalography (EEG) monitoring over 7 hours showed that SD mice were awake 97.0 ± 2.1% of the time, whereas mice with undisturbed sleep (non-SD) were awake only 26.4 ± 2.9% of the time ($P < 0.05$) (Fig. 2, B and C). There was a significant reduction in learning-induced spine formation over the entire 8 hours in SD mice when compared to non-SD mice (Fig. 2D). Sleep deprivation specifically reduced spine formation on HFBs (4.9 ± 0.7% versus 9.3 ± 0.7%; $P < 0.0001$), but not on LFBs (2.4 ± 0.4% versus 1.8 ± 0.4%; $P = 0.16$). To investigate whether the effect of sleep deprivation on spine formation might be stress-related, we administered the stress hormone corticosterone (2.5 mg/kg) to non-SD mice after motor training (fig. S3). Corticosterone administration had no significant effects on spine formation on either HFBs or LFBs in the course of 8 hours (Fig. 2D), which suggested that the elevation of stress hormones associated with sleep deprivation is not important for the reduction in spine formation after learning.

To better understand the importance of sleep in dendritic spine formation, we tested whether the reduced spine formation after sleep deprivation could be compensated for by additional training. Although spine formation on HFBs was significantly higher with intensive training (two 40-trial sessions) than with regular training (one 40-trial session) or no training in SD mice ($P < 0.05$) (Fig. 2, A and D), it remained significantly lower than in non-SD mice with regular training ($P < 0.05$). There was no significant difference in spine formation on LFBs among all five groups [$P = 0.35$, one-way analysis of variance (ANOVA)] (Fig. 2D). We also tested whether the reduction in spine formation could be compensated for by subsequent sleep by allowing animals to sleep during the next 16 hours after the initial 7-hour sleep deprivation (Fig. 2A). Over the subsequent 16 hours, the rate of spine formation on either HFBs or LFBs was found to be significantly lower in SD mice than non-SD mice ($P < 0.05$) (Fig. 2E and fig. S4). Thus, the reduction in spine formation after the 7-hour sleep deprivation could not be rescued by either an additional training session or subsequent sleep.

A fraction of learning-induced new spines persists over time, and the number of persisting new spines correlates with long-term retention of motor skills (*18*, *36*). We followed the fate of all new spines that were formed during 8 hours with or without posttraining sleep (Fig. 3A). The survival of new spines on HFBs was significantly higher during the next day in mice with sleep after learning than without ($P < 0.05$) (Fig. 3B). In contrast, the survival of new spines on LFBs was not significantly different between mice with and without sleep ($P = 0.97$) (Fig. 3B). The performance improvement in mice with posttraining sleep, when tested 1 or 5 days after the initial training, was significantly larger when compared to that of SD mice ($P < 0.05$) (Fig. 3C and fig. S5). These results suggest that sleep contributes significantly to the formation of persistent new spines on HFBs, as well as motor skill retention.

Previous studies have shown that the survival of new spines is modulated by subsequent experiences (*18*, *36*). To better understand the

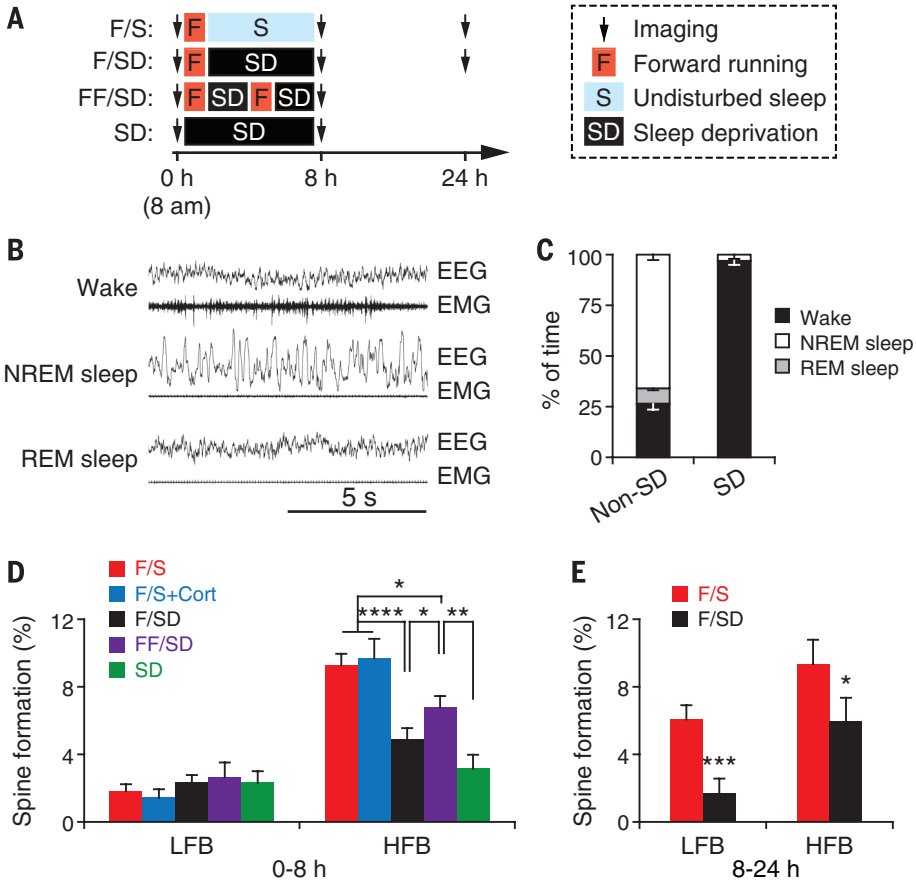

Fig. 2. Postlearning sleep promotes branch-specific spine formation. (**A**) Schematic of experimental paradigm. After imaging and training (40 trials per session), the animals were either subjected to sleep deprivation or left undisturbed to assess the effect of sleep deprivation. (**B**) Examples of the EEG and EMG traces. (**C**) Sleep structure in undisturbed control and SD animals. (**D**) Percentage of spine formation on the sibling branches over the course of 8 hours under various conditions. Sleep deprivation significantly reduced the rate of spine formation on HFBs, but not LFBs, after training. Corticosterone injection (2.5 mg/kg; $n = 4$ mice) into non-SD mice had no significant effect on spine formation on HFBs or LFBs during 8 hours. Spine formation on HFBs was significantly higher in SD mice with intensive training (5 mice) than with regular training (9 mice) or no training (4 mice), but significantly lower than that in non-SD mice with regular training (9 mice). (**E**) Over the course of 16 hours after sleep deprivation, new spine formation on HFBs or LFBs was significantly lower in SD mice than in non-SD mice. Data are presented as means ± SEM. *$P < 0.05$. **$P < 0.01$. ***$P < 0.001$. ****$P < 0.0001$, nonparametric test.

persistence of new spines formed during postlearning sleep, we examined how new spines induced by forward running are affected by subsequent motor learning experiences (Fig. 3D). The survival rate of new spines on HFBs was significantly higher when animals were trained again with the forward-running task than when animals were not trained or were subjected to backward running (Fig. 3E). Notably, the survival rate of new spines on LFBs was significantly lower in mice subjected to backward running when compared with mice subjected to either forward training or no training ($P < 0.01$) (Fig. 3, D and E). This reduction in new dendritic spine survival on LFBs could be related to the fact that backward training tended to promote new spine formation on LFBs (Fig. 1M). Because the majority (78%) of total new spines were formed on HFBs after forward running, the persistence of the total new spines induced by forward running was not significantly affected after backward running (Fig. 3E). The persistence of new spines formed during postlearning sleep may underlie a well-known feature of motor skill learning that, once a skill is learned, it persists for long periods of time with minimum interference by other learning tasks.

How does sleep promote branch-specific spine formation after learning? Sleep consists of two basic states, rapid eye movement (REM) sleep and non-REM (NREM) sleep. To explore the mechanisms underlying sleep-dependent spine formation, we first examined whether REM sleep is required for spine formation after rotarod learning. Mice were subjected to rotarod training (40 trials, ~1 hour) and deprived of REM sleep (REMD) for 7 hours (Fig. 4A). REM sleep was monitored continuously by EEG and electromyography (EMG) recordings and disrupted by gentle touching upon detection. EEG and EMG monitoring in the course of 7 hours showed that REM sleep in REMD mice was significantly reduced when compared to control mice (6.9 ± 1.1 min versus 32.1 ± 4.0 min; $P < 0.01$) (Figs. 2C and 4A). REM deprivation during 7 hours did not disrupt branch-specific spine formation induced by learning (Fig. 4B). Similar to mice with undisturbed sleep, spine formation during 8 hours after training was ~3.1 times as much on HFBs as on LFBs in REMD mice.

Neurons associated with wakeful experience are reactivated in multiple brain regions during subsequent NREM sleep, and this sleep reactivation occurs after the prior wakeful experience (*6*–*11*). Because neuronal activity is critical for regulating synaptic plasticity, neuronal reactivation during NREM sleep could be involved in promoting spine formation. We therefore examined whether motor task–related neurons are reactivated in the primary motor cortex during NREM sleep by performing calcium imaging of layer V pyramidal neurons expressing the genetically encoded calcium indicator GCaMP6 (*39*) (Fig. 4, C and D) (see methods). In this experiment, head-restrained mice were trained to run on a custom-built treadmill under a two-photon microscope. We found that, similar to rotarod motor learning, forward and backward running on the treadmill induced branch-specific spine formation in the course of 8 hours (fig. S6). Many layer V pyramidal neurons showed increased activity, as indicated by elevated levels of Ca^{2+} in cell somata, during forward running on the treadmill as compared to a state of quiet wakefulness (Fig. 4E). Over the 5-min recording period, ~41% (250 out of 617) of neurons showed a large increase (>50%) in somatic Ca^{2+} level ($\Delta F_{running}/\Delta F_{quiet} > 1.5$) and ~39% (242 out of 617) of neurons showed no or moderate increase ($\Delta F_{running}/\Delta F_{quiet}$ = 1.0–1.5). When the same neurons were followed over the next 8 hours, neurons with >50% increase in somatic Ca^{2+} during running ($\Delta F_{running}/\Delta F_{quiet} > 1.5$, defined as task-related neurons) also showed higher levels of somatic Ca^{2+} during NREM sleep when compared to that under the quiet awake state ($P < 0.0001$) (Fig. 4F). To rule out the possibility that certain neurons active during postrunning sleep were not task-related, we removed neurons highly active during prerunning sleep from the analysis of sleep reactivation during postrunning sleep (fig. S7). We found that neurons highly activated during forward running but not during prerunning sleep ($\Delta F_{running}/\Delta F_{quiet} > 1.5$; $\Delta F_{prerun\ sleep}/\Delta F_{quiet} < 1.5$) were reactivated during the postrunning sleep episode (Fig. 4F). In contrast, neurons with no or moderate increase (<50%) in somatic Ca^{2+} level during running did not show a significant increase of Ca^{2+} activity during NREM sleep. These observations are consistent with previous electrophysiological studies of sleep replay in several brain regions (*6*–*11*) and suggest that neuronal reactivation of prior motor experience also occurs in the motor cortex during extended periods of time (>4 hours).

To test whether neuronal reactivation might be involved in branch-specific spine formation, we first blocked *N*-methyl-D-aspartate (NMDA) receptors with MK801 and examined branch-specific spine formation. MK801 (0.25 mg/kg) injection after training significantly reduced the activity of forward running–related neurons during NREM sleep within 8 hours after training ($P < 0.001$) (Fig. 4F). MK801 administration also blocked branch-specific spine formation after training ($P < 0.0001$) (Fig. 4H).

MK801 not only reduces neuronal activity during sleep but also alters the animals' locomotion behavior in the first few hours after drug administration (*40*). Therefore, the effect of MK801 on spine formation may not be specifically related to altered neuronal activity during sleep. To manipulate the extent of neuronal reactivation more specifically, we took advantage of the findings that sleep reactivation is related to prior wakeful experience. We trained mice to run forward and allowed them to sleep for 4 hours. Subsequently, mice either received no further training (F-N) or were trained to run forward (F-F) or backward (F-B) (Fig. 4G). During the second 4-hour sleep period, the reactivation of neurons specific to forward running in the F-B group was significantly reduced when compared to neurons specific to backward-running

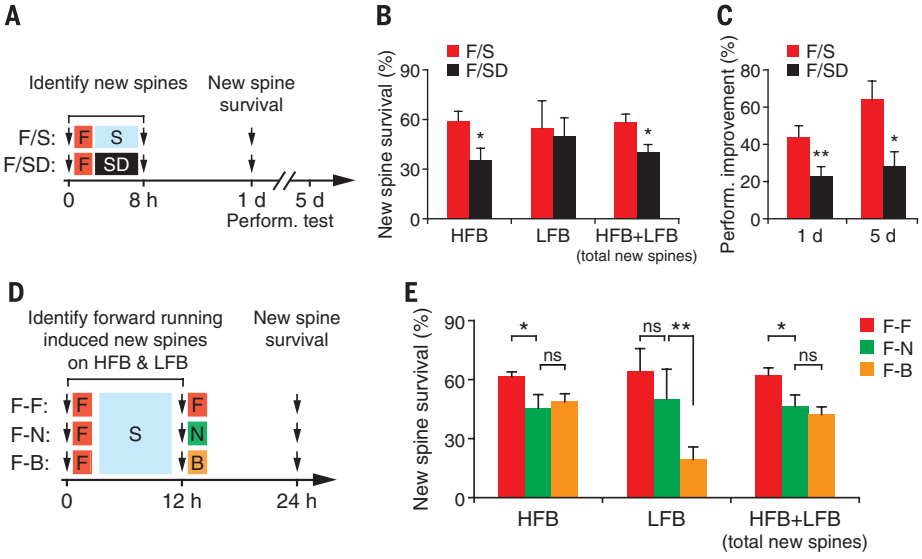

Fig. 3. New spines formed during postlearning sleep persist. (**A**) Schematic of experimental paradigm. (**B**) More new spines formed on HFBs during hours 0 to 8 persist at 24 hours in non-SD mice ($n = 7$) than in SD mice ($n = 8$). (**C**) Performance improvement is significantly larger in non-SD mice than in SD mice 1 or 5 days after training. (**D**) New spines formed within 12 hours after forward running were followed over the next 12 hours when the animals were either not trained ($n = 5$), trained again with the same task ($n = 6$), or trained with a new task (backward running) ($n = 8$). (**E**) Continued training with the same forward-running task facilitates the maintenance of new spines that are formed previously on HFBs. Training with a different task (backward running) significantly reduced the survival of new spines that are formed on LFBs. Data are presented as means ± SEM. *$P < 0.05$. **$P < 0.01$, nonparametric test.

or neurons activated during both forward and backward running in the same F-B group (P < 0.01) (Fig. 4G). The reactivation of neurons specific to forward running in the F-B group was also significantly less than neurons activated during forward running in the F-F and F-N groups (P < 0.01) (Fig. 4G). Notably, when spine formation on sibling branches was examined over the course of 8 hours, the rate of spine formation on HFBs was significantly reduced in the F-B group when compared to the F-F or F-N group (P < 0.05) (Fig. 4H). The ratio of spine formation rates between HFBs and LFBs was 1.8 in the F-B group, substantially lower than 3.5 and 5.6 in the F-F and F-N groups, respectively. Because all three experimental groups experienced a similar amount of sleep but differed in the extent of neuronal reactivation associated with forward training, these results provide further evidence for the role of sleep reactivation in branch-specific spine formation.

Sleep is widely believed to be important for memory consolidation, but the underlying processes remain elusive. There are conflicting views as to whether non-REM sleep contributes to memory consolidation by either promoting or down-regulating synaptic plasticity (*19*–*22*, *29*). By directly imaging postsynaptic dendritic spines over time in the mouse cortex, our results indicate that sleep after learning promotes new spine formation on different sets of apical tuft branches of individual layer V pyramidal neurons. Furthermore, this sleep-dependent, branch-specific spine formation facilitates new spine survival when animals learn different tasks. These findings suggest that sleep promotes learning-induced synapse formation to aid long-term memory storage.

Different motor learning tasks cause spine formation on different sets of dendritic branches. Furthermore, additional training without sleep

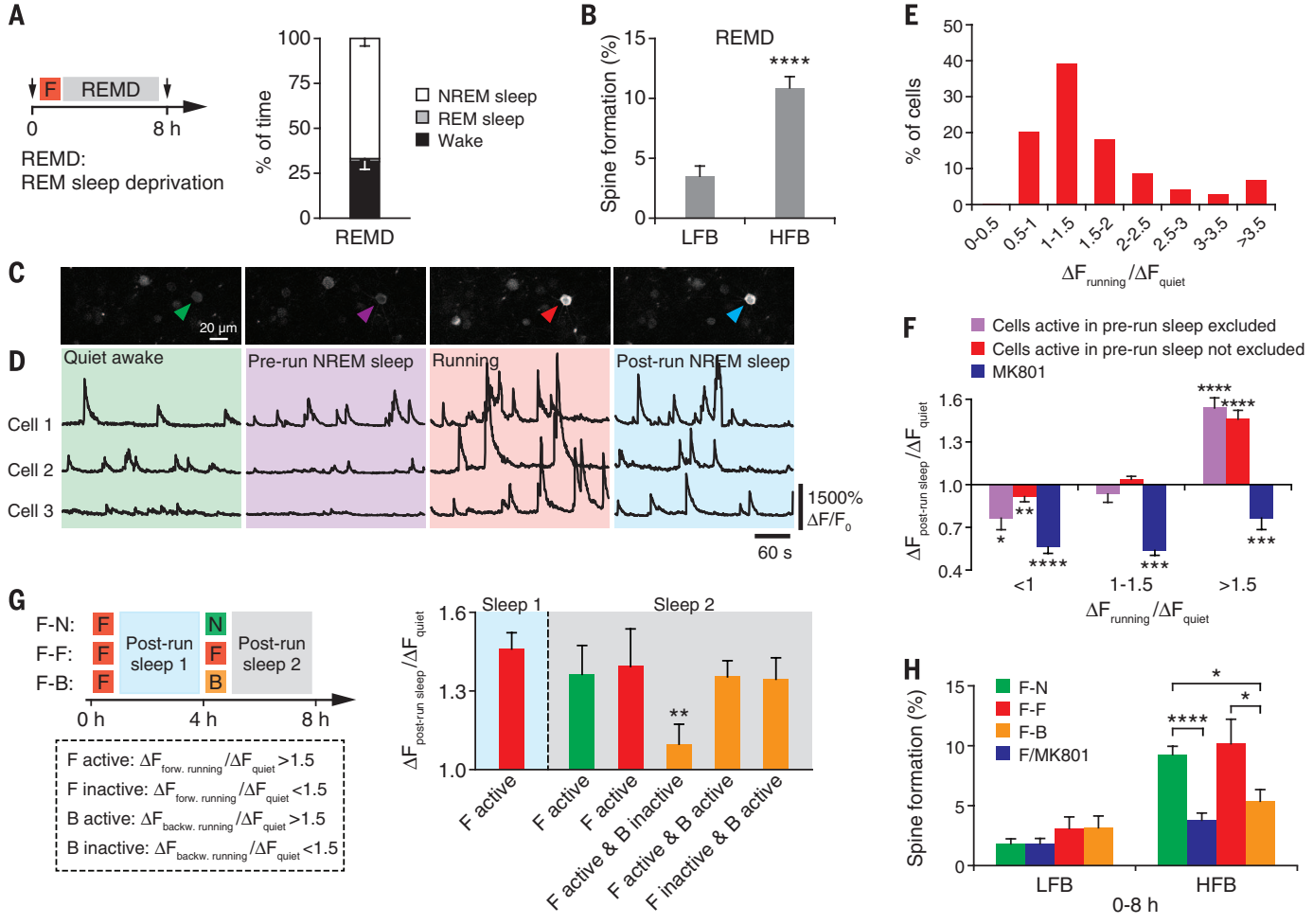

Fig. 4. Branch-specific spine formation involves neuronal reactivation during NREM sleep. (**A**) Mice were deprived of REM sleep (REMD) over the course of 7 hours after rotarod training. (**B**) Learning-induced branch-specific spine formation was not affected by REMD (n = 5 mice). (**C**) Two-photon calcium imaging of layer V neurons from mice expressing GCaMP6 during quiet awake state, prerunning NREM sleep, running, and postrunning NREM sleep. Red arrow points to a soma activated during forward running, and blue arrow points to the same soma reactivated during NREM sleep. (**D**) Calcium fluorescence traces of three neurons under various states. Examples of 5-min traces are shown. (**E**) Frequency distribution of cells with somatic Ca^{2+} change during forward running (617 cells, 17 mice). About 41% of cells show a large increase (>50%) of Ca^{2+} level in somata during forward running (>1.5 relative to the quiet awake state). (**F**) Cells (either inactive or active during prerunning sleep) show a large increase (>50%) in somatic Ca^{2+} level both during running and during postrunning NREM sleep. MK801 administration after running reduced somatic Ca^{2+} level during NREM sleep. (**G**) Experimental design to reduce reactivation of forward-running neurons during sleep. Three groups of mice were trained to run forward and allowed to sleep for 4 hours. Subsequently, each group was either subjected to no training (F-N) or trained to run backward (F-B) or forward (F-F), then allowed to sleep for another 4 hours. Reactivation of forward running–specific cells ($\Delta F_{forw.\ running}/\Delta F_{quiet}$ > 1.5 and $\Delta F_{backw.\ running}/\Delta F_{quiet}$ < 1.5) was significantly reduced during the second 4-hour sleep after mice were trained with a backward-running task (F-B). (**H**) Experimental design is the same as in (G). The rate of spine formation on HFBs was significantly reduced either after MK801 administration or in the F-B group as compared to the F-F or F-N group. Data are presented as means ± SEM. *P < 0.05. **P < 0.01. ***P < 0.001. ****P < 0.0001, nonparametric test.

could promote branch-specific formation (Fig. 2D). Thus, it appears that which set of dendritic branches forms new spines is determined by specific features (input or activity patterns) of a learning task, rather than by sleep. Our data suggest that reactivation of task-specific neurons during NREM sleep is involved in forming new synapses after learning, although definitive proof that reactivation causes synaptic formation would require simultaneous imaging of both reactivation and synapses in the same neurons over time. Neuronal reactivation during sleep may promote branch-specific spine formation in a manner similar to awake learning experiences (Fig. 2D), and its effectiveness in promoting spine formation may vary at different times of the day (fig. S8). Sleep reactivation could also allow the expression of specific genes critical for the growth of new synaptic connections (*32*, *33*). Future studies are needed to address these questions in order to better understand how sleep contributes to memory storage in the brain.

REFERENCES AND NOTES

1. P. Maquet, *Science* **294**, 1048–1052 (2001).
2. J. M. Siegel, *Nature* **437**, 1264–1271 (2005).
3. R. Stickgold, *Nature* **437**, 1272–1278 (2005).
4. S. Diekelmann, J. Born, *Nat. Rev. Neurosci.* **11**, 114–126 (2010).
5. J. H. Benington, M. G. Frank, *Prog. Neurobiol.* **69**, 71–101 (2003).
6. C. Pavlides, J. Winson, *J. Neurosci.* **9**, 2907–2918 (1989).
7. W. E. Skaggs, B. L. McNaughton, *Science* **271**, 1870–1873 (1996).
8. A. S. Dave, D. Margoliash, *Science* **290**, 812–816 (2000).
9. M. A. Wilson, B. L. McNaughton, *Science* **265**, 676–679 (1994).
10. D. Ji, M. A. Wilson, *Nat. Neurosci.* **10**, 100–107 (2007).
11. S. Ribeiro *et al.*, *PLOS Biol.* **2**, E24 (2004).
12. A. S. Dave, A. C. Yu, D. Margoliash, *Science* **282**, 2250–2254 (1998).
13. R. R. Llinás, M. Steriade, *J. Neurophysiol.* **95**, 3297–3308 (2006).
14. V. Crunelli, S. W. Hughes, *Nat. Neurosci.* **13**, 9–17 (2010).
15. C. H. Bailey, E. R. Kandel, *Annu. Rev. Physiol.* **55**, 397–426 (1993).
16. J. W. Lichtman, H. Colman, *Neuron* **25**, 269–278 (2000).
17. D. H. Bhatt, S. Zhang, W. B. Gan, *Annu. Rev. Physiol.* **71**, 261–282 (2009).
18. G. Yang, F. Pan, W. B. Gan, *Nature* **462**, 920–924 (2009).
19. I. Timofeev, *Prog. Brain Res.* **193**, 121–144 (2011).
20. G. Wang, B. Grone, D. Colas, L. Appelbaum, P. Mourrain, *Trends Neurosci.* **34**, 452–463 (2011).
21. M. G. Frank, *Neural Plast.* **2012**, 264378 (2012).
22. J. Born, G. B. Feld, *Neuron* **75**, 933–935 (2012).
23. C. Cirelli, G. Tononi, *Ann. Med.* **31**, 117–124 (1999).
24. V. V. Vyazovskiy, C. Cirelli, M. Pfister-Genskow, U. Faraguna, G. Tononi, *Nat. Neurosci.* **11**, 200–208 (2008).
25. S. Maret, U. Faraguna, A. B. Nelson, C. Cirelli, G. Tononi, *Nat. Neurosci.* **14**, 1418–1420 (2011).
26. G. Yang, W. B. Gan, *Dev. Neurobiol.* **72**, 1391–1398 (2012).
27. J. M. Donlea, N. Ramanan, P. J. Shaw, *Science* **324**, 105–108 (2009).
28. D. Bushey, G. Tononi, C. Cirelli, *Science* **332**, 1576–1581 (2011).
29. G. Tononi, C. Cirelli, *Brain Res. Bull.* **62**, 143–150 (2003).
30. M. G. Frank, N. P. Issa, M. P. Stryker, *Neuron* **30**, 275–287 (2001).
31. S. Chauvette, J. Seigneur, I. Timofeev, *Neuron* **75**, 1105–1113 (2012).
32. S. J. Aton *et al.*, *Neuron* **61**, 454–466 (2009).
33. J. Seibt *et al.*, *Curr. Biol.* **22**, 676–682 (2012).
34. H. P. Roffwarg, J. N. Muzio, W. C. Dement, *Science* **152**, 604–619 (1966).
35. D. Jouvet-Mounier, L. Astic, D. Lacote, *Dev. Psychobiol.* **2**, 216–239 (1969).
36. C. Liston *et al.*, *Nat. Neurosci.* **16**, 698–705 (2013).
37. G. Yang, F. Pan, P. C. Chang, F. Gooden, W. B. Gan, *Methods Mol. Biol.* **1010**, 35–43 (2013).
38. P. V. Zelenin *et al.*, *J. Neurophysiol.* **105**, 2698–2714 (2011).
39. T. W. Chen *et al.*, *Nature* **499**, 295–300 (2013).
40. I. G. Campbell, I. Feinberg, *J. Neurophysiol.* **76**, 3714–3720 (1996).

ACKNOWLEDGMENTS

We thank all the members in the Gan laboratory and T. Franke for comments on the manuscript. This work was supported by NIH R01 NS047325 and P01 NS074972 to W.-B.G. and by a Whitehall Foundation research grant and an American Federation for Aging Research grant to G.Y.

SUPPLEMENTARY MATERIALS

www.sciencemag.org/content/344/6188/1173/suppl/DC1
Materials and Methods
Figs. S1 to S8
References (*41*–*43*)

28 November 2013; accepted 28 April 2014
10.1126/science.1249098

SCHIZOPHRENIA

Specific disruption of thalamic inputs to the auditory cortex in schizophrenia models

Sungkun Chun, Joby J. Westmoreland, Ildar T. Bayazitov, Donnie Eddins, Amar K. Pani, Richard J. Smeyne, Jing Yu, Jay A. Blundon, Stanislav S. Zakharenko*

Auditory hallucinations in schizophrenia are alleviated by antipsychotic agents that inhibit D2 dopamine receptors (Drd2s). The defective neural circuits and mechanisms of their sensitivity to antipsychotics are unknown. We identified a specific disruption of synaptic transmission at thalamocortical glutamatergic projections in the auditory cortex in murine models of schizophrenia-associated 22q11 deletion syndrome (22q11DS). This deficit is caused by an aberrant elevation of Drd2 in the thalamus, which renders 22q11DS thalamocortical projections sensitive to antipsychotics and causes a deficient acoustic startle response similar to that observed in schizophrenic patients. Haploinsufficiency of the microRNA-processing gene *Dgcr8* is responsible for the Drd2 elevation and hypersensitivity of auditory thalamocortical projections to antipsychotics. This suggests that *Dgcr8*-microRNA-Drd2–dependent thalamocortical disruption is a pathogenic event underlying schizophrenia-associated psychosis.

Schizophrenia (SCZ) is one of the most debilitating forms of mental illness (*1*). Positive symptoms of SCZ, including auditory hallucinations, are among the most enigmatic. Antipsychotic agents acting via D2 dopamine receptors (Drd2s) alleviate auditory hallucinations in most patients (*2*, *3*) but do not treat other symptoms (such as cognitive deficits, dampened emotions, and social withdrawal) (*4*). Sensory cortex malfunction has been implicated in hallucinations (*5*, *6*), but which neural circuits become faulty and how they develop selective sensitivity to antipsychotics are unknown.

We tested synaptic transmission at excitatory projections in the auditory cortex (ACx) of *Df(16)1*/+ mice (*7*, *8*), a mouse model of schizophrenia-associated 22q11 deletion syndrome (22q11DS) (*9*) (Fig. 1A). Because positive symptoms emerge during adolescence or early adulthood, we used mature (4- to 5-month-old) mice. We measured evoked AMPA receptor (AMPAR)–mediated excitatory postsynaptic currents (EPSCs) from layer (L) 3/4 pyramidal neurons, the main thalamorecipient neurons in the ACx (*10*), in response to stimulation of thalamocortical (TC) or corticocortical [CC (L3/4-L3/4 or L1-L3/4)] projections in slices containing the auditory thalamus [the ventral medial geniculate nucleus (MGv)], ACx, and hippocampus (Fig. 1, B to E). We also measured synaptic transmission at corticothalamic (CT) projections by recording CT EPSCs in MGv thalamic neurons (Fig. 1F) and at hippocampal CA3-CA1 projections by recording field excitatory postsynaptic potentials (fEPSPs) (Fig. 1G). Only TC projections were deficient in *Df(16)1*/+ mice as compared to wild-type (WT) littermates [30 (WT)/30 (*Df(16)1*/+) neurons] (Fig. 1C and fig. S1), and this deficit occurred in both female and male mice (fig. S2). Synaptic transmission at CC [19 out of 19 (19/19) and 17/16 neurons for L3/4-L3/4 and L1-L3/4, respectively], CT (14/16 neurons), or hippocampal (24/29 slices) projections was normal (Fig. 1, D to G, and fig. S1).

Several findings supported the idea that TC deficiency in *Df(16)1*/+ mice is presynaptic. Two-photon calcium imaging in dendritic spines of L3/4 neurons loaded with the calcium indicator Fluo-5F and cytoplasmic dye Alexa 594 (Fig. 1H) identified functional TC inputs (Fig. 1I). The

Department of Developmental Neurobiology, St. Jude Children's Research Hospital, Memphis, TN 38105, USA.
***Corresponding author. E-mail: stanislav.zakharenko@stjude.org**

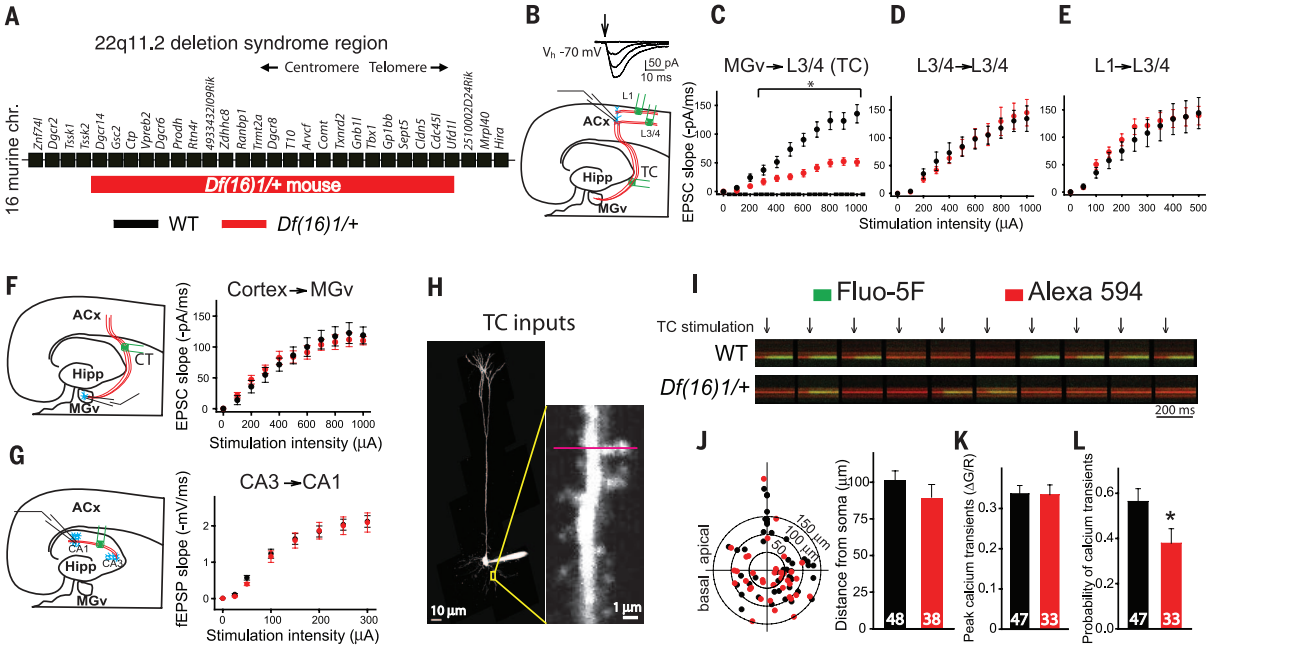

Fig. 1. Specific deficit of TC synaptic transmission to the ACx of 22q11DS mice. (**A**) Map of 22q11DS orthologs in *Df(16)1/+* mice. (**B**) Voltage-clamp recordings in thalamorecipient L3/4 pyramidal neurons. Arrow, electrical stimulation (top). TC slices showing the MGv, hippocampus (Hipp), and ACx (bottom). (**C** to **E**) Input-output relationships between stimulation intensity and EPSCs at TC (MGv-L3/4) (C), L3/4-L3/4 (D), and L1-L3/4 (E) projections. (**F** and **G**) CT EPSC and CA3-CA1 fEPSP recordings (left) and input-output relationship (right). (**H**) L3/4 pyramidal neuron filled with Fluo-5F and Alexa 594 (left) to visualize dendritic spines (right). The red line represents the line scan. (**I**) Calcium transients in a dendritic spine in response to a single TC stimulation (arrows) repeated 10 times (0.1 Hz). (**J**) TC input locations on dendritic trees of L3/4 pyramidal neurons [48 (WT)/38 (*Df(16)1/+*) spines from 17 (WT)/11 (*Df(16)1/+*) neurons] (left); (0;0), soma coordinates. Average distances from soma to TC inputs (right) are shown. (**K** and **L**) Calcium transient amplitudes (K) and probabilities (L) in response to 10 single TC stimulations. The numbers of spines tested are shown inside columns. *$P < 0.05$ [(C) and (L)].

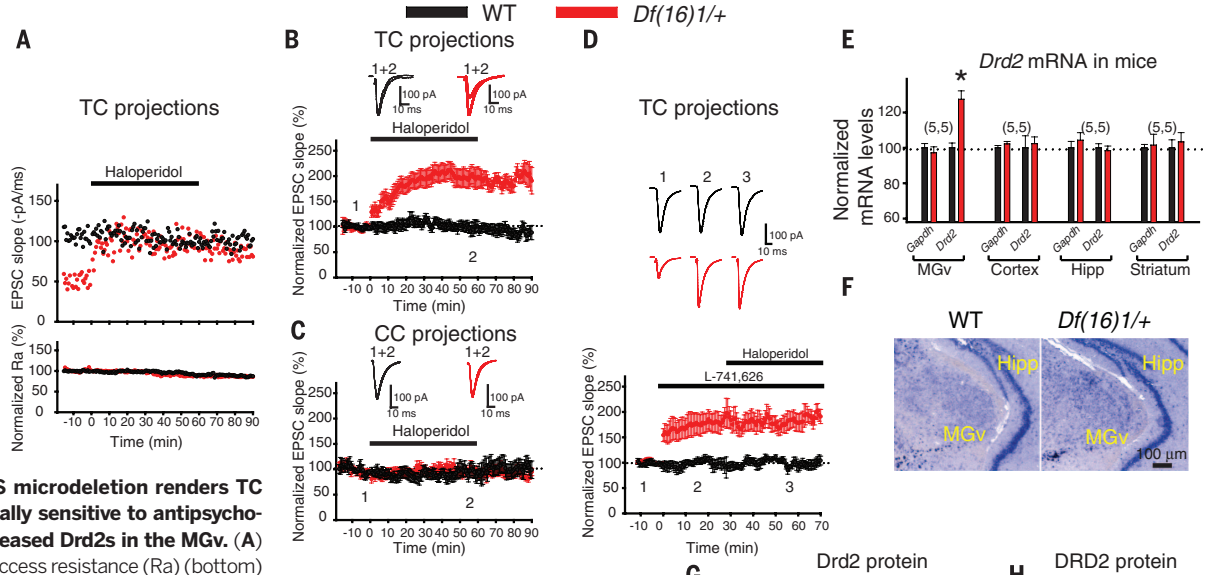

Fig. 2. The 22q11DS microdeletion renders TC projections abnormally sensitive to antipsychotics because of increased Drd2s in the MGv. (**A**) TC EPSCs (top) and access resistance (Ra) (bottom) during repeated TC stimulations (0.05 Hz, 600 μA) before and after haloperidol (1 μM). (**B** and **C**) Mean EPSCs normalized to initial baseline at TC ($P < 0.001$, 16/21 neurons) (B) and L3/4-L3/4 CC projections ($P = 0.75$, 15/14 neurons) (C) before and after haloperidol. (**D**) Normalized TC EPSCs before and after L-741,626 (20 nM) and haloperidol (5/12 neurons). (Insets) Representative EPSC traces. (**E**) Average mRNA levels of *Drd2* normalized to *Gapdh* in different brain regions. (**F**) *Drd2* in situ hybridization. (**G** and **H**) Average Drd2 and DRD2 protein levels normalized to β-actin in mice (G) and the MGv from postmortem tissues of healthy human controls and patients with SCZ (H). Numbers of mice or human samples are shown inside columns or parentheses. *$P < 0.05$ [(E), (G), and (H)].

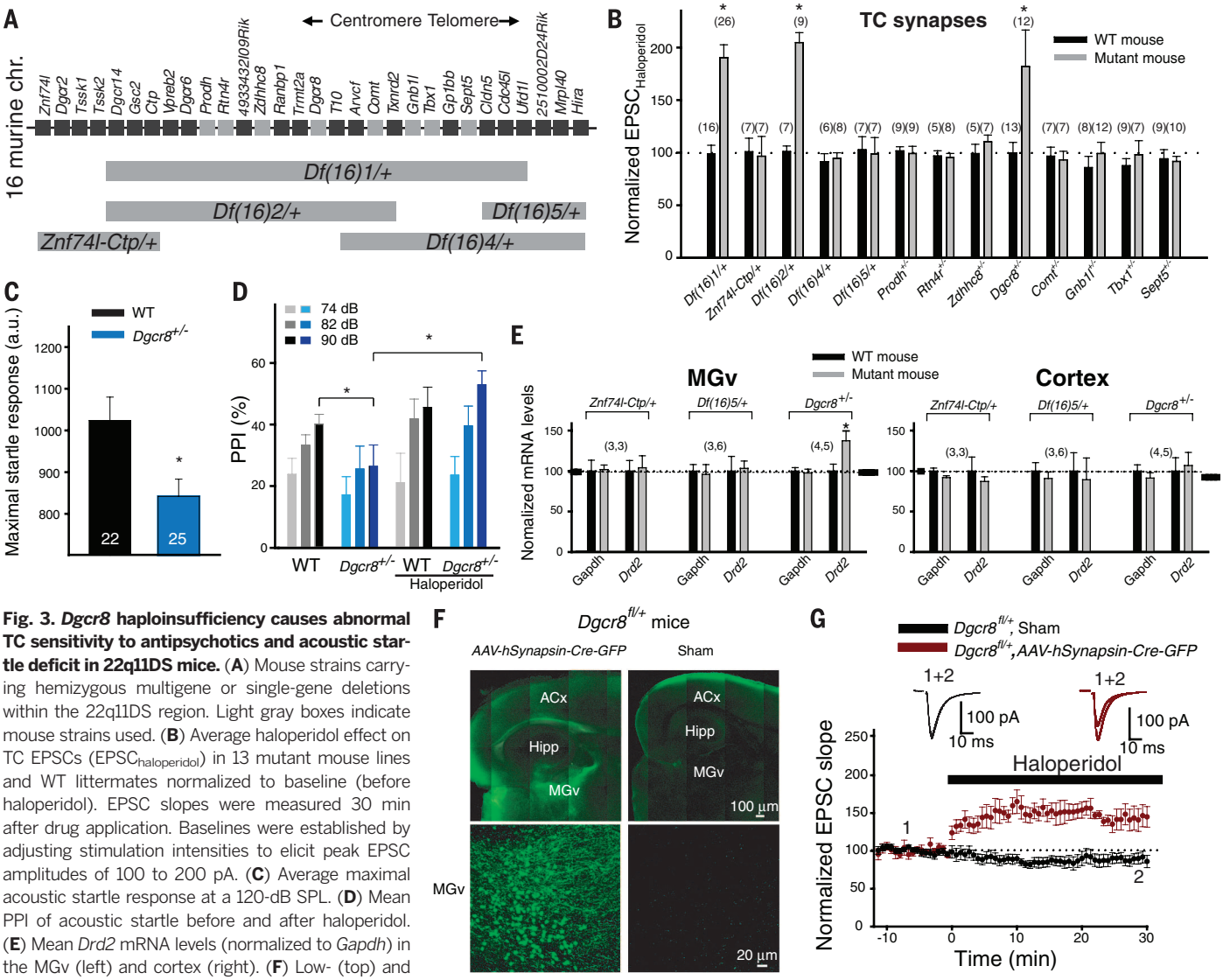

Fig. 3. *Dgcr8* haploinsufficiency causes abnormal TC sensitivity to antipsychotics and acoustic startle deficit in 22q11DS mice. (**A**) Mouse strains carrying hemizygous multigene or single-gene deletions within the 22q11DS region. Light gray boxes indicate mouse strains used. (**B**) Average haloperidol effect on TC EPSCs ($EPSC_{haloperidol}$) in 13 mutant mouse lines and WT littermates normalized to baseline (before haloperidol). EPSC slopes were measured 30 min after drug application. Baselines were established by adjusting stimulation intensities to elicit peak EPSC amplitudes of 100 to 200 pA. (**C**) Average maximal acoustic startle response at a 120-dB SPL. (**D**) Mean PPI of acoustic startle before and after haloperidol. (**E**) Mean *Drd2* mRNA levels (normalized to *Gapdh*) in the MGv (left) and cortex (right). (**F**) Low- (top) and high- (bottom) magnification images of a TC slice from $Dgcr8^{fl/+}$ mice injected with *AAV-hSynapsin-Cre-GFP* (left) or ACSF (sham, right). (**G**) Mean TC EPSCs before and after haloperidol in $Dgcr8^{fl/+}$ mice injected in vivo with *AAV-hSynapsin-Cre-GFP* or sham ($P < 0.05$, 8/6 neurons). Insets show representative TC EPSCs. The dotted line indicates the baseline. Numbers of neurons (B) or mice [(C) and (E)] are shown inside columns or parentheses.*$P < 0.05$.

distribution of thalamic inputs on dendritic trees and the calcium-transient amplitudes were normal (Fig. 1, J and K), but calcium-transient probability was deficient at TC synapses of *Df(16)1/+* mice (Fig. 1L). Paired-pulse depression evoked electrically or optogenetically was reduced at *Df(16)1/+* TC projections (fig. S3). The FM 1-43 assay (*11*) showed slower dye release from TC terminals in mutant mice (fig. S4). Monosynaptic TC *N*-methyl-D-aspartate receptor (NMDAR)–dependent EPSCs were also deficient in *Df(16)1/+* mice (fig. S5). However, the NMDAR/AMPAR ratio was unaffected (fig. S6). Minimal electrical stimulation of the thalamic radiation that typically evoked unitary EPSCs (successes) or no ESPCs (failures) revealed reduced release probability in TC projections of *Df(16)1/+* mice (fig. S7). A synaptic deficiency rather than a decrease in the excitability of thalamic neurons seemed to cause the presynaptic deficit at *Df(16)1/+* TC projections (fig. S8).

The antipsychotics haloperidol (1 µM) and clozapine (40 µM) reversed the synaptic defect of *Df(16)1/+* TC connections (Fig. 2 and fig. S9). Normalized EPSC data revealed that *Df(16)1/+* (but not WT) TC projections are sensitive to antipsychotics (Fig. 2B and fig. S9A). CC projections of both genotypes remained insensitive to the drugs (Fig. 2C and figs. S9B and S10 to S12). The response of mutant TC projections to antipsychotics was dose-dependent (fig. S13). Approximately 85% of mutant TC neurons responded more strongly than WT neurons to antipsychotics (fig. S14). In contrast to the ACx, TC projections in *Df(16)1/+* somatosensory or visual cortices were not sensitive to haloperidol (fig. S15).

The sensitivity of *Df(16)1/+* TC projections to antipsychotics was mediated by Drd2s. The Drd2-specific antagonist L-741,626 (20 nM) enhanced TC EPSCs in *Df(16)1/+* but not WT mice (Fig. 2D). Subsequent application of haloperidol did not induce an additional effect, suggesting that both agents act through Drd2s (Fig. 2D). Drd2 agonist quinpirole (0.5 to 20 µM) did not affect TC or CC EPSCs in WT or *Df(16)1/+* mice (fig. S16). Dopaminergic projections from the ventral tegmental area were present in the thalamic radiation and ACx (fig. S17) and therefore may deliver dopamine to TC projections. We hypothesized that ambient dopamine in the MGv and ACx may activate abnormally upregulated Drd2 in TC projections of *Df(16)1/+* mice. Quantitative real-time polymerase chain reaction (Fig. 2E) and in situ hybridization (Fig. 2F and fig. S18) revealed an increase in *Drd2* transcript levels in the *Df(16)1/+* MGv. Splice variants of *Drd2* (*D2Short* and *D2Long*) (fig. S19) and Drd2 protein levels (Fig. 2G) were comparably increased in the *Df(16)1/+* MGv. Transcript and protein levels

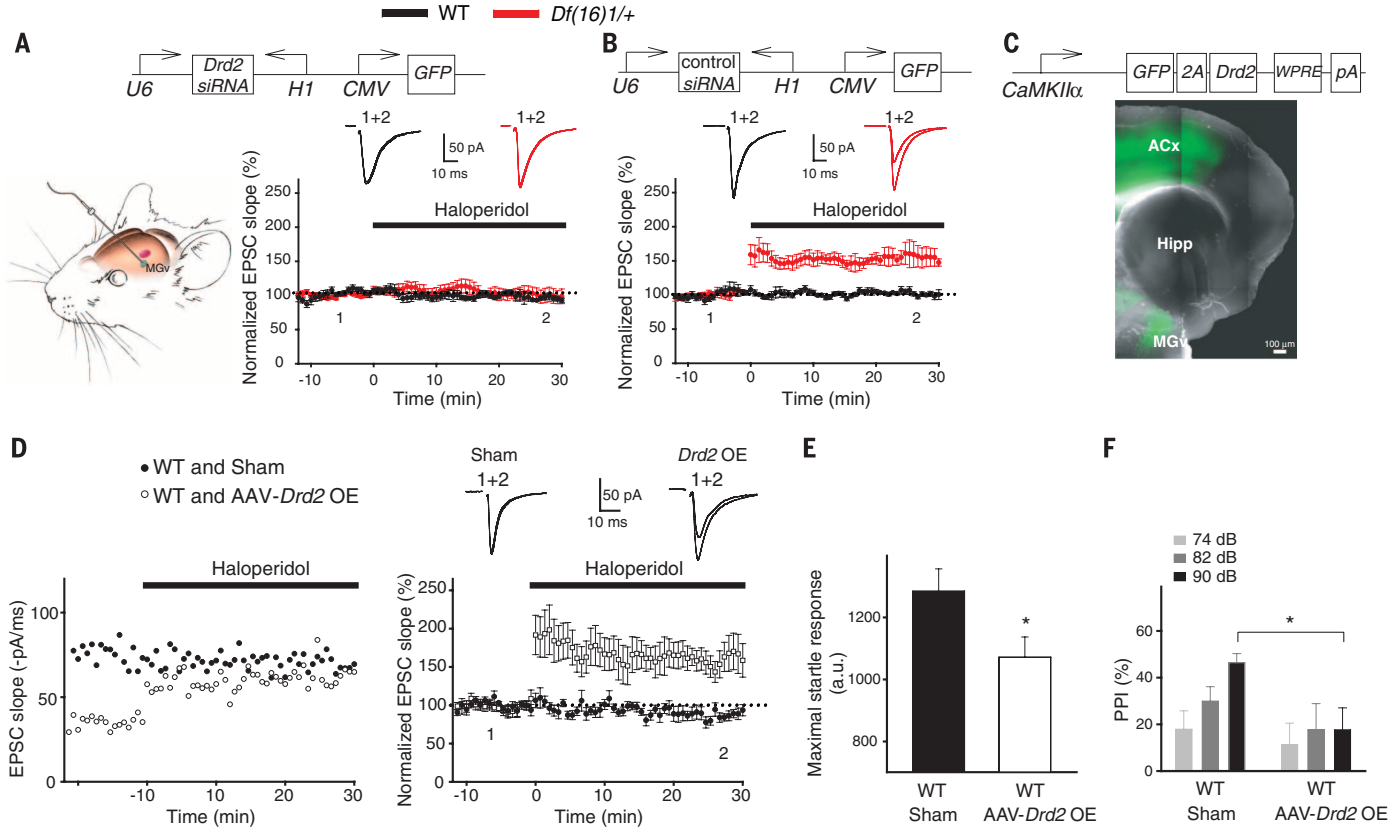

Fig. 4. Aberrant Drd2 elevation in MGv neurons is necessary and sufficient to render TC projections sensitive to antipsychotics. (**A** and **B**) *Drd2* [(A), top] and control [(B), top] siRNA viruses. In vivo MGv viral injection [(A), bottom left]. Mean TC EPSCs before and after haloperidol in mice injected with *Drd2* siRNA [(A), bottom right] ($P = 0.67$, 9/11 neurons) or control siRNA viruses (B, bottom) ($P = 0.016$, 7/9 neurons) are shown. (**C**) Composition of the *Drd2*-OE virus [woodchuck hepatitis posttranscriptional regulatory element (*WPRE*), polyA signal (*pA*)] (top) and TC slice showing green fluorescent protein (*GFP*) in MGv neurons (bottom). (**D**) Representative TC EPSCs (left) and mean normalized TC EPSCs (right) before and after haloperidol from WT mice injected with *Drd2*-OE or sham ($P < 0.05$, 7/9 neurons). (**E** and **F**) Acoustic startle response (E) at a 120-dB SPL and PPI (F) in WT mice injected with *Drd2*-OE or sham (10 mice each) into the MGv, $^*P < 0.05$. Dotted lines, baseline; insets, representative TC EPSCs.

increased in the thalamus but not the cortex, hippocampus, and striatum (Fig. 2, E and G). However, total dopamine levels in all regions assayed were comparable between both genotypes (fig. S20). In postmortem human tissues (Fig. 2H and table S1), DRD2 protein levels in the MGv were higher in SCZ patients than in healthy controls ($P < 0.001$, 13 patients per group).

We next screened 12 mouse strains carrying hemizygous deletions of gene clusters or individual genes within the microdeletion for haloperidol sensitivity (Fig. 3A). We measured TC EPSCs before and after haloperidol application in mutants and WT littermates. In addition to *Df(16)1/+*, only *Df(16)2/+* and *Dgcr8*$^{+/-}$ mice responded to haloperidol (Fig. 3B). The microRNA-processing gene *Dgcr8* is encoded within the *Df(16)2* region (Fig. 3A). Like *Df(16)1/+*, approximately 80% of *Dgcr8*$^{+/-}$ neurons responded more strongly than WT neurons to the antipsychotics (figs. S21 and S22), implying an impaired flow of acoustic information in *Dgcr8*$^{+/-}$ mice. The acoustic startle response was lower in mature *Dgcr8*$^{+/-}$ mice than in WT littermates (22/25 mice, $P < 0.05$) (Fig. 3C). This deficit may affect prepulse inhibition (PPI) of acoustic startle, a characteristic feature of SCZ in animal models and human patients. *Dgcr8*$^{+/-}$ mice were deficient in PPI [24/29 mice, $P < 0.05$ at a 90-dB sound pressure level (SPL)] (Fig. 3D), and this deficit was rescued by haloperidol ($P < 0.05$ at a 90-dB SPL) (Fig. 3D).

Consistent with the notion that *Dgcr8* haploinsufficiency underlies the sensitivity of TC projections to antipsychotics in 22q11DS, *Drd2* mRNA levels were found to be increased in the MGv but not the cortex of *Dgcr8*$^{+/-}$ mice (Fig. 3E). *Znf74l-Ctp/+* and *Df(16)5/+* microdeletions, which do not include *Dgcr8*, produced no increase in *Drd2* (Fig. 3E), but *Df(16)2/+* mice carrying a *Dgcr8*-containing microdeletion did (fig. S23).

Conditional *Dgcr8* hemizygous deletion in MGv neurons (Fig. 3F) rendered TC projections sensitive to antipsychotics (Fig. 3G), indicating that MGv-specific reduction in *Dgcr8* underlies TC deficiency in 22q11DS mice.

To test whether Drd2 elevation causes TC deficiency, we knocked down *Drd2* in MGv neurons (Fig. 4A and fig. S24A). *Drd2* small interfering RNA (siRNA) but not scrambled (control) siRNA decreased *Drd2* levels in the MGv (fig. S24B) and eliminated the sensitivity of mutant TC projections to antipsychotics (Fig. 4, A and B). Drd2 overexpression in MGv excitatory neurons (Fig. 4C) made WT TC projections sensitive to haloperidol (Fig. 4D) and caused deficits in acoustic startle and PPI in WT mice (Fig. 4, E and F).

Thus, we have identified that an SCZ-associated microdeletion up-regulates Drd2 in thalamic neurons and disrupts glutamatergic synaptic transmission at TC projections to the ACx, and this is caused by haploinsufficiency of *Dgcr8*. This mechanism integrates several competing SCZ models such as dopamine hyperfunction theory (*2*), glutamatergic hypofunction theory (*12*), TC disconnectivity theory (*13*), and TC loop dysfunction models (*14*). Our results indicate disturbances in the *Dgcr8*-microRNA-Drd2 pathway in thalamic projections to the ACx as a pathogenic mechanism that alters the normal flow of auditory information and thereby contributes to positive symptoms of SCZ.

REFERENCES AND NOTES

1. T. R. Insel, *Nature* **468**, 187–193 (2010).
2. A. Carlsson, *Neuropsychopharmacology* **1**, 179–186 (1988).
3. S. H. Snyder, *Philos. Trans. R. Soc. London Ser. B* **354**, 1985–1994 (1999).
4. S. Miyamoto, N. Miyake, L. F. Jarskog, W. W. Fleischhacker, J. A. Lieberman, *Mol. Psychiatry* **17**, 1206–1227 (2012).
5. T. Dierks *et al.*, *Neuron* **22**, 615–621 (1999).

6. D. Hubl, T. Koenig, W. K. Strik, L. M. Garcia, T. Dierks, *Br. J. Psychiatry* **190**, 57–62 (2007).
7. E. A. Lindsay *et al*., *Nature* **401**, 379–383 (1999).
8. E. A. Lindsay *et al*., *Nature* **410**, 97–101 (2001).
9. 22q11DS is caused by the hemizygous deletion of a 1.5- to 3-megabase region of the q arm of human chromosome 22, and SCZ develops in approximately 30% of patients with 22q11DS. *Df(16)1/+* mice carry a hemizygous deletion of 23 genes in the syntenic region of chromosome 16.
10. P. H. Smith, L. C. Populin, *J. Comp. Neurol.* **436**, 508–519 (2001).
11. S. S. Zakharenko, L. Zablow, S. A. Siegelbaum, *Nat. Neurosci.* **4**, 711–717 (2001).
12. J. T. Coyle, *Harv. Rev. Psychiatry* **3**, 241–253 (1996).
13. N. D. Woodward, H. Karbasforoushan, S. Heckers, *Am. J. Psychiatry* **169**, 1092–1099 (2012).
14. R. P. Behrendt, *Conscious. Cogn.* **12**, 413–451 (2003).

ACKNOWLEDGMENTS

This work was supported, in part, by NIH grants R01 MH097742, R01 MH095810, and R01 DC012833 and the American Lebanese Syrian Associated Charities. We thank E. Illingworth, P. Scambler, A. Wynshaw-Boris, J. Gogos, S. Strittmatter, B. Morrow, and E. Fuchs for providing mutant mice; A. Lessard and the Maryland Brain Collection for providing postmortem human brain samples; K. J. Sample and P. Devaraju for technical assistance; and St. Jude Children's Research Hospital, University of Tennessee, University of North Carolina, and University of Pennsylvania Vector Cores for producing adeno-associated viruses and lentiviruses.

SUPPLEMENTARY MATERIALS

www.sciencemag.org/content/344/6188/1178/suppl/DC1
Materials and Methods
Figs. S1 to S24
Table S1
References (*15*–*20*)

25 March 2014; accepted 14 May 2014
10.1126/science.1253895

NEURODEVELOPMENT

Cell-intrinsic requirement of Dscam1 isoform diversity for axon collateral formation

Haihuai He,[1,2,3]* Yoshiaki Kise,[1,2]* Azadeh Izadifar,[1,2] Olivier Urwyler,[1,2] Derya Ayaz,[1,2]† Akhila Parthasarthy,[3] Bing Yan,[1,2] Maria-Luise Erfurth,[1,2,4] Dan Dascenco,[1,2] Dietmar Schmucker[1,2]‡

The isoform diversity of the *Drosophila* Dscam1 receptor is important for neuronal self-recognition and self-avoidance. A canonical model suggests that homophilic binding of identical Dscam1 receptor isoforms on sister dendrites ensures self-avoidance even when only a single isoform is expressed. We detected a cell-intrinsic function of Dscam1 that requires the coexpression of multiple isoforms. Manipulation of the Dscam1 isoform pool in single neurons caused severe disruption of collateral formation of mechanosensory axons. Changes in isoform abundance led to dominant dosage-sensitive inhibition of branching. We propose that the ratio of matching to nonmatching isoforms within a cell influences the Dscam1-mediated signaling strength, which in turn controls axon growth and growth cone sprouting. Cell-intrinsic use of surface receptor diversity may be of general importance in regulating axonal branching during brain wiring.

Several classes of neuronal cell surface receptors exhibit an exceptional degree of protein diversity and have been implicated in important aspects of neuronal differentiation (*1*–*5*). Evidence for the importance of isoform diversity during development has been provided for the *Drosophila* Down syndrome cell adhesion molecule (Dscam1) and the mouse clustered protocadherins (PCDHs) (*6*–*14*). The *Dscam1* gene uses combinatorial alternative splicing to generate tens of thousands of different receptor isoforms, whereas the clustered PCDHs rely on combinatorial oligomerization to provide a huge diversification of their binding specificities (*2*, *7*, *9*, *11*). The isoform diversity is thought to provide neurons with distinct "surface tags," thereby endowing them with unique molecular identities. Such complex molecular recognition mechanisms are particularly important for the development of highly branched neurite compartments.

Many neuronal circuits depend on the presence of highly branched axons or dendrites, which serve to increase either the wiring complexity or the size of the input/output fields. The development of branched dendritic fields requires a dedicated mechanism—often referred to as self-avoidance—that ensures correct spacing between sister neurites and prevents hypo- or hyperinnervation (*7*). For Dscam1 it has been shown that isoform-specific homophilic binding on the surface of sister dendrites provides the molecular recognition mechanism that underlies neurite repulsion and self-avoidance (*12*–*14*). This molecular model of self-avoidance has also been proposed for the vertebrate PCDH gamma receptors (*10*).

This model, which we refer to as the canonical model of Dscam1/PCDH function, states that isoform-specific homophilic receptor binding on the surface of sister dendrites initiates neurite repulsion, and that the expression of a single Dscam1 isoform per neuron is sufficient for Dscam1 function (*12*–*15*). The question of whether this canonical role provides the mechanistic basis of all Dscam1 functions is still open to debate (*3*, *7*, *9*). Addressing this point, we found evidence for a strictly cell-intrinsic requirement of multiple diverse Dscam1 isoforms and describe a function of isoform diversity specifically required for the patterning of complex axonal arborizations.

To examine the role of Dscam1 diversity, we generated bacterial artificial chromosome (BAC)–based conditional alleles (*16*) that express Dscam1 protein at endogenous levels and allow for the manipulation of Dscam1 diversity in a spatially and temporally specific manner (Fig. 1A) (*17*). We found that the *[Dscam1]EX6.1-FRT* allele recapitulates all known neuronal wiring functions of Dscam1 and is functionally equivalent to the endogenous *Dscam1* (Fig. 1, fig. S1, and table S1). We analyzed thoracic mechanosensory (MS) neurons, which innervate the macrochaetae of adult flies and show a stereotypic axonal branching pattern in the ventral nerve cord (VNC) (*3*) (Fig. 1B). The loss of *Dscam1* in MS neurons causes severe MS axon growth and branch patterning defects (*3*) (Fig. 1C). However, replacing the endogenous *Dscam1* locus with the BAC-based *[Dscam1]EX6.1-FRT* allele rescued all mutant defects (fig. S1).

In sharp contrast to the *[Dscam1]EX6.1-FRT* allele, the *[Dscam1]EX6.1-Flpd* allele lacking all but one of the exon 6 variants (Fig. 1A) did not restore the axon collateral formation (Fig. 1, D and E). Often only an ipsilateral primary axon shaft was formed (Fig. 1E), but collateral branches were missing (78%, $n = 37$). In some cases, primary branches were formed but lacked higher-order branches and varicosities (fig. S2) (22%, $n = 37$). Because similar branching defects have been observed in experiments where exon 9 diversity was lacking in whole flies (*8*), we conclude that any substantial and global reduction in Dscam1 isoform diversity causes a loss of MS axon collaterals.

The use of BAC-based *Dscam1* alleles allowed us to combine multiple engineered and endogenous *Dscam1* alleles and revealed a striking dominant and dosage-dependent influence of Dscam1 diversity on axonal branching (Fig. 1, F to I). A single copy of *[Dscam1]EX6.1-Flpd* in a wild-type background dominantly caused a specific lack of a primary anterior ipsilateral branch (86%) (Fig. 1H). When two copies of *[Dscam1]EX6.1-Flpd* were added, the dominant phenotype was enhanced such that additional primary branches were missing in 45% of the

[1]Neuronal Wiring Laboratory, Vlaams Instituut voor Biotechnologie (VIB) Vesalius Research Center, 3000 Leuven, Belgium. [2]Department of Oncology, School of Medicine, University of Leuven, 3000 Leuven, Belgium. [3]Department of Cancer Biology, Dana-Farber Cancer Institute, Boston, MA 02215, USA. [4]Institute of Biochemistry, Christian-Albrechts-University of Kiel, 24118 Kiel, Germany.
*These authors contributed equally to this work. †Present address: Laboratory of Ion Channel Research, University of Leuven, 3000 Leuven, Belgium. **‡Corresponding author. E-mail: dietmar.schmucker@vib-kuleuven.be**

flies (n = 29) (Fig. 1F). Overall, higher severity and penetrance of the branching phenotype were observed by increasing the ratio of *[Dscam1]EX6.1-Flpd* to endogenous *Dscam1*. Conversely, the dominant effect was partially suppressed by adding a normal *Dscam1* allele (i.e., *[Dscam1]EX6.1-FRT*) and was completely suppressed by having three copies of wild-type *Dscam1* alleles (Fig. 1I).

Similar branching defects were observed when using the analogous *[Dscam1]EX6.7-Flpd* and *[Dscam1]EX6.21-Flpd* alleles in which exon 6 variants have been swapped (fig. S2). Profiling the *Dscam1* mRNA in flies bearing *[Dscam1]EX6.n-Flpd* alleles revealed that alternative exons 4 and 9 of transgenic and endogenous *Dscam1* can still be normally spliced and their protein expression is not impaired (fig. S1 and tables S2

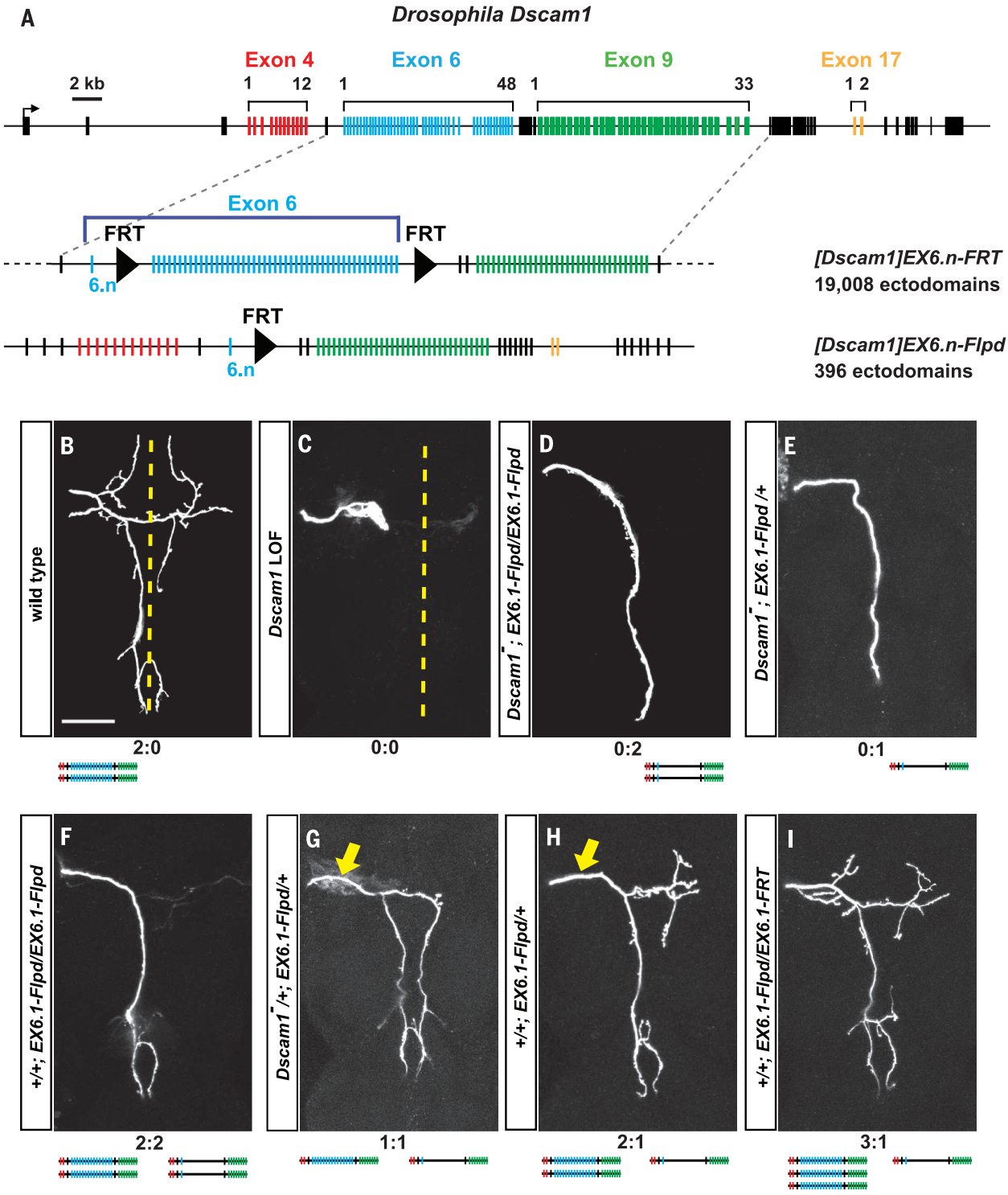

Fig. 1. Reduction of Dscam1 diversity causes dominant and dosage-dependent impairment of axonal branching. (**A**) Schematic representation of the genomic structure of the *Dscam1* gene and *Dscam1* BAC alleles, used for manipulation of Dscam1 diversity. (**B** to **I**) Axonal branching patterns of MS neurons resulting from different combinations of endogenous Dscam1 (left) and the *[Dscam1]EX6.1-Flpd* allele (right) as indicated below panels. Phenotypic defects have been quantified (Table 1). The dashed line indicates the midline of the central nervous system; arrows indicate missing primary branches. Scale bar, 50 μm.

and S3). Taken together, the dominant nature of the branching defects makes it unlikely that the lack of axonal branches resulted from potentially reduced levels of Dscam1 protein.

On the basis of the role of *Dscam1* in self versus nonself discrimination (*4*–*9*), one might assume that global reduction of the Dscam1 diversity in *[Dscam1]EX6.1-Flpd* flies results in an increased frequency of "same-isoform" encounters between neurons contacting each other. To investigate this possibility, we used the *[Dscam1]EX6.1-FRT* allele to reduce the Dscam1 diversity by Flp recombinase expression in a cell-specific fashion (Fig. 2, A and B, and figs. S3 and S4) (*17*). We found that the selective elimination of exon 6 diversity in a subset of peripheral sensory neurons also caused strong axon branching defects at high penetrance (80 to 90%), despite spatial and temporal differences in Flp recombinase expression (Fig. 2B, Table 1, and figs. S3 and S4) (*17*). Frequently, only the main axon shaft was formed (Fig. 2B and fig. S3C), or only distal branches (figs. S3D and S4G), or only short stubs or varicosities were detected (fig. S3E and fig. S4, C, E, and H).

We also used double dye fills to compare the axon branching pattern of two MS neurons innervating the same VNC target area. We found, without exception, that only MS neurons expressing Flp recombinase exhibited branch patterning defects (Fig. 2B and figs. S3G and S4); their neighboring MS neurons were unaffected (Fig. 2B′ and figs. S3G′ and S4).

In contrast to the strong branching defects observed in MS neurons, we did not observe any defect in dendritic branch formation of class I dendritic arborization (DA) neurons (fig. S5). Therefore, consistent with previous reports (*12*–*15*), we found no indication for a cell-intrinsic requirement of Dscam1 isoform diversity for dendrite morphogenesis of DA neurons.

To investigate further why a potential repertoire of *396* Dscam1 isoforms in MS neurons is not sufficient for proper MS axon branching, we directly examined Dscam1 isoform expression in single posterior scutellar (pSc) neurons (fig. S6). In single wild-type pSc neurons, many isoforms are expressed with no clear preference of exon 6 variants. However, in agreement with previous multicell profiling experiments (*18*–*21*), we found that expression of exon 4 and exon 9 was highly biased and that exon 4.2 and exon 4.8 were the most frequently identified exon 4 variants (>65%) in pSc neurons.

In single pSc neurons of *Dscam1-null;[Dscam1]EX6.1-Flpd* flies, we found a similar strong bias in exon 4 and exon 9 variants, but all variants contained exon 6.1. We found no evidence that the excision of exon 6.2–6.48 would indirectly or aberrantly influence splicing of isoforms (tables S2 and S3).

Taken together, these results indicate that a much smaller set of isoforms than the hypothetically available repertoire of up to *396* isoforms is used in mutant MS neurons. Because of strong quantitative differences in expression levels (*19*), we conclude that very few Dscam1 isoform variants are predominantly expressed in MS neurons of *[Dscam1]EX6.1-Flpd* flies.

This increase of identical isoforms in neurons with reduced exon 6 diversity supports the hypothesis that too many "same-isoform" interactions within MS neurons are causing an overactivation of Dscam1 function cell-intrinsically, but does not strictly exclude other possibilities. To exclude a potential role of axon-axon interactions, we used several approaches to restrict the isoform reduction to single neurons (Fig. 2, C and E, and figs. S7, S8, S9, and S11). Even if the reduction of exon 6 diversity was limited to only one MS neuron, pronounced axon branching defects were frequently detected (80 to 85%; Fig. 2D, Table 1, and fig. S7). The phenotypic spectra were similar to those observed in flies in which Dscam1 diversity was reduced in broad tissue domains (Fig. 2B and figs. S3 and S4). Performing double dye-fill experiments, we found that the branching pattern of the neighboring anterior scutellar neuron (aSc) was normal despite strong defective branch patterning of the pSc neuron (Fig. 2D′ and fig. S7), which is in direct contact with the aSc axon (fig. S7). The penetrance of the phenotypes was high (80 to 85%), although the expressivity differed depending on the respective GAL4 transactivator used (Table 1 and figs. S7 to S10) (*17*).

In a complementary approach, we used heat shock–mediated induction of sparse stochastic Flp recombinase expression (figs. S11 and S12) (*17*) to generate flies in which single MS neurons had reduced Dscam1 diversity (Fig. 2, E and F, and fig. S11). We found that a significant number of green fluorescent protein (GFP)–positive cells with reduced Dscam1 diversity (47%) exhibited strong or moderate axon branching defects (Fig. 2F, Table 1, and fig. S11).

To further test the cell-autonomous function of Dscam1 diversity in MS axons, we overexpressed a Dscam1 isoform selectively in single MS neurons (fig. S13). Consistent with our single-cell Flp-out experiments, we observed strong defects in axonal branching of posterior dorsocentral (pDc) neurons (fig. S13 and fig. S17, G and H).

We also examined whether Dscam1 isoform interactions between axons of MS neurons and processes or cells of potential target neurons contribute to branch patterning, and found that Dscam1 diversity in the VNC is dispensable for

Table 1. Quantification of branching phenotypes of pSc neurons. Branching phenotypes were classified into two groups: In strong phenotypes, the midline crossing branch is not formed (i.e., Fig. 1, D to F; Fig. 2, B, D, and F; fig. S2, B, D, and F; fig. S3, C, D, and G; fig. S4, C, D, G, and H; fig. S7, C, C′, D, D′, F, and G; fig. S11, E, E′, and G). In moderate phenotypes, the midline-crossing branch or a stub is formed but is missing other primary and higher-order branches (i.e., Fig. 1, G and H; fig. S2, C and E; fig. S3E; fig. S4E; fig. S7, C″ and D″; fig. S11E″).

Genotype	*n*	Strong	Moderate	Normal branching
Wild type	171	0%	2.9%	97.1%
Reduced diversity in all neurons, wild type versus EX6.n-Flpd				
0:1 (6.1)	37	78%	22%	0%
0:2 (6.1)	33	73%	27%	0%
0:1 (6.7)	41	73%	27%	0%
0:1 (6.21)	39	79%	21%	0%
Dominant effects, wild type versus EX6.1-Flpd				
2:2	29	45%	55%	0%
1:1	37	11%	89%	0%
2:1	35	0%	86%	14%
3:1	32	0%	3.1%	96.9%
Reduced diversity in sensory field				
455-Gal4	201	62%	18%	20%
pnr-Gal4	34	62%	29%	9%
Reduced diversity in single MS neurons				
R36D01-Gal4	40	67%	18%	15%
R15E08-Gal4	39	31%	49%	20%
Heat shock single clones	45	38%	9%	53%
Reduced diversity in target area				
worniu-Gal4	37	0%	2.7%	97.3%

the overall mechanism of axon collateral formation of MS axons (figs. S14 to S16) (*17*).

These results indicate that the presence of too many identical isoforms within MS axons is detrimental to axon growth and branching. This suggests that in contrast to self-avoidance in DA neuron dendrites, the Dscam1 isoform diversity in MS axons is required cell-intrinsically.

Finally, we asked how reduction of Dscam1 isoform diversity impairs the ability of axons to elaborate collateral branches during development. We examined single growth cones of MS axons, comparing pDc axon growth of neurons from wild-type flies, flies with *Dscam1* knockdown through RNA interference (RNAi), and flies with Dscam1 isoform reduction (Fig. 3) (*17*). In wild-type neurons, a characteristic sprouting phase could initially be identified, with a plethora of long filopodia-like extensions starting to project in many different directions (Fig. 3A). This was followed by a more ordered redistribution of filopodia-like extensions along the anterior-posterior axis as well as toward the midline (Fig. 3B). In the next phase, the consolidated axon collaterals and the main axon shaft were growing in length (fig. S17A).

In MS axons with reduced Dscam1 protein levels, the early growth cones exhibited a defective morphology with abnormally dense and short filopodia-like extensions (Fig. 3, C and D, and fig. S17B). In contrast, growth cones with a reduced Dscam1 diversity appeared to have fewer filopodia-like extensions (Fig. 3, E and F, and fig. S17C). Note that for mutant pDc neurons, the earliest onset of growth cone sprouting occurs with an 8- to 10-hour delay, suggesting the possibility of an impairment of axon growth per se. However, although Dscam1 has a role in axon growth, several observations suggest that Dscam1 diversity may also contribute directly to growth cone sprouting and branching (figs. S18 and S19). For example, a moderate increase in Dscam1-Dscam1 homophilic interactions does not cause any axon growth delay but causes branching defects (figs. S17I and S18). Similarly, single isoform expression does not lead to a delay but nonetheless leads to dominant axon branching defects (fig. S13 and fig. S17, G and H). In summary, the developmental analysis suggests that changes in the abundance and diversity of Dscam1 isoforms influence axon growth and growth cone sprouting, resulting in disrupted growth cone morphologies.

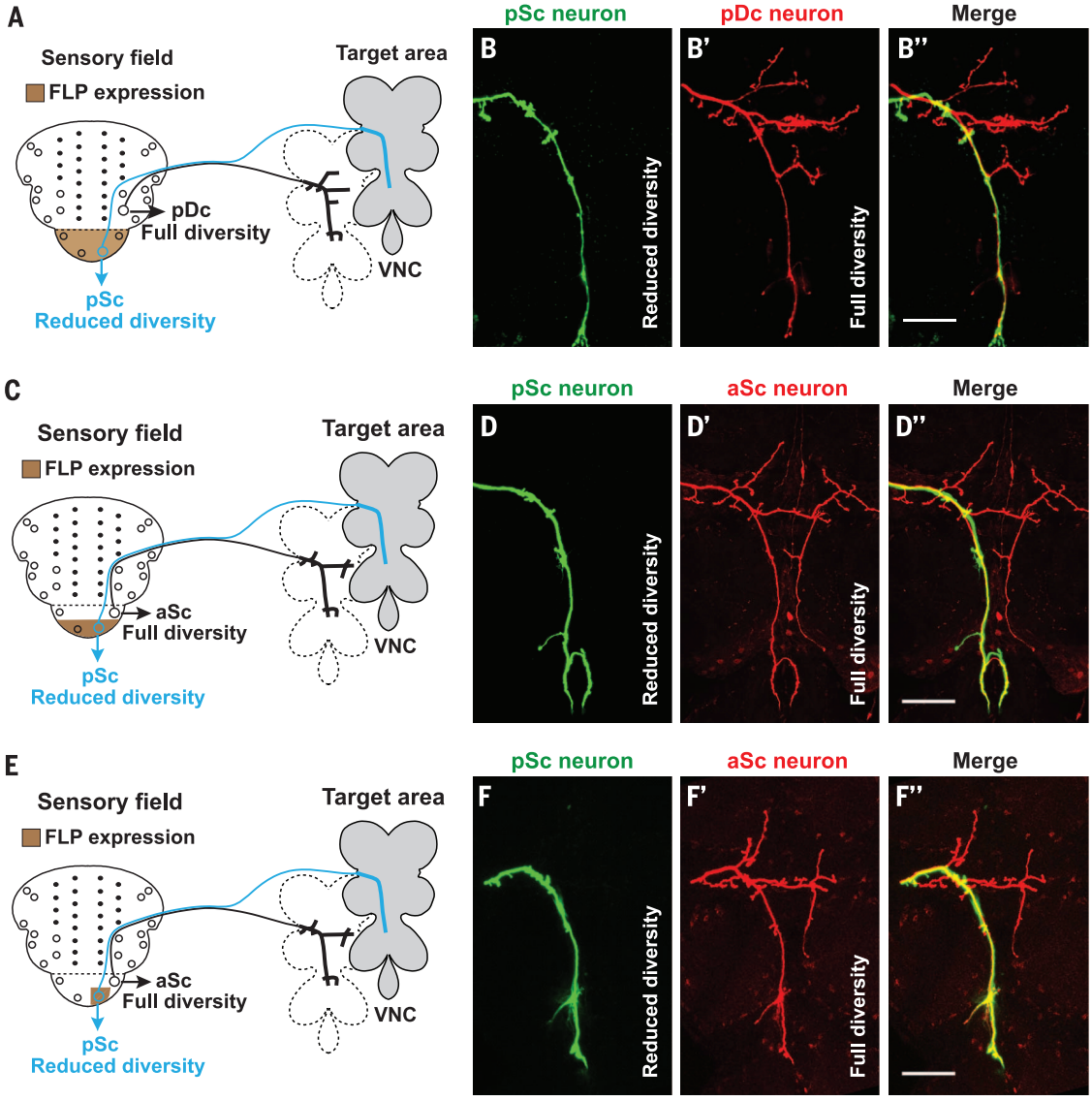

Fig. 2. Cell-Intrinsic requirement of Dscam1 isoform diversity for axonal branching pattern of MS neurons. (**A**, **C**, and **E**) Schematic representation of reducing Dscam1 diversity in two pairs of neurons (pSc, aSc) (A), in both pSc neurons (C), or in a single pSc neuron (E) by using *455-Gal4*, *R36D01-Gal4*, or mild heat shock, respectively, to induce Flp recombinase expression (*17*). For illustration purposes, the axon branching patterns are sketched separately. (**B**, **D**, and **F**) Despite strong branching defects in the mutant pSc neuron, the pDc neuron (B) and aSc neuron with full Dscam1 diversity [(D) and (F)] both show a normal branching pattern (see also figs. S3, S7, and S11). Branching patterns of pSc and neighboring pDc or aSc neurons were visualized by double dye labeling (*17*). Quantification of phenotypic defects is summarized in Table 1. Scale bars, 50 μm.

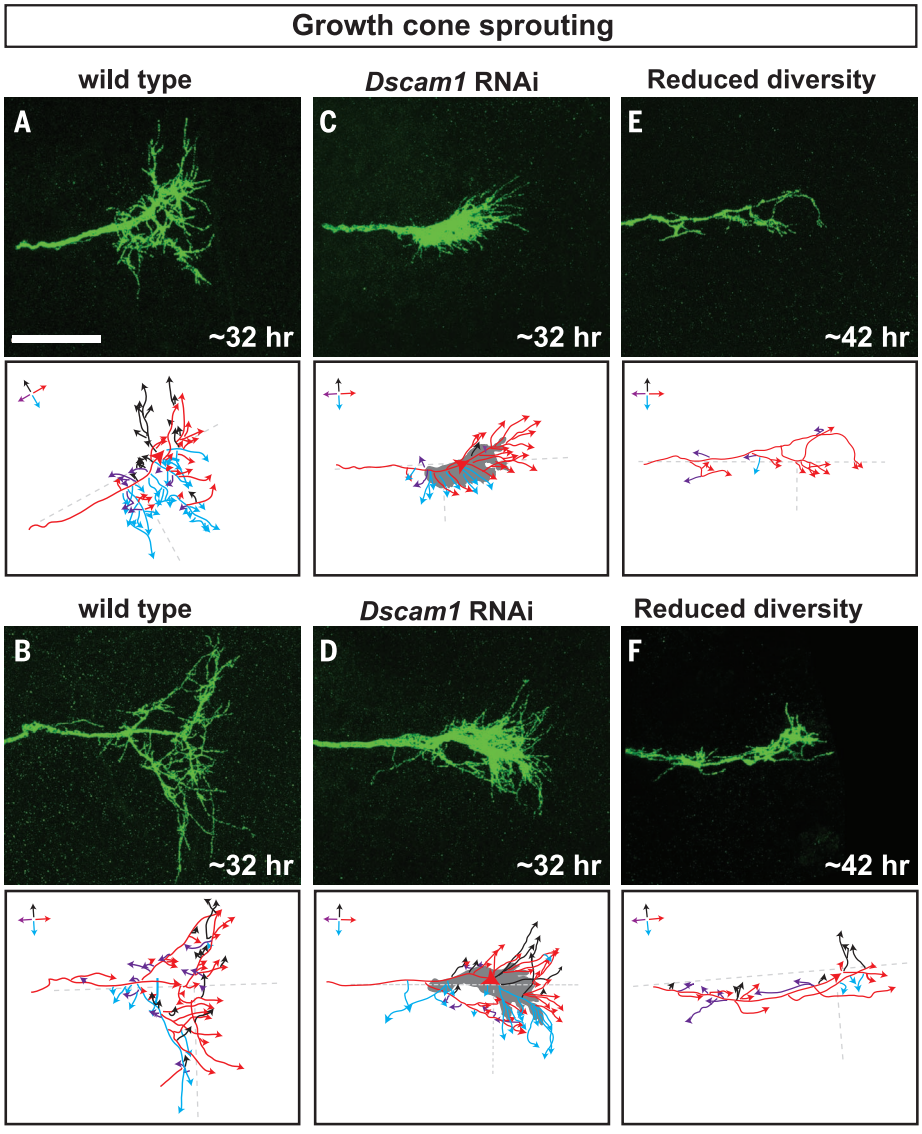

Fig. 3. Manipulation of Dscam1 activity affects growth cone sprouting. Images show growth cone morphology of single pDc neurons at the sprouting stage. Tracings of filopodia-like extensions are color-coded; arrowheads indicate growth direction of single filopodia-like extensions. (**A** and **B**) Growth cones of wild-type pDc at ~32 hours APF (after puparium formation) show a complex morphology with many long filopodia-like extensions projecting into all directions. (**C** and **D**) Growth cones of pDc neurons with Dscam1 RNAi knockdown at ~32 hours APF. The abnormally dense filopodia-like extensions do not separate well and within the center (gray area) are too dense to be traced individually. Filopodia-like extensions "escaping" from the central domain often project in the same direction. (**E** and **F**) Growth cones of pDc neurons with reduced Dscam1 diversity at ~42 hours APF. Axon growth is delayed by ~10 hours and the growth cones are highly abnormal, exhibiting a reduced number of filopodia-like extensions. Scale bar, 20 μm.

Why does cell-intrinsic isoform reduction cause axonal branching defects in single MS neurons? Given that our single-cell isoform profiling revealed that the reduction of isoform diversity leads to the presence of more identical Dscam1 isoforms in MS neurons, it seems prudent to assume that this results in more homophilic Dscam1-Dscam1 binding in mutant growth cones and causes a gain of *Dscam1* function. The dominant dosage-sensitive effects of *[Dscam1]EX6.1-Flpd* (Fig. 1, G to I, and fig. S17I) and the cell-autonomous single isoform overexpression (fig. S13), as well as the sensory neuron–specific Flp-out experiments (Fig. 2), are all consistent with the interpretation that the observed axon branching defects result from Dscam1 gain-of-function signaling. In molecular terms, we propose a model in which growth cones of MS axons are exquisitely responsive to quantitative differences in Dscam1 signaling. Specifically, we propose that when more identical-type isoforms are present in growth cones, more Dscam1 signaling occurs, and as a consequence, axon growth as well as growth cone dynamics (e.g., regulation of filopodia-like extensions) are strongly impaired (model in fig. S20).

REFERENCES AND NOTES

1. Q. Wu, T. Maniatis, *Cell* **97**, 779–790 (1999).
2. D. Schmucker *et al.*, *Cell* **101**, 671–684 (2000).
3. B. E. Chen *et al.*, *Cell* **125**, 607–620 (2006).
4. D. Schmucker, *Nat. Rev. Neurosci.* **8**, 915–920 (2007).
5. D. Hattori *et al.*, *Nature* **449**, 223–227 (2007).
6. D. Hattori, S. S. Millard, W. M. Wojtowicz, S. L. Zipursky, *Annu. Rev. Cell Dev. Biol.* **24**, 597–620 (2008).
7. Y. Kise, D. Schmucker, *Curr. Opin. Neurobiol.* **23**, 983–989 (2013).
8. D. Hattori *et al.*, *Nature* **461**, 644–648 (2009).
9. S. L. Zipursky, J. R. Sanes, *Cell* **143**, 343–353 (2010).
10. J. L. Lefebvre, D. Kostadinov, W. V. Chen, T. Maniatis, J. R. Sanes, *Nature* **488**, 517–521 (2012).
11. D. Schreiner, J. A. Weiner, *Proc. Natl. Acad. Sci. U.S.A.* **107**, 14893–14898 (2010).
12. M. E. Hughes *et al.*, *Neuron* **54**, 417–427 (2007).
13. B. J. Matthews *et al.*, *Cell* **129**, 593–604 (2007).
14. P. Soba *et al.*, *Neuron* **54**, 403–416 (2007).
15. W. Wu, G. Ahlsen, D. Baker, L. Shapiro, S. L. Zipursky, *Neuron* **74**, 261–268 (2012).
16. K. J. Venken, Y. He, R. A. Hoskins, H. J. Bellen, *Science* **314**, 1747–1751 (2006).
17. See supplementary materials on *Science* Online.
18. X. L. Zhan *et al.*, *Neuron* **43**, 673–686 (2004).
19. W. Sun *et al.*, *EMBO J.* **32**, 2029–2038 (2013).
20. A. M. Celotto, B. R. Graveley, *Genetics* **159**, 599–608 (2001).
21. G. Neves, J. Zucker, M. Daly, A. Chess, *Nat. Genet.* **36**, 240–246 (2004).

ACKNOWLEDGMENTS

Supported by NIH grant 2RO1NS046747-05A1 (D.S.); Fonds Wetenschappelijk Onderzoek (FWO) grants G059611N, G078913N, and G077013N (D.S.); BELSPO IUAP VII-20 "WIBRAIN project" (D.S.); VIB funding; a JSPS postdoctoral fellowship and a Human Frontier Science Program long-term fellowship (Y.K.); an FWO Ph.D. fellowship (D.D.); a Swiss National Science Foundation postdoctoral fellowship (O.U.); and a Boehringer Ingelheim Fonds Ph.D. fellowship (M.-L.E.). We thank members of the lab and especially B. Hassan (VIB, Center for the Biology of Disease) for critical reading of the manuscript, discussions, and insightful comments.

SUPPLEMENTARY MATERIALS

www.sciencemag.org/content/344/6188/1182/suppl/DC1
Materials and Methods
Supplementary Text
Figs. S1 to S20
Tables S1 to S3
References (*22*–*35*)

6 February 2014; accepted 8 May 2014
Published online 15 May 2014;
10.1126/science.1251852

Gel Protein Recovery System

The Gel Protein Recovery GPR-850 instrument delivers efficient recovery of gel separated intact proteins through a multiplexed, automated, microfluidics chip-based process. The GPR System (consisting of the GPR-850 instrument, GPRchips, and GPR Buffers and Reagents) enables researchers to recover intact proteins and peptides for subsequent top-down proteomics experiments. This process facilitates effective protein identification, characterization, and quantitation by mass spectrometry. The effectiveness of the system is enhanced by the use of proprietary reagents together with the microfluidic-based GPRchip. The GPR System combines these components to provide a high throughput recovery platform for researchers interested in studying intact proteins. The GPR system features several kits specifically designed for specialized downstream mass spec applications, including ESI-MS and LC-MALDI. The new GPR-850 instrument features an updated user interface, improved mechanical and industrial design, and comes in six different colors to match the personalities of researchers, laboratories, or institutions.

Protea Biosciences Group
For info: 304-284-2600
www.proteabio.com

Gel Image Capture & Documentation System

The new gel documentation and analysis systems omniDOC and omniDOCi provide researchers with a quick, simple, and flexible solution for their gel documentation needs in a compact and affordable benchtop unit. The integral five megapixel camera combined with CSL basic gel analysis software ensures a perfect image every time along with the provision for image analysis. Each omniDOC system provides a simple yet sophisticated imaging solution for most laboratories and most budgets. The five megapixel camera with slide-out ultraviolet transilluminator, optional blue epi-illumination module and white light table, makes the omniDOC suitable for imaging most fluorescent and colormetric gels. The USB port requires a cable to connect the dark room assembly to an external PC for control, while imaging applications are simplified by the pre-focused camera that requires little, or no manual adjustment. The result is easy one-click image acquisition with analysis software guiding the user through every step of the gel documentation process.

Cleaver Scientific
For info: +44-(0)-1788-565300
www.cleaverscientific.com

Gel Imaging Systems

The high sensitivity G:BOX Chemi XX6 and XX9 image analysis systems utilize the power of the latest CCD camera technology. These versatile systems are capable of exceptional imaging of 1-D and 2-D gels, as well as chemi and fluorescent blots. The G:BOX Chemi XX6 and XX9 feature high resolution, high-quantum efficiency (73% quantum efficiency at 425 nm) low noise CCD cameras with the highest level (f0.95) auto-focus lens and six and nine megapixel resolution respectively. Since the cameras are cooled to -53°C, the XX9 and XX6 systems can generate excellent images of chemi blots with minimal background noise and the system's large imaging areas (32.3 cm x 25.6 cm) also mean both systems are ideal for accurately imaging larger blots, as well as larger 1-D and 2-D gels. These systems can be fitted with a range of LED lighting and filter options making them suitable for fluorescence, chemi-luminescence, IR, and 2-D gel applications.

Syngene
For info: 800-686-4407
www.syngene.com

Gel Imaging System

The sensitive and robust Amersham Imager 600 series is designed to enable capture and analysis of high-resolution digital images of protein and DNA samples in gels and membranes. These multipurpose imagers deliver high performance imaging to chemiluminescence, fluorescence, and colorimetric applications and the wide dynamic range allows weak and strong signals to be quantitated accurately at the same time. Full system automation means that after startup, there is no need for focusing, insertion of light sources, changing of filters, calibrations, or other adjustments. In each capture mode, images are automatically corrected for both geometric and intensity distortion therefore minimizing the hassle of post-processing for publication. The seamless workflow allows users to readily detect and quantitate bands, determine molecular weight, and perform normalization. With integrated analysis software controllable via a touchscreen device, the results are presented in both tabular and graphical formats, enabling quick and easy generation and analysis of data.

GE Life Sciences
For info: 800-526-3593
www.gelifesciences.com/amershamwesternblotting

Protein Delivery Reagent

The BioPORTER Protein Delivery Reagent is a unique lipid formulation that allows direct translocation of proteins into living cells. Comprising a unique cationic lipid mixture that interacts non-covalently with the protein, BioPORTER creates a protective vehicle for immediate protein delivery. BioPORTER makes studying protein functionality faster and easier than ever before by bypassing the traditional DNA transfection, transcription, and protein translation processes. After capturing the protein, the reagent transports the lipid protein complex into the target cell. The delivered proteins retain their structure and function while leaving the transduced cells unharmed. Because of its simple delivery mechanism and because there's no fusion partner or covalent bond formation, BioPORTER can efficiently deliver functionally active proteins into a wide range of cell types. The reagent is especially useful when studying protein function in cells that are difficult to transfect using traditional DNA transfection reagents.

AMS Biotechnology
For info: +44-(0)-1235-828200
www.amsbio.com

Electronically submit your new product description or product literature information! Go to www.sciencemag.org/products/newproducts.dtl for more information.

Newly offered instrumentation, apparatus, and laboratory materials of interest to researchers in all disciplines in academic, industrial, and governmental organizations are featured in this space. Emphasis is given to purpose, chief characteristics, and availability of products and materials. Endorsement by *Science* or AAAS of any products or materials mentioned is not implied. Additional information may be obtained from the manufacturer or supplier.

By **Jacopo Marino**

On the road again

"Is your English good enough?" Gian Luigi Rossi, my former supervisor, asked as we left the biochemistry building at the University of Parma in Italy on a hot afternoon in June 2006. My English was OK—but before I could ask, "Good enough for what?" he jumped in his car and drove away. When I saw him again the next day, the reason for the question became clear: I had an opportunity to spend the summer abroad, working at the University of Zurich (UZH) in Switzerland and learning state-of-the-art purification techniques for membrane proteins in the group led by Andreas Plückthun. Later, I returned to UZH to pursue a Ph.D. in the lab of Oliver Zerbe, applying nuclear magnetic resonance to the study of membrane proteins. I'm now finishing my Ph.D.

With good research infrastructure and nature all around, Switzerland is a great place to do science. The country ranks in the top six nations in investing in science and in the top three for the impact of its scientific publications. Coming from Italy (where things are quite different), I find the wealth of resources here fascinating. With such easy access to materials and services, it is easy to test out a new idea.

Similarly, when traveling the Zurich streets, one often finds nice things left streetside with a note attached: "Gratis zum Mitnehmen," indicating that this piece of furniture, stereo, or flat-screen TV is free for whoever wants it. I am passionate about well-designed furniture and have picked up several pieces that were left beside the road. Once, as I was going to the lab on a Sunday evening to start up some bacterial cultures, I encountered an old woman emptying her cellar, happy to give me a lovely Danish-style sideboard from the 1970s.

Today, I am no longer thinking about furnishing my Zurich apartment, as I am preparing to move again. I have decided to join the group of Gunnar von Heijne at Stockholm University, one of the top labs studying the biophysics of membrane proteins. I have to bring my own funding, so deadlines for applying for postdoctoral mobility fellowships are among the many other deadlines that loom.

The Swiss National Science Foundation has mobility fellowship programs for people who have obtained a Ph.D. in this country, which give young researchers the opportunity to travel abroad for a postdoc and then, in conjunction with its Ambizione program, to return to Switzerland and set up their own research labs.

As a latter-day Ulysses, I realize that travel and relocation are essential steps for personal and cultural growth, and arguably the only way to ensure opportunities to carry out cutting-edge scientific research. But professional lives can collide with personal lives. The Ph.D. period can seriously delay or hinder life decisions like settling down with a partner or starting a family. Frustrated with this prolonged adolescence, many of my peers have decided to leave the academic track and remain here in Zurich, taking jobs in the country's healthy pharmaceuticals industry or in consulting.

Going abroad to do science has disadvantages, but the advantages are greater.

Going abroad to do science has disadvantages, but the advantages are greater. My visits to conferences and foreign labs have made it clear that the leading European groups in my field are connected like members of a widely dispersed family. Moving to a new lab in a new place will give me the opportunity to share ideas, have collaborations that otherwise would be difficult to start, build a great network, and in time establish a node of my own. I have ideas I'm eager to pursue, and I am looking forward to working in a new environment.

That is sufficient reason to leave, for a while at least, my beloved Zurich. As to my personal life, my girlfriend is coming. She works for a pharmaceutical company in Lucerne, close to Zurich. She will either apply for relocation within the same company or look for a similar position in Sweden. We will move together.

What is more, the Nordic countries have a pretty good reputation for furniture. I have already learned what "Gratis! Varsågod!" means in Swedish. We'll see how it goes.

Jacopo Marino is finishing his Ph.D. in the Department of Chemistry at the University of Zurich in Switzerland. For more on life and career issues, see http://www.sciencecareers.org.

ILLUSTRATION: MARC ROSENTHAL

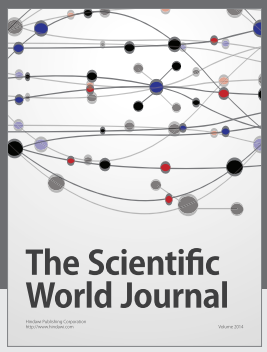

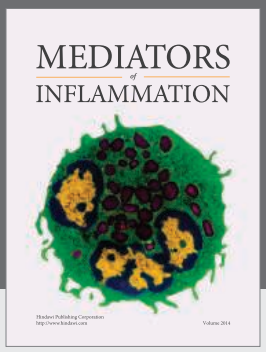

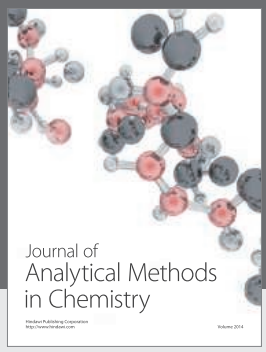

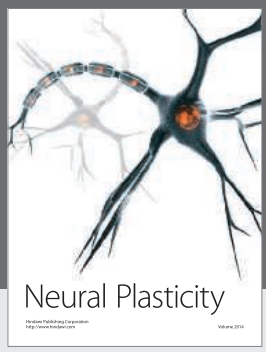

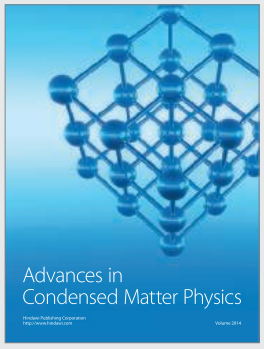

Hindawi

Submit your manuscripts at
http://www.hindawi.com

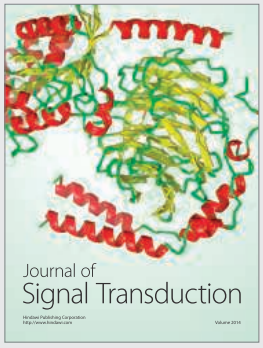

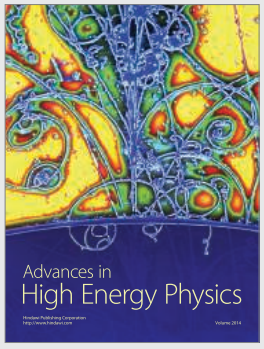

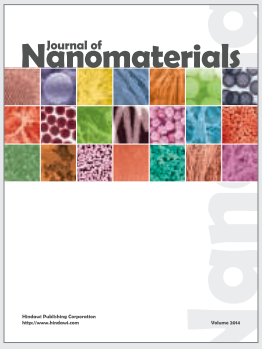

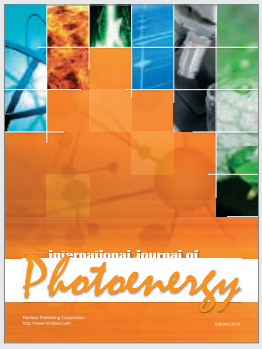

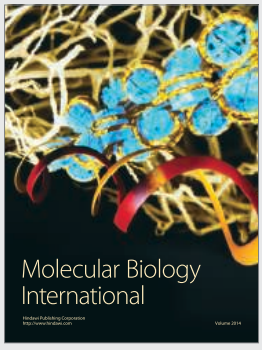

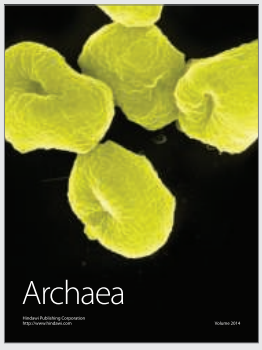

Personal Flow Cytometry from BD Biosciences

BD Pharmingen™ reagents and BD Accuri™ C6

BD

Helping all people live healthy lives

Best-in-class meets best time to buy.

10% OFF

40% OFF

Now you can speed discovery with the power of multiparameter cell analysis using the best-in-class BD Accuri™ C6 personal flow cytometer. Never before have the power and insight of personal flow cytometry been more within reach. Today, you can take advantage of an unprecedented value package including 10% savings on the BD Accuri C6 and 40% savings on the high quality BD reagents you'll use with it for a full two years.

With this package, you get 4-color cell analysis in an affordable, transportable, and easy-to-use format that serves both novice and experienced researchers well, right from the benchtop.

The software's intuitive interface guides you through workflows, making it easy to begin collecting and analyzing data—even if you have little flow cytometry know-how. Setup and maintenance are also simplified to increase availability and up-time.

Take advantage of this value package today at bdbiosciences.com/go/accuri.

Flow cytometry within reach.™

Some limitations apply. Vist bdbiosciences.com/go/accuri for more information.

23-14402-00

BD Biosciences
2350 Qume Drive
San Jose, CA 95131
bdbiosciences.com

NEW ENGLAND BioLabs® Inc.
enabling technologies in the life sciences

Make ends meet.

Gibson Assembly® Cloning Kit

New England Biolabs has revolutionized your laboratory's standard cloning methodology. The Gibson Assembly Cloning Kit combines the power of the Gibson Assembly Master Mix with NEB 5-alpha Competent *E. coli*, enabling fragment assembly and transformation in just under two hours. Save time, without sacrificing efficiency.

Making ends meet is now quicker and easier than ever before, with the Gibson Assembly Cloning Kit from NEB.

Gibson Assembly Cloning Kit provides robust transformation efficiencies

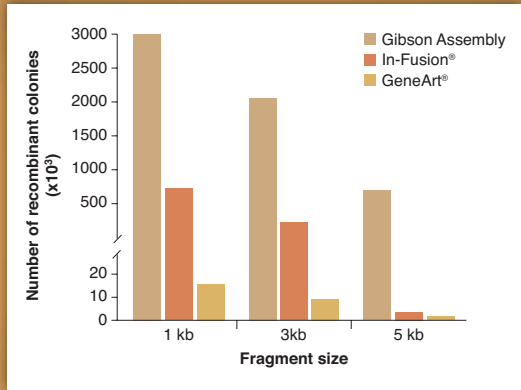

Assembly reactions containing 25 ng of linear pUC19 vector and 0.04 pmol of each fragment were performed following individual suppliers' recommended protocols and using the competent cells provided with the kit. The total number of recombinant colonies was calculated per 25 ng of linear pUC19 vector added to the assembly reaction.

NEBuilder™ for Gibson Assembly

Visit **NEBGibson.com** to view the latest tutorials and to try our primer design tool.

SGI-DNA

Some components of this product are manufactured by New England Biolabs, Inc. under license from Synthetic Genomics, Inc.

eppendorf & Science

PRIZE FOR NEURO BIOLOGY

2013 Winner
Dr. Michael Yartsev
CV Starr Research Fellow
Princeton Neuroscience Institute

Application Deadline
June 15, 2014

Call for Entries

Eppendorf & Science Prize for Neurobiology
The annual Eppendorf & Science Prize for Neurobiology, an international award, honors young scientists for their outstanding contributions to neurobiological research based on methods of molecular and cell biology.
The winner and finalists are selected by a committee of independent scientists, chaired by Science's Senior Editor, Dr. Peter Stern. To be eligible, you must be 35 years of age or younger.

You could be next to win this prize and to receive
> Prize money of US$25,000
> Publication of your work in Science
> Full support to attend the Prize Ceremony held in conjunction with the Annual Meeting of the Society for Neuroscience in the USA
> An invitation to visit Eppendorf in Hamburg, Germany

It's easy to apply!

Learn more at: www.eppendorf.com/prize

eppendorf

Science AAAS

immunogenomics 2014

September 29 - October 1, 2014

HudsonAlpha Biotechnology Campus
Huntsville, Alabama, USA

Join us at the intersection of Immunology and Genomics!

Keynote Speakers

Christophe Benoist, Harvard Medical School
Mary Ellen Conley, University of Tennessee, College of Medicine, Memphis
Mark Davis, Howard Hughes Medical Institute;
Stanford University School of Medicine

Session Chairs

Lou Bridges, University of Alabama at Birmingham, AL, USA • **Jean-Laurent Casanova**, Howard Hughes Medical Institute, Rockefeller • **Alain Fischer**, Imagine Institute, Necker Hospital, Paris, France • **Dan Littman**, New York University, NY, USA • **Sara Marsal**, University of Barcelona, Spain • **Kristen Mueller**, *Science* • **Harlan Robins**, University of Washington/Fred Hutchinson Cancer Research Center

Session Speakers

Scott Boyd, Stanford University School of Medicine, CA • **Zhijian James Chen**, UT Southwestern, TX • **Yanick Crow**, University of Manchester, UK • **Malek Faham**, Sequenta, CA • **Wendy Garrett**, Harvard University School of Public Health, MA • **Peter Gregersen**, Feinstein Institute for Medical Research, NY • **Jian Han**, HudsonAlpha Institute for Biotechnology, AL • **Lionel Ivashkiv**, Hospital for Special Surgery, NY • **Thirumala-Devi Kanneganti**, St. Jude Children's Research Hosp. • **Julian Knight**, Merton College , University of Oxford, UK • **Mike Lenardo**, National Institutes of Health, Washington D.C. • **Xochitl Morgan**, Harvard University School of Public Health, MA • **Barbara Methe**, J. Craig Venter Institute, MD • **Kees Murre**, University of California, San Diego, CA • **Richard M. Myers**, HudsonAlpha Institute for Biotechnology, AL • **Soumya Raychaudhuri**, Broad Institute, MA • **Lars Steinmetz**, European Molecular Biology Laboratory, Germany • **Barbara Stranger**, University of Chicago, IL USA

Platinum Sponsors

BAY CITY CAPITAL

iRepertoire, Inc.

Gold Sponsors

UAB COMPREHENSIVE ARTHRITIS, MUSCULOSKELETAL, AND AUTOIMMUNITY CENTER

Silver Sponsors

GenapSys

illumina

Bronze Sponsors

SEQUENTA

follow @immunogenomics on twitter

Register today at

immunogenomics.com

presented by

HUDSONALPHA INSTITUTE FOR BIOTECHNOLOGY

Science AAAS

Science Careers Advertising

For full advertising details, go to ScienceCareers.org and click For Employers, or call one of our representatives.

Tracy Holmes
Worldwide Associate Director
Science Careers
Phone: +44 (0) 1223 326525

THE AMERICAS

E-mail: advertise@sciencecareers.org
Fax: 202-289-6742

Tina Burks
Phone: 202-326-6577

Nancy Toema
Phone: 202-326-6578

Marci Gallun
Sales Administrator
Phone: 202-326-6582

Online Job Posting Questions
Phone: 202-312-6375

EUROPE / INDIA / AUSTRALIA / NEW ZEALAND / REST OF WORLD

E-mail: ads@science-int.co.uk
Fax: +44 (0) 1223 326532

Axel Gesatzki
Phone: +44 (0)1223 326529

Sarah Lelarge
Phone: +44 (0) 1223 326527

Kelly Grace
Phone: +44 (0) 1223 326528

JAPAN

Yuri Kobayashi
Phone: +81-(0)90-9110-1719
E-mail: ykobayas@aaas.org

CHINA / KOREA / SINGAPORE / TAIWAN / THAILAND

Ruolei Wu
Phone: +86-186-0082-9345
E-mail: rwu@aaas.org

Science Careers
From the journal *Science* AAAS

ScienceCareers.org

SANFORD RESEARCH

ASSOCIATE SCIENTIST/ASSISTANT PROFESSOR
CHILDREN'S HEALTH RESEARCH CENTER, SANFORD RESEARCH

The Children's Health Research Center (CHRC, Sioux Falls, SD **http://www.sanfordresearch.org/researchcenters/childrenshealth/**), invites applications from researchers for full time faculty at the rank of Associate Scientist within Sanford Research (**http://www.sanfordresearch.org/**) with commensurate rank of Assistant Professor in the Department of Pediatrics of the Sanford School of Medicine at The University of South Dakota. An historic $400 million gift by philanthropist Denny Sanford has allowed for expansion of Sanford Research and development of the CHRC, an energetic and collegial research community focused on pediatric research.

We seek outstanding scientists with research programs on the underlying mechanisms and/or treatment of congenital defects, developmental disorders, and pediatric diseases. Applicants should hold a PhD, MD or MD/PhD degree and complement the existing strengths and the interdisciplinary and collaborative nature of the CHRC. Candidates will be expected to develop independent research programs with extramural funding.

Significant institutional support, including modern laboratory space and state-of-the-art facilities, will be provided at the Sanford Center. In addition, a comprehensive compensation package will be tailored to the individual's qualifications.

Sanford Health is an Equal Opportunity/Affirmative Action Employer. Candidates should submit a single PDF including a detailed *curriculum vitae*, description of research experience and future research plans with specific details on the relevance of their research to pediatric research. Candidates should also submit at least three letters of recommendation. Incomplete candidate packages will not be accepted.

All application materials should be sent by email to:

David A. Pearce, Ph.D.
Director, Children's Health Research Center
Sanford Research
Professor, Department of Pediatrics
Sanford School of Medicine of The University of South Dakota
2301 E. 60th Street North, Sioux Falls, SD 57104
Telephone: 605-312-6004 FAX: 605-312-6071
Email: researchrecruitment@sanfordhealth.org

AAAS is here – helping scientists achieve career success.

Every month, over 400,000 students and scientists visit ScienceCareers.org in search of the information, advice, and opportunities they need to take the next step in their careers.

A complete career resource, free to the public, *Science* Careers offers a suite of tools and services developed specifically for scientists. With hundreds of career development articles, webinars and downloadable booklets filled with practical advice, a community forum providing answers to career questions, and thousands of job listings in academia, government, and industry, *Science* Careers has helped countless individuals prepare themselves for successful careers.

As a AAAS member, your dues help AAAS make this service freely available to the scientific community. If you're not a member, join us. Together we can make a difference.

To learn more, visit
aaas.org/plusyou/sciencecareers

AAAS + U = Δ

Alexander von Humboldt
Stiftung / Foundation

Seeking outstanding research talents

Sofja Kovalevskaja Award – cutting-edge research award for the best junior researchers from abroad

The Alexander von Humboldt Foundation is now calling for applications for the Sofja Kovalevskaja Award, one of the most valuable academic awards in Germany. The award amount of up to 1.65 million euros allows excellent researchers to carry out academic work under unique conditions: For a period of five years, they are able to work on their own research projects at an institute of their own choice in Germany and set up their own working groups – independently and virtually unaffected by administrative constraints. Scientists and scholars from all disciplines from abroad who have completed their doctorates within the last six years are eligible to apply. The award targets outstanding talent and a creative approach to research.

The Humboldt Foundation actively promotes equal opportunities and therefore particularly welcomes applications of women academics.

The closing date for applications is 1 September 2014. More information:
www.humboldt-foundation.de/SKP_en

Exzellenz verbindet –
be part of a worldwide network.

Alexander von Humboldt Foundation
Jean-Paul-Str. 12
53173 Bonn
Germany
e-mail: info@avh.de

www.humboldt-foundation.de

UNIVERSITÄT BASEL

Professor in Biomolecular NMR Spectroscopy

The Biozentrum of the University of Basel in Switzerland invites applications for a professorship in biomolecular NMR spectroscopy. The position will be filled open rank depending on the qualifications of the applicant. The ideal candidate should apply and further develop NMR spectroscopy in order to generate fundamental, new insights into specific, relevant biological mechanisms. This activity will require excellent spectroscopic expertise combined with a deep understanding of biology and biochemistry.

The candidate should have a strong research record, complementing the research portfolio of the Biozentrum, and a desire to engage in local collaborations. He/she should have very good communication skills, and is expected to actively participate in teaching at the undergraduate and postgraduate level.

The Biozentrum offers an outstanding scientific environment and an attractive research endowment. The NMR center of the Biozentrum currently encompasses state-of-the art 900 and 600 MHz NMR spectrometers. High-level expertise and equipment is also available in X-ray crystallography, electron microscopy and a variety of biophysical methods.

The city of Basel is the home of a vibrant international life science community and provides a high standard of living and a superb cultural atmosphere. Applications, including CV, list of publications and a short research summary, should be sent by e-mail (pdf or zip) to Prof. Dr. Jörg Schibler, Dean, Faculty of Science, University of Basel, Klingelbergstrasse 50, 4056 Basel, Switzerland, to dekanat-philnat@unibas.ch. For informal inquiries please contact Prof. Dr. Erich A. Nigg (erich.nigg@unibas.ch, phone: +41-61-267 16 56).

The deadline for receipt of applications is August 31, 2014. The University of Basel is an equal opportunity employer and encourages applications from female candidates.

UNI BASEL

南京理工大学
NANJING UNIVERSITY OF SCIENCE & TECHNOLOGY

Recruitments of talents abroad by Nanjing University of Science and Technology

http://rczp.njust.edu.cn/urp-portal/portal/group/Recruit

Nanjing University of Science and Technology (NUST) is one of the first national "211 Project" universities affiliated with the Ministry of Industry and Information Technology. It has become a multi-disciplinary and coordinated developing engineering-based university along with science, liberal arts, economics, management, law, education, etc. It is an ideal place for research work for its strong scientific research ability, prominent advantages, perfect construction of infrastructural facilities and it's also a pleasant place to live in since the beautiful scenery of Dr. Sun Yat-sen's Mausoleum which is only less than one mile away.

Please refer to the following application guidelines and we welcome your applications.

Majors for recruitment:

Related disciplines of Ordnance Science and Technology, Mechanical Engineering, Instrumentation Science and Technology, Chemical Engineering and Technology, Chemical, Electronic Science and Technology, Information and Communication Engineering, Optics, Optical Engineering, Computer Science and Technology, Control Science and Technology, Electrical Engineering, Transportation Engineering, Aerospace Science and Technology, Power Engineering and Thermal Physics, New Energy, Mechanics, Mathematics, Physics, Civil Engineering, Materials Science and Engineering, Environmental Science and Engineering, Biomedical Engineering, Law, Intellectual Property, Public Administration, Sociology, Economics, Management Science, (Applied) Linguistics and Literature, Art and Design.

Position and requirements:

Recruiting position: "Zijin scholars" distinguished professor, "Young Talents Professors", Professor, Associate Professor, Assistant Professor.

Basic qualities: Overseas talents with a doctorate degree, passion for education, high academic achievement and strong research capability and, good professionalism, academic character and team spirit as well. Among them, the candidates for "Young Talent Professor" staff position should be under 35 years old.

Related treatment:

The full-time employed teachers will be directly categorized into national institution, enjoying free medical care, pensions and other state welfare, and the family issues such as children's nursery and schooling will be addressed. We provide the high-level personnel and young talents with transitional housing, financial relief, research funding and other supports with generous salaries, comfortable working and living conditions. For high-level talents, we help settle down in terms of team building, work, housing, etc. Specific treatment will be determined by personal discussion.

1. For the full-time "Thousands of Plans" and other leading talents, NUST will provide 600 thousand to 1 million RMB annual salary and no less than 8 million RMB research start-up funds.
2. For the "Thousands Youth Talents" and other related talents, we provide no less than 300 thousand RMB annual salary, 1 million RMB financial relief and 2-4 million RMB research start-up funds.
3. For the "Zijin scholars" distinguished professor, we provide 500 thousand to 2 million RMB financial relief, 1 to 5 million RMB research funds and stipulated wages and other benefits along with certain amount of professor allowances per year.
4. For the "Young Talented Professors", we provide 300 thousand RMB annual salary, with certain financial relief and start-up funds.
5. For the professor, associate professor, assistant professor, we will provide salary and financial relief which is competitive in the same region, as well as starter home, and provide appropriate amount of research funds.

Way for recruitment:

The recruitments of talents abroad by NUST is under way regularly, please log in NUST Recruitment Network http://rczp.njust.edu.cn/urp-portal/portal/group/Recruit to have a registration, or contact us directly.

Contact us:

JI Wenchao Meng Yang
Tel: 86-25-84316943
Mail: rcb@njust.edu.cn
NUST website: www.njust.edu.cn

南京工业大学
NANJING TECH UNIVERSITY

海外领军人才招聘

Overseas Talents Recruitment

Nanjing Tech University, with a history of more than one hundred years, is a multidisciplinary university with a particular strength in engineering.

Aiming at excellence and innovation, Nanjing Tech University is set to become a first-class research university with a global vision. We are now seeking outstanding academic and research leaders in the following and related fields: Basic disciplines from within the Physical Sciences; Cutting edge disciplines from within the Life Sciences; Applied disciplines from within the Information Sciences; Humanities represented by Management Science.

Applicants should have a Ph.D. with at least 3-years research experience from leading universities or institutes. Candidates should demonstrate an internationally recognized research record and outstanding achievements. Successful candidates are expected to develop vigorous research programs and lead an independent research team. Successful candidates will be provided with a competitive relocation fee and salary package, generous start-up funds and spacious laboratories.

Interested candidates should visit **http://rczyb.njtech.edu.cn** for application details.

Phone: **Ms. Wang +86-25-58139148.**

E-mail: **job@njtech.edu.cn**

Opening of the Director's Position and Faculty Positions in the New Institute of Health Informatics at Peking University

DIRECTOR'S POSITION AND FACULTY POSITIONS

Peking University is establishing a new Institute of Health Informatics that aims to advance research and teaching in all areas of health informatics. Director's position and several faculty positions at all academic levels are open for application.

Faculty in the new institute can have joint appointments at Peking University's Medical Center and the School of Interdisciplinary Research. Faculty are expected to develop new methodologies and technologies to manage, query, and analyze clinical data and/or perform innovative analysis to find new patterns and trends that have significant impact on clinical practice or health policy. Faculty are especially encouraged to interact with the university's nine affiliated hospitals and other health care organizations in China to take advantage of China's vast clinical resource. Faculty are expected to teach core courses on the curriculum.

The Director, in addition to his/her role as a faculty member,is also expected to lead the institute in world-class research, develop a comprehensive curriculum, recruit faculty members, and establish collaborations with the university's nine affiliated hospitals and other health care organizations in China.

Candidates should have a doctorate degree and strong research background in a related field. Hiring levels will be commensurate with experience and achievements. Interested applicants please send CV, research statement, teaching statement, five representative publications, and contact information of three references to Ms Siyuan Gong *(gongsy@pku.edu.cn)*, and include a cover letter indicating the position applying to.

Peking University provides competitive salary and funding support for research and teaching. Successful candidates may also be supported by the Peking-Tsinghua Center for Life Sciences. The recruitment continues until all the positions are filled.

POSITIONS OPEN

POSTDOCTORAL FELLOWSHIPS

Postdoctoral fellowships are available to pursue research supported by NIH grants including the Center of Excellence for Complementary and Alternative Medicine on Autoimmune and Inflammatory Diseases (**website: http://camcenter.med.sc.edu/**). Studies will address the effects of plant products such as resveratrol, indoles, and cannabinoids on inflammation, autoimmunity, and cancer. Ph.D. in Immunology or related areas is required. Other projects include role of CD44, estrogens and dioxins on immune response. Experience in -omics and microbiome preferred. Send curriculum vitae and three references to: **Dr. Mitzi Nagarkatti, Carolina Distinguished Professor and Chair, Department of Pathology, Microbiology and Immunology, University of South Carolina School of Medicine, Columbia, SC 29229** or **e-mail: postdoccam@uscmed.sc.edu.** *University of South Carolina Columbia is an Equal Opportunity/Affirmative Action Employer and encourages applications from women and minorities.*

Department of Health and Human Services
National Institutes of Health
National Institute of General Medical Sciences
Division of Training, Workforce Development, and Diversity

DIVISION DIRECTOR

The National Institute of General Medical Sciences (NIGMS), a major research component of the National Institutes of Health (NIH) and the Department of Health and Human Services (DHHS), is seeking exceptional candidates for the position of Director, Division of Training, Workforce Development, and Diversity (TWD). Information about TWD is available at **http://www.nigms.nih.gov/About/Overview/pages/twd.aspx.**

TWD funds research training, career development, diversity and capacity-building activities that foster the development of a strong and diverse biomedical research workforce. The TWD Director will be responsible for the scientific and administrative management of the Division, and coordinating the development of NIGMS goals, objectives, policies, plans and guidelines for research and research training programs. Specifically, the TWD Director is responsible for: 1) overall oversight and supervision of Division programs, including programmatic review of research grant, research training grant and fellowship applications, and priority setting in regard to payment of grants; 2) development and implementation of strategic plans to enable NIGMS to improve the effectiveness of its programs aimed at increasing participation in biomedical research; 3) coordination of Institute policies related to research and research training programs; and 4) liaison with groups at NIH, DHHS, and other federal agencies, as well as with the extramural scientific community on these matters. This individual will report to the NIGMS Director and may also coordinate activities across NIH and among other federal agencies.

Qualifications: Candidates must have an M.D., Ph.D. or equivalent degree in a field relevant to the position. The ideal candidate will have considerable research experience and will possess a broad spectrum of scientific knowledge related to the NIGMS mission. He/she will also have professional experience in the training of research scientists, as well as programs aimed at developing a diverse biomedical and behavioral research workforce. In addition, candidates should possess recognized research management and leadership abilities. This position will be filled under a Title 42(f) excepted service appointment.

Salary/Benefits: Salary is competitive and will be commensurate with the experience of the candidate. A recruitment or relocation bonus may be available, and relocation expenses may be paid. A full package of Federal Civil Service benefits is available, including: retirement, health and life insurance, long term care insurance, leave and a Thrift Savings Plan (401K equivalent). The successful candidate is subject to a background investigation and public financial disclosure requirements.

How to Apply: Applicants must submit a current curriculum vitae, bibliography, copy of degree and full contact details for three references. In addition, applicants are asked to prepare two statements: a vision statement and a statement that addresses the specific qualification requirements (please limit both statements to two pages each). NIGMS will be accepting applications from **June 1, 2014, to July 15, 2014**. Please send your application package to **NIGMSTWDDirector@mail.nih.gov**. You may contact Krystal Kelly with questions about this vacancy at **NIGMSTWDDirector@mail.nih.gov** or 301-594-3827.

DHHS, NIH and NIGMS are Equal Opportunity Employers

LSU Health Shreveport

FACULTY TEACHING POSITION

The Department of Cellular Biology and Anatomy at the LSU Health Sciences Center School of Medicine in Shreveport invites applications for a full-time Instructor/Assistant/Associate/Full Professor that possess expertise in teaching Cellular Biology and Anatomy to medical, graduate, and allied health students. The candidate will instruct in required courses in the department including, but not limited to, Histology, Embryology, Gross Anatomy, Neuroscience and Neuroanatomy. The candidate should have a Ph.D. or equivalent degree and experience teaching in the proposed disciplines. Special consideration will be given to those candidates that demonstrate the ability to attract extramural funding, but extramural funding is not a requirement. The candidate will be encouraged to collaborate with investigators in research projects currently ongoing within the department. The position will be supported by state-of-the-art teaching facilities, competitive salary and start-up packages based upon experience/need.

This is an exciting opportunity for an appropriate candidate to play a significant role in the education of future scientists, allied health professionals and physicians. In addition, exciting opportunities to interact with investigators and participate in cutting-edge research projects are available.

Please submit application with full curriculum vitae and names of three references via email to: **Dr. William G. Mayhan (wmayha@LSUHSC.edu), Professor and Head, Department of Cellular Biology and Anatomy, LSU Health Sciences Center, School of Medicine in Shreveport, Shreveport, LA 71130**. Please include a letter that summarizes your teaching experiences and teaching philosophy. Review of applications will begin immediately and will continue until the position is filled.

LSU Health- Shreveport is an Equal Opportunity Employer and all qualified applicants will receive consideration for employment without regard to race, color, religion, sex, national origin, disability status, protected veteran status, or any other characteristic protected by law.

WASHINGTON STATE UNIVERSITY

Director of the Health Professions Student Center

The College of Arts and Sciences, Washington State University, in Pullman, WA seeks an open-ranked 12-month Clinical Faculty member to serve as the Director of the Health Professions Student Center. The Director is responsible for the programmatic design, development, and administrative and financial oversight of the Center's services to help WSU's pre-health students interested in careers as a healthcare professional. The ideal candidate is expected to assist students as they are considering a career in the health professions and teach course(s), such as medical terminology and/or careers in health professions.

The ideal candidate will have a terminal degree in Sciences or related appropriate field. Candidates must have the ability to think creatively and effectively, and work collaboratively with faculty, staff and students. Candidates must also be committed to working effectively with a diverse population, have an energetic approach to student services, an excellent understanding of professions available in healthcare, and an ability to engage in outreach with professional health schools. Preferred qualifications include experience working with medical or dental professionals and pre-health students, demonstrated experience supervising staff colleagues, budgetary experience, and effective written communication skills. Please address each of the required and preferred qualifications within your letter of application.

WASHINGTON STATE UNIVERSITY IS AN EQUAL OPPORTUNITY/ AFFIRMATIVE ACTION EDUCATOR AND EMPLOYER.

To apply for this position, please visit:
https://www.wsujobs.com/postings/11436